

**TRANSIENT DISCHARGE OF A PRESSURISED
INCOMPRESSIBLE FLUID THROUGH A PIPE AND
ANALYTICAL SOLUTION FOR UNSTEADY
TURBULENT PIPE FLOW**

AUTHOR: F. JAVIER GARCIA GARCIA

DOCTORAL THESIS UDC / 2017

DIRECTOR: DR PABLO FARIÑAS ALVARIÑO

OFFICIAL DOCTORAL PROGRAM IN NAVAL AND INDUSTRIAL ENGINEERING



UNIVERSIDADE DA CORUÑA


Acknowledgements

Foremost I am indebted to Pablo Fariñas, my Thesis' Director, for his permanent insistence on accuracy and perfection. He has never ceased to spur my brain with ever more complicated challenges, and the extent and depth of most of the findings herein presented are as much his offspring as mine. I, left to my own devices, would have never been able to reach so farther.

I also wish to express my gratitude to the Centro de Supercomputacion de Galicia (CESGA), for its standing support and for lending to this project abundant supercomputer time and memory.


Last, but by no means least, I must thank my loving family for allowing me to disappear for endless hours in my dungeon while preparing this years-long Dissertation, frequently disregarding my family duties as father and husband. Now I am back. This work, as well as my life, is dedicated to you, with all my love.

Resumo / Resumen / Short Abstract

 Estúdase a dinámica do proceso de descarga súbita dun líquido presurizado á atmosfera, de amplo interese en Enxeñaría de protección contra incendios. Preséntase o estado da arte respecto ao estudo do proceso de descarga. Elabórase un modelo hidráulico unidimensional para ese fluxo, que adopta a forma dunhas ecuacións integro-diferenciais ordinarias que resólvense numericamente. Efectúase unha análise de sensibilidade respecto a todos os parámetros dos que depende o modelo, con especial fincapé na fricción xerada pola turbulencia.


Analízanse os métodos xenéricos de descrición da turbulencia, incluíndo a representación estatística, o filtrado de magnitudes turbulentas e a plena descrición analítica. Desenvólvese unha solución analítica xeral para o fluxo turbulento, incompresible e non estacionario nunha tubaxe.

Elabórase un modelo computacional tridimensional para o fluxo descrito. A modelización da turbulencia resulta ser o punto máis importante e conflictivo de dito modelo. Compáranse os resultados obtidos con eles preditos polo modelo hidráulico unidimensional desenvolto previamente. Preséntanse resultados diso á estrutura interna da turbulencia en fluxos fortemente acelerados, prevéndose un aumento notable da devandita turbulencia nas proximidades do muro, que non se explica unicamente polo número de Reynolds.

 Se estudia la dinámica del proceso de descarga súbita de un líquido presurizado a la atmósfera, de amplio interés en Ingeniería de protección contra incendios. Se presenta el estado del arte en la literatura que trata dicho proceso de descarga. Se elabora un modelo hidráulico unidimensional para ese flujo, que adopta la forma de unas ecuaciones integro-diferenciales ordinarias que se resuelven numericamente. Se efectúa un análisis de sensibilidad respecto a todos los parámetros de los que depende el modelo, con especial hincapié en la fricción generada por la turbulencia.

Se analizan los métodos genéricos de descripción de la turbulencia, incluyendo la representación estadística, el filtrado de magnitudes turbulentas y la plena descripción analítica. Se desarrolla una solución analítica general para el flujo turbulento, incompresible y no estacionario en un tubo.

Se elabora un modelo computacional tridimensional para el flujo descrito. La modelización de la turbulencia resulta ser el punto más importante y conflictivo de dicho modelo. Se comparan los resultados obtenidos con los predichos por el modelo hidráulico unidimensional desarrollado previamente. Se presentan resultados respecto a la estructura interna de la turbulencia en flujos fuertemente acelerados, previéndose un aumento notable de dicha turbulencia en las proximidades de la pared, que no se explica únicamente por el número de Reynolds.

 The dynamics involved in the process of sudden discharge of a pressurized liquid to the atmosphere is studied, a case of broad interest in fire protection Engineering. The state of the art in the literature regarding such discharge process is presented. A one-dimensional hydraulic model is developed for this flow, which takes the form of ordinary integro-differential equations that are solved numerically. A sensitivity analysis is carried out with respect to all the parameters on which the model depends, with special emphasis on the friction generated by the turbulence.

The generic methods of describing turbulence are analysed, including the statistical representation, the filtering of turbulent quantities and the full analytical description. A general analytical solution for the turbulent, incompressible and unsteady flow in a pipe is developed.

A three-dimensional computational model for the described flow is elaborated. The modelling of turbulence turns out to be the most important and conflicting point of such model. The results obtained are compared with those predicted by the one-dimensional hydraulic model previously developed. Results are presented regarding the internal structure of the turbulence in strongly accelerated flows. A remarkable increase of said turbulence is anticipated in the proximities of the wall, that could not be explained only with the Reynolds number.

Abstract

In the realm of Fire Protection Engineering (FPE), the use of highly pressurised extinguishing agents that are suddenly discharge to protected areas, in case of fire, it is not infrequent. This very effective method of fire extinction is carried out with agents that are normally in gaseous state at Normal Temperature and Pressure (NTP),, at least for low concentrations, although within the pressurised vessels they are in liquid state. This Dissertation explores the Dynamics of such fast transient discharge flows, assuming an incompressible liquid flowing through a straight pipe of constant diameter.

First a State of the Art investigation is performed on the existing literature for discharge flows, specifically for FPE applications. The technique of fire extinction through discharge of clean agents is explained, and the thermophysical properties of some of them are presented. The most relevant research works on discharge flow are surveyed, highlighting the features that later will be reproduced in the models developed herein, and a synoptic evaluation is presented. The extinction mechanisms of two of the most frequently used clean agents will be discussed, over their pressure-enthalpy diagrams.

An one-dimensional Analytical Hydraulic Model (AHM) is developed to describe and explain the discharge of an incompressible liquid from a vessel pressurised with a compressed ideal gas. The model assumes a fast transient flow through a straight open-ended pipe, highly accelerated and subjected only to pressure and friction forces. A set of dynamic equations has been found which should provide an exact solution within the AHM limitations, assumptions and hypothesis. The dynamic equations are ordinary non-linear integro-differential equations for which no direct analytical solution could be found. A computer program has also been developed to solve the 1D problem numerically. The program includes well-known algorithms suited for point-wise solution of ordinary differential equations and to perform numerical integration. The AHM is thoroughly studied, including a detailed sensitivity analysis upon every quantity or parameter it depends on. Bulk velocity curves are shown for various configurations, in expectation for CFD models to reproduce them.

Due to the relevant role played by turbulence in such transient flows, a general discussion is raised on the different methods to represent turbulent fields, before describing the 3D CFD model itself. The statistical approach, based on the concept of statistical average, is discussed first, including those properties of the averaging operation necessary to yield viable Reynolds-Averaged Navier-Stokes Equations (RANSE) upon applying them to the Navier-Stokes equations (Reynolds operator). The available averaging methods for incompressible flow are presented with great detail, including their mathematical properties, the functional form of the RANSE derived therefrom and the scope within which they remain valid. It is stressed that each averaging method produces an unique set of RANS equations which are accurate only within the specified limits. The error incurred for disregarding such limits is also examined, and a general equation is introduced to estimate the error, particularly when using URANS methods with time-averaged mean fields, a rather frequent practice. The so-called triple decomposition is discussed too, and an alternative formulation free of mathematical inconsistencies is offered.

Secondly is introduced the filtering approach, based on the convolution integral. When applied to physical fields, the filtering operation produces filtered fields and fluctuating fields. Derivative and filtering operations, in general, do not commute. Conditions for commutation are studied, and the Filtered Navier-Stokes Equations (FNSE) are derived in such circumstances. A general expression is offered to estimate the commutation error and the expected accuracy of FNSE outside their scope of application.

Thirdly, a fully analytical approach to the problem of turbulence is devised. All the known analytical solutions for incompressible pipe flow are explored: Hagen-Poiseuille's (ca. 1840) for steady laminar flow, Piotr Szymanski's (1932) for transient laminar flow, and Shih-I Pai's (1953) for steady turbulent flow. Beginning from ensemble averaged RANSE, a General Analytical Solution (GAS) for unsteady turbulent incompressible pipe flow is deduced from first principles, thus closing the sequence of proposed solutions. Possibly, this be the major contribution of the present Dissertation. The GAS is composed of three different terms, whose detailed description is offered in the text. The GAS is also applied to various simple flows, as an illustration of the general method herein devised to obtain fully analytical solutions for particular problems.

Last, an exercise has been made to deduce a simplified steady state version of the Navier-Stokes equations from the cornerstone of Mechanics, namely the Principle of Least Action (PLA).

A 3D Computational Fluid Dynamics (CFD) model has been developed to achieve detailed knowledge of the internal structure of this transient discharge flow. The CFD model is based on the open-source suite OpenFOAM, itself based on the Finite Volume Method (FVM) formalism. The CFD model is comprehensively described: the geometry of the mesh, the equations solver, the establishment of the initial conditions for the flow, the wall-functions proposed, the differencing schemes... Up to twenty different turbulence models, already available in OpenFOAM, have been tested. Since no experimental data has been found for such a fast transient flow, the bulk velocity curves provided by the AHM played the role of benchmark for the CFD models. Only two turbulence models were able to reproduce the intense friction causing the high decelerations observed in the flow. One of those two models provides a mean velocity profile at the wall not compatible with the law of the wall, and was discarded as unreliable. The single remaining turbulence model shows a mean velocity profile compatible with the law of the wall. Besides, it predicts an important role for deceleration in the description of turbulence for fast transient flows. It would appear that Reynolds number alone would be insufficient to characterise the turbulence in such flows.

Finally, conclusions are presented and a research program is proposed to further explore the various paths opened upon discovery of the GAS, and to devise experiments in order to confirm the interesting, and so far unreported, internal structure of turbulence predicted by the 3D CFD model for highly decelerated pipe flows.

Keywords: fire suppression, clean agent discharge, transient fluid dynamics, unsteady pipe flow, CFD, turbulence description, FK-5-1-12

Contents

Nomenclature	iii
Acronyms	viii
Nomenclature	ix
List of Figures	xii
List of Tables	xiii
1 State of the Art in FPE	1
1.1 Introduction	1
1.2 Description of the Technique	4
1.3 Hydraulics of Discharge: Literature Review	12
1.4 Extinction Mechanisms for FK-5-1-12	20
1.5 Change of Phase During Discharge	24
1.6 Conclusions	28
2 1D Analytical Model	29
2.1 Introduction	29
2.2 Presentation of the 1D Model of Discharge of an Incompressible Fluid	32
2.3 Derivation of Dynamic Equations	36
2.3.1 Cross-Section Average of Fields	37
2.3.2 Reynolds' Transport Theorem Approach	39
2.3.3 Navier-Stokes' Equations Approach	42
2.3.4 Equations for Pressure	45
2.3.5 Brief Considerations About Friction	49
2.3.6 Cross-Section Averaged Dynamic Equations of the 1D AHM	51
2.4 Dimensionless Dynamic Equations	54
2.4.1 Reference Quantities and Values	54
2.4.2 Method of Dimensionality	55
2.5 Numerical Solution of Dimensionless Equations	57
2.6 Results and Discussions	58
2.6.1 Sensitivity Analysis of the 1D AHM	60
2.6.1.1 Variations with p_0	62
2.6.1.2 Variations with L	63
2.6.1.3 Variations with G_f	64
2.6.1.4 Variations with ζ_D	65

2.6.1.5	Variations with L_v	66
2.6.1.6	Variations with Δ_f	67
2.6.2	Force Balance	69
3	Introduction to Turbulence Description	71
3.1	Introduction	71
3.2	The Statistical Approach (or the Averaging Problem)	76
3.2.1	The Statistical Averages	82
3.2.1.1	The Ensemble Average	82
3.2.1.2	The General Space-Time Average	86
3.2.1.3	The Time Average	88
3.2.1.4	The Spatial Average	90
3.2.1.5	The Phase Average	93
3.2.2	A Critique to Certain Kind of URANS Simulations	97
3.2.3	A Light Critique to the Triple Decomposition	115
3.3	The Filtering Approach (or LES method)	132
3.4	Turbulence as an Additional Term to Laminar Solution	148
3.4.1	Steady State Turbulence as an Additional Term to Laminar Solution	149
3.4.2	General Transient/Unsteady Analytical Solution of RANSE for Incompressible Pipe Flow	160
3.5	Derivation of Navier-Stokes Equations from First Principles	197
4	3D CFD Model	202
4.1	Introduction to the 3D CFD Model	202
4.2	Brief Description of OpenFOAM	208
4.3	OpenFOAM's Solver Description	214
4.4	Initial conditions for turbulence quantities	217
4.5	Near-Wall Modelling	222
4.6	Mesh Selection	243
4.7	Discretisation Method and Differencing Scheme	247
4.8	Independence of the Results with Mesh, Δt and Differencing Schemes	249
4.9	Turbulence Modelling	252
4.10	Results and Discussions	257
4.10.1	$k - \omega$ SST SAS	257
4.10.2	$k - \epsilon$ Launder-Sharma	275
5	Conclusions and Research Program	283
A	Anexo : Resumen en Castellano	287
	Bibliography	i
	Index	xiv

Nomenclature

LATIN SYMBOLS

A	[-] Average dimensionless acceleration of the turbulent flow
A	[m^2] Cross-section area of a pipe
a	[-] Dimensionless acceleration of the flow
\tilde{A}	[-] Cross-section averaged dimensionless mean acceleration of the turbulent flow
\tilde{a}	[-] Cross-section averaged dimensionless acceleration of the flow
B	[-] Additive inner layer scaling constant for the log-law, taken ≈ 5.57
C_f	[-] Fanning friction factor or Skin friction coefficient ($C_f = f/4$)
$d\mathbf{s}$	[m^2] Vector surface element normal to $\partial\Omega$, pointing outwards
E	[-] Multiplicative inner layer scaling constant for the log-law, taken ≈ 9.8
E_k	[m^2/s^2] Specific kinetic energy of the fluid (per unit mass)
f	[-] Darcy-Weisbach friction factor ($f = 4C_f$)
f_e	[-] Effective Friction Factor, Darcy-Weisbach friction factor f times friction modulator Δ_f
F_f	[N] Friction force within the pipe
F_p	[N] Pressure force within the pipe
g_i	[m/s^2] Vector acceleration of gravity
G_f	[-] Dimensionless geometric factor equal to $\pi D^3/4V_{g_0}$
K	[m^2/s^2] Specific kinetic energy of the mean flow (per unit mass)
k	[m^2/s^2] Specific average turbulence kinetic energy (per unit mass)
ℓ	[m] Inertial length scale in a turbulent flow
\mathcal{L}	[-] Sturm-Liouville operator
\mathcal{L}	[m] Integral length scale in a turbulent flow
L	[m] Length of the liquid's discharge pipe
L_v	[m] Length of the discharge valve, minimal length over which the pressure gradient develops

m_l	[kg] Total mass of the liquid involved in the process
\mathbf{n}	[-] Unit vector normal to the boundary surface $\partial\Omega$, pointing outwards
n	[-] Polytropic index. Used only in chapter 2
\mathfrak{P}	[m^2/s^3] Turbulence production term in the turbulent kinetic energy transport equation
P	[Ns] Momentum of the liquid mass inside the pipe
p_0	[Pa] Absolute pressure within the vessel at instant $t = 0$
$p(t, z)$	[Pa] Absolute pressure of the liquid within the pipe ($z > 0$), at position z and instant t
$p_g(t)$	[Pa] Absolute pressure of the gas within the vessel at instant t
$p_l(t)$	[Pa] Absolute pressure of the liquid within the vessel ($z \leq 0$) at instant t
Q	[m^3/s] Volumetric flow
R	[m] Radius of the pipe in which the liquid discharges
R_{ij}	[Pa] Reynolds stress tensor
\mathfrak{R}_T	[-] Rectangular or normalised boxcar function of width T
\mathcal{R}_{ij}	[m^2/s^2] Fluctuating velocity autocorrelation function
\mathcal{R}_ψ	[-] Fluctuating field ψ' autocorrelation function
${}^{(n)}r_{\psi_i}^{[t]}$	[-] Residual error of discretised field ψ at mesh-node i , for the n^{th} iteration of time-step t
\mathfrak{S}	[J s] Action of a mechanical system
s_{ij}	[1/s] Instantaneous strain rate tensor
S_{ij}	[1/s] Mean strain rate tensor
s'_{ij}	[1/s] Fluctuating strain rate tensor
S_w	[m^2] Wet surface within the pipe ($= 2\pi Rz_f$ or $2\pi RL$)
\mathcal{T}	[m^2/s^3] Turbulence transport term in the turbulent kinetic energy transport equation
\mathfrak{T}	[s] Integral time scale in a turbulent flow
t	[s] Inertial time scale in a turbulent flow
t_f	[s] Time at which the fluid's front reaches the pipe's end for the first time
\mathfrak{T}_w	[-] Distribution/generalised function with kernel $w(t, \mathbf{x})$
\mathfrak{U}	[m/s] Integral velocity scale in a turbulent flow
u	[m/s] Inertial velocity scale in a turbulent flow
\mathbf{u}, u_i	[m/s] Velocity in a turbulent flow
U	[m/s] Mean velocity in a turbulent flow

u_∞	[m/s] Mean velocity at the pipe's centreline
u^+	[-] Dimensionless mean velocity, in wall-units
u^*	[-] Dimensionless mean velocity, in the ν/R normalisation
u_τ	[m/s] Friction velocity. Velocity scale used in wall turbulence
\tilde{v}	[m/s] Average velocity of the liquid in the cross-section of the pipe. Bulk velocity
v_f	[m/s] Liquid velocity as it reaches the pipe's end ($v_f = \tilde{v}(t_f)$)
V_{g0}	[m ³] Volume occupied by N_2 gas at instant $t = 0$
$V_g(t)$	[m ³] Volume occupied by N_2 gas at instant t (no gas has left the vessel)
V_{l0}	[m ³] Volume occupied by the liquid at instant $t = 0$
$V_l(t)$	[m ³] Volume occupied by the liquid at any instant t
\mathbf{v}_Ω	[m/s] Velocity of the control surface points
\mathbf{v}, v_i	[m/s] Velocity vector at any point in the liquid within the pipe in the analytical model
$w^{[n]}$	[-] Probability of the n^{th} realisation in ensemble average
y^+	[-] Distance to the wall expressed in the friction length scale
\check{y}	[-] Outer variable expressing the distance to the wall
z_f	[m] Distance of liquid's front within the pipe, measured from the pipe's origin ($z = 0$)

GREEK SYMBOLS

α	[-] Liquid fraction field in a two-phase flow
α	[-] Dimensionless cylindrical radial coordinate r/R
γ	[-] Adiabatic index. Ratio between ideal gas' constant pressure and constant volume specific heats ($\gamma = c_p/c_v$, $\gamma = 1.4$ for an ideal diatomic gas at NTP conditions)
γ	[-] Dimensionless time, in the ν/R normalisation
δ	[m] Boundary layer thickness
δ^+	[-] Ratio of inner to outer length scales, or boundary layer thickness in wall-units
Δ_f	[-] Friction modulator. Coefficient multiplying the Darcy-Weisbach friction factor f to obtain the Effective Friction Factor f_e
δ_L	[m] Height of the laminar sublayer within the turbulent boundary layer
Δ	[m] Filter spatial width for LES applications
Δp	[Pa] Pressure drop over the full length of the pipe during liquid discharge (depends on t)
δ_*	[m] Displacement thickness in the turbulent boundary layer
ϵ	[m ² /s ³] Turbulent kinetic energy dissipation rate per unit mass

ε	$[m^2/s^3]$ Instantaneous turbulent energy dissipation rate per unit mass
ζ	$[1/s]$ Vorticity
ζ_D	$[-]$ Relative pipe roughness
ζ_r	$[m]$ Absolute pipe roughness. Average height of roughness protrusions on pipe's inner surface
η	$[m]$ Kolmogorov length scale
Θ	$[-]$ Ratio of maximum centreline velocity for laminar to turbulent pipe flow
ϑ	$[-]$ Ratio of pipe wall-shear stress for steady state turbulent and laminar flow
Θ	$[s]$ Filter temporal width for LES applications
κ	$[m^{-1}]$ Spatial wavenumber, the reciprocal variable to \mathbf{x} in Fourier transform
κ	$[-]$ von Karman's constant for the log-law, taken ≈ 0.41
λ_t	$[m]$ Taylor length scale in a turbulent flow
μ	$[kg\ m^{-1}\ s^{-1}]$ Dynamic viscosity of the liquid agent. It is assumed constant
ν	$[m^2/s]$ Kinematic viscosity of the liquid agent. It is assumed constant
$\nu(t)$	$[-]$ Random-spike function
ν_s	$[m^2/s]$ Subgrid-scale viscosity in the filter approach to turbulence
ν_t	$[m^2/s]$ Turbulent eddy viscosity according to Boussinesq's hypothesis
ξ	$[-]$ Local mean pressure gradient at the pipe's centreline
Π	$[Pa/m]$ Pressure gradient along the pipe (with minus sign)
Π	$[-]$ In near-wall modelling section represents the Coles' wake parameter
ρ	$[kg/m^3]$ Density of the liquid agent. It is assumed constant
σ	$[-]$ Dimensionless mean squared fluctuation velocity, in wall-units
ς	$[-]$ Dimensionless mean squared fluctuation velocity, in the ν/R normalisation
τ_η	$[s]$ Kolmogorov time scale in a turbulent flow
τ_{ij}^r	$[m^2/s^2]$ Residual stress tensor in the filter approach to turbulence
τ_w	$[Pa]$ Shear friction stress in the pipe's wall
$\tilde{\tau}_w$	$[Pa]$ Average shear friction stress along the perimeter of the pipe's wall
v_η	$[m/s]$ Kolmogorov velocity scale in a turbulent flow, η/τ_η
χ	$[-]$ Dimensionless Reynolds stress function, in wall-units
ω	$[1/s]$ Specific turbulence dissipation rate or dissipation per unit turbulence kinetic energy
ω	$[rad/s]$ Angular frequency, in sections where Fourier analysis is employed

$\partial\Omega$	$[m^2]$ Closed boundary of the control volume Ω
ϖ	$[-]$ Dimensionless Reynolds stress function, in the ν/R normalisation
Ω	$[m^3]$ Control volume in which Reynolds' Transport Theorem and Leibniz's Rule are applied
\mathcal{V}	$[m^3]$ Material volume in which Reynolds' Transport Theorem is applied

SPECIAL SYMBOLS

\tilde{f}	Cross-section average of field f in the pipe
$\partial_i = \frac{\partial}{\partial x_i}$	Partial derivative with respect to x_i
$\partial_t = \frac{\partial}{\partial t}$	Partial derivative with respect to time
∂	Closed boundary (surface/line) of an open domain (volume/surface)
$\langle f \rangle$	Ensemble average of field f . Also general average of field f
\bar{f}	Time average of field f
\overbrace{f}	Spatial average of field f
\overleftarrow{f}	Phase average of field f
$\langle f \rangle_T$	Moving average of width T for field f
\ddot{f}	Cumulative average of field f
$\triangle f$	General space-time average of field f
$\hat{f} = \mathcal{F}(f)$	Fourier transform of field f
\underline{f}	Filtered component of field f
$\overset{\circ}{f}$	DC component of T -periodic field f
$a_i b_i = \mathbf{a} \cdot \mathbf{b}$	Einstein's summation convention over repeated indices is followed in this text
$\mathbb{1}$	Identity operator in Hilbert space, $\mathbb{1} \psi = \psi$
\mathbb{C}	Complex numbers
\mathbb{N}	Natural numbers = 1, 2, 3, ...
\mathbb{Q}	Rational numbers
\mathbb{R}	Real numbers
\mathbb{R}^+	Positive real numbers ($x \geq 0$)
\mathbb{Z}	Integer numbers = 0, ± 1 , ± 2 , ± 3 , ...
\mathbb{Z}^+	Positive integer numbers = 0, 1, 2, 3, ... $\equiv \mathbb{N} \cup \{0\}$

Acronyms

AHM Analytical Hydraulic Model.

CESGA Centro de Supercomputacion de Galicia.

CFD Computational Fluid Dynamics.

CFL Courant-Friedrichs-Lewy.

DES Detached Eddy Simulation.

DNS Direct Numerical Simulation.

FCT Flux-Corrected Transport.

FNSE Filtered Navier-Stokes Equations.

FPE Fire Protection Engineering.

FVM Finite Volume Method.

GAS General Analytical Solution.

GSTA General Space-Time Average.

GWP Global Warming Potential.

HFC Hydrofluorocarbons.

HOTWC Halon Options Technical Working Conference.

HRLTM Hybrid RANS-LES Turbulence Models.

IDDES Improved Delayed Detached Eddy Simulation.

LANS- α Lagrangian-averaged Navier Stokes- α .

LES Large Eddy Simulation.

MULES Multidimensional Universal Limiter with Explicit Solution.

NGP Next Generation Fire Suppression Technology Program.

NIST National Institute of Standards and Technology.

NS- α Navier-Stokes- α .

NTP Normal Temperature and Pressure.

PDF Probability Density Function.

PISO Pressure Implicit with Splitting of Operator.

PLA Principle of Least Action.

RANS Reynolds-Averaged Navier-Stokes.

RANSE Reynolds-Averaged Navier-Stokes Equations.

RAS Reynolds-Averaged Simulation.

RMSE Root-Mean-Square Error.

RSTM Reynolds Stress Transport Method.

RVN Residuals Vector Norm.

SAS Scale Adaptive Simulation.

SFCD Self-Filtered Central Differencing.

SIMPLE Semi-Implicit Method for Pressure-Linked Equations.

SNSE Stochastic Navier-Stokes Equations.

SST Shear Stress Transport.

SSTM Shear Stress Transport Model.

SSTSAS Shear Stress Transport with Scale Adaptive Simulation.

STP Standard Temperature and Pressure.

TQ Turbulence Quantities.

TVD Total Variation Diminishing.

URANS Unsteady Reynolds Averaged Navier-Stokes.

VoF Volume of Fluid.

List of Figures

1.1	The largest Antarctic ozone hole recorded as of September 2006.	2
1.2	Thermophysical properties of most used Hydrofluorocarbons (HFC) extinction agents.	4
1.3	Chemical formula of FK-5-1-12 molecule.	6
1.4	3-D image of FK-5-1-12 molecule	6
1.5	Chemical formula of HFC-227ea molecule.	7
1.6	3-D image of HFC-227ea molecule.	7
1.7	Typical battery of HFC-227ea cylinders for fire extinction applications.	9
1.8	Typical small installation of HFC-227ea fire extinction.	9
1.9	Vapour pressure curve of FK-5-1-12.	10
1.10	Vapour pressure curve of HFC-227ea.	10
1.11	Discharge of HFC-227ea agent in a protected room.	11
1.12	Isometric diagram for FK-5-1-12 superpressurised with N_2 to 25 bar at 21°C.	12
1.13	Isometric diagram for HFC-227ea superpressurised with N_2 to 25 bar at 21°C.	12
1.14	Experimental arrangement in [PYG ⁺ 94] experiments.	13
1.15	Internal pressure during downward discharges of HFC-227ea (after [PYG ⁺ 94]).	14
1.16	Theoretical and experimental discharge pressure for HFC-227ea (after [PYG ⁺ 94]).	15
1.17	Near-field dynamic pressure for releases of HFC-227ea. Trace B is offset by 100 kPa. (A) 476 g, release pressure 4.45 MPa; (B) 489 g, release pressure 4.41 MPa (after [PYG ⁺ 94]).	15
1.18	Far-field dynamic pressure for releases of HFC-227ea. Trace B is offset by 100 kPa. (A) 489 g, release pressure 4.41 MPa; (B) 476 g, release pressure 4.45 MPa (after [PYG ⁺ 94]).	16
1.19	Pressure inside the cylinder and at nozzle for HFC-227ea discharge (after [Wys96]).	16
1.20	Pressure inside the cylinder and at nozzle for clean agent discharge (after [DFP ⁺ 94]).	17
1.21	Qualitative mass flow rate for discharge of Halon 1301 (after [CHM92]).	18
1.22	Experimental vs. calculated steady mass flow rate (after [CYK ⁺ 95]).	18
1.23	Model/measured pressure in 34m ³ room upon HFC-227ea discharge @5.9% (after [SP95]).	19
1.24	Room pressure during the discharge of 30.9% V/V IG541 (after [RFS05]).	20
1.25	Room pressure during the discharge of 6.1% V/V HFC-227ea (after [RFS05]).	20
1.26	Predicted/measured enclosure pressures for 8 s HFC-227ea discharge @ 9.8% (after [RFS05]).	21
1.27	Thermodynamic path followed by FK-5-1-12 to extinguish a fire.	23
1.28	Thermodynamic path followed by HFC-227ea to extinguish a fire.	25
1.29	Spinodal lines for a simple compressible substance.	27
1.30	Extinction system with very small length of discharge's pipe.	28
2.1	Transient mass flow rate for liquid discharge (after [Val98]).	30
2.2	Initial state of the system.	32
2.3	Typical nozzles used for fire extinction applications with agent FK-5-1-12.	34
2.4	Coordinate system for the pipe.	35

2.5	Fast stage of the liquid's discharge process.	36
2.6	Slow stage of the liquid's discharge process.	37
2.7	Pipe's cross-section. Average over ring dr	37
2.8	Control volume over which integration is performed.	40
2.9	Detail of the liquid's discharge process.	46
2.10	Discharge process and pressure gradient for $0 < t < t_f$	47
2.11	Discharge process and pressure gradient for $t > t_f$	48
2.12	Moody diagram.	50
2.13	Skin friction coefficient for unsteady accelerated flow (source: [JC12]).	51
2.14	Dynamic equation's solution up to complete liquid discharge.	53
2.15	Dimensionless dynamic equation's solution up to complete liquid discharge.	58
2.16	Standard curves for parameters' standard values.	60
2.17	Velocity curve during the filing of a pipeline, after [KLA ⁺ 11].	61
2.18	Velocity curve (thick line) during the filing of a pipeline, after [VW07].	61
2.19	Velocity curves for various initial pressures p_0	62
2.20	Velocity curves for various pipe's lengths L	63
2.21	Bulk velocity for $L = 1$	64
2.22	Velocity curves for various geometrical factors G_f	65
2.23	Velocity curves for various pipe roughness ζ_D	66
2.24	Velocity curves for various equivalent valve lengths L_v	67
2.25	Evolution of Darcy-Weisbach friction factor f for standard pipe.	68
2.26	Velocity curves for various friction modulators Δ_f	68
2.27	Dimensionless force balance in the standard pipe.	70
3.1	Flow field ψ and its phase average. The graph needs to repeat itself to be periodic.	95
3.2	Rect function or normalised boxcar of width $T = 1$, $\mathfrak{R}_1(t)$	101
3.3	Fourier transform of rect function of width $T = 1$, $\text{sinc}(\omega) = \widehat{\mathfrak{R}}_1(\omega)$	103
3.4	Convolution of rect function of width $T = 1$ with itself, $\mathfrak{R}_1(t) \star \mathfrak{R}_1(t)$	104
3.5	Spectrum of a flow which could be approximately modelled with URANS.	108
3.6	The moving average filter affects mostly the high-frequency part of the spectrum.	109
3.7	Decomposition of field $\psi = 5 + 3 \sin t + \sin(\sqrt{23} t)$	119
3.8	Decomposition of field $\psi = 5 + 3 \sin t + 1.5 e^{-0.05t} \sin(\sqrt{23} t)$	120
3.9	An example of positive random-spike function.	121
3.10	Gaussian filter $G(x; 1)$ for different values of the shape parameter.	136
3.11	Gaussian filter $G(x; \Delta)$ for different values of the filter width Δ , $\gamma = 6$	137
3.12	Filter range for point \mathbf{x}_1 within the flow, and for point \mathbf{x}_2 close to the boundary $\partial\Omega$	146
3.13	Geometry of Hagen-Poiseuille flow.	149
3.14	Analytic, log-law and CFD velocity profiles for turbulent Hagen-Poiseuille flow (analytic profiles with $U_m = 2.2708$: (1) $\vartheta = 13.4$, $n = 16$, and (2) $\vartheta = 36.8$, $n = 45$).	159
3.15	Analytic and CFD Reynolds stress profile for turbulent Hagen-Poiseuille flow (analytic with $U_m = 2.2708$, $\vartheta = 13.4$, $n = 16$ and $U_m = 2.2708$, $\vartheta = 36.8$ and $n = 45$).	160
3.16	Bessel functions of the first and second kind $J_0(x)$, $Y_0(x)$, $J_1(x)$ and $Y_1(x)$. Note how similar are Y_0 and J_1 as $x \rightarrow \infty$	171
3.17	Profile of Reynolds stress in turbulent channel flow ($y/\delta = 1 - \alpha$). From fig. 7.3 of [Pop00].	184
3.18	Reynolds stress and mean velocity profiles for equations (3.475) and (3.476) with $A = 0.99$, $b = 0.01$, $Re^+ = 152.5 (R_2, U_2)$, and for figures 3.14 and 3.15 (R_1, U_1).	185

3.19	Reynolds stress and mean velocity profiles for equations (3.475) and (3.476) with $A = 0.995$, $b = 0.011$, $Re^+ = 169$ (R_3, U_3), and for figures 3.14 and 3.15 (R_1, U_1).	186
3.20	Decay of pressure gradient in pipe according to AHM and to $\Pi^*(\gamma) = 0.01 + \frac{0.03}{(0.001\gamma+1)^4}$	193
4.1	Figure 4.29 of reference [Wil06].	219
4.2	Figure 12, page 394 of reference [Cha00].	220
4.3	Theoretical velocity profiles for κ and B according to OpenFOAM and [ASKS07].	227
4.4	Turbulent Boundary Layer according to [McD07].	228
4.5	Turbulent Boundary Layer evolution.	228
4.6	(a) Low Re , the pipe is considered smooth; (b) high Re , it behaves as rough.	238
4.7	Meaning of velocity offset Δu^+ due to rough wall (from figure 4.25 of [Ceb13]).	240
4.8	Mean velocity profiles for smooth ($\zeta_r^+ < 4$) and transitional-rough flows (from figure 3 of [SF07]).	241
4.9	Mean velocity profiles for a range of Re in rough-walled pipe (from [SAS06]).	242
4.10	Complete mesh for the CFD model.	245
4.11	Cross-section of the mesh for the CFD model.	246
4.12	The log-layer develops within the first wall-cell.	247
4.13	Velocity curves for $k - \omega$ Shear Stress Transport with Scale Adaptive Simulation (SSTSAS) model in 3 different solver executions.	261
4.14	Velocity curves for DES simulation and AM ($L_v = 7.6 \cdot 10^{-3}$, $\zeta_D = 8.75 \cdot 10^{-5}$, $\Delta_f = 1$).	261
4.15	Sequence of discharge of liquid in the pipe for $k - \omega$ SSTSAS model.	263
4.16	Cross-section averaged flow acceleration for $k - \omega$ SSTSAS model.	265
4.17	Mean pressure along Z axis at instants in fast stage for $k - \omega$ SSTSAS model.	266
4.18	Mean pressure and velocity along centreline at $t = 9, 10$, $k - \omega$ SSTSAS model.	266
4.19	Mean velocity profiles for unsteady $t = 49$ (u) and steady (s) flow in $k - \omega$ SSTSAS model for positions $z = 5, 12.5, 20$ and 24.5 . Also theoretical log-law profile.	268
4.20	Law of the wall for unsteady $t = 49$ (u), steady (s) and theoretical (Theor.) flows in $k - \omega$ SSTSAS model for position $z = 20$	269
4.21	Reynolds stress R_{xz} profiles for unsteady $t = 49$ (u) and steady (s) flow in $k - \omega$ SSTSAS model for positions $z = 5, 12.5, 20$ and 24.5	270
4.22	Turbulent kinetic energy k profiles for unsteady $t = 49$ (u) and steady (s) flow in $k - \omega$ SSTSAS model for positions $z = 5, 12.5, 20$ and 24.5	271
4.23	Turbulent energy dissipation ϵ profiles for unsteady $t = 49$ (u) and steady (s) flow in $k - \omega$ SSTSAS model for positions $z = 5, 12.5, 20$ and 24.5	272
4.24	Turbulence dissipation rate ω profiles for unsteady $t = 49$ (u) and steady (s) flow in $k - \omega$ SSTSAS model for positions $z = 5, 12.5, 20$ and 24.5	273
4.25	Vorticity ζ profiles for unsteady $t = 49$ (u) and steady (s) flow in $k - \omega$ SSTSAS model for positions $z = 5, 12.5, 20$ and 24.5	273
4.26	Dimensionless number evolution for $k - \omega$ SSTSAS model.	275
4.27	Velocity curves for $k - \epsilon$ Launder-Sharma model in 6 different solver executions.	277
4.28	Velocity curves for $k - \epsilon$ simulation and AHM ($L_v = 1.833 \cdot 10^{-3}$, $\zeta_D = 2.0 \cdot 10^{-4}$, $\Delta_f = 1$).	278
4.29	Cross-section averaged flow acceleration for $k - \epsilon$ Launder-Sharma model.	279
4.30	Dimensionless number evolution for $k - \epsilon$ Launder-Sharma model.	280
4.31	Sequence of discharge of liquid in the pipe for $k - \epsilon$ Launder-Sharma model.	281
4.32	Mean velocity profiles for unsteady (u) and steady (s) flow in $k - \epsilon$ Launder-Sharma model for time $t = 53$ and positions $z = 5, z = 12.5, z = 20$ and $z = 24.5$	282

List of Tables

1.1	Thermophysical properties of FK-5-1-12 (at 25°C unless otherwise specified).	6
1.2	Thermophysical properties of HFC-227ea (at 25°C unless otherwise specified).	7
2.1	Values for dimensionless quantities of a standard pipe.	59
2.2	Reference quantities and units for standard pipe.	61
2.3	Key values defining the dynamics for varying p_0	62
2.4	Key values defining the dynamics for varying L	63
2.5	Key values defining the dynamics for varying G_f	64
2.6	Key values defining the dynamics for varying ζ_D	65
2.7	Key values defining the dynamics for varying L_v	67
2.8	Key values defining the dynamics for varying Δ_f	69
3.1	Complete set of analytical solutions for incompressible pipe flow.	161
4.1	y^+ for first wall-node for bulk velocities \tilde{U} , according to Blasius correlation (4.24).	246
4.2	Turbulence models tested in CFD simulations.	254
4.3	Comparison of flow events for 3D CFD and 1D AHM models.	262
4.4	Features of the 6 models executed in figure 4.27.	277
4.5	Comparison of flow events for 3D CFD and 1D AHM models.	278

Chapter 1

State of the Art in Fire Protection Engineering

1.1 Introduction

This Chapter¹ aims to summarise the current state of the art regarding the physical phenomena behind an ever more frequent method of firefighting: the hydrodynamical modelling of processes in which a liquid is kept highly pressurised by a seemingly ideal gas, both contained within a vessel provided with a fast valve, which is suddenly opened and the liquid released to atmosphere at high speed through a length of discharge's pipe. A special emphasis is made on the theoretical and mathematical models which attempt to explain such phenomena.

In the realm of Fire Protection Engineering (FPE) it is not infrequent the use of highly pressurised extinguishing agents that are suddenly discharged to protected areas in case of outbreak of fire. This very effective method of fire extinction is carried out with agents that normally are in gaseous state at standard conditions of pressure and temperature (with a remarkable exception), although within the pressurised vessels can very well be in liquid state. Upon discharging, the agent's vaporisation enthalpy is retrieved from the ambient, thus decreasing its temperature until fire is quenched.

A number of years ago, Halons (a subclass of the general family of Haloalkanes) were the main extinction agents used to prevent the initiation of flames within small-to-medium rooms in which fires were deemed specially catastrophic, such as computer rooms, critical documentation vaults, museum's restoration halls, process control rooms, etc. They were so effective in stopping the combustion reactions, that little discussion existed about the possibility of finding some other kinds of extinction agents.

As it was established the role played by BFCs and CFCs (Haloalkanes containing *Br* and *Cl*) in ozone layer depletion (see figure 1.1), and it became evident that those compounds were doomed to perish for any industrial application as a result of 1987 Montreal's Protocol, a vast scientific and engineering endeavour was originated with the purpose of finding new substances that could substitute Halons in such important applications. Thus, there were established the Halon Options Technical Working Conference (HOTWC), or the International CFC and Halon Alternatives Conferences and Exhibitions, and similar scientific and engineering meetings. Probably, the most ambitious program was the Next Generation Fire Suppression Technology Program (NGP) of the National Institute of Standards and

¹The present Chapter is addressed to Engineers interested in the field of Fire Protection Engineering (FPE), specially in fire extinction through the discharge of clean agents into protected rooms. Readers not fitting this category are most welcome to this Chapter, although possibly they might prefer to skip it altogether and plunge directly into the next one 2.

Technology (NIST) (USA), which ran from 1991 to 2006 under the supervision of renowned scientists like Richard G. Gann and others (see [Gan95], [Gan98], [Gan03] or [Gan05])

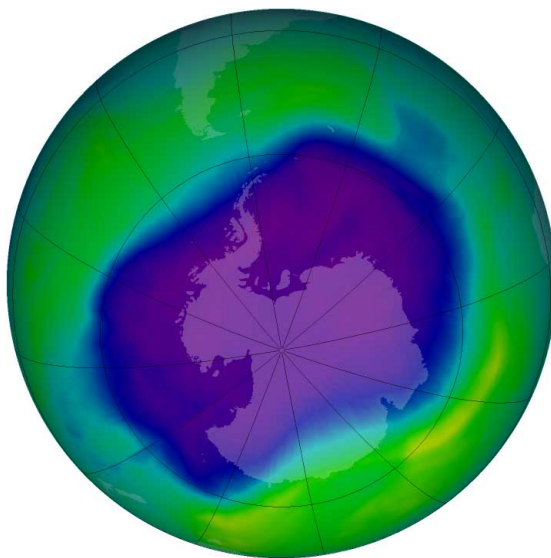


Figure 1.1: The largest Antarctic ozone hole recorded as of September 2006.

As a result of such standing and extensive research, a number of agents were found that fulfilled acceptably the role of Halons for fire extinction applications, and the literature is full of articles, papers and proceedings describing them (see, for instance, [Coo94], [GGP94], [HGG⁺94], [HTSC94], [BGF⁺95], [MDK98], [NBHT98], [GHCP00], [Sas01], [RRC01], [Lin06], [PYB⁺06] or [BBFY08])

Those fire extinction compounds are members of the HFC family (a subclass of Haloalkanes containing only *C*, *H* and *F*), also called colloquially **Clean Agents**, because they have no noticeable effect on Earth's ozone layer. Some of these agents actually showed design concentrations to quench test fires not too different from those corresponding to Halons. This last feature is quite desirable, because it means that, in many cases, the existing installations (pipes, valves, manifolds, etc.) could be preserved and only the actual agent's cylinders had to be replaced, thus rendering more affordable the initiative of banning Halons and having them replaced by less environmentally hazardous compounds. Notably, one of the most suitable agents (with an acceptable price tag) was found to be HFC-227ea, which could readily be used as a replacement agent in existing installations of Halon 1301 (see [Sen01]).

But once the problem of Earth's ozone layer depletion was given a temporary solution, the world, with the exception of a few stubborn characters, became conscious of a new threat to the Planet: the global warming of the atmosphere due to greenhouse effect and the climate change it might engender. A great number of studies were conducted in order to measure the greenhouse effect attached to any gaseous substance that might be released to the atmosphere. Nowadays, every industrial compound exhibits in its Material Safety Data Sheet the degree of Global Warming Potential (Global Warming Potential (GWP)) it carries, usually referred to that of CO_2 which is taken as a reference unit ($GWP_{CO_2} = 1$).

The most effective clean agents, from the extinction power's point of view, normally exhibit a very high degree of GWP, several thousand times higher than CO_2 ² (see figure 1.2). With raising worldwide concern about climate change, it is only natural to try to find extinction agents as effective as those, but

²HFC-227ea has a GWP= 2900, that is, 1 kg of HFC-227ea has the equivalent global warming effect of 2.9 tons of CO_2 . Other extinction agents have a much higher GWP: for instance, HFC-23 has GWP= 11700 (14800 for a 100 years period). See thermophysical properties of HFC-227ea in table 1.2.

much less hazardous for the environment. While this research is being conducted, with varying degree of success, growing concern arises in rationalising the use of existing clean agents, with the aim that just the strictly sufficient amount to extinguish a potential fire is released to the atmosphere, and nothing else. There exists founded suspicions that, possibly, current regulations and standards concerning such fire protection techniques, do not adequately address the necessity of reducing the amount of agent to be released to environment, to the actual minimum which guarantees fire extinction.

Thus in the long term, those Clean Agents were not so *clean* after all, and a new endeavour is again necessary to replace them with other agents that could undertake the task. In the meantime, the emphasis is set on techniques which might improve the efficiency of existing clean agents, allowing for smaller amounts of them to guarantee the same extinction performance. This could very well be obtained with improved methods of discharge, that take into account the specific hydrodynamic features of this process. All that justifies the necessity of developing new models that could be used in the design of better systems, which fully exploit the intrinsic capabilities of clean agents to quench fires.

Although there exist ample empirical research regarding the effectiveness of those clean agents to extinguish various kinds of fire (see, for instance, [Coo94], [HGG⁺94], [HTSC94], [KSMKK96], [MDK98], [KOYS01], [RRC01], [Sas01], [Ska02], [Fri03], [SAA⁺03], [SAAMO4], [Ben06], [Lin06], [PYB⁺06] or [YK06], among many others), to the author's knowledge, very few studies have been reported regarding the hydrodynamics aspects of the phenomenon, specially from the transient point of view. It would be expected that a deeper understanding of the dynamical processes involved in agent's release, would help in reducing and optimising the amounts of clean agent that currently are regulated and established as suitable for extinction applications.

The information summarised in this State of the Art Chapter is gathered with the intention of contributing to such endeavour: to provide a physico-mathematical model, and the associated dynamic equations thereof, which will permit the description, comprehension and prediction of the free discharge process of a highly pressurised liquid agent into the atmosphere. It is also expected that the model would open up the possibility of incorporating its results into the current set of regulations and standards related with this field of FPE.

Although this problem has been approached before within the realm of FPE (see, for instance, [PYG⁺94] or [Coo93]), the treatment found in the literature has always been from a hydraulic³ steady state perspective. To the author's knowledge, there is not yet a model for the problem's transient hydrodynamic behaviour. Along the Dissertation it will become evident that such a fast process as this agent's discharge (which normally elapses less than 10 s, with a frenzy evolution in the first second), could not be accurately described with the equations of steady state hydraulics. Instead, full transient regime equations must be used, which will allow for new and interesting hydrodynamic behaviour to emerge.

The present Chapter is devoted to investigate the findings that exist in the literature regarding this

³In this Dissertation the following distinction will be made between *hydrodynamic model* and *hydraulic model*. A hydrodynamic model refers to the study of a flow from the perspective of Mechanics of Continua, which is best described through fields that determine the detailed structure of the flow, whereas a hydraulic model deals with quantities not requiring the treatment of fields, but rather are considered dependent variables which characterise the flow as a whole, and are unable to provide information about the internal structure of the flow. Hydrodynamic models are usually 3D, while hydraulic models are systematically 1D. The connecting bridge between both types of model is the cross-section average to be introduced in section 2.3.1. This distinction applies only within the scope of the present work and has no pretension to be universal.

	FE-13™	FE-25™	FE-227™	FE-36™	FE-241™	Halon 1211	Halon 1301
Application	Flooding (Occupied)	Flooding (Occupied for Class Hazards)	Flooding (Occupied)	Streaming Flooding (Local application) (Occupied)	Flooding Streaming (Unoccupied)	Streaming Flooding (Local application) (Unoccupied)	Flooding (Unoccupied)
Halocarbon Name	HFC-23	HFC-125	HFC-227ea	HFC-236fa	HCFC-124	BCFC-12B1	BCF-1301
Chemical Name	Trifluoromethane	Pentafluoroethane	1,1,1,2,3,3,3-Heptafluoropropane	1,1,1,3,3,3-Hexafluoropropane	Chlorotetrafluoroethane	Bromochlorodifluoromethane	Bromotrifluoromethane
Chemical Formula	CHF_3	CF_3CHF_2	$\text{CF}_3\text{CHF}_2\text{CF}_3$	$\text{CF}_3\text{CH}_2\text{CF}_3$	CF_3CHClF	CBrClF_2	CBrF_3
Molecular Weight	70.01	120.02	170	152.04	136.48	165.38	148.9
Boiling Point at 1 atm, °C (°F)	-82.0 (-115.7)	-48.3 (-55.0)	-16.3 (-2.6)	-1.4 (29.5)	-10.95 (12.2)	-3.4 (26)	-57.7 (-71.9)
Liquid Density at 25°C, kg/m ³ (77°F, lb/ft ³)	670 (41.82)	1189.7 (74.27)	1386 (86.53)	1360 (84.89)	1364 (85.15)	1810 (113)	1538 (96.01)
Heat of Vaporization at Boiling Point, kJ/kg (Btu/lb)	240 (103.02)	164.4 (70.7)	132.6 (56.7)	160.04 (68.77)	162.6 (70)	132.6 (57)	118.8 (51.08)
US EPA SNAP Approval	Accepted	Accepted	Accepted	Accepted	Accepted	NA	NA
Ozone Depletion Potential (CFC-11=1)	0	0	0	0	0.02	4	16
Atmospheric Lifetime, years	264	33	37	209	6	15	65
Global Warming Potential, 100-year time horizon (CO ₂ =1.0)	11700	2800	2900	6300	480	1300	5600
NOAEL, vol%	30	7.5	9	10	1	0.5	5
LOAEL, vol%	>50	10	10.5	15	2.5	1	7.5
Extinguishing Concentration (cup burner, heptane) ^(a)	12.9	8.7	6.7	6.3	6.6	4.1	3.5
Design Concentration, vol% ^(b)	16-18	9.6-11.3	7.4-8.7	6.9-8.2	7.3-8.6	5.0-5.8	5
Agent Required for 28.32 m ³ at 21°C (1,000 ft ³ at 70°F), per NFPA 2001 kg (lb)	15.7-18.1 (34.7-40.0)	15.2-18.2 (33.5-40.2)	16.4-19.6 (36.2-43.2)	13.7-16.5 (30.1-36.4)	13.0-15.6 (28.7-34.3)	10.6-12.9 (23.4-28.4)	9.3 (20.6)
Storage Volume Equivalent (Halon 1301=1)	2.2-2.5	2.1-2.5	1.7-2.0	1.4-1.6	1.3-1.6	NA	1
Max Fill Density, kg/m ³ (lb/ft ³) ^(c)	865 (54) ^(d)	865 (54)	1153 (72)	1201 (75)	1185 (74)	NA	1121 (70)

(a) Average for n-Heptane
 (b) Fuel and application dependent
 (c) In 500 psi working pressure container pressurized with nitrogen to 360 psi at 70°F
 (d) In 1,800 psi working pressure container (no superpressurization)

Figure 1.2: Thermophysical properties of most used HFC extinction agents.

phenomenon, always within the realm of FPE (hence the Chapter’s title). Works studying similar processes in fields not related with FPE will be considered in other Chapters.

A final word on a new generation of clean agents that have arisen with suitable characteristics for being used as fire quenching agents replacing Halons and HFC. To date, the most promising extinction agent that has no impact on the ozone layer and boasts a remarkably low GWP= 1 is a member of the perfluorinated ketones identified as FK-5-1-12, also known as NOVEC-1230. Its thermophysical properties are presented in table 1.1, and the models to be developed in this Dissertation will take the transport quantities of FK-5-1-12 as a reference. Another interesting family of agents is the BromoTri-fluoroPropene (BTP) group, with members like 2-bromo-3,3,3-trifluoropropene (2-BTP) or 1-bromo-3,3,3-trifluoropropene (1-BTP) and chemical relatives like 4-bromo-3,3,4,4-tetrafluorobutene (BTFB) or 2-bromo-3,3,4,4,4-pentafluorobutene (BPFB). Unfortunately, this State of the Art investigation could not find any paper related with the discharge hydrodynamics of any of the above new clean agents.

1.2 Description of the Technique

A well tested technique for fire-fighting in closed rooms, used all over to protect valuable assets, consists of discharging an extinction agent very rapidly into the room which is meant to be protected, as soon as an outbreak of fire is detected. It is specially adequate for the initial stages of fire development, when the amount of combustible involved in the reaction is still small and accessible for the agent to actuate.

The high velocity attained by the flooded agent upon releasing creates a turbulence within the vault which favours its thorough mixing with the existing air. According to the nature and amount of agent discharged into the room, the fire is quenched by one or more of the following mechanisms:

Heat removal: The combustion reaction is halted due to a sudden decrease of temperature, below flammability limit. The agent's concentration in the room need not be very high, as long as it exhibits enough cooling properties. Such heat removal is mainly attained by rapid agent's vaporisation, which is favoured by the generation of tiny droplets as the liquid agent collides with the nozzle's sharp edges.

Oxygen removal: The chemical reaction is halted due to the scarcity of a basic reactive (suffocation). The agent's concentration in the ambient needs to be very high, since it must displace oxygen from the room below the suffocation limit.

Reaction hindrance: The combustion reaction is hindered, and eventually halted, due to new chemical compounds that interfere with the radicals created in the original chain reaction. The agent's concentration need not be very high, as long as it has the property of generating intermediate compounds with those radicals.

Haloalkane-based clean agents rely primarily on the first mechanism, being the others of secondary importance. Inert-gas clean agents use almost exclusively the second mechanism, somewhat aided by the blowing effect the gas jets have on the burning surface. The third mechanism is typical of Halons, which also employ profusely the first.

Around year 2003 a new kind of clean agent was introduced in the market for this same application. Under the ASHRAE name of FK-5-1-12 (FK stands for 'FluoroKetone') this new agent boasts a GWP of 1 (equal to CO_2), and has set a standard that other manufacturers will follow. FK-5-1-12 presents, among others, a distinct characteristic not equalled by competing clean agents: it is liquid at NTP⁴ conditions. Therefore, it undergoes negligible vaporisation while being convected inside the discharge pipe. This feature represents a remarkable advantage for the practitioner Engineer, since it is possible to develop a hydraulic model for the FK-5-1-12 discharge without further concern on the difficulties of two-phase flow. The main models developed in this Dissertation will also be particularised for the FK-5-1-12 agent. FK-5-1-12's formula and molecule are shown in figures 1.3 and 1.4, respectively. Table 1.1 lists its main thermophysical properties. Note that agent FK-5-1-12 has a kinematic viscosity lower than water, $0.4 cSt$ versus $1 cSt$.

Since this research cannot delve into every Haloalkane employed in FPE, it will concentrate instead in one of the most used clean agents, namely HFC-227ea, also known as R227, Heptafluoropropane, HFP, C_3HF_7 , $CF_3 - CFH - CF_3$... It is also commercialised under the trade registered names of FM-200, FE-227, Solkaflam 227, MH-227, NAF S 227... It is a colourless and odourless gaseous halocarbon at NTP conditions, although it is liquid at the conditions reigning in the cylinders being used in FPE. Agent HFC-227ea adopts the chemical formula depicted on figure 1.5, while its main thermophysical properties are listed in table 1.2. The molecule $CF_3 - CFH - CF_3$ is a reagent to generate sources of radical $CF_3 - CF^- - CF_3$ by deprotonation. This ability would be clearly understood upon examining its 3D molecular model, figure 1.6 By considering HFC-227ea, other members of the family of HFCs would be adequately represented, since their properties are not so different⁵

⁴Nominal NTP conditions are set at $101.325 kPa = 1 atm$ and $20 ^\circ C = 293.15 K$, while Standard Temperature and Pressure (STP) is set by the IUPAC as $100 kPa = 1 bar$ and $0 ^\circ C = 273.15 K$.

⁵With the exception of HFC-23, which is in a class by itself. However, HFC-23 is currently banned in Europe for obvious environmental reasons: GWP= 11700.

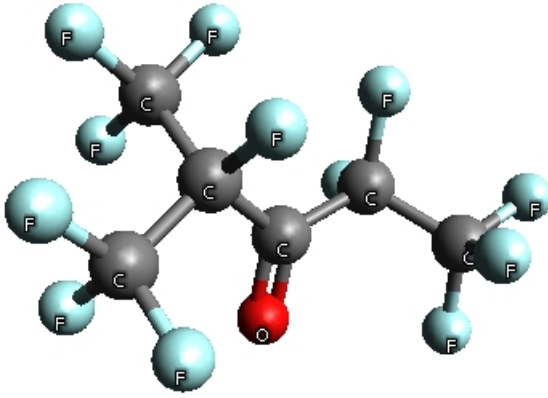


Figure 1.3: Chemical formula of FK-5-1-12 molecule.



Figure 1.4: 3-D image of FK-5-1-12 molecule

Properties	Value
Chemical Formula	$CF_3CF_2C(O)CF(CF_3)_2$
Boiling point @ 1 atm ($^{\circ}C$)	49.2
Freezing Point ($^{\circ}C$)	-108
Molecular Weight (g/mol)	316
Critical Temperature ($^{\circ}C$)	168.7
Critical Pressure (MPa)	1.865
Critical Volume ($cc/mole$)	494.5
Critical Density (kg/m^3)	639.1
Vapour Pressure (kPa)	40.4
Heat of Vaporization @ boiling point (kJ/kg)	88
Liquid Density (kg/m^3)	1616.34 @ $20^{\circ}C$
Gas Density @ 1 atm (kg/m^3)	13.6
Specific Volume, gas @ 1 atm (m^3/kg)	0.0733
Coefficient of Expansion (K^{-1})	0.0018
Kinematic Viscosity @ $20^{\circ}C$ (cSt)	0.40
Absolute Viscosity (cP)	0.64
Specific Heat, liquid ($J/kg K$)	1103
Specific Heat, vapour @ 1 atm ($J/kg K$)	891
Thermal Conductivity ($W/m K$)	0.059
Surface Tension (mN/m)	11.39 @ $20^{\circ}C$
Solubility of Water in Fluid (ppm by weight)	20
Dielectric Strength, 0.1" gap (kV)	> 40
Relative Dielectric Strength @ 1 atm ($N_2 = 1.0$)	2.3
Dielectric Constant @ 1kHz	1.8
Volume Resistivity (Ωcm)	10^{12}
Global Warming Potential (GWP)	1

Table 1.1: Thermophysical properties of FK-5-1-12 (at $25^{\circ}C$ unless otherwise specified).

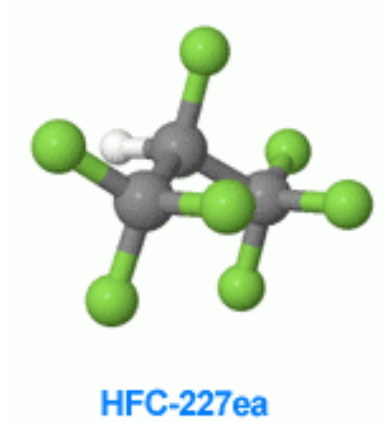


Figure 1.5: Chemical formula of HFC-227ea molecule.

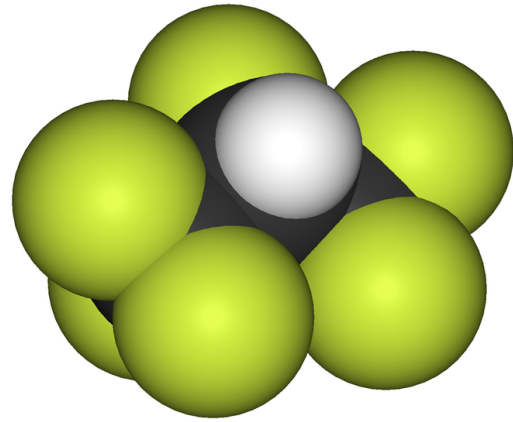


Figure 1.6: 3-D image of HFC-227ea molecule.

Properties	Value
Chemical name	1,1,1,2,3,3,3-Heptafluoropropane
Chemical formula	CF ₃ CHF ₂ CF ₃
Molecular Weight	170.03
Boiling Point @ 1 atm (°C)	-16.34
Freezing Point (°C)	-131
Critical Temperature (°C)	101.75
Critical Pressure (kPa)	2925.0
Critical Density (kg/m ³)	594.25
Liquid Density (kg/m ³)	1387.7
Density, saturated vapour @ boiling point (kg/m ³)	8.4860
Vapour Density @ 1 atm (kg/m ³)	7.1461
Specific Heat, liquid (Cp) (kJ/kg°C)	1.1816
Specific Heat, vapour (Cp) @ 1 atm (kJ/kg°C)	0.81327
Vapour Pressure, saturated (kPa)	454.73
Heat of Vaporization @ boiling point (kJ/kg)	131.77
Thermal Conductivity, liquid (W/m°C)	0.060491
Thermal Conductivity, vapour @ 1 atm (W/m°C)	0.013336
Viscosity, liquid (cP)	0.23935
Viscosity, vapour @ 1 atm (cP)	0.011590
Relative dielectric strength @ 1 atm (N ₂ = 1)	2.00
Solubility of Water in HFC-227ea @ 20°C (ppm)	600
Solubility of HFC-227ea in water @ 20°C (mg/L)	260
Ozone Depletion Potential (CFC-11 = 1)	0.0
GWP (100 yr ITH. GWP _{CO₂} = 1)	3220
Atmospheric Lifetime (yr)	34.2
Inhalation Exposure Limit (AEL)	1000 ppm 8 hr/12 hr TWA

Table 1.2: Thermophysical properties of HFC-227ea (at 25°C unless otherwise specified).

The basic features and Engineering aspects of automatic fire extinction systems based on HFC-227ea

could be found in general reference handbooks such as [DiNO2] and [DiNO3]. Unfortunately, those extensive references do not mention agent FK-5-1-12.

Commercially, the agents FK-5-1-12 and HFC-227ea are supplied in cylinders of different standardised volumes, normally at 24 *bar* or 42 *bar* of relative pressure at normal room temperature, although other pressures are possible. The pressure is maintained by means of compressed gas N_2 , being both the agent and N_2 within the cylinder. Should the application demand more than one cylinder, several of them could be deployed together forming a battery, as shown in figure 1.7. In such cases, normally the released pressure of one tripped cylinder is used to trigger the next one in the battery.

The cylinders are connected, *via* rigid pipe (normally with high pressure rating), to a number of nozzles which warrant the adequate distribution of agent within the protected room (see figure 1.8). The trigger which releases the agent is normally an automatic fire detection system, usually of the very-early-warning type.

Figure 1.8 shows a typical small installation that demands just one cylinder to guarantee fire extinction. The elements which constitute an automatic fire suppression system based on clean agent are:

- Agent cylinder Clean agent and N_2 are both contained inside the cylinder, both compressed to the designed pressure. The cylinder is endowed with a manometer.
- Valve A fast-opening valve releases the agent to the ambient. It could be electrically or pneumatically activated. In a battery of cylinders either a pilot bottle triggers pneumatically all cylinders, or the first one is tripped electrically and the remaining are triggered pneumatically with the pressure released by the first, or any other similar combination. The cylinder has a manual release lever which acts directly on this valve.
- Piping It conducts the clean agent to the atomising nozzles, guaranteeing that discharge elapses less than a established time (usually 10 s).
- Nozzles Allow for the agent to break into tiny droplets (case of FK-5-1-12) or to vaporise directly (case of HFC-227ea), and distribute the agent evenly enough inside the protected room. The set of droplets present an enormously larger interface than an equal-mass pool liquid, thus favouring rapid vaporisation.
- Fire detectors They could detect the presence of smoke, rising temperature, flame, or any other property associated with fire. Usually there are a redundant set of detectors in each protected room, to avoid false alarms. Each activated detector sends an alarm signal to the fire detection panel.
- Detection panel Called Releasing Panel in figure 1.8, it is the electronic unit which receives the early-warning alarm signal from fire detectors, and triggers the agent's release, according to whatever sequence has been programmed.
- Horn/strobe An audible/visible warning signal for the people inside the room, announcing that agent's release is coming. People must leave the room and lock the door upon hearing this horn.
- Manual release A push-button which sends a signal to the Detection Panel, causing the release of agent to the room.
- Manual abort A push-button which sends a signal to the Detection Panel, aborting the extinction sequence and granting manual control to whomever has pressed such button (not shown in figure 1.8).

Fire suppression with clean agents FK-5-1-12 or HFC-227ea is mainly based on its ability to vaporise and rapidly remove heat from its surroundings. This causes a sudden temperature decrease in the protected



Figure 1.7: Typical battery of HFC-227ea cylinders for fire extinction applications.

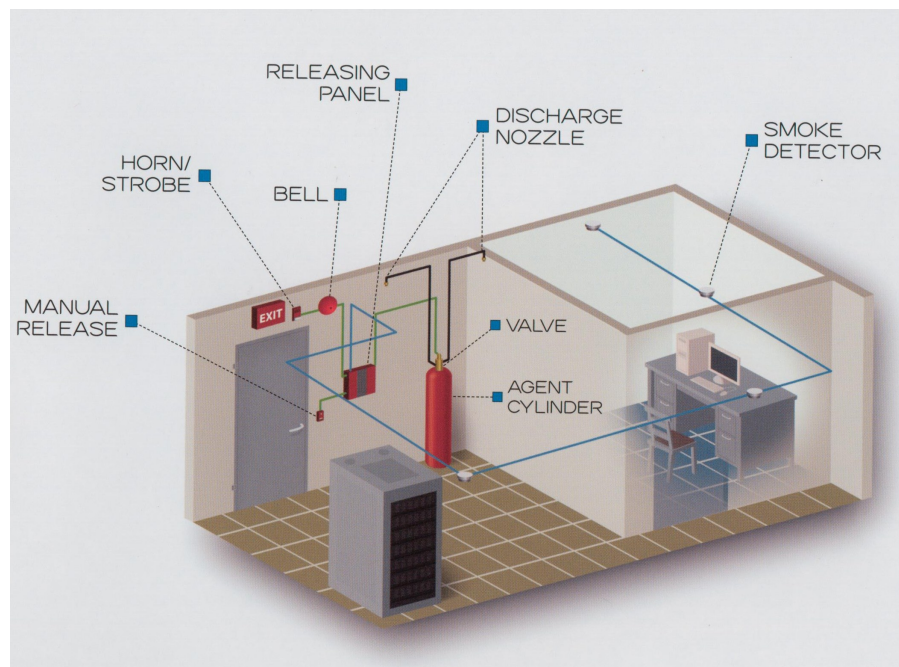


Figure 1.8: Typical small installation of HFC-227ea fire extinction.

room, which plunges below the flammability limit, thus quenching any attempted fire that might have initiated. The rate of vaporisation, which in turn determines the efficiency of the extinction agent, is directly related with its vapour pressure at the conditions reigning in the protected room.

Figure 1.9 shows the vapour pressure of FK-5-1-12 as a function of temperature. It has the expected exponential behaviour predicted by Thermodynamics. For normal room temperature (some 20°C), this pressure is slightly higher than 32 kPa , that is, concentrations of FK-5-1-12 up to 32% are possible before reaching saturation. Therefore, at the concentrations this agent is normally used in actual installations (around 6%), it can vaporise completely and its extinguishing action would not be hindered by saturation, being the maximum achievable partial pressure after discharge (some 6 kPa) neatly lower than saturation pressure at normal room temperature. Thus, FK-5-1-12 exits the nozzle in liquid phase,

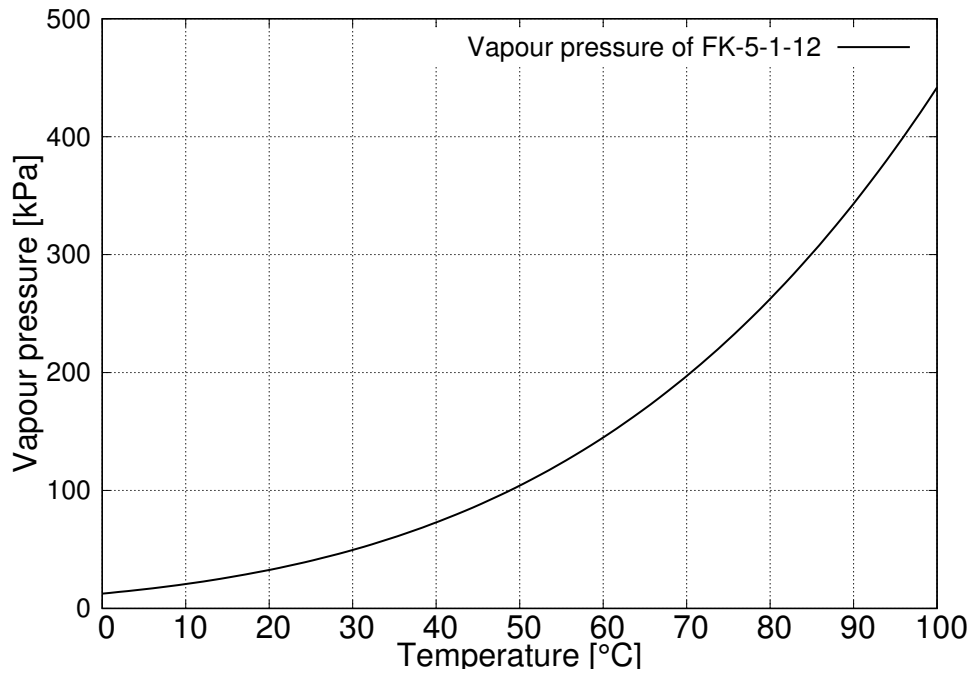


Figure 1.9: Vapour pressure curve of FK-5-1-12.

and it is the conversion in droplets upon colliding with the nozzle that makes it vaporise quickly.

Figure 1.10 shows the vapour pressure of HFC-227ea as a function of temperature. For normal room temperature (some 20°C) this pressure is slightly above 4 bar , and that explains the flashing behaviour of HFC-227ea as it exits the discharge nozzles. The excellent photograph of figure 1.11 displays how the agent has fully vaporised as it displaces some 1 m away from the nozzle. The vaporisation begins before reaching the nozzle, inside the discharge pipe. Flashing of HFC-227ea will be further explained in section 1.5 .

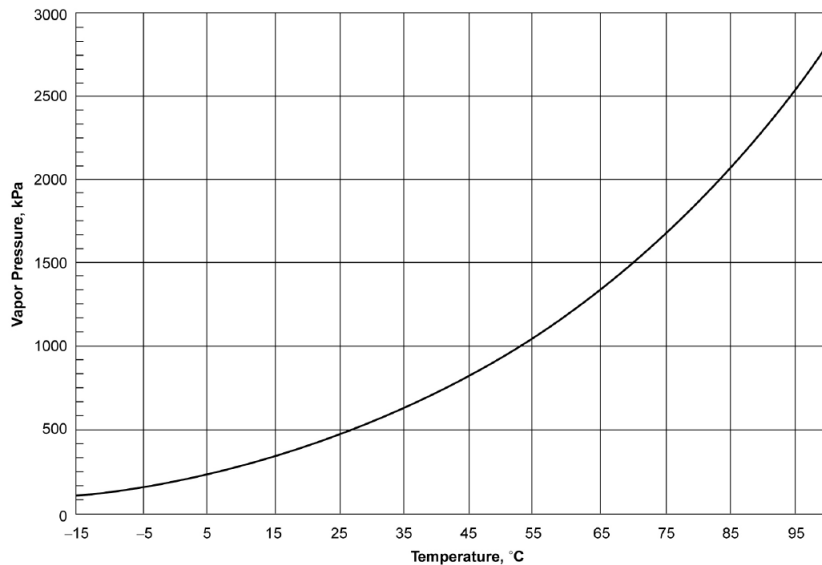


Figure 1.10: Vapour pressure curve of HFC-227ea.

The calculation of the heat removed from ambient as clean agent vaporises during the discharge process,

is suitably described in general handbooks such as [DiNO2] and [DiNO3] (see also sections 1.4 and 1.5). This cooling effect, although the most important, is not the only suppression mechanism taking place during agent's discharge: the high speed fluid also removes partially some oxygen from the fire, and disperses and mixes with pyrolysis products, thus interfering with the combustion reaction. It is worth mentioning the interesting experimental work related with fire suppression, [BBFY08], which shows with detail the successive stages being developed in a typical fire extinction process.



Figure 1.11: Discharge of HFC-227ea agent in a protected room.

The main mechanism to attain the desired discharge velocity is to N_2 -pressurise correctly the agent in the cylinders. Thus, a certain amount of N_2 must be added to obtain the right pressurisation, but always above a minimum threshold, since the pressure within the cylinders would raise rapidly with increasing room temperature, perhaps above their pressure rating. The relationship between N_2 and clean agent inside the cylinder is called the **filling density**, and its measured in kg of clean agent per m^3 of cylinder capacity. The higher the filling density the lower the mass of N_2 within the cylinder⁶.

In order to understand the importance of such pressurisation, figure 1.12 shows the pressure increase of a typical cylinder as a function of temperature, taking into account several filling densities of FK-5-1-12. In the FPE jargon, it is called the **isometric diagram** for a given agent. The diagram has been drawn for a cylinder with 25 bar at $21^\circ C$, and similar ones must be determined for different design pressures (42 bar or any other). Alternatively, figure 1.13 shows the corresponding isometric diagram for HFC-227ea at the same design pressure of 25 bar at $21^\circ C$. Such isometric diagrams determine the maximum filling density for an agent in a cylinder with a given pressure rating, the rule being that the pressure attained at $54^\circ C$ must not exceed $5/4$ of its design pressure. For example, the maximum filling density for HFC-227ea with 25 bar at $21^\circ C$ is $1153\text{ kg}/m^3$ (see figure 1.13).

A second means to achieve a high discharge velocity, complementary to the former, is an optimised piping design. It is thus necessary to develop comprehensive dynamic models of pipe flow which take

⁶The filling density is related with the geometric factor G_f to be introduced in section 2.4. The higher the filling density the larger the geometric factor.

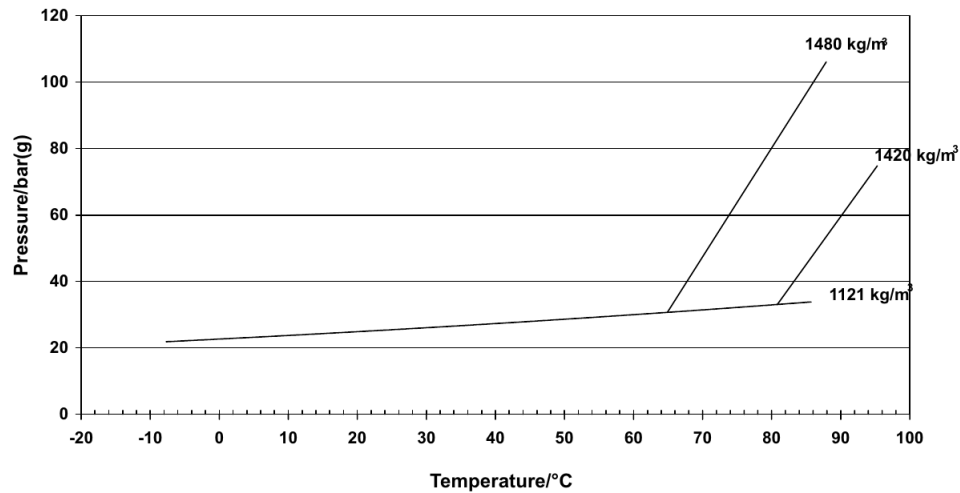


Figure 1.12: Isometric diagram for FK-5-1-12 superpressurised with N_2 to 25 bar at 21°C.

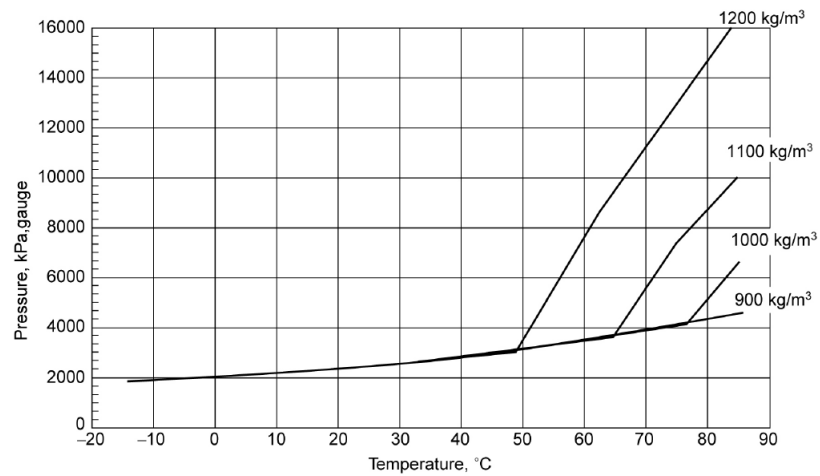


Figure 1.13: Isometric diagram for HFC-227ea superpressurised with N_2 to 25 bar at 21°C.

into account the transient character of the discharge process. Besides, those models should describe accurately the dependence of the transient friction factor on flow parameters, since friction is the most important effect opposing agent's motion. The following section is devoted to assess the current State of the Art of this particular aspect of those extinguishing systems. New mathematical models will be introduced in the coming Chapters, which derive the transient dynamic equations of agent's flow directly from First Principles.

1.3 Hydraulics of Discharge: Literature Review

Even though there exist a large number of works studying and documenting the effectiveness of clean agents (and other extinction agents) for various kinds of test fires, few papers can be found conducting extensive research on the hydrodynamics behaviour of the discharge process of such agents to protected areas.

[GGP94], is probably the most comprehensive work ever written on the subject of agent's discharge over fires in protected areas. It covers most areas of research which have a relationship with this

issue: thermodynamic properties of agents, hydrodynamical modelling of discharge, hydrodynamic experimentation of these phenomena, flame suppression effectiveness of such agents, flame inhibition chemistry, agent stability under storage and discharge residue, corrosion of metals, elastomer seal compatibility, and human exposure and environmental impact. It contains interesting developments from a theoretical point of view, viable numerical models, ingenious experimental set-ups, and valuable results and findings.

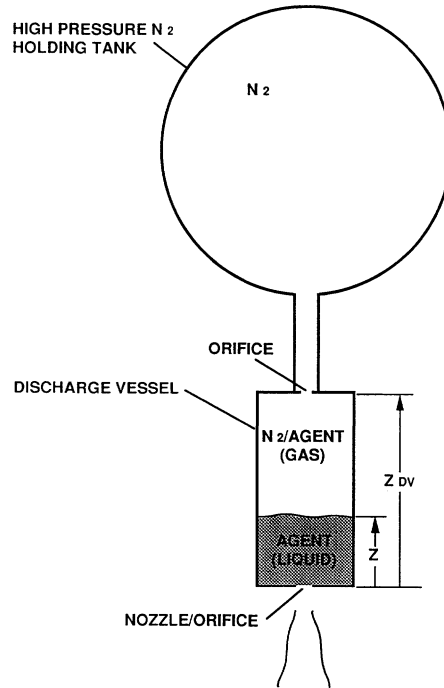


Figure 1.14: Experimental arrangement in [PYG⁺94] experiments.

The Chapter devoted to hydrodynamics of agent discharge, [PYG⁺94], is exhaustive and covers most aspects of this subject. It defines a mathematical model for an experimental set-up in which the process can be studied and monitored, and the model's predictions compared with the measurement results. It is complete, full and detailed, and the model is quite analytical, but it is based on the equations found in [Sha53], which are developed under the assumptions of isentropic steady regime flow, and it does not take into account the transient flow equations which are deduced in [Sha54].

[PYG⁺94] describes an experimental apparatus, shown in figure 1.14, and the associated mathematical model that explains the agent's behaviour as it is discharged through it. Their approach to the problem considers the agent as a compressible fluid and makes use of the equations for steady isentropic compressible flow. The model also includes the possibility of agent flashing⁷.

It considers also a discharge flow coefficient for the orifice (nozzle) through which the agent is released to the ambient, according to [Sha53]. The dimensionless equations are then presented and solved numerically, for a set of initial values typical of standard extinction installations. The results are depicted in graphs and then compared to actual measurements. There is a comprehensive set of curves which shows most of the situations that can be subjected to experimental control. The experiments are

⁷Flash evaporation is produced when a saturated liquid undergoes a sudden reduction in pressure. The liquid begins to boil until the energy removed from the remaining liquid drops its temperature below saturation point, or until it vaporises completely, whatever occurs first.

conducted with a number of different extinction agents, such as HFC-227ea, FC-218, FC-236, FC-31-10, HFC-32, HFC-125, Halon 1301, HCFC-22, HCFC-124, HFC-236fa, FC-318, FC-116 and HFC-134a.

One of such curves is shown on figure 1.15, representing the results for the temporal variation of the internal pressure during downward discharges of HFC-227ea. Pressures reported in the figure are gauge dimensionless pressures, referred to the actual burst pressure, P_i , which is taken to be the pressure at $t = 0$ s. The curves show two distinct regions, separated by an inflection point. The first region corresponds to the time interval during which the liquid agent is being propelled from the vessel. The second region corresponds to the period when the remaining vapour (mostly N_2) is being vented from the vessel. The inflection point corresponds to the time at which the liquid agent has just been completely expelled from the vessel. [PYG⁺94] also includes abundant pictures taken from high speed cameras. Those pictures show with great detail the development of flow in the discharge process.

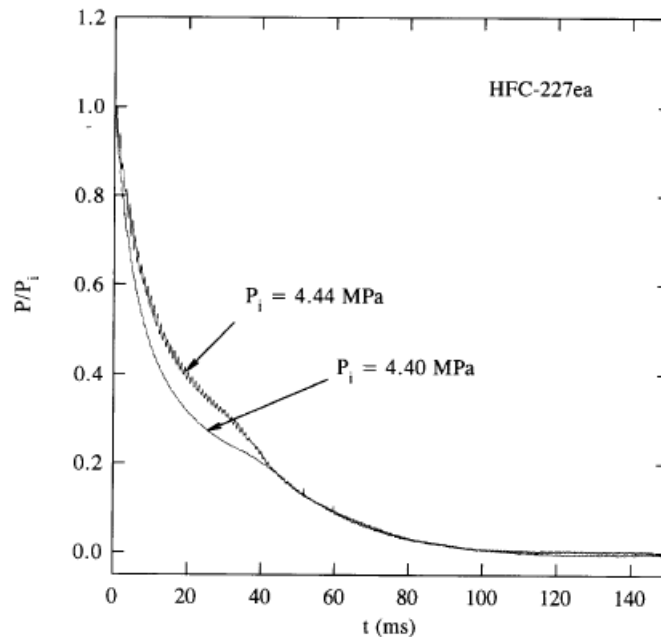


Figure 1.15: Internal pressure during downward discharges of HFC-227ea (after [PYG⁺94]).

Figure 1.16 shows the comparison of the actual measured values of discharge pressures for HFC-227ea with the model's predicted results. Despite not using transient flow dynamic equations, the agreement is excellent⁸.

Perhaps the most interesting results, from a Hydrodynamics point of view, are those shown in figures 1.17 and 1.18. They correspond to the dynamic pressure curves as measured by two pressure transducers: one located near the exit orifice (some 13 mm downstream, figure 1.17), and another placed further away (some 1.3 m downstream of the vessel's exit, figure 1.18). In both cases, two measurements have been conducted with different agent masses and release pressures. Those curves are plotted with an offset, so that they could be clearly distinguished. Despite air entrainment alters the jet, far-field curves are qualitatively not too different from near-field's, although their values are over 60% higher, a somewhat surprising result.

⁸Possibly, the transient is negligible because the discharge length is zero, that is, the agent is discharged directly to the atmosphere through an orifice made on the vessel itself. In chapter 2 it will be seen that the transient duration is related with the discharge being conducted through a pipe of length L .

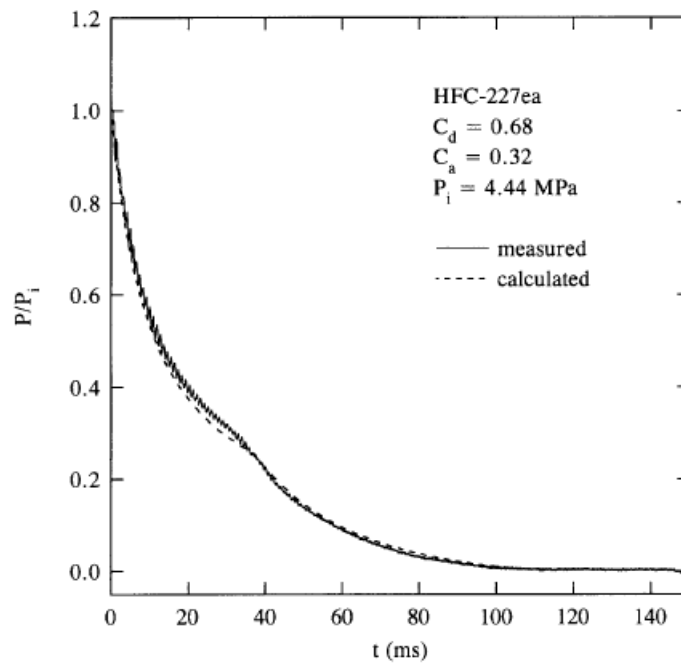


Figure 1.16: Theoretical and experimental discharge pressure for HFC-227ea (after [PYG⁺94]).

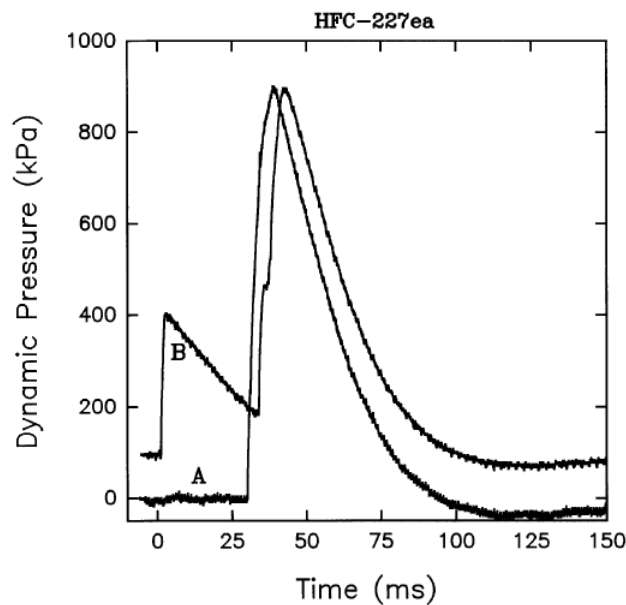


Figure 1.17: Near-field dynamic pressure for releases of HFC-227ea. Trace B is offset by 100 *kPa*. (A) 476 *g*, release pressure 4.45 *MPa*; (B) 489 *g*, release pressure 4.41 *MPa* (after [PYG⁺94]).

[Coo93] is a research work very much in the line of [PYG⁺94] above, although it studies the agent R22, with slightly different properties than HFCs like HFC-227ea. As remarked above, the discharge treatment is done under the assumption of steady compressible flow. Also [PYBG93] develops this same issue from an experimental point of view for various HFC, although it is less exhaustive than [PYG⁺94].

[Wys96] also reports the discharge process of clean agents, including HFC-227ea. He uses Bernoulli's equation in the Hesson's adaptation form, and does not consider explicitly the transient nature of the dynamics, although most of the work is experimental rather than theoretical. Pressure data is provided

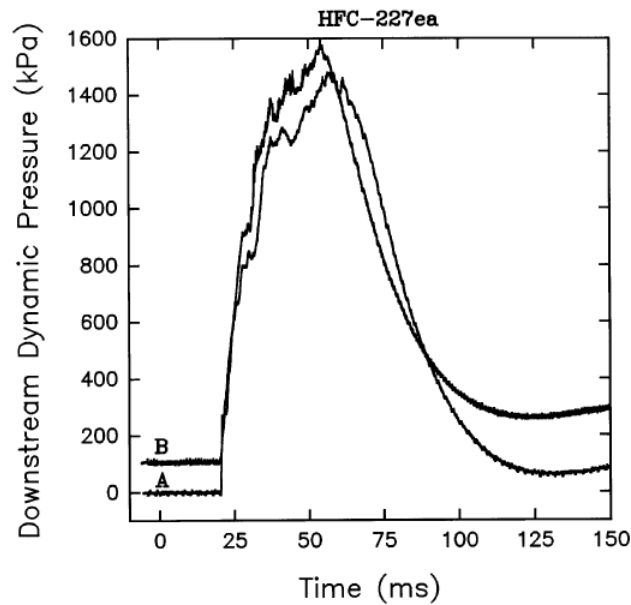


Figure 1.18: Far-field dynamic pressure for releases of HFC-227ea. Trace B is offset by 100 *kPa*. (A) 489 *g*, release pressure 4.41 *MPa*; (B) 476 *g*, release pressure 4.45 *MPa* (after [PYG⁺94]).

for both, inside the vessel and at the nozzle (see figure 1.19). The pressure curves for the discharge of HFC-227ea show the time-decreasing pressure drop between cylinder and nozzle. This standing decrease is interrupted on two occasions: the peak in cylinder pressure at 2.5 *s* that indicates the beginning of flashing, in which the agent's flow changes from single-phase to two-phase; and the peak in the nozzle pressure trace at 9.6 *s* indicating a transition from two-phase flow to vapour flow. Note the pressure at the nozzle changes slowly, except after pure vapour flow.

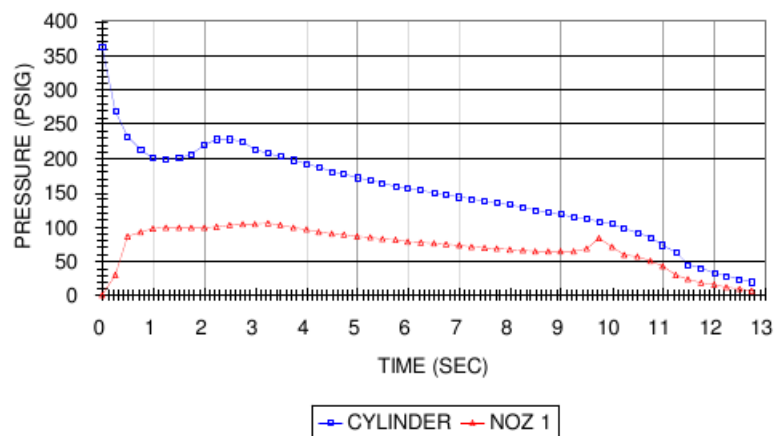


Figure 1.19: Pressure inside the cylinder and at nozzle for HFC-227ea discharge (after [Wys96]).

[DFF⁺94] presents a study of the clean agent's discharge process, based on the model developed by [EGK⁺84] for Halon 1301. It offers a mathematical model for the phenomenon, but it does not take into account a transient dynamic equation, but rather considers quasi-steady flow. The agent is assumed to flow in liquid, two-phase and vapour modes. It reports interesting experimental pressure data for the first few seconds of process, displayed in figure 1.20. In this figure the flow has been divided into five distinctive sections (see the four vertical dashed lines).

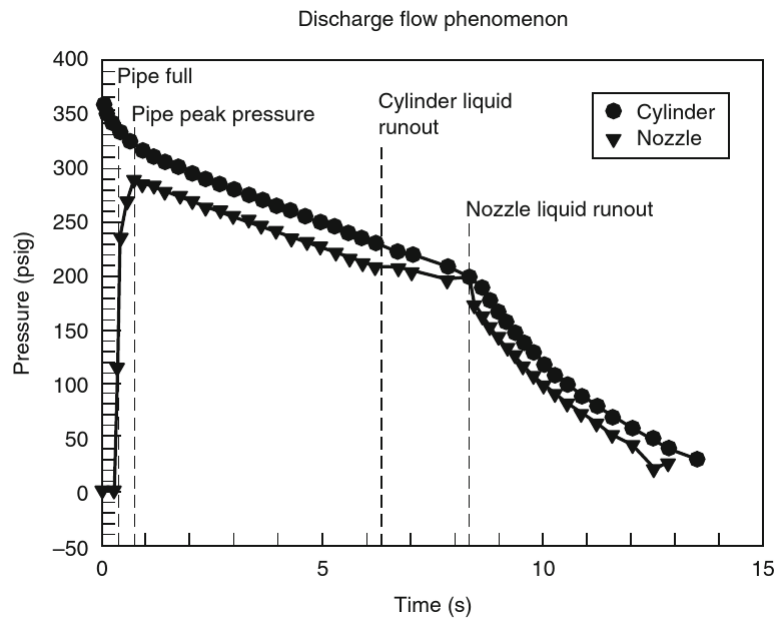


Figure 1.20: Pressure inside the cylinder and at nozzle for clean agent discharge (after [DFF⁺94]).

[ZW96] develops a mathematical model based on mass and energy conservation, in which no transient dynamic equation is considered. The paper shows curves of HFC-227ea concentration versus time, both from analytical calculations and from actual test results. The agreement is good in the long term, even though no comparison is made between experimental and theoretical results in the first few seconds. Actually, the discharge concentration curves are modelled as straight lines. A theoretical pressure curve is offered, but it corresponds to room pressure, not to pipe flow pressure. Therefore, scarce information is offered about the discharge's dynamics.

[BGH⁺94] measures the discharge process of HFC-227ea, and other clean agents, in an experimental set-up, and compares the results with a computer model named Transient Flow Analysis (TFA), which is not described in the paper. TFA is presented and explained in [KLG94], which describes the computer model used to calculate the discharge process, but the program and its numerical output are not shown on the paper. TFA is the result of a modification to an already existing computer program for modelling Halon 1301 discharge, described in [CHM92]. Figure 1.21 displays the qualitative mass flow rate for Halon 1301 predicted by [CHM92]. In Chapter 2 it will be developed a velocity curve qualitatively similar to that presented in figure 1.21.

TFA is further explored in [BGF⁺95], which studies the discharge of HFC-227ea and HFC-23 in large piping distribution systems, with several cylinders (4 to 14) installed in battery. The discharge pressure is monitored in up to 9 nozzles, and also inside the pipe. TFA's predicted results are compared to actual measurements. Unfortunately, no mathematical model is presented in this work, nor any graph similar to figure 1.21.

The flow within pipes during discharge is studied in [CGY94], which characterises the flow as transient and two-phase. The experimental set-up includes a high-speed camera that records the liquid evolution inside the pipe, and the authors test the agents HFC-227ea and Halon 1301. The paper displays the pictures of the flow from the beginning fractions of first second, although only presents experimental curves with no theoretical predictions nor computer programs. Pipe pressure traces, corresponding to a transducer located some 2 m downstream the release valve, show an interesting transient spike at around 700 ms, probably related with N_2 flowing alone in the pipe.

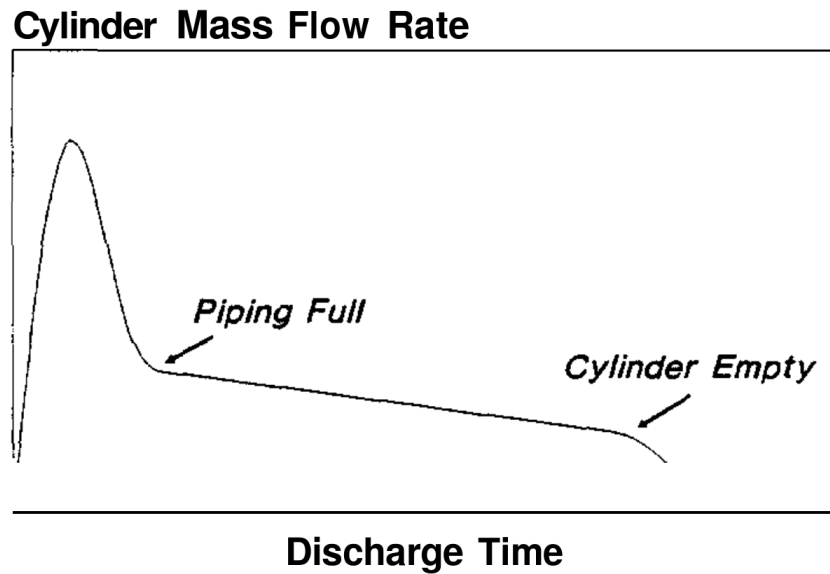


Figure 1.21: Qualitative mass flow rate for discharge of Halon 1301 (after [CHM92]).

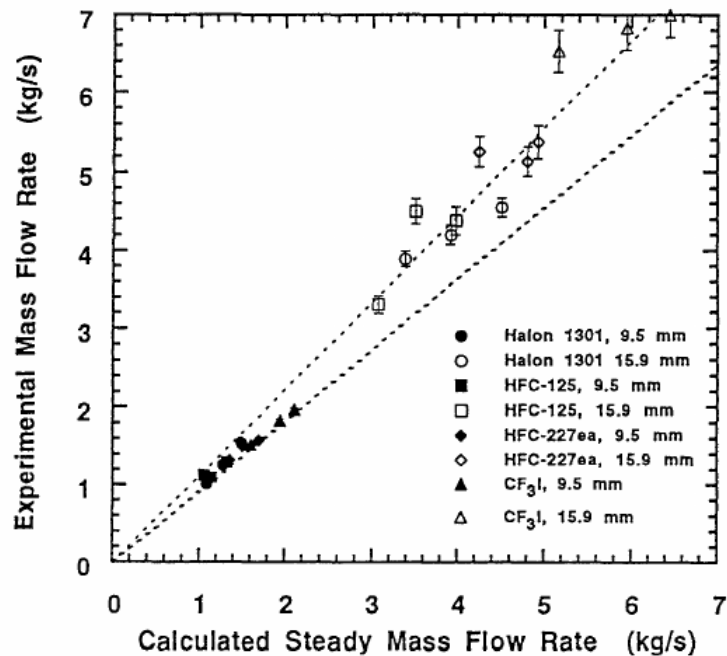


Figure 1.22: Experimental vs. calculated steady mass flow rate (after [CYK⁺95]).

Using the same experimental set-up as in [CGY94] above, [CYK⁺95] studies the discharge process after the agent exits the pipe and is released into test engine's nacelles. Several extinction agents are employed in the experiments, and the pressure traces are presented for a number of tests. Figure 1.22 shows the deviation of the actual experimental results from the calculated steady state mass flow rate, according to the model the authors were using. Such model, though, is not offered explicitly in the paper, which just mentions its source: the model for discharge of Halon 1301 developed in [EGK⁺84]. The observed deviations measure the limitations of a steady state flow model to correctly predict the experimental data. The transient spike in the pipe transducers described above is also present in this paper, surely due to flow of N_2 alone as the liquid agent runs out of the vessel.

A computer model for the discharge of several agents (water, Halon 1301, CO_2 , HFC-227ea and HFC-125) is profusely described in [TPC⁺00]. The program bears the name of FSP and it represents an improvement to the computer model presented in [EGK⁺84]. It covers transient phenomena and two-phase flow. The computer model is tested against the same experimental apparatus used in [CGY94] and [CYK⁺95], providing acceptable results when the predicted curves are compared with the actual experimental data.

Also transient experimental phenomena are studied in [WC96], although it treats inert agent IG541⁹, not Haloalkanes. It is mentioned herein for its study on pure gas discharge, without consideration for flashing or two-phase flow. Some experimental curves are offered which could be compared with those corresponding to HFCs.

A different approach to the discharge problem is offered in [SP95]. It presents a mathematical model of discharge to a control room, and shows the results of experiments measuring the pressure variation within a 34 m^3 leak-tight room (i.e. a room with a one-way vent that releases excess pressure, but is leak-proof at negative pressure), which undergoes the discharge of agent HFC-227ea. The pressure is monitored for relatively long time (some 30 s), compared to the actual discharge's time. The agreement between model and experiment is noteworthy. A remarkable outcome of this study: the pressure within the room turns negative (below atmospheric) for some time after discharge (see figure 1.23). Also the HFC-227ea dispersion throughout the room is observed and monitored.

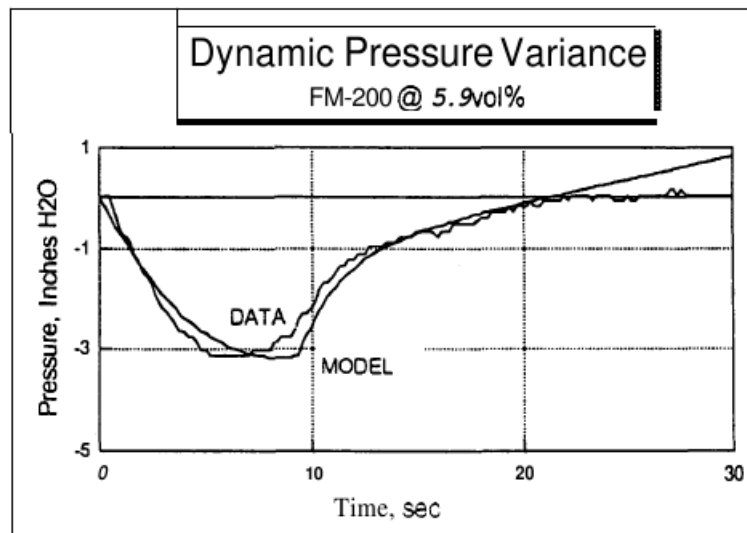


Figure 1.23: Model/measured pressure in 34m^3 room upon HFC-227ea discharge @5.9% (after [SP95]).

The same negative pressure in rooms suffering HFC-227ea discharge is reported in [RFS05]. This work offers a comparison between the room pressure curves of two extinction agents: inert gas IG541, which is always in gaseous state along this process, and clean agent HFC-227ea, which exhibits a flashing behaviour and vaporises entirely after a few seconds. Figure 1.24 displays a *positive* pressure within the room at every instant after IG541 discharge, while figure 1.25 shows alternatively positive, *negative* and again positive room pressures after HFC-227ea discharge. The paper also compares the actual test

⁹IG541 is a blend of inert gases, Ar 40%, N_2 52%, CO_2 8%, and it quenches the fire suffocating the flames, that is, removing oxygen from the combustion reaction. This agent is stored at very high pressures (normally 200 or 300 bar) and is never in liquid state within the cylinders.

results with the predictions of a computer model, even though no details are given thereof (see figure 1.26).

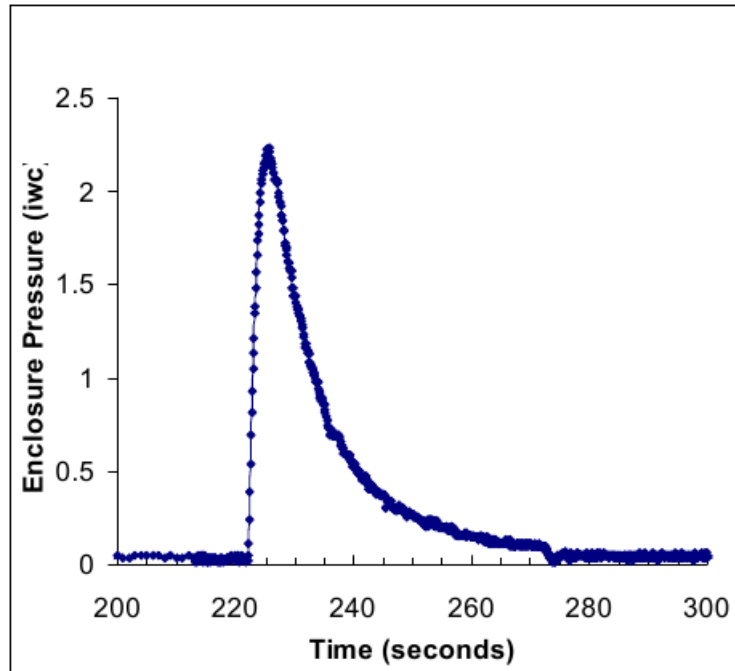


Figure 1.24: Room pressure during the discharge of 30.9% V/V IG541 (after [RFS05]).

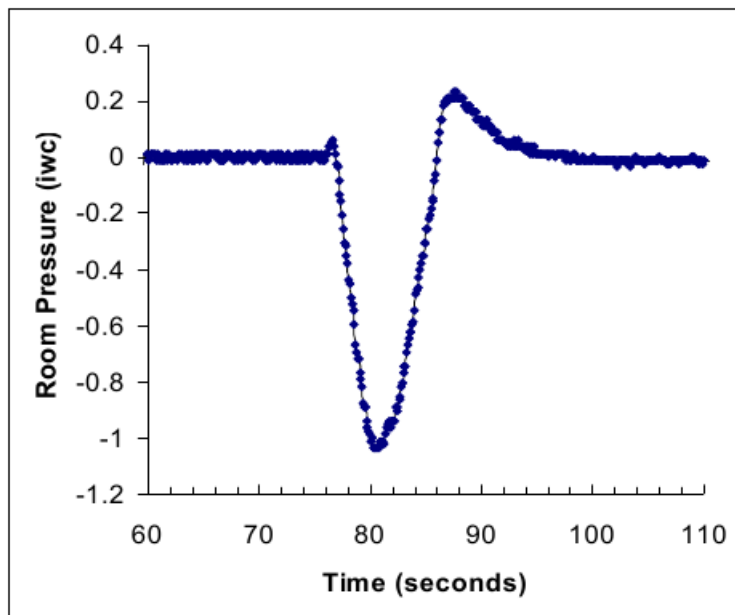


Figure 1.25: Room pressure during the discharge of 6.1% V/V HFC-227ea (after [RFS05]).

1.4 Extinction Mechanisms for FK-5-1-12

The main mechanism used by FK-5-1-12 (and other clean agents) to extinguish a fire is the sudden temperature reduction caused in the surrounding air when the agent vaporises as it floods the protected

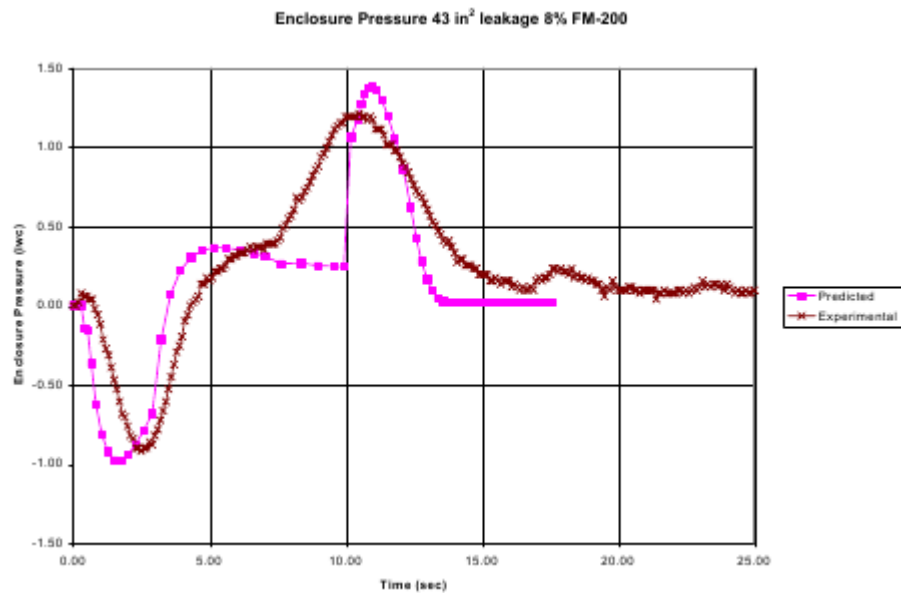


Figure 1.26: Predicted/measured enclosure pressures for 8 s HFC-227ea discharge @ 9.8% (after [RFS05]).

room. This cooling effect is supposed to bring the room's temperature below the flash point of the pyrolysed material, thus quenching the fire as long as the heat source be not powerful enough to overcome the temperature descent. That kind of extinguishing mechanism will now be studied in detail with the aid of figure 1.27, which shows the pressure-enthalpy diagram of agent FK-5-1-12. Some rule-of-thumb basic calculations will be performed, to serve as estimates without any pretension of accuracy. The calculations follow the guidelines expressed in the regulation EN 15004-2:2008. Hopefully, the practitioner Engineer will find them useful, and is invited to repeat them any time for specific applications in FPE. Similar rules are applicable to other clean agents, and the results would provide an estimate of their quenching capacity.

Assume a mass of agent FK-5-1-12 is kept in cylinders with a pressure of 25 bar, although that might change depending on the system's manufacturer. Assume also the cylinder temperature is 20°C, just as the room temperature. While in the cylinder, the agent's state is represented by the point *A* in figure 1.27. Assume now a fire is detected, usually in a very early stage, and as a result an automatic command is issued to initiate the agent's release to the room. Upon discharge, the agent's state follows the thermodynamic path from *A* to *B* in figure 1.27. The process is roughly isenthalpic and isothermal, and it goes on until all agent reaches the atmospheric pressure. Note that at point *B* the agent FK-5-1-12 has a specific enthalpy around 65 kJ/kg, is in liquid state and still needs some additional 30 kJ/kg to begin to boil (point *C*), because at $p = 1 \text{ bar}$, $T = 49.2^\circ\text{C}$ vaporisation begins at around 95 kJ/kg. The remarkable fact is that, thermodynamically, FK-5-1-12 should be in liquid state at $p = 1 \text{ bar}$, $T = 20^\circ\text{C}$, except the fraction needed to generate the agent's vapour pressure. Actually, at 20°C the vapour concentration of FK-5-1-12 in air can raise up to 32% in volume before reaching saturation. Compared with water, the combination of a relatively low heat of vaporisation (some 25 times less) and a high vapour pressure (some 12.7 times more), causes FK-5-1-12 to evaporate more than 50 times faster than water. Besides, the mixture (air)+(FK-5-1-12) has a much higher heat capacity than air alone, thus removing more heat from fire for each additional degree of temperature increase.

In order for FK-5-1-12 to boil completely at atmospheric pressure, point *D* in figure 1.27, the liquid agent in state *C* needs some $185 - 95 = 90 \text{ kJ/kg}$ of additional energy (88 kJ/kg according to table 1.1). The balance for some agent just discharged (point *B*) is thus: 30 kJ/kg to start vaporising (point *C*) and

88 kJ/kg additional energy to fully boil (point *D*). That is the maximum margin the agent possesses for rapidly removing heat from the fire, although eventually it would be less than that.

Some energy is also contributed by the agent's high velocity upon discharging. Assuming perfect conditions that enable Bernoulli's principle to be applicable to this problem,

$$\frac{1}{2}\rho v_1^2 + p_1 + \rho g h_1 = \frac{1}{2}\rho v_2^2 + p_2 + \rho g h_2$$

with $h_1 = h_2$, $v_1 = 0$, $p_2 = 1 \text{ atm}$, $p_1 - p_2 = 25 \text{ bar}$ and $\rho = 1600 \text{ kg/m}^3$, the final velocity v_2 is obtained

$$v_2 = \sqrt{\frac{2(p_1 - p_2)}{\rho}} \approx 177 \text{ m/s}$$

contributing with an additional kinetic energy of 15.6 kJ/kg. This kinetic energy can only be extracted from the liquid's initial enthalpy. Thus, taking it into account the discharge path would not really be isenthalpic, but rather it would go from state *A* to state *B'* in figure 1.27. Note *B'* is offset 15.6 kJ/kg from *B*. In the end, the agent's kinetic energy serves to increase the surrounding air's internal energy through molecular collisions, thus it balances out and can be ignored in what follows.

Upon reaching the nozzle the agent impacts with its sharp edges and converts itself into a spray of myriad micro-droplets. FK-5-1-12 surface tension is seven times lower than water's; therefore it creates much smaller droplets for the same kinetic energy. With much-increased surface for heat transfer, due to atomisation, the agent's vaporisation advances even faster. Once the discharge is over at atmospheric pressure, most of the agent will either be vaporised (up to 32% in volume) or forming micro-droplets floating in the protected room's air, ready to contribute to heat removal through further vaporisation. In the process it will have removed from the fire a sizeable fraction of the $30 + 88 \text{ kJ/kg} = 118 \text{ kJ/kg}$ available enthalpy.

As an exercise, it will be calculated the maximum temperature descent the agent could create in a mass of air. The air's specific heat is 1.005 kJ/kg K, and it is reasonably constant from 40°C to -50°C. Therefore, each kg of FK-5-1-12 can decrease the temperature of a kg of air up to

$$\frac{118 \text{ kJ/kg}}{1.005 \text{ kJ/kg K}} = 117.4 \text{ K}$$

Of course, this is an absolute maximum not reachable in practice, but it provides an estimate of the agent FK-5-1-12's cooling capacity.

The exercise could still be taken further. Assume a typical fire extinction application in a 100 m³ room, with a design concentration of 5.5% in volume. The mass of agent FK-5-1-12 needed for such a room volume, according to [NFPO8], is given by

$$W = \frac{V}{s} \left(\frac{C}{100 - C} \right) [\text{kg}]$$

with *C* the volumetric design concentration in air, *V* the room's volume and *s* the specific volume of superheated FK-5-1-12 vapour given approximately by (see EN 15004-2:2008 or [NFPO8])

$$s = 0.0664 + 0.0002741 T [\text{m}^3/\text{kg}]$$

with *T* the temperature in °C. Assuming $T = 20^\circ\text{C}$ then $s = 0.07188 \text{ m}^3/\text{kg}$ and $W = 80.97 \text{ kg} \approx 81 \text{ kg}$. Since $\rho_{\text{air}} = 1.204 \text{ kg/m}^3$ at 20°C, a room of 100 m³ contains 120.4 kg of air, resulting in 1 kg of

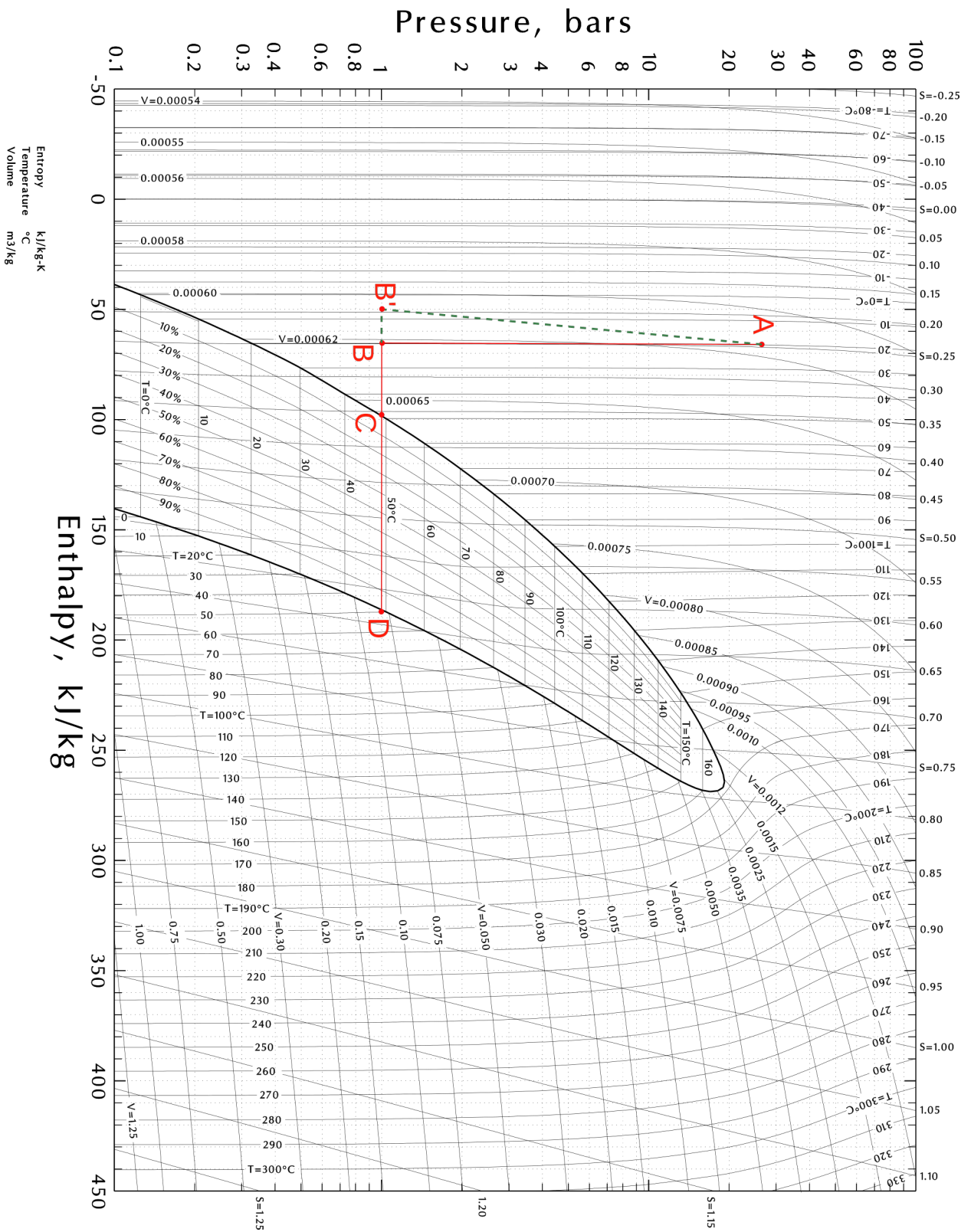


Figure 1.27: Thermodynamic path followed by FK-5-1-12 to extinguish a fire.

FK-5-1-12 for each $1.49 \text{ kg} \approx 1.5 \text{ kg}$ of air. Repeating the previous calculation, the 81 kg of agent could, as an unreachable maximum, cool the 100 m^3 room some

$$\frac{81 \text{ kg } 118 \text{ kJ/kg}}{120.4 \text{ kg } 1.005 \text{ kJ/kg K}} = 79 \text{ K}$$

This sort of simple (and not entirely accurate) calculation suggests how the agent acts in order to quench a fire. Obviously, the release of FK-5-1-12 in a room modifies the thermodynamic conditions within such space, and this variation affects dynamically to the enthalpy interchange between agent, air and heat source, rendering the result of 79°C out of proportion. However, even more than halving this figure, a temperature drop of 30°C ought to be sufficient to halt the fire, because the surrounding temperature would be well below the flash point. Therefore, at the prescribed concentration the agent FK-5-1-12 holds enough cooling power to extinguish most fires detected at a sufficiently early stage.

1.5 Change of Phase During Discharge

A similar analysis to that carried out in last section will now be performed for the class of clean agents that are gaseous at NTP conditions. Clean agent HFC-227ea will be taken as a representative of such class, whose pressure-enthalpy diagram is shown in Figure 1.28.

The main problem for characterising the flow of HFC-227ea inside the discharge pipe is simply this: during the discharge process, at some given time, the initially liquid agent will begin to boil as it is convected through the pipe. That causes a two-phase flow inside the pipe, which will steadily transit from pure liquid to pure gas. The closer to the nozzle, the more gaseous the flow would be. Depending on the length of pipeline and the discharge time, the vapour quality¹⁰ of the stream could be as high as 1 by the time the agent reaches the nozzle, or it could be negligibly small for short pipes or short discharge times. In the second case, a single-phase discharge flow model would describe the agent's flow with reasonable accuracy, provided a clear criterion could be established to determine when a *short* pipe or time are short enough.

Two-phase flows complicate extraordinarily the hydraulic calculations for agent's release, since no detailed information is available regarding the pressure and temperature at each cross-section of the discharge pipe. Moreover, the vaporisation effect interacts with the flow's temperature (decreasing) and pressure (increasing), at a rate which is also influenced by the interchange of heat with the environment through the metal pipe walls. [HP58] is one of the first works studying the two-phase discharge problem. Devoted exclusively to CO_2 , the paper offers a method to determine the flow rate through nozzles, whose equations are based on the MSc and PhD thesis of Hesson. No transient dynamics was considered in [HP58], and only steady state two-phase flows are regarded. Since then, the so-called Hesson method has been thoroughly used to calculate two-phase discharge flow of CO_2 . Later [Wil76] improved the Hesson method to make it applicable to other extinguishing agents, namely Halon-1301. The result is known as the Hesson-Williamson method and is the standard for calculating two-phase flow. The equation for Halon-1301 is

$$Q = \frac{1.013D^{5.25}Y}{L + 8.08D^{1.25}Z} \quad (1.1)$$

¹⁰The vapour quality of a two-phase mixture is defined as the ratio of the mass of vapour to the total mass of the mixture:

$$\chi = \frac{m_{\text{vapour}}}{m_{\text{total}}}$$

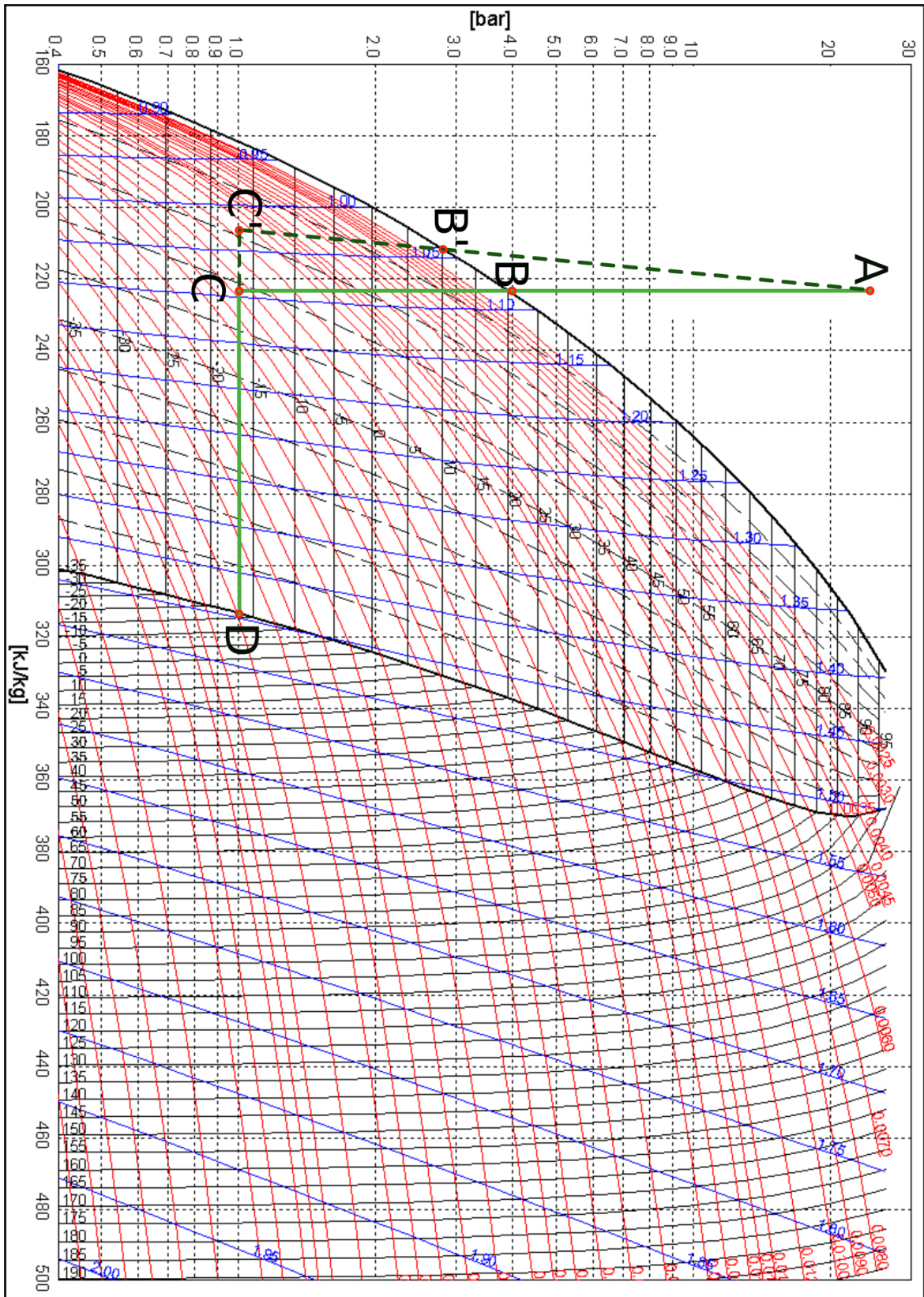


Figure 1.28: Thermodynamic path followed by HFC-227ea to extinguish a fire.

where Q is the flow rate [lbs/sec], D is the inside pipe diameter [in], L the equivalent length of pipe [ft], and Y and Z are factors depending upon the density and line pressure of Halon-1301. Note equation (1.1) has no provision for transient flows. [Gra85] uses the Hesson-Williamson method to develop a computer program to calculate the hydraulics of two-phase discharge flow for Halon-1301. [Wys96] introduces corrections in the Hesson-Williamson method in order to make it applicable to HFCs.

The path followed by HFC-227ea in the pressure-enthalpy diagram during the discharge process is illustrated in figure 1.28. Initially, the clean agent is contained in cylinders at 25 bar and 20°C (point A), in liquid state. Upon release, the liquid agent begins to flow through the pipe until it reaches the state designated by point B , since so far the process could be considered isenthalpic and isothermal. At point B the liquid agent begins to vaporise, and still has 4 bar of remaining pressure drop before reaching atmospheric pressure (which is attained at the nozzles). At point C the agent, a mixture of liquid and vapour, reaches the nozzle at atmospheric pressure and undergoes no further expansion. It could be safely assumed that the transit from B to C is a vertical straight line, that is, an isenthalpic process, because the potential discrepancy would be due to the heat interchanged with the surrounding pipe: since the flow progresses very fast, it would have little time to receive any significant heat input from the pipe's walls. Besides, the pipe's walls present a relatively small surface to interchange energy. The heat needed for vaporisation is obtained mainly from the liquid matrix, which decreases abruptly its temperature (point C is some -17°C , to be compared with the room's 20°C).

Should the pipe be very long, that assumption may not be correct and the agent would reach the nozzle with a vapour quality approaching 1. The final journey, from C to D , would normally be traversed while the agent is already discharged in the room. Note the full vaporisation of clean agent is not attained instantly: from B to C and then to D would rather need some time since it must gather up energy. Nevertheless, upon discharge at the nozzles the remaining liquid agent disintegrates into micro-droplets, thus increasing dramatically the available surface to interchange heat, and the rate of vaporisation.

At this point, it is necessary to take into account the agent's kinetic energy during the discharge, estimated in last section as some 15.6 kJ/kg . Such kinetic energy is extracted from the agent's initial enthalpy, and thus the thermodynamic path it describes would rather be from A to B' and to C' . B' has a pressure of less than 3 bar, while C' is offset from C in 15.6 kJ/kg . Note C' has a higher proportion of liquid phase than C , meaning that a larger fraction than initially estimated would be liquid upon reaching the nozzle, with a lower vapour quality. Or in other words, that the flow would be less two-phase than originally thought over.

Therefore, at least five are the facts that would lead to consider the clean agent's discharge flow as quasi-single-phase within the pipe, provided the pipe be not too long:

- i. The flow velocity is very high during the first instants of the discharge, typically well over 150 m/s . Thus, the agent has practically no time to remove heat from the room while rushing within the pipe, and the necessary heat to boil is mainly extracted from the liquid itself, delaying the vaporisation¹¹.
- ii. During the first instants of discharge the pressure gradient between cylinder and nozzle is very high. Thus, the 4 bar associated with point B in figure 1.28 (or better still, the 3 bar of point B') would be attained relatively near the nozzle, which is at atmospheric pressure. This effect further

¹¹This is a desirable effect, since the pipe might run through rooms not affected by fire, and nobody wishes to cool down those adjacent rooms. It is generally a bad idea to cool down the pipe itself. The clean agent is best used when all its cooling power is developed *after* the nozzles.

delays the beginning of vaporisation, which could occur at short distance from the nozzles. The above possibly would not be true if the pipe has many bends and bifurcations.

- iii. The available surface to interchange heat with the surroundings is relatively small: the pipe's wall. Heat flux ought to be very high to transport a significant amount of heat through such walls, but the flow has no time since it is rushing down the pipe. Besides, condensation of ambient water vapour on the outside pipe-wall would hinder the expected heat flux.
- iv. The agent's kinetic energy displaces the state attained at the nozzle from C to C' , some 15.6 kJ/kg closer to the liquid side. Thus, a lower fraction of vapour is present at the nozzle.
- v. A metastable liquid state could well occur in those conditions, thus further retarding the beginning of vaporisation. The point C in figure 1.28 would probably not be too far from the liquid spinodal line of HFC-227ea,¹² and point C' would do even better (see figure 1.29 obtained from www.thermalfluidscentral.org). Should that be the case, the liquid would probably begin to boil abruptly upon colliding with the nozzle's sharp edges, out in the open air. This situation corresponds to the maximum efficacy of the clean agent, since all the vaporisation develops in the air surrounding the fire, thus extracting the maximum possible heat therefrom and decreasing its temperature.

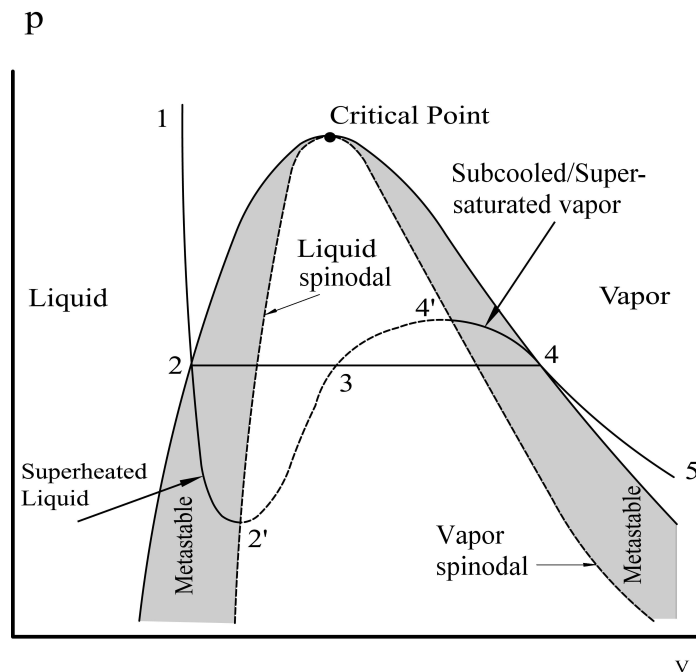


Figure 1.29: Spinodal lines for a simple compressible substance.

From those rough estimates made above it could be concluded that, at least during the first few seconds of agent's discharge, the error incurred by considering the discharge flow quasi-single-phase might be acceptably low. Therefore, the models that are going to be developed in the coming Chapters

¹²Spinodal lines and metastable states are conveniently explained in [SL93]. When a substance is changing phase, frequently the initial phase reaches a metastable state and extends its life beyond theoretical conditions, that is, the expected phase change is delayed until certain conditions are met. At some given points, defining the spinodal line, the phase changes abruptly to the expected mixed state. This particularly occurs with processes that require the presence of nuclei to start up, like condensation or boiling. Such nuclei might not develop exactly at the phase space point they were expected to.

would probably find application to HFC-227ea discharge flow, and to other similar Haloalkanes as well, provided the conveying pipeline is straight and short enough. That would significantly simplify the resolution of the hydraulics problem of such clean agent's discharge.

1.6 Conclusions

As a conclusion, in the realm of FPE there are abundant works, articles, papers, technical reports, etc. concerning experimental and empirical aspects of clean agent discharge; a few studying the steady state hydraulics of the discharge process, both single- and two-phase; but no one (to the author's knowledge) dealing with its transient behaviour from a theoretical perspective, derived from First Principles. In the next Chapters, some references will be given regarding transient flows, although they were not developed for fire extinguishing applications, or so it would seem upon reading them.



Figure 1.30: Extinction system with very small length of discharge's pipe.

Thus, it would appear suitable that Hydraulic and Hydrodynamic models be developed and proposed to the FPE Community, as potentially valuable tools for improving the calculations and design of actual clean agent fire suppression systems. Such models will be presented in this Dissertation, in the Chapters that follow. It might even be possible, perhaps, that those models will prevent any Engineer from ever designing a fire suppression system like the one shown in figure 1.30, whereby the agent's discharge is carried out with no significant length of pipe, thus making it possible that liquid at extremely high speed and cold temperature can impinge directly on people standing by.

Chapter 2

1D Analytical Hydraulic Model with Steady Wall Friction

2.1 Introduction

Within the realm of FPE an useful and frequent technique to quench just-started fires in closed rooms is to flood them with countless droplets of a liquid agent which rapidly vaporises and upon that phase change removes heat from the fire. The detailed description of such process includes the study of the discharge's hydrodynamics through the piping, the distribution of ejected droplets within the protected room, the heat transfer mechanisms that lead to agent's vaporisation, and the potential thermo-chemical reactions that causes the extinction of the fire. In this Dissertation only the first of these processes is considered.

This Chapter is devoted to provide an analytical model, and the attached dynamic equations, which will permit the description, understanding and prediction of hydraulic ¹ events in the free discharge process of a highly pressurised liquid agent into atmosphere. It would also be expected that this model open up the possibility of incorporating the results obtained therefrom, into the actual regulations and standards related to this very active field of FPE.

The Analytical Hydraulic Model (AHM) is a one-dimensional model and its development is based on the much studied turbulent flow in pipes (see, for instance [Tan64], [Tow76] or [Dur08], just to name a few). The turbulent nature of the flow is represented in the AHM by a single parameter, the friction factor f to be introduced later, and it must be admitted that turbulence is far too complex to be condensed in such a simple way. Engineering experience shows that under the simplifying assumptions of one-dimensional steady state flows, the friction factor provides convenient means for calculating the relevant variables in Hydraulics: pressure drop and flow.

The situation is noticeably different with unsteady flows. They are not so well studied as steady state flows, and the wide difference in the number of available references ought to prove this assertion ². Beginning with the somewhat forgotten work of [Szy32], the research of unsteady flows has progressed slowly, and the majority of publications are related with experimental studies. [Zie66] was a pioneering theoretical study of unsteady frequency-dependent flow, which has later served as a reference for a

¹This Dissertation distinguishes between *hydrodynamic models* and *hydraulic models*. See footnote 3 in page 3 and section 2.3.1.

²There are a number of publications dealing with the type of transients flows occurring in water-hammer-like applications. Such flows will not be considered herein.

wide range of publications on unsteady friction. The book [Tel81] represents one of the first systematic and comprehensive approaches to unsteady flows, including analytical results and computational modelling. Some interesting works centred on theoretical or analytical aspects of unsteady flows are those of [GM84] and [MY10], although they do not consider turbulence. Within the realm of Hydraulics, [Jov13] also presents some practical results regarding the sudden discharge of liquid from a pressurised tank, using simplified 1D models.

A group of works regard the discharge process not only from the perspective of Fluid Mechanics, but rather from the Thermodynamics point of view. The sudden pressure reduction associated with the discharge renders many liquids unstable, the flow becomes superheated and the change of phase takes place, often violently. One of the first works to study this transient situation is [KE81], which considers the two-phase flow occurring when a liquid is rapidly depressurised. The author develops a computer model and carry out experiments to validate it, with scarce success. More thorough is the work of [Val98], which considers the discharge of a pressurised liquid producing a choking two-phase flow. The author develops two alternative mathematical models: a homogeneous model and an Equal Velocity Unequal Temperature (EVUT) model. Then designs experiments to validate them, with remarkable results. Figure 2.1 shows the prediction for the mass flow rate at the beginning of the discharge.

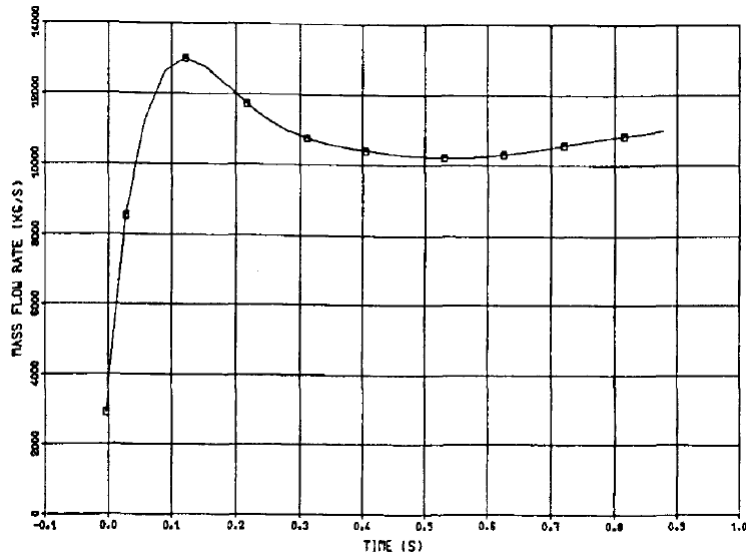


Figure 2.1: Transient mass flow rate for liquid discharge (after [Val98]).

[OMERO3] studies the transient flow obtained when a pressurised pipeline is punctured. The authors develop a computer model which is then compared with data taken from actual oil pipeline tests. The computer model is further improved in [MORO6], considering transport equations for the main thermodynamical quantities. [Den09] is a PhD Thesis after the results and previous works of [OMERO3] and [MORO6], studying the transient flow following a pipeline rupture. It develops a CFD program to simulate highly transient flows, and it offers the results of such simulations for a number of interesting cases, notably the discharge of pressurised fluids through orifices. Along similar lines, [NBZR10] presents a computer model for the transient gas flow in a pipe after a localised rupture. The paper considers compressible single-phase gas flow, disregarding flashing phenomena. Other references with liquids producing two-phase flows have already been mentioned in the previous Chapter.

The nearest set of references for the subject developed in this Dissertation is that provided by members of Tallinn Technical University, who have conducted a very comprehensive research on start-up

accelerated flows in pipes. Some of the publications that have relationship with the theme being studied herein are [ALSL81], [KAO6], [KLA⁺11], [Ann11], [L⁺12] and [AKSA13]. [ALSL81] provides the theoretical background the other works are based thereon. [KAO6] identifies the transition to turbulence in start-up flows, which are characterised analytically. [KLA⁺11] will be cited later, since it presents a velocity curve qualitatively similar to the one describing the agent's discharge phenomenon to be developed here. [Ann11] and [AKSA13] present a remarkable set of velocity profiles, both analytical and experimental, for start-up pipe flow subjected to moderate accelerations. The present research departs from those cited works in some key aspects: it considers a pipe initially empty of liquid, the flow progresses with the liquid-air interface within the pipe, the range of velocities and Reynolds numbers is orders of magnitude larger and, above all, the accelerations undergone by the liquid are enormously greater than those reported by the Tallinn's team. Besides, the analytical approach to the problem being considered herein is different from that reported in the above references: the 1D AHM dynamic equations developed in this Chapter and, specially, the 3D General Analytical Solution (GAS) presented in section 3.4.2, follow different guidelines.

Accelerated start-up flow from rest is also studied experimentally in [MKM78] and [Mos89], although for moderate Re ($5 \cdot 10^3 \sim 5 \cdot 10^4$). [MKM78] obtains mean velocity profiles which show a considerably smaller gradient at the wall than those provided by [Ann11]-[AKSA13], leading to lower wall-shear stress. Both measure the ensemble average velocity profile across the pipe.

Moving now to the field of FPE, the hydraulic problem of the discharge of a liquid agent has been approached before (see, for instance, [Coo93]), but the treatment found in the literature has usually been from a steady state perspective. Such a fast process as the sudden agent's discharge, which normally elapses less than 10 s to be completely depleted, although most of the mass is released in the first few seconds, could not be accurately described with the equations of steady state hydraulics. Instead, full transient regime equations must be used, which will allow for new and interesting hydrodynamic behaviour to emerge. This is what has been attempted herein, hopefully with insight enough to permit further research and development in this field.

This section develops a mathematical model for a problem which is of real interest in the realm of FPE. And it does so from the transient hydraulics point of view. It makes no attempt to describe the effectiveness of agents in extinguishing fires: as a matter of fact, the model ceases to explain the phenomenon as the agent exits the discharge's pipe. Although the simplifying assumptions could be considered somewhat ideal for certain practical applications, the model is intended to fill a gap existing in present literature: to provide for a simple but fully analytical hydraulic model, which might allow for explanation, estimation and prediction of fast discharge phenomena.

The model could be used for a number of extinction clean agents, although it will be particularised for FK-5-1-12 (commercial name Novec-1230), since it fits aptly into its discharge behaviour. The model does not take into account the agent vapourisation within the pipe, therefore it would only be valid for agents that undergo low vapourisation whilst transiting from the vessel to the discharge nozzle into the room. Agent FK-5-1-12 fully presents the desired behaviour, whereas agents like HFC-227ea, (commercial name FM-200), which is liquid within the pressurised vessel but is a gas if equilibrium is reached in the normal conditions of a room, only partially fulfil that condition if the transit from vessel to nozzle is sufficiently fast. With due changes to the main transport quantities (viscosity, density, surface tension, etc.) the AHM could be applied to other extinction agents.

Although simple, the proposed model still takes into account most aspects that are relevant for this application:

- Friction.
- The expansion of an ideal gas as the driving force which sets the liquid into motion.
- The liquid's finite volume within the vessel.
- The phenomenon's very fast nature and the transient treatment of it.

In actual FPE applications through the use of agents discharged to protected rooms, the nozzles constitute a narrowing in the flow intended to vaporise and disperse the agent into the room, rather than hamper its release. In other words, the hydraulic diameter of the joint set of holes drawn in the nozzle is not much smaller than the pipe diameter. Therefore, there is not a great error in assuming that the flow proceeds along an open pipe, with no nozzle at the end. Since the present study is only concerned with the hydrodynamic behaviour of the fluid *within* the pipe, and does not consider what happens to the agent after exiting the pipe, the assumption of a free discharge through an open tube without nozzle avoids the complication of having to characterise the discharge properties of each type of nozzle.

2.2 Presentation of the 1D Model of Discharge of an Incompressible Fluid

This section is devoted to study the free discharge process of an incompressible liquid which is kept at rest within a pressurised vessel, and suddenly released to the atmosphere until exhaustion. In FPE applications the initial pressure p_0 is somewhat moderate (some 25 ~ 50 bar), and is maintained by an ideal gas (N_2) which is also compressed within the vessel.

At time $t = 0$ a very fast valve is suddenly opened and the liquid is rapidly discharged to the atmosphere through a pipe of length L and constant diameter $D = 2R$. The expansion of the ideal gas from p_0 to atmospheric pressure p_∞ is the agent which sets the liquid into rapidly accelerating motion (see figure 2.2).

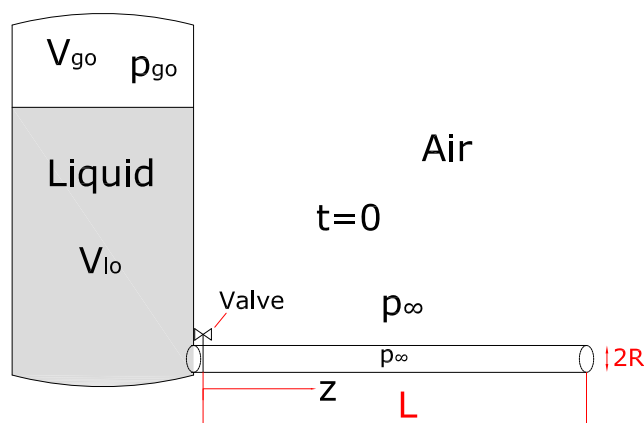


Figure 2.2: Initial state of the system.

It might be argued that this model lacks a nozzle at the pipe's outlet, as it is customary in fire extinction applications with clean agents. The tube in the model is not ending with any narrowing that could

resemble a nozzle, but rather it is left open discharging directly into the atmosphere, without any change in its diameter. Figure 2.3 shows some typical nozzles employed with clean agent FK-5-1-12. It can be appreciated that the holes drilled in the nozzle are by no means fine, and the cumulative area of all holes is not very different from the pipe's cross-section area. Actually the mission of the holes is not to create a narrowing which would delay the discharge, but rather to dispose of multiple edges against which the liquid could impact to form droplets that favour the agent's rapid vaporisation. Therefore it is justified in the AHM to leave the pipe open at the outlet, since this study does not cover the agent's vaporisation once it exits the tube.

The following assumptions³ are adopted in the development of the mathematical model associated with this system:

- i. The flow is one-dimensional (1D).
- ii. At the conditions present in the vessel and pipe until liquid exhaustion, the clean agent (typically FK-5-1-12) is an incompressible Newtonian fluid. The density, dynamic and kinematic viscosities, ρ , μ and ν respectively, ought to be considered constants.
- iii. The pressurisation gas N_2 is considered to behave as an ideal bimolecular gas. Thus, its adiabatic index is $\gamma = c_p/c_v = 1.4$, a very well known result of Statistical Mechanics.
- iv. Within the vessel, the discharge process is adiabatic for the pressurisation gas N_2 , that is, the ideal gas N_2 inside the vessel interchanges a negligibly small amount of heat with the surroundings during the short-time expansion⁴. This assumption leads to consider the polytropic equation for the ideal gas' expansion, that will be introduced later.
- v. The gas' pressure within the vessel equals the total pressure in the vessel. That is, within the vessel N_2 and liquid are in mechanical equilibrium at all times, and the pressure is one and common for both ($p_g(t) = p_l(t)$). The pressure gradient begins when the liquid enters the pipe ($z \geq 0$), but not in the vessel ($z < 0$).
- vi. The air within the pipe is always at atmospheric pressure p_∞ (pressure in dry zone equals p_∞)⁵. In other words, during the discharge process the air is not supposed to compress itself within the pipe, due to the pushing force exerted by the liquid. The liquid will just displace the air (pushing it ahead), without compressing it. Thus, the pressure gradient develops exclusively in the wet zone of the pipe (see figure 2.10)⁶.

³This work adopts the following definition of **hypothesis**: 'A prediction based on theory, an educated guess derived from various assumptions, which can be tested using a range of methods, but is most often associated with experimental procedure, a proposition put forward for proof or discussion'. On the other hand, an **assumption** will be 'a proposition that is taken for granted, as if it were true based upon presupposition without preponderance of the facts', and also, 'a proposition that may be used to prove further propositions, in the expectation that the assumption will be discharged in due course by proving it via a separate argument'.

⁴The assumption of polytropic and adiabatic expansion of an ideal gas also conveys the notion of quasi-static process. Although the liquid's discharge is a relatively fast process for the pressurisation gas N_2 , it is still well below its sound velocity and the changes occurring through the gas' interfaces are rapidly transmitted to its whole volume, which can readily reach a certain homogeneity of properties at all instants. Plausibly, the error committed for assuming the gas expansion in such conditions as quasi-static is not very large. In such case, the polytropic index coincides with the adiabatic index $n = \gamma = c_p/c_v$.

⁵It should be noted that this assumption is dynamically equivalent to suppose that the pressure inside the vessel is $p_0 - p_\infty$, while the liquid discharges in the vacuum (assuming no boiling of liquid).

⁶This assumption is confirmed in the CFD simulation: the pressure gradients develops exclusively in the wet zone, while the air within the pipe is always at atmospheric pressure (see figure 4.17 in page 266).

- vii. No fluid mixture liquid-air is considered and no vaporisation of the agent (HFC-227ea or FK-5-1-12) is taken into account. That is, once the liquid-air interface has reached the pipe's outlet, the discharge process within the pipe will remain single-phase all the time.
- viii. The N_2 gas does not exit the vessel until all the liquid has been exhausted. The model ceases to be valid when the liquid exits the discharge pipe and no further liquid remains in the vessel and pipe. No gas leaves the vessel (pipe) until all liquid has abandoned that space. The discharge process shall be (artificially) ended when the liquid has left the discharge pipe, and the N_2 gas begins to pour into the atmosphere.⁷
- ix. The liquid is supposed to be at rest within the vessel. That is, v is negligibly small for $z < 0$, and the liquid has velocity only for $z > 0$.⁸
- x. Gravity effects are neglected.
- xi. The Darcy-Weisbach friction factor f (or, equivalently, the Fanning friction factor or skin friction coefficient $C_f = f/4$) is assumed to be a valid relationship between dynamic pressure and wall-shear stress for this transient flow. That is, the following general relationship

$$\tau_w = C_f \frac{\rho v^2}{2} = f \frac{\rho v^2}{8} \quad (2.1)$$

is supposed to be true during the fast discharge process. Besides, f is assumed to be calculated at all times through the Moody diagram of the equivalent Colebrook-White correlation⁹ (see section 2.3.5 below).

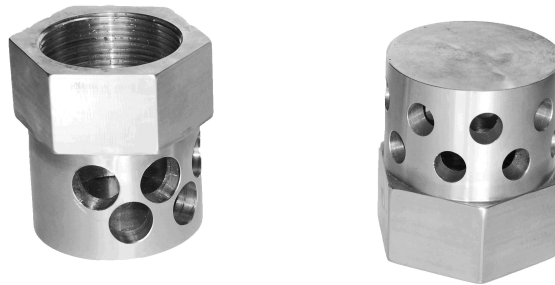


Figure 2.3: Typical nozzles used for fire extinction applications with agent FK-5-1-12.

Note that no assumption has been made regarding the pipe length L , nor diameter D . Although L/D could easily be higher than 500 in actual installations, and it could be safely presumed that $L/D \gg 1$, no restriction has been imposed on these geometrical parameters.

As has been said, the pressure within the dry zone is assumed equal to ambient's pressure. This implies that no nozzle can exist at the pipe's end; otherwise it would be necessary to justify that the air within the dry zone is not compressed by the liquid's advance through the pipe. Thus, it will be assumed that the pipe's diameter is constant from inlet to outlet, without any narrowing at the end, as it is customary

⁷Or when the pressure within the vessel equals the atmospheric pressure.

⁸What happens at $z = 0$ is irrelevant as it is a null-measure set.

⁹For steady state flows, the relationship between wall-shear stress and dynamic pressure, equation (2.1), is known to be accurate for *constant* values of f (and C_f). Herein it is assumed that such relationship is still valid for transient flow, though perhaps for a *time dependent* friction factor f . Although f ought to be considered variable throughout the flow, its actual values will in reality be almost constant, due to the high Reynolds numbers Re attained in flow. See section 2.3.5 for further information.

in actual FPE installations¹⁰. That is, perhaps, the harshest simplifying assumption that has been made to this 1D AHM.

The transient process of free discharge of a liquid through a pipe is going to be studied in these conditions. The geometry of the problem suggests the use of a cylindrical coordinate system, in which the Z axis is set along the symmetry longitudinal axis of the discharge pipe (see figure 2.4).

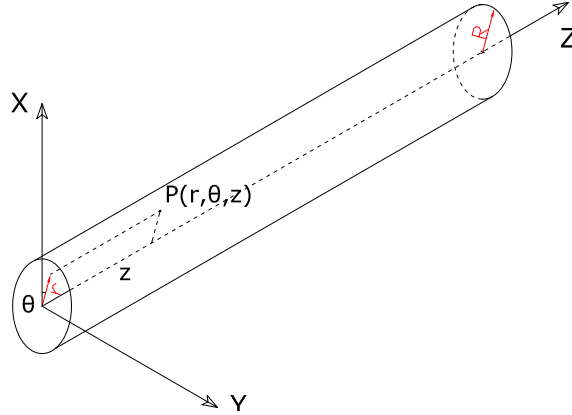


Figure 2.4: Coordinate system for the pipe.

The flow in the pipe is considered one-dimensional. Thus the velocity field can be expressed as:

$$\mathbf{v}(t, r, \theta, z) = [v_r, v_\theta, v_z] = [0, 0, v] \quad (2.2)$$

with $v = v(t, r, \theta, z)$. The only possible macroscopic displacement of liquid is along the Z axis.

In principle, the pressure field is given by $p = p(t, r, \theta, z)$. For symmetry reasons, the pressure p cannot depend on θ and, besides, if $\partial p / \partial \theta$ were different from zero so would be v_θ , against the assumption of one-dimensional flow (equation (2.2)). Following such one-dimensional assumption, neither can p depend on r , because in such case there might exist a motion's component in the radial direction, v_r , contrary to said assumption. Thus, $p = p(t, z)$ and $\nabla p = \partial p / \partial z \hat{\mathbf{z}}$, where $\hat{\mathbf{z}}$ is the unit vector along the Z axis.

The liquid is assumed incompressible, thus ρ is constant. Having into account (2.2) the Continuity equation in cylindrical coordinates takes the form:

$$\frac{\partial \rho}{\partial t} + \nabla \cdot (\rho \mathbf{v}) = \rho \nabla \cdot \mathbf{v} = 0 \quad \Rightarrow \quad \nabla \cdot \mathbf{v} = 0$$

$$\frac{1}{r} \frac{\partial}{\partial r} (r \cdot v_r) + \frac{1}{r} \frac{\partial v_\theta}{\partial \theta} + \frac{\partial v}{\partial z} = \frac{\partial v}{\partial z} = 0 \quad (2.3)$$

This last result is particularly important: inside the pipe v does not depend on z , that is, within the wet zone the velocity field has the form $\mathbf{v} = v(t, r, \theta) \hat{\mathbf{z}}$. Note that no independence of v with θ is invoked: later it will be seen that it is an unnecessary assumption.

¹⁰A planned research work to be conducted next is the upgrading of this model in order to consider the narrowing associated with discharge nozzles, so that air within the dry zone cannot escape to ambient as fast as in the present model, and it gets rapidly compressed by liquid being discharged, and as a result the liquid's advance is retarded, and the overall dynamics changed. This development would show that p_∞ must be substituted within the dynamic equations by a more complex, time dependent expression. This upgraded model will describe more faithfully the actual phenomenon happening in real fire extinction installations.

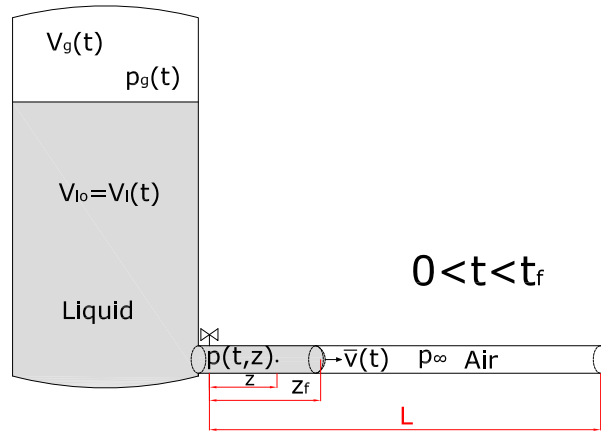


Figure 2.5: Fast stage of the liquid's discharge process.

Let $z_f(t)$ be the position of the liquid front, that is the liquid-air interface, measured from the pipe's inlet (see figure 2.5). As the liquid progresses, the gas pressure $p_g(t)$ and volume $V_g(t)$ change, while the liquid volume remains constant $V_l(t) = V_l(0) \equiv V_{l_0}$, since it is incompressible. Let t_f be the time at which the liquid front reaches the pipe's outlet, that is, $z_f(t_f) = L$. Two stages should be distinguished in the discharge process:

- i. **Fast stage**¹¹ ($0 < t < t_f$) (see figure 2.5). The liquid-air interface has not yet reached the pipe's end, that is, it has not yet covered the full length L . There exists a fraction of pipe full of liquid (with a pressure different from p_∞), while the other is full of air at atmospheric pressure p_∞ . The former will be named the **Wet Zone** and the latter the **Dry Zone**. $z_f(t)$ is the length of the wet zone, and it is measured from the opening valve up to an average point in the *meniscus* which forms the liquid front as it advances through the pipe.
- ii. **Slow stage** ($t > t_f$) (see figure 2.6). The liquid front has already passed through the pipe's end and it is directly pouring into ambient. The whole inside of the pipe is the wet zone. It should be noted that, according to this model, the liquid which has already exited the pipe is not subjected to any pressure gradient or friction (neither to gravity, by assumption (x) of section 2.2), and thus it undergoes no acceleration.

2.3 Derivation of Dynamic Equations

This section is devoted to the deduction of the model's dynamic equations, under the assumptions established above and within the limitations expressed therein. Before proceeding, some remarks regarding the method to obtain the quantities appearing in such equations are in order.

¹¹Do not mistake the *Fast stage* with the *Transient regime*, or the *Slow stage* with the *Steady state*. The whole process develops in a very fast and transient regime, although within its short duration some stages are more *transient* than others, if such an expression be allowed. Also the name Slow stage is somewhat misleading, as the liquid still moves very fast, although slower than in the Fast stage. Later on the reason for such names will become clear.

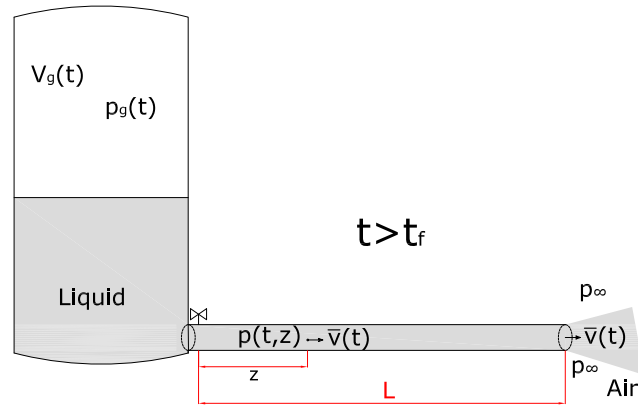
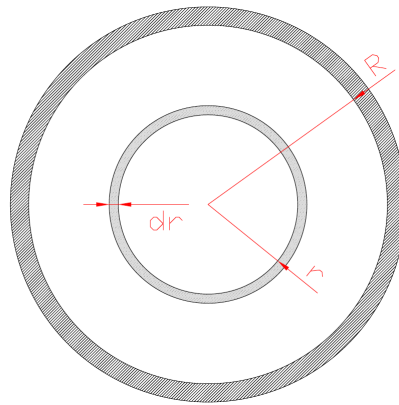


Figure 2.6: Slow stage of the liquid's discharge process.

2.3.1 Cross-Section Average of Fields

As this Chapter deals with the dynamics of fast discharge of a liquid by means of an ideal gas adiabatic expansion, in what constitutes a highly transient process, it is only natural to focus attention on the overall behaviour of the liquid along the axis in which most of the dynamics takes place, that is, along the Z -axis. Thus, the velocity profile of the liquid within the pipe (that is, the dependence of v on r) is of secondary importance, allowing for the assumption of one-dimensional flow. Such profiles will be later discussed in Chapters 3 and 4.

It is, then, pertinent to average the flow equations over the pipe's cross-section, in order to eliminate the dependence on r ¹².

Figure 2.7: Pipe's cross-section. Average over ring dr .

Let S be any flat surface within a fluid flow. Assume, without loss of generality, that the Z axis is chosen normal to this surface. Then for any smooth function $\psi = \psi(t, \mathbf{x})$ a **surface average** can be defined

¹²This average procedure is consistent with the fact that most pipe flow formulae of Hydraulics are based on the average velocity (understood as $V = Q/A$), and not on the centreline or any other point velocity.

according to the following expression:

$$\tilde{\psi}(t, z) := \frac{1}{S} \int_S \psi(t, x, y, z) dx dy \quad (2.4)$$

$\tilde{\psi}$ is conventionally used to denote surface average, while reserving the more common $\bar{\psi}$ for time average.

In many situations the flow function $\tilde{\psi}(t, z)$ could be used instead of the flow field $\psi(t, \mathbf{x})$. It can then be said that the initial flow problem has been converted into a one-dimensional problem, because the dependence on other coordinates has been removed, ironed out through this surface averaging procedure. If the flow develops within a pipe of circular cross-section, then it is only natural to use cylindrical coordinates (r, θ, z) (see figure 2.4) and to define the **cross-section average** for the quantity $\psi = \psi(t, \mathbf{x}) = \psi(t, r, \theta, z)$ as

$$\tilde{\psi}(t, z) = \frac{1}{\pi R^2} \int_0^R \int_0^{2\pi} r \psi(t, r, \theta, z) d\theta dr \quad (2.5)$$

If the pipe flow exhibits circular symmetry, that is, no quantity related to the flow depends on θ , then the cross-section average of $\psi(t, r, z)$ is given by (see figure 2.7)

$$\tilde{\psi}(t, z) = \frac{1}{\pi R^2} \int_0^R 2\pi r \psi(t, r, z) dr = \frac{2}{R^2} \int_0^R r \psi(t, r, z) dr \quad (2.6)$$

The particular case of $\psi(t, r) = \rho v(t, r)$ (no dependence on z), gives the following result

$$\tilde{\rho v}(t) = \rho \tilde{v}(t) = \frac{2\rho}{R^2} \int_0^R r v(t, r) dr \quad (2.7)$$

where \tilde{v} is also known as the **bulk velocity**. It should be noted that, with this definition,

$$\tilde{\rho \frac{\partial v}{\partial t}} = \rho \frac{d\tilde{v}}{dt}$$

Moreover, for any flow quantity $\psi(t, z)$ not depending on r , $\tilde{\psi}(t, z) = \psi(t, z)$ holds.

The cross-section average constitutes the bridge between **hydrodynamic** and **hydraulic** models, which are considered different in this Dissertation (see footnote 3 in page 3). A hydrodynamic model refers to the study of a flow from the perspective of Mechanics of Continua, which is best described through fields that determine the detailed structure of the flow, whereas a hydraulic model deals with quantities not requiring the treatment of fields, but rather are considered dependent variables which characterise the flow as a whole, and are unable to provide information about the internal structure of the flow. Hydrodynamic models consider usually 3D flows, while hydraulic models deal systematically with 1D flows. This distinction is applied within the realm of the present Dissertation and has no pretension to be universal.

2.3.2 Reynolds' Transport Theorem Approach

Let Ω be a control volume within a fluid flow and $\partial\Omega$ its closed and oriented boundary, which do not have to be fixed and could be time-dependent ($\Omega(t)$). Let \mathcal{U} be the material volume (a volume always composed of the same fluid particles or system) occupying the control volume Ω at time t . \mathcal{U} is a mechanical system upon which the conservation laws could be applied. Then for such a system the Reynolds' Transport Theorem establishes that

$$\frac{D\Psi}{Dt} \equiv \frac{D}{Dt} \int_{\mathcal{U}} \psi \, d\mathcal{U} = \frac{d}{dt} \int_{\Omega} \psi \, d\Omega + \int_{\partial\Omega} \psi(\mathbf{v} - \mathbf{v}_{\Omega}) \cdot d\mathbf{S} \quad (2.8)$$

where $\Psi(t)$ is any extensive tensorial physical quantity and $\psi(t, \mathbf{x})$ is the corresponding intensive field, \mathbf{v} is the fluid velocity at (t, \mathbf{x}) , and \mathbf{v}_{Ω} is the velocity of the boundary point corresponding to the boundary surface element $d\mathbf{S}$ ($\mathbf{v}_{\Omega} = 0$ if the control volume is static). Note $\mathbf{v} - \mathbf{v}_{\Omega}$ is the relative velocity of the fluid respect to $\partial\Omega$. The boundary surface element $d\mathbf{S}$ is to be understood as $\mathbf{n}dS$, where the unit vector \mathbf{n} is always normal to the boundary $\partial\Omega$, and pointing outwards. This theorem can be further explored in [Sch08].

In order to calculate the first integral in the right-hand side of equation (2.8), the Leibniz's rule¹³ could be used (see [Fla73]). It establishes that for any smooth function $\psi(t, \mathbf{x})$ defined in the volume $\Omega(t)$, the derivative of the variable-volume integral is split into two components:

$$\frac{d}{dt} \int_{\Omega} \psi \, d\Omega = \int_{\Omega} \frac{\partial\psi}{\partial t} \, d\Omega + \int_{\partial\Omega} \psi(\mathbf{v}_{\Omega} \cdot d\mathbf{S}) \quad (2.9)$$

Thus equation (2.8) could be written as

$$\frac{D\Psi}{Dt} \equiv \frac{D}{Dt} \int_{\mathcal{U}} \psi \, d\mathcal{U} = \int_{\Omega} \frac{\partial\psi}{\partial t} \, d\Omega + \int_{\partial\Omega} \psi(\mathbf{v} \cdot d\mathbf{S}) \quad (2.10)$$

Note that \mathbf{v}_{Ω} does not appear explicitly in (2.10), although the movement of the surface element $d\mathbf{S}$ would follow from that of the boundary integration limits $\partial\Omega$.

The application of the Reynolds' Transport Theorem to the 1D AHM proceeds as follows. Let $\psi(t, \mathbf{x}) = \rho\mathbf{v}(t, \mathbf{x})$ be the intensive vector field defining the fluid flow. Then, equation (2.10) above is expressed as;

$$\frac{D}{Dt} \int_{\mathcal{U}} \rho\mathbf{v} \, d\mathcal{U} = \int_{\Omega} \frac{\partial(\rho\mathbf{v})}{\partial t} \, d\Omega + \int_{\partial\Omega} \rho\mathbf{v}(\mathbf{v} \cdot d\mathbf{S}) \quad (2.11)$$

But the integral in the left-hand side is the linear momentum of the system \mathcal{U} . Then it can be established that

$$\frac{D}{Dt} \int_{\mathcal{U}} \rho\mathbf{v} \, d\mathcal{U} = \sum \mathbf{F}_{ext} \quad (2.12)$$

where \mathbf{F}_{ext} are the external forces acting on the system.

¹³Some texts name this result as Reynolds' Transport Theorem. Though quite similar in form, the Reynolds' Transport theorem is different in scope and application from the Leibniz's Rule. Nevertheless, the Leibniz's Rule is more general and implies Reynold's Transport Theorem. See [Sch08]

Consider the control volume Ω defined by the limiting surfaces (sides) A, B and C of figure 2.8. At time t the control volume Ω is coincident with the material volume or system \mathcal{U} . Neglecting gravity (assumption x of section 2.2), there are only two external forces acting on the system: pressure force and friction force (which depends on the wet surface $S_w = 2\pi R z_f(t)$). Their expressions are (see figures 2.5 and 2.6):

$$F_p(t) = (p_g(t) - p_\infty) \pi R^2 \quad (2.13)$$

and¹⁴

$$F_f(t) = \tilde{\tau}_w S_w = -\rho C_f \tilde{v}^2 \pi R z_f \quad (2.15)$$

with $\tilde{\tau}_w$ the average wall-shear stress and S_w the area of wet surface.

Since $\mathbf{v} = [0, 0, v(t, r, \theta)] = v(t, r, \theta)\hat{\mathbf{z}}$, with $\hat{\mathbf{z}}$ the unit vector in the Z direction, it is only necessary to consider the Z component. Notice that v does not depend on z .

The dynamic equation (2.12) is rewritten for the single non-zero component as (with $C_f = \frac{f}{4}$):

$$\int_{\Omega} \frac{\partial(\rho v)}{\partial t} d\Omega + \int_{\partial\Omega} \rho v (\mathbf{v} \cdot d\mathbf{S}) = (p_g - p_\infty) \pi R^2 - \rho \frac{f}{4} \tilde{v}^2 \pi R z_f \quad (2.16)$$

It is convenient to distinguish two different stages in this dynamical process:

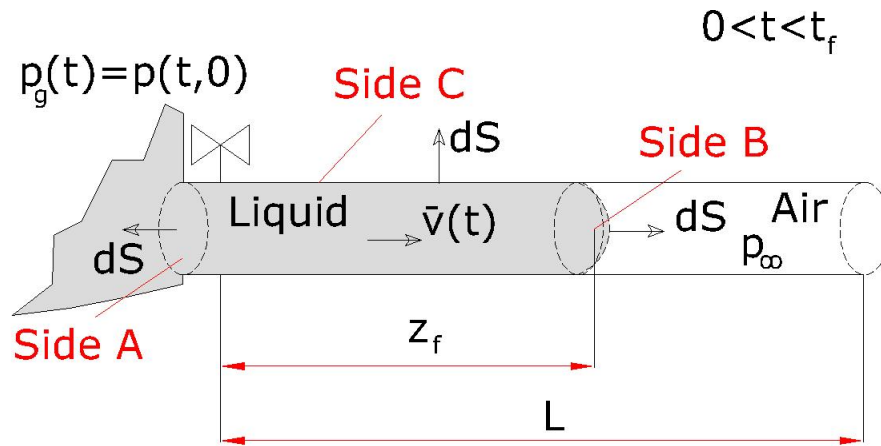


Figure 2.8: Control volume over which integration is performed.

Fast stage $0 < t < t_f$ (see figure 2.8)

In this case a cylindrical control volume $\Omega(t)$ coincident with the wet zone will be considered. This volume Ω grows from zero at $t = 0$ to $\pi R^2 L$ at $t = t_f$, with a value of $\pi R^2 z_f$ at any time $0 \leq t \leq t_f$,

¹⁴Note the skin friction coefficient C_f (also called the Fanning Friction Factor) is defined by means of the cross-section averaged velocity for steady state flows \tilde{v} (also called bulk velocity), as

$$C_f = \frac{\tilde{\tau}_w}{\frac{1}{2}\rho\tilde{v}^2} \quad (2.14)$$

that is, the quotient between average wall-shear stress and average dynamic pressure. The friction force exerted on the moving fluid is equal to $\tilde{\tau}_w$ times the area of wet surface. According to assumption (xi) in section 2.2, C_f and equation (2.14) are supposed to be also applicable to the AHM, and the transient friction force would be given by (2.15). Moreover, $C_f = f/4$, being f the Darcy-Weisbach friction factor.

in which it is coincident with the system \mathcal{U} . The control volume Ω has a moving boundary; a fact irrelevant for the derivation, as it has already been established that \mathbf{v}_Ω does not appear in equation (2.16).

The fluid is assumed incompressible, thus ρ is constant and can be removed from the integrals. Having into account that the volume element in cylindrical coordinates is $d\Omega = r dr d\theta dz$, and noting that v is independent of z , the first integral of equation (2.16) yields:

$$\int_{\Omega} \frac{\partial v}{\partial t} r dr d\theta dz = \int_0^R \int_0^{2\pi} \int_0^{z_f} \frac{\partial v}{\partial t} r dr d\theta dz = z_f \int_0^R \int_0^{2\pi} \frac{\partial v}{\partial t} r dr d\theta \quad (2.17)$$

But the last integral is, precisely, the definition of the cross-section average of $\frac{\partial v}{\partial t}$ times the cross-section area. Thus,

$$\int_{\Omega} \frac{\partial v}{\partial t} d\Omega = \pi R^2 z_f \frac{d\tilde{v}}{dt} \quad (2.18)$$

as \tilde{v} only depends on t .

The surface integral remains to be calculated. The control surface can be divided into three sub-surfaces, A, B and C (see figure 2.8). Note that since v does not depend on z , v is the same for equivalent points of surfaces A and B. The following equality holds with generality:

$$\int_{\partial\Omega} v(\mathbf{v} \cdot d\mathbf{S}) = \int_A v(\mathbf{v} \cdot d\mathbf{S}) + \int_B v(\mathbf{v} \cdot d\mathbf{S}) + \int_C v(\mathbf{v} \cdot d\mathbf{S}) \quad (2.19)$$

Note the integrals on A and B are proportional to the cross-section average of squared velocity in the pipe.

- On surfaces A and B the cross-section averaged velocities are the same, but $d\mathbf{S}$ have opposite senses. Thus

$$\int_A v^2(\hat{\mathbf{z}} \cdot d\mathbf{S}) + \int_B v^2(\hat{\mathbf{z}} \cdot d\mathbf{S}) = 0$$

Note this last result would hold for any function not depending on z .

- On surface C $\mathbf{v} \cdot d\mathbf{S} = 0$, because \mathbf{v} is always normal to $d\mathbf{S}$ (whatever the value \mathbf{v} might have). Thus

$$\int_C v(\mathbf{v} \cdot d\mathbf{S}) = 0$$

The result for the surface integral is then:

$$\int_{\partial\Omega} \rho v(\mathbf{v} \cdot d\mathbf{S}) = 0 \quad (2.20)$$

and equation (2.16) can be written as

$$\rho \frac{d\tilde{v}}{dt} \pi R^2 z_f = (p_g - p_\infty) \pi R^2 - \rho \frac{f}{4} \tilde{v}^2 \pi R z_f \quad (2.21)$$

or rather

$$\boxed{\frac{d\tilde{v}}{dt} = \frac{p_g(t) - p_\infty}{\rho z_f} - \frac{f}{4R} \tilde{v}^2} \quad (2.22)$$

Notice just how naturally the cross-section averaged velocity \tilde{v} has appeared in this dynamic equation. Only two assumptions were necessary: \mathbf{v} is a vector parallel to the Z axis and the flow is incompressible (which lead to independence of v on z).

Equation (2.22) is far more complicated than what at first sight seems, as

$$z_f(t) = \int_0^t \tilde{v}(\tau) d\tau \quad (2.23)$$

Using the notation $\dot{z}_f = \tilde{v}$, equation (2.22) can be written as:

$$\ddot{z}_f = \frac{p_g(t) - p_\infty}{\rho z_f} - \frac{f}{4R} \dot{z}_f^2 \quad (2.24)$$

which, again, is not as simple as it looks, since $p_g(t)$ also depends on z_f , as will be seen later.

Slow stage $t > t_f$ (see figure 2.6)

In the Slow stage the control volume Ω is fixed and equal to $\pi R^2 L$. As seen in the Fast stage, the surface integral of equation (2.16) is zero.

In Slow stage the volume integral results in

$$\int_{\Omega} \frac{\partial \rho v}{\partial t} d\Omega = \rho \pi R^2 L \frac{d\tilde{v}}{dt} \quad (2.25)$$

and the dynamic equation for this case becomes:

$$\rho \pi R^2 L \frac{d\tilde{v}}{dt} = (p_g - p_\infty) \pi R^2 - \frac{f}{4} \rho \pi R L \tilde{v}^2 \quad (2.26)$$

or rather

$$\frac{d\tilde{v}}{dt} = \frac{p_g(t) - p_\infty}{\rho L} - \frac{f}{4R} \tilde{v}^2 \quad (2.27)$$

a seemingly simple equation, should $p_g(t)$ not depend on z_f .

2.3.3 Navier-Stokes' Equations Approach

It is also very illustrative to obtain the dynamic equations from an Eulerian perspective, using the Navier-Stokes' differential field equations, instead of the integral approach developed in last section. As the model's geometry is a pipe, it seems only natural to use cylindrical coordinates.

Continuity equation (2.3) shows that the assumptions of incompressibility and one-dimensional flow lead to $\partial_z v = 0$. Thus, only the z -component of Navier-Stokes equations will be considered:

$$\frac{\partial v}{\partial t} + v_r \frac{\partial v}{\partial r} + \frac{v_\theta}{r} \frac{\partial v}{\partial \theta} + v \frac{\partial v}{\partial z} = -\frac{1}{\rho} \frac{\partial p}{\partial z} + \nu \left\{ \frac{1}{r} \frac{\partial}{\partial r} \left(r \frac{\partial v}{\partial r} \right) + \frac{1}{r^2} \frac{\partial^2 v}{\partial \theta^2} + \frac{\partial^2 v}{\partial z^2} \right\} \Rightarrow \quad (2.28)$$

$$\rho \frac{\partial v}{\partial t} = -\frac{\partial p}{\partial z} + \frac{\mu}{r} \left\{ \frac{\partial}{\partial r} \left(r \frac{\partial v}{\partial r} \right) + \frac{1}{r} \frac{\partial^2 v}{\partial \theta^2} \right\} \quad (2.29)$$

In this equation¹⁵ all quantities (ρ, v, p, μ) refer to the liquid within the pipe. Note that, although in general $v = v(t, r, \theta)$, p cannot depend on r nor θ , and thus $p = p(t, z)$. In effect, if $p = p(r)$ then $\partial p / \partial r \neq 0$ and $v_r \neq 0$, for there would exist a radial force, against the assumption of one-dimensional flow. For the same token, $p = p(\theta)$ would imply $\partial p / \partial \theta \neq 0$ and $v_\theta \neq 0$, against said assumption.

One conclusion could be drawn upon close exam of equation (2.29): since $\rho \partial_t v$ does not depend on z , neither does the right-hand side of said equation. But the diffusion term does not depend on z either. It follows that $\partial_z p$ must also be independent of z . Thus, there must exist a function $\Pi = \Pi(t)$ such that¹⁶

$$\Pi(t) = -\frac{\partial p}{\partial z} \quad (2.30)$$

With the help of such function Π the equation (2.29) can be written as:

$$\rho \frac{\partial v}{\partial t} = \Pi(t) + \frac{\mu}{r} \left\{ \frac{\partial}{\partial r} \left(r \frac{\partial v}{\partial r} \right) + \frac{1}{r} \frac{\partial^2 v}{\partial \theta^2} \right\} \quad (2.31)$$

From (2.30) it follows that $p(t, z)$ must necessarily be of the form¹⁷:

$$p(t, z) = -\Pi(t)z + \chi(t) \quad (2.32)$$

where $\chi(t)$ is a continuous function of t that must be found from the problem's initial and boundary conditions. Thus, p can only depend linearly on z . For $z = 0$ the liquid pressure equals the gas pressure within the vessel, $p(t, 0) \equiv p_l(t) = p_g(t)$, and the functional form of the liquid pressure within the pipe is:

$$p(t, z) = -z \Pi(t) + p_g(t) \quad (2.33)$$

Equation (2.31) can also be written as:

$$\rho \frac{\partial v}{\partial t} = \Pi(t) + \frac{\mu}{r} \left\{ \frac{\partial v}{\partial r} + r \frac{\partial^2 v}{\partial r^2} + \frac{1}{r} \frac{\partial^2 v}{\partial \theta^2} \right\} \quad (2.34)$$

Now it is time to average equation (2.34) over the pipe's cross-section. Note $\Pi(t)$ does not depend on spatial coordinates, and it is identical to its cross-section average $\bar{\Pi}(t) = \Pi(t)$. The results of the averaging process are:

i. The left-hand side of equation (2.34) is clearly $\rho \partial \bar{v} / \partial t = \rho d \bar{v} / dt$, since $\bar{v} = \bar{v}(t)$.

ii. The first term $\frac{\mu}{r} \partial_r v$ averages as:

$$\frac{\mu}{r} \bar{\frac{\partial v}{\partial r}} = \frac{\mu}{\pi R^2} \int_0^R \int_0^{2\pi} \frac{1}{r} \frac{\partial v}{\partial r} r \, dr \, d\theta = \frac{\mu}{\pi R^2} \int_0^{2\pi} (0 - v_{max}) \, d\theta = -\frac{\mu}{\pi R^2} \int_0^{2\pi} v_{max} \, d\theta \quad (2.35)$$

because $v(t, R, \theta) = 0$ (no-slip condition) and $v(t, 0, \theta) = v_{max}(t, \theta)$.

iii. The second term $\mu \partial_r \partial_r v$ averages as:

$$\mu \bar{\frac{\partial^2 v}{\partial r^2}} = \frac{\mu}{\pi R^2} \int_0^R \int_0^{2\pi} \frac{\partial^2 v}{\partial r^2} r \, dr \, d\theta \quad (2.36)$$

¹⁵Note the convective term has disappeared from equation (2.29). It is the expected result for incompressible flow within a pipe full of liquid.

¹⁶It should be noted that $\Pi(t) \geq 0$.

¹⁷The expression (2.32) for p can only be true if the liquid's incompressibility assumption is maintained.

This integral can be solved by parts,

$$\int f dg = fg - \int g df$$

with $f = r$, $df = dr$ and $g = \frac{\partial v}{\partial r}$, $dg = \frac{\partial^2 v}{\partial r^2} dr$, which leads to:

$$\int r \frac{\partial^2 v}{\partial r^2} dr = r \frac{\partial v}{\partial r} - \int \frac{\partial v}{\partial r} dr = r \frac{\partial v}{\partial r} - v \quad (2.37)$$

The cross-section average is then

$$\widetilde{\frac{\partial^2 v}{\partial r^2}} = \frac{\mu}{\pi R^2} \int_0^{2\pi} \left(R \left[\frac{\partial v}{\partial r} \right]_R + v_{max} \right) d\theta \quad (2.38)$$

iv. The third term $\frac{\mu}{r^2} \partial_\theta \partial_\theta v$ averages as:

$$\widetilde{\frac{\mu}{r^2} \frac{\partial^2 v}{\partial \theta^2}} = \frac{\mu}{\pi R^2} \int_0^R \int_0^{2\pi} \frac{1}{r} \frac{\partial^2 v}{\partial \theta^2} dr d\theta = \frac{\mu}{\pi R^2} \int_0^R \frac{1}{r} \left(\left[\frac{\partial v}{\partial \theta} \right]_{2\pi} - \left[\frac{\partial v}{\partial \theta} \right]_0 \right) dr \quad (2.39)$$

But $v(t, r, \theta)$ is a physical quantity, not just an abstract mathematical function. Thus, from physical considerations, $v(t, r, 0) = v(t, r, 2\pi) \forall t, r \in \mathbb{R}^+$, and the same is true for $\partial_\theta v$. It follows the cross-section average of $\frac{\mu}{r^2} \partial_\theta \partial_\theta v$ is always zero. By now it should be evident why it was unnecessary to assume $v \neq v(\theta)$: whatever the dependence on θ it would have been ironed out by the cross-section averaging process.

Putting together all the terms above, the cross-section average of equation (2.34) yields

$$\rho \frac{d\tilde{v}}{dt} = \Pi(t) + \frac{\mu}{\pi R^2} \int_0^{2\pi} \left(-v_{max} + R \left[\frac{\partial v}{\partial r} \right]_R + v_{max} \right) d\theta = \Pi(t) + \frac{\mu}{\pi R} \int_0^{2\pi} \left[\frac{\partial v}{\partial r} \right]_R d\theta \quad (2.40)$$

But, according to Newton's Law of viscosity, the shear friction stress at the pipe's wall is:

$$\tau_w = \tau_w(t, \theta) = \mu \left[\frac{\partial v}{\partial r} \right]_{r=R} \quad (2.41)$$

Note the above integral (2.40) is the average of the wall-shear stress $\tau_w(t, \theta)$ along the perimeter of the pipe's wall¹⁸:

$$\tilde{\tau}_w(t) = \frac{\mu}{2\pi} \int_0^{2\pi} \left[\frac{\partial v}{\partial r} \right]_R d\theta \quad (2.42)$$

Thus the dynamic equation could be written as:

$$\rho \frac{d\tilde{v}}{dt} = \Pi(t) + \frac{2 \tilde{\tau}_w(t)}{R} \quad (2.43)$$

It should be noted that, in this particular problem, $\tilde{\tau}_w$ does not depend on z , as neither does v nor μ . On the other hand, $\tilde{\tau}_w$ does depend on t .

¹⁸Note how the friction term appears as a natural outcome of the calculation process. The integration by parts has yielded such result. Equation (2.41) is a consequence of assuming the liquid Newtonian.

Now it only remains to substitute the average wall-shear stress $\tilde{\tau}_w$ by its squared bulk velocity equivalent expression $C_f \rho \tilde{v}^2 / 2 \equiv f \rho \tilde{v}^2 / 8$ (see assumption xi in page 34), to obtain the already familiar dynamic equation in average form:

$$\rho \frac{d\tilde{v}}{dt} = \Pi(t) - \frac{f \rho}{4R} \tilde{v}^2 \quad (2.44)$$

which constitutes an ordinary non-linear differential equation. Since Π is the pressure gradient along the pipe, not depending on z , it can only take the following form:

Fast stage $0 < t < t_f$ (Figure 2.5)

$$\Pi(t) = \frac{p_g(t) - p_\infty}{z_f(t)} \quad (2.45)$$

Slow stage $t > t_f$ (Figure 2.6)

$$\Pi(t) = \frac{p_g(t) - p_\infty}{L} \quad (2.46)$$

and the resulting dynamic equations are identical to (2.22) and (2.27), respectively. Thus the dynamic equations have been derived through two different methods.

2.3.4 Equations for Pressure

Assumption iv of page 33 states the discharge to be a polytropic and adiabatic expansion process for the gas. Therefore, considering N_2 an ideal gas, the following polytropic relation could be applied thereupon¹⁹:

$$p_0 V_{g_0}^\gamma = p_g(t) (V_g(t))^\gamma \quad (2.48)$$

in which

$$\gamma = \frac{c_p}{c_v} \quad (2.49)$$

is the adiabatic index, in this case $\gamma = 1.4$ for an ideal diatomic gas at NTP conditions. According to the initial assumption v in page 33, within the vessel the liquid and gas pressures are the same at every instant

$$p_g(t) = p_l(t) \equiv p(t, 0) \quad (2.50)$$

It is also assumed that the pressure gradient begins exactly where (and when) the liquid exits the vessel and enters the pipe. That is, within the vessel ($z < 0$) there is no pressure gradient. Moreover, the pressure within the pipe has the form shown in equation (2.33).

Let $z_f = z_f(t)$ be the position of the liquid's front within the pipe²⁰, measured from a central point of the *meniscus* formed upwind (see figure 2.9). Then, the following relationships hold for the gas within the vessel:

$$V_g(t) = V_{g_0} + \pi R^2 z_f \quad (2.51)$$

¹⁹Two considerations are in order: (i) equation (2.48) is only valid when using absolute pressures; and (ii) it would be plausible to assume other polytropic processes for the ideal gas, having been its quasi-static character already discussed in footnote 4 in page 33. In this case, the general polytropic relation would be

$$p_0 V_{g_0}^n = p_g(t) (V_g(t))^n \quad (2.47)$$

with $0 \leq n < \infty$ the polytropic index, and $n = \gamma$ for adiabatic, $n = 1$ for isothermal, etc.

²⁰ z_f only has physical meaning while $t < t_f$, that is, before the front reaches the pipe's outlet at $z_f = L$. On the other hand, $\int_0^t \tilde{v}(\tau) d\tau$ (see equation (2.54) below) has a physical meaning for any $t > 0$.

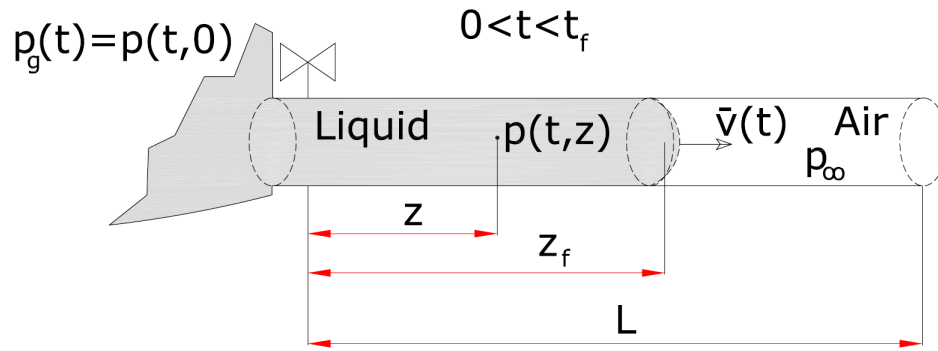


Figure 2.9: Detail of the liquid's discharge process.

and

$$p_g(t) = p_0 \left(\frac{V_{g0}}{V_g(t)} \right)^\gamma = p_0 \left(\frac{V_{g0}}{V_{g0} + \pi R^2 z_f} \right)^\gamma = \frac{p_0}{\left(1 + z_f \frac{\pi R^2}{V_{g0}} \right)^\gamma} \quad (2.52)$$

Note the parameter $\pi R^2/V_{g0}$ is completely geometric and is always known in advance²¹. The equation above provides the pressure at the pipe's inlet, $z = 0$. The pressure at the pipe's outlet, $z = L$, is always the atmospheric p_∞ , according to the assumptions established on section 2.2.

Defining $z_f(t)$ as the liquid-air interface's position implies that $\dot{z}_f(t) \equiv dz_f/dt$ must be its velocity, that is, the average velocity of all liquid particles which make up such interface. But this average velocity is, by definition, $\tilde{v}(t)$ (see figures 2.7 and 2.9)

$$\tilde{v}(t) = \frac{1}{\pi R^2} \int_0^R \int_0^{2\pi} v r d\theta dr \quad (2.53)$$

and therefrom follows $dz_f/dt = \tilde{v}(t)$. It is in this sense of *average*, for it can be referred to liquid front's position and velocity, that is used herein.

Since $dz_f/dt = \tilde{v}$, equation (2.51) could also be expressed as:

$$V_g(t) = V_{g0} + \pi R^2 \int_0^t \tilde{v}(\tau) d\tau \quad (2.54)$$

where the last term refers to the full volumetric flow circulating within the pipe until instant t . Note this last expression is valid even if $t > t_f$, in which case there is not an obvious physical meaning for z_f . With this same criterion, equation (2.52) could be written as:

$$p_g(t) = p_0 \left(\frac{V_{g0}}{V_g(t)} \right)^\gamma = \frac{p_0}{\left(1 + \frac{\pi R^2}{V_{g0}} \int_0^t \tilde{v}(\tau) d\tau \right)^\gamma} \quad (2.55)$$

and now a direct relationship between $p_g(t)$ and $\tilde{v}(t)$ has been established.

²¹The vessel containing the clean agent and gas N_2 is assumed to be kept in a protected room at roughly constant temperature, thus the thermal dilatation which would make V_{g0} change could be neglected.

But $\Pi(t) = -\partial p/\partial z$, where $p(t, z)$ is the pressure within the pipe (not the pressure in the vessel, which is $p(t, 0) = p_g(t)$), and since Π does not depend upon z , the only option for p is a linear decrease along the pipe.

As usual, two cases should be considered:

Case $0 < t < t_f$ (**Fast stage**) (Figure 2.10)

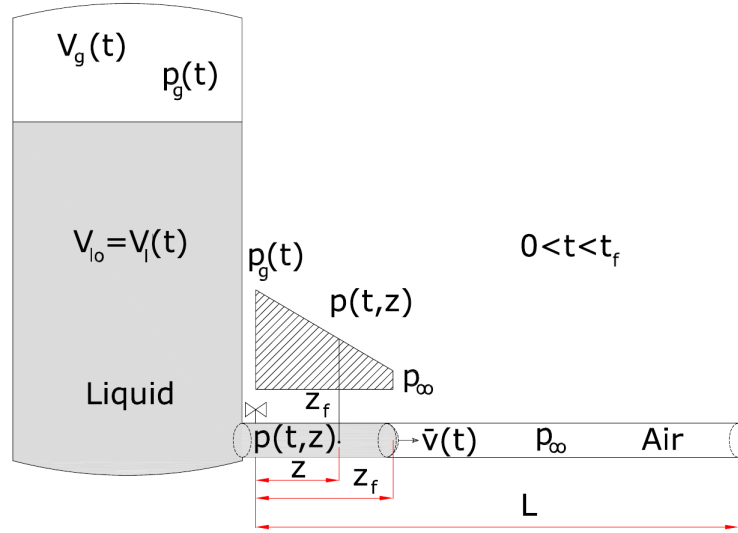


Figure 2.10: Discharge process and pressure gradient for $0 < t < t_f$.

In this case the pressure has the form (see equation (2.33))

$$p(t, z) = -\Pi(t) z + p_g(t) = \frac{p_\infty - p_g(t)}{z_f(t)} z + p_g(t) \quad (0 < z < z_f) \quad (2.56)$$

But $z_f(t) = \int_0^t \tilde{v}(\tau) d\tau$ ($0 < t < t_f$), and the equation above could be written as:

$$p(t, z) = \frac{p_\infty - p_g(t)}{\int_0^t \tilde{v}(\tau) d\tau} z + p_g(t) \quad (0 < z < z_f) \quad (0 < t < t_f) \quad (2.57)$$

and taking into account equation (2.55), the following result holds

$$\Pi(t) = \frac{1}{\int_0^t \tilde{v}(\tau) d\tau} \left(\frac{p_0}{\left(1 + \frac{\pi R^2}{V_{g0}} \int_0^t \tilde{v}(\tau) d\tau\right)^\gamma} - p_\infty \right) \quad (0 < t < t_f) \quad (2.58)$$

and with this expression the dynamic equation (2.44) is converted into the following ordinary non-linear integro-differential equation:

$$\rho \frac{d\tilde{v}(t)}{dt} = \frac{1}{\int_0^t \tilde{v}(\tau) d\tau} \left(\frac{p_0}{\left(1 + \frac{\pi R^2}{V_{g0}} \int_0^t \tilde{v}(\tau) d\tau\right)^\gamma} - p_\infty \right) - \frac{f\rho[\tilde{v}(t)]^2}{4R} \quad (0 < t < t_f) \quad (2.59)$$

in which all quantities that do not exhibit explicit dependence on t are assumed to be constant²².

Case $t > t_f$ (Slow stage) (Figure 2.11)

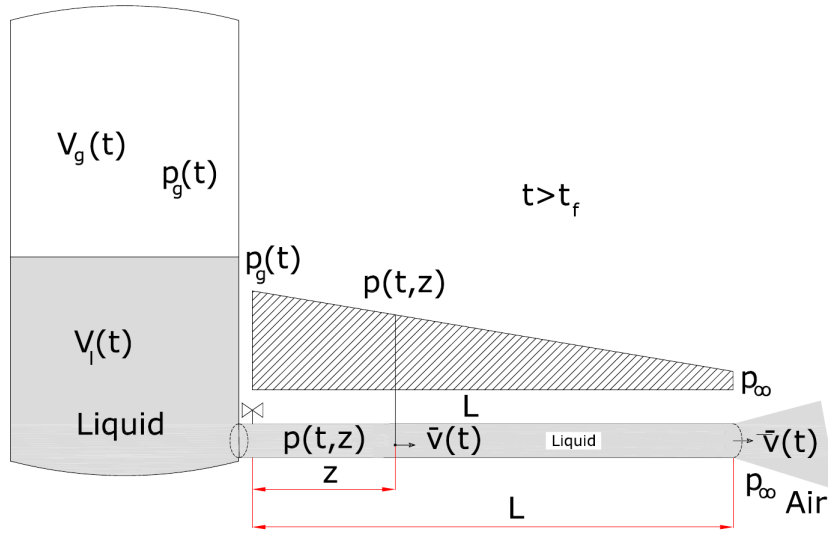


Figure 2.11: Discharge process and pressure gradient for $t > t_f$.

In this case the pressure has the form (see equation (2.33)):

$$p(t, z) = \frac{p_\infty - p_g(t)}{L} z + p_g(t) \quad (0 < z < L) \quad (2.60)$$

which, using equation (2.55), leads to:

$$\Pi(t) = \frac{p_g(t) - p_\infty}{L} = \frac{1}{L} \left(\frac{p_0}{\left(1 + \frac{\pi R^2}{V_{g0}} \int_0^t \tilde{v}(\tau) d\tau\right)^\gamma} - p_\infty \right) \quad (t > t_f) \quad (2.61)$$

and with this result equation (2.44) transforms into the following ordinary non-linear integro-differential equation:

$$\rho \frac{d\tilde{v}(t)}{dt} = \frac{1}{L} \left(\frac{p_0}{\left(1 + \frac{\pi R^2}{V_{g0}} \int_0^t \tilde{v}(\tau) d\tau\right)^\gamma} - p_\infty \right) - \frac{f\rho[\tilde{v}(t)]^2}{4R} \quad (t > t_f) \quad (2.62)$$

in which all quantities not exhibiting explicit dependence on t are presumed constant (see footnote 22).

²²With one exception: the friction factor f is also time dependent, though only for a brief period. See next section 2.3.5

2.3.5 Brief Considerations About Friction

It should be noted that in equations (2.22)/(2.59) and (2.27)/(2.62) the time dependence has been explicitly signalled in all quantities which exhibit such a relationship, whereas variables not showing it are deemed constant. Nevertheless, those results hide a time dependence which, in principle, is far from being fully understood: in a transient flow the friction factor (C_f or f) cannot be constant. Note the derivation of the dynamic equations does not require f to be constant: it simply assumes a proportionality at all times between wall-shear stress (friction) and dynamic pressure. Constant f is just a convenient feature, not a request of the model.

Although equations (2.59) and (2.62) are exact within the limitations of the model, it must be noticed that f , as it is normally calculated for steady state flows, might not accurately represent the friction phenomena when one is to delve into the realm of highly transient flows.

The operational definition of Darcy-Weisbach friction factor f is through the pressure drop undergone by a turbulent steady state pipe flow of bulk velocity \tilde{v} :

$$\Delta p = -f \frac{\rho \tilde{v}^2 L}{4R} \quad (2.63)$$

and f itself is a constant for a given steady state flow, determined by the Moody Diagram, figure 2.12, or the equivalent Colebrook-White correlation²³

$$\frac{1}{\sqrt{f}} = -2 \log \left(\frac{2.51}{Re\sqrt{f}} + \frac{\zeta_r}{3.7 D} \right) \quad (2.64)$$

Thus the friction factor f depends on the Reynolds number $Re = \tilde{v}D/\nu$, which in turn depends on \tilde{v} . By construction, correlation (2.64) is only applicable to turbulent *steady state* flow.

In principle, **two approaches** to the problem of determining the functional dependence of f with \tilde{v} are possible for the transient model presented herein:

- i. Assume the functional form given by equation (2.64) is also valid for transient accelerated pipe flow, and use it to calculate at each time step the f resulting from the current value of \tilde{v} . A time-dependent friction factor $f(t)$ would be obtained, although the general proportionality between wall-shear stress (friction) and dynamic pressure would be maintained. This is the approach followed in the present Dissertation, and that is the precise meaning of assumption xi of page 34.

A computer program has been developed to solve the dynamic equation of the AHM. The equation is solved through a time-marching algorithm, step by step, with a Δt conveniently small. At each time-step t_n the value of f_n is determined from the \tilde{v}_{n-1} obtained in the previous step t_{n-1} , using equation (2.64)²⁴. (see [Cla09]). Such f_n serves to calculate the current value of \tilde{v}_n through the dynamic equations (2.59) and (2.62).

²³Alternative correlations to calculate f in steady state flows are offered in [Bra09], [Cla09], [Den09], [GS08], [KM86], [KY78], [RHC98], [RK06], [SG06] and [TCK05]. [GCC07] provides a unified formulation for the friction factor in pipes and channels. Any of the above correlations is compatible with the AHM.

²⁴The Reynolds number grows so fast, that after a few time-steps the flow regime is fully turbulent ($Re \gtrsim 4000$), and (2.64) becomes applicable. During those first few time-steps f is calculated by means of the simple laminar relationship

$$f = \frac{64}{Re} \quad (2.65)$$

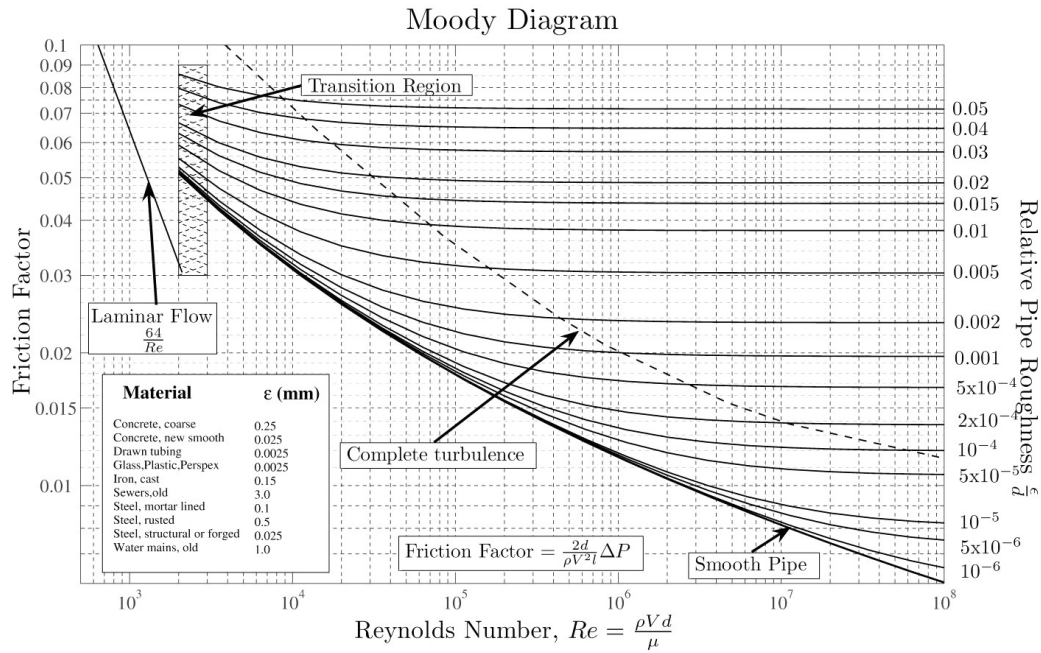


Figure 2.12: Moody diagram.

With growing Re the friction factor $f(t)$ tends asymptotically to a constant value, fixed by the relative roughness $\zeta_D = \zeta_r/D$ (see the horizontal lines of Moody diagram and section 2.6.1.6). In the AHM Re attains so high a value so early, that f could be considered constant for most of the duration of the transient. Besides, in the acceleration stage the effect of friction on the flow is negligible (see sections 2.5 and 4.9). Thus, in this approach no significant error is expected if f is assumed constant, with a value given by the relative pipe roughness, and such practice is recommended for practical calculations.

- ii. Determine a new functional dependence of f with \tilde{v} (and possibly with the acceleration). It is not clear the Colebrook-White correlation could be applied to transient flows, specially if they undergo high accelerations. Figure 2.13, borrowed from [JC12], shows the departure of the skin friction coefficient $C_f = f/4$ for unsteady turbulent flows from that attained in steady state.

[JC12] discusses differences in excess of 20% for the skin friction coefficient, for Reynolds numbers Re ranging from 7000 to 28000. The study also shows a noticeable coincidence from $Re = 28000$ to 36000, though it does not reach any further and the acceleration attained by the flow is moderate. In the AHM $Re \gtrsim 10^7$ and the acceleration is extremely high (hundreds of g), therefore reasonable doubt exists on the application of equation (2.64) to such transient flow. No publication could be found reporting skin friction for those figures.

The transient friction is explained in papers like [AL⁺81], [Shu95], [Shu96], [KA06], [Ann11], [AKSA13] and the references cited therein. [KM86] introduces the concept of transient friction factor and offers an estimate in which the difference between transient and steady friction factors is proportional to the dimensionless acceleration of the fluid. To the author's knowledge, none of the correlations that have been proposed for transient flows has gained a fair level of acceptance within the scientific community.

The AHM still requires a linear relationship between wall-shear stress and dynamic pressure, similar to (2.14), although in this second approach such proportionality would not be obtained

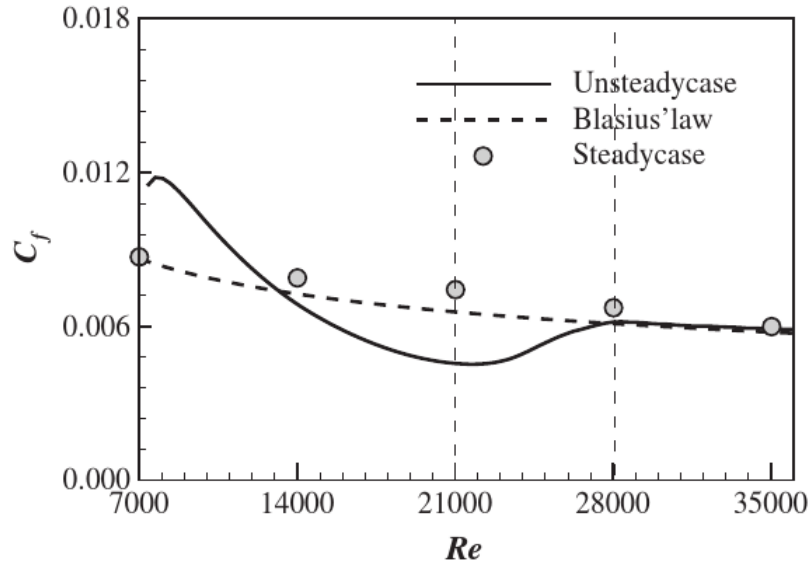


Figure 2.13: Skin friction coefficient for unsteady accelerated flow (source: [JC12]).

from the Colebrook-White correlation, but instead through some other functional dependence that might even include the acceleration.

In principle, the problem of finding f for a transient flow might have an analytic solution. In section 3.4.2, the GAS for transient/unsteady turbulent incompressible pipe flow will be derived and explained (equation (3.469)). The functional form of f could be found from the solution herewith: the general velocity profile would permit to calculate the bulk velocity \tilde{v} , as well as the wall-shear stress

$$\tau_w = \mu \left[\frac{\partial v}{\partial r} \right]_{r=R}$$

and a new transient C_f would follow naturally from equation (2.14). However, this is easier said than done and will be relayed to a future research work, since the study of transient friction is beyond the scope of this Dissertation.

In all that follows, the requirements of the first approach to transient friction will be assumed.

2.3.6 Cross-Section Averaged Dynamic Equations of the 1D AHM

The considerations, assumptions and elaborations carried out in the preceding sections, lead finally to the dynamic equations corresponding to the liquid's discharge problem, which are summarised in the following ordinary non-linear integro-differential equations:

$$\frac{d\tilde{v}(t)}{dt} = \frac{1}{\rho \int_0^t \tilde{v}(\tau) d\tau} \left(\frac{p_0}{\left(1 + \frac{\pi R^2}{V_{90}} \int_0^t \tilde{v}(\tau) d\tau \right)^\gamma} - p_\infty \right) - \frac{f \tilde{v}(t)^2}{4R} \quad (0 < t < t_f) \quad (2.66)$$

$$\frac{d\tilde{v}(t)}{dt} = \frac{1}{\rho L} \left(\frac{p_0}{\left(1 + \frac{\pi R^2}{V_{g0}} \int_0^t \tilde{v}(\tau) d\tau\right)^\gamma} - p_\infty \right) - \frac{f \tilde{v}(t)^2}{4R} \quad (t > t_f) \quad (2.67)$$

which constitute the definition of the AHM. Note the AHM is entirely based on First Principles: the Navier-Stokes equations and some generically acceptable assumptions. These equations are too intricate to be solved analytically, and thus it is necessary to resort to numerical algorithms. Remember f could be considered constant for rapid practical calculations, although for a rigorous solver it would be preferred to implement a routine yielding f through correlation (2.64).

The resolution of the integro-differential equations demands initial conditions, fixed as: $\tilde{v}_1(0) = 0$ for equation 2.66, and $\tilde{v}_2(t_f) = \tilde{v}_1(t_f)$ for equation 2.67, being \tilde{v}_1 and \tilde{v}_2 the velocities calculated through 2.66 and 2.67, respectively. Upon numerical solution of these equations, it will be seen that resulting velocities are very large after a few hundredths of a second elapse. Thus, it is justified the assumption of very large Re during the discharge process, which in turn would justify to consider f as a constant in the equations above.

The dynamic equations contains a singularity for $t = 0^+$, since $z_f(0) = 0$. The pressure gradient is formally infinite immediately after $t = 0$, when the valve is assumed to be instantaneously opened and the pressure difference is developed over a zero length. In order to avoid this singularity, a finite (though small) length of the equivalent to a Discharge Valve, L_v , will be introduced in the computer algorithm, which actually is no more than the finite length over which the first pressure gradient (the maximum) is exerted. Fortunately, this mathematical artifice turns into a quantity with physical sense, since a fast valve actually exists in FPE applications. The computer algorithm will show that a few millimetres of discharge valve suffice to circumvent this singularity problem. Although L_v does not appear explicitly in the dynamic equation 2.66, it must be defined before running the computer solver.

This 1D AHM describes analytically the discharge flow of a clean extinction agent, like FK-5-1-12, through a pipe. Later, in Chapter 4, the AHM will be compared with equivalent results obtained from CFD simulations. The 3D CFD model will supply internal flow data the 1D AHM would by no means provide, though both models would validate each other.

The AHM counts with three additional degrees of freedom to adjust to matching CFD flow simulations or to experimental data ²⁵:

- i. The pipe roughness ζ_r or, equivalently, the dimensionless relative pipe roughness $\zeta_D = \zeta_r/D$. It serves to determine the asymptotic value of f as Re grows with the flow.
- ii. The length of equivalent discharge valve L_v . It serves to determine how fast will the velocity grow immediately after opening the valve, that is, the acceleration level attained by the flow.
- iii. The **friction modulator** Δ_f . The second approach to the transient friction problem described in

²⁵Actually, the AHM counts with a fourth degree of freedom: the polytropic index n . The expansion of the ideal gas N_2 inside the vessel has been assumed polytropic and adiabatic (see assumption iv in page 33), and that means $n = \gamma = c_p/c_v$. However, the expansion could also be thought of as isothermal, since the N_2 temperature inside the vessel is not expected to change much during the process. In this case, the polytropic index would be $n = 1$. It would even be plausible to think of other values for n , which could be adjusted to fit experimental or simulation data. Nevertheless, no sensitivity analysis upon the polytropic index will be performed, since in all CFD simulations carried out in this work has been set $n = \gamma$.

page 50, introduces the possibility that the friction factor be not calculated through the Colebrook-White correlation, or any other steady state correlation found in the literature. Thus, it would be possible that the unsteady friction factor were functionally different and even depend on the acceleration. Therefore, it would seem sensible to introduce in the AHM a factor which could modify (modulate) the values of f obtained through the steady state Colebrook-White correlation. Such factor is the **friction modulator** Δ_f , a dimensionless coefficient that produces an **effective friction factor** $f_e = f\Delta_f$, which would replace f in equations 2.66 and 2.67. Should the CFD simulation yield a time-velocity curve not compatible with steady state friction factor f , the effective friction factor f_e would enable the adjustment of the AHM time-velocity curve with that of the CFD. Although in general Δ_f would be variable, only constant friction modulators will be considered herein.

Those degrees of freedom should be adjusted at will for each particular case, until the best fit is obtained with the 3D CFD data, or experimental results. The CFD models essayed in this Dissertation do not have a provision for such parameters; thus they are not fixed in advance in the AHM and could be fine-tuned within reason. Other quantities involved in the AHM ($L, R, G_f, p_0, p_\infty, \gamma, \dots$) are fixed by equivalent ones in the CFD model and cannot be modified for each simulation.

A graphical representation of the dynamic equation's solution is offered in figure 2.14, as an advance of the results that will be analysed later in detail, so that the reader can have an early idea of the liquid's behaviour during the discharge process, prior to plunging into the sections that come next. The values for the transport quantities ρ, μ and ν correspond to clean agent FK-5-1-12, while the initial values p_0 and V_{g0} are chosen according to the conditions in which such agent is normally installed in actual FPE applications. The whole discharge process until agent's exhaustion lasts some 5 s; according to standing regulations it should take less than 10 s.

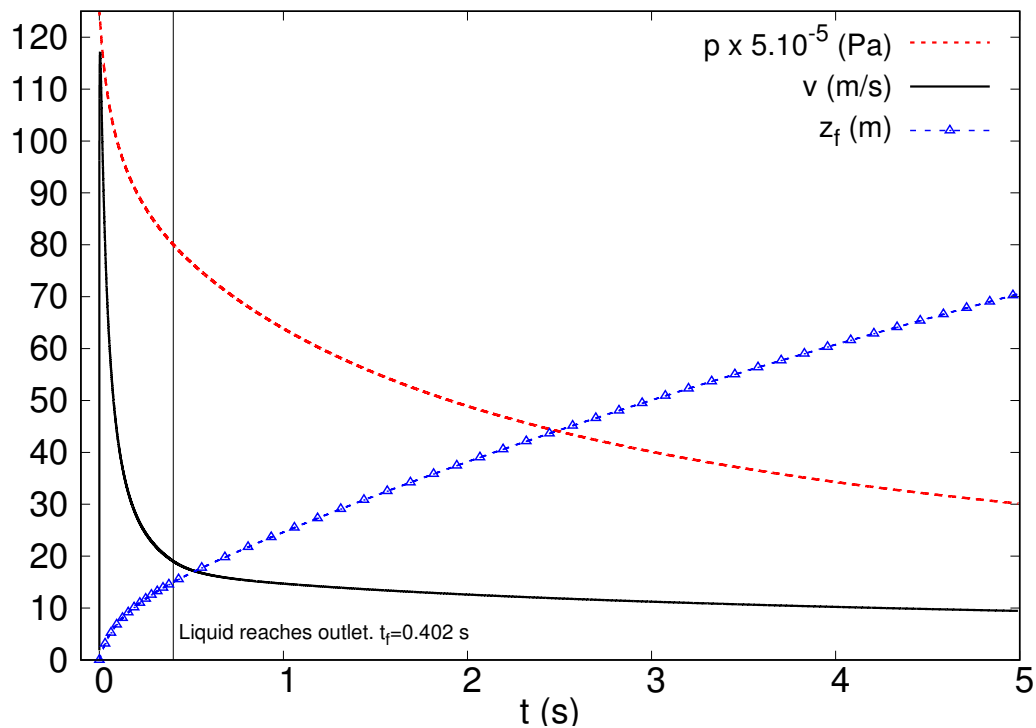


Figure 2.14: Dynamic equation's solution up to complete liquid discharge.

2.4 Dimensionless Dynamic Equations

As there are many variables present in this phenomenon, of differing importance, it is generally a good idea to reduce their number by converting the dynamic equations to a dimensionless form.

In this approach a method of dimensionality will be used in which some reference quantities are chosen, and the other quantities are expressed as combinations of the formers. Attached to each reference quantity there exist a reference unit. Those reference quantities ought to be selected to fulfil two basic conditions: they must be very representative of the phenomenon, and they should be determined directly from the model prior to beginning any actual calculation. Another feature is also desirable, namely, that the reference units be of similar order of magnitude than the calculated quantity values. Obviously, the selection is not unique and an unfortunate choice could complicate the equations rather than helping to their resolution.

In this section a suitable set of reference quantities will be chosen, together with their reference units, an explanation offered for such selection, and the final dimensionless dynamic equations will be derived. At the end of this derivation, some remarks will help explain the physical meaning of those equations. In the next section, the dimensionless dynamic equations will be solved numerically and the solution curves will be shown graphically.

To avoid subscripts, primes ('), or stars (*) which unnecessarily complicate the notation, dimensionless quantities will be expressed with the same characters as the original ones, using instead a Sans Serif font.

2.4.1 Reference Quantities and Values

Three reference quantities are chosen, all others could be derived therefrom. They are:

- i. **Length:** Traditionally, the reference unit for length in flow phenomena involving pipes is the pipe diameter itself, $L_{ref} = D$. No reason is found to change this criterion and the study herein adheres to such custom. Thus the lengths involved in the AHM are expressed as $z = zD$, $z_f = z_f D$, $L = LD...$
- ii. **Density:** The reference unit will be the density of the liquid filling the vessel at an ambient temperature of $20^\circ C$. In this study it corresponds to extinction agent FK-5-1-12, $\rho_{ref} = \rho_{FK-5-1-12} = 1616.34 \text{ kg/m}^3 @ 20^\circ C$ (see table 1.1).
- iii. **Pressure:** The relative pressure in the vessel is adopted as the reference unit, $p_{ref} = p_0 - p_\infty$. Thus $p_g(t) = p_g(t)(p_0 - p_\infty)$, $p_0 = p_0(p_0 - p_\infty)$ and $p_\infty = p_\infty(p_0 - p_\infty)$.

Other quantities are expressed as a function of the references:

Velocity: The reference velocity is chosen as that attained by an ideal liquid exiting a large deposit of height $h = (p_0 - p_\infty)/g\rho$, namely, $v_{ref} = \sqrt{2(p_0 - p_\infty)/\rho}$ through Bernoulli's principle. Note in the AHM p_0 is the vessel's absolute pressure and $p_0 - p_\infty$ is relative to the atmosphere. Thus $\tilde{v} = \tilde{v}\sqrt{2(p_0 - p_\infty)/\rho}$.

Time: A suitable time reference unit is length/velocity, that is, $t_{ref} = D/\sqrt{2(p_0 - p_\infty)/\rho} = D\sqrt{\rho/2(p_0 - p_\infty)}$. Thus any time will be expressed as $t = t D\sqrt{\rho/2(p_0 - p_\infty)}$.

Force: The reference unit of force equals the reference pressure times the reference area: $F_{ref} = (p_0 - p_\infty)D^2$. Thus $F = F (p_0 - p_\infty)D^2$ for any force F .

The selection of those references is justified by the simplicity of the dimensionless equations obtained, and their fulfilling the requirements stated above. They are summarised in table 2.2.

2.4.2 Method of Dimensionality

Fast stage ($0 < t < t_f$) (Figure 2.10) With the reference quantities on hand, every term of equation (2.66) is converted into a dimensionless form by the following procedure:

- $\frac{d\tilde{v}}{dt}$. The elaboration of this term is:

$$\frac{d\tilde{v}}{dt} = \sqrt{\frac{2(p_0 - p_\infty)}{\rho}} \frac{d\tilde{v}}{dt} \frac{1}{D} \sqrt{\frac{2(p_0 - p_\infty)}{\rho}} = \frac{2(p_0 - p_\infty)}{\rho D} \frac{d\tilde{v}}{dt} \quad (2.68)$$

- $\left(\rho \int_0^t \tilde{v}(t) dt \right)^{-1} \left(\frac{p_0}{\left(1 + \frac{\pi R^2}{V_{g0}} \int_0^t \tilde{v}(t) dt \right)^\gamma} - p_\infty \right)$. The elaboration of this term is:

$$\begin{aligned} & \left(\rho D \int_0^t \tilde{v}(t) dt \right)^{-1} \left(\frac{p_0(p_0 - p_\infty)}{\left(1 + \frac{\pi R^2 D}{V_{g0}} \int_0^t \tilde{v}(t) dt \right)^\gamma} - p_\infty(p_0 - p_\infty) \right) = \\ & = \frac{p_0 - p_\infty}{\rho D \int_0^t \tilde{v} dt} \left(\frac{p_0}{\left(1 + G_f \int_0^t \tilde{v} dt \right)^\gamma} - p_\infty \right) \end{aligned} \quad (2.69)$$

where the geometric factor $G_f = \frac{\pi R^2 D}{V_{g0}} = \frac{\pi D^3}{4V_{g0}}$ is already a dimensionless number²⁶.

- $\frac{f\tilde{v}(t)^2}{4R}$. Since f is already a dimensionless number, this term results in:

$$\frac{f\tilde{v}^2}{4R} = \frac{f}{4R} \frac{2(p_0 - p_\infty)}{\rho} \tilde{v}^2 = \frac{f(p_0 - p_\infty)}{\rho D} \tilde{v}^2 \quad (2.70)$$

Combining now all the above terms, the following dimensionless equation is obtained:

$$\begin{aligned} \frac{2(p_0 - p_\infty)}{\rho D} \frac{d\tilde{v}}{dt} &= \frac{p_0 - p_\infty}{\rho D \int_0^t \tilde{v} dt} \left(\frac{p_0}{\left(1 + G_f \int_0^t \tilde{v} dt \right)^\gamma} - p_\infty \right) - \frac{f(p_0 - p_\infty)}{\rho D} \tilde{v}^2 \Rightarrow \\ \Rightarrow 2 \frac{d\tilde{v}}{dt} &= \left(\int_0^t \tilde{v} dt \right)^{-1} \left(\frac{p_0}{\left(1 + G_f \int_0^t \tilde{v} dt \right)^\gamma} - p_\infty \right) - f\tilde{v}^2 \end{aligned} \quad (2.71)$$

²⁶Note that G_f equals 3/2 times the ratio (volume of a sphere of diameter D)/ V_{g0} , and it is a pure geometric factor. It is related to the filling density of the cylinders described in section 1.2

or, arranging the terms:

$$\frac{d\tilde{v}}{dt} = \left(2 \int_0^t \tilde{v} dt \right)^{-1} \left(\frac{p_0}{\left(1 + G_f \int_0^t \tilde{v} dt \right)^\gamma} - p_\infty \right) - \frac{f \tilde{v}^2}{2} \quad (2.72)$$

This is a fully dimensionless equation in which all the quantities, except $\tilde{v}(t)$, are constant (f is mathematically variable, but it is physically constant, see section 2.3.5). Thus, it can be classified as a non-linear ordinary integro-differential equation with constant coefficients.²⁷

Slow stage ($t > t_f$) (Figure 2.11) The process is identical to that already seen for Fast stage, using instead the equation (2.67). Thus

$$\frac{d\tilde{v}}{dt} = \frac{2(p_0 - p_\infty)}{\rho D} \frac{d\tilde{v}}{dt} \quad (2.73)$$

and

$$\frac{1}{\rho L} \left(\frac{p_0}{\left(1 + \frac{\pi R^2}{V_{g0}} \int_0^t \tilde{v}(t) dt \right)^\gamma} - p_\infty \right) = \frac{p_0 - p_\infty}{\rho L D} \left(\frac{p_0}{\left(1 + G_f \int_0^t \tilde{v} dt \right)^\gamma} - p_\infty \right) \quad (2.74)$$

and

$$\frac{f \tilde{v}^2}{4R} = \frac{f(p_0 - p_\infty)}{\rho D} \tilde{v}^2 \quad (2.75)$$

All together yield the result

$$\frac{d\tilde{v}}{dt} = \frac{1}{2L} \left(\frac{p_0}{\left(1 + G_f \int_0^t \tilde{v} dt \right)^\gamma} - p_\infty \right) - \frac{f \tilde{v}^2}{2} \quad (2.76)$$

which is another non-linear ordinary integro-differential equation with constant coefficients (same remark for f as before).

The dimensionless equations that have just been obtained are quite similar to their dimensional counterparts. The presence of the integral $z_f = \int_0^t \tilde{v}(t) dt$ in the Fast stage means that the evolution of the main variable, \tilde{v} , depends not only on the instantaneous values of the present forces, but also on the history of the discharge process, on its past. That is, whatever occur in the first instants will determine the later evolution of \tilde{v} , until the Slow stage is reached. Thus, the Fast stage could also be dubbed as *'the stage in which history matters'*, or *'the stage in which the discharge process has memory'*, because in order to calculate \tilde{v} at a certain instant t , what has happened to \tilde{v} in all previous instants must be taken into account. This dependence is also present in the Slow stage, but its influence is much smaller and limited to the denominator of p_0 , namely $\left(1 + G_f \int_0^t \tilde{v}(t) dt \right)^\gamma$.

²⁷An almost identical result is obtained (with factors of 2 placed elsewhere) if the following reference quantities are considered: $t_{ref} = D^2/\nu$, $p_{ref} = \rho\nu^2/D^2$ and $v_{ref} = D/t_{ref} = \nu/D$. Note that with this selection $\tilde{v} \equiv Re$.

2.5 Numerical Solution of Dimensionless Equations

It has already been said that the model's dynamic equations are too intricate to attempt a direct analytical solution. Since they are ordinary integro-differential equations, classical algorithms could be used in their solution, as most traditional numerical methods yield accurate results provided Δt is chosen small enough. With growing computer power, a very small time-step is not usually a problem and the solver output's accuracy could be chosen as high as needed. This section is devoted to explain the numerical algorithm used to solve the dimensionless dynamic equations (2.72) and (2.76), and to show the results graphically for various quantities.

The algorithm has been implemented into a computer program which could be used to perform hydraulic calculations for actual practical cases of fire extinction with clean agent FK-5-1-12. It resorts to very powerful techniques of classical Numerical Analysis, which are accurate to fourth order. With minor modifications, it could be used for other clean agents as well, provided they do not undergo significant vaporisation during the transit within the pipe.

In order to properly calculate $\tilde{v}(t)$ at each time-step, the integral $\int_0^t \tilde{v} dt$ must be calculated simultaneously with the velocity itself. To solve both, equation and integral, the following procedures are employed:

- The integral will be solved with the One Third Simpson's Rule (S1/3), in the version suitable for a large number of points (see [Vah86] or [Ant91]).
- The integro-differential equation will be solved with the Fourth Order Runge-Kutta's method (RK4), with constant interval Δt (see [DR05], [Vah86] or [Ant91]).

Some other aspects had to be solved in the algorithm, although they were not so evident in the theoretical development presented herein, namely:

- i. The problem of the singularity at $t = 0^+$.²⁸ At this point the equation is singular and the computer algorithm crashes (overflow error). This problem is circumvented just by defining a minimal finite length in which the pressure gradient develops. This variable is L_v and it may be considered as the length of the opening valve, although it merely is an artifice to avoid the singularity at the origin.
- ii. The value of the friction factor f , and the correlation used to calculate it, depend on whether the liquid's motion develops on laminar or turbulent regime. Thus, a method has been implemented to pass smoothly from one correlation to another, without breaking the continuity, when $64/Re$ equals the value yielded by Colebrook-White. Possibly, this procedure is not very accurate. However, it must be said that after few iteration steps the regime becomes fully turbulent, f tends asymptotically to a constant value, and the error committed is negligible.
- iii. One Third Simpson's Rule (S1/3) and Fourth Order Runge-Kutta's method (RK4) require a careful treatment of the very first steps of the iteration loop. The computer program deals explicitly with the first three iteration steps, in which some quantities (such as the integral) are not yet properly defined.
- iv. The algorithm also takes into account the two different denominators appearing in the equations when the liquid reaches the pipe's outlet.

²⁸The problem of the *impulsive start* of an incompressible flow is amply discussed and explained in [Gre91] and [Gre92], some must-read references for whoever interested in the study of transient flows.

- v. In order to optimize the time step Δt in the algorithm, a first integration of the equation is carried out with a total discharge time equalling the maximum admissible time established by regulations and standards (namely $T_{max} = 10$ s), and taking $\Delta t = T_{max}/N$, with N the number of integration points. After the first execution, the actual time of full discharge up to exhaustion is found (which must be below 10 s according to current regulations). and T_{max} is replaced by this new value, resulting in a $\Delta t = T_{max}/N$ smaller than in the first round. Thus, a slightly different Δt is used in each simulation.
- vi. In order to optimize the algorithm, more calculation power should be applied to the Fast stage, where the most interesting phenomena happen, than to the Slow stage. To this end, the time interval Δt in the Fast stage is chosen smaller than the corresponding to Slow stage, while maintaining unchanged the total number of points N . A procedure has been written to smoothly change from Δt for Fast stage to Δt for Slow stage. Typically, $\Delta t_{fast} \leq \Delta t_{slow}/2$.

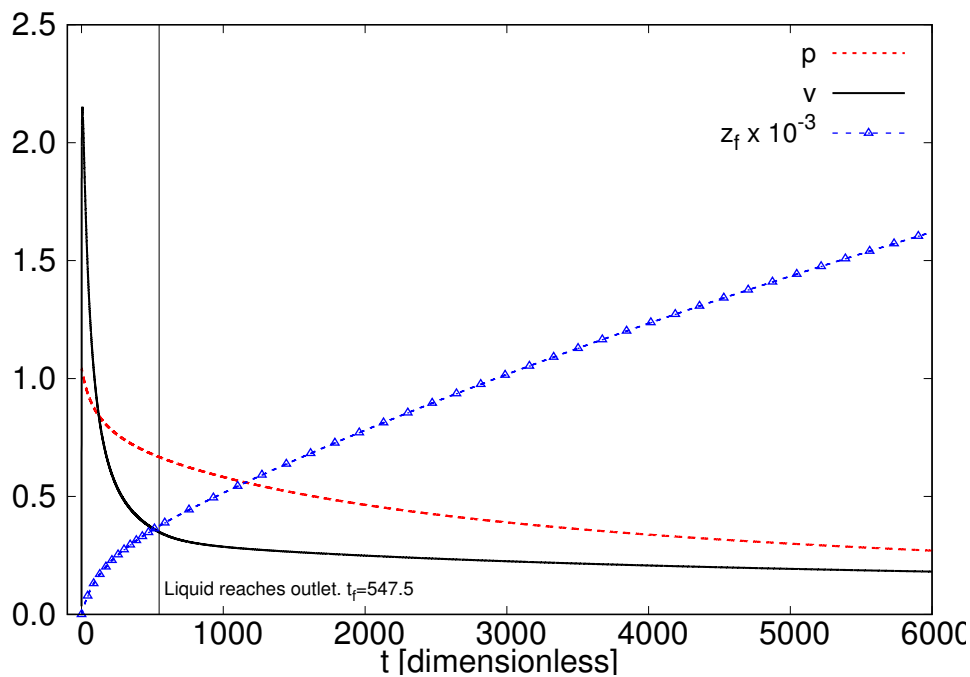


Figure 2.15: Dimensionless dynamic equation's solution up to complete liquid discharge.

The dimensionless version of figure 2.14 is presented in figure 2.15. The graph shows the variation of relevant quantities along the discharge process, until agent has been exhausted from the vessel.

2.6 Results and Discussions

Equations (2.72) and (2.76) exhibit explicit dependence only on four dimensionless parameters, namely: the vessel's initial pressure p_0 , the discharge pipe's length L , the geometric factor G_f , and the Darcy-Weisbach friction factor f . The atmospheric pressure p_∞ and the adiabatic index γ are presumed rigorously constant²⁹. The Darcy-Weisbach friction factor f is calculated each time, thus no value could be assigned to it beforehand. That leaves three parameters to define in the solver prior to execution.

²⁹Recall the adiabatic index γ could be substituted by a general polytropic index n , should the expansion process occurring in the ideal gas N_2 be assumed polytropic but not adiabatic. This possibility, though, will not be considered in this Dissertation, since all CFD simulations have been executed with $n = \gamma$.

Besides, those equations exhibit an implicit dependence on the three dimensionless parameters that have been called the *degrees of freedom* of the 1D AHM: pipe roughness ζ_D , equivalent length valve L_v , and friction modulator Δ_f . These implicit parameters are inserted in the computer code which solves the equations (2.72) and (2.76), and could be tweaked at will (within reason) to adjust to CFD or experimental data.

This section will conduct a detailed study of the equation's behaviour under controlled changes in all these 3 + 3 dimensionless parameters. As will be seen, the Fast stage proves quite insensitive to such changes, except for ζ_D , L_v and Δ_f . On the other hand, the velocity curve in the Slow stage vary noticeably with those parameters, except for p_0 and L_v .

Quantity	Value	Reference Unit
p_0	1.04224	$p_0 - p_\infty = 2\,398\,675\ Pa$
L	375	$D = 0.04\ m$
G_f	0.0010	$V_{g_0} = 0.0502656\ m^3, D = 0.04\ m$
ζ_D	$8.25 \cdot 10^{-4}$	$D = 0.04\ m$
L_v	0.125	$D = 0.04\ m$
Δ_f	1	—

Table 2.1: Values for dimensionless quantities of a standard pipe.

The methodology will be straightforward: a set of standard values for the 3 + 3 parameters will be established, and variations around these will be introduced in the computer solver, one at a time, and the results displayed and analysed. The selection of such standard values is based on those conditions that frequently occur is FPE applications with clean agent FK-5-1-12. The dimensionless values that are considered standard are shown in table 2.1³⁰: A **standard pipe** is defined as a test set like that of figure 2.2 with the standard values given in table 2.1. The dimensioned and dimensionless curves of figures 2.14 and 2.15, respectively, correspond to a standard pipe, and they present the evolution of the dynamic quantities until the agent is completely depleted from the vessel.

In order to foster the comparison among different flow situations, in the remainder of this Chapter the graphs will only show the evolution from $t = 0$ to the beginning of the asymptotic zone for velocity. Figure 2.16 displays this situation for a standard pipe, where the asymptotic zone for \tilde{v} is attained around $t = 1000$. Upon examining the velocity curve in figure 2.16, three stages could be identified³¹:

- i. The **acceleration stage**. It is characterised by an extremely fast growth of velocity: acceleration surpasses $1000\ g$. Such high accelerations are confirmed by the 3D CFD simulations. In this stage the driving force for the flow is the pressure exerted by the ideal gas within the vessel. Wall-friction plays a negligible role here. In the standard pipe of figure 2.16 the acceleration stage runs from $t = 0^+$ to approximately $t = 5$.
- ii. The **transition stage**. Pressure and friction forces are roughly balanced in this short stage, and the relevant driving force for the flow switches over. This stage is developed around the velocity maximum and represents a major change in the cross-section velocity profile within the pipe. The

³⁰ $G_f = 0.001$ corresponds to a 120 litre cylinder filled with 112.7145 kg of FK-5-1-12, a filling density well within industry standards.

³¹Note this classification is different from that made in section 2.2 regarding the Fast and Slow stages: there the event separating both stages is the liquid reaching the outlet, here it is the value of the acceleration.

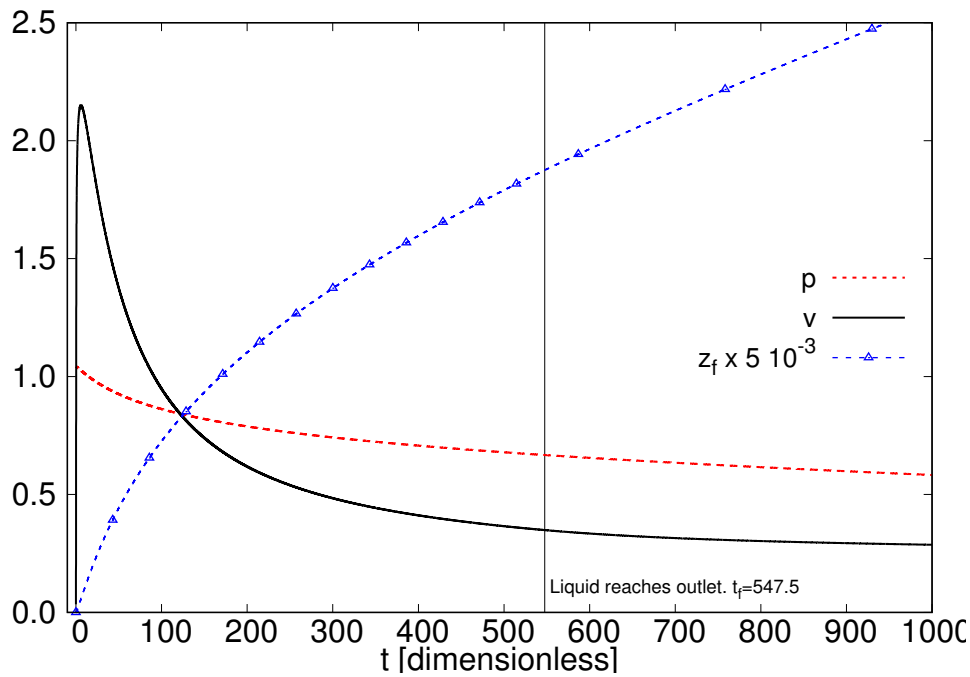


Figure 2.16: Standard curves for parameters' standard values.

maximum velocity (zero acceleration) for the standard pipe of figure 2.16 occurs at $t = 5.8393$. Thus the transition stage elapses roughly from $t = 5$ to $t = 7$.

- iii. The **deceleration stage**. The driving force is the wall-friction, which acts once enough liquid is present in the pipe. Pressure, though still noteworthy, cannot counteract the resistance offered by the wall and is not so important. It is the longest stage: it elapses until the liquid depletes the vessel. Note that, contrary to what one might have thought at first sight, the flow spends most of the time *decelerating*.

Note the velocity curve of figure 2.16 is remarkably similar to that predicted by [CHM92], shown in figure 1.21 of page 18, or, to a lesser degree, to the curve predicted by [Val98] in figure 2.1. Besides, it is also similar to figures 2.17 and 2.18, obtained respectively from [KLA⁺11] and [VW07]. Figures 2.17 and 2.18 correspond to a flow of water filling a pipeline previously empty (full of air). The initial pressure in both papers is much lower than the one assumed herein, but the velocity present a dynamic behaviour not markedly different from that revealed in figure 2.16: they also have acceleration, transition and deceleration stages. In figure 2.17 the parameter f^* corresponds to $f^* = f L/D$.

Other quantities of interest could be expressed by means of the reference units introduced previously. A non exhaustive list for the standard pipe is shown in table 2.2.

2.6.1 Sensitivity Analysis of the 1D AHM

This section will study the effects on the flow dynamics caused by changes in the dimensionless parameters listed in table 2.1. The departing point will always be the standard pipe (see page 59), All parameters adopt their standard values except one, which will be varied above and below its standard value, in some cases up to one or two orders of magnitude. A single parameter will be changed at a time.

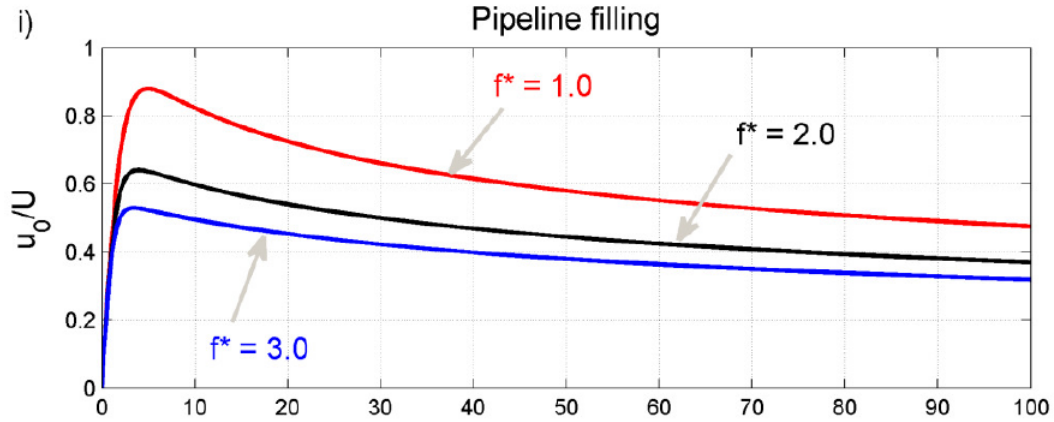
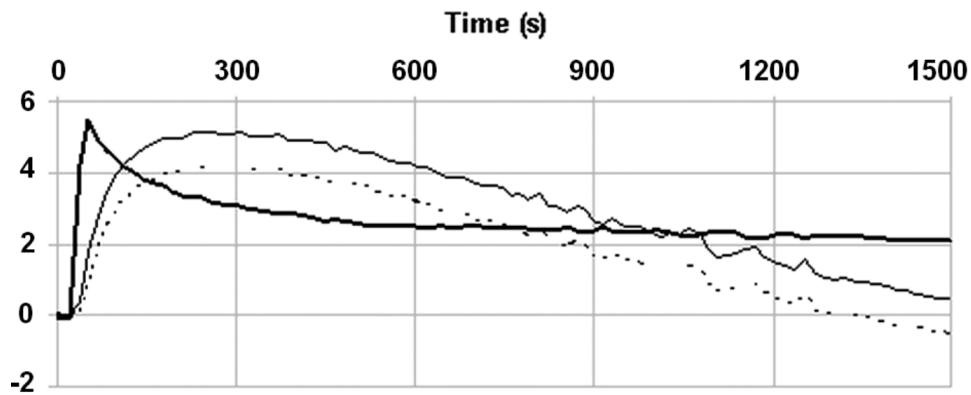
Figure 2.17: Velocity curve during the filing of a pipeline, after [KLA⁺11].

Figure 2.18: Velocity curve (thick line) during the filing of a pipeline, after [VW07].

Reference Quantity	Expression	Reference Unit
z_{ref}	D	0.04 m
v_{ref}	$\sqrt{\frac{2(p_0 - p_\infty)}{\rho}}$	54.47965 m/s
p_{ref}	$p_0 - p_\infty$	2.398675 MPa
t_{ref}	$D\sqrt{\frac{\rho}{2(p_0 - p_\infty)}}$	$7.342191 \cdot 10^{-04} \text{ s}$
F_{ref}	$(p_0 - p_\infty)D^2$	$3.83788 \cdot 10^3 \text{ N}$
ρ_{ref}	$\rho_{FK-5-1-12}$	1616.34 kg/m^3
a_{ref}	z_{ref}/t_{ref}^2	$7.420082 \cdot 10^4 \text{ m/s}^2$

Table 2.2: Reference quantities and units for standard pipe.

The results will be examined and the sensitivity of the 1D AHM to such variations will be analysed³².

In the coming examples, t_{\max} is the time at which the velocity maximum v_{\max} is achieved, t_f is the time

³²No sensitivity analysis will be performed upon the adiabatic index γ , regarding its potential substitution by a general polytropic index n .

at which the liquid first reaches the pipe's outlet (end of Fast stage and beginning of Slow stage), while v_f is its velocity at t_f , and $p_g(t_f)$ is the pressure within the vessel at the same instant.

2.6.1.1 Variations with p_0

A typical value of $p_0 = p_0/(p_0 - p_\infty)$ for actual FPE applications involving clean agent FK-5-1-12 is 1.04224, corresponding to $p_0 = 2.5 \text{ MPa}$. Although other pressures are possible, this is the standard value adopted herein.

Figure 2.19 displays the dimensionless bulk velocity curves corresponding to the p_0 values shown in table 2.3 (**bold** typeface belongs to the standard pipe)³³.

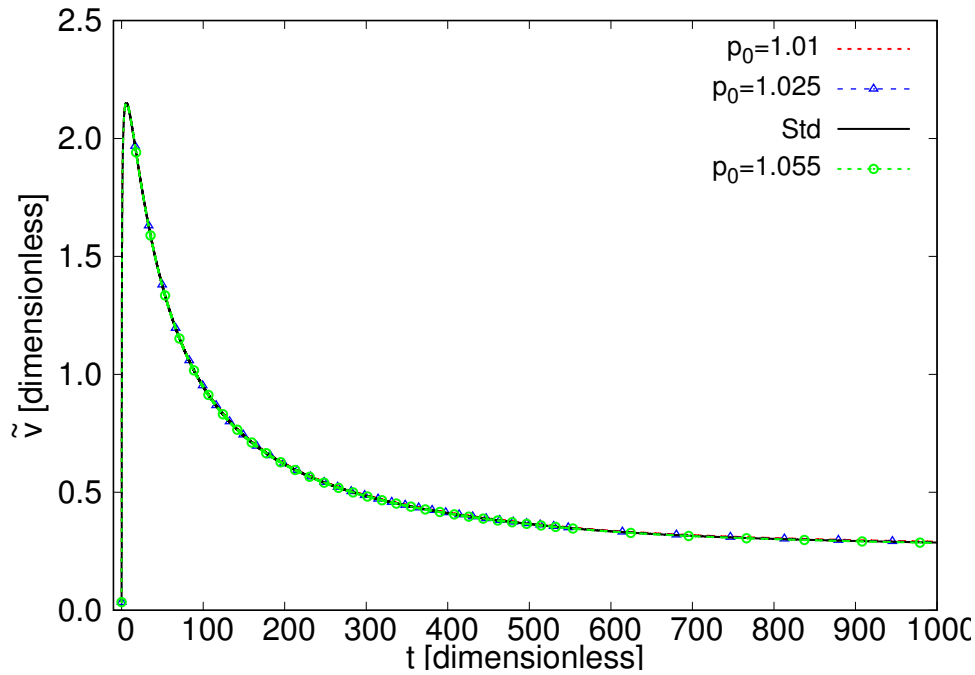


Figure 2.19: Velocity curves for various initial pressures p_0 .

p_0	$p_0 \text{ (MPa)}$	t_{\max}	v_{\max}	t_f	v_f	$p_g(t_f)$
1.01	10.233825	5.84830	2.149192	544.409805	0.352742	0.636692
1.025	4.154325	5.84206	2.149053	545.969730	0.350966	0.631296
1.04224	2.500000	5.83927	2.149094	547.536641	0.349139	0.625094
1.055	1.943597	5.84024	2.148703	584.024014	0.347848	0.620505

Table 2.3: Key values defining the dynamics for varying p_0 .

The results obtained should cause no surprise: the curves are almost insensitive to p_0 variations. This is due to the particular selection of v_{ref} and p_{ref} made in this work. However, the dimensional velocities are quite dependent on the p_0 values: $v_{max} = 240.6 \text{ m/s}$ for $p_0 = 1.01$, $v_{max} = 152.2 \text{ m/s}$ for $p_0 = 1.025$, $v_{max} = 117.1 \text{ m/s}$ for the standard pipe, and $v_{max} = 102.6 \text{ m/s}$ for $p_0 = 1.055$.

³³The dimensional values of p_0 are also offered, should the reader want to calculate the reference pressure $p_{ref} = p_0 - p_\infty$ and the rest of reference units.

2.6.1.2 Variations with L

Figure 2.20 displays the dimensionless bulk velocity curves corresponding to the L values shown in table 2.4. Note that, unlike the previous section, the reference units do not change for the cases being considered, and the results are directly comparable. Slight variations on v_{\max} are due to the different Δt used by the algorithm in each simulation.

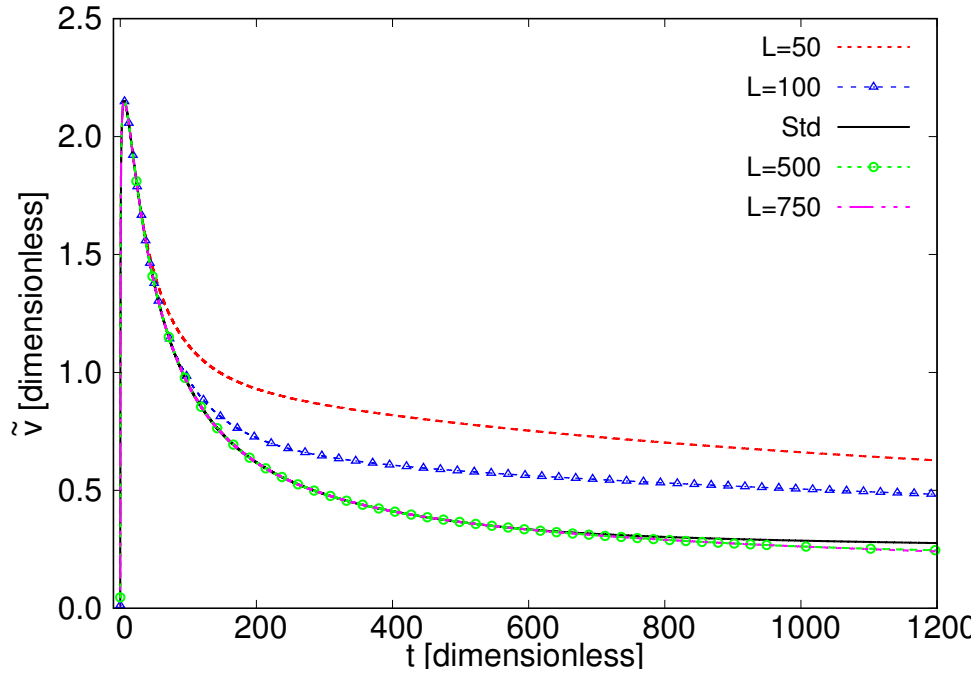


Figure 2.20: Velocity curves for various pipe's lengths L.

L	t_{\max}	v_{\max}	t_f	v_f	$p_g(t_f)$
50	5.84054	2.148799	25.3359866	1.778290	0.931183
100	5.84248	2.148807	58.7052872	1.272181	0.869804
375	5.83927	2.149094	547.536641	0.349139	0.625094
500	5.83636	2.148919	961.946191	0.266750	0.548557
750	5.83686	2.149730	2103.55755	0.186059	0.433876

Table 2.4: Key values defining the dynamics for varying L.

Several conclusions could be drawn from the graphs above:

- Except for very short pipe lengths, the acceleration and transition stages are almost identical for varying L. Thus, the acceleration/transition stage dynamics is completely insensitive to pipe length.
- The maximum value \tilde{v} is also insensitive to L (this ceases to be true for $L \rightarrow 0$).
- The bulk velocity curves depart in the deceleration stage: the shorter L the sooner the departure begins. Standard pipe and $L = 500$ start to depart significantly around $t \approx 900$.

For very short pipe lengths the AHM predicts a high dependence on L . Figure 2.21 shows the bulk velocity curve for $L = 1$. The agent depletes the vessel at $t = 282.06$. Maximum predicted bulk velocity for the liquid is $v_{\max} = 6.5906 \approx 359$ m/s, that is, a supersonic projectile cruising the surrounding air. Therefore, the AHM is not to be trusted for very short pipe lengths. However, the velocity attained by the agent in such cases is extremely high: it should be strictly forbidden to install fire extinction systems with pipes too short (see figure 1.30 in page 28).

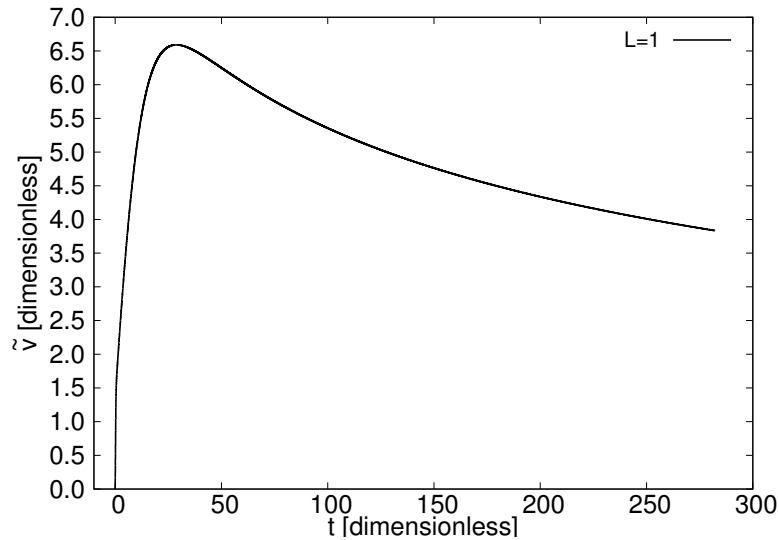


Figure 2.21: Bulk velocity for $L = 1$.

2.6.1.3 Variations with G_f

A typical value of $G_f = \pi D^3 / 4V_{g0}$ for actual FPE applications involving agent FK-5-1-12 is $G_f = 0.001$, corresponding to $D = 0.04$ m, $V_{g0} = 0.0503$ m³, and assigned to the standard pipe. Figure 2.22 displays the dimensionless bulk velocity curves corresponding to the G_f values shown in table 2.5. The reference units do not change for the cases being considered and the results are directly comparable.

G_f	t_{\max}	v_{\max}	t_f	v_f	$p_g(t_f)$
$4 \cdot 10^{-3}$	5.66450	2.139410	675.315250	0.241386	0.246725
$2 \cdot 10^{-3}$	5.77703	2.146075	593.788528	0.301617	0.433876
10^{-3}	5.83927	2.149094	547.536641	0.349139	0.625094
$5 \cdot 10^{-4}$	5.87502	2.150539	522.558871	0.380995	0.777130
$2 \cdot 10^{-4}$	5.89462	2.151694	506.835222	0.403984	0.899640

Table 2.5: Key values defining the dynamics for varying G_f .

Several conclusions could be drawn from the graphs above:

- The acceleration and transition stages are quite independent of G_f .
- The maximum value v_{\max} does not depend much on G_f either.
- In the deceleration stage the curves behave very similarly for different G_f values, although with an offset.

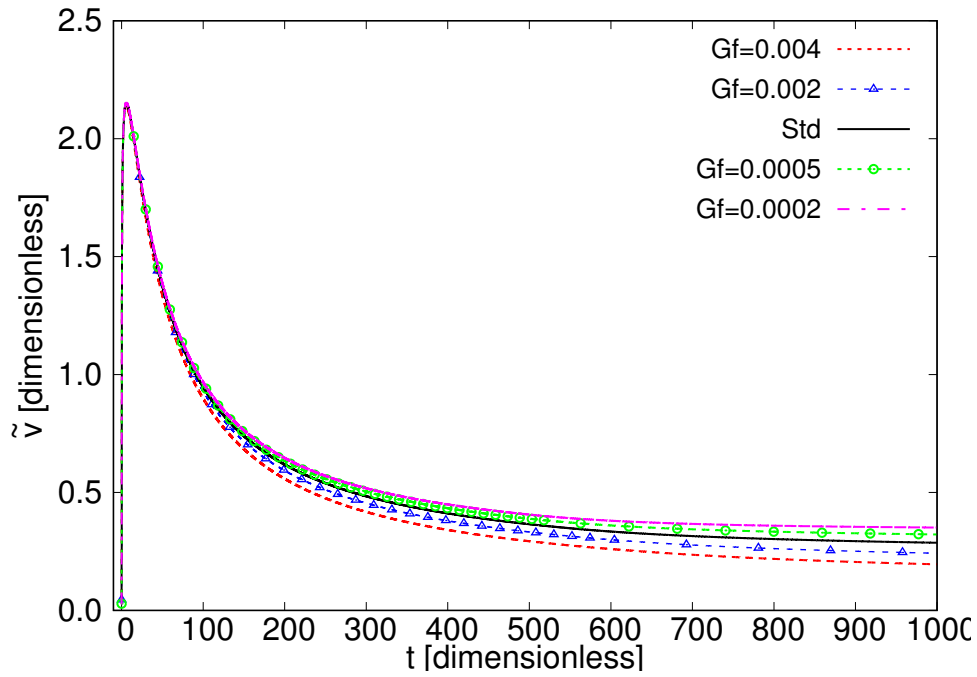


Figure 2.22: Velocity curves for various geometrical factors G_f .

- The pressure drop is very sensitive to G_f . This is probably the most remarkable feature.
- For very small G_f (formally, $G_f \rightarrow 0$) the bulk velocity is insensitive to G_f .

2.6.1.4 Variations with ζ_D

According to AFTA (<http://www.afta-asociacion.com/>), $\zeta_r = 3.3 \cdot 10^{-5} m$ is a typical value for the absolute roughness of steel galvanised pipe. It corresponds to the standard pipe adopted herein. Figure 2.23 displays the dimensionless bulk velocity curves corresponding to the ζ_D values shown in table 2.6. The first row of that table, $\zeta_D = 0$, is referred to hydraulically smooth flow. The reference units do not change for the cases being considered and the results are directly comparable.

ζ_D	t_{\max}	v_{\max}	t_f	v_f	$p_g(t_f)$
0	10.8464	2.303676	273.256528	0.794981	0.625093
$2 \cdot 10^{-5}$	9.45053	2.271046	308.060874	0.673912	0.625094
10^{-4}	7.94670	2.228299	371.832043	0.527807	0.625092
$8.25 \cdot 10^{-4}$	5.83927	2.149094	547.536641	0.349139	0.625094
$2 \cdot 10^{-3}$	5.00718	2.107669	661.348339	0.296597	0.625094
$5 \cdot 10^{-3}$	4.19244	2.059359	808.379470	0.251975	0.625093

Table 2.6: Key values defining the dynamics for varying ζ_D .

Several conclusions could be drawn from the graphs above:

- Compare figure 2.23 with 2.26 below to realise that the effect on the flow of changing ζ_D is not equivalent to modifying Δ_f .
- The acceleration stage is quite insensitive to ζ_D , that is, the rising slope is unaltered by ζ_D .

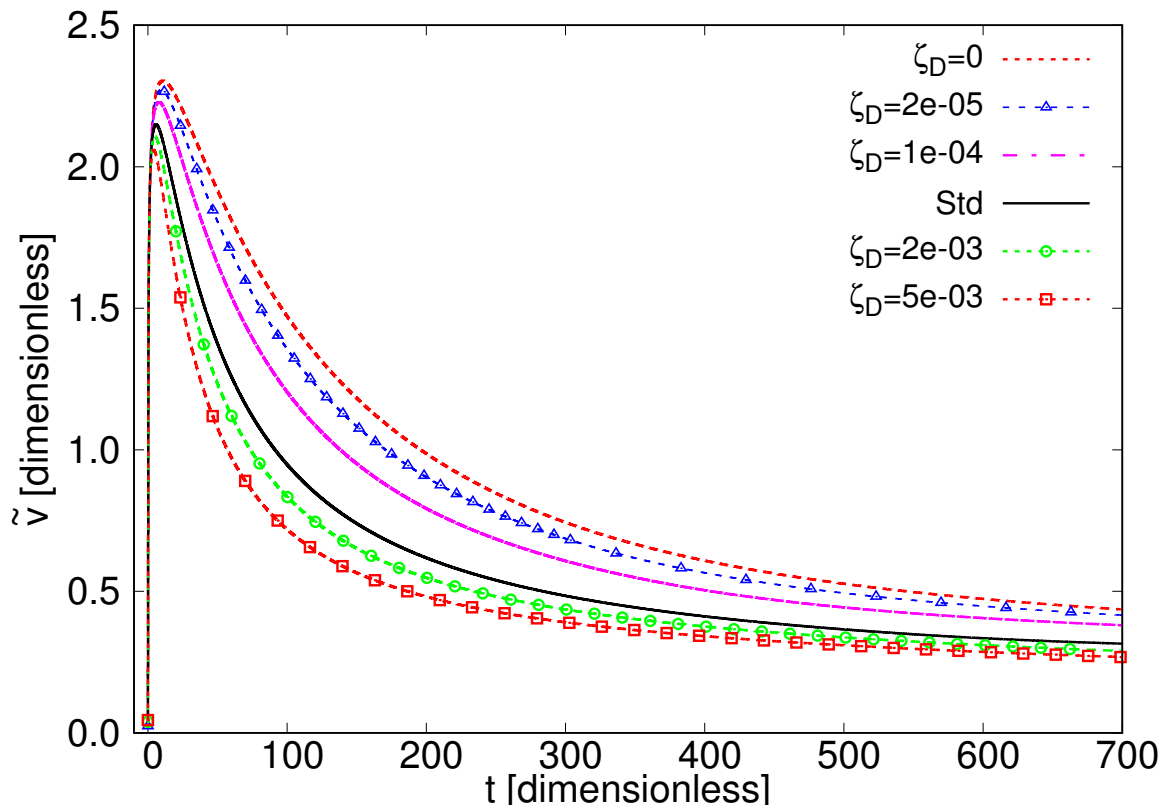


Figure 2.23: Velocity curves for various pipe roughness ζ_D .

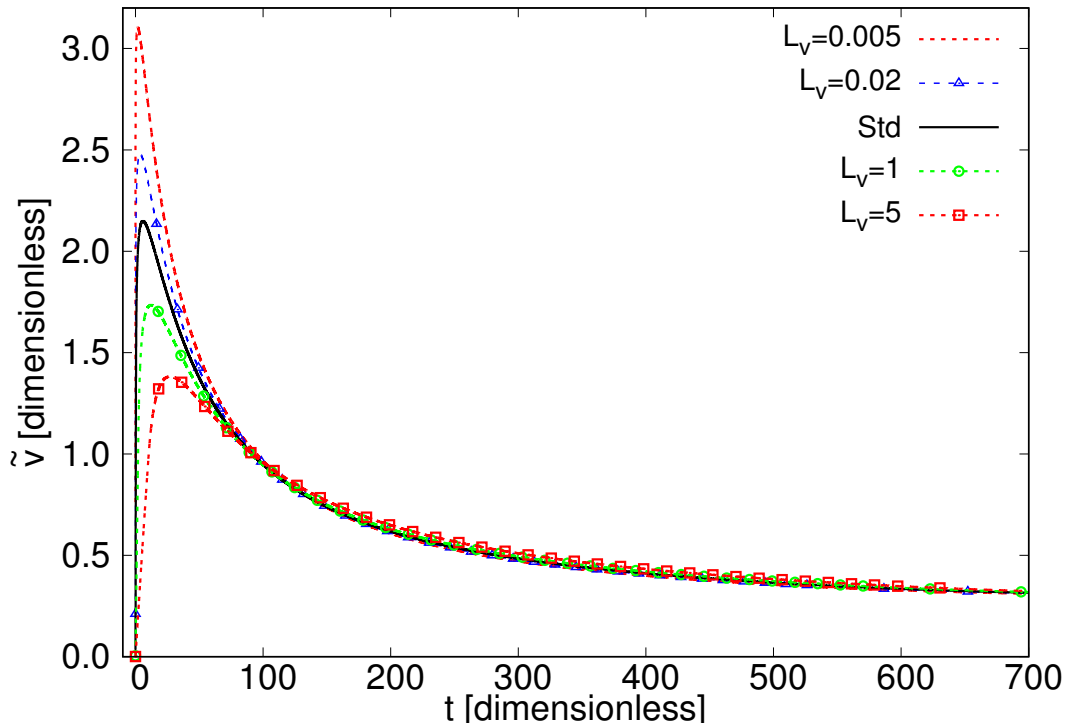
- The transition stage depends on pipe roughness: the maximum velocity v_{\max} and the time for maximum t_{\max} , both, grow for decreasing ζ_D . Note the variation of t_{\max} is more accused than that of v_{\max} .
- The slope in the deceleration stage is very dependent on ζ_D , something to be expected since friction is the dominant force in this stage.

2.6.1.5 Variations with L_v

The introduction of parameter L_v in the solver algorithm is compulsory if the singularity at $t = 0^+$ is to be avoided. L_v is an empirical parameter to be determined from experiment or CFD simulation, since it does not explicitly appear in the dynamic equations. From a physical point of view, it could be resembled to an opening valve of length L_v . The standard pipe has $L_v = 0.125$. Figure 2.24 displays the dimensionless bulk velocity curves corresponding to the L_v values shown in table 2.7. The reference units do not change for the cases being considered and the results are directly comparable.

Several conclusions could be drawn from the graphs above:

- This time the acceleration stage is sensitive to L_v , since the rising slope is altered by L_v . This should cause no surprise, because the acceleration is directly determined by the pressure gradient, and such gradient is relatively small for large L_v . Note the pressure is the dominant force in the acceleration stage.
- Likewise, the transition stage depends on L_v : not only the maximum velocity v_{\max} , but also t_{\max} change noticeably.

Figure 2.24: Velocity curves for various equivalent valve lengths L_v .

L_v	t_{\max}	v_{\max}	t_f	v_f	$p_g(t_f)$
0.005	1.83822	3.102247	495.366588	0.356267	0.625094
0.02	3.66812	2.479196	527.990666	0.351413	0.625092
0.125	5.83927	2.149094	547.536641	0.349139	0.625094
1	12.1784	1.734895	576.514905	0.346534	0.625093
5	27.0710	1.381771	610.421163	0.344471	0.625093

Table 2.7: Key values defining the dynamics for varying L_v .

- The deceleration stage is only sensitive to L_v immediately after the transition stage. Once the effect of the initial pressure gradient disappears, the behaviour of all curves is almost identical, since the friction equals things up.

2.6.1.6 Variations with Δ_f

Although f is not considered an input datum, but rather is calculated as part of the numerical algorithm designed in this Dissertation, it might be convenient to investigate what would happen to the bulk velocity if f were really different from what the Colebrook-White correlation dictates. This issue has already been dealt with in section 2.3.5, page 52.

Figure 2.25 shows f during the complete discharge process for the standard pipe, as calculated by the computer program with the Colebrook-White correlation. Except for initial instants, corresponding to laminar flow with $f = 64/Re$, the calculated f value is almost constant during the flow. It would have served the purpose equally well to have supposed a constant f from the beginning.

The friction modulator Δ_f is introduced to modify f , in order to obtain an effective friction factor

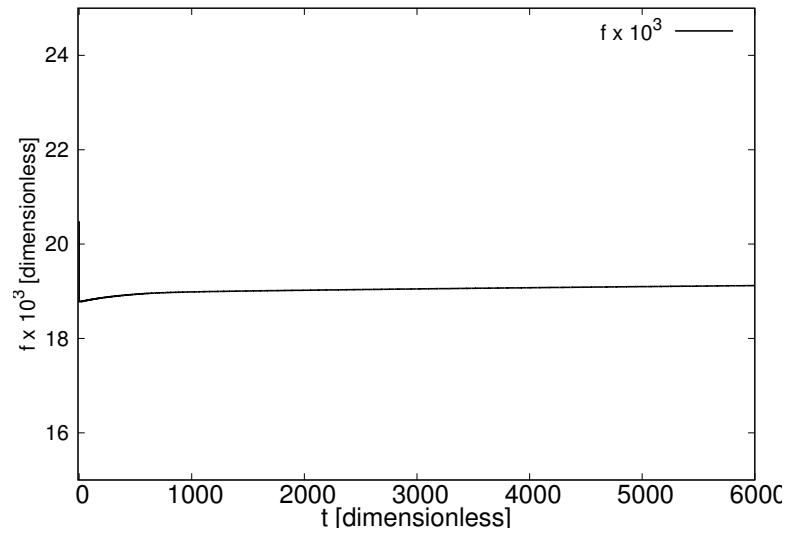


Figure 2.25: Evolution of Darcy-Weisbach friction factor f for standard pipe.

$f_e = f\Delta_f$ which could resemble the actual dynamics of transient turbulent flows. Δ_f is an empirical function to be determined from experiment or CFD simulation, since it does not explicitly appear in the dynamic equations. In general, it would be a variable although herein it will be considered constant. Possibly, the idea of a constant friction modulator would be unsupported by CFD simulations or measurements on actual transient turbulent flows, but meanwhile it is an additional resource the AHM provides to adjust to other trustworthy results. The standard pipe has $\Delta_f = 1$. Figure 2.26 displays the dimensionless bulk velocity curves corresponding to the Δ_f values shown in table 2.8. The reference units do not change for the cases being considered and the results are directly comparable.

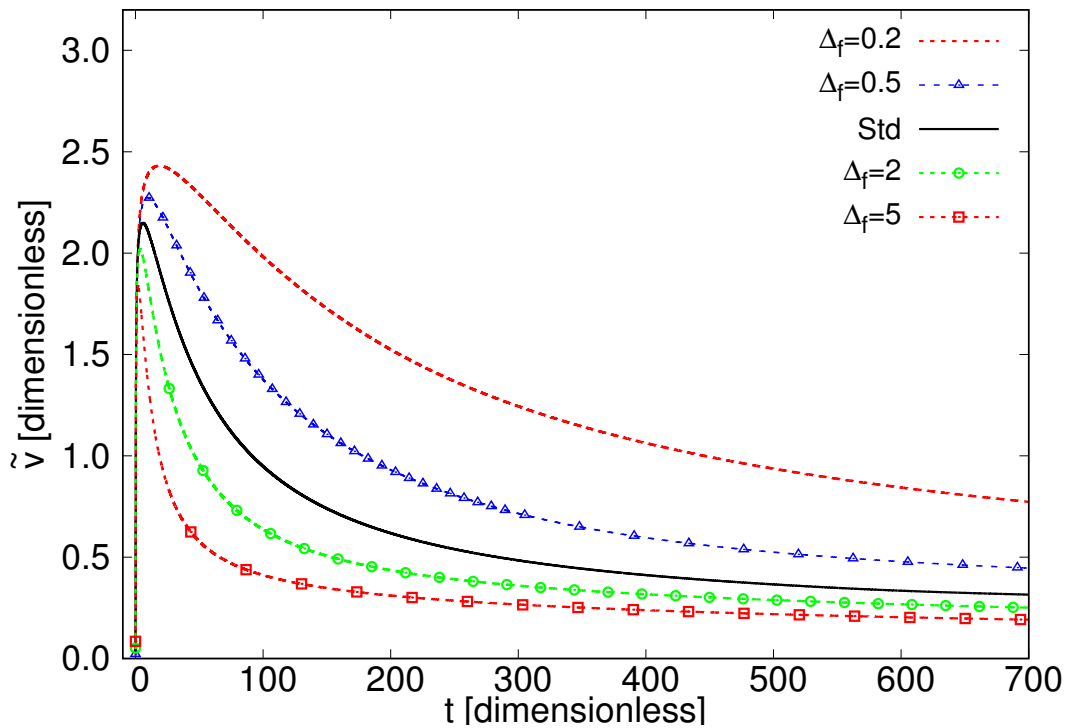


Figure 2.26: Velocity curves for various friction modulators Δ_f .

Δ_f	t_{\max}	v_{\max}	t_f	v_f	$p_g(t_f)$
0.2	18.6257	2.430505	185.738007	1.576889	0.625092
0.5	9.55415	2.274163	298.763860	0.717481	0.625093
1	5.83927	2.149094	547.536641	0.349139	0.625094
2	3.63925	2.018305	943.081856	0.221302	0.625092
5	2.02993	1.836759	1648.13205	0.134361	0.625093

Table 2.8: Key values defining the dynamics for varying Δ_f .

Several conclusions could be drawn from the graphs above:

- Comparing figure 2.26 with 2.23 above, see that the effect of changing ζ_D is not equivalent to modifying Δ_f . Values of v_{\max} span a wider range in figure 2.26.
- The acceleration stage, or rather its slope, is quite insensitive to Δ_f changes. This is compatible with the statement that friction is not the relevant force during the acceleration stage.
- The transition stage is very dependent on Δ_f . Not only v_{\max} changes, but more so does t_{\max} .
- The deceleration stage undergoes major changes with Δ_f . Again, this is compatible with the assertion that friction is the dominant force in that stage.

It remains as an open question to find better correlations for the transient friction factor, since the AHM (or any other which could be envisaged) has proven very dependent on the actual values of f_e .

2.6.2 Force Balance

A very interesting result is attained when a force balance within the pipe is carried out. Forces favouring and opposing motion are compared, and the results depicted in graphs. There is just one force favouring movement: the pressure force, evaluated as

$$F_p = \pi R^2 (p_g(t) - p_\infty) \quad (2.77)$$

or rather, in dimensionless form:

$$F_p = \frac{\pi}{4} (p_g(t) - p_\infty) \quad (2.78)$$

The assumption (vi) of section 2.2 should be remembered: the liquid's front is always moving against atmospheric pressure p_∞ .

On the other hand, the force opposing motion is the friction force, which develops exclusively on the pipe's wet zone. Its expression depends on the stage of the flow:

- Fast stage ($0 < t < t_f$):

$$F_f = \frac{f}{4} \rho \tilde{v}^2 \pi R z_f \quad (2.79)$$

or, in dimensionless form

$$F_f = \frac{f \pi}{4} z_f \tilde{v}^2 \quad (2.80)$$

- Slow stage ($t > t_f$):

$$F_f = \frac{f}{4} \rho \tilde{v}^2 \pi R L \quad (2.81)$$

or

$$F_f = \frac{f\pi}{4} L \tilde{v}^2 \quad (2.82)$$

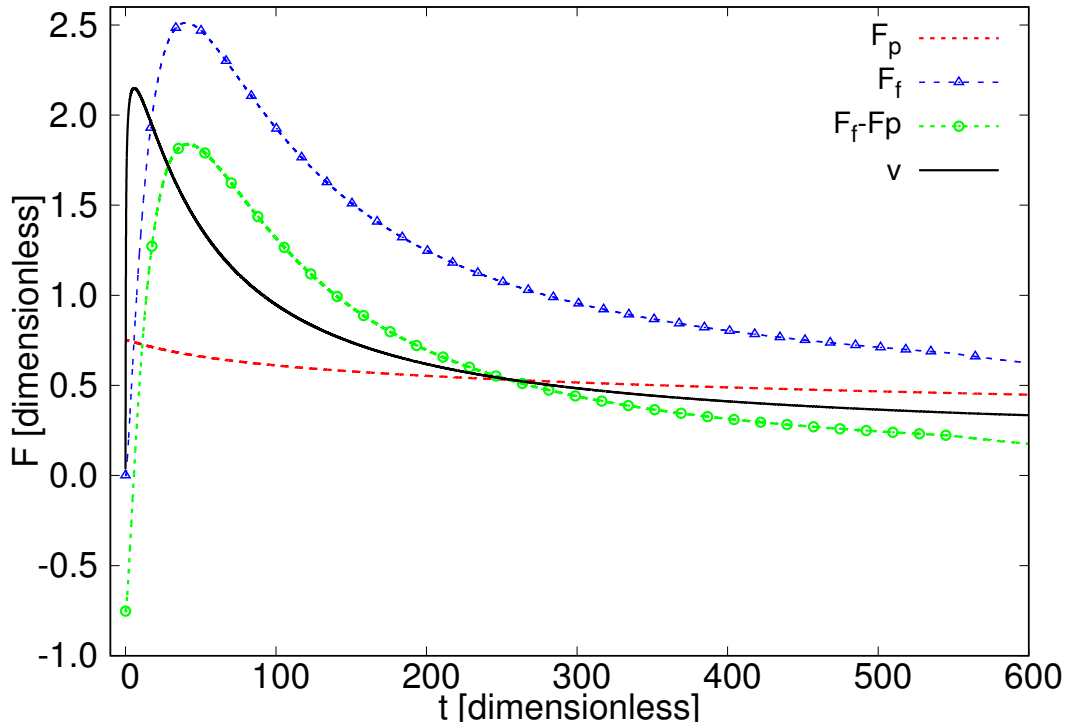


Figure 2.27: Dimensionless force balance in the standard pipe.

The instantaneous balance of those dimensionless forces developing inside the standard pipe, favouring and opposing motion, can be seen in figure 2.27 : F_p , F_f and $F_f - F_p$. The bulk velocity is also shown, for synchronisation purposes. Some remarkable features are:

- The net force on the liquid $F_p - F_f$ becomes rapidly negative, that is, the force opposing movement is dominant during most of the flow. At $t = 5.6206$ (very close to the maximum bulk velocity at $t_{\max} = 5.83927$) both forces are equal $F_f = F_p$.
- During the Fast stage the friction force grows due to, both, increased bulk velocity and increased wet surface on the pipe. In the Slow stage the wet surface is constant.
- In dimensionless units, the pressure force decreases very slowly, whereas the friction force changes rapidly and abruptly, assuming f obeys the Colebrook-White correlation.
- There is a time offset between the maximum bulk velocity v_{\max} and the maximum net force. The bulk velocity curve moderates its falling slope after the friction force maximum has been reached.
- Friction and pressure forces converge after sufficiently long time (formally $t \rightarrow \infty$).

Chapter 3

Introduction to the Description of Turbulence

3.1 Introduction

The AHM described so far assumes the existence of a turbulent flow only through the Darcy-Weisbach friction factor included in the equations. Nowhere else any clue is obtained regarding the type of flow developing in the pipe. But Reynolds number for this case surpasses 10^7 in a split-second, surely leading to very intense turbulence being created and developed within the pipe. The description of that turbulence constitutes an integral part in the study of the phenomenon occurring in the transient discharge of the liquid to the atmosphere.

Turbulence is probably the most cited instance of chaotic behaviour, meaning that it is almost impossible to describe with detail what is happening in the system, although the dynamical governing equations can be obtained from first principles. The observer can see a very complex behaviour that apparently seems to be fully random, but can also distinguish some general patterns. No intent is made herein to explain what turbulence is, a task well beyond the scope of this Dissertation, which have already been attempted by some of the past century brightest minds, and the reader is referred to any of the excellent textbooks cited in the bibliography. However, some small contribution will be offered regarding the description of the quantities and fields that characterise the turbulent flow of fluids.

Turbulence encompasses a wide range of scales, in space and time. The basic structure in a turbulent flow is the **eddy**, which roughly can be thought of as a parcel of vorticity. The larger eddies have a size comparable to the integral length scale $\mathfrak{L} \approx D$, while the smallest belong to the Kolmogorov (dissipation) length scale ¹ $\eta = (\nu^3/\epsilon)^{1/4}$; in between those scales is the inertial length scale or inertial subrange ℓ (see, for example, [Pop00]). Beyond that, only the realm of laminar flow exists, like, for example, the laminar sublayer within the turbulent boundary layer. The time scales are related to the length scales: from integral time scale \mathfrak{T} to Kolmogorov time scale $\tau_\eta = (\nu/\epsilon)^{1/2}$, passing through inertial time scales t . The time scale t associated with a length scale ℓ is usually called the **eddy turnover time**, and represents the typical time scale necessary for an eddy of size ℓ to undergo a significant distortion (see [Fri95]), or in other words, the typical time for the transfer of energy from scale ℓ to smaller scales, since the said distortion is the main mechanism for energy transfer among length scales.

The ratio between the extreme length scales, integral and Kolmogorov, is of the order of $\mathfrak{L}/\eta \sim Re^{3/4}$, for large Re . As Re grows the dynamic range of length scales widens, and the flow contains a continuous

¹ ν is the fluid's kinematic viscosity, while ϵ is the energy dissipation rate per unit mass to be defined in page 80.

spectrum of length and time scales². According to [Gib91], the first eddies to be generated in the flow are the small ones, the viscous scales: little energy is removed from the flow, and some dissipation appears exclusively as viscous stress. With increasing Re , gradually the larger length scales emerge and the flow becomes more complex. The higher Re the wider the spectrum of length scales.

Fluid flow is an instance of dynamical system, and the full mathematical apparatus of such systems can be applied to it, including integrals of motion, conserved quantities, Lyapunov exponent and degrees of freedom. The turbulent flow presents a large amount of degrees of freedom which depend on the Reynolds number as well. According to [MY71], the number N of degrees of freedom for a flow limited to a finite volume is also finite, though quite large, of the order of $N \sim Re^{9/4}$, again for large Re .³ In this scheme, a pure steady laminar flow has zero degrees of freedom. Any closed dynamical system with such a high number N of degrees of freedom will be very difficult, if not outright impossible, to be described analytically, since the number of integrals of motion is $2N - 1$. Besides, the governing equations are non-linear and the Lyapunov exponent is of the order of $\lambda \sim \sqrt{Re}/\mathfrak{T}$, with $\mathfrak{T} \approx \mathfrak{L}/\mathfrak{U}$ the turnover time of the largest eddies of length scale \mathfrak{L} , also for large Re (see [BJPV98]). Therefore, the motion is highly unstable and even infinitesimal perturbations lead to great differences in the macroscopic behaviour of the system. Small variations on initial or boundary conditions produce greatly different patterns of eddies in the flow. Two arbitrarily close points in phase space are exponentially taken apart, with Lyapunov exponent, until not long after they are sufficiently separated to represent fully different system states. The chaotic (in the sense of Lyapunov) character of turbulence is of utmost importance to understand the phenomenon. Both, the high number of degrees of freedom and the high instability to small disturbances, confer the turbulence a quasi-stochastic character despite being deterministic the governing equations. Thus, although turbulence should be considered a deterministic phenomenon, its description is too complicated to be approached without the tools of statistical analysis.

A simple example will help to understand the statements made above. Consider a pipe flow with $Re = 2300$, which is conventionally taken as the beginning of turbulent behaviour for such flows. $Re = 2300$ cannot be considered to belong to the $Re \rightarrow \infty$ limit mentioned above, but let's not worry about it just now. The biggest eddies will be some $2300^{0.75} \approx 332$ times larger than Kolmogorov length scale. With $\eta = (\nu^3/\epsilon)^{1/4}$ and $\epsilon \approx U^3/D$ then $\eta \approx (\nu^3 D/U^3)^{1/4}$, and this approximation gives an idea of the smallest length scales. The number of degrees of freedom is $N \sim 2300^{9/4} \approx 3.7 \cdot 10^7$, the integrals of motion are almost 10^8 , and the nearby phase space points separate exponentially at a rate of $e^{48 t/\mathfrak{T}}$ (Lyapunov exponent $\lambda \sim \sqrt{Re}/\mathfrak{T} \approx 48/\mathfrak{T}$). These figures lead to consider this dynamical system as complex, although the turbulence has just all but begun. For the discharge flow under study $Re \sim 10^7$, a value for which the assumption $Re \rightarrow \infty$ is more accurate, and the relevant figures are $\mathfrak{L}/\eta \sim 2 \cdot 10^5$, $N \sim 6 \cdot 10^{15}$ and $\lambda \sim 3000/\mathfrak{T}$. Although still far from Avogadro's number $6.022 \cdot 10^{23}$ (typical range of degrees of freedom for systems in Statistical Mechanics), surely $6 \cdot 10^{15}$ is calling for some kind of statistical description, the deterministic nature of the turbulence notwithstanding.

The pattern of large scale eddies are flow dependent and have certain coherent structures, like hairpins, ribs, rings or Lagrangian coherent structures (see [Hus86]), which are roughly simulated with powerful computer models. However, the smallest length scales do not appear to have a flow-dependent structure, and they may be modelled as statistically isotropic and apparently random (see [Nel94]). The smallest length scale fluctuations seem to have the property of universality: they are roughly equal for

²This continuous scale of lengths and times is only interrupted by the phenomenon called turbulence intermittency. The reader is referred to [Hin75].

³In this interpretation of turbulent fluid flow as a dynamical system, the role of degree of freedom corresponds loosely to an eddy. Each eddy undergoes transformations under the action of inertia, pressure and viscous forces. See [Piq99].

all kinds of flows. Therefore it is possible, in principle, to develop a general theory or model to describe the turbulence behaviour at those small scales. Isotropy at smaller scales in presence of anisotropy at larger scales receives the name of **locally isotropic turbulence**. If the hypothesis of local isotropy were true, then the large scale flow could be computed directly, with all its particularities, while the smaller scale fluctuations would be replaced by their universal statistical properties. This program may fairly be called the **statistical representation of turbulence**,⁴ with the larger scales still represented by some sort of averages which are largely free from the extreme variations and fluctuations shown by quantities describing a turbulent flow. For a random vector field $\mathbf{u}(t, \mathbf{x})$ isotropy implies zero mean value (see [MY75]). Therefore, the isotropic turbulence is presented devoid of the mean flow, and the turbulent fluctuations are assumed to interact among themselves, not with the mean flow. Thus, only fluctuating components of the flow fields are considered in isotropic turbulence. The isotropic and locally isotropic turbulence are extraordinarily well studied in [MY75], and to that textbook refer most of the papers on the subject.

However, as much as it might be wished to obtain a reliable statistical representation of turbulence, the governing equations are still deterministic, and it is by no means straightforward to produce stochastic fields from deterministic equations. In principle there are, at least, two main ways to turn a deterministic differential equation into stochastic:

- i. Inserting a random term in the otherwise deterministic equation. This approach is followed, for instance, in [BIL06], where the Stochastic Navier-Stokes Equations (SNSE) are expressed by:

$$\partial_t \mathbf{u} + (\mathbf{u} \cdot \nabla) \mathbf{u} - \frac{1}{Re} \nabla^2 \mathbf{u} + \nabla p = \mathbf{f} + \mathbf{n} \quad (3.1)$$

with two body forces, \mathbf{f} the familiar term representing gravity or any other slowly varying force, and $\mathbf{n}(t, \mathbf{x})$ the **noise** term corresponding to fast random fluctuations of the force, which is to be considered as an external non-controllable perturbation, and need not be continuous or differentiable. As discussed in [BIL06], the observed fact that no two experiments conducted in laboratory are truly identical, because the Navier-Stokes equations for large Re are chaotic and any microscopic perturbation, even at a molecular scale, is amplified to macroscopic scales; leads to the conclusion that constructing such SNSE is plausible even if it is not known how to formalise the underlying probability space. Since \mathbf{n} is a random field, the solution of the SNSE $\mathbf{u}(t, \mathbf{x}, \mathbf{n})$ is also a random field.

- ii. Inserting random boundary or initial conditions in the otherwise deterministic equation. This approach is followed, for instance, in [Dei84]. In this case the equation itself does not contain any noise term, but the initial or boundary conditions impose the stochastic character to the solutions. A typical example would be a rough wall, where the wall's little peaks and crevices could be considered a random variable (wall roughness height ζ_r) which might have a lasting influence on the flow, provided the roughness protrude above the laminar sublayer. The rough wall's relief is an external non-controllable small perturbation to the flow, which is amplified through the non-linear turbulence production process to macroscopic scales, and would be perfectly characterised as a random variable. The classic Navier-Stokes equations together with such initial or boundary conditions may also be considered as SNSE, and the solution $\mathbf{u}(t, \mathbf{x}, \zeta_r)$ to this SNSE would be a random field, conferring to the flow a random behaviour as well.

In both cases just described, what makes the system stochastic is an external non-controllable factor whose influence on the flow is random, and because this small perturbation is not damped and

⁴The expressions '*statistical description of turbulence*' and '*statistical representation of turbulence*' will be considered synonyms in this work.

dissipated but, on the contrary, is amplified to larger scales, it turns the otherwise deterministic equation into a stochastic one.

It is worth having a look at Statistical Mechanics, possibly the most successful Physics theory dealing with random variables, with permission of Quantum Mechanics, and see what can be imported therefrom to the description of turbulence. It should not be forgotten that Classical Statistical Mechanics is the approach chosen when one gives up to fully describe a deterministic mechanical system (a gas in equilibrium, for instance) using the deterministic Lagrange-Hamilton equations of Mechanics, because the number of degrees of freedom is impossibly high, of the order of Avogadro's number (see, for instance, [Haa95]). The deterministic nature of the particles' motion within the gas is no hindrance to use stochastic tools to describe the system. It is, then, not far-fetched to suggest that Classical Statistical Mechanics is a statistical representation of the underlying dynamical system. Four important points need to be highlighted upon trying to extend this formalism to turbulence:

- i. To start with, Classical Statistical Mechanics aims *directly* to find the probability distribution, by determining the Probability Density Function (PDF) $\rho(t, \mathbf{q}, \mathbf{p})$ in phase space for a given system, and the related partition function Z . The probability distribution is defined as

$$\mathcal{P}(\Omega) := \int_{\Omega} \rho(t, \mathbf{q}, \mathbf{p}) \, d^N \mathbf{q} \, d^N \mathbf{p} \quad (3.2)$$

with $\Omega \subset \mathbb{R}^{2N}$ a domain in the phase space associated to the physical system of N degrees of freedom. $\mathcal{P}(\Omega)$ is the probability of finding the system's state within Ω , with a state being defined by a point (\mathbf{q}, \mathbf{p}) in phase space, characterised by N generalised coordinates \mathbf{q} and N generalised momenta \mathbf{p} . The PDF ρ for a system obeys the Liouville theorem, and that provides an initial equation for this quantity. The knowledge of the PDF ρ , and the attached partition function Z , provides the full solution and the maximum information about the physical system that can be obtained from Statistical Mechanics. Quantities like internal energy, temperature, pressure, entropy, etc. can be easily and exactly derived from Z .

Much effort is being devoted to find such a PDF for turbulence. However, in this case the main challenge is to define what is meant by '*state of turbulence*' or, in other words, how to construct the equivalent to a phase space for turbulence, in the sense that each point of such a phase space define an unique state of turbulence. A line of research is to define, in steady isotropic turbulence, the PDF for velocity difference $\Delta \mathbf{u} = \mathbf{u}(\mathbf{x} + \mathbf{r}) - \mathbf{u}(\mathbf{x})$ in space points separated by a fixed vector \mathbf{r} (see [MY75]). The PDF $\rho(\Delta \mathbf{u}, \mathbf{r})$ is defined such that $\rho(\Delta \mathbf{u}, \mathbf{r}) \, d^3 \mathbf{u}$ is the probability of finding a velocity difference $\Delta \mathbf{u} = \mathbf{u}(\mathbf{x} + \mathbf{r}) - \mathbf{u}(\mathbf{x})$ within the interval $(\Delta \mathbf{u}, \Delta \mathbf{u} + d\mathbf{u})$, for infinitesimal $d\mathbf{u}$. Being the turbulence isotropic, the direction of \mathbf{r} is unimportant for the definition just given.

Another approach is to attain mean values, one- and two-point correlations, double- or triple-velocity correlations, etc., with the expectation that those correlations represent moments of the distribution wherefrom the characteristic function could be approximately obtained ⁵ *via* its expansion in terms of all moments (see [Lum98]), and from the characteristic function extract the probability distribution itself.

- ii. Each point (\mathbf{q}, \mathbf{p}) in phase space characterises what is called a **microstate** of the mechanical system. Therefore, the microstate is determined univocally by the phase space generalised coordinates and momenta. On the other hand, macroscopically the system is characterised by a set of

⁵The characteristic function of a probability distribution is also called the moment-generating function. See [Lum98].

Thermodynamic quantities: temperature, pressure, internal energy, entropy... This is called a **macrostate** of the system. For a system in equilibrium, to each macrostate correspond (infinitely) many microstates compatible with it. A system in equilibrium will be for ages in its macrostate, while the molecules are continuously changing from one compatible microstate to another. Any little perturbation on the system will change the microstate to another compatible microstate, thus leaving the macrostate unchanged. Besides, the equipartition theorem guarantees that the energy is shared evenly among all degrees of freedom, and thus all compatible microstates are equivalent from the macroscopic point of view.

This situation cannot be directly extrapolated to turbulence, because the correspondence between a macrostate and the set of compatible microstates is not so straightforward: each little local perturbation in the flow (change of microstate) is amplified by the turbulence and converted into a different eddy pattern (change of macrostate). The pressure field within the flow would transmit the change of motion at any given point to other distant points, thus affecting their motions too. While it is possible to envisage two different flow configurations yielding the same mean value, possibly they will not produce identical values for higher distribution moments (two-point correlations, triple-velocity correlations...), and thus they cannot be considered compatible microstates. It seems that micro- and macrostate describe the same flow configuration, and changing one means changing the other. Moreover, the equipartition theorem is not expected to be valid in turbulence, as the energy attached to the largest eddies is higher than that corresponding to smaller ones ⁶.

- iii. Most systems dealt with in Classical Statistical Mechanics are conservative, and thus it is possible to thoroughly study systems in equilibrium characterised by their partition functions. The Hamiltonian is a conserved quantity and can be used to determine the probability distribution function that governs the whole system. The wealth of results obtained from Statistical Mechanics, including most of Thermodynamics, is based on this hypothesis. Armed with this knowledge, it is then possible to attempt the exploration of the thousand-fold more complex realm of Dissipative Statistical Mechanics, with varying degree of success. Had not been for the previous equilibrium theory, it would have been almost impossible to approach the more difficult non-equilibrium counterpart.

Turbulence cannot be separated from viscosity, that is, from dissipation. It does not exist such a thing as an *equilibrium state of turbulence*, with conserved quantities and state functions. There must always exist an external input of energy into the flow, if turbulence is to be maintained. Therefore, it is not possible to construct a theory of equilibrium turbulence from which later to explore the domains of ordinary turbulence. Even the most simple instance of turbulence, namely the steady, homogeneous and isotropic turbulence, is still too complex to assign a *partition function* to it. This lack of guidance is, possibly, what is challenging most the foundation of a general theory of turbulence.

- iv. Although extremely high, the number of particles within any system studied by Classical Statistical Mechanics is discrete. The phase space (\mathbf{q}, \mathbf{p}) is continuous, but the index characterising each particle's generalised coordinates and momenta is an integer, $(q_i(t), p_i(t))$, $i = 1, \dots, 3N$, and that integer covers all the phase space dimensions. The very concept of *ensemble* devised by Gibbs rests on a phase space whose dimension is numerable, namely $3N + 3N$. The mathematical formalism is based on statistics over ordinary differential equations, with time t as the independent variable.

On the other hand, Fluid Dynamics owes its existence to the hypothesis of continuous media.

⁶See footnote 3 in page 72

The numerable set of generalised coordinates and momenta is now replaced by the concept of continuous field. The ordinary differential equations turn into partial differential equations, and the statistics does not deal with random variables but with random fields. The phase space manifold is no longer the support of the dynamics, but rather this role is taken by a functional space, the Hilbert space of all flow fields compatible with the turbulence conditions existing in the flow. All this added complication makes it even more difficult the transposition of a formalism similar to that used in Classical Statistical Mechanics to the theory of turbulence.

Thus, the application of the underlying ideas of Statistical Mechanics to turbulence is beset with extreme difficulties which were, and still are, the main struggle of many bright researchers, which have been attracted to this extraordinary form of movement so universally present in nature. In any case, the statistical representation of turbulence is a tool for describing the mean behaviour of the flow, but it is not, it cannot be, a set of dynamical equations derived from first principles which encompass the underlying foundations for such a form of movement. There is no much dynamics in the derivatives of averages like $\overline{u'_i u'_j}$ or $\overline{u'_i u'_j u'_k}$, just to name a few of the formalism's offspring. Rather, it would be justified to consider them as mathematical artefacts, outputs of an average procedure over otherwise sound dynamical equations, specially if their actual numerical values depend on the averaging method employed.

This introduction has tried to highlight the fact that accepting the use of statistical tools does not imply to cease acknowledging the deterministic-chaotic nature of turbulence. The language, the methods, the formalism belong to the realm of Statistics, whilst the governing dynamical equations are non-linear and deterministic. The same equations contain the orderly laminar movement and the chaotic turbulent behaviour. The statistical representation of turbulence is the shortcut used by scholars, who accept with helplessness that the subject is much too complex to attempt a direct approach.

3.2 The Statistical Approach (or the Averaging Problem)

Last section has shown the great temptation for an observer to consider the turbulence as a stochastic process. This results in a confusion between the most successful methods used for its representation, and the actual nature of the phenomenon itself. The disturbing behaviour of the turbulent flow fields brings out the idea of separating any field into two components, the average and the fluctuating.

A characteristic of the turbulent motion of a fluid is the existence of disordered fluctuations in the dynamic variables of the flow. Thus, a seemingly random variation is expected in both, the spatial and temporal evolution of the field quantities describing the turbulent flow. Turbulence is probably the most outstanding instance of chaos and, as a result, if a turbulent flow is set up repeatedly under exactly the same conditions, the actual values of those fields, in time and space, will be different in each attempt.

According to the statistical approach to turbulence, the spatio-temporal fluctuations for each dynamic field have a wide range of amplitude, frequency, wavelength and direction, and the fields themselves can be assimilated to what is called **random fields**. Since no analytical expression can be found for each dynamic field in a turbulent regime, the most that can be achieved is only a collection of measured values for various positions and time frames. It is not possible, nor desirable, nor interesting, to have the exact value of each flow field at all points and instants.

On the contrary, what in principle is possible, and definitively desirable, is to obtain an analytical expression for the mean value of each dynamic field, and possibly some other statistical moments. Those mean values are expected to be smoother and much more regular. Of course, the equations that govern

the mean values of the fields need not be the same than those governing the fields themselves. Thus, a method for averaging the flow fields must be defined, which should separate the mean evolution from the fluctuating random variation of each quantity. Moreover, the attached equations to such average fields must be obtained from the original dynamic governing equations ⁷. The resulting relationships receive the name of **Reynolds-Averaged Navier-Stokes Equations** (RANSE), as they are derived directly from the Navier-Stokes relations.

The statistical description of turbulence is associated with the decomposition of physical quantities into two parts: one is relatively smooth and regular, whereas the other concentrates the rapid variations attached to the turbulent motion. For any flow field $\psi(t, \mathbf{x})$ ⁸ that dissection, known as **Reynolds decomposition**, is expressed in a general form as:

$$\psi(t, \mathbf{x}) = \langle \psi(t, \mathbf{x}) \rangle + \psi'(t, \mathbf{x}) \quad (3.3)$$

where ψ is called the instantaneous quantity, $\langle \psi \rangle$ the mean or average quantity, and ψ' the fluctuating quantity ⁹. Only the instantaneous quantities are directly bounded by the conservation principles that govern the Mechanics, that is, only instantaneous quantities can reach the status of *constants of the motion*. Any constraint affecting the mean or fluctuating quantities is inherited from those basic principles affecting the instantaneous ones. As pointed out by [BIL06], the main challenge of simulating turbulence rests in the fact that the equations describing the mean flow cannot be directly derived from the Physics of fluids.

The description of turbulence and turbulent quantities through the use of statistical functions like average, correlations, higher-order moments... is appropriate when a procedure for defining such functions be readily available. The problem with very transient turbulent phenomena is the difficulty to find a suitable method to define the moments of the random variables, one which could be of direct use in Engineering applications. The averaging issue is elegantly presented and discussed in [MY71].

Note that in equation (3.3) only ψ and $\langle \psi \rangle$ have a sharp clear meaning: ψ is the actual physical field and $\langle \psi \rangle$ is the result of an accurately defined averaging method. However, ψ' could only be defined as “whatever is left after subtracting $\langle \psi \rangle$ from ψ ”. Of course, one might (and must) attempt to provide a physical explanation to enlighten the meaning of ψ' , and derive some mathematical properties of this new fluctuating field. But reality is a stubborn thing and, in the end, one must always resort to its definition as $\psi' = \psi - \langle \psi \rangle$ in order to demonstrate any mathematical result regarding ψ' . It is important to stress this fact, and to understand that ψ' is as intrinsically linked to the averaging method as $\langle \psi \rangle$ is, and that different averaging methods will not only render different mean fields $\langle \psi \rangle$, but also different fluctuating fields ψ' .

The averaging method, whatever it might be, must fulfil the following conditions in order to be applicable to the theory of turbulence. If ψ and ϕ are two random fields of the turbulent flow, then the **Reynolds conditions** are established as:

⁷One resists to use the adjective ‘dynamic’ to refer to the average fields equations. Although the mean fields have governing equations determining their evolution, it is preferable to reserve such term for equations directly obtained from First Principles, wherefrom Integrals of Motion can be defined.

⁸The field $\psi(t, \mathbf{x})$ could be a velocity component $u_i(t, \mathbf{x})$, or the velocity vector $\mathbf{u}(t, \mathbf{x})$, or the pressure $p(t, \mathbf{x})$ at a given time and position, or it could be a more complicated tensorial field derived from other flow fields at different times and positions.

⁹This fluctuating part receives different names in the literature: the turbulence component [HR70], the incoherent background turbulence [GHL96]...

- **LINEAR CONDITION.** Averaging is a linear operation:

$$\begin{aligned}\langle \psi + \phi \rangle &= \langle \psi \rangle + \langle \phi \rangle \\ \langle c\psi \rangle &= c\langle \psi \rangle \quad \text{if } c = \text{constant} \\ \langle c \rangle &= c \quad \text{if } c = \text{constant}\end{aligned}\tag{3.4}$$

- **COMMUTATION CONDITION.** The averaging operation commutes with derivation

$$\left\langle \frac{\partial \psi(t, \mathbf{x})}{\partial s} \right\rangle = \frac{\partial}{\partial s} \langle \psi(t, \mathbf{x}) \rangle\tag{3.5}$$

where s is any space-time variable t, x_1, x_2, x_3 .

- **IDEMPOTENT CONDITION.** The averaging operation is idempotent

$$\langle \langle \psi \rangle \phi \rangle = \langle \psi \rangle \langle \phi \rangle\tag{3.6}$$

This last condition is more frequently seen as

$$\langle \langle \psi \rangle \rangle = \langle \psi \rangle\tag{3.7}$$

which can be easily derived from (3.6) by setting $\phi = 1$.

It is trivial to prove that equation (3.7) leads to

$$\langle \psi' \rangle = 0\tag{3.8}$$

for the fluctuating component of ψ . Also, as a corollary, it can be easily deduced from the above Reynolds conditions the following rule for the product average:

$$\langle \psi \phi \rangle = \langle \psi \rangle \langle \phi \rangle + \langle \psi' \phi' \rangle\tag{3.9}$$

Any operation like $\langle \cdot \rangle$ acting on flow fields ψ , fulfilling the Reynolds conditions, will be called a **Reynolds operator**. A Reynolds operator will always produce valid RANSE when applied to the Navier-Stokes equations.

The last two conditions (3.5) and (3.6)-(3.7) are the most difficult to meet for ordinary averaging procedures. It will be seen that in most practical cases one can only work with approximations, since it is impossible to cover the whole statistical universe of each random field: temporal and spatial averages cannot be extended to infinity in Engineering application, and ensemble average (see later) cannot be expected to contain all possible realisations.

Along this text the mean value of a physical field ψ will be denoted by the same symbol in capitals $\Psi = \langle \psi \rangle$, and thus it will not be necessary to use overbars, angled brackets or similar signs to refer to the mean quantities. The fluctuating part of the field will be denoted with primes ψ' . The notation for the Reynolds decomposition of the turbulence quantities and fields appearing in this work is the following:

- Velocity¹⁰ [m/s]

$$\mathbf{u} = \mathbf{U} + \mathbf{u}' \quad u_i = U_i + u'_i\tag{3.10}$$

¹⁰From now onwards, as it is customary in turbulence and CFD formalisms, the velocity field in a turbulent flow will be denoted by \mathbf{u} or u_i , instead of \mathbf{v} or v_i employed so far. This change of notation has two benefits: allows for the direct comparison of results with existing turbulence literature, and neatly distinguishes between the hydraulic (treated before) and the hydrodynamic (to be treated next) cases (see footnote 3 in page 3).

- Pressure [$kg\ m^{-1}\ s^{-2}$]

$$p = P + p' \quad (3.11)$$

- Strain rate tensor [s^{-1}] Defined by the matrix

$$s_{ij} = \frac{1}{2} \{ \partial_j u_i + \partial_i u_j \} \quad (3.12)$$

and the Reynolds decomposition is

$$s_{ij} = S_{ij} + s'_{ij} \quad (3.13)$$

with

$$S_{ij} = \frac{1}{2} \{ \partial_j U_i + \partial_i U_j \} \quad (3.14)$$

$$s'_{ij} = \frac{1}{2} \{ \partial_j u'_i + \partial_i u'_j \} \quad (3.15)$$

- Specific turbulent kinetic energy ¹¹ [$m^2/s^2 = J/kg$]

The specific kinetic energy of the fluid is defined by the expression:

$$E_k(t, \mathbf{x}) = \frac{1}{2} \mathbf{u}(t, \mathbf{x}) \cdot \mathbf{u}(t, \mathbf{x}) = \frac{1}{2} u_i(t, \mathbf{x}) u_i(t, \mathbf{x}) \quad (3.16)$$

Applying the Reynolds decomposition (3.10) of \mathbf{u} to E_k , the expected mean and fluctuating components of the specific kinetic energy are obtained. The fluctuating component is of lesser importance and no further attention will be paid to it.

Upon describing the turbulent motion, emphasis is placed on the average specific kinetic energy $\langle \frac{1}{2} u_i u_i \rangle$ (sum in repeated indices implicit), since the instantaneous value (3.16) is of limited usefulness due to the energy cascade existing among the turbulent eddies in the flow. This average quantity transforms into:

$$\begin{aligned} \frac{1}{2} \langle u_i u_i \rangle &= \frac{1}{2} \langle (U_i + u'_i)(U_i + u'_i) \rangle = \frac{1}{2} \langle U_i U_i + u'_i u'_i + 2U_i u'_i \rangle = \\ &= \frac{1}{2} U_i U_i + \frac{1}{2} \langle u'_i u'_i \rangle = K(t, \mathbf{x}) + k(t, \mathbf{x}) \end{aligned} \quad (3.17)$$

where use has been made of the idempotent condition (3.6), and as a result $\langle U_i U_i \rangle = U_i U_i$ and $\langle U_i u'_i \rangle = U_i \langle u'_i \rangle = 0$. The first term K is the specific kinetic energy corresponding to a hypothetical flow whose velocity be U_i , and is thus called the **specific kinetic energy of the mean flow**. Whether U_i be a function of t , or \mathbf{x} , or both, depends on the type of average method carried out to obtain U_i , as it will be shown later. The second term k is the specific kinetic energy associated with the fluctuating velocity field u'_i . It corresponds to the energy which is going to be dissipated along the flow ¹², at a rate defined by ϵ (see below), and it could be said that it is the energy fraction pertaining to the turbulence itself.

¹¹In the present context 'specific' means 'per unit mass'.

¹²The energy represented by k is not only dissipated at the smallest scales of turbulence, it is also generated as it is being extracted from the mean flow at the largest scales. There is a net transport of energy from the largest to the smallest scales of turbulence.

The division of a field given in (3.17) is not a Reynolds decomposition, because it is not the addition of an average plus a fluctuating component, but rather is the addition of two averages: one over mean velocities and the other over fluctuating velocities. Nevertheless, it serves well the purpose of splitting a mean flow field into a *stable* component and an *unsettled* one, over which the effects of turbulence operate. It will be seen that Reynolds-Averaged Navier-Stokes (RANS) formalism uses $k = \frac{1}{2} \langle u'_i u'_i \rangle$ almost exclusively, disregarding K , and some of the most widespread CFD turbulence models have an equation for k in their solvers.

- Turbulent kinetic energy dissipation rate per unit mass [$m^2/s^3 = W/kg$]

The instantaneous specific energy dissipation rate is defined by 2ν times the matrix norm of the instantaneous strain rate tensor $s_{ij}(t, \mathbf{x})$

$$\varepsilon(t, \mathbf{x}) = 2\nu \| (s_{ij}) \|^2 = 2\nu s_{ij} s_{ij} \quad (3.18)$$

or, equivalently, ν times the scalar product of vorticity with itself

$$\varepsilon(t, \mathbf{x}) = \nu \boldsymbol{\zeta} \cdot \boldsymbol{\zeta} \quad (3.19)$$

Just as it was done with the specific kinetic energy in last paragraph, the Reynolds decomposition could also be applied to ε and the fluctuating part discarded as less important. Thus, an average specific energy dissipation rate is obtained with the following form¹³:

$$\langle \varepsilon \rangle = 2\nu \langle s_{ij} s_{ij} \rangle = 2\nu S_{ij} S_{ij} + 2\nu \langle s'_{ij} s'_{ij} \rangle = \bar{\varepsilon}(t, \mathbf{x}) + \varepsilon(t, \mathbf{x}) \quad (3.20)$$

with S_{ij} and s'_{ij} defined in (3.14) and (3.15), respectively.

The average energy dissipation rate is also made up of two terms, one *stable* and another *unsettled*: the first one $\bar{\varepsilon}$ is the dissipation rate due to the mean flow movement, while the second, ε , is the dissipation of turbulent kinetic energy produced by the viscosity (thermal dissipation due to internal friction caused by viscosity), usually simply called *the* dissipation. This last field determines the rate of dissipation of the turbulent kinetic energy k in the flow: the kinetic energy is transformed into internal energy.

According to [Pop00], the mean flow dissipation $\bar{\varepsilon}$ is of order Re^{-1} . Thus, for high Re the mean flow dissipation is negligible when compared with the dissipation rate ε , that is, $\langle s'_{ij} s'_{ij} \rangle \gg S_{ij} S_{ij}$. It follows that the energy dissipation in turbulent flows is almost entirely viscous, $\bar{\varepsilon} \ll \varepsilon$ and $\langle \varepsilon \rangle \approx \varepsilon$. Therefore, $\langle \varepsilon \rangle$ and ε can be freely interchanged in most equations, and for simplicity only ε will be used with the following meaning¹⁴:

$$\varepsilon(t, \mathbf{x}) = \frac{\nu}{2} \langle (\partial_i u'_j + \partial_j u'_i) (\partial_i u'_j + \partial_j u'_i) \rangle \quad (3.22)$$

The dissipation ε is parallel in importance to the kinetic energy k . RANS formalism uses ε almost exclusively, disregarding $\bar{\varepsilon}$, and some of the most widespread CFD turbulence models have an equation for ε in their solvers.

¹³The remaining terms contain products of the form $S_{ij} s'_{ij}$ which have null average and, therefore, belong to the fluctuating component of ε .

¹⁴[Hin75] deduces the following exact expression for ε

$$\varepsilon = \nu \langle (\partial_j u'_i + \partial_i u'_j) \partial_i u'_j \rangle \quad (3.21)$$

- Specific turbulence dissipation rate [$s^{-1} = \text{Hz}$]

The specific turbulence dissipation rate ω is closely related to the specific turbulent kinetic energy k [J/kg] and the specific turbulent kinetic energy dissipation rate ϵ [W/kg]. The relationship among those quantities is one of proportionality

$$\omega \sim \frac{\epsilon}{k} \quad (3.23)$$

Different turbulence models provide different proportionality constants for ω .

- Specific Reynolds stress tensor [$m^2/s^2 = J/kg$]

Another field always present in the RANS formalism is the specific Reynolds stress tensor $-\langle u'_i u'_j \rangle$, which is itself an average of fluctuating velocity products. Actually, k is proportional to the trace of this tensor. It represents the stress associated with the interaction of turbulent eddies among themselves with rapidly varying velocities. Reynolds stress is a direct mathematical consequence of the RANS method and it will be studied in the coming sections.

Reynolds decomposition through a Reynolds operator has the advantage of providing a set of equations for the averaged fields very similar to the original Navier-Stokes equations, plus the extra Reynolds stress terms which cause the closure problem. This formal likeness of equations is very convenient, since it permits to classify the averaged terms into convective, diffusive, inertial... so familiar to students of the original Navier-Stokes equations, and to make use of the known properties the equations show according to the relative importance of such terms.

On the other hand, the Reynolds decomposition is difficult to obtain in practice, it represents a very radical separation of two conflicting behaviours; the two resulting components, average and fluctuating, are too ideal to be physically realisable. It would seem that the main reason to use the Reynolds decomposition be one of mathematical convenience: as long as the averages are suitably defined, the fluctuating components disappear cleanly, leaving neat average equations devoid of disturbing fluctuating fields (except the Reynolds stress, whose presence is easy to explain from a physical standpoint). Whether this decomposition be actually possible in practice, seems to be a secondary matter for this somewhat *naïve* approach.

Statistical description of turbulence provides exactly this: a description. No Dynamics in the classic rigorous sense can be found within the statistics, no equations of motion which can be derived from First Principles like Hamilton's Least Action. The fluctuating part of Reynolds decomposition depends essentially on the averaging method chosen for such decomposition. Actually, the fluctuating component could be defined as: *'Take the instantaneous value and remove the average. Whatever is left is the fluctuating component'*. It will be seen that different averaging methods produce different fluctuating parts and, moreover, the fluctuating component corresponding to one averaging procedure does not yield zero when averaged by a different method.

A disturbing situation, found in a number of papers dealing with turbulent flow simulations, arises when some authors use lightly the statistical representation of turbulence, defining averages which are far from being Reynolds operators, whose definitions fail to meet some of the Reynolds conditions, or conferring to averaged quantities a time or space dependence they should not possess, or comparing results obtained from different averaging methods as if all of them were equivalent, or assigning to some averages mathematical properties they do not enjoy, or some other not manifestly accurate practice. Not all results spewed up by a computer are physically sound, and usually the averaged fields calculated in CFD are of one type (namely, ensemble average) different from the averaged experimental values they

are compared with (often, short time average), and that difference in averaging method must produce offsets in numerical data which are frequently not taken into consideration.

Hopefully, the issues presented and discussed in this section would help the simulation Engineer to understand some of the concepts which are always latent in any CFD publication dealing with turbulence, but are usually not patently explained.

3.2.1 The Statistical Averages

In this section the different types of statistical averages will be introduced and discussed. Thus, a detailed study of most frequent averaging methods for incompressible flow will be presented, together with the Reynolds conditions and RANSE stemming from each. It will be highlighted that different averaging methods provide divergent results, that the fluctuating component is as inherently linked to each averaging method as the mean one, and the applicability limits for each average type will also be considered.

Five main averaging methods could be defined to obtain the mean quantities of interest in a turbulent flow. The methods are conveniently introduced and discussed in several references, for example, [GHL96] or [Pop00]. Those mean quantities should be coupled through governing equations which are formally almost identical to the ones obeyed by their instantaneous counterparts, except for the Reynolds stress terms which bring the closure problem. Roughly speaking, the mean quantities carry most of the flow dynamics while the fluctuating components account for most of the dissipation.

Compressible flow is beyond the scope of this work, therefore averaging methods like Favre average will not be considered herein.

3.2.1.1 The Ensemble Average

This averaging method is the most universal but has the drawback of being very impractical. In case of doubt, the ensemble average is always dynamically right and it is the standard with which any other averaging method is compared. The ensemble average assumes that the same phenomenon can be repeated an indefinite number of times, N , each time in the same conditions. As it is almost impossible to reproduce *exactly* the same conditions in any two experiments, it will be assumed that these conditions will be as closed as could possibly be, and the two experiments will be called **similar**¹⁵. The statistical ensemble of all similar repetitions of the same phenomenon will be simply called the **ensemble**. The set of measured quantities in each repetition is called a **realisation**. The n^{th} realisation for the physical field $\psi(t, \mathbf{x})$ is denoted by $\psi^{[n]}(t, \mathbf{x})$. The closer the initial conditions for two different realisations of the same experiment, n^{th} and m^{th} , the more similar the results $\psi^{[n]}(t, \mathbf{x})$ and $\psi^{[m]}(t, \mathbf{x})$ of the same field will be. Suppose now that N similar experiments (realisations) are conducted, and that the result obtained for the field $\psi(t, \mathbf{x})$ in each one of them is $\psi^{[n]}(t, \mathbf{x})$, $1 \leq n \leq N$. Suppose also, for the moment, that all realisations are equally probable and that they constitute a numerable set. Then, the **ensemble average** for the field ψ is defined as

$$\langle \psi(t, \mathbf{x}) \rangle := \lim_{N \rightarrow \infty} \frac{1}{N} \sum_{n=1}^N \psi^{[n]}(t, \mathbf{x}) \quad (3.24)$$

¹⁵The concept of *similar experiments* is related to the sensitive dependence on initial conditions (see [Dev89]). It is not equal to the concept of *similarity* as defined in Dimensional Analysis.

The ensemble average thus defined retains the t and/or \mathbf{x} dependence of the realisation fields ψ themselves: if $\psi = \psi(t, \mathbf{x})$, then so is $\langle \psi(t, \mathbf{x}) \rangle$ a function of t and \mathbf{x} . The departure of any particular realisation from the average field is considered to be due to the turbulence; it actually is identified with turbulent behaviour. Or in other words, each realization is distinguished from any other only through its fluctuating component.

The ensemble average fulfils the Reynolds conditions (3.4)-(3.7):

- LINEAR CONDITION.

$$\langle \psi + \phi \rangle = \lim_{N \rightarrow \infty} \frac{1}{N} \sum_{n=1}^N (\psi^{[n]} + \phi^{[n]}) = \lim_{N \rightarrow \infty} \frac{1}{N} \left(\sum_{n=1}^N \psi^{[n]} + \sum_{n=1}^N \phi^{[n]} \right) = \langle \psi \rangle + \langle \phi \rangle \quad (3.25)$$

$$\langle c\psi \rangle = \lim_{N \rightarrow \infty} \frac{1}{N} \sum_{n=1}^N c\psi^{[n]} = \lim_{N \rightarrow \infty} \frac{1}{N} c \sum_{n=1}^N \psi^{[n]} = c \lim_{N \rightarrow \infty} \frac{1}{N} \sum_{n=1}^N \psi^{[n]} = c \langle \psi \rangle \quad (3.26)$$

$$\langle c \rangle = \lim_{N \rightarrow \infty} \frac{1}{N} \sum_{n=1}^N c = \lim_{N \rightarrow \infty} \frac{1}{N} Nc = \lim_{N \rightarrow \infty} c = c \quad (3.27)$$

- COMMUTATION CONDITION.

$$\left\langle \frac{\partial \psi}{\partial s} \right\rangle = \lim_{N \rightarrow \infty} \frac{1}{N} \sum_{n=1}^N \frac{\partial \psi^{[n]}}{\partial s} = \lim_{N \rightarrow \infty} \frac{1}{N} \frac{\partial}{\partial s} \left(\sum_{n=1}^N \psi^{[n]} \right) = \frac{\partial}{\partial s} \left(\lim_{N \rightarrow \infty} \frac{1}{N} \sum_{n=1}^N \psi^{[n]} \right) = \frac{\partial}{\partial s} \langle \psi \rangle \quad (3.28)$$

- IDEMPOTENT CONDITION.

$$\langle \langle \phi \rangle \psi \rangle = \lim_{N \rightarrow \infty} \frac{1}{N} \sum_{n=1}^N \langle \phi \rangle \psi^{[n]} = \lim_{N \rightarrow \infty} \frac{1}{N} \langle \phi \rangle \sum_{n=1}^N \psi^{[n]} = \langle \phi \rangle \lim_{N \rightarrow \infty} \frac{1}{N} \sum_{n=1}^N \psi^{[n]} = \langle \phi \rangle \langle \psi \rangle \quad (3.29)$$

Note that $\langle \phi \rangle$ can exit the sum because it is not affected by the summation index n (there are no different *realisations* of the ensemble average $\langle \phi \rangle$)

The ensemble average $\langle \cdot \rangle$ is a Reynolds operator, since it meets the Reynolds conditions, and it is thus a suitable average to derive the RANSE from. Note that N can be allowed to be finite: the Reynolds conditions are still met. Thus, a finite ensemble average is an approximation of the physical process which is still a Reynolds operator, that is, a suitable averaging method to obtain the RANSE from the Navier-Stokes equations. The accuracy is partially lost, but no inconsistencies appear in the derivation and use of the RANSE.

A further step can be taken if the assumption of equally probable realisations is dropped. Assume then that some realisations are more likely than others. Let $w^{[n]}$ be the probability of obtaining the n^{th} realisation in a similar repetition of the flow experiment. The set of probabilities must fulfil the normalisation condition, given by:

$$\lim_{N \rightarrow \infty} \sum_{n=1}^N w^{[n]} = 1 \quad (3.30)$$

where N might be allowed to be finite (a finite number of realisations). The new ensemble average is defined by:

$$\langle \psi(t, \mathbf{x}) \rangle := \lim_{N \rightarrow \infty} \sum_{n=1}^N \psi^{[n]}(t, \mathbf{x}) w^{[n]} \quad (3.31)$$

where $\psi^{[n]}$ is the value adopted by the n^{th} realisation of the field $\psi(t, \mathbf{x})$. The definition (3.24) corresponds to the case of equally probable realisations, $w^{[n]} = 1/N$. Note $w^{[n]}$ affects to the realisation, not to the field. Thus, the added ensemble average of fields ψ and ϕ would be:

$$\langle \psi + \phi \rangle = \lim_{N \rightarrow \infty} \sum_{n=1}^N (\psi^{[n]} + \phi^{[n]}) w^{[n]} = \lim_{N \rightarrow \infty} \sum_{n=1}^N (\psi^{[n]} w^{[n]} + \phi^{[n]} w^{[n]}) = \langle \psi \rangle + \langle \phi \rangle \quad (3.32)$$

It can readily be seen that, as long as $w^{[n]}$ is independent of (t, \mathbf{x}) , the newly defined ensemble average is a Reynolds operator and, therefore, it is appropriate for developing the RANSE.

Still a further step can be taken if the assumption of numerability of the realisations is also dropped. This means that realisations are allowed to develop continuously, and no longer is valid to refer to the n^{th} realisation. Instead of using an index n , they must be characterised by a set of continuous parameters χ which reveal how near is any given realisation from any other, that is, how close are the initial conditions from one another. All the realisations whose initial conditions are close enough are called **similar** and they are included in the **ensemble**.

Let Ξ be an open set in the space of initial conditions for a dynamical system. All the realisations which originate within Ξ are similar and belong to the ensemble. The measure of Ξ (its size) would normally be very small, and depends on how different are the initial conditions allowed to be before the realisations are no longer deemed similar. The realisations of the field ψ are denoted by $\psi(t, \mathbf{x}; \chi)$, with $\chi \in \Xi$. Define a probability distribution $w(\chi)$ for the realisations whose initial conditions lie within Ξ . This probability distribution fulfils the normalisation condition:

$$\int_{\Xi} w(\chi) d\chi = 1 \quad (3.33)$$

Define now the ensemble average for this continuous set of realisations of the field ψ by the expression:

$$\langle \psi(t, \mathbf{x}) \rangle := \int_{\Xi} \psi(t, \mathbf{x}; \chi) w(\chi) d\chi \quad (3.34)$$

The particular case of equally probable realisations corresponds to the constant probability distribution $w(\chi) = 1/\mu(\Xi)$, where $\mu(\Xi)$ is a measure of the open set Ξ , usually its volume in initial-conditions space. Note that as long as $w(\chi)$ do not depend on (t, \mathbf{x}) , the ensemble average just defined in (3.34) is a Reynolds operator.

The averaging methods described by either (3.24), (3.31) or (3.34) render averages that are space and time dependent, which is very suitable for unsteady turbulent flows. On the contrary, this definition is not very practical from the Engineering point of view, as it normally will not be possible to carry out the high number of identical repetitions that would produce a reliable average.

The RANSE derived from ensemble average are the only ones which are complete, because of the retained dependence of the averaged fields on (t, \mathbf{x}) . It can be asserted that ensemble average is the most suitable from a physical standpoint, since it reproduces the results of any other averaging method, being the reciprocal usually not true. From now on, the standard nomenclature employed in turbulence and CFD textbooks will be used, so that the reader can compare the results obtained herein therewith.

RANSE are obtained applying ensemble average $\langle \cdot \rangle$ to the Navier-Stokes equations (3.35)

$$\partial_t u_i + u_j \partial_j u_i = -\frac{1}{\rho} \partial_i p + \partial_j \left[\nu (\partial_j u_i + \partial_i u_j) \right] + g_i \quad (3.35)$$

where $\mathbf{g} = (g_i)$ is a vector representing the external volumetric forces (typically the gravity).

The Reynolds decomposition is denoted by:

$$\mathbf{u}(t, \mathbf{x}) = \langle \mathbf{u}(t, \mathbf{x}) \rangle + \mathbf{u}'(t, \mathbf{x}) \equiv \mathbf{U}(t, \mathbf{x}) + \mathbf{u}'(t, \mathbf{x}) \quad (3.36)$$

$$p(t, \mathbf{x}) = \langle p(t, \mathbf{x}) \rangle + p'(t, \mathbf{x}) \equiv P(t, \mathbf{x}) + p'(t, \mathbf{x}) \quad (3.37)$$

First substitute the Reynolds decomposition of \mathbf{u} and p in (3.35)

$$\begin{aligned} \partial_t(U_i + u'_i) + (U_j + u'_j)\partial_j(U_i + u'_i) &= \\ &= -\frac{1}{\rho}\partial_i(P + p') + \partial_j \left\{ \nu \left[\partial_j(U_i + u'_i) + \partial_i(U_j + u'_j) \right] \right\} + g_i \end{aligned} \quad (3.38)$$

and then apply the ensemble average $\langle \cdot \rangle$ to each term of the resulting equation, having into account that $\langle u'_i \rangle = 0$ and $\langle p' \rangle = 0$. The advection term is the only one presenting some difficulty:

$$\langle (U_j + u'_j)\partial_j(U_i + u'_i) \rangle = \langle U_j\partial_jU_i + u'_j\partial_jU_i + U_j\partial_ju'_i + u'_j\partial_ju'_i \rangle = U_j\partial_jU_i + \langle u'_j\partial_ju'_i \rangle \quad (3.39)$$

because $\langle u'_j \rangle = 0$ and $\langle \partial_ju'_i \rangle = 0$ does not imply $\langle u'_j\partial_ju'_i \rangle = 0$.

Therefore, the RANSE *à la* ensemble average for incompressible Newtonian flow are

$$\partial_tU_i + U_j\partial_jU_i = \partial_j \left[-\frac{P}{\rho}\delta_{ij} + \nu(\partial_jU_i + \partial_iU_j) - \langle u'_iu'_j \rangle \right] + \langle g_i \rangle \quad (3.40)$$

plus the Reynolds-averaged continuity equation:

$$\nabla \cdot \mathbf{u}(t, \mathbf{x}) = \nabla \cdot \mathbf{U}(t, \mathbf{x}) = \nabla \cdot \mathbf{u}'(t, \mathbf{x}) = 0 \quad (3.41)$$

The RANSE retain all terms of the original Navier-Stokes equations plus one: the Reynolds stress divergence term $\partial_jR_{ij} = -\partial_j\langle \rho u'_iu'_j \rangle$. Therefore, this particular form of RANSE could be used to simulate the mean motion of any turbulent flow, regardless of its character (unsteady, inhomogeneous, anisotropic, potentially periodic...), because the mean fields $\mathbf{U}(t, \mathbf{x})$ and $P(t, \mathbf{x})$ are time- and position-dependent, and likewise occurs with the Reynolds stress tensor $R_{ij}(t, \mathbf{x})$ *à la* ensemble average. Of course, always provided a suitable expression for Reynolds stress $-\rho\langle u'_iu'_j \rangle$ in terms of the mean fields could be found, or a solution for the Reynolds stress differential equation. The conventional approach to this problem is the **Boussinesq's eddy viscosity hypothesis**, which assumes the Reynolds stress tensor could be expressed as (see [Pop00]):

$$R_{ij}(t, \mathbf{x}) = -\rho\langle u'_iu'_j \rangle = \rho\nu_t \left[\partial_jU_i + \partial_iU_j \right] - \frac{2}{3}\rho k\delta_{ij} \equiv 2\mu_t S_{ij} - \frac{2}{3}\rho k\delta_{ij} \quad (3.42)$$

with $\nu_t = \mu_t/\rho$ the **turbulent eddy viscosity**, a single quantity that intends to summarise the complex behaviour of R_{ij} . With the help of this eddy viscosity the RANSE yield

$$\partial_tU_i + U_j\partial_jU_i = \partial_j \left[-\frac{P}{\rho}\delta_{ij} + (\nu + \nu_t)(\partial_jU_i + \partial_iU_j) \right] + \langle g_i \rangle \quad (3.43)$$

CFD solvers, like OpenFOAM, which discretise and solve RANSE in the form of (3.40) or (3.43), are actually obtaining the mean fields $\mathbf{U}(t, \mathbf{x})$ and $P(t, \mathbf{x})$ as ensemble averages. Comparison of those CFD results with actual data taken from experiments must be executed with care, since most laboratory instruments record and measure the time-average of fields, and these are not the results provided by the computer upon solving the equation (3.40).

3.2.1.2 The General Space-Time Average

An averaging method that does not depend on realisations, but rather applies on the full measured record of a given turbulent flow, is the General Space-Time Average (GSTA), which is the most comprehensive averaging method that can be performed on a single realisation of a turbulent flow.¹⁶

A remarkable introduction to the GSTA is found in [MY71], and the description presented herein follows to certain extent that reference. Let $\psi(t, \mathbf{x})$ be a turbulent flow field defined in the space-time domain $\mathcal{U} \subset \mathbb{R}^4$, with the customary requirements of boundedness, differentiability and integrability one expects from physical fields. The GSTA is defined as

$$\overset{\Delta}{\psi}(t, \mathbf{x}) := \int_{\mathcal{U}} \psi(\tau, \boldsymbol{\xi}) w(t - \tau, \mathbf{x} - \boldsymbol{\xi}) d\tau d^3\xi \quad (3.44)$$

where $w(t, \mathbf{x})$ is a weighting function which satisfies the normalisation condition:

$$\int_{\mathcal{U}} w(\tau, \boldsymbol{\xi}) d\tau d^3\xi = 1 \quad (3.45)$$

An alternative definition is to set the integration domain equal to \mathbb{R}^4 , and let either the weighting function $w(t, \mathbf{x})$ or the flow field $\psi(t, \mathbf{x})$ limit the region in which the average is defined; that is, one or both of these functions have compact support. In this case the expression for the GSTA is:

$$\overset{\Delta}{\psi}(t, \mathbf{x}) := \int_{-\infty}^{+\infty} \int \int \int \psi(\tau, \boldsymbol{\xi}) w(t - \tau, \mathbf{x} - \boldsymbol{\xi}) d\tau d^3\xi \equiv \int_{\mathbb{R}^4} \psi(\tau, \boldsymbol{\xi}) w(t - \tau, \mathbf{x} - \boldsymbol{\xi}) d\tau d^3\xi \quad (3.46)$$

and the normalisation condition reads:

$$\int_{-\infty}^{+\infty} \int \int \int w(\tau, \boldsymbol{\xi}) d\tau d^3\xi \equiv \int_{\mathbb{R}^4} w(\tau, \boldsymbol{\xi}) d\tau d^3\xi = 1 \quad (3.47)$$

According to this second definition, corresponds to the product $\psi(\tau, \boldsymbol{\xi}) w(t - \tau, \mathbf{x} - \boldsymbol{\xi})$ to be zero outside of the space-time region in which the turbulent flow develops.

From the definition given in (3.46), the GSTA of a flow field $\psi(t, \mathbf{x})$ could be thought of as the convolution of a distribution \mathfrak{T}_w with a test function $\psi(t, \mathbf{x})$ ¹⁷ (see [Con80]).

$$(\mathfrak{T}_w \star \psi)(t, \mathbf{x}) = \int_{\mathbb{R}^4} \psi(\tau, \boldsymbol{\xi}) w(t - \tau, \mathbf{x} - \boldsymbol{\xi}) d\tau d^3\xi \quad (3.48)$$

¹⁶Actually, that assertion is not true. The most general GSTA takes the form

$$\overset{\Delta}{\psi}(t, \mathbf{x}) = \int_{\mathbb{R}^4} \psi(\tau, \boldsymbol{\xi}) w(t, \tau; \mathbf{x}, \boldsymbol{\xi}) d\tau d^3\xi$$

with the *kernel* w depending also on the space-time point being integrated, instead of the difference of positions. But this sort of anisotropic average is beyond the scope of the present Dissertation.

¹⁷The rigorous definition of a **distribution** \mathfrak{T}_w (also known as **generalised function**) requires that the test functions be infinitely differentiable (C^∞) and of compact support (see [Con80]). But in reference [Sch66] it is pointed out that in Physics sometimes the test functions do not have compact support, although the *kernel* w associated to the distribution does, and the net effect is the same. This approach is followed herein, demanding that the product of w and ψ have compact support.

The function $w(t, \mathbf{x})$ is called the **kernel** of the distribution \mathfrak{T}_w . Note that the integrals extended to $\pm\infty$ exist as long as either:

- The integrand $\psi(\tau, \boldsymbol{\xi})w(t - \tau, \mathbf{x} - \boldsymbol{\xi})$ has a compact support and, therefore, it is zero outside this domain.
- The integrand is non-zero in an unbounded domain, but the following limit is approached sufficiently rapid

$$\lim_{\sigma \rightarrow \infty} \psi(\tau, \boldsymbol{\xi})w(t - \tau, \mathbf{x} - \boldsymbol{\xi}) = 0$$

where $\sigma = \tau$ or $\sigma = \xi_i$

Considering the GSTA of a flow field ψ as its convolution with a distribution \mathfrak{T}_w , enjoys the added benefit of having the rich theory of generalised functions at one's disposal to be applied to the turbulence problem. Either reference [Sch66] or [Con80] contains the relevant theorems and results on generalised functions.

The GSTA would be a suitable averaging method to generate RANSE from, as long as it satisfy the Reynolds conditions (3.4)-(3.7). Herefrom will be obtained the general properties that must be satisfied by the weighting function $w(t, \mathbf{x})$ in order for GSTA to be a Reynolds operator.

- **LINEAR CONDITION.** It is obvious because the integral is a linear operator:

$$\begin{aligned} \overline{a\psi + b\phi}(t, \mathbf{x}) &= \int_{\mathbb{R}^4} (a\psi + b\phi) w(t - \tau, \mathbf{x} - \boldsymbol{\xi}) d\tau d^3\boldsymbol{\xi} = \\ &= a \int_{\mathbb{R}^4} \psi(\tau, \boldsymbol{\xi})w(t - \tau, \mathbf{x} - \boldsymbol{\xi}) d\tau d^3\boldsymbol{\xi} + b \int_{\mathbb{R}^4} \phi(\tau, \boldsymbol{\xi})w(t - \tau, \mathbf{x} - \boldsymbol{\xi}) d\tau d^3\boldsymbol{\xi} = a\overline{\psi} + b\overline{\phi} \end{aligned} \quad (3.49)$$

Thus, any convolution with the form given on (3.46) will be linear.

- **COMMUTATION CONDITION.** This is a general property of the convolution with distributions, and is offered herein without proof (see [Con80])

$$\partial_s(\mathfrak{T}_w \star \psi) = \partial_s(\mathfrak{T}_w) \star \psi = \mathfrak{T}_w \star \partial_s\psi \quad (3.50)$$

with $s = t$ or $s = x_i$. Written in integral form it yields:

$$\partial_s(\overline{\psi}(t, \mathbf{x})) = \int_{\mathbb{R}^4} \partial_\sigma \phi(\tau, \boldsymbol{\xi}) w(t - \tau, \mathbf{x} - \boldsymbol{\xi}) d\tau d^3\boldsymbol{\xi} = \quad (3.51)$$

$$= \int_{\mathbb{R}^4} \phi(\tau, \boldsymbol{\xi}) \partial_\sigma w(t - \tau, \mathbf{x} - \boldsymbol{\xi}) d\tau d^3\boldsymbol{\xi} = \overline{\partial_s\psi}(t, \mathbf{x}) \quad (3.52)$$

where $\sigma = \tau$ or $\sigma = \xi_i$. Thus far, any generalised function \mathfrak{T}_w is suitable for yielding RANSE. The truly restrictive condition is that of idempotency, treated next.

- **IDEMPOTENT CONDITION.** The alternative expression (3.7) for the idempotent condition will be used:

$$\overline{\overline{\psi}}(t, \mathbf{x}) = \int_{\mathbb{R}^4} \overline{\psi}(\tau, \boldsymbol{\xi}) w(t - \tau, \mathbf{x} - \boldsymbol{\xi}) d\tau d^3\boldsymbol{\xi} = \quad (3.53)$$

$$\begin{aligned}
&= \int_{\mathbb{R}^4} \int_{\mathbb{R}^4} \psi(\lambda, \boldsymbol{\eta}) w(\tau - \lambda, \boldsymbol{\xi} - \boldsymbol{\eta}) w(t - \tau, \mathbf{x} - \boldsymbol{\xi}) d\tau d^3\boldsymbol{\xi} d\lambda d^3\boldsymbol{\eta} \stackrel{?}{=} \\
&\stackrel{?}{=} \int_{\mathbb{R}^4} \psi(\lambda, \boldsymbol{\eta}) w(t - \lambda, \mathbf{x} - \boldsymbol{\eta}) d\lambda d^3\boldsymbol{\eta} = \overset{\Delta}{\psi}(t, \mathbf{x})
\end{aligned} \tag{3.54}$$

For this to be true, the *kernel* must satisfy the following relationship:

$$w(t - \lambda, \mathbf{x} - \boldsymbol{\eta}) = \int_{\mathbb{R}^4} w(\tau - \lambda, \boldsymbol{\xi} - \boldsymbol{\eta}) w(t - \tau, \mathbf{x} - \boldsymbol{\xi}) d\tau d^3\boldsymbol{\xi} \tag{3.55}$$

This last property singles out the sort of generalised functions \mathfrak{T}_w that will turn the GSTA a suitable averaging method to derive RANSE from, that is, a Reynolds operator.

The most outstanding example of generalised function fulfilling the three conditions mentioned above is the Dirac's δ distribution. Actually, the three most prominent averaging methods (leaving aside the ensemble average) are derived from Dirac's δ , namely:

- If the weighting function has the form

$$w(t, \mathbf{x}) = \frac{1}{T} \delta(\mathbf{x}) \tag{3.56}$$

with T the time interval in which the flow exists (theoretically $(0, \infty)$), then the GSTA coincides with the time average to be introduced in section 3.2.1.3. Note that w actually does not depend on t .

- Likewise, if

$$w(t, \mathbf{x}) = \frac{1}{\Omega} \delta(t) \tag{3.57}$$

with Ω the space region in which the flow exists, then the GSTA coincides with the space average which will be described in section 3.2.1.4. Likewise, w does not depend on \mathbf{x} .

- Finally, if the weighting function has the form

$$w(t, \mathbf{x}) = \frac{1}{N} \sum_{n=0}^{N-1} \delta(t + nT) \delta(\mathbf{x}) = \frac{1}{N} \sum_{n=0}^{N-1} \delta(t_n) \delta(\mathbf{x}) \tag{3.58}$$

with $t_n = t + nT$ and T the period of a periodic agent acting on the flow, then the GSTA corresponds to the phase average, to be treated in section 3.2.1.5. In this case w depends on t and \mathbf{x} .

Any other more sophisticated averaging method will still require that the corresponding weighting function $w(t, \mathbf{x})$ fulfil the Reynolds conditions (3.49)-(3.55), in order for it to lead to RANSE when applied over the Navier-Stokes equations.

3.2.1.3 The Time Average

Time average is the most familiar method for obtaining the turbulence mean fields, and in the vast majority of cases the only one available in laboratory. Most textbooks on CFD assume, or explicitly establish, that the mean quantities are to be obtained through time average.

The time average of a field $\psi(t, \mathbf{x})$ is defined as¹⁸

$$\overline{\psi}(\mathbf{x}) := \lim_{T \rightarrow \infty} \frac{1}{T} \int_0^T \psi(t, \mathbf{x}) dt \quad (3.59)$$

where it is assumed that the turbulent flow begins at $t = 0$, and ψ is a bounded function for which the limit exists. Note $\overline{\psi}(\mathbf{x})$ is not a function of time. The mean fields provided by the time averaging method are always stationary in time, invariant to time-shifts, so the mean flow is steady. Therefore, it is not possible to reproduce an unsteady turbulent flow using RANSE which are obtained through time average.

The time average fulfils the Reynolds conditions (3.4)-(3.7):

- **LINEAR CONDITION.** The integral is a linear operator:

$$\overline{\psi + \phi} = \lim_{T \rightarrow \infty} \frac{1}{T} \int_0^T (\psi + \phi) dt = \lim_{T \rightarrow \infty} \frac{1}{T} \left[\int_0^T \psi dt + \int_0^T \phi dt \right] = \overline{\psi} + \overline{\phi} \quad (3.60)$$

$$\overline{c\psi} = \lim_{T \rightarrow \infty} \frac{1}{T} \int_0^T c \psi dt = \lim_{T \rightarrow \infty} \frac{1}{T} \left[c \int_0^T \psi dt \right] = c \overline{\psi} \quad (3.61)$$

$$\overline{c} = \lim_{T \rightarrow \infty} \frac{1}{T} \int_0^T c dt = \lim_{T \rightarrow \infty} c \frac{1}{T} \int_0^T dt = \lim_{T \rightarrow \infty} c \cdot 1 = c \quad (3.62)$$

- **COMMUTATION CONDITION.** Using the rule of differentiation under the integral sign:

$$\frac{\partial \overline{\psi}}{\partial x_i} = \lim_{T \rightarrow \infty} \frac{1}{T} \int_0^T \frac{\partial \psi}{\partial x_i} dt = \lim_{T \rightarrow \infty} \frac{1}{T} \frac{\partial}{\partial x_i} \left[\int_0^T \psi dt \right] = \frac{\partial}{\partial x_i} \overline{\psi} \quad (3.63)$$

$$\frac{\partial \overline{\psi}}{\partial t} = \lim_{T \rightarrow \infty} \frac{1}{T} \int_0^T \frac{\partial \psi}{\partial t} dt = \lim_{T \rightarrow \infty} \frac{\psi(T) - \psi(0)}{T} = 0 \equiv \frac{\partial}{\partial t} \overline{\psi} \quad (3.64)$$

because $\psi(t, \mathbf{x})$ is a bounded function $\forall t \in \mathbb{R}^+$, and $\overline{\psi}(\mathbf{x})$ does not depend on t .¹⁹

- **IDEMPOTENT CONDITION.**

$$\overline{\overline{\psi}} = \lim_{T \rightarrow \infty} \frac{1}{T} \int_0^T \overline{\psi} dt = \lim_{T \rightarrow \infty} \frac{1}{T} \overline{\psi} \int_0^T dt = \overline{\psi} \quad (3.65)$$

$\overline{\psi}$ can exit the integral because it does not depend on t .

¹⁸From equation (3.56) and the Fubini's theorem

$$\overline{\psi}(t, \mathbf{x}) = \int_{\mathbb{R}^4} \psi(\tau, \boldsymbol{\xi}) w(t - \tau, \mathbf{x} - \boldsymbol{\xi}) d\tau d^3\boldsymbol{\xi} = \lim_{T \rightarrow \infty} \frac{1}{T} \int_{\mathbb{R}^4} \psi(\tau, \boldsymbol{\xi}) \delta(\mathbf{x} - \boldsymbol{\xi}) d\tau d^3\boldsymbol{\xi} = \overline{\psi}(\mathbf{x})$$

and thus the time average is a particular case of the GSTA (note that $\delta(\mathbf{x}) = \delta(-\mathbf{x})$).

¹⁹If T were allowed to remain finite, as in the case of a time average over a finite period, then $\overline{\partial_t \psi} \neq 0$ and the commutation condition would not be fulfilled.

Therefore, the time average $\bar{\cdot}$ is a Reynolds operator.

The Reynolds decomposition for the main turbulence fields is given by:

$$\mathbf{u}(t, \mathbf{x}) = \bar{\mathbf{u}}(\mathbf{x}) + \mathbf{u}'(t, \mathbf{x}) \equiv \mathbf{U}(\mathbf{x}) + \mathbf{u}'(t, \mathbf{x}) \quad (3.66)$$

$$p(t, \mathbf{x}) = \bar{p}(\mathbf{x}) + p'(t, \mathbf{x}) \equiv P(\mathbf{x}) + p'(t, \mathbf{x}) \quad (3.67)$$

Note that all time dependence existing in \mathbf{u} and p is entirely transmitted to \mathbf{u}' and p' , because no time dependence remains in the mean fields.

Inserting this Reynolds decomposition into Navier-Stokes equation (3.35), and applying time average $\bar{\cdot}$ to each term, the RANSE *à la* time average for incompressible Newtonian flow are obtained:

$$U_j \partial_j U_i = \partial_j \left[-\frac{P}{\rho} \delta_{ij} + \nu (\partial_j U_i + \partial_i U_j) - \overline{u'_i u'_j} \right] + \bar{g}_i \quad (3.68)$$

The Reynolds-averaged continuity equation is

$$\nabla \cdot \mathbf{u}(t, \mathbf{x}) = \nabla \cdot \mathbf{U}(\mathbf{x}) = \nabla \cdot \mathbf{u}'(t, \mathbf{x}) = 0 \quad (3.69)$$

Thus, the time average meets the Reynolds conditions and is a suitable average method to derive the RANSE therefrom. The Reynolds stress tensor *à la* time average $R_{ij} = -\rho \overline{u'_i u'_j}$ would, in general, be different from the Reynolds stress tensor $-\rho \langle u'_i u'_j \rangle$ derived from ensemble averaging method, although its physical meaning is similar and the role played in the equations is identical. R_{ij} is as dependent on the averaging method as the mean fields themselves, and care should be taken before comparing results involving Reynolds stresses from different sources. As a matter of fact, $R_{ij} = -\rho \overline{u'_i u'_j}$ is the time average of a quantity and thus can only produce a steady, time-independent result, $R_{ij} = R_{ij}(\mathbf{x})$ and $\partial_t R_{ij} = 0$, while the Reynolds stress tensor *à la* ensemble average is time-dependent.

Note that T cannot be allowed to be finite: the Reynolds conditions will not be fulfilled. Thus, a finite time average would not only mean a loss of accuracy (because it is an approximation), but also the appearance of inconsistencies in the derivation and use of the RANSE. Any solution to the equation (3.68) corresponds to a steady mean flow.

3.2.1.4 The Spatial Average

Spatial average is not so frequently used to obtain the mean fields in experiment related with turbulence. Normally, it makes sense when dealing with homogeneous and isotropic turbulent flows.

The spatial average of a field $\psi(t, \mathbf{x})$ is defined as

$$\widehat{\psi}(t) := \lim_{L \rightarrow \infty} \frac{1}{8L^3} \int_{-L}^{+L} \int_{-L}^{+L} \int_{-L}^{+L} \psi(t, \mathbf{x}) \, d^3 \mathbf{x} \quad (3.70)$$

where it is assumed that ψ is a bounded function for which the limit exists. $\widehat{\psi}(t)$ is not a function of space variables \mathbf{x} . The mean fields provided by the spatial averaging method are invariant to translations in space, so the mean flow is homogeneous and isotropic.

In the case of bounded flows, confined to an open finite domain Ω and subjected to the condition $\psi(t, \mathbf{x}) = 0$ for $\mathbf{x} \notin \Omega$, being ψ any field defined in the bounded flow, the definition of spatial average of the flow field $\psi(t, \mathbf{x})$ is straightforward:²⁰

$$\widehat{\psi}(t) := \frac{1}{\Omega} \int \int \int_{\Omega} \psi(t, \mathbf{x}) \, d^3\mathbf{x} \quad (3.71)$$

Actually, the average for bounded flow (3.71) can be considered a particular case of the more general definition (3.70). Therefore, in all that follows the general definition will be used.

The spatial average fulfils the Reynolds conditions (3.4)-(3.7):

- LINEAR CONDITION. The integral is a linear operator:

$$\widehat{\psi + \phi} = \lim_{L \rightarrow \infty} \frac{1}{8L^3} \int_{-L}^{+L} \int_{-L}^{+L} \int_{-L}^{+L} (\psi + \phi) \, d^3\mathbf{x} = \widehat{\psi} + \widehat{\phi} \quad (3.72)$$

$$\widehat{c\psi} = \lim_{L \rightarrow \infty} \frac{1}{8L^3} \int_{-L}^{+L} \int_{-L}^{+L} \int_{-L}^{+L} c\psi \, d^3\mathbf{x} = c \widehat{\psi} \quad (3.73)$$

$$\widehat{c} = \lim_{L \rightarrow \infty} \frac{1}{8L^3} \int_{-L}^{+L} \int_{-L}^{+L} \int_{-L}^{+L} c \, d^3\mathbf{x} = \lim_{L \rightarrow \infty} c \cdot 1 = c \quad (3.74)$$

- COMMUTATION CONDITION. Using the rule of differentiation under the integral sign:

$$\begin{aligned} \frac{\partial \widehat{\psi}}{\partial x_i} &= \lim_{L \rightarrow \infty} \frac{1}{8L^3} \int_{-L}^{+L} \int_{-L}^{+L} \int_{-L}^{+L} \frac{\partial \psi}{\partial x_i} \, d^3\mathbf{x} = \\ &= \lim_{L \rightarrow \infty} \frac{1}{4L^2} \int_{-L}^{+L} \int_{-L}^{+L} \frac{\psi(L, x_j, x_k) - \psi(-L, x_j, x_k)}{2L} \, dx_j \, dx_k = 0 \equiv \frac{\partial}{\partial x_i} \widehat{\psi} \end{aligned} \quad (3.75)$$

$$\frac{\partial \widehat{\psi}}{\partial t} = \lim_{L \rightarrow \infty} \frac{1}{8L^3} \int_{-L}^{+L} \int_{-L}^{+L} \int_{-L}^{+L} \frac{\partial \psi}{\partial t} \, d^3\mathbf{x} = \lim_{L \rightarrow \infty} \frac{1}{8L^3} \frac{\partial}{\partial t} \int_{-L}^{+L} \int_{-L}^{+L} \int_{-L}^{+L} \psi \, d^3\mathbf{x} = \frac{\partial}{\partial t} \widehat{\psi} \quad (3.76)$$

because $\psi(t, \mathbf{x})$ is a bounded function $\forall x_i \in \mathbb{R}$, and $\widehat{\psi}(t)$ does not depend on \mathbf{x} .²¹

²⁰From equation (3.57) and the Fubini's theorem

$$\widehat{\Delta \psi}(t, \mathbf{x}) = \int_{\mathbb{R}^4} \psi(\tau, \boldsymbol{\xi}) w(t - \tau, \mathbf{x} - \boldsymbol{\xi}) \, d\tau \, d^3\boldsymbol{\xi} = \frac{1}{\Omega} \int_{\mathbb{R}^4} \psi(\tau, \boldsymbol{\xi}) \delta(t - \tau) \, d\tau \, d^3\boldsymbol{\xi} = \widehat{\psi}(t)$$

and thus the space average is a particular case of the GSTA (note that $\delta(t) = \delta(-t)$).

²¹If L is allowed to remain finite in a general unbounded flow, as in the case of a spatial average performed over just a finite domain, then $\widehat{\partial_j \psi} \neq 0$ and the commutation condition would not be fulfilled. On the contrary, if ψ is zero outside a finite open domain Ω (bounded flow), then the commutation condition would be satisfied, as long as L stretches farther away than Ω .

- IDEMPOTENT CONDITION.

$$\overbrace{\phi}^{\psi} = \lim_{L \rightarrow \infty} \frac{1}{8L^3} \int_{-L}^{+L} \int_{-L}^{+L} \int_{-L}^{+L} \overbrace{\phi}^{\psi} \psi \, d^3 \mathbf{x} = \lim_{L \rightarrow \infty} \frac{1}{8L^3} \overbrace{\phi}^{\psi} \int_{-L}^{+L} \int_{-L}^{+L} \int_{-L}^{+L} \psi \, d^3 \mathbf{x} = \overbrace{\phi}^{\psi} \overbrace{\psi}^{\psi} \quad (3.77)$$

$\overbrace{\phi}^{\psi}$ can exit the integral because it does not depend on \mathbf{x} .

Therefore, the spatial average $\overbrace{\cdot}^{\psi}$ is a Reynolds operator.

The Reynolds decomposition for the main turbulence fields is given by:

$$\mathbf{u}(t, \mathbf{x}) = \overbrace{\mathbf{u}}^{\mathbf{U}}(t) + \mathbf{u}'(t, \mathbf{x}) \equiv \mathbf{U}(t) + \mathbf{u}'(t, \mathbf{x}) \quad (3.78)$$

$$p(t, \mathbf{x}) = \overbrace{p}^P(t) + p'(t, \mathbf{x}) \equiv P(t) + p'(t, \mathbf{x}) \quad (3.79)$$

Note that all dependence on position coordinates existing in \mathbf{u} and p is entirely transmitted to \mathbf{u}' and p' , since no spatial dependence remains in the mean fields.

Inserting this Reynolds decomposition into Navier-Stokes equation (3.35), and applying the spatial average $\overbrace{\cdot}^{\psi}$ to each term, the RANSE *à la* spatial average for incompressible Newtonian flow are obtained:

$$\partial_t U_i = - \overbrace{u'_j \partial_j u'_i} + \overbrace{g_i} = - \overbrace{\partial_j (u'_j u'_i)} + \overbrace{g_i} \quad (3.80)$$

The resulting equation is short because no mean quantity survives the derivation with respect to space variables. Note also the term $\overbrace{u'_j \partial_j u'_i} = \overbrace{\partial_j (u'_j u'_i)}$. In this case, it cannot appear as $\partial_j (\overbrace{u'_i u'_j})$, because any space derivative of any space-averaged field would be identically zero. Therefore, the Reynolds stress tensor does not appear explicitly in the RANSE, but rather a related quantity does which, perhaps, would require a modelling different than Boussinesq's turbulent viscosity. This ought to be taken into consideration upon writing CFD code.

The Reynolds-averaged continuity equation is

$$\nabla \cdot \mathbf{u}(t, \mathbf{x}) = \nabla \cdot \mathbf{u}'(t, \mathbf{x}) = 0 \quad (3.81)$$

because $\partial_i U_j \equiv 0 \, \forall i, j = 1, 2, 3$.

Thus, the spatial average meets the Reynolds conditions and is a suitable average to derive the RANSE therefrom. The Reynolds stress tensor *à la* spatial average $R_{ij} = -\rho \overbrace{u'_i u'_j}$ would, in general, be different from the Reynolds stress tensor $-\rho \langle u'_i u'_j \rangle$ derived from ensemble averaging method. As it has already been said elsewhere, the Reynolds stress tensor is as dependent on the averaging method as the mean fields themselves. It fulfils the same role of concentrating the turbulence diffusion effects in the governing equations, but the values acquired by this version of R_{ij} are different from those corresponding to other versions. As a matter of fact, $R_{ij} = -\rho \overbrace{u'_i u'_j}$ is the space average of a quantity and thus can only produce a homogeneous, space-independent result, $R_{ij} = R_{ij}(t)$ and $\partial_k R_{ij} = 0$, while the Reynolds stress tensor *à la* ensemble average is space-dependent. That is the reason why $R_{ij} = -\rho \overbrace{u'_i u'_j}$ does not appear explicitly in equation (3.80), but rather $\overbrace{u'_j \partial_j u'_i} = \overbrace{\partial_j (u'_j u'_i)}$, which is not the same as the identically null quantity $\partial_j R_{ij}$.

Note that L cannot be allowed to be finite: the Reynolds conditions will not be fulfilled. Thus, a finite spatial average would not only mean a loss of accuracy (because it is an approximation), but also the appearance of inconsistencies in the derivation and use of the RANSE. Of course, the flow could be bounded, in which case $\mathbf{u}(t, \mathbf{x})$ and $p(t, \mathbf{x})$ would be zero outside a bounded domain Ω , and the integral over $-L$ to L would be equal to that over $-\infty$ to ∞ , as long as L reach beyond the bounded domain Ω .

Any solution to the equation (3.80) corresponds to a homogeneous and isotropic mean flow.

3.2.1.5 The Phase Average

Some flows of interest in Engineering develop in almost periodic conditions. Examples of such flows are found in internal combustion motors and rotating machinery, and in others not so obvious as vortex shedding behind a cylinder or water-hammer. There is a periodic agent of period T which acts on the fluid, exerting an influence which manifests itself in a quasi-periodic behaviour of the turbulence fields. This agent could be a periodic force or some periodic boundary conditions, or any other cause. The resulting flow fields are unsteady, not purely periodic because of their turbulent nature. However, upon analysis of their Fourier spectra one can see a large component in the frequency range generated by the periodic agent.

The phase average was first introduced in [HR70], although in a different context than the one intended herein, whence is meant for flows where an organised motion exists. Let be a flow developing on a domain $\Omega \subset \mathbb{R}^3$ upon which a periodic agent with period T acts. Then the **phase-average**²² of the field $\psi(t, \mathbf{x})$ (ψ is a physical field and thus is a continuous and bounded function with continuous derivatives) is defined as:²³

$$\overleftrightarrow{\psi}(t, \mathbf{x}) := \lim_{N \rightarrow \infty} \frac{1}{N} \sum_{n=0}^{N-1} \psi(t + nT, \mathbf{x}) \quad (3.82)$$

provided the series converge. Note that $\overleftrightarrow{\psi}(t, \mathbf{x})$, if it exists, is a periodic function of t with period T . For brevity, they will be called here **T -periodic functions**, to distinguish them from any other periodic function with period $T' \neq T$.

One might feel tempted to think that $\overleftrightarrow{\psi}(t, \mathbf{x}) \neq \overleftrightarrow{\psi}(t + T, \mathbf{x})$, because the later is

$$\overleftrightarrow{\psi}(t + T, \mathbf{x}) = \lim_{N \rightarrow \infty} \frac{1}{N} \sum_{n=0}^{N-1} \psi(t + T + nT, \mathbf{x}) = \lim_{N \rightarrow \infty} \frac{1}{N} \sum_{n=1}^N \psi(t + nT, \mathbf{x}) \quad (3.83)$$

and the first term $\psi(t, \mathbf{x})$ corresponding to $n = 0$ is absent. The following derivation will prove that thought without foundation:

$$\overleftrightarrow{\psi}(t, \mathbf{x}) - \overleftrightarrow{\psi}(t + T, \mathbf{x}) = \lim_{N \rightarrow \infty} \frac{1}{N} \left[\sum_{n=0}^{N-1} \psi(t + nT, \mathbf{x}) - \sum_{n=1}^N \psi(t + nT, \mathbf{x}) \right] =$$

²²When any confusion may exist regarding the period T , it will be called **phase average of period T** , or **T -phase average** for short. Such situations may occur when a bundle of periodic motions with different periods are present in the flow.

²³From equation (3.58) and the Fubini's theorem

$$\overset{\Delta}{\psi}(t, \mathbf{x}) = \int_{\mathbb{R}^4} \psi(\tau, \boldsymbol{\xi}) w(t - \tau, \mathbf{x} - \boldsymbol{\xi}) \, d\tau \, d^3\boldsymbol{\xi} = \lim_{N \rightarrow \infty} \frac{1}{N} \sum_{n=0}^{N-1} \int_{\mathbb{R}^4} \psi(\tau, \boldsymbol{\xi}) \delta(t_n - \tau) \delta(\mathbf{x} - \boldsymbol{\xi}) \, d\tau \, d^3\boldsymbol{\xi} = \overleftrightarrow{\psi}(t, \mathbf{x})$$

with $t_n = t + nT$, and thus the phase average is a particular case of the GSTA (note that $\delta(\mathbf{x}) = \delta(-\mathbf{x})$, $\delta(t) = \delta(-t)$).

$$= \lim_{N \rightarrow \infty} \frac{\psi(t, \mathbf{x}) - \psi(t + NT, \mathbf{x})}{N} = 0 \quad (3.84)$$

because $\psi(t, \mathbf{x})$ is a bounded real function $\forall t \in \mathbb{R}^+$ and $\forall \mathbf{x} \in \Omega \subset \mathbb{R}^3$. With the same argument, it can be proven that $\overleftrightarrow{\psi}(t, \mathbf{x}) = \overleftrightarrow{\psi}(t + mT, \mathbf{x})$, $m \in \mathbb{Z}^+$. Therefore, $\overleftrightarrow{\psi}(t, \mathbf{x})$ is a T -periodic function of t , that is, the phase average is independent of the time origin.²⁴ According to this result, suffices to define $\overleftrightarrow{\psi}(t, \mathbf{x})$ for $t \in [0, T)$, $\mathbf{x} \in \Omega \subset \mathbb{R}^3$, and to study its properties only in that domain, although t must be extended to \mathbb{R}^+ for fields ψ and ψ' .

A physical field $\psi(t, \mathbf{x}) = \overleftrightarrow{\psi}(t, \mathbf{x}) + \psi'(t, \mathbf{x})$ for which $\psi(t_0, \mathbf{x}) \neq 0$ for some $t_0 \in \mathbb{R}^+$ implies $\overleftrightarrow{\psi}(t, \mathbf{x}) \neq 0 \forall t \in \mathbb{R}^+$ except in a set of measure zero, and $\psi(t, \mathbf{x})$ will be called a **T -potentially periodic field**²⁵. A T -potentially periodic field can have regions in which $\psi(t, \mathbf{x}) = 0$ and $\overleftrightarrow{\psi}(t, \mathbf{x}) = 0$, for example the velocity field on a wall (no-slip condition). But if $\psi(t, \mathbf{x}) \neq 0$ at some instant, then $\overleftrightarrow{\psi}(t, \mathbf{x}) \neq 0$ at all instants, except in a numerable set of them (the periodic crossing of zero, if that exists). Note that if $\psi(t + nT, \mathbf{x})$ does not add significantly to $\psi(t, \mathbf{x})$, then the sum will not be large enough to counteract the $1/N$ factor and the limit will be zero as $N \rightarrow \infty$, and the field ψ would not be T -potentially periodic. In a T -potentially periodic field, $\psi(t + nT, \mathbf{x})$ adds significantly to $\psi(t, \mathbf{x})$ for almost every n , even if the flow is not markedly periodic. In conclusion, $\overleftrightarrow{\psi}(t, \mathbf{x})$ is a T -periodic function of t by construction. It could either be zero (the $\psi(t + nT, \mathbf{x})$ terms do not add significantly), infinite (the series does not converge) or T -periodic. A flow whose fields are T -potentially periodic will be called a **T -potentially periodic flow**. This does not necessarily mean that the flow show a pronounced periodic behaviour.

The phase average fulfils the Reynolds conditions (3.4)-(3.7):

- **LINEAR CONDITION.** The sum is a linear operator:

$$\overleftrightarrow{a\psi(t, \mathbf{x}) + b\phi(t, \mathbf{x})} = \lim_{N \rightarrow \infty} \frac{1}{N} \sum_{n=0}^{N-1} [a\psi(t + nT, \mathbf{x}) + b\phi(t + nT, \mathbf{x})] = a \overleftrightarrow{\psi}(t, \mathbf{x}) + b \overleftrightarrow{\phi}(t, \mathbf{x}) \quad (3.85)$$

- **COMMUTATION CONDITION.** Obvious because $\frac{\partial}{\partial t} = \frac{\partial}{\partial(t+nT)} \frac{\partial(t+nT)}{\partial t} = \frac{\partial}{\partial(t+nT)}$,

$$\overleftrightarrow{\partial_s \psi(t, \mathbf{x})} = \lim_{N \rightarrow \infty} \frac{1}{N} \sum_{n=0}^{N-1} \partial_s \psi(t + nT, \mathbf{x}) = \lim_{N \rightarrow \infty} \frac{1}{N} \partial_s \left[\sum_{n=0}^{N-1} \psi(t + nT, \mathbf{x}) \right] = \partial_s \overleftrightarrow{\psi}(t, \mathbf{x}) \quad (3.86)$$

where s is any space-time variable t, x_1, x_2, x_3 .

- **IDEMPOTENT CONDITION.** Easy to prove because $\overleftrightarrow{\phi}(t, \mathbf{x})$ is a T -periodic function of t and $\overleftrightarrow{\phi}(t, \mathbf{x}) = \overleftrightarrow{\phi}(t + nT, \mathbf{x}) \forall n \in \mathbb{N}, \forall t \in \mathbb{R}^+, \forall \mathbf{x} \in \Omega \subset \mathbb{R}^3$:

$$\overleftrightarrow{\overleftrightarrow{\phi} \psi} = \lim_{N \rightarrow \infty} \frac{1}{N} \sum_{n=0}^{N-1} \overleftrightarrow{\phi}(t + nT, \mathbf{x}) \psi(t + nT, \mathbf{x}) = \lim_{N \rightarrow \infty} \frac{1}{N} \sum_{n=0}^{N-1} \overleftrightarrow{\phi}(t, \mathbf{x}) \psi(t + nT, \mathbf{x}) = \quad (3.87)$$

²⁴Special emphasis is placed on the period T . The phase average method only produces fields that are periodic in time with period T . If ψ also has components with period $T' \neq T$, these will not be included in $\overleftrightarrow{\psi}$ as defined by (3.82), unless T is a multiple of T' . See section 3.2.3 for an actual example.

²⁵The non- T -periodic components of ψ will be sent to ψ' by this averaging method; only T -periodic components remain in $\overleftrightarrow{\psi}$. Note that any T' -periodic component of ψ , with $T/T' \notin \mathbb{Z}$ and $T'/T \notin \mathbb{Z}$ (non-integer numbers), will also be sent to ψ' . Again, see section 3.2.3 for an actual example.

$$= \lim_{N \rightarrow \infty} \frac{1}{N} \overleftrightarrow{\phi}(t, \mathbf{x}) \sum_{n=0}^{N-1} \psi(t + nT, \mathbf{x}) = \overleftrightarrow{\phi}(t, \mathbf{x}) \overleftrightarrow{\psi}(t, \mathbf{x})$$

$\overleftrightarrow{\phi}(t, \mathbf{x})$ can exit the sum because it is not affected by the summation index n .

Hence, the phase average $\overleftrightarrow{\cdot}$ is a Reynolds operator, that is, a correct averaging method to derive RANSE from the Navier-Stokes counterpart.

In the just described situation of a T -periodic agent acting on the flow, the T -phase average assumes that any T -potentially periodic field $\psi(t, \mathbf{x}) = \overleftrightarrow{\psi}(t, \mathbf{x}) + \psi'(t, \mathbf{x})$ can be decomposed into two parts (see figure 3.1):

- i. A pure T -periodic function, following the periodic agent acting on the flow, called the **mean periodic field** $\overleftrightarrow{\psi}(t, \mathbf{x})$.
- ii. A non- T -periodic part, due entirely to the turbulence or to any other agent, called the **fluctuating field** $\psi'(t, \mathbf{x})$. This fluctuating component has by construction the property $\overleftrightarrow{\psi'}(t, \mathbf{x}) = 0$. Note that ψ' could be non- T -periodic for a variety of reasons. Two of them, with no pretension to make the list exhaustive, would be:
 - ψ' is completely non periodic, it does not possess any period whatsoever.
 - ψ' has T' -periodic components, with $T'/T \notin \mathbb{Z}$ and $T/T' \notin \mathbb{Z}$ (non-integer numbers).

According to this decomposition, whatever non- T -periodicity existing in the flow is assumed to be caused by the turbulence, and is removed from the mean field by the phase averaging method, and passed over to the fluctuating field. As it has been stated in section 3.2, the fluctuating component is as inherently linked to the averaging method as the mean component, and it can be roughly defined as *that part of ψ which is not included in the mean periodic component*.

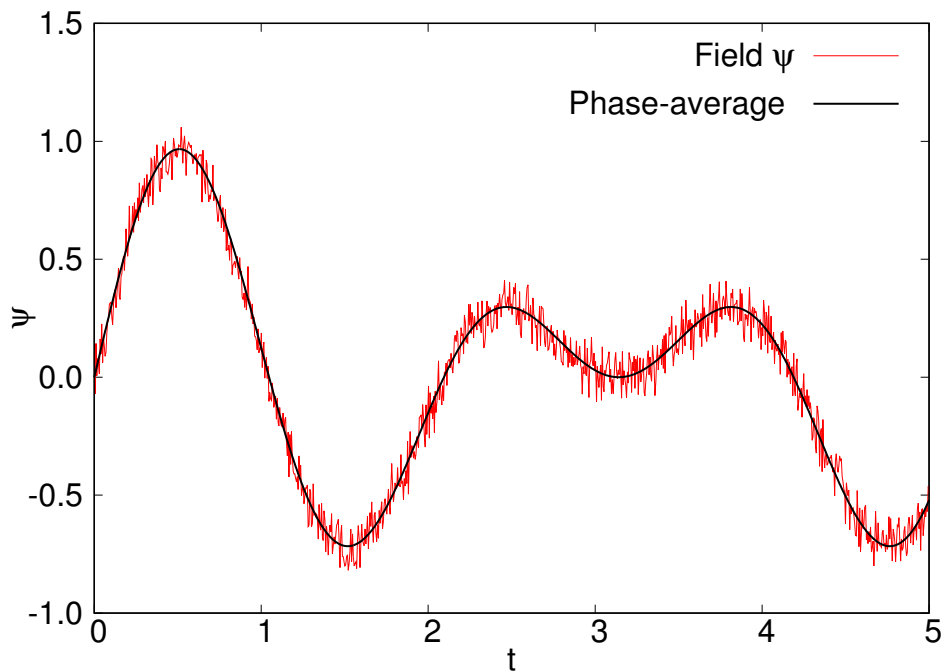


Figure 3.1: Flow field ψ and its phase average. The graph needs to repeat itself to be periodic.

The Reynolds decomposition for the main turbulence fields is given by:

$$\mathbf{u}(t, \mathbf{x}) = \overleftarrow{\mathbf{u}}(t, \mathbf{x}) + \mathbf{u}'(t, \mathbf{x}) \equiv \mathbf{U}(t, \mathbf{x}) + \mathbf{u}'(t, \mathbf{x}) \quad (3.88)$$

$$p(t, \mathbf{x}) = \overleftarrow{p}(t, \mathbf{x}) + p'(t, \mathbf{x}) \equiv P(t, \mathbf{x}) + p'(t, \mathbf{x}) \quad (3.89)$$

Note how similar this decomposition is to equations (3.36)-(3.37) for ensemble average: the mean fields depend on (t, \mathbf{x}) .

Before inserting this Reynolds decomposition into the Navier-Stokes equations, the periodic agent acting on the flow should be explicitly written in them. This agent is not necessarily a force, but most times it could be expressed as such. Therefore, let $\pi_i(t, \mathbf{x})$ be a T -periodic volumetric force field applied to the flow. g_i represents, as usual, the external volumetric forces acting on the flow (typically the gravity). Note that for a steady force field the phase average yields $\overleftarrow{g}_i = g_i$ and for a T -periodic force field is also $\overleftarrow{\pi}_i = \pi_i$, thus their Reynolds decomposition is trivial.

With such provisions, the Navier-Stokes equations for incompressible flow are written as:

$$\partial_i u_i + u_j \partial_j u_i = -\frac{1}{\rho} \partial_i p + \partial_j (\nu \partial_j u_i) + g_i + \pi_i \quad (3.90)$$

Inserting now the Reynolds decomposition of fields (3.88)-(3.89) into this equation and applying phase average $\overleftarrow{\cdot}$ to each term, the RANSE *à la* phase average for incompressible Newtonian flow are obtained:

$$\partial_i U_i + U_j \partial_j U_i = \partial_j \left[-\frac{P}{\rho} \delta_{ij} + \nu (\partial_j U_i + \partial_i U_j) - \overleftarrow{u'_i u'_j} \right] + g_i + \pi_i \quad (3.91)$$

plus the Reynolds-averaged continuity equation:

$$\nabla \cdot \mathbf{u}(t, \mathbf{x}) = \nabla \cdot \mathbf{U}(t, \mathbf{x}) = \nabla \cdot \mathbf{u}'(t, \mathbf{x}) = 0 \quad (3.92)$$

As it has been pointed out in other occasions, the Reynolds stress tensor *à la* phase average $R_{ij} = -\rho \overleftarrow{u'_i u'_j}$ appearing in this equation is not the same than the like-named $-\rho \langle u'_i u'_j \rangle$ derived from the ensemble averaging method. The Reynolds stress tensor is as dependent on the averaging method as the mean fields themselves. It fulfils the same role of concentrating the turbulence diffusion effects in the governing equations, but the values acquired by this version of R_{ij} are different from those corresponding to other averaging methods. Care should be taken before comparing values of R_{ij} obtained from different sources, because it is as much a mathematical artifice as a physical entity. As a matter of fact, $R_{ij}(t, \mathbf{x}) = -\rho \overleftarrow{u'_i u'_j}$ is the phase average of a quantity and this operation can only produce a T -periodic function of t , $R_{ij}(t, \mathbf{x}) = R_{ij}(t + nT, \mathbf{x})$, whereas the Reynolds stress tensor *à la* ensemble average would not in general be periodic.

Note that, leaving aside the T -periodic π_i term which might be absent from the equation, the RANSE *à la* phase average (3.91) are indistinguishable from the RANSE *à la* ensemble average (3.40). A CFD code solving those equations would equally provide a mean field obtained from phase average or from ensemble average. Only the boundary conditions would make the code yield one of those two options. Of course, if the T -periodic force field $\pi_i(t, \mathbf{x})$ were present in the equations, then the mean fields would be also T -periodic and would correspond to phase average.

3.2.2 A Critique to Certain Kind of URANS Simulations

Unsteady Reynolds Averaged Navier-Stokes (URANS) simulations literally make reference to those applications of the RANSE in which the mean flow fields are supposed to be unsteady, that is, to change with time (see [Tuc01]). This, in principle, should not be a problem, since the theory behind RANSE permits perfectly well the existence of arbitrarily fast-varying mean velocity and pressure fields. As a matter of fact, the very presence of the term *unsteady* is quite unnecessary in this context, because the time derivative $\partial \mathbf{U} / \partial t$ of the mean field is already included in some versions of RANSE, and need not be expressly highlighted.

Leaving aside potential unexplored versions of the GSTA, two possibilities clearly stand out to realise mathematically sound URANS simulations:

- Modelling the turbulent flow through the equation (3.40), with \mathbf{U} and P the ensemble average of the flow fields \mathbf{u} and p . This approach is always the most suitable from a mathematical and physical standpoint, since the ensemble average constitutes the highest reference for any other averaging method, that is, the standard against which any other average type is compared. Whatever the simulation one mean to attempt, ensemble average will always be a right choice. Besides, equation (3.40) poses no limits to the variation of \mathbf{U} with t , other than the usual requirements of continuity and differentiability.
- If the turbulent flow is being acted upon by a T -periodic agent, it would also be possible to use equation (3.91) following a phase average. In that case, the outcome would be a set of T -periodic mean fields U , P and Reynolds stress R_{ij} . No result other than a T -periodic mean field should be expected from phase average. Of course, ensemble average is again the best mathematical and physical option even for potentially periodic flow.

Having said that, what the term URANS normally means in the contexts this section intends to pinpoint (which are not all where such term could be found), applies to a particular class of *unsteady simulations through the use of finite time average*. And here, yes, there is a problem. Such URANS models are being used frequently in industry to simulate the unsteady flow occurring in many situations of interest related with hydraulic machinery, motors, boundary layer meteorology, etc. The simulation results need to be compared with experimental data which, usually, are taken with instruments that perform some degree of integration, that is, a finite time average. Whether this average be over sufficiently long time, is a different discussion. The relevant point is that mean velocities are unsteady, and one writes in the computer solver an equation like (3.40), and one expects the computer's outcome to be plausibly comparable with the experimental values. But this procedure harbours a fundamental flaw, even though in some cases it might yield some degree of agreement: every time an equation like (3.40) is written in a solver, the computer will spew an ensemble average of the velocity field. Whether these results can be safely compared with the experimental data, is the object of the critique raised herein.

The possibility of comparing data thus averaged over time (or space) with results obtained through a CFD simulation, usually expressed in terms of ensemble averaged fields, is closely related with a property that since the dawn of turbulence science has been attached to most turbulent flows: ergodicity. Ergodicity opens quite a convenient prospect: instead of studying turbulence through many identically repeated experiments (realisations), why not carry out detailed observations of a single experiment over long times or large spatial breadths? Shouldn't it be the same? Ergodicity was first envisioned by Ludwig Boltzmann during the development of Statistical Mechanics (see [Haa95]), and has since then found a prominent role in many fields of Physics.

A distinction must be made between the **Ergodic theorem** and the **Ergodic hypothesis**. The ergodic hypothesis states that within the general set of phenomena comprised under the name of turbulence, there exists a subset that could be considered ergodic, that is, the ergodic theorem is applicable to certain classes of turbulent flows. Since this is extremely difficult to prove, to the point that (to the author's knowledge) no one has yet done so, it is customary to issue the hypothesis and to expect it to be true: the scientific community accepts it somewhat reluctantly, but does not cease to use it.

Now it remains to see the scope and enunciate of the ergodic theorem. It is explained, for instance, in [MY71] or [Fri95]. Three cases are being considered in the statement of the **Ergodic theorem**:

i. Statistically stationary fields.

If the probability distribution of a random function $\psi(t, \mathbf{x})$ is such that it does not change when there is a time shift ²⁶ affecting all the variables it depends on, then the random function will be called a **stationary random function** (or a statistically stationary field). This, in turn, implies that all statistical moments corresponding to that random function (mean, variance, skewness, kurtosis, autocorrelation...) be independent of time. These moments are calculated using the ensemble average, which is always a physically correct method.

Assume a given turbulent flow is statistically stationary, that is, all fields related to the turbulence have mean, variance,... and the rest of moments independent of time. Let $\langle \psi \rangle = \Psi(\mathbf{x})$ be the mean of the field $\psi(t, \mathbf{x})$ at a point \mathbf{x} . Let $\bar{\psi}(\mathbf{x})$ be the time average defined by (3.59)

$$\bar{\psi}(\mathbf{x}) = \frac{1}{T} \int_0^T \psi(t, \mathbf{x}) dt$$

taken at the same point \mathbf{x} . Then, the ergodic theorem establishes that both means converge when $T \rightarrow \infty$:

$$\lim_{T \rightarrow \infty} \langle |\bar{\psi}(\mathbf{x}) - \Psi(\mathbf{x})|^2 \rangle = 0 \quad (3.93)$$

Note the double condition: statistically stationary flow *and* average over infinitely long time. Similar convergence results could be established for other higher-order statistical moments of the field ψ .

ii. Statistically homogeneous fields.

Likewise, if the probability distribution of a random function $\psi(t, \mathbf{x})$ is such that it does not change with a space shift ²⁷ affecting all the variables it depends on, then the random function is called **homogeneous** (or statistically homogeneous field). Again, this implies that all statistical moments related with ψ be independent of \mathbf{x} . These moments are determined through ensemble average.

Assume a given turbulent flow is statistically homogeneous. Let $\langle \psi \rangle = \Psi(t)$ be the mean of the field $\psi(t, \mathbf{x})$ at an instant t . Let $\widehat{\psi}(t)$ be the spatial average defined by (3.70)

$$\widehat{\psi}(t) = \frac{1}{8L^3} \int_{-L}^{+L} \int_{-L}^{+L} \int_{-L}^{+L} \psi(t, \mathbf{x}) d^3\mathbf{x}$$

²⁶A statistical system is said to undergo a **time shift** given by τ , if the samples previously taken at instants t_1, t_2, \dots are replaced by others taken at $t_1 + \tau, t_2 + \tau, \dots$. If that time shift changes nothing in the system, then it is said to be statistically stationary.

²⁷A statistical system is said to undergo a **space shift** given by the vector $\boldsymbol{\xi}$, if the samples previously taken at points $\mathbf{x}_1, \mathbf{x}_2, \dots$ are replaced by others taken at $\mathbf{x}_1 + \boldsymbol{\xi}, \mathbf{x}_2 + \boldsymbol{\xi}, \dots$. If that space shift changes nothing in the system, then it is said to be statistically homogeneous.

taken at the same instant t . Then, the ergodic theorem establishes that both means converge when $L \rightarrow \infty$ ²⁸:

$$\lim_{L \rightarrow \infty} \langle \left| \widehat{\psi}(t) - \Psi(t) \right|^2 \rangle = 0 \quad (3.94)$$

Note the double condition: statistically homogeneous flow *and* average over infinitely large spatial domain (or, at least, a domain exceeding the flow boundaries). Similar convergence results could be enunciated for other higher-order statistical moments of the field ψ .

iii. Statistically stationary homogeneous fields.

In this case, aside from the convergence between $\langle \psi \rangle$ and $\bar{\psi}$ on one hand, and $\langle \psi \rangle$ and $\widehat{\psi}$ on the other, it is also verified the convergence

$$\lim_{T \rightarrow \infty} \lim_{L \rightarrow \infty} \langle \left| \widehat{\psi} - \bar{\psi} \right|^2 \rangle = 0 \quad (3.95)$$

Thus the time and space averages can be freely interchanged in any statistical calculation affecting the stationary and homogeneous turbulent flow. This also applies to other higher-order moments.

Note the validity of the ergodic hypothesis is confined to the limits of the ergodic theorem expressed above. Any turbulent flow outside of the ergodic theorem's scope, cannot claim the right to be treated according to the ergodic hypothesis. Neither can any time/space average calculated over too short time/space breadths. Of course, if the averaging time/space is sufficiently larger than the turbulent flow's time/space fluctuations, it could reasonably be expected that the convergence relations (3.93)/(3.94) be still approximately valid. Much harder is to admit the ergodic hypothesis retain its validity with non-stationary/homogeneous flows **and** not very large integration time/space. And a remarkable number of measurements made over turbulent flows suffer from both predicaments. ■

Once exposed the cautions that need to be taken before attempting to compare experimental data with CFD simulations, specially in cases where some unsteadiness is present, it is time to get back to the issue that gives title to this section, namely, the unsteady simulation of flows through the use of finite time averages. The rationale behind this sort of URANS models lies in a particular class of averaging methods, known by the name of moving average (also called running or rolling average). Typically it is defined in time-domain, although it can also be employed in space-, frequency- or wavenumber-domain (to be defined later).

Let $\psi(t, \mathbf{x})$ be a generic flow field defined in a domain $t \in [0, +\infty)$, $\mathbf{x} \in \Omega \subset \mathbb{R}^3$. The running or **moving time average** of width T of the field ψ is defined as

$$\langle \psi(t, \mathbf{x}) \rangle_T := \frac{1}{T} \int_{t-T}^t \psi(\tau, \mathbf{x}) \, d\tau = \frac{1}{T} \int_{-T}^0 \psi(t + \tau, \mathbf{x}) \, d\tau = \frac{-1}{T} \int_0^T \psi(t - \tau, \mathbf{x}) \, d\tau \quad (t \geq T) \quad (3.96)$$

The three integrals are identical and will be used interchangeably. If $t < T$, then the definition corresponds to the first integral with the lower limit set to zero.

²⁸Actually, it is possible to consider random fields which are homogeneous in one direction, or in one plane. In those cases, the integrals should be executed in one variable (unidirectional homogeneity) or in two variables (plane homogeneity). The ergodic theorem will then have validity only in the affected geometry.

Alternatively, it is possible to define a global moving average, or **cumulative time average** (with no mention to any width T) as²⁹

$$\ddot{\psi}(t, \mathbf{x}) := \frac{1}{t} \int_0^t \psi(\tau, \mathbf{x}) \, d\tau \quad (3.97)$$

without forcing $t \rightarrow \infty$. Note that for $t < T$, $\langle \psi(t, \mathbf{x}) \rangle_T \equiv \ddot{\psi}(t, \mathbf{x})$, and also for $t \rightarrow \infty$ the cumulative time average approaches the standard time average $\ddot{\psi} \rightarrow \bar{\psi}$. It will always be assumed that $\ddot{\psi}(t, \mathbf{x})$ is a bounded function $\forall t \in \mathbb{R}^+$.

Yet another alternative definition of the moving average of width T , that provides similar results, is given by:

$$\langle \psi(t, \mathbf{x}) \rangle_T = \frac{1}{T} \int_{t-T/2}^{t+T/2} \psi(\tau, \mathbf{x}) \, d\tau = \frac{1}{T} \int_{-T/2}^{T/2} \psi(t + \tau, \mathbf{x}) \, d\tau \quad (3.98)$$

Equation (3.96) should be used in real-time processes in which control commands are issued based on the smoothed real-time value of a variable, while (3.98) could be used if one would mean to evaluate the evolution of a smoothed variable based on stored data.

Finally, the moving average of width T can still be formulated in another equivalent form, as the following convolution integral (see page 102):

$$\langle \psi(t, \mathbf{x}) \rangle_T := \int_{-\infty}^{+\infty} \psi(\tau, \mathbf{x}) \mathfrak{R}_T(t - \tau) \, d\tau \quad (3.99)$$

where $\mathfrak{R}_T(t)$ is the rectangular or **normalised boxcar function** (**rect function** for short) of width T , defined by (see figure 3.2):

$$\mathfrak{R}_T(t) := \begin{cases} 0 & \text{if } |t| > T/2 \\ \frac{1}{2T} & \text{if } |t| = T/2 \\ \frac{1}{T} & \text{if } |t| < T/2 \end{cases} \quad (3.100)$$

which fulfils the normalisation condition³⁰:

$$\int_{-\infty}^{+\infty} \mathfrak{R}_T(t) \, dt = 1 \quad (3.105)$$

²⁹Four dots will be used in the notation if the expression to be averaged were long and could not be adequately spanned by three dots, e.g. $\psi\phi$ or $\partial_i\psi$.

³⁰The normalised boxcar is a particular case of the **general boxcar function** $\mathfrak{R}(t; a, b)$, $a \leq b$, given by

$$\mathfrak{R}(t; a, b) := \begin{cases} 0 & \text{if } t < a \\ \frac{1}{2} & \text{if } t = a \\ 1 & \text{if } a < t < b \\ \frac{1}{2} & \text{if } t = b \\ 0 & \text{if } t > b \end{cases} \quad (3.101)$$

which takes the particular form

$$\mathfrak{R}_T(t) = \frac{1}{T} \mathfrak{R}(t; -\frac{T}{2}, \frac{T}{2}) \quad (3.102)$$

The general boxcar function verifies

$$\mathfrak{R}(t; a, b) = H(t - a) - H(t - b) \quad (3.103)$$

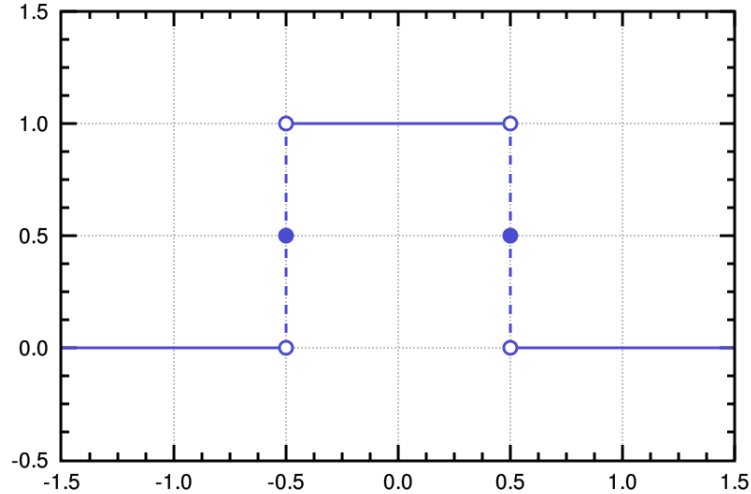


Figure 3.2: Rect function or normalised boxcar of width $T = 1$, $\mathfrak{R}_1(t)$

The main advantage of this formulation is that one can consider the moving average as a filter (actually a low-pass filter) executed on the original field ψ , by means of the convolution (see page 102). This concept of filter will be dealt with later in this section.

The moving averaging/filtering on a field ψ could also be applied to space variables \mathbf{x} by means of a rect function $\mathfrak{R}_L(\mathbf{x})$ of width L , of like definition (see equation (3.253) for a full description)

$$\mathfrak{R}_L(\mathbf{x}) = \begin{cases} 0 & \text{if } |x_i| > L/2 \\ \frac{1}{8L^3} & \text{if } |x_i| = L/2 \\ \frac{1}{L^3} & \text{if } |x_i| < L/2 \end{cases} \quad (i = 1, 2, 3) \quad (3.106)$$

The moving average is commonly used in practice for experimental data, because most instruments perform by construction some degree of integration.

The proper mathematical formalism to work with filters is the Fourier transform, since it is in the frequency domain where the filtering is best understood. Herein the following normalisation for the Fourier transform will be used:

$$\mathcal{F}(\psi) \equiv \hat{\psi}(\omega) = \int_{-\infty}^{+\infty} \psi(t) e^{-i\omega t} dt \quad (3.107)$$

and its inverse

$$\mathcal{F}^{-1}(\hat{\psi}) \equiv \psi(t) = \frac{1}{2\pi} \int_{-\infty}^{+\infty} \hat{\psi}(\omega) e^{i\omega t} d\omega \quad (3.108)$$

with $H(t)$ the **Heaviside step function** given by

$$H(t) = \begin{cases} 0 & \text{if } t < 0 \\ \frac{1}{2} & \text{if } t = 0 \\ 1 & \text{if } t > 0 \end{cases} \quad (3.104)$$

with ω the angular frequency ³¹

$$\omega = \frac{2\pi}{\tau} \quad (3.109)$$

and τ the period of the harmonic ³².

In Fourier transform formalism the equation (3.99) for moving average of ψ is called the **convolution** \star of the functions $\psi(t, \mathbf{x})$ and $\mathfrak{R}_T(t)$.

$$\langle \psi(t, \mathbf{x}) \rangle_T = \psi(t, \mathbf{x}) \star \mathfrak{R}_T(t) \equiv \int_{-\infty}^{+\infty} \psi(\tau, \mathbf{x}) \mathfrak{R}_T(t - \tau) d\tau \quad (3.110)$$

The Fourier transform of the convolution of two functions is the product of the Fourier transforms of convolved functions:

$$\mathcal{F}(\psi \star \mathfrak{R}_T) \equiv \mathcal{F} \left(\int_{-\infty}^{+\infty} \psi(\tau, \mathbf{x}) \mathfrak{R}_T(t - \tau) d\tau \right) \equiv \langle \widehat{\psi} \rangle_T = \widehat{\psi}(\omega, \mathbf{x}) \widehat{\mathfrak{R}}_T \quad (3.111)$$

The Fourier transform of the rect function $\mathfrak{R}_T(t)$ is the well known $\text{sinc}(\omega T)$ function (see figure 3.3)

$$\widehat{\mathfrak{R}}_T(\omega) = \text{sinc}(\omega T) := \frac{\sin(\omega T/2)}{\omega T/2} \quad (3.112)$$

■

³¹Along sections 3.2.2 to 3.3, ω will be used to appoint the angular frequency $2\pi/T$, as it is customary in Fourier analysis, instead of the specific dissipation rate of the turbulence kinetic energy, which is the designation for ω in the rest of the Dissertation

³²Two other normalisations are also commonly used to define the Fourier transform. The first one introduces a 2π factor in the exponential and uses a variable $\nu = 1/t$ for the direct transform

$$\mathcal{F}(\psi) \equiv \widehat{\psi}(\nu) = \int_{-\infty}^{+\infty} \psi(t) e^{-i2\pi\nu t} dt$$

with inverse transform

$$\mathcal{F}^{-1}(\widehat{\psi}) \equiv \psi(t) = \int_{-\infty}^{+\infty} \widehat{\psi}(\nu) e^{i2\pi\nu t} d\nu$$

whereas the second normalisation uses as variable $\omega = 2\pi\nu$ and treats symmetrically the direct and inverse transform with a factor $(2\pi)^{1/2}$:

$$\mathcal{F}(\psi) \equiv \widehat{\psi}(\omega) = \frac{1}{\sqrt{2\pi}} \int_{-\infty}^{+\infty} \psi(t) e^{-i\omega t} dt$$

and the inverse

$$\mathcal{F}^{-1}(\widehat{\psi}) \equiv \psi(t) = \frac{1}{\sqrt{2\pi}} \int_{-\infty}^{+\infty} \widehat{\psi}(\omega) e^{i\omega t} d\omega$$

The first normalisation has the advantage that $\mathcal{F}^{-1}[\mathcal{F}(\psi(t))] \equiv \mathcal{F}^{-1}(\widehat{\psi}(\omega)) = \psi(t)$, while in the normalisation (3.107) adopted herein $\mathcal{F}^{-1}[\widehat{\psi}(\omega/2\pi)] = \psi(t)$.

It is also frequent to see the definition of Fourier transform with a change of sign in the exponentials.

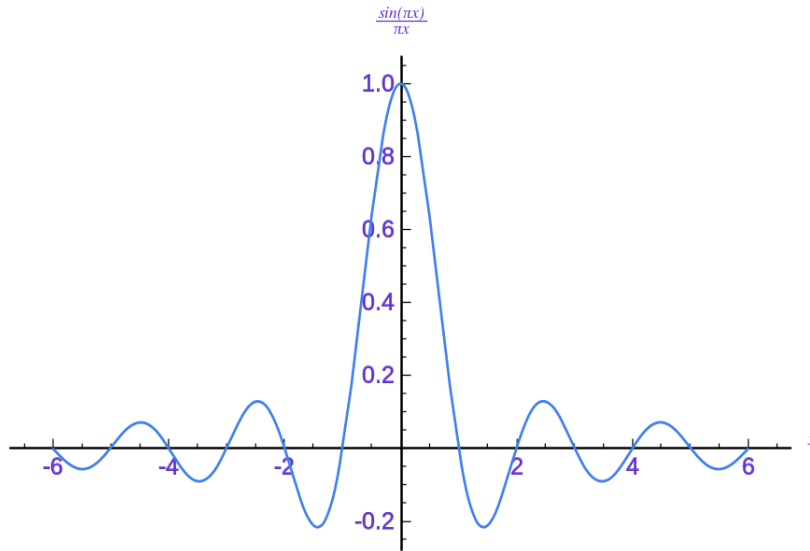


Figure 3.3: Fourier transform of rect function of width $T = 1$, $\text{sinc}(\omega) = \widehat{\mathfrak{R}}_1(\omega)$.

Having introduced the moving average of width T and the cumulative average of a field $\psi(t, \mathbf{x})$, it is pertinent to consider whether such averages are suitable to derive RANSE from, that is, if they fulfil the Reynolds conditions (3.4)-(3.9). From their definitions, it is clear that $\langle \psi(t, \mathbf{x}) \rangle_T$ and $\dot{\psi}(t, \mathbf{x})$ are in general functions of (t, \mathbf{x}) . Therefore, it would not be expected for these averages to fulfil the Reynolds conditions and, in principle, should not be used to derive RANSE from the Navier-Stokes equations. This last statement can be easily proven for both averages:

MOVING AVERAGE OF WIDTH T , $\langle \psi(t, \mathbf{x}) \rangle_T$

- LINEAR CONDITION. It is obvious because the integral is a linear operator.
- COMMUTATION CONDITION. For the $\partial_i \equiv \frac{\partial}{\partial x_i}$ derivative it follows:

$$\langle \partial_i \psi(t, \mathbf{x}) \rangle_T \equiv \frac{1}{T} \int_{t-T}^t \partial_i \psi(\tau, \mathbf{x}) d\tau \quad (3.113)$$

and

$$\partial_i \langle \psi(t, \mathbf{x}) \rangle_T \equiv \partial_i \left[\frac{1}{T} \int_{t-T}^t \psi(\tau, \mathbf{x}) d\tau \right] = \frac{1}{T} \int_{t-T}^t \partial_i \psi(\tau, \mathbf{x}) d\tau \quad (3.114)$$

in the last step use has been made of Leibniz's rule for differentiation under the integral sign. Therefore the moving average fulfils the commutation condition for ∂_i .

For $\partial_t = \frac{\partial}{\partial t}$ is equally obvious:

$$\langle \partial_t \psi(t, \mathbf{x}) \rangle_T \equiv \frac{1}{T} \int_{t-T}^t \partial_t \psi(\tau, \mathbf{x}) d\tau = \frac{1}{T} [\psi(t, \mathbf{x}) - \psi(t-T, \mathbf{x})] \quad (3.115)$$

and

$$\partial_t \langle \psi(t, \mathbf{x}) \rangle_T \equiv \partial_t \left[\frac{1}{T} \int_{t-T}^t \psi(\tau, \mathbf{x}) d\tau \right] = \frac{1}{T} [\psi(t, \mathbf{x}) - \psi(t-T, \mathbf{x})] \quad (3.116)$$

and therefore the commutation condition is also fulfilled for ∂_t .

- IDEMPOTENT CONDITION. It is best demonstrated through the use of convolution \star with the rect function $\mathfrak{R}_T(t)$.

$$\langle\langle\psi(t, \mathbf{x})\rangle\rangle_T = [\psi(t, \mathbf{x}) \star \mathfrak{R}_T(t)] \star \mathfrak{R}_T(t) \quad (3.117)$$

The convolution has the associative property (see [Bra00]):

$$[\psi(t, \mathbf{x}) \star \mathfrak{R}_T(t)] \star \mathfrak{R}_T(t) = \psi(t, \mathbf{x}) \star [\mathfrak{R}_T(t) \star \mathfrak{R}_T(t)]$$

The convolution of the general boxcar function (3.103) with itself verifies:

$$\begin{aligned} \mathfrak{R}(t; a, b) \star \mathfrak{R}(t; c, d) = & (t - a - c) H(t - a - c) - (t - b - c) H(t - b - c) - \\ & - (t - a - d) H(t - a - d) + (t - b - d) H(t - b - d) \end{aligned} \quad (3.118)$$

In the particular case of $a = c = -T/2$ and $b = d = T/2$, this results in (see equation (3.102))

$$\begin{aligned} \mathfrak{R}_T(t) \star \mathfrak{R}_T(t) &= \frac{1}{T^2} \mathfrak{R}(t; -T/2, T/2) \star \mathfrak{R}(t; -T/2, T/2) = \\ &= \frac{1}{T^2} [(t + T) H(t + T) - 2t H(t) + (t - T) H(t - T)] \end{aligned} \quad (3.119)$$

Figure 3.4 shows the convolution (3.119) of the normalised boxcar of width $T = 1$ with itself.

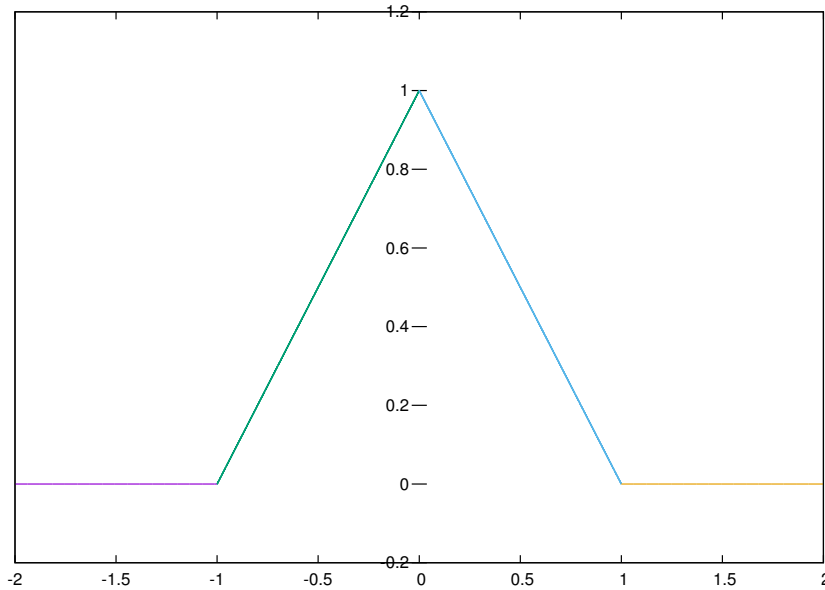


Figure 3.4: Convolution of rect function of width $T = 1$ with itself, $\mathfrak{R}_1(t) \star \mathfrak{R}_1(t)$.

The resulting triangular function is clearly different from the normalised boxcar itself, shown in figure 3.2. Both figures have an area below the curve equal to one, although the distribution of that area is different in each case. This difference disappears when $T \rightarrow \infty$, yielding the regular time average (3.59).

Substituting this result in equation (3.117) leads to

$$\langle\langle\psi(t, \mathbf{x})\rangle\rangle_T = \psi(t, \mathbf{x}) \star [\mathfrak{R}_T(t) \star \mathfrak{R}_T(t)] = \quad (3.120)$$

$$\begin{aligned}
&= \frac{1}{T^2} \int_{-\infty}^{+\infty} \psi(t - \tau, \mathbf{x}) [(t + T) H(t + T) - 2t H(t) + (t - T) H(t - T)] d\tau \neq \\
&\neq \frac{1}{T} \int_{-\infty}^{+\infty} \psi(t - \tau, \mathbf{x}) [H(t + T/2) - H(t - T/2)] d\tau = \int_{-\infty}^{+\infty} \psi(t - \tau, \mathbf{x}) \mathfrak{R}_T(\tau) d\tau = \langle \psi(t, \mathbf{x}) \rangle_T
\end{aligned}$$

where use has been made of (3.103) and the convolution's commutative property (see [Bra00]):

$$\psi(t, \mathbf{x}) \star \mathfrak{R}_T(t) \equiv \int_{-\infty}^{+\infty} \psi(\tau, \mathbf{x}) \mathfrak{R}_T(t - \tau) d\tau = \mathfrak{R}_T(t) \star \psi(t, \mathbf{x}) \equiv \int_{-\infty}^{+\infty} \psi(t - \tau, \mathbf{x}) \mathfrak{R}_T(\tau) d\tau$$

Therefore, the idempotent condition is not fulfilled and the moving average of width T is not a Reynolds operator, and then should not be used to derive RANSE from Navier-Stokes equations.

CUMULATIVE AVERAGE $\ddot{\psi}(t, \mathbf{x})$

- LINEAR CONDITION. Again, is obvious because the integral is a linear operator.
- COMMUTATION CONDITION. For the $\partial_i \equiv \frac{\partial}{\partial x_i}$ derivative it follows:

$$\partial_i \ddot{\psi}(t, \mathbf{x}) \equiv \frac{1}{t} \int_0^t \partial_i \psi(\tau, \mathbf{x}) d\tau = \frac{1}{t} \partial_i \int_0^t \psi(\tau, \mathbf{x}) d\tau = \partial_i \ddot{\psi}(t, \mathbf{x}) \quad (3.121)$$

where use has been made of Leibniz's rule for differentiation under the integral sign. Therefore, the cumulative average fulfils the commutation condition for ∂_i .

For $\partial_t = \frac{\partial}{\partial t}$ the result is completely different:

$$\partial_t \ddot{\psi}(t, \mathbf{x}) \equiv \frac{1}{t} \int_0^t \partial_t \psi(\tau, \mathbf{x}) d\tau = \frac{1}{t} [\psi(t, \mathbf{x}) - \psi(0, \mathbf{x})] \quad (3.122)$$

and

$$\partial_t \ddot{\psi}(t, \mathbf{x}) \equiv \partial_t \left[\frac{1}{t} \int_0^t \psi(\tau, \mathbf{x}) d\tau \right] = \frac{-1}{t^2} \int_0^t \psi(\tau, \mathbf{x}) d\tau + \frac{1}{t} [\psi(t, \mathbf{x}) - \psi(0, \mathbf{x})] \quad (3.123)$$

that is,

$$\partial_t \ddot{\psi}(t, \mathbf{x}) = \partial_t \ddot{\psi}(t, \mathbf{x}) + \frac{1}{t} \ddot{\psi}(t, \mathbf{x}) = \left(\partial_t + \frac{1}{t} \right) \ddot{\psi}(t, \mathbf{x}) \quad (3.124)$$

This is a major drawback for the cumulative average: it does not fulfil the commutation condition for ∂_t . Nevertheless, for steady-state flow situations the commutation condition with ∂_t is unnecessary. Note for t sufficiently large this commutation condition is met approximately, since $\ddot{\psi}(t, \mathbf{x})$ is a bounded function.

- IDEMPOTENT CONDITION. In this case, it is more convenient to check the version (3.6) of the idempotent condition

$$\ddot{\psi} \phi(t, \mathbf{x}) = \frac{1}{t} \int_0^t d\tau \psi(\tau, \mathbf{x}) \ddot{\phi}(\tau, \mathbf{x}) = \frac{1}{t} \int_0^t \frac{d\tau}{\tau} \psi(\tau, \mathbf{x}) \int_0^\tau d\sigma \phi(\sigma, \mathbf{x}) \quad (3.125)$$

This double integral must be equal to $\ddot{\psi}(t, \mathbf{x})\ddot{\phi}(t, \mathbf{x})$ in order for the idempotent condition to be true. Let's evaluate the following differential (the \mathbf{x} dependence is omitted for brevity):

$$\begin{aligned} d \left[\int_0^\tau d\sigma \psi(\sigma) \cdot \frac{1}{\tau} \int_0^\tau d\sigma \phi(\sigma) \right] &= d\tau \psi(\tau) \cdot \frac{1}{\tau} \int_0^\tau d\sigma \phi(\sigma) + \int_0^\tau d\sigma \psi(\sigma) \cdot d \left[\frac{1}{\tau} \int_0^\tau d\sigma \phi(\sigma) \right] = \\ &= \frac{d\tau}{\tau} \psi(\tau) \int_0^\tau d\sigma \phi(\sigma) + \frac{d\tau}{\tau} \phi(\tau) \int_0^\tau d\sigma \psi(\sigma) - \frac{d\tau}{\tau^2} \int_0^\tau d\sigma \psi(\sigma) \int_0^\tau d\varsigma \phi(\varsigma) \end{aligned} \quad (3.126)$$

Integrate now respect to τ from 0 to t ³³

$$\begin{aligned} \int_0^t d \left[\int_0^\tau d\sigma \psi(\sigma) \cdot \frac{1}{\tau} \int_0^\tau d\sigma \phi(\sigma) \right] &= \int_0^t d\sigma \psi(\sigma) \cdot \frac{1}{t} \int_0^t d\sigma \phi(\sigma) = \\ &= \int_0^t \frac{d\tau}{\tau} \psi(\tau) \int_0^\tau d\sigma \phi(\sigma) + \int_0^t \frac{d\tau}{\tau} \phi(\tau) \int_0^\tau d\sigma \psi(\sigma) - \int_0^t \frac{d\tau}{\tau^2} \int_0^\tau d\sigma \psi(\sigma) \int_0^\tau d\varsigma \phi(\varsigma) \end{aligned} \quad (3.127)$$

Divide this expression by t and it turns into the following identity:

$$\ddot{\psi}(t, \mathbf{x})\ddot{\phi}(t, \mathbf{x}) = \ddot{\psi}\ddot{\phi}(t, \mathbf{x}) + \ddot{\phi}\ddot{\psi}(t, \mathbf{x}) - \ddot{\psi}\ddot{\phi}(t, \mathbf{x})$$

or, grouping terms:

$$\ddot{\psi}(t, \mathbf{x})\ddot{\phi}(t, \mathbf{x}) + \ddot{\psi}\ddot{\phi}(t, \mathbf{x}) = \ddot{\psi}\ddot{\phi}(t, \mathbf{x}) + \ddot{\phi}\ddot{\psi}(t, \mathbf{x}) \quad (3.128)$$

This result is not the idempotent condition, which should read

$$\ddot{\psi}\ddot{\phi}(t, \mathbf{x}) = \ddot{\psi}(t, \mathbf{x})\ddot{\phi}(t, \mathbf{x})$$

Therefore, the cumulative average does not fulfil the idempotent condition, and it is an averaging method that cannot be used to derive RANSE from Navier-Stokes equations.

Note that if $t \rightarrow \infty$ then $\ddot{\psi}$ becomes time-independent (just as the regular time average $\overline{\psi}$) and can exit the integral which defines the cumulative average. In that limiting case the equation (3.128) yields:

$$2\ddot{\psi}\ddot{\phi} = 2\ddot{\psi}\ddot{\phi}$$

which is the expected idempotent condition. ■

It has been mentioned, while introducing the convolution with the normalised boxcar function, that the moving average might behave like a low-pass filter. The moving average is indeed a true low-pass filter, which respects the lower frequency content of the signal, and attenuates the higher frequency spectrum. In order to proof this assertion, the following properties of Fourier transform are needed (see [Bra00]):

³³For $t \rightarrow 0$ the expression

$$\int_0^t d\sigma \psi(\sigma) \cdot \frac{1}{t} \int_0^t d\sigma \phi(\sigma)$$

is zero because $\ddot{\phi}(t) \equiv \frac{1}{t} \int_0^t d\sigma \phi(\sigma)$ is a bounded function $\forall t \in \mathbb{R}^+$.

- Linearity

$$\mathcal{F}[a\psi + b\phi] = a\hat{\psi} + b\hat{\phi} \quad a, b \in \mathbb{C} \quad (3.129)$$

- Time shift

$$\mathcal{F}[\psi(t \pm T)] = \hat{\psi}(\omega)e^{\pm i\omega T} \quad (3.130)$$

- Time integration

$$\mathcal{F}\left[\int_{-\infty}^t \psi(\tau) d\tau\right] = \frac{\hat{\psi}(\omega)}{i\omega} + \pi\hat{\psi}(\omega)\delta(\omega) \quad (3.131)$$

where $\delta(\omega)$ is the Dirac's delta distribution³⁴.

Let $\psi(t)$ be a function of time, the ψ dependence on \mathbf{x} be momentarily forgotten. It is required that the Fourier transform of ψ exists, that is, ψ fulfils the condition³⁵

$$\int_{-\infty}^{+\infty} |\psi(t)| dt < \infty \quad (3.132)$$

The condition (3.132) implies that $|\psi(t)| \rightarrow 0$ sufficiently rapid as $t \rightarrow \pm\infty$. From equations (3.129) to (3.132), it can be deduced that the Fourier transform of the moving average results in:

$$\begin{aligned} \mathcal{F}[\langle\psi(t)\rangle_T] &\equiv \mathcal{F}\left[\frac{1}{T}\int_{t-T}^t \psi(\tau) d\tau\right] = \frac{1}{T}\mathcal{F}\left[\int_{-\infty}^t \psi(\tau) d\tau - \int_{-\infty}^{t-T} \psi(\tau) d\tau\right] = \\ &= \frac{1}{T}\mathcal{F}\left[\int_{-\infty}^t \psi(\tau) d\tau\right](1 - e^{-i\omega T}) = \frac{1 - e^{-i\omega T}}{T}\left(\frac{\hat{\psi}(\omega)}{i\omega} + \pi\hat{\psi}(0)\delta(\omega)\right) \end{aligned}$$

that is,

$$\mathcal{F}[\langle\psi(t)\rangle_T] = \frac{1 - e^{-i\omega T}}{T}\left(\frac{\hat{\psi}(\omega)}{i\omega} + \pi\hat{\psi}(0)\delta(\omega)\right) \quad (3.133)$$

The second term $\pi\hat{\psi}(0)\delta(\omega)$ only plays a role at $\omega \rightarrow 0$. It could be omitted outside of this range. Note the existence of the inverse Fourier transform also implies a condition symmetrical to (3.132),

$$\int_{-\infty}^{+\infty} |\hat{\psi}(\omega)| d\omega < \infty \quad (3.134)$$

so that $|\hat{\psi}(\omega)| \rightarrow 0$ sufficiently rapid as $\omega \rightarrow \pm\infty$.

³⁴Due to the properties of Dirac's delta, one could equally well write $\pi\hat{\psi}(0)\delta(\omega)$ for the second term of equation (3.131).

³⁵A function $\psi(t) : \mathbb{R} \rightarrow \mathbb{R}$, defined in all \mathbb{R} , is said to be of class $L^p(\mathbb{R})$, $1 \leq p < \infty$, if

$$\int_{-\infty}^{+\infty} |\psi(t)|^p dt < \infty$$

The Fourier transform of a function $\psi(t)$ exists as long as $\psi \in L^1(\mathbb{R})$.

Now making use of Euler's formula

$$e^{-it} = \cos t - i \sin t$$

and McLaurin's series for cos and sin,

$$\cos t = 1 - \frac{t^2}{2!} + \frac{t^4}{4!} - \dots \quad ; \quad \sin t = t - \frac{t^3}{3!} + \frac{t^5}{5!} - \dots$$

the expression (3.133) could be written as:

$$\begin{aligned} \mathcal{F} [\langle \psi(t) \rangle_T] &\approx \frac{i\omega T + \mathcal{O}(\omega^2)}{T} \left(\frac{\hat{\psi}(\omega)}{i\omega} + \pi \hat{\psi}(0) \delta(\omega) \right) = \\ &= \hat{\psi}(\omega) + i\omega \pi \hat{\psi}(0) \delta(\omega) + \frac{1}{T} \left(\frac{\hat{\psi}(\omega)}{i\omega} + \pi \hat{\psi}(0) \delta(\omega) \right) \mathcal{O}(\omega^2) \end{aligned} \quad (3.135)$$

When $\omega \rightarrow 0$ the only term that survives is the first one $\hat{\psi}(\omega)$. Thus $\mathcal{F} [\langle \psi(t) \rangle_T] \rightarrow \hat{\psi}(0)$ with $\omega \rightarrow 0$. The Fourier transform of the moving average tends to $\hat{\psi}(0)$ when $\omega \rightarrow 0$, and to zero when $\omega \rightarrow \infty$, which is the expected behaviour of a low-pass filter. In other words, the moving average low-pass filter leaves mostly unchanged the lower part of the spectrum, while greatly attenuates the higher-frequency band.



This sort of finite time average, as it has already been proven, does not fulfil the idempotent condition, and thus it is not possible to obtain a proper RANSE therefrom. However, it would be interesting to explore under which conditions a finite time average would yield acceptable URANS simulations, if any. The following paragraphs aim to this purpose.

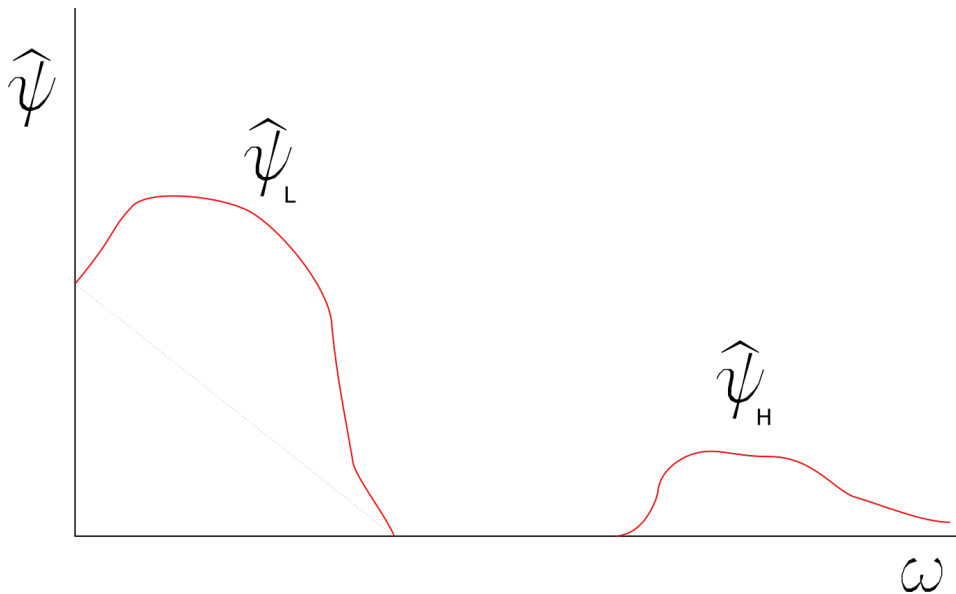


Figure 3.5: Spectrum of a flow which could be approximately modelled with URANS.

In principle, it would be feasible to approximately meet the idempotent condition if the field $\psi(t)$ would have a frequency spectrum $\hat{\psi}(\omega)$ similar to the one shown in figure 3.5 ³⁶. The spectrum has a high-

³⁶This type of frequency spectrum is not unknown in boundary layer meteorology, where it receives the name of *spectral gap problem*. See [Stu03].

amplitude lower-frequency band, then it is zero (or very close to zero) in the mid-frequency band, and finally it has a higher-frequency band starting with finite amplitude values that later continuously decrease to zero, as it is demanded by the $\hat{\psi}(\omega \rightarrow \infty) \rightarrow 0$ condition. Assume the mid-frequency band to be very wide, so that the lower- and higher-frequency bands be quite far apart. Let's call, somewhat artificially, $\hat{\psi}_L(\omega)$ to the lower portion of the spectrum and $\hat{\psi}_H(\omega)$ to the higher. Then, the following decomposition of $\hat{\psi}(\omega)$ is therefore possible:

$$\hat{\psi}(\omega) = \hat{\psi}_L(\omega) + \hat{\psi}_H(\omega)$$

The linear property of the Fourier transform implies then

$$\psi(t) = \psi_L(t) + \psi_H(t)$$

with $\psi_L = \mathcal{F}^{-1}[\hat{\psi}_L]$ and $\psi_H = \mathcal{F}^{-1}[\hat{\psi}_H]$.

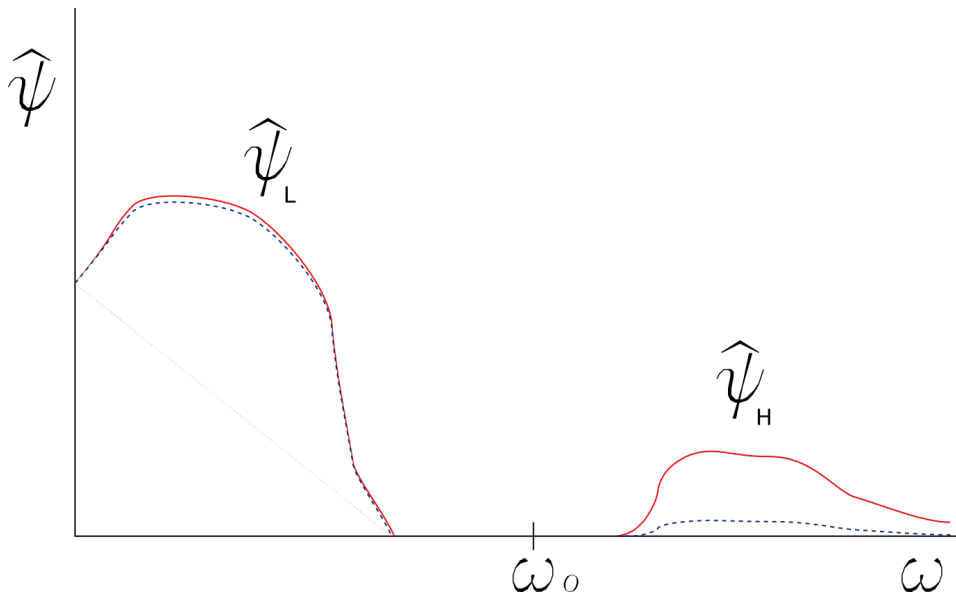


Figure 3.6: The moving average filter affects mostly the high-frequency part of the spectrum.

This decomposition makes possible the following procedure:

- Given a spectrum like the one shown in figure 3.5, with a wide mid-frequency range of zero amplitude, select a time interval T such that its associated angular frequency $\omega_0 = 2\pi/T$ lie approximately in the middle, far enough from both low- and high-frequency bands (see figure 3.6).
- With such time interval T generate a moving average of width T , equation (3.96), and the corresponding Fourier transform, low-pass filter equation (3.133).
- Apply equation (3.133) to both, $\hat{\psi}_L(\omega)$ and $\hat{\psi}_H(\omega)$. Since the lower-frequency band is sufficiently far from ω_0 , the effect of moving average on $\hat{\psi}_L(\omega)$ is not important. Let's see how this statement would be true. Equation (3.135) could be expanded with more detail, rejecting the terms with $\pi\hat{\psi}(0)\delta(\omega)$ because there is no need to consider $\omega = 0$, since it has already been proven that $\mathcal{F}[\langle\psi(t)\rangle_T] \rightarrow \hat{\psi}(0)$ with $\omega \rightarrow 0$. Therefore, the Fourier transform for $\omega \ll \omega_0$ results in ($\omega \neq 0$):

$$\mathcal{F}[\langle\psi(t)\rangle_T] = \hat{\psi}(\omega) \frac{1 - e^{-i\omega T}}{i\omega T} \approx \hat{\psi}(\omega) \left(1 + \frac{\omega T}{2i} - \frac{\omega^2 T^2}{3!} + \dots \right) \approx$$

$$\approx \hat{\psi}(\omega) + \hat{\psi}(\omega) \left(\frac{\pi}{i} \frac{\omega}{\omega_0} - \frac{2\pi^2}{3} \frac{\omega^2}{\omega_0^2} + \dots \right) \approx \hat{\psi}(\omega) + \hat{\psi}(\omega) \mathcal{O} \left(\frac{\omega}{\omega_0} \right) \quad (3.136)$$

As long as $\omega/\omega_0 \ll 1$ the dominant term is $\hat{\psi}(\omega)$. For example, if $\omega/\omega_0 = 0.001$ then the difference between $\mathcal{F} [\langle \psi(t) \rangle_T]$ and $\hat{\psi}(\omega)$ is around one thousandth. Note the use of McLaurin series is justified because ω is not too far from zero. Besides, for $\omega/\omega_0 < 1$, $\hat{\psi}(\omega) \approx \hat{\psi}_L(\omega)$, and the following very approximate result can be offered

$$\mathcal{F} [\langle \psi(t) \rangle_T] \approx \hat{\psi}_L(\omega)$$

which, upon Fourier inversion, means

$$\langle \psi(t) \rangle_T \approx \psi_L(t) \quad (3.137)$$

- Likewise, a parallel result is obtained for the higher-frequency portion of the spectrum. For $\omega/\omega_0 \gg 1$ the McLaurin series (3.136) cannot be used, and one must go back to the original equation (3.133) without the term $\pi \hat{\psi}(0) \delta(\omega)$, and perform an order of magnitude estimation. In these conditions, the factor $1 - e^{-\omega T}$ is of lesser importance because its modulus is order of one ($0 \leq |1 - e^{-\omega T}| \leq 2$). Thus, taking $1 - e^{-\omega T} \approx 1$, equation (3.133) yields:

$$\mathcal{F} [\langle \psi(t) \rangle_T] \approx \frac{\hat{\psi}(\omega)}{i\omega T} = \hat{\psi}(\omega) \frac{1}{2\pi i} \frac{\omega_0}{\omega} \approx \hat{\psi}_H(\omega) \frac{1}{2\pi i} \frac{\omega_0}{\omega} \sim \frac{\hat{\psi}_H(\omega)}{\omega}$$

because $\hat{\psi}(\omega) \approx \hat{\psi}_H(\omega)$ for $\omega/\omega_0 \gg 1$. The above expression is very small for large ω , and this effect is still enhanced because condition (3.134) implies that $\hat{\psi}(\omega)$ must decrease much faster than $1/\omega$, otherwise the integral extended from $-\infty$ to $+\infty$ would not converge. Therefore, through the combined effect of $\hat{\psi}(\omega \rightarrow \infty) \rightarrow 0$ and $\omega_0/\omega \rightarrow 0$, it can be concluded that

$$\omega/\omega_0 \gg 1 \quad \Rightarrow \quad \mathcal{F} [\langle \psi(t) \rangle_T] \approx \mathcal{F} [\langle \psi_H(t) \rangle_T] \approx 0$$

since for $\omega/\omega_0 > 1$, $\hat{\psi}(\omega) \approx \hat{\psi}_H(\omega)$, and the outcome can be written as

$$\langle \psi_H(t) \rangle_T \approx 0 \quad (3.138)$$

These results are graphically shown in figure 3.6. The blue dashed-line curve represents the finite time averaged spectrum $\mathcal{F} [\langle \psi(t) \rangle_T]$ of the red solid-line spectrum curve $\hat{\psi}(\omega)$. The moving average affects very little to $\hat{\psi}_L$, and very much to $\hat{\psi}_H$. As expected, the low-pass filter selects the low-frequency range of the flow's spectrum.

- The results $\langle \psi_L(t) \rangle_T \approx \psi_L(t)$ and $\langle \psi_H(t) \rangle_T \approx 0$ are almost identical to those one would expect from classical Reynolds decomposition. Therefore, calling $\Psi(t, \mathbf{x}) = \psi_L(t, \mathbf{x})$ the mean field component, and $\psi'(t, \mathbf{x}) = \psi_H(t, \mathbf{x})$ the fluctuating component, the familiar Reynolds decomposition is obtained

$$\psi(t, \mathbf{x}) = \Psi(t, \mathbf{x}) + \psi'(t, \mathbf{x}), \quad \langle \Psi(t, \mathbf{x}) \rangle_T \approx \Psi(t, \mathbf{x}), \quad \langle \psi'(t, \mathbf{x}) \rangle_T \approx 0 \quad (3.139)$$

and it will yield approximately exact RANSE of the form (3.40), suitable for URANS simulations. The time variation of the mean field $\Psi(t, \mathbf{x})$ will be rather slow, since it corresponds to the low-frequency spectrum assigned thereto.

The procedure just described fixes the limits within which URANS simulations based on finite time average could be safely executed. Any situation not similar to that shown in figure 3.6 could not be accurately (not even approximately) simulated with moving average-based URANS. Unfortunately, few of the many flows likely to be found in Engineering will present the required spectrum behaviour. ■

Once shown the approximate conditions a turbulent flow should meet in order to be properly described by URANS equations obtained through moving average, it is pertinent to question which would be the error committed in the Reynolds decomposition if a finite time average be used instead of a regular time average (3.59). This question has been answered by [MY71], [TL72] or [MS00]. In what follows, it will be assumed the turbulence is statistically stationary, so that the mean field $\langle \psi \rangle$ do not depend on time.

Let $\Psi(\mathbf{x}) \equiv \langle \psi \rangle$ be the ensemble average of the flow field $\psi(t, \mathbf{x})$, which is always an apt average for any situation, and $\psi'(t, \mathbf{x}) = \psi(t, \mathbf{x}) - \Psi(\mathbf{x})$ the fluctuating component of ψ à la ensemble average. Ψ is the standard whereby the accuracy of $\langle \psi(t, \mathbf{x}) \rangle_T$ is to be referenced and, in order to assess the error incurred upon using one instead of the other, it is convenient to determine the ensemble average of their difference, since this mean difference will be taken as a measure of such error. Before proceeding to the demonstration, two previous results should be clear:

$$\Psi(\mathbf{x}) = \frac{1}{T} \int_0^T \Psi(\mathbf{x}) dt = \frac{1}{T} \int_{-T}^0 \Psi(\mathbf{x}) dt$$

because $\Psi(\mathbf{x})$ does not depend on t , and

$$\langle \psi(t, \mathbf{x}) \rangle_T - \Psi(\mathbf{x}) = \frac{1}{T} \int_{-T}^0 [\psi(t + \tau, \mathbf{x}) - \Psi(\mathbf{x})] d\tau = \frac{1}{T} \int_{-T}^0 \psi'(t + \tau, \mathbf{x}) d\tau$$

with $\psi'(t + \tau, \mathbf{x})$ the fluctuating component à la ensemble average of $\psi(t, \mathbf{x})$ calculated at instant $t + \tau$.

Armed with those two intermediate results, the ensemble average of the squared difference between $\Psi(\mathbf{x})$ and $\langle \psi(t, \mathbf{x}) \rangle_T$, which is the best estimate of the error committed, is given by:

$$\begin{aligned} \langle [\langle \psi(t, \mathbf{x}) \rangle_T - \Psi(\mathbf{x})]^2 \rangle &= \frac{1}{T^2} \left\langle \left[\int_{-T}^0 [\psi(t + \tau, \mathbf{x}) - \Psi(\mathbf{x})] d\tau \right]^2 \right\rangle = \\ &= \frac{1}{T^2} \left\langle \int_{-T}^0 \int_{-T}^0 [\psi(t + \tau, \mathbf{x}) - \Psi(\mathbf{x})][\psi(t + \sigma, \mathbf{x}) - \Psi(\mathbf{x})] d\tau d\sigma \right\rangle = \\ &= \frac{1}{T^2} \left\langle \int_{-T}^0 \int_{-T}^0 \psi'(t + \tau, \mathbf{x}) \psi'(t + \sigma, \mathbf{x}) d\tau d\sigma \right\rangle = \frac{1}{T^2} \int_{-T}^0 \int_{-T-\tau}^{-\tau} \langle \psi'(t + \tau, \mathbf{x}) \psi'(t + \tau + \alpha, \mathbf{x}) \rangle d\alpha d\tau \end{aligned} \quad (3.140)$$

where the change of variables $\alpha = \sigma - \tau$ has been made. Note that, whatever the value of $t + \tau$, the expression $\langle \psi'(t + \tau, \mathbf{x}) \psi'(t + \tau + \alpha, \mathbf{x}) \rangle$ is the autocorrelation à la ensemble average of $\psi'(t, \mathbf{x})$ respect to time, $\mathcal{R}_\psi(\alpha, \mathbf{x})$, defined generically by³⁷

$$\mathcal{R}_\psi(\tau, \mathbf{x}) := \langle \psi'(t + \tau, \mathbf{x}) \psi'(t, \mathbf{x}) \rangle \quad (3.141)$$

³⁷There exists a similar autocorrelation function for each averaging method discussed in this Chapter. Of course, the resulting function depends on the type of average and, in general, will be different for each one. The ensemble average autocorrelation is always the most physically accurate for any situation.

Since the turbulence has been assumed statistically stationary, the autocorrelation in time $\mathcal{R}_\psi(\tau, \mathbf{x})$ depends only upon the time difference between both instances of ψ' . It has the property

$$\mathcal{R}_\psi(\tau, \mathbf{x}) = \mathcal{R}_\psi(-\tau, \mathbf{x})$$

Whatever the field ψ , for each \mathbf{x} the autocorrelation $\mathcal{R}_\psi(\tau, \mathbf{x})$ has a maximum at $\tau = 0$

$$\mathcal{R}_\psi(\tau, \mathbf{x}) \leq \mathcal{R}_\psi(0, \mathbf{x})$$

and the following quantity has dimensions of time:

$$\mathfrak{T}_\psi(\mathbf{x}) := \frac{1}{\mathcal{R}_\psi(0, \mathbf{x})} \int_0^\infty \mathcal{R}_\psi(\tau, \mathbf{x}) \, d\tau \quad (3.142)$$

$\mathfrak{T}_\psi(\mathbf{x})$ is time-independent and represents the **correlation time** of the statistically stationary field $\psi(t, \mathbf{x})$. The correlation time marks approximately the frontier wherefrom the field ψ' begins not to correlate with itself or, in other words, $\mathcal{R}_\psi(\mathfrak{T}_\psi(\mathbf{x}), \mathbf{x})$ is small (or rather, $\mathcal{R}_\psi(\mathfrak{T}_\psi(\mathbf{x}), \mathbf{x})/\mathcal{R}_\psi(0, \mathbf{x}) \ll 1$). Note the correlation time can change from one point \mathbf{x} to another within the flow domain, unless the turbulence be also homogeneous and then \mathfrak{T}_ψ would also be space-independent.

In the particular case in which ψ is a component of the velocity field $u_i(t, \mathbf{x})$, then

$$\mathcal{R}_{ii}(\tau, \mathbf{x}) = \langle u'_i(t + \tau, \mathbf{x}) u'_i(t, \mathbf{x}) \rangle \quad (\text{no sum implied}) \quad (3.143)$$

and $\mathfrak{T}_i(\mathbf{x})$ is called the **integral time scale** of turbulence corresponding to direction i .

$$\mathfrak{T}_i(\mathbf{x}) = \frac{1}{\langle u'_i(t, \mathbf{x}) u'_i(t, \mathbf{x}) \rangle} \int_0^\infty \langle u'_i(t + \tau, \mathbf{x}) u'_i(t, \mathbf{x}) \rangle \, d\tau = \frac{1}{\mathcal{R}_{ii}(0, \mathbf{x})} \int_0^\infty \mathcal{R}_{ii}(\tau, \mathbf{x}) \, d\tau \quad (3.144)$$

For a scalar field there is just one integral time scale, whereas for a vector field there are three integral time scales, one for each direction. The integral time scale characterises the maximum time over which the fluctuating component of velocity retains some significant correlation with itself.

The integral time scale is closely related to the **integral length scale** $\mathfrak{L}_i(t)$ of homogeneous turbulence³⁸. The integral in α of equation (3.140) is smaller or equal than the integral defining the correlation time

$$\int_{-T}^{-T-\tau} \langle \psi'(t + \tau, \mathbf{x}) \psi'(t + \tau + \alpha, \mathbf{x}) \rangle \, d\alpha \leq \int_0^\infty \mathcal{R}_\psi(\alpha, \mathbf{x}) \, d\alpha = \mathfrak{T}_\psi(\mathbf{x}) \mathcal{R}_\psi(0, \mathbf{x})$$

³⁸The integral length scale is similarly defined (see [Pop00]). Assume the turbulence be statistically homogeneous, that is,

$$u_i(t, \mathbf{x}) = \langle u_i \rangle + u'_i(t, \mathbf{x}) \equiv U_i(t) + u'_i(t, \mathbf{x}) \quad (3.145)$$

for the velocity field $u_i(t, \mathbf{x})$, with $\langle u_i \rangle$ the ensemble average. Let the autocorrelation of u'_i for the homogeneous flow be defined by

$$\mathcal{R}_{ii}(t, \mathbf{r}) := \langle u'_i(t, \mathbf{x} + \mathbf{r}) u'_i(t, \mathbf{x}) \rangle \quad (\text{no sum implied}) \quad (3.146)$$

From this definition it is possible to obtain several integral length scales, depending upon the component u'_i of the fluctuating velocity field, and the direction $\hat{\mathbf{e}}_j$ in which that length scale is considered, being $\hat{\mathbf{e}}_j$ the unit vector along the j^{th} axis ($u_j = \mathbf{u} \cdot \hat{\mathbf{e}}_j$). For example, the integral length scale for u_i along the j^{th} direction is given by:

$$\mathfrak{L}_i(t, \hat{\mathbf{e}}_j) := \frac{1}{\mathcal{R}_{ii}(t, \mathbf{0})} \int_0^\infty \mathcal{R}_{ii}(t, r \hat{\mathbf{e}}_j) \, dr \quad (3.147)$$

Therefore, the ensemble average of the squared difference between $\Psi(\mathbf{x})$ and $\langle \psi(t, \mathbf{x}) \rangle_T$ satisfies

$$\langle [\langle \psi(t, \mathbf{x}) \rangle_T - \Psi(\mathbf{x})]^2 \rangle \leq \frac{1}{T^2} \int_{-T}^0 \mathfrak{T}_\psi(\mathbf{x}) \mathcal{R}_\psi(0, \mathbf{x}) \, d\tau \quad (3.149)$$

Since the product $\mathfrak{T}_\psi(\mathbf{x}) \mathcal{R}_\psi(0, \mathbf{x})$ does not depend on time, it exits the integral sign and the remaining integral is equal to T , and the following result holds ³⁹:

$$\langle [\langle \psi(t, \mathbf{x}) \rangle_T - \Psi(\mathbf{x})]^2 \rangle \leq \frac{\mathfrak{T}_\psi(\mathbf{x})}{T} \mathcal{R}_\psi(0, \mathbf{x}) \quad (3.151)$$

Equation (3.151) proves that the necessary and sufficient condition for the finite time average $\langle \psi(t, \mathbf{x}) \rangle_T$ to converge to the ensemble average $\Psi(\mathbf{x})$, is that

$$\lim_{T \rightarrow \infty} \frac{1}{T} \int_0^T \mathcal{R}_\psi(\tau, \mathbf{x}) \, d\tau = \lim_{T \rightarrow \infty} \frac{1}{T} \int_0^T \langle \psi'(t + \tau, \mathbf{x}) \psi'(t, \mathbf{x}) \rangle \, d\tau = 0 \quad (3.152)$$

The integral length scale depends on t but it is independent of position for homogeneous turbulence. The set of length scales \mathfrak{L}_i characterises the size of the most energetic eddies existing in the flow. The two other important length scales in turbulence are the Kolmogorov length scale η and the Taylor length scale λ_t , given respectively by

$$\eta = \left(\frac{\nu^3}{\epsilon} \right)^{\frac{1}{4}} \quad \text{and} \quad \lambda_t \approx \sqrt{15 \frac{\nu k}{\epsilon}}$$

with k the turbulence kinetic energy per unit mass and ϵ the turbulent energy dissipation rate per unit mass. Taylor length scale characterises the size of eddies which are significantly affected by the viscous forces, whereas Kolmogorov length scale corresponds to those eddies that directly dissipate into heat (thermal dissipation range). In the \mathfrak{L}_i range only inertial effects are important for turbulence. In the Taylor λ_t range any fluctuating velocity component is strongly correlated with itself. The three length scales satisfy

$$\eta \ll \lambda_t \ll \mathfrak{L}_i$$

Calling (for convenience subscript i is omitted)

$$Re_{\mathfrak{L}} = \frac{\mathfrak{L} \sqrt{k}}{\nu} \approx \frac{k^2}{\epsilon \nu}$$

then the relationship among turbulence length scales is given by

$$\frac{\lambda_t}{\mathfrak{L}} = \sqrt{\frac{10}{Re_{\mathfrak{L}}}} \quad , \quad \frac{\eta}{\mathfrak{L}} = Re_{\mathfrak{L}}^{-\frac{3}{4}} \quad . \quad \lambda_t = \sqrt{10} \eta^{\frac{2}{3}} \mathfrak{L}^{\frac{1}{3}} \quad (3.148)$$

³⁹This inequality turns into an equality upon observing that

$$\frac{1}{T^2} \int_{-T}^0 \int_{-T-\tau}^{-\tau} \langle \psi'(t + \tau, \mathbf{x}) \psi'(t + \tau + \alpha, \mathbf{x}) \rangle \, d\alpha \, d\tau = \frac{1}{T^2} \int_{-T}^0 \int_{-T}^0 \mathcal{R}_\psi(\sigma - \tau, \mathbf{x}) \, d\sigma \, d\tau$$

because \mathcal{R}_ψ depends only on the time difference and $\mathcal{R}_\psi(\tau) = \mathcal{R}_\psi(-\tau)$, and then

$$\langle [\langle \psi(t, \mathbf{x}) \rangle_T - \Psi(\mathbf{x})]^2 \rangle = \frac{1}{T^2} \int_{-T}^0 \int_{-T}^0 \mathcal{R}_\psi(\sigma - \tau, \mathbf{x}) \, d\sigma \, d\tau \quad (3.150)$$

The error tends to zero for $T \rightarrow \infty$, since the integral of $\mathcal{R}_\psi(\sigma - \tau, \mathbf{x})$ always converges for actual turbulent flows.

As $\mathcal{R}_\psi(0, \mathbf{x})$ is a bounded field (and usually not too large) for actual turbulent flows, then the error incurred by using finite time average instead of regular time average (3.59) is small, as long as T be much larger than correlation time \mathfrak{T}_ψ ($T \gg \mathfrak{T}_\psi$). To be exact, the requirement is to take T such that

$$\frac{\mathfrak{T}_\psi(\mathbf{x})}{T} \mathcal{R}_\psi(0, \mathbf{x}) \leq \delta^2 \quad (3.153)$$

being δ the maximum admissible error in the moving average of ψ with respect to the time average $\Psi = \overline{\psi}$. Note that δ has dimensions of ψ . ■

The expression (3.151) provides a practical limit for the use of URANS simulations based on moving time averages, from which some CFD practitioners could very well profit. If ψ were a velocity component u_i , then $\mathcal{R}_{ii}(0, \mathbf{x})$ (no sum implied) would be proportional to the squared turbulence intensity I_i^2 along the i^{th} direction. In the case of homogeneous isotropic turbulence $\mathcal{R}_{ii}(\tau, \mathbf{r}) = \mathcal{R}_{jj}(\tau, \mathbf{r})$ (no sum implied), the integral time scale \mathfrak{T} could be estimated from the integral length scale \mathfrak{L} and the mean velocity U as⁴⁰

$$\mathfrak{T} \sim \frac{\mathfrak{L}}{U} \quad (3.154)$$

The integral length scale has usually a value similar to the geometric length scale of the turbulent flow. For instance, the geometric length scale for a pipe is conventionally taken as the diameter.

Thus, a convenient estimate for a suitable finite time T , to be used in moving average operations, could be obtained if the turbulent flow's geometric length scale L_G , mean velocity U , and turbulence intensity I were known, or could be guessed. This estimate is given by

$$\frac{L_G U}{T} I^2 \leq \delta^2 \quad (3.155)$$

with $I = \sqrt{\mathcal{R}}/U$ (see equation (4.22)) and δ measured in m/s . There exist rules of thumb for those quantities in most flows of interest for Engineering applications. Therefore, it should not be very difficult to obtain an estimate for T in most practical cases.

In summary, the use of finite time moving average in certain URANS simulations brings forward two different error types in the results obtained:

- i. Since the idempotent condition is not met, the RANSE could not be properly derived from Navier-Stokes equations, and an error is committed by forcing them into a CFD code.
- ii. The ergodic hypothesis ceases to be valid, even in the case of statistically stationary turbulent flow, and the comparison of the ensemble averaged CFD output results with the finite time averaged data is also subjected to errors.

By selecting T sufficiently large, those errors could be reduced to acceptable levels, although in such cases the field's dependence on t is much diminished, due to excessive time smoothing.

To end up with this section, it is worth remarking that similar results to the ones exposed herein would have been obtained upon substitution of *time-average* for *space-average*, and of *statistically stationary* for *statistically homogeneous* turbulence.

⁴⁰Actually, the general relationship calls for the use of the **convection velocity** U_c , which is the velocity demanded in Taylor's frozen turbulence hypothesis, in order to relate space and time scales for a turbulent flow. In most cases, the convection velocity U_c can be approximated by the mean velocity U , and this is the convention adopted herein (see [TYF07]).

3.2.3 A Light Critique to the Triple Decomposition

The triple decomposition of a turbulence field was first introduced in [HR70], and later expanded in the reference paper [RH72]. Since then, this technique has been employed by many authors, some very renowned, to deal with turbulence problems whose mean flow presents some sort of unsteadiness. The interested reader is also recommended to check the references [Tel81], [GHL96], [Spe87], [KCB⁺10] and [BK92]. Some extreme examples leading to "quadruple" decomposition can be found in [PMN08] and some references cited therein.

The original authors' intentions were '*...to extract an organised wave motion from a background field of finite turbulent fluctuation*'. In order to obtain such results, their approach was to decompose any turbulent flow field $\psi(t, \mathbf{x})$ in three terms, namely (in the notation followed herein)

$$\psi(t, \mathbf{x}) = \bar{\psi}(\mathbf{x}) + \tilde{\psi}(t, \mathbf{x}) + \psi'(t, \mathbf{x}) \quad (3.156)$$

where:

- $\bar{\psi}$ is the time average of field ψ defined by equation (3.59),
- $\tilde{\psi}$ is given by

$$\tilde{\psi}(t, \mathbf{x}) = \overleftarrow{\psi}(t, \mathbf{x}) - \bar{\psi}(\mathbf{x}) \quad (3.157)$$

with $\overleftarrow{\psi}$ the phase average defined by equation (3.82)⁴¹. The authors called $\tilde{\psi}$ '*the (statistical) contribution of the organized wave*' ([HR70]) or '*the periodic wave*' ([RH72]).

- ψ' is simply called '*the turbulence*' ([HR70]) or '*the turbulent motion*' ([RH72]). From equations (3.156) and (3.157) it is clear that

$$\psi'(t, \mathbf{x}) = \psi(t, \mathbf{x}) - \overleftarrow{\psi}(t, \mathbf{x}) \quad (3.158)$$

thus, ψ' can only be the fluctuating part of ψ à la phase average, that is, the fluctuating component that results upon applying the phase averaging method to the field ψ .

The triple decomposition thus presented is a sort of tautology of the phase average introduced in section 3.2.1.5, although written in a slightly different manner, with a third member that, supposedly, highlights the steady component of the turbulent flow.

[HR70]-[RH72] attach to the components of equation (3.156) a set of Reynolds-like conditions (see equations (3.4)-(3.7)), involving the four field types present in the triple decomposition: $\bar{\psi}$, $\tilde{\psi}$, $\overleftarrow{\psi}$ and ψ' . For the present discussion, the relevant conditions introduced in [HR70] and [RH72] are:

$$\overline{\psi'} = 0 \quad (3.159)$$

$$\overleftrightarrow{\psi} = \bar{\psi} \quad (3.160)$$

⁴¹Actually, [HR70] defines the phase average in equation (1.3) of their paper with the literal expression

$$\langle f(\mathbf{x}, t) \rangle = \lim_{N \rightarrow \infty} \frac{1}{N} \sum_{n=0}^N f(\mathbf{x}, t + n\tau)$$

but herein the symbol $\langle \cdot \rangle$ is reserved for the ensemble average, and the fact that the sum reaches up to N instead of $N - 1$ is unimportant.

From Navier-Stokes equation and that set of Reynolds-like conditions, [RH72] obtains the RANSE for the phase averaged velocity field

$$\partial_t \tilde{u}_i + \bar{u}_j \partial_j \bar{u}_i + \bar{u}_j \partial_j \tilde{u}_i + \tilde{u}_j \partial_j \bar{u}_i + \partial_j \overleftrightarrow{u'_i u'_j} + \partial_j (\tilde{u}_i \tilde{u}_j) = -\partial_i \bar{p} - \partial_i \tilde{p} + \frac{1}{Re} \left(\partial_j \partial_j \bar{u}_i + \partial_j \partial_j \tilde{u}_i \right) \quad (3.161)$$

and the RANSE for the time-averaged mean velocity field as:

$$\bar{u}_j \partial_j \bar{u}_i = -\partial_i \bar{p} + \frac{1}{Re} \partial_j \partial_j \bar{u}_i - \partial_j (\overline{u'_i u'_j}) - \partial_j (\overline{\tilde{u}_i \tilde{u}_j}) \quad (3.162)$$

and the RANSE for the 'organised wave':

$$\partial_t \tilde{u}_i + \bar{u}_j \partial_j \tilde{u}_i + \tilde{u}_j \partial_j \bar{u}_i = -\partial_i \tilde{p} + \frac{1}{Re} \partial_j \partial_j \tilde{u}_i + \partial_j (\overline{\tilde{u}_i \tilde{u}_j} - \tilde{u}_i \tilde{u}_i) - \partial_j (\overleftrightarrow{u'_i u'_j} - \overline{u'_i u'_j}) \quad (3.163)$$

Therefore, if conditions (3.159)-(3.160) were not correct or could not be satisfied, the derivation of equations (3.161)-(3.163) would also be incorrect, and the equations themselves would be lacking terms that would have been erroneously omitted.

As it has repeatedly been said along this Dissertation, the fluctuating component ψ' is as inherently linked to the averaging method as the mean component is. According to equation (3.158), ψ' is the fluctuating component corresponding to the phase average. It is not, it cannot be, the fluctuating component corresponding to the time average, or to any other averaging method. Thus only $\overleftrightarrow{\psi'} = 0$ is guaranteed, and there would be no reason to think this apply to any other averaging method, and in general the results would be $\langle \psi' \rangle \neq 0$, $\overline{\psi'} \neq 0$, $\widehat{\psi'} \neq 0 \dots$

In effect, by construction $\overleftrightarrow{\psi'}(t, \mathbf{x})$ is a T -periodic function of t . Therefore, it can be expressed as a Fourier series

$$\overleftrightarrow{\psi'}(t, \mathbf{x}) = a_0(\mathbf{x}) + \sum_{n=1}^{\infty} [a_n(\mathbf{x}) \cos n\omega t + b_n(\mathbf{x}) \sin n\omega t] \quad (3.164)$$

with a_0 , a_n and b_n functions of \mathbf{x} and $\omega = 2\pi/T$. The phase average $\overleftrightarrow{\psi'}(t, \mathbf{x})$ has a time average equal to a_0 (also called in Electric Engineering the **dc component**). The demonstration is straightforward:

$$\overleftrightarrow{\overline{\psi'}}(\mathbf{x}) = \lim_{\tau \rightarrow \infty} \frac{1}{\tau} \left\{ \int_0^{\tau} a_0(\mathbf{x}) dt + \sum_{n=1}^{\infty} \left[a_n(\mathbf{x}) \int_0^{\tau} \cos n\omega t dt + b_n(\mathbf{x}) \int_0^{\tau} \sin n\omega t dt \right] \right\} \quad (3.165)$$

The first term is clearly

$$\lim_{\tau \rightarrow \infty} \frac{1}{\tau} a_0(\mathbf{x}) \int_0^{\tau} dt = \lim_{\tau \rightarrow \infty} \frac{1}{\tau} a_0(\mathbf{x}) \tau = \lim_{\tau \rightarrow \infty} a_0(\mathbf{x}) = a_0(\mathbf{x})$$

The following improper integrals have no definite value:

$$\int_0^{\infty} \cos n\omega t dt \quad \int_0^{\infty} \sin n\omega t dt$$

Nevertheless, for any $n, m \in \mathbb{N}$ the following identities hold:

$$\int_0^{mT} \sin n\omega t dt = \int_0^{mT} \cos n\omega t dt = 0 \quad (3.166)$$

Any real number $\tau \in \mathbb{R}$ can be decomposed into an integer part $\lfloor \tau \rfloor \in \mathbb{Z}$ (floor function), and a fractional part $\{\tau\} \in \mathbb{R}$, $0 \leq \{\tau\} < 1$, resulting in $\tau = \lfloor \tau \rfloor + \{\tau\}$. Therefore, the following decomposition is always true

$$\tau = \lfloor \frac{\tau}{T} \rfloor T + \{\frac{\tau}{T}\} T \quad (3.167)$$

With this decomposition, the time average integral for cosine is:

$$\lim_{\tau \rightarrow \infty} \frac{1}{\tau} \int_0^{\tau} \cos n\omega t \, dt = \lim_{\tau \rightarrow \infty} \frac{1}{\tau} \left[\int_0^{\lfloor \frac{\tau}{T} \rfloor T} \cos n\omega t \, dt + \int_{\lfloor \frac{\tau}{T} \rfloor T}^{\lfloor \frac{\tau}{T} \rfloor T + \{\frac{\tau}{T}\} T} \cos n\omega t \, dt \right] \quad (3.168)$$

According to equation (3.166), the first integral in the right-hand side is identically zero, and the second integral is a finite number $B \in \mathbb{R}$. Therefore, the time average for cosine is zero:

$$\lim_{\tau \rightarrow \infty} \frac{1}{\tau} \int_0^{\tau} \cos n\omega t \, dt = \lim_{\tau \rightarrow \infty} \frac{B}{\tau} = 0 \quad (3.169)$$

Likewise, the time average for the sine integral is zero, and then it has been proven that

$$\overleftrightarrow{\psi}(\mathbf{x}) = a_0(\mathbf{x}) \quad (3.170)$$

Accordingly, the time average for the field $\psi(t, \mathbf{x})$ is

$$\overline{\psi}(\mathbf{x}) = \overleftrightarrow{\psi}(\mathbf{x}) + \overline{\psi'}(\mathbf{x}) = a_0(\mathbf{x}) + \overline{\psi'}(\mathbf{x}) \quad (3.171)$$

with $\overline{\psi'}(\mathbf{x}) \neq 0$ in general. The time average $\overline{\psi}$ of a turbulent flow field ψ is the dc component a_0 of the periodic field $\overleftrightarrow{\psi}$, plus something else⁴². Note the dc component of any field is also periodic: its value at t equals its value at $t + T$. It is only natural that this dc term be within the phase averaged component, although not all time average of the field need to be included in the dc component. Nevertheless, it would seem reasonable that actual physical fields would verify equations (3.159)-(3.160).

Therefore, equations (3.159)-(3.160) are to be taken with caution, and so happens with equations (3.161)-(3.163). This should come as no surprise after the derivation made in section 3.2.1.5 : once it has been proven that the triple decomposition is actually the phase average decomposition in disguise, the only RANSE that can be derived therefrom is (3.91).

Some examples presented next will attempt to highlight the assertions made herein.

EXAMPLE (i)

Let ψ be the following T -potentially periodic field, which could well be an actual physical field:

$$\psi(t, \mathbf{x}) = a_0(\mathbf{x}) + a_1(\mathbf{x}) \sin \omega t + a_2(\mathbf{x}) \sin \omega' t \quad (3.172)$$

where $\omega = 2\pi/T$ and $\omega' = 2\pi/T'$; T and T' are real numbers non-multiple of each other ($T/T' \notin \mathbb{Z}$ and $T'/T \notin \mathbb{Z}$); and a_0 , a_1 and a_2 are sufficiently smooth functions of $\mathbf{x} \in \Omega \subset \mathbb{R}^3$. Note that ψ is as well a T' -potentially periodic field.⁴³

The T -phase average of ψ is calculated term by term:

⁴²Note that a_0 is the dc component of the phase averaged field $\overleftrightarrow{\psi}$. It is not the dc component of the physical field ψ because ψ is not, in general, a periodic function of t . In this section, the term 'dc component' is always used to appoint the time average of a periodic function.

⁴³Similar results would be obtained using cosines instead of sines in (3.172), or any linear combination of sines and cosines. The key issue is to have T - and T' -periodic components within ψ .

- First term is trivial:

$$\overleftarrow{a_0(\mathbf{x})} = \lim_{N \rightarrow \infty} \frac{1}{N} \sum_{n=0}^{N-1} a_0(\mathbf{x}) = \lim_{N \rightarrow \infty} \frac{1}{N} a_0(\mathbf{x}) \sum_{n=0}^{N-1} 1 = a_0(\mathbf{x}) \frac{N}{N} = a_0(\mathbf{x})$$

because $a_0(\mathbf{x})$ is not affected by the summation index n .

- The second term is also trivial:

$$\overleftarrow{a_1(\mathbf{x}) \sin \omega t} = \lim_{N \rightarrow \infty} \frac{1}{N} \sum_{n=0}^{N-1} a_1(\mathbf{x}) \sin \omega(t + nT) = \lim_{N \rightarrow \infty} \frac{a_1(\mathbf{x})}{N} \sum_{n=0}^{N-1} \sin \omega t = a_1(\mathbf{x}) \sin \omega t$$

because $a_1(\mathbf{x})$ and $\sin \omega t$ are not affected by the summation index n and can exit the sum.

- The third term is more elaborated:

$$\overleftarrow{a_2(\mathbf{x}) \sin \omega' t} = \lim_{N \rightarrow \infty} \frac{1}{N} \sum_{n=0}^{N-1} a_2(\mathbf{x}) \sin \omega'(t + nT) = \lim_{N \rightarrow \infty} \frac{a_2(\mathbf{x})}{N} \sum_{n=0}^{N-1} \sin \left(\omega' t + 2\pi n \frac{T}{T'} \right)$$

[GR07] offers the following formula for a sum of sines:

$$\sum_{n=0}^{N-1} \sin(x + ny) = \frac{\sin(x + \frac{N-1}{2}y) \sin \frac{Ny}{2}}{\sin \frac{y}{2}} \quad (3.173)$$

With this formula, the third term's T -phase average results in

$$\overleftarrow{a_2(\mathbf{x}) \sin \omega' t} = \lim_{N \rightarrow \infty} \frac{a_0(\mathbf{x})}{N} \frac{\sin(\omega' t + (N-1)\pi \frac{T}{T'}) \sin N\pi \frac{T}{T'}}{\sin \pi \frac{T}{T'}} \quad (3.174)$$

For any $N \in \mathbb{N}$, $t \in \mathbb{R}$ the second numerator is a real number with an absolute value ≤ 1 , and the denominator is a finite non-zero real number, because T/T' is not an integer. Thus, the fraction in sines is a finite real number $B \in \mathbb{R}$, and the function a_0 is also bounded. Then

$$\overleftarrow{a_2(\mathbf{x}) \sin \omega' t} = \lim_{N \rightarrow \infty} \frac{Ba_0}{N} = 0 \quad (3.175)$$

and, by definition, the third term is the fluctuating component ψ' of ψ , because it yields zero under the operation of phase average.

Hence,

$$\overleftarrow{\psi}(t, \mathbf{x}) = a_0(\mathbf{x}) + a_1(\mathbf{x}) \sin \omega t \quad , \quad \psi'(t, \mathbf{x}) = a_2(\mathbf{x}) \sin \omega' t$$

By the way, ψ' is a T' -periodic function, although it cannot be a T -periodic one.

Calculating now the time average of ψ according to equation (3.59), the following obvious result is obtained:

$$\overline{\psi} = \overleftarrow{\psi} = a_0, \quad \overline{\psi'} = 0$$

Thus, the field (3.172) is hardly a counter-example to highlight the assertions made herein. For this kind of regular functions, like sines and cosines, the assumptions made in [HR70] and [RH72] are correct. Figure 3.7 shows an instance of field (3.172). The fluctuating component ψ' has both averages, phase and time, equal to zero. ■

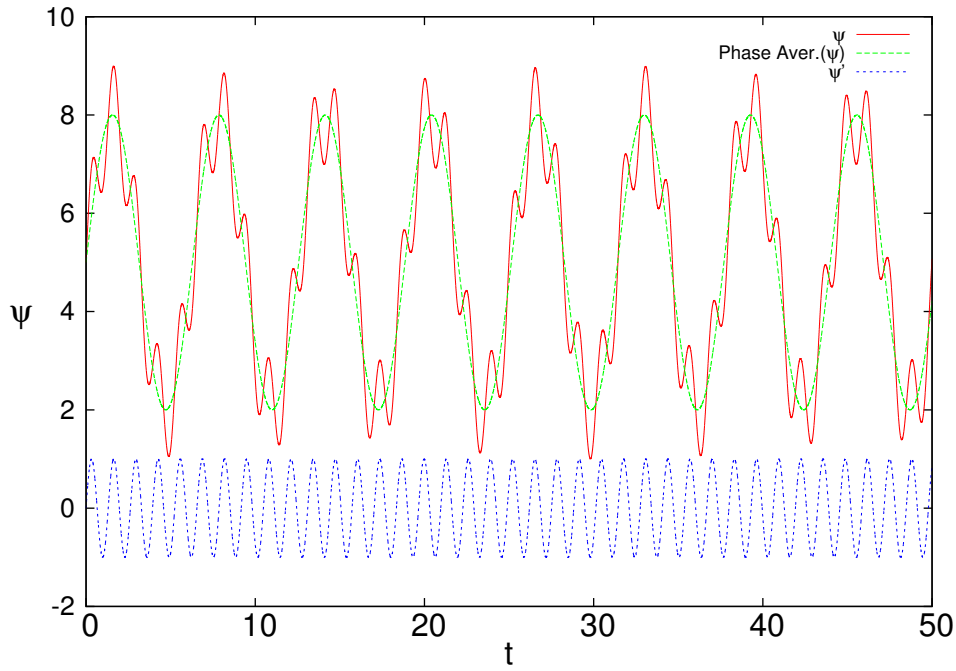


Figure 3.7: Decomposition of field $\psi = 5 + 3 \sin t + \sin(\sqrt{23} t)$.

EXAMPLE (ii)

Now a damped version of the example (3.172) will be presented herein. Let ψ be the following T' -potentially periodic field, which could also be an actual physical field:

$$\psi(t, \mathbf{x}) = a_0(\mathbf{x}) + a_1(\mathbf{x}) \sin \omega t + a_2(\mathbf{x}) e^{-\lambda t} \sin \omega' t \quad (3.176)$$

where $\lambda \in \mathbb{R}^+$ and all other quantities are as defined in (3.172). Now, the third term is a damped sine which tends to zero as $t \rightarrow \infty$. This sort of damped T' -potentially periodic field is not alien to Physics: a great number of natural phenomena exhibit that behaviour, including turbulence. Note that $0 < e^{-\lambda t} \leq 1$.

The phase average of the third term must be calculated:

$$\overleftarrow{a_2(\mathbf{x}) e^{-\lambda t} \sin \omega' t} = \lim_{N \rightarrow \infty} \frac{1}{N} \sum_{n=0}^{N-1} a_2(\mathbf{x}) e^{-\lambda(t+nT')} \sin \omega'(t+nT') \leq \lim_{N \rightarrow \infty} \frac{a_2(\mathbf{x})}{N} \sum_{n=0}^{N-1} \sin(\omega' t + 2\pi n \frac{T'}{T'}) \quad (3.177)$$

The last limit has already been proven equal to zero. Thus the phase average of the third term is zero and, by definition, that term is ψ' :

$$\overleftarrow{\psi}(t, \mathbf{x}) = a_0(\mathbf{x}) + a_1(\mathbf{x}) \sin \omega t \quad , \quad \psi'(t, \mathbf{x}) = a_2(\mathbf{x}) e^{-\lambda t} \sin \omega' t$$

It remains to calculate the time average of ψ' :

$$\overline{\psi'}(\mathbf{x}) = \lim_{\tau \rightarrow \infty} \frac{1}{\tau} \int_0^\tau a_2(\mathbf{x}) e^{-\lambda t} \sin \omega' t \, dt = \lim_{\tau \rightarrow \infty} \frac{a_2(\mathbf{x})}{\tau} \int_0^\tau e^{-\lambda t} \sin \omega' t \, dt \quad (3.178)$$

[Boi61] offers the following indefinite integral

$$\int e^{ax} \sin bx \, dx = \frac{e^{ax}(a \sin bx - b \cos bx)}{a^2 + b^2} \quad (3.179)$$

which in the present case is:

$$\int e^{-\lambda t} \sin \omega' t \, dt = -\frac{e^{-\lambda t} (\lambda \sin \omega' t + \omega' \cos \omega' t)}{\lambda^2 + \omega'^2} \quad (3.180)$$

For $t \rightarrow \infty$ this expression is clearly zero. For $t = 0$ it is equal to $-\omega' / (\lambda^2 + \omega'^2)$. Thus, the time average results in:

$$\overline{\psi'}(\mathbf{x}) = \lim_{\tau \rightarrow \infty} \frac{a_2(\mathbf{x}) \omega'}{\tau (\lambda^2 + \omega'^2)} = 0 \quad (3.181)$$

A similar result than in example (i) above is obtained: ψ' has both, phase and time average, equal to zero. Again, for this kind of regular functions, like damped sines and cosines, the assumptions made in [HR70] and [RH72] are also correct. Figure 3.8 shows an instance of field (3.176).

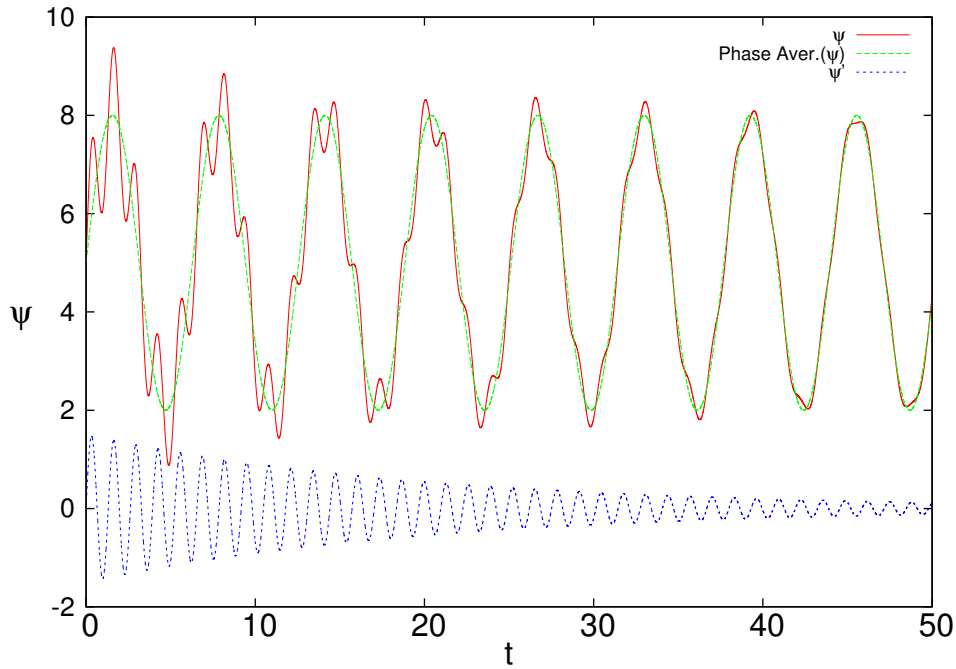


Figure 3.8: Decomposition of field $\psi = 5 + 3 \sin t + 1.5 e^{-0.05t} \sin(\sqrt{23} t)$.

EXAMPLE (iii)

Finally, it will be essayed a truly random function that could be assimilated to statistical noise. Let $\{\delta_n, n \in \mathbb{N}, 0 < \delta_n < 1\}$ and $\{y_n, n \in \mathbb{N}, 0 < |y_n| < 1\}$ be two numerable infinite sets of random numbers. Let

$$t_n = \sum_{i=1}^{2n-2} \delta_i + \delta_{2n-1} \quad (3.182)$$

be a sequence of random real numbers, and $y(t)$ the random function defined by (see figure 3.9):

$$y(t) = \begin{cases} \frac{y_n}{\delta_{2n-1}} (t - t_n + \delta_{2n-1}) & t_n - \delta_{2n-1} < t \leq t_n \\ -\frac{y_n}{\delta_{2n}} (t - t_n - \delta_{2n}) & t_n < t \leq t_n + \delta_{2n} \end{cases} \quad (3.183)$$

such that its time average is a finite non-zero real number:

$$B = \lim_{T \rightarrow \infty} \frac{1}{T} \int_0^T y(t) dt, \quad 0 < B < \infty \quad (3.184)$$

Let $\nu(t)$ be a normalised random function defined by:

$$\nu(t) = \frac{y(t)}{B}, \quad \bar{\nu} = \lim_{T \rightarrow \infty} \frac{1}{T} \int_0^T \nu(t) dt = 1 \quad (3.185)$$

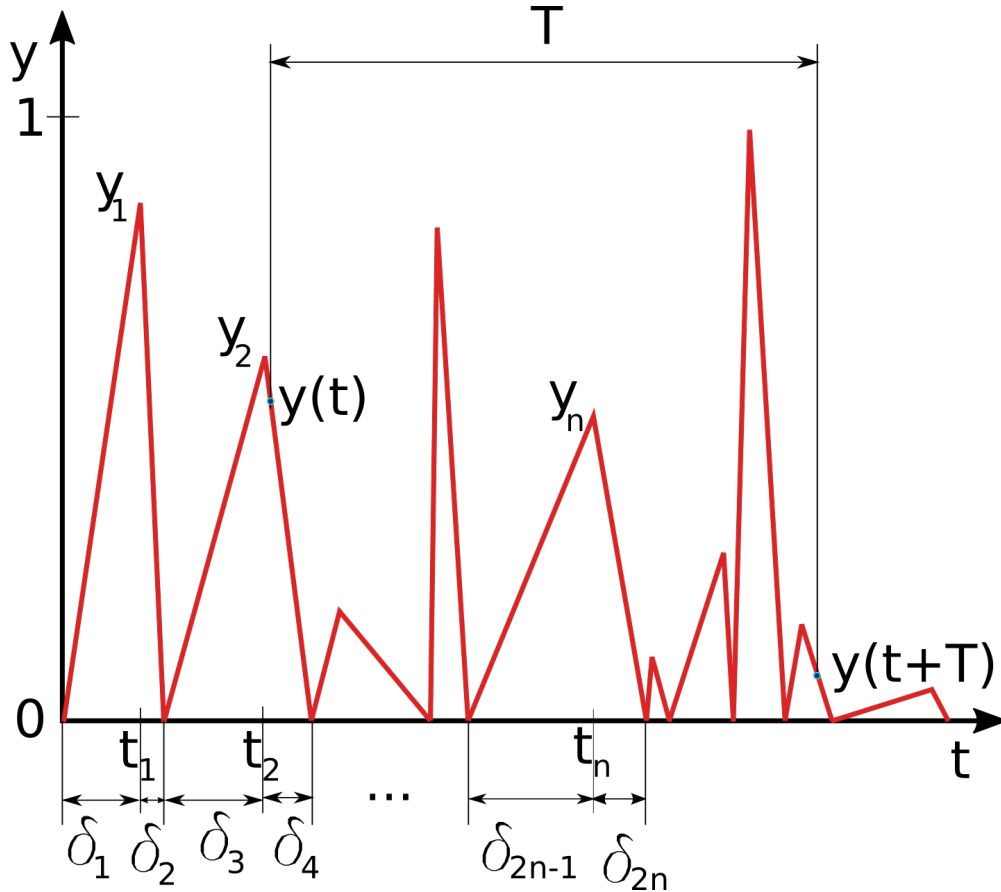


Figure 3.9: An example of positive random-spike function.

$\nu(t)$ could be considered a sort of random noise generator, hopefully white noise, which will be called the **random-spike function** because it has an irregular sawtooth profile. Figure 3.9 shows an example of a positive random-spike function, with $0 < y_n < 1, \forall n \in \mathbb{N}$. Note $\nu(t)$ is completely non-periodic and not even potentially periodic, and that implies the phase average will leave the function mostly untouched, with a negligible (or null) phase averaged component. Herein it cannot be proven that $\overleftarrow{\nu}(t) = 0$, but surely it will be very small: the phase average of width T selects only a few non-representative values of $\nu(t)$, ignoring the rest (see $y(t), y(t+T)$ in figure 3.9), whereas the time average ignores nothing since the time integral (3.185) is calculated along all \mathbb{R}^+ . This situation could be expressed as:

$$\nu(t) = \overleftarrow{\nu}(t) + \nu'(t), \quad \overleftarrow{\nu}(t) \ll \nu'(t), \quad \nu(t) \simeq \nu'(t), \quad \bar{\nu} \simeq \bar{\nu} = 1 \quad (3.186)$$

Let $\phi(t, \mathbf{x})$ be a flow field, and as physical field it would be assumed that $\overline{\phi'}(\mathbf{x}) = 0$. Let $\psi(t, \mathbf{x}) = \phi(t, \mathbf{x}) + \nu(t)$ be a flow field with an added noise source. For this field hold the following results:

$$\psi(t, \mathbf{x}) = \overleftrightarrow{\psi}(t, \mathbf{x}) + \psi'(t, \mathbf{x}), \quad \overleftrightarrow{\psi}(t, \mathbf{x}) \simeq \overleftrightarrow{\phi}(t, \mathbf{x}), \quad \psi'(t, \mathbf{x}) = \phi'(t, \mathbf{x}) + \nu'(t) \simeq \phi'(t, \mathbf{x}) + \nu(t) \quad (3.187)$$

and most important of all:

$$\overline{\psi'}(\mathbf{x}) = \overline{\nu'} \simeq \overline{\nu} = 1 \neq 0 \quad (3.188)$$

Therefore, it has been found an instance of noisy field not verifying equations (3.159)-(3.160). ■

According to these examples, it is pertinent to question whether that sort of behaviour is general. It would appear that physical fields with no strange noisy functions, like the random-spike, would meet [HR70]-[RH72] requirements; but if they were affected by random noise, the classical triple average could be flawed. Does ψ' always present a time average equal to zero for physical fields? (note its phase average is zero by construction). And one answer seems to be: for sufficiently regular functions, phase average and time average are almost equivalent, provided T is small enough. This assertion will be proven next.

Let $\psi(t, \mathbf{x})$ be a sufficiently regular field. It is beyond the scope of this Dissertation to establish what is meant by "*sufficiently regular*": one expects most functions found in Physics and Engineering fulfil that condition. Note this time no assumption is made regarding the periodicity, exact or potential, of ψ .

The phase average of ψ , equation (3.82) can be transformed into an expression very similar to the time average equation (3.59). Assume T is small and $T = \delta t$. Also, let's write $t_n = t + n\delta t$. Then, the phase average is

$$\overleftrightarrow{\psi}(t, \mathbf{x}) = \lim_{N \rightarrow \infty} \frac{1}{N} \sum_{n=0}^{N-1} \psi(t + n\delta t, \mathbf{x}) = \lim_{N \rightarrow \infty} \frac{1}{N\delta t} \sum_{n=0}^{N-1} \psi(t_n, \mathbf{x})\delta t$$

Let $\tau = N\delta t$ and assume, without loss of generality,⁴⁴ that the initial time is $t = 0$. Then

$$\overleftrightarrow{\psi}(0, \mathbf{x}) = \lim_{N \rightarrow \infty} \frac{1}{N} \sum_{n=0}^{N-1} \psi(n\delta t, \mathbf{x}) = \lim_{\tau \rightarrow \infty} \frac{1}{\tau} \sum_{t_n=0}^{\tau} \psi(t_n, \mathbf{x})\delta t \approx \lim_{\tau \rightarrow \infty} \frac{1}{\tau} \int_0^{\tau} \psi(t, \mathbf{x}) dt = \overline{\psi}(\mathbf{x}) \quad (3.189)$$

because the last sum is approximately the integral. A surprising result has been obtained: for small δt phase average and time average are roughly equal functions, $\overleftrightarrow{\psi} \approx \overline{\psi}$, provided ψ is sufficiently regular. Of course, roughly equal functions *on average*. If $\delta t = T$ could not be reduced, because of the T -periodic nature of the agent acting on the flow, then the approximation (3.189) would be very coarse, or even outright erroneous. Said in other words: if phase average were applied to a T -potentially periodic field ψ , then the result would be a T -periodic field $\overleftrightarrow{\psi}$ which could be very different from $\overline{\psi}$; but if it were applied to a non T -potentially periodic field ϕ , then the outcome would be approximate to $\overline{\phi}$, provided ϕ be sufficiently regular. The phase average only produces T -periodic results if applied to the right functions, otherwise it irons out the functions and yields (roughly) time averages. This is also true for the dc component of a sufficiently regular function.

⁴⁴The sum needs a finite number of terms to overtake t from zero, $t \leq n_0\delta t$ for finite n_0 . The limit $\lim_{N \rightarrow \infty} \frac{1}{N} \sum_{n=0}^{n_0} \psi(n\delta t, \mathbf{x})$ is zero and, therefore, it is irrelevant to start the sum with $\psi(0)$ or with $\psi(t)$. This is called the independence of phase average with respect to time origin. (see remark in page 94 leading to equation (3.84)).

Equation (3.189) leads to another interesting result: for sufficiently regular functions $\overleftrightarrow{\psi} = \bar{\psi}$. In other words, whatever small difference existing between $\overleftrightarrow{\psi}$ and $\bar{\psi}$ is obliterated after a second time average. Thus, it may be concluded that

$$\overleftrightarrow{\psi}(\mathbf{x}) = \bar{\psi}(\mathbf{x}) \quad , \quad \overleftrightarrow{\psi}'(\mathbf{x}) = 0$$

and equations (3.159)-(3.160) are satisfied for sufficiently regular fields like, hopefully, physical fields.

Summarising, from equation (3.189) the following conclusions can be derived for sufficiently regular functions ψ (with no assumptions on periodicity):

- If $\overleftrightarrow{\psi} = 0$ then $\bar{\psi} = 0$. That is, if ψ is the fluctuating component *à la* phase average of another field (hence $\overleftrightarrow{\psi} = 0$), then equation (3.189) implies $\bar{\psi} = 0$ as well. Thus the approximation " \approx " turns into equality when $\overleftrightarrow{\psi} = 0$.
- If $\overleftrightarrow{\psi} = \infty$ (the series does not converge), then $\bar{\psi} = \infty$ as well (the integral does not converge either). Again, the approximation turns into equality.
- If $\overleftrightarrow{\psi} \neq 0$ for a non T -potentially periodic field ψ , then $\overleftrightarrow{\psi} \approx \bar{\psi}$, provided $T = \delta t$ is sufficiently small. Of course, if ψ is T -potentially periodic then $\overleftrightarrow{\psi} \neq \bar{\psi}$.
- A further time average over $\overleftrightarrow{\psi} \approx \bar{\psi}$ turns the approximation into an equality: $\overleftrightarrow{\overleftrightarrow{\psi}} = \bar{\psi}$, and hence $\overleftrightarrow{\overleftrightarrow{\psi}}' = 0$.

Herein it is not investigated (nor even hinted) the conditions that ψ must fulfil for the above conclusions to be false. If ψ is sufficiently regular, the above conclusions are true. ■

The results just enunciated have been presented in a scarcely rigorous form. Surely, there are functions for which those conclusions are false, like the noisy random-spike function of example (iii) above, but herein it is believed that such fields are extremely unlikely to be found in any turbulent flow of actual interest in Engineering. Many other examples, not shown here for reasons of space, have been tested and the results are consistent with the four points above. It corresponds to skilled Mathematicians to demonstrate (or to refute) the conclusions exposed herein. Meanwhile, it seems safe to accept the results obtained in [HR70] and [RH72], because the cases they are being applied to involve turbulent flows with physical fields \mathbf{u} and p sufficiently regular. However, it cannot be fully discarded that some extreme turbulence phenomena would generate fluctuating components with such non-regular behaviour, that would render false some of the assertions made above.

For those researchers who might not be comfortable with a potentially erroneous triple decomposition, as introduced in [HR70] and [RH72], the following slightly different triple decomposition for a T -potentially periodic turbulent flow field $\psi(t, \mathbf{x})$ is proposed:

$$\psi(t, \mathbf{x}) = \overset{\circ}{\psi}(\mathbf{x}) + \tilde{\psi}(t, \mathbf{x}) + \psi'(t, \mathbf{x}) \equiv \overleftrightarrow{\psi}(t, \mathbf{x}) + \psi'(t, \mathbf{x}) \quad (3.190)$$

where:

- $\overset{\circ}{\psi}(\mathbf{x}) = a_0(\mathbf{x})$ is the time average of $\overleftrightarrow{\psi}(t, \mathbf{x})$, the first term in the Fourier series (3.164), the dc component of $\overleftrightarrow{\psi}(t, \mathbf{x})$.

- $\tilde{\psi}(t, \mathbf{x}) = \overleftrightarrow{\psi}(t, \mathbf{x}) - \overset{\circ}{\psi}(\mathbf{x})$ is the part of $\overleftrightarrow{\psi}$ with null time average, that is:

$$\tilde{\psi}(t, \mathbf{x}) = \sum_{n=1}^{\infty} [a_n(\mathbf{x}) \cos n\omega t + b_n(\mathbf{x}) \sin n\omega t] \quad (3.191)$$

$\tilde{\psi}(t, \mathbf{x})$ is still a T -periodic function of t , albeit with no dc component. It will be called the **oscillating component** of $\overleftrightarrow{\psi}(t, \mathbf{x})$.⁴⁵

- $\psi'(t, \mathbf{x})$ is the fluctuating component *à la* phase average of ψ .

From this point onwards and up to the end of this section, it will be assumed that equations (3.159)-(3.160) are in general erroneous (which they are not for most cases of interest in Physics and Engineering). Thus, all past remarks made about them being physically correct will be ignored.

The following Reynolds-like conditions apply:

$$\overline{\overset{\circ}{\psi}(\mathbf{x})} = \overset{\circ}{\psi}(\mathbf{x}) \quad , \quad \overline{\overleftrightarrow{\psi}(\mathbf{x})} = \overset{\circ}{\psi}(\mathbf{x}) \quad , \quad \overline{\tilde{\psi}(\mathbf{x})} \neq \overset{\circ}{\psi}(\mathbf{x}) \quad (3.192)$$

$$\overline{\overleftrightarrow{\psi}'(\mathbf{x})} = \overset{\circ}{\psi}'(\mathbf{x}) \quad (3.193)$$

$$\overline{\overleftrightarrow{\psi}(t, \mathbf{x})} = \tilde{\psi}(t, \mathbf{x}) \quad , \quad \overline{\tilde{\psi}(\mathbf{x})} = 0 \quad (3.194)$$

$$\overline{\overleftrightarrow{\psi}'(t, \mathbf{x})} = 0 \quad , \quad \overline{\tilde{\psi}'(\mathbf{x})} \neq 0 \quad (3.195)$$

Starting with the Navier-Stokes equation (3.90) and the new triple decomposition for fields $\mathbf{u}(t, \mathbf{x})$ and $p(t, \mathbf{x})$

$$\mathbf{u}(t, \mathbf{x}) = \overset{\circ}{\mathbf{u}}(\mathbf{x}) + \tilde{\mathbf{u}}(t, \mathbf{x}) + \mathbf{u}'(t, \mathbf{x}) \equiv \overleftrightarrow{\mathbf{u}}(t, \mathbf{x}) + \mathbf{u}'(t, \mathbf{x}) \quad (3.196)$$

$$p(t, \mathbf{x}) = \overset{\circ}{p}(\mathbf{x}) + \tilde{p}(t, \mathbf{x}) + p'(t, \mathbf{x}) \equiv \overleftrightarrow{p}(t, \mathbf{x}) + p'(t, \mathbf{x}) \quad (3.197)$$

and the set of continuity equations⁴⁶

$$\nabla \cdot \mathbf{u} = \nabla \cdot \overleftrightarrow{\mathbf{u}} = \nabla \cdot \overset{\circ}{\mathbf{u}} = \nabla \cdot \tilde{\mathbf{u}} = \nabla \cdot \mathbf{u}' = 0 \quad (3.198)$$

after substituting these fields in equation (3.90) and phase averaging it, the RANSE *à la* triple decomposition is obtained:

$$\begin{aligned} \partial_t \tilde{u}_i + \overset{\circ}{u}_j \partial_j \overset{\circ}{u}_i + \overset{\circ}{u}_j \partial_j \tilde{u}_i + \tilde{u}_j \partial_j \overset{\circ}{u}_i + \tilde{u}_j \partial_j \tilde{u}_i &= \\ = -\frac{1}{\rho} (\partial_i \overset{\circ}{p} + \partial_i \tilde{p}) + \partial_j \left[\nu \partial_j \overset{\circ}{u}_i + \nu \partial_j \tilde{u}_i - \overleftrightarrow{u'_i u'_j} \right] + g_i + \pi_i \end{aligned} \quad (3.199)$$

It should come as no surprise that equation (3.199) is identical to (3.91), because $\overleftrightarrow{\mathbf{u}} = \overset{\circ}{\mathbf{u}} + \tilde{\mathbf{u}}$, $\overleftrightarrow{p} = \overset{\circ}{p} + \tilde{p}$, $\partial_t \overset{\circ}{\mathbf{u}} = 0$, and equation (3.91) corresponds to RANSE *à la* phase average.

⁴⁵According to this decomposition, $\overleftrightarrow{\psi}(t, \mathbf{x})$ has two components: the dc $\overset{\circ}{\psi}(\mathbf{x})$ and the oscillating $\tilde{\psi}(t, \mathbf{x})$.

⁴⁶ $\nabla \cdot \overleftrightarrow{\mathbf{u}} = 0$ is obtained after phase averaging $\nabla \cdot \mathbf{u} = 0$. Then it follows $\nabla \cdot \mathbf{u}' = 0$. $\nabla \cdot \overset{\circ}{\mathbf{u}} = 0$ is obtained after time averaging $\nabla \cdot \overleftrightarrow{\mathbf{u}} = 0$. Then it follows $\nabla \cdot \tilde{\mathbf{u}} = 0$.

To derive equation (3.199) the following non-obvious intermediate steps are necessary:

$$\overleftarrow{\dot{u}_j \partial_j u'_i} = \lim_{N \rightarrow \infty} \frac{1}{N} \sum_{n=0}^{N-1} \dot{u}_j(\mathbf{x}) \partial_j u'_i(t + nT, \mathbf{x}) = \lim_{N \rightarrow \infty} \frac{\dot{u}_j(\mathbf{x})}{N} \sum_{n=0}^{N-1} \partial_j u'_i(t + nT, \mathbf{x}) = \dot{u}_j \overleftrightarrow{\partial_j u'_i} = 0 \quad (3.200)$$

$\dot{u}_j(\mathbf{x})$ can exit the sum because it does not depend on t and is not affected by the summation index n .

Likewise, using the same argument that $\dot{u}_j(\mathbf{x})$ can exit the sum, it can be proven that:

$$\overleftarrow{\dot{u}_j \partial_j \dot{u}_i} = \dot{u}_j \partial_j \dot{u}_i \quad (3.201)$$

$$\overleftarrow{\dot{u}_j \partial_j \tilde{u}_i} = \dot{u}_j \partial_j \overleftrightarrow{\tilde{u}_i} = \dot{u}_j \partial_j \tilde{u}_i \quad (3.202)$$

$$\overleftarrow{\tilde{u}_j \partial_j \dot{u}_i} = \overleftrightarrow{\tilde{u}_j} \partial_j \dot{u}_i = \tilde{u}_j \partial_j \dot{u}_i \quad (3.203)$$

because $\tilde{\mathbf{u}}(t, \mathbf{x})$ is already a T -periodic vector field.

It is also necessary to check the value of $\overleftrightarrow{\tilde{u}_j \partial_j \tilde{u}_i}$. It will be shown that \tilde{u}_i exits the sum too.

$$\begin{aligned} \overleftrightarrow{\tilde{u}_j \partial_j \tilde{u}_i} &= \lim_{N \rightarrow \infty} \frac{1}{N} \sum_{n=0}^{N-1} \tilde{u}_j(t + nT, \mathbf{x}) \partial_j \tilde{u}_i(t + nT, \mathbf{x}) = \lim_{N \rightarrow \infty} \frac{1}{N} \sum_{n=0}^{N-1} \tilde{u}_j(t, \mathbf{x}) \partial_j \tilde{u}_i(t + nT, \mathbf{x}) = \\ &= \lim_{N \rightarrow \infty} \frac{\tilde{u}_j(t, \mathbf{x})}{N} \partial_j \left[\sum_{n=0}^{N-1} \tilde{u}_i(t + nT, \mathbf{x}) \right] = \tilde{u}_j \overleftrightarrow{\partial_j \tilde{u}_i} = 0 \end{aligned} \quad (3.204)$$

\tilde{u}_j exits the sum because it is a T -periodic function of t and $\tilde{u}_j(t + nT, \mathbf{x}) = \tilde{u}_j(t, \mathbf{x})$, and thus it is not affected by the summation index n .

Likewise, using the same argument that $\tilde{u}_j(t, \mathbf{x})$ can exit the sum, it can be proven that:

$$\overleftrightarrow{\tilde{u}'_j \partial_j \tilde{u}_i} = \overleftrightarrow{\tilde{u}'_j} \partial_j \tilde{u}_i = 0 \quad (3.205)$$

The last term to check is $\overleftrightarrow{\tilde{u}_j \partial_j \tilde{u}_i}$, whose result is:

$$\begin{aligned} \overleftrightarrow{\tilde{u}_j \partial_j \tilde{u}_i} &= \lim_{N \rightarrow \infty} \frac{1}{N} \sum_{n=0}^{N-1} \tilde{u}_j(t + nT, \mathbf{x}) \partial_j \tilde{u}_i(t + nT, \mathbf{x}) = \lim_{N \rightarrow \infty} \frac{1}{N} \sum_{n=0}^{N-1} \tilde{u}_j(t, \mathbf{x}) \partial_j \tilde{u}_i(t, \mathbf{x}) = \\ &= \lim_{N \rightarrow \infty} \tilde{u}_j(t, \mathbf{x}) \partial_j \tilde{u}_i(t, \mathbf{x}) \frac{1}{N} \sum_{n=0}^{N-1} 1 = \lim_{N \rightarrow \infty} \tilde{u}_j(t, \mathbf{x}) \partial_j \tilde{u}_i(t, \mathbf{x}) \frac{N}{N} = \tilde{u}_j \partial_j \tilde{u}_i \end{aligned} \quad (3.206)$$

using the same argument that \tilde{u}_i is a T -periodic function of t , and is not affected by the summation index n .

Equations (3.200)-(3.206) suffice to obtain equation (3.199).

Leaving aside the terms g_i and π_i in equations (3.199), corresponding to the steady and T -periodic force densities, the main differences between equations (3.161) and (3.199) are:

- The time averaged fields \bar{u}_i and \bar{p} in (3.161) are now substituted by the dc components \dot{u}_i and \dot{p} in (3.199). It should be considered that this substitution fixes an error and a potential source of inaccuracies, specially if the turbulent flow fields' behaviour is not markedly T -periodic and the fluctuating components \mathbf{u}' , p' are not negligible.

- The fields \tilde{u}_i and \tilde{p} in (3.161) are not identical to the like-named in (3.199). In the later, \tilde{u}_i and \tilde{p} are T -periodic functions devoid of their dc component, and thus still T -periodic functions. But in the former $\tilde{u}_i = \overleftarrow{u'_i} - \overline{u_i}$ and $\tilde{p} = \overleftarrow{p'} - \overline{p}$, and while $\overleftarrow{u'_i}$, $\overleftarrow{p'}$ are T -periodic functions, the subtraction of the time average (not the dc component) renders \tilde{u}_i and \tilde{p} T -periodic functions with some dc component. Therefore, $\overline{\tilde{u}_i} \neq 0$ and $\overline{\tilde{p}} \neq 0$ in the formalism of [RH72].
- The term $\partial_j(\tilde{u}_i\tilde{u}_j)$ in (3.161) appears as $\tilde{u}_j\partial_j\tilde{u}_i$ in (3.199), but at this stage it is not a problem because $\tilde{\mathbf{u}}$ fulfils the continuity equation (3.198). However, it might be a problem after time averaging this term. Fortunately, it will be seen that, even after time averaging, both terms remain identical

Following the same sequence than [RH72], now a time average should be applied on equation (3.199) in order to obtain the RANSE for the mean fields. Having into account the Reynolds-like conditions (3.192)-(3.195), only the combined terms need to be explicitly calculated. After applying time average (3.59) to every term in equation (3.199), and discarding the obviously null ones, the result is ⁴⁷:

$$\overline{\dot{u}_j \partial_j \dot{u}_i} + \overline{\dot{u}_j \partial_j \tilde{u}_i} + \overline{\tilde{u}_j \partial_j \dot{u}_i} + \overline{\tilde{u}_j \partial_j \tilde{u}_i} = -\frac{1}{\rho} \partial_i \dot{p} + \partial_j \left[\nu \partial_j \dot{u}_i - \overleftarrow{u'_i u'_j} \right] + g_i + \dot{\pi}_i \quad (3.207)$$

Note that g_i is supposed to be a steady force field and $\overline{g_i} = \overleftarrow{g'_i} = g_i$, while π_i is a T -periodic field and $\overline{\pi_i} = \dot{\pi}_i$, the dc component. Let's examine each term in equation (3.207). $\overline{\dot{u}_j \partial_j \dot{u}_i}$ is easy to calculate because $\dot{u}_j(\mathbf{x})$ does not depend on t .

$$\overline{\dot{u}_j \partial_j \dot{u}_i} = \lim_{\tau \rightarrow \infty} \frac{1}{\tau} \int_0^\tau \dot{u}_j(\mathbf{x}) \partial_j \dot{u}_i(\mathbf{x}) dt = \lim_{\tau \rightarrow \infty} \frac{1}{\tau} \dot{u}_j(\mathbf{x}) \partial_j \dot{u}_i(\mathbf{x}) \int_0^\tau dt = \lim_{\tau \rightarrow \infty} \dot{u}_j(\mathbf{x}) \partial_j \dot{u}_i(\mathbf{x}) \frac{\tau}{\tau} = \dot{u}_j \partial_j \dot{u}_i \quad (3.208)$$

This possibility of $\dot{u}_j(\mathbf{x})$ exiting the time integral will be exploited in the coming derivations.

Thus the term $\overline{\dot{u}_j \partial_j \tilde{u}_i}$ results in:

$$\begin{aligned} \overline{\dot{u}_j \partial_j \tilde{u}_i} &= \lim_{\tau \rightarrow \infty} \frac{1}{\tau} \int_0^\tau \dot{u}_j(\mathbf{x}) \partial_j \tilde{u}_i(t, \mathbf{x}) dt = \lim_{\tau \rightarrow \infty} \frac{1}{\tau} \dot{u}_j(\mathbf{x}) \int_0^\tau \partial_j \tilde{u}_i(t, \mathbf{x}) dt = \\ &= \lim_{\tau \rightarrow \infty} \frac{1}{\tau} \dot{u}_j(\mathbf{x}) \partial_j \int_0^\tau \tilde{u}_i(t, \mathbf{x}) dt = \dot{u}_j \partial_j \overline{\tilde{u}_i} = 0 \end{aligned} \quad (3.209)$$

because it has been proven in equation (3.170) that $\overline{\tilde{u}_i} = 0$. Likewise, the term $\overline{\tilde{u}_j \partial_j \dot{u}_i} = 0$.

The remaining term $\overline{\tilde{u}_j \partial_j \tilde{u}_i}$ requires a more elaborated approach. First, it must be clear that $\overleftarrow{u'_j}(t, \mathbf{x})$ is a T -periodic function of t . Therefore, it can be expressed as a Fourier series

$$\overleftarrow{u'_i}(t, \mathbf{x}) = \dot{u}_i(\mathbf{x}) + \sum_{n=1}^{\infty} \left[a_n^{(i)}(\mathbf{x}) \cos n\omega t + b_n^{(i)}(\mathbf{x}) \sin n\omega t \right] = \dot{u}_i(\mathbf{x}) + \tilde{u}_i(t, \mathbf{x}) \quad (3.210)$$

where the dc and oscillating components are shown separately. According to this decomposition, the time average $\overline{\tilde{u}_j \partial_j \tilde{u}_i}$ would be expressed as a sum of integrals in which $\cos n\omega t$ and $\sin n\omega t$ would appear

⁴⁷Note that $\overleftarrow{u'_i u'_j} \equiv u'_i u'_j$ because $\overleftarrow{u'_i u'_j}$ is a T -periodic function whose dc component is obtained through time average. Both expressions will be used along this text, specially when confusion might arise regarding which quantities are under the little circle \circ above them.

multiplying each other in every possible combination. Namely:

$$\begin{aligned}
\overline{\tilde{u}_j \partial_j \tilde{u}_i(\mathbf{x})} &= \lim_{\tau \rightarrow \infty} \frac{1}{\tau} \int_0^\tau \tilde{u}_j(t, \mathbf{x}) \partial_j \tilde{u}_i(t, \mathbf{x}) dt = \\
&= \lim_{\tau \rightarrow \infty} \frac{1}{\tau} \int_0^\tau \sum_{n=1}^{\infty} \left[a_n^{(j)}(\mathbf{x}) \cos n\omega t + b_n^{(j)}(\mathbf{x}) \sin n\omega t \right] \partial_j \sum_{m=1}^{\infty} \left[a_m^{(i)}(\mathbf{x}) \cos m\omega t + b_m^{(i)}(\mathbf{x}) \sin m\omega t \right] dt = \\
&= \lim_{\tau \rightarrow \infty} \frac{1}{\tau} \sum_{n=1}^{\infty} \sum_{m=1}^{\infty} \left[a_n^{(j)} \partial_j a_m^{(i)} \int_0^\tau \cos n\omega t \cos m\omega t dt + a_n^{(j)} \partial_j b_m^{(i)} \int_0^\tau \cos n\omega t \sin m\omega t dt + \right. \\
&\quad \left. + b_n^{(j)} \partial_j a_m^{(i)} \int_0^\tau \sin n\omega t \cos m\omega t dt + b_n^{(j)} \partial_j b_m^{(i)} \int_0^\tau \sin n\omega t \sin m\omega t dt \right] \quad (3.211)
\end{aligned}$$

where $a_n^{(j)}(\mathbf{x})$ to $b_m^{(i)}(\mathbf{x})$ exit the integral because they do not depend on t .

The following indefinite integrals can be found at [Boi61]:

$$\int \sin at \sin bt dt = \frac{1}{2} \left\{ \frac{\sin(a-b)t}{a-b} - \frac{\sin(a+b)t}{a+b} \right\} \quad (a \neq b) \quad (3.212)$$

$$\int \cos at \cos bt dt = \frac{1}{2} \left\{ \frac{\sin(a-b)t}{a-b} + \frac{\sin(a+b)t}{a+b} \right\} \quad (a \neq b) \quad (3.213)$$

$$\int \sin at \cos bt dt = -\frac{1}{2} \left\{ \frac{\cos(a-b)t}{a-b} + \frac{\cos(a+b)t}{a+b} \right\} \quad (a \neq b) \quad (3.214)$$

$$\int \sin at \cos at dt = \frac{1}{2a} \sin^2 at = -\frac{1}{4a} \cos 2at \quad (3.215)$$

$$\int \sin^2 at dt = \frac{t}{2} - \frac{\sin 2at}{4a} \quad (3.216)$$

$$\int \cos^2 at dt = \frac{t}{2} + \frac{\sin 2at}{4a} \quad (3.217)$$

Moreover, for any natural numbers $p, n, m \in \mathbb{N}$ the above integrals fulfil:

$$\int_0^{pT} \sin n\omega t \sin m\omega t dt = \frac{\sin(n-m)p2\pi}{2(n-m)\omega} - \frac{\sin(n+m)p2\pi}{2(n+m)\omega} = 0 \quad (n \neq m) \quad (3.218)$$

$$\int_0^{pT} \cos n\omega t \cos m\omega t dt = \frac{\sin(n-m)p2\pi}{2(n-m)\omega} + \frac{\sin(n+m)p2\pi}{2(n+m)\omega} = 0 \quad (n \neq m) \quad (3.219)$$

$$\begin{aligned}
&\int_0^{pT} \sin n\omega t \cos m\omega t dt = \\
&-\frac{\cos(n-m)p2\pi}{2(n-m)\omega} - \frac{\cos(n+m)p2\pi}{2(n+m)\omega} + \frac{1}{2(n-m)\omega} + \frac{1}{2(n+m)\omega} = 0 \quad (n \neq m) \quad (3.220)
\end{aligned}$$

$$\int_0^{pT} \sin n\omega t \cos n\omega t \, dt = -\frac{1}{4n\omega} \cos 4np\pi + \frac{1}{4n\omega} = 0 \quad (3.221)$$

$$\int_0^{pT} \sin^2 n\omega t \, dt = \frac{pT}{2} - \frac{\sin 4np\pi}{4n\omega} = \frac{pT}{2} \quad (3.222)$$

$$\int_0^{pT} \cos^2 n\omega t \, dt = \frac{pT}{2} + \frac{\sin 4np\pi}{4n\omega} = \frac{pT}{2} \quad (3.223)$$

because $(n - m)p \in \mathbb{Z}$ and $(n + m)p \in \mathbb{Z}^+$

Now it will be invoked the general decomposition of any real number into integer and fractional parts (3.167). For the four integrals (3.218)-(3.221) the following result holds:

$$\begin{aligned} \lim_{\tau \rightarrow \infty} \frac{1}{\tau} \int_0^{\tau} \begin{Bmatrix} \sin n\omega t \sin m\omega t \\ \cos n\omega t \cos m\omega t \\ \sin n\omega t \cos m\omega t \\ \sin n\omega t \cos n\omega t \end{Bmatrix} dt &= \lim_{\tau \rightarrow \infty} \frac{1}{\tau} \left[\int_0^{\lfloor \frac{\tau}{T} \rfloor T} + \int_{\lfloor \frac{\tau}{T} \rfloor T}^{\lfloor \frac{\tau}{T} \rfloor T + \{\frac{\tau}{T}\}T} \right] \begin{Bmatrix} \sin n\omega t \sin m\omega t \\ \cos n\omega t \cos m\omega t \\ \sin n\omega t \cos m\omega t \\ \sin n\omega t \cos n\omega t \end{Bmatrix} dt = \\ &= \lim_{\tau \rightarrow \infty} \frac{1}{\tau} \int_{\lfloor \frac{\tau}{T} \rfloor T}^{\lfloor \frac{\tau}{T} \rfloor T + \{\frac{\tau}{T}\}T} \begin{Bmatrix} \sin n\omega t \sin m\omega t \\ \cos n\omega t \cos m\omega t \\ \sin n\omega t \cos m\omega t \\ \sin n\omega t \cos n\omega t \end{Bmatrix} dt = \lim_{\tau \rightarrow \infty} \frac{B}{\tau} = 0 \end{aligned} \quad (3.224)$$

where the first set of integrals is identically zero and $B \in \mathbb{R}$ is a finite real number.

Using the same decomposition of τ into integer and fractional parts, the integrals (3.222)-(3.223) verify:

$$\begin{aligned} \lim_{\tau \rightarrow \infty} \frac{1}{\tau} \int_0^{\tau} \begin{Bmatrix} \sin^2 n\omega t \\ \cos^2 n\omega t \end{Bmatrix} dt &= \lim_{\tau \rightarrow \infty} \frac{1}{\tau} \left[\frac{t}{2} \mp \frac{\sin 2n\omega t}{4n\omega} \right]_0^{\tau} = \\ &= \lim_{\tau \rightarrow \infty} \frac{1}{\tau} \left\{ \left[\frac{t}{2} \right]_0^{\tau} \mp \left[\frac{\sin 2n\omega t}{4n\omega} \right]_0^{\lfloor \frac{\tau}{T} \rfloor T} \mp \left[\frac{\sin 2n\omega t}{4n\omega} \right]_{\lfloor \frac{\tau}{T} \rfloor T}^{\lfloor \frac{\tau}{T} \rfloor T + \{\frac{\tau}{T}\}T} \right\} = \\ &= \lim_{\tau \rightarrow \infty} \frac{1}{\tau} \left\{ \frac{\tau}{2} \mp 0 \mp B \right\} = \lim_{\tau \rightarrow \infty} \left\{ \frac{1}{2} \mp \frac{B}{\tau} \right\} = \frac{1}{2} \end{aligned} \quad (3.225)$$

where, again, $B \in \mathbb{R}$ is a finite real number.

Therefore, the single set of terms which survive in the series of equation (3.211) are:

$$\overline{\tilde{u}_j \partial_j \tilde{u}_i(\mathbf{x})} = \frac{1}{2} \sum_{n=1}^{\infty} \left[a_n^{(j)}(\mathbf{x}) \partial_j a_n^{(i)}(\mathbf{x}) + b_n^{(j)}(\mathbf{x}) \partial_j b_n^{(i)}(\mathbf{x}) \right] \quad (3.226)$$

which in general are non-zero. Putting together the partial results obtained so far, the time-phase averaged RANSE appear as:

$$\dot{u}_j \partial_j \dot{u}_i + \overline{\tilde{u}_j \partial_j \tilde{u}_i} = -\frac{1}{\rho} \partial_i \dot{p} + \partial_j \left[\nu \partial_j \dot{u}_i - \overleftrightarrow{u_i' u_j'} \right] + g_i + \dot{\pi}_i \quad (3.227)$$

All terms above are steady, not depending on t .

Comparing equation (3.227) with (3.162) it is possible to see three main differences:

- Equation (3.162) contains the time mean values $\overline{u_i}$ and \overline{p} , whereas in equation (3.227) the dc components $\overset{\circ}{u}_i$ and $\overset{\circ}{p}$ appear. It has already been shown that both quantities are not equal.
- The term $\partial_j(\overline{u_i u_j})$ in equation (3.162) appears as $\overline{\tilde{u}_j \partial_j \tilde{u}_i}$ in equation (3.227). In principle, they do not seem equal. However, both will be proven identical. In effect, assuming \tilde{u}_i takes the form given by equation (3.210), and having into account the equations (3.211)-(3.226), the $\partial_j(\overline{u_i u_j})$ term yields:

$$\begin{aligned} \partial_j(\overline{u_i u_j})(\mathbf{x}) &= \lim_{\tau \rightarrow \infty} \frac{1}{\tau} \partial_j \int_0^\tau \tilde{u}_i(t, \mathbf{x}) \tilde{u}_j(t, \mathbf{x}) dt = \\ &= \lim_{\tau \rightarrow \infty} \frac{1}{\tau} \partial_j \int_0^\tau \sum_{n=1}^{\infty} \left[a_n^{(i)}(\mathbf{x}) \cos n\omega t + b_n^{(i)}(\mathbf{x}) \sin n\omega t \right] \sum_{m=1}^{\infty} \left[a_m^{(j)}(\mathbf{x}) \cos m\omega t + b_m^{(j)}(\mathbf{x}) \sin m\omega t \right] dt = \\ &= \lim_{\tau \rightarrow \infty} \frac{1}{\tau} \partial_j \sum_{n=1}^{\infty} \left[a_n^{(i)} a_n^{(j)} \int_0^\tau \cos^2 n\omega t dt + b_n^{(i)} b_n^{(j)} \int_0^\tau \sin^2 n\omega t dt \right] = \frac{1}{2} \partial_j \sum_{n=1}^{\infty} \left[a_n^{(i)} a_n^{(j)} + b_n^{(i)} b_n^{(j)} \right] \end{aligned} \quad (3.228)$$

which, in principle, does not look similar to (3.226). But the continuity equation (3.198) implies

$$\partial_j \tilde{u}_j = 0 = \partial_j \sum_{n=1}^{\infty} \left[a_n^{(j)} \cos n\omega t + b_n^{(j)} \sin n\omega t \right] = \sum_{n=1}^{\infty} \left[\partial_j a_n^{(j)} \cos n\omega t + \partial_j b_n^{(j)} \sin n\omega t \right] \quad (3.229)$$

However this series is zero $\forall t \in \mathbb{R}$, and the only possibility for this to be true is:

$$\partial_j a_n^{(j)} = \partial_j b_n^{(j)} = 0 \quad \forall n \in \mathbb{N} \quad (3.230)$$

Then equation (3.228) converts into:

$$\begin{aligned} \partial_j(\overline{u_i u_j})(\mathbf{x}) &= \frac{1}{2} \partial_j \sum_{n=1}^{\infty} \left[a_n^{(i)} a_n^{(j)} + b_n^{(i)} b_n^{(j)} \right] = \frac{1}{2} \sum_{n=1}^{\infty} \left[\partial_j (a_n^{(i)} a_n^{(j)}) + \partial_j (b_n^{(i)} b_n^{(j)}) \right] \\ &= \frac{1}{2} \sum_{n=1}^{\infty} \left[a_n^{(j)} \partial_j a_n^{(i)} + b_n^{(j)} \partial_j b_n^{(i)} \right] = \overline{\tilde{u}_j \partial_j \tilde{u}_i}(\mathbf{x}) \end{aligned} \quad (3.231)$$

and now it has been proven that both terms are identical. Eventually, an interesting side-result has been obtained:

$$\overline{\tilde{u}_i \tilde{u}_j}(\mathbf{x}) = \frac{1}{2} \sum_{n=1}^{\infty} \left[a_n^{(i)}(\mathbf{x}) a_n^{(j)}(\mathbf{x}) + b_n^{(i)}(\mathbf{x}) b_n^{(j)}(\mathbf{x}) \right] \quad (3.232)$$

- The term $\partial_j(\overline{u'_i u'_j})$ in equation (3.162) appears as $\partial_j(\overline{u'_i u'_j})$ in (3.227). However, this time it is not possible to assume that both are identical. To start with, $\overline{u'_i u'_j}$ is a T -periodic function and $\overline{u'_i u'_j} \equiv u'_i u'_j$ its dc component, whereas $\overline{u'_i u'_j}$ is no dc component because $u'_i u'_j$ is not even a T -periodic function. Moreover, it should not be forgotten that u'_i is the fluctuating component *à la* phase average of u_i , and this very interpretation of u'_i is also implicit in [HR70] and [RH72]. Thus it is possible to write

$$\overline{u'_i u'_j}(\mathbf{x}) = \overline{(u_i - \overleftarrow{u}_i)(u_j - \overleftarrow{u}_j)} = \overline{u_i u_j} - \overline{u_i \overleftarrow{u}_j} - \overline{u_j \overleftarrow{u}_i} + \overline{\overleftarrow{u}_i \overleftarrow{u}_j} \quad (3.233)$$

⁴⁸See footnote 47 in page 126.

and this expression is hardly similar to $u'_i u'_j$.

As an exercise, the expression for $\overline{u_i \overleftarrow{u'_j}}$ is offered next:

$$\begin{aligned}
\overline{u_i \overleftarrow{u'_j}}(\mathbf{x}) &= \lim_{\tau \rightarrow \infty} \frac{1}{\tau} \int_0^\tau u_i(t, \mathbf{x}) \overleftarrow{u'_j}(t, \mathbf{x}) dt = \\
&= \lim_{\tau \rightarrow \infty} \frac{1}{\tau} \int_0^\tau u_i \left\{ \overset{\circ}{u}_j(\mathbf{x}) + \sum_{n=1}^{\infty} [a_n^{(j)}(\mathbf{x}) \cos n\omega t + b_n^{(j)}(\mathbf{x}) \sin n\omega t] \right\} dt = \\
&= \lim_{\tau \rightarrow \infty} \frac{1}{\tau} \left[\overset{\circ}{u}_j \int_0^\tau u_i dt + \sum_{n=1}^{\infty} a_n^{(j)} \int_0^\tau u_i \cos n\omega t dt + \sum_{n=1}^{\infty} b_n^{(j)} \int_0^\tau u_i \sin n\omega t dt \right] = \\
&= \overline{u_i}(\mathbf{x}) \overset{\circ}{u}_j(\mathbf{x}) + \sum_{n=1}^{\infty} a_n^{(j)}(\mathbf{x}) \overline{u_i \cos n\omega t} + \sum_{n=1}^{\infty} b_n^{(j)}(\mathbf{x}) \overline{u_i \sin n\omega t} \tag{3.234}
\end{aligned}$$

where use has been made of the Fourier series expansion (3.210), and only the t -dependent quantities have remained inside the integral⁴⁹. An equivalent expression is obtained for $\overline{u_j \overleftarrow{u'_i}}$, and it is not repeated herein. Finally, the expression for $\overline{\overleftarrow{u'_i} \overleftarrow{u'_j}}$ is:

$$\begin{aligned}
\overline{\overleftarrow{u'_i} \overleftarrow{u'_j}}(\mathbf{x}) &= \overline{(\overset{\circ}{u}_i + \tilde{u}_i)(\overset{\circ}{u}_j + \tilde{u}_j)} = \overline{\overset{\circ}{u}_i \overset{\circ}{u}_j} + \overline{\overset{\circ}{u}_i \tilde{u}_j} + \overline{\tilde{u}_i \overset{\circ}{u}_j} + \overline{\tilde{u}_i \tilde{u}_j} = \\
&= \overset{\circ}{u}_i \overset{\circ}{u}_j + \overset{\circ}{u}_i \overline{\tilde{u}_j} + \overline{\tilde{u}_i} \overset{\circ}{u}_j + \overline{\tilde{u}_i \tilde{u}_j} = \overset{\circ}{u}_i \overset{\circ}{u}_j + \overline{\tilde{u}_i \tilde{u}_j} = \overset{\circ}{u}_i \overset{\circ}{u}_j + \frac{1}{2} \sum_{n=1}^{\infty} [a_n^{(i)} a_n^{(j)} + b_n^{(i)} b_n^{(j)}] \tag{3.235}
\end{aligned}$$

where $\overset{\circ}{u}_i$ can exit the time-integral because it does not depend on t , $\overline{\tilde{u}_i} = 0$, and use has been made of equation (3.232). To end with this proof the complete expression for the $\overline{u'_i u'_j}$ term is offered:

$$\begin{aligned}
\overline{u'_i u'_j}(\mathbf{x}) &= \overline{u_i u_j} - \overline{u_i} \overset{\circ}{u}_j - \sum_{n=1}^{\infty} a_n^{(j)} \overline{u_i \cos n\omega t} - \sum_{n=1}^{\infty} b_n^{(j)} \overline{u_i \sin n\omega t} - \\
&- \overline{u_j} \overset{\circ}{u}_i - \sum_{n=1}^{\infty} a_n^{(i)} \overline{u_j \cos n\omega t} - \sum_{n=1}^{\infty} b_n^{(i)} \overline{u_j \sin n\omega t} + \overset{\circ}{u}_i \overset{\circ}{u}_j + \frac{1}{2} \sum_{n=1}^{\infty} [a_n^{(i)} a_n^{(j)} + b_n^{(i)} b_n^{(j)}] \tag{3.236}
\end{aligned}$$

which is not identical to $\overline{\overleftarrow{u'_i} \overleftarrow{u'_j}} \equiv \overline{u'_i u'_j}$, and the results shown in [RH72] cannot be held without discussion.

The last step carried out by [RH72] is to subtract the time-averaged RANSE (3.227) from the phase-averaged RANSE (3.199). The result is shown next:

$$\partial_i \tilde{u}_i + \overset{\circ}{u}_j \partial_j \tilde{u}_i + \tilde{u}_j \partial_j \overset{\circ}{u}_i + \tilde{u}_j \partial_j \tilde{u}_i - \overline{\tilde{u}_j \partial_j \tilde{u}_i} = -\frac{1}{\rho} \partial_i \tilde{p} + \partial_j [\nu \partial_j \tilde{u}_i - \overline{u'_i u'_j}] + \tilde{\pi}_i \tag{3.237}$$

where

$$\overleftarrow{u'_i u'_j} - \overset{\circ}{u'_i u'_j} \equiv \overleftarrow{u'_i u'_j} - \overleftarrow{u'_i u'_j} \equiv \overline{u'_i u'_j}$$

because $\overleftarrow{u'_i u'_j}$ is a T -periodic function with dc component $\overset{\circ}{u'_i u'_j}$. Equation (3.237) is to be compared with (3.163). [RH72] calls the later the 'dynamical equations for the organized wave', and herein it will be called

⁴⁹Note that if u_i were a T -periodic function, then the integral of $u_i \cos n\omega t$ would be proportional to the coefficient $a_n^{(i)}$, and that of $u_i \sin n\omega t$ to $b_n^{(i)}$; but in general this is not the case.

the RANS oscillating equation. Before comparing both equations, some elaboration about the terms $\tilde{u}_j \partial_j \tilde{u}_i - \overline{\tilde{u}_j \partial_j \tilde{u}_i}$ is pertinent.

The continuity equation (3.198) makes possible the equalities (see equation (3.231)):

$$\tilde{u}_j \partial_j \tilde{u}_i = \partial_j (\tilde{u}_i \tilde{u}_j), \quad \overline{\tilde{u}_j \partial_j \tilde{u}_i} = \partial_j (\overline{\tilde{u}_i \tilde{u}_j})$$

But $\tilde{u}_i(t, \mathbf{x})$ is a T -periodic function of t , although without dc component. [Cor89] proves that the product of two T -periodic functions is also a T -periodic function. Thus, $\tilde{u}_i \tilde{u}_j$ is a T -periodic function, albeit with dc component, and it makes sense to write

$$\tilde{u}_i \tilde{u}_j - \overline{\tilde{u}_i \tilde{u}_j} \equiv \tilde{u}_i \tilde{u}_j - \overset{\circ}{\tilde{u}_i \tilde{u}_j} \equiv \widetilde{\tilde{u}_i \tilde{u}_j}$$

and the RANS oscillating equation (3.237) can be written with oscillating components $\widetilde{\tilde{u}_i \tilde{u}_j}$ and $\widetilde{u'_i u'_j}$ as:

$$\partial_t \tilde{u}_i + \overset{\circ}{u}_j \partial_j \tilde{u}_i + \tilde{u}_j \partial_j \overset{\circ}{u}_i = \partial_j \left[-\delta_{ij} \frac{\tilde{p}}{\rho} + \nu \partial_j \tilde{u}_i - \widetilde{\tilde{u}_i \tilde{u}_j} - \widetilde{u'_i u'_j} \right] + \tilde{\pi}_i \quad (3.238)$$

A remarkable feature about this equation is that only contains dc and oscillating components. Comparison of (3.238) with (3.163) reveals:

- The much repeated observation that $\overset{\circ}{u}_i$ is different from \overline{u}_i .
- The already pointed remark that \tilde{u}_i has a different meaning in equation (3.238) than it has in (3.163) and [RH72] (see page 126).
- (3.238) refers directly to the oscillating components of Reynolds stress-like quantities $\widetilde{\tilde{u}_i \tilde{u}_j}$ and $\widetilde{u'_i u'_j}$, thus enhancing the oscillating nature of this equation, whereas the (3.163) terms $\tilde{u}_i \tilde{u}_i - \overline{\tilde{u}_i \tilde{u}_i}$ and $\overleftarrow{u'_i u'_i} - \overline{u'_i u'_i}$ do not correspond to oscillating components.

The above does not imply, in any way, that the results published in [HR70] and [RH72] would need to be revised, nor those of the many authors who have chosen to follow the triple decomposition idea initiated therefrom, since those results correspond to physical flows whose turbulence fields appear to be sufficiently regular. The new formalism just proposes a new writing of equations, fully devoid of potential errors for those extreme cases that would not be foreseen in advance. Even then, a possible way out of this situation would occur when the fluctuating component be much smaller than the phase average one, $|u'_i| \ll |\overleftarrow{u'_i}|$ and $|p'| \ll |\overleftarrow{p'}|$. In that case, the following approximate results hold:

$$u_i = \overleftarrow{u'_i} + u'_i \approx \overleftarrow{u'_i}, \quad \overline{u}_i \approx \overleftarrow{\overline{u'_i}} \equiv \overset{\circ}{u}_i, \quad \tilde{u}_i \approx \overleftarrow{u'_i} - \overline{u}_i, \quad \widetilde{\tilde{u}_i} \approx \overleftarrow{\overline{u'_i}} - \overline{u}_i \approx 0 \quad (3.239)$$

and similar ones for p .

A T -potentially periodic field $\psi(t, \mathbf{x})$ verifying $|\psi'(t, \mathbf{x})| \ll |\overleftarrow{\psi'}(t, \mathbf{x})| \forall t \in \mathbb{R}$, except in a set of null measure, will be called a **T -quasi-periodic field**⁵⁰. Such field will fulfil a set of relations similar to (3.239), even for non-sufficiently regular functions. A flow whose fields are T -quasi-periodic will be called a **T -quasi-periodic flow**. T -quasi-periodic flows satisfy approximately the equations and results shown in [HR70] and [RH72]. The degree of approximation which would be deemed acceptable is application-dependent, and cannot be settled before-hand.

⁵⁰This concept is very similar to the definition of **almost periodic function** given in [Cor89]: if ψ is almost periodic, then it would be considered quasi-periodic in most applications.

3.3 The Filtering Approach (or LES method)

The averaging problem has already been thoroughly studied along this Chapter. RANS methods assume implicitly that the average is carried out over all scales of motion, and thus no scale separation is prescribed nor required. The fluctuating component stems directly from subtracting the mean to the physical field, and no scale affiliation ought to be attached to that component either. However, there is another approach to the natural trend of separating the slowly or long-range varying portion of any flow field $\psi(t, \mathbf{x})$ from the rapidly or short-range fluctuating part, which is not based on statistical grounds but, instead, on the filtering concept. The name of this section is borrowed from the reference [Ger92], who performed a bright attempt to bridge the statistical and the filtered representations of turbulence.

Filtered turbulence quantities $\underline{\psi}(t, \mathbf{x})$, defined as the convolution of the actual flow field $\psi(t, \mathbf{x})$ with a kernel or weighting function $G(t, \mathbf{x})$, have already been introduced in section 3.2.1.2, although in a different context and with another name. They also have been described in section 3.2.2, referring to them as an alternative averaging method, not yielding Reynolds operators. In both cases, the filter was defined under the scope of space or time averages, against which it was compared. Here the filter will be studied by itself, as an alternative method to produce a decomposition of the physical field into a slow changing component and a fluctuating and rapidly varying one, where *slow* and *rapid* refer not only to time but also to space dimensions.

The filtering approach is based upon the existence of a wide range of scales in any turbulent flow, and the possibility of separating those scales into bandwidths, and subject each one to a different mathematical treatment. It has little or no relationship to the statistical description of physical phenomena seen so far. The filter is associated with Hilbert space and the Fourier transform that permits the transit from one domain to another. This wide spectrum of scales will be considered continuous, although a discrete spectrum could also be described by using a generalised definition of integral.

The filter thus introduced is an operator, a functional, which acts on the turbulent field $\psi(t, \mathbf{x})$ producing a softened and smoothed version of itself $\underline{\psi}(t, \mathbf{x})$. This operator need not be, cannot be, a Reynolds operator, and the Filtered Navier-Stokes Equations (FNSE) it leads to will not be like RANSE, however similar they might seem at first sight. Filters do not enjoy the idempotent property, they do not commute with derivative, are highly dependent on the kernel function and produce different results with shifting filter widths. Instead, they are more *physical* than infinite time or space averages.

The above introduction justifies this new approach to the problem of turbulence representation: the methods, the language, the formalism, the scope, the results, are different from those already seen for the statistical representation of turbulence. However, the knowledge gained along the past sections of this Chapter will be an useful guide for what comes next.

The use of filters in turbulence representation is directly linked to the simulation of turbulent flows in CFD, specifically with the formalism known as Large Eddy Simulation (LES). The flow spatial domain Ω is divided into cells, constituting a mesh, and it is only natural to try to average (filter) the flow fields over each cell or group of cells. Following [BIL06], the strategy of filtering along the mesh might not be such a good idea, since the resulting model would not be rotationally invariant, the solution would be sensitive to mesh orientation and the problem of determining the convergence error will be difficult to deal with. Also, the resulting model would not be smooth, as it would be mesh dependent, and the ensuing FNSE might not even be deterministic.

It is, therefore, convenient to select filter kernels $G(t, \mathbf{x})$ that are rotationally symmetric, aside from the usual requirements of smoothness, integrability and convergence. This desirable feature renders

filters independent of the chosen mesh. Of course, for this approach to make sense, the mesh's typical size should be smaller than the filter's length scale. A similar reasoning ought to be applied to time: the filter's time scale should be larger than the time step employed in CFD calculations.

Let $G(t, \mathbf{x})$ be a filter kernel assumed smooth, integrable over \mathbb{R}^4 , rotationally symmetric and with the properties (see [BIL06])⁵¹:

$$0 \leq |G(t, \mathbf{x})| \leq 1, \quad G(0, \mathbf{0}) = 1, \quad \int_{\mathbb{R}^4} G(t, \mathbf{x}) dt d^3\mathbf{x} = 1 \quad (3.240)$$

The filter is said to be positive if $0 \leq G(t, \mathbf{x}) \leq 1 \forall (t, \mathbf{x}) \in \mathbb{R}^4$. Note the normalisation condition implies $G(t, \mathbf{x}) \rightarrow 0$ so long as any of the variables $t, x_i \rightarrow \pm\infty$.

Select a filter range or **width** given by $\square = (\Theta, \mathbf{\Delta}) \subset \mathbb{R}^4$, also called the filter's time and length scales, where $\Theta > 0$ is the time window and $\mathbf{\Delta} = (\Delta_1, \Delta_2, \Delta_3)$, $\Delta_i > 0$, the space extent over which the filter develops; and define

$$G(t, \mathbf{x}; \square) := \frac{1}{\Theta \mathbf{\Delta}^3} G\left(\frac{t}{\Theta}, \frac{\mathbf{x}}{\mathbf{\Delta}}\right) \quad (3.241)$$

with $\mathbf{\Delta}^3 := \Delta_1 \Delta_2 \Delta_3$ and $\frac{\mathbf{x}}{\mathbf{\Delta}} := \left(\frac{x_1}{\Delta_1}, \frac{x_2}{\Delta_2}, \frac{x_3}{\Delta_3}\right)$ ⁵². Note $G(t, \mathbf{x}; \square)$ thus defined also satisfies the normalisation condition:

$$\int_{\mathbb{R}^4} G(t, \mathbf{x}; \square) dt d^3\mathbf{x} = 1 \quad (3.242)$$

and therefore

$$\lim_{s \rightarrow \pm\infty} G(t, \mathbf{x}; \square) = 0 \quad (s = t, x_i) \quad (3.243)$$

Moreover, $G(t, \mathbf{x}; \square) \rightarrow 0$ very rapidly, typically $G(t, \mathbf{x}; \square) \ll 1$ for (t, \mathbf{x}) a few times $(\Theta, \mathbf{\Delta})$.

The filtered component $\underline{\psi}(t, \mathbf{x})$ of the field $\psi(t, \mathbf{x})$ is defined by the convolution⁵³ (see [Sag06])

$$\underline{\psi}(t, \mathbf{x}) := \psi(t, \mathbf{x}) \star G(t, \mathbf{x}; \square) = \int_{\mathbb{R}^4} G(t - t', \mathbf{x} - \mathbf{x}'; \square) \psi(t', \mathbf{x}') dt' d^3\mathbf{x}' \quad (3.244)$$

⁵¹To be fully rigorous, the kernel should depend on a dimensionally homogeneous set of variables $\boldsymbol{\varkappa} = (x_0, x_1, x_2, x_3)$, all with dimensions of length, being $x_0 = ct$ the 'time' variable with c a suitably chosen constant velocity scale. Thus, $G(\boldsymbol{\varkappa})$ would have dimensions of L^{-4} and the integral

$$\int_{\mathbb{R}^4} G(\boldsymbol{\varkappa}) d^4\boldsymbol{\varkappa} = 1$$

would be dimensionally flawless. Nevertheless, it is customary to write $G(t, \mathbf{x})$ for the filter kernel and this Dissertation will adhere to such custom.

⁵²Note the role played by each one of the three different length scales present in the filter and LES concepts: (i) **Kolmogorov length scale** η and time scale τ_η , that mark the bare minimum over which the filter approach makes sense when applied to turbulence phenomena. (ii) The **mesh size** δx_i and **time step** δt used in the CFD model, which characterises the desired level of approximation to the actual flow to be simulated. (iii) The **filter width** $\square = (\Theta, \mathbf{\Delta})$, which determines how far and how long is the smoothing process going to be executed for each space-time point (t, \mathbf{x}) . In the filtering approach introduced here, each spatial direction is allowed to have a different length scale Δ_i .

⁵³Although equation (3.244) appears to be formally identical to equation (3.48) defining the GSTA, there is an important difference: in the GSTA the integral extends to the whole volume actually occupied by the fluid (either $\psi(t, \mathbf{x})$ and/or $w(t, \mathbf{x})$ are functions of compact support), whereas in (3.244) the integral practically extends only a few times beyond the filter width \square .

The filter width $\square = (\Theta, \Delta)$ is chosen according to the extent over which the filter is expected to develop and execute its effects on the physical field $\psi(t, \mathbf{x})$. As a minimum, it should be selected no smaller than the foreseeable time step and mesh-cell size in the CFD. Note that neither Θ nor Δ depend on (t, \mathbf{x}) , that is, they are supposed to be constant throughout the flow. \square is defined such that

$$\left| \frac{G(t_2, \mathbf{x}_2; \square)}{G(t_1, \mathbf{x}_1; \square)} \right| \ll 1 \quad \text{for} \quad |t_1| < \frac{\Theta}{2}, \quad |x_{1i}| < \frac{\Delta_i}{2} \quad \text{and} \quad |t_2| > \frac{\Theta}{2}, \quad |x_{2i}| > \frac{\Delta_i}{2} \quad (3.245)$$

In other words, the function G takes negligible values outside the filter width \square , much smaller than those acquired within \square .

In order for a filter to be applicable to turbulent flows, its kernel must depend on the difference $(t-t', \mathbf{x}-\mathbf{x}')$, instead of the actual space-time points (t, \mathbf{x}) and (t', \mathbf{x}') . This requirement is not necessary for a general filter, but it will be demanded for filters representing turbulence fields, since $\psi(t, \mathbf{x})$ is defined as the convolution of two fields.

A valid filter for a turbulence field $\psi(t, \mathbf{x})$ is such that the integral (3.244) verifies

$$\int_{\mathbb{R}^4} G(t-t', \mathbf{x}-\mathbf{x}'; \square) \psi(t', \mathbf{x}') dt' d^3\mathbf{x}' \approx \int_{\square} G(t-t', \mathbf{x}-\mathbf{x}'; \square) \psi(t', \mathbf{x}') dt' d^3\mathbf{x}' \quad (3.246)$$

where the last integral means:

$$\int_{\square} dt' d^3\mathbf{x}' := \int_{\Theta} \int_{\Delta} dt' d^3\mathbf{x}' = \int_{t-\frac{\Theta}{2}}^{t+\frac{\Theta}{2}} \int_{x_1-\frac{\Delta_1}{2}}^{x_1+\frac{\Delta_1}{2}} \int_{x_2-\frac{\Delta_2}{2}}^{x_2+\frac{\Delta_2}{2}} \int_{x_3-\frac{\Delta_3}{2}}^{x_3+\frac{\Delta_3}{2}} dt' dx'_1 dx'_2 dx'_3 \quad (3.247)$$

Condition (3.246) is a consequence of (3.245), because the integrand turns negligible outside the filter width \square .

In \mathbb{R}^4 the Fourier transform and its inverse are defined as:

$$\mathcal{F}(\psi) \equiv \hat{\psi}(\omega, \boldsymbol{\kappa}) := \int_{-\infty}^{+\infty} \int_{-\infty}^{+\infty} \int_{-\infty}^{+\infty} \int_{-\infty}^{+\infty} \psi(t, \mathbf{x}) e^{-i(\omega t + \boldsymbol{\kappa} \cdot \mathbf{x})} dt d^3\mathbf{x} \quad (3.248)$$

$$\mathcal{F}^{-1}(\hat{\psi}) \equiv \psi(t, \mathbf{x}) := \frac{1}{(2\pi)^4} \int_{-\infty}^{+\infty} \int_{-\infty}^{+\infty} \int_{-\infty}^{+\infty} \int_{-\infty}^{+\infty} \hat{\psi}(\omega, \boldsymbol{\kappa}) e^{i(\omega t + \boldsymbol{\kappa} \cdot \mathbf{x})} d\omega d^3\boldsymbol{\kappa} \quad (3.249)$$

with

$$\omega = \frac{2\pi}{\tau}$$

the angular frequency, with τ the period of the harmonic, and

$$\kappa_i = \frac{2\pi}{\lambda_i} \quad \equiv \quad \boldsymbol{\kappa} := \frac{2\pi}{\boldsymbol{\lambda}}$$

the spatial frequency or **wavenumber**, with λ_i the wavelength of the harmonic in the i^{th} direction, $\boldsymbol{\kappa} = (\kappa_1, \kappa_2, \kappa_3)$, $\boldsymbol{\lambda} = (\lambda_1, \lambda_2, \lambda_3)$.

The filter width $\square = (\Theta, \Delta)$ in physical space (t, \mathbf{x}) originates in Fourier space $(\omega, \boldsymbol{\kappa})$ (also called spectral space) the associated **cut-off wavenumber** and **frequency** given by:

$$\kappa_{c_i} = \frac{2\pi}{\Delta_i} \quad \equiv \quad \boldsymbol{\kappa}_c := \frac{2\pi}{\Delta} \quad (3.250)$$

$$\omega_c = \frac{2\pi}{\Theta} \quad (3.251)$$

The filter leaves rather unaffected the Fourier components with wavenumbers $|\boldsymbol{\kappa}| < |\boldsymbol{\kappa}_c|$ and frequencies $\omega < \omega_c$ for each turbulent flow field $\hat{\psi}(\omega, \boldsymbol{\kappa})$, and greatly attenuates the remaining wavenumber and frequency components.

In Fourier space $(\omega, \boldsymbol{\kappa})$ the definition (3.244) adopts the simple form:

$$\hat{\psi}(\omega, \boldsymbol{\kappa}) = \hat{\psi}(\omega, \boldsymbol{\kappa}) \hat{G}(\omega, \boldsymbol{\kappa}; \square) \quad (3.252)$$

since the Fourier transform of the convolution is the simple product of transformed functions, with $\hat{G}(\omega, \boldsymbol{\kappa}; \square)$ the Fourier transform of the kernel function $G(t, \mathbf{x}; \square)$.

Some kernel functions frequently used in the filter formalism are:

- The boxcar filter, already introduced in equations (3.100), (3.106), with its Fourier transform:⁵⁴

$$G(t, \mathbf{x}; \square) = \begin{cases} 0 & \text{if } |t| > \Theta/2 \text{ or } |x_i| > \Delta_i/2 \\ \frac{1}{2^4 \Theta \Delta^3} & \text{if } |t| = \Theta/2 \text{ and } |x_i| = \Delta_i/2 \quad (i = 1, 2, 3) \\ \frac{1}{2^n \Theta \Delta^3} & \text{if } n \text{ variables on border and } 4 - n \text{ inside } (0 \leq n \leq 4) \\ \frac{1}{\Theta \Delta^3} & \text{if } |t| < \Theta/2 \text{ and } |x_i| < \Delta_i/2 \end{cases} \quad (3.253)$$

$$\hat{G}(\omega, \boldsymbol{\kappa}; \square) = \frac{\sin(\omega\Theta/2)}{\omega\Theta/2} \frac{\sin(\kappa_1\Delta_1/2)}{\kappa_1\Delta_1/2} \frac{\sin(\kappa_2\Delta_2/2)}{\kappa_2\Delta_2/2} \frac{\sin(\kappa_3\Delta_3/2)}{\kappa_3\Delta_3/2} \quad (3.254)$$

with $\Delta^3 := \Delta_1\Delta_2\Delta_3$. The boxcar filter is related to the sinc function in Fourier space $(\omega, \boldsymbol{\kappa})$.

- The ideal low pass filter, given by the reciprocal of the boxcar filter, shows the sinc function in ordinary space-time:

$$G(t, \mathbf{x}; \square) = \frac{\sin(2\pi t/\Theta)}{\pi t} \frac{\sin(2\pi x_1/\Delta_1)}{\pi x_1} \frac{\sin(2\pi x_2/\Delta_2)}{\pi x_2} \frac{\sin(2\pi x_3/\Delta_3)}{\pi x_3} \quad (3.255)$$

$$\hat{G}(\omega, \boldsymbol{\kappa}; \square) = \begin{cases} 0 & \text{if } |\omega| > 2\pi/\Theta \text{ or } |\kappa_i| > 2\pi/\Delta_i \\ \frac{1}{2^4} & \text{if } |\omega| = 2\pi/\Theta \text{ and } |\kappa_i| = 2\pi/\Delta_i \quad (i = 1, 2, 3) \\ \frac{1}{2^n} & \text{if } n \text{ variables on border and } 4 - n \text{ inside } (0 \leq n \leq 4) \\ 1 & \text{if } |\omega| < 2\pi/\Theta \text{ and } |\kappa_i| < 2\pi/\Delta_i \end{cases} \quad (3.256)$$

The ideal low pass filter has the convenient property of being idempotent in Fourier space $(\omega, \boldsymbol{\kappa})$, that is, the n -repeated applications of the filter yields the same result as the single application:

$$\hat{G} \cdot \hat{G} \dots \hat{G} = \hat{G}^n = \hat{G}$$

Unfortunately, this filter is not realisable in practice, since it carries the burden of being *ideal*.

⁵⁴In equation (3.253) in the first case at least one variable (t, x_1, x_2, x_3) is outside of the range defined by \square , in the second case all variables are on the border $|t| = \Theta/2$ and $|x_i| = \Delta_i/2$, in the third case $0 \leq n \leq 4$ variables are on the border and $4 - n$ are inside \square , and in the fourth case all variables are inside \square , defined by $|t| < \Theta/2$ and $|x_i| < \Delta_i/2$. In equation and (3.256) replace (t, \mathbf{x}) for $(\omega, \boldsymbol{\kappa})$.

- The Gaussian filter in space-time with its Fourier transform

$$G(t, \mathbf{x}; \square) = \frac{\gamma_t^{\frac{1}{2}} \gamma_x^{\frac{3}{2}}}{\pi^2 \Theta \Delta^3} e^{-\left[\frac{\gamma_t t^2}{\Theta^2} + \gamma_x \delta_{ij} \frac{x_i x_j}{\Delta_i \Delta_j} \right]} = \frac{\gamma_t^{\frac{1}{2}} \gamma_x^{\frac{3}{2}}}{\pi^2 \Theta \Delta^3} e^{-\xi_\alpha \xi_\alpha} \quad (\alpha = 0, 1, 2, 3) \quad (3.257)$$

$$\hat{G}(\omega, \boldsymbol{\kappa}; \square) = e^{-\left[\frac{\Theta^2 \omega^2}{4\gamma_t} + \frac{\kappa_i \kappa_j \Delta_i \Delta_j}{4\gamma_x} \right]} = e^{-\varsigma_\alpha \varsigma_\alpha} \quad (\alpha = 0, 1, 2, 3) \quad (3.258)$$

where

$$\xi_0 = \frac{\sqrt{\gamma_t} t}{\Theta}, \quad \xi_i = \frac{\sqrt{\gamma_x} x_i}{\Delta_i} \quad (i = 1, 2, 3)$$

$$\varsigma_0 = \frac{\omega \Theta}{2\sqrt{\gamma_t}}, \quad \varsigma_i = \frac{\kappa_i \Delta_i}{2\sqrt{\gamma_x}} \quad (i = 1, 2, 3)$$

and $\gamma_t > 0$, $\gamma_x > 0$ are known as the **shape parameter** for time and space, respectively⁵⁵. The Gaussian filter decays so rapidly that, provided $\gamma_t, \gamma_x \geq 6$, it is negligible outside the range

$$[-\Theta, \Theta] \times [-\Delta_1, \Delta_1] \times [-\Delta_2, \Delta_2] \times [-\Delta_3, \Delta_3] \equiv [-\Theta, \Theta] \times [-\boldsymbol{\Delta}, \boldsymbol{\Delta}] \equiv [-\square, \square]$$

for physical space-time (t, \mathbf{x}) , and

$$\left[-\frac{2\pi}{\Theta}, \frac{2\pi}{\Theta} \right] \times \left[-\frac{2\pi}{\Delta_1}, \frac{2\pi}{\Delta_1} \right] \times \left[-\frac{2\pi}{\Delta_2}, \frac{2\pi}{\Delta_2} \right] \times \left[-\frac{2\pi}{\Delta_3}, \frac{2\pi}{\Delta_3} \right] \equiv \left[-\frac{2\pi}{\Theta}, \frac{2\pi}{\Theta} \right] \times \left[-\frac{2\pi}{\boldsymbol{\Delta}}, \frac{2\pi}{\boldsymbol{\Delta}} \right] \equiv \left[-\frac{2\pi}{\square}, \frac{2\pi}{\square} \right]$$

for Fourier space $(\omega, \boldsymbol{\kappa})$.

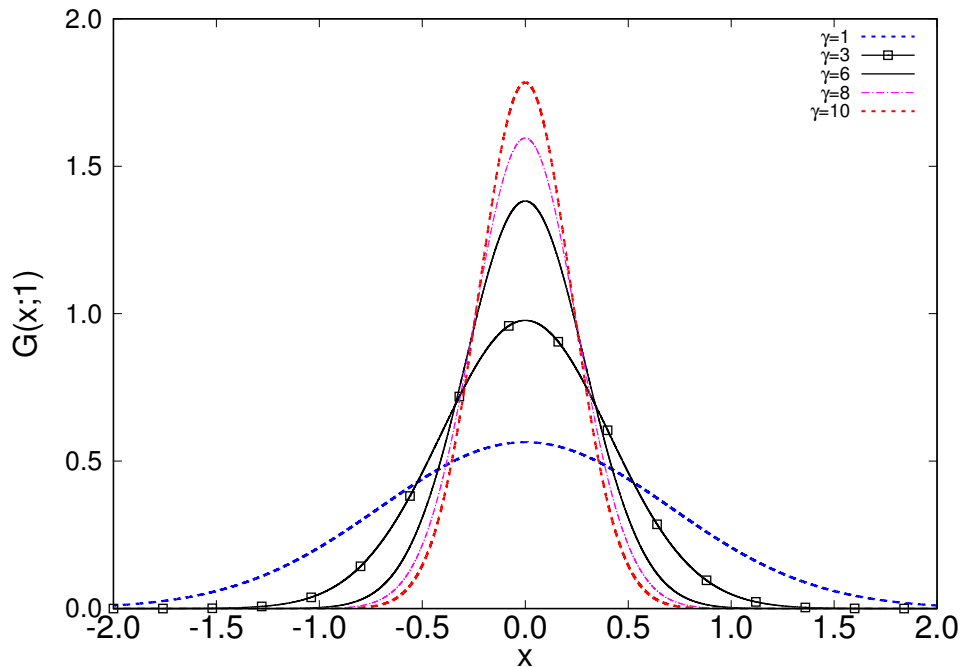


Figure 3.10: Gaussian filter $G(x;1)$ for different values of the shape parameter.

Figure 3.10 shows the one-dimensional Gaussian filter for $\Delta = 1$ and different values of the shape parameter γ . Note that for $\gamma \geq 6$ the filter is almost zero for $|x| \geq \Delta$, while for $\gamma = 1$ the filter still has a relatively high value at $|x| = \Delta$.

⁵⁵ The space shape parameter is frequently taken as $\gamma_x = 6$, because it is the integer most approximate to 2π . The time shape parameter is rarely used, since most simulations are carried out in the framework of LES, where the time filtering is seldom called for. It is also recommended to bestow the value $\gamma_t = 6$ to it.

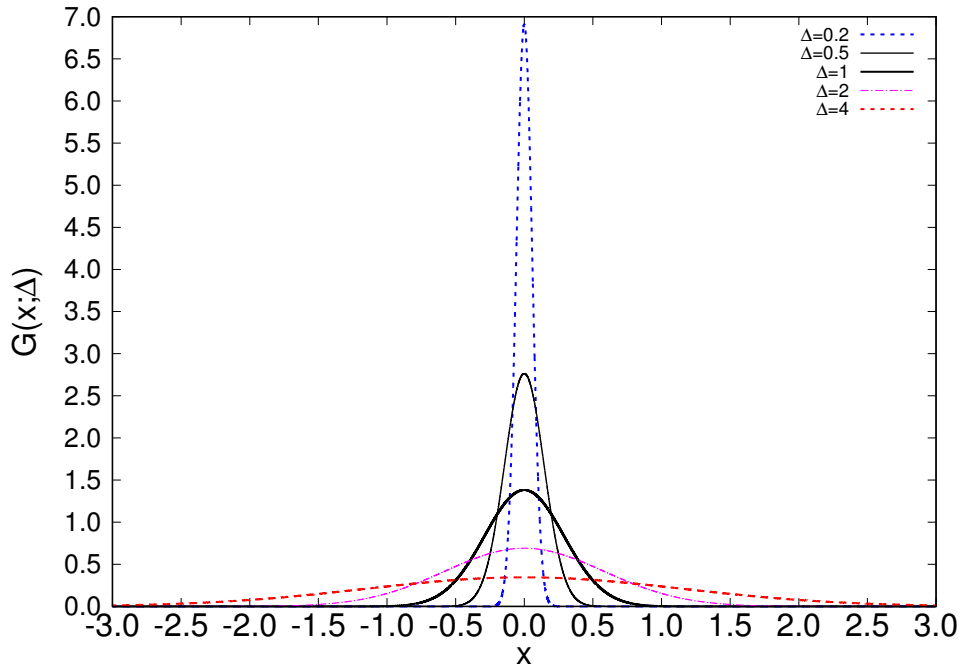


Figure 3.11: Gaussian filter $G(x; \Delta)$ for different values of the filter width Δ , $\gamma = 6$.

Figure 3.11 shows the one-dimensional Gaussian filter for $\gamma = 6$ and different values of the filter width Δ . Note that, in any case, the filter is almost zero for $|x| \geq \Delta$. With $\Delta \leq 0.1$ the filter gets extremely peaky, and starts resembling the Dirac's delta $\delta(x)$.

According to the filter approach, any flow field $\psi(t, \mathbf{x})$ can be decomposed into two components

$$\psi(t, \mathbf{x}) = \underline{\psi}(t, \mathbf{x}) + \psi'(t, \mathbf{x}) \quad (3.259)$$

It receives the name of the **filter decomposition**. The filtered component $\underline{\psi}(t, \mathbf{x})$ is also called the **filtered field** or the **resolved part** of the physical field $\psi(t, \mathbf{x})$, while the fluctuating component $\psi'(t, \mathbf{x})$ is also named the **fluctuating field** or the **unresolved part**. This nomenclature stems from LES formalism. Again, as it was highlighted during the introduction of the Reynolds decomposition (see section 3.2), the unresolved component could be defined as *'whatever is left from the physical field after the filtered component has been removed'*. The difference now, with respect to Reynolds decomposition, being that ψ' depends not only on the type of filter, but also on the filter width \square ; that is, customisable ψ' are feasible. This possibility does not exist in Reynolds decomposition: the fluctuating component is linked to the averaging method, and once such average is chosen ψ' is fixed. Besides, in this new context ψ' possesses some other different properties than it has in the statistical case. To start with, the idempotent property is lost, $\underline{\psi}' \neq 0$, and it is non-zero even in an ideal case.

Note that from equations (3.244) and (3.252), the unresolved component $\psi'(t, \mathbf{x})$ could be expressed as

$$\psi'(t, \mathbf{x}) = (1 - G(t, \mathbf{x}; \square)) \star \psi(t, \mathbf{x}) \quad , \quad \hat{\psi}'(\omega, \boldsymbol{\kappa}) = \left(1 - \hat{G}(\omega, \boldsymbol{\kappa}; \square)\right) \hat{\psi}(\omega, \boldsymbol{\kappa}) \quad (3.260)$$

The filter decomposition brings about the possibility of obtaining Filtered Navier-Stokes Equations (FNSE), in a similar fashion as Reynolds decomposition enacts the RANSE. The conditions demanded to filter operators $\underline{\cdot}$ to produce FNSE are somewhat simpler than those applied to Reynolds operator:

- LINEARITY

$$\underline{(a\psi + b\phi)}(t, \mathbf{x}) = a\underline{\psi}(t, \mathbf{x}) + b\underline{\phi}(t, \mathbf{x}) \quad a, b \in \mathbb{R} \quad (3.261)$$

This property is automatically fulfilled, since the integral defining the convolution is linear. Note also that, through normalisation condition (3.242), constants are conserved in a filter operation:

$$\underline{a} = a \quad a \in \mathbb{R}$$

This result trivially follows with $\psi(t, \mathbf{x}) = \delta(t)\delta(\mathbf{x})$ (Dirac's delta) and $\phi = 0$ in equation (3.261).

• COMMUTATION WITH DERIVATION

$$\frac{\partial \psi}{\partial \underline{s}} = \frac{\partial \psi}{\partial s} \quad (s = t, x_i) \quad (3.262)$$

The demonstration of this condition follows:

$$\begin{aligned} \partial_s \underline{\psi} &= \partial_s \int_{\mathbb{R}^4} G(t - t', \mathbf{x} - \mathbf{x}'; \square) \psi(t', \mathbf{x}') dt' d^3 \mathbf{x}' = \int_{\mathbb{R}^4} \partial_s G(t - t', \mathbf{x} - \mathbf{x}'; \square) \psi(t', \mathbf{x}') dt' d^3 \mathbf{x}' = \\ &= - \int_{\mathbb{R}^4} \partial_{s'} G(t - t', \mathbf{x} - \mathbf{x}'; \square) \psi(t', \mathbf{x}') dt' d^3 \mathbf{x}' = - G(t - t', \mathbf{x} - \mathbf{x}'; \square) \psi(t', \mathbf{x}') \Big]_{s'=-\infty}^{s'+\infty} + \\ &\quad + \int_{\mathbb{R}^4} G(t - t', \mathbf{x} - \mathbf{x}'; \square) \partial_{s'} \psi(t', \mathbf{x}') dt' d^3 \mathbf{x}' = \underline{\partial_s \psi} \end{aligned} \quad (3.263)$$

where the derivative ∂_s enters the integral because the limits do not depend upon s , and use has been made of $\partial_s G(t - t', \mathbf{x} - \mathbf{x}'; \square) = -\partial_{s'} G(t - t', \mathbf{x} - \mathbf{x}'; \square)$, and the resulting integral has been solved by parts, and the condition (3.243) has been applied to zero the product $G(t - t', \mathbf{x} - \mathbf{x}'; \square) \psi(t', \mathbf{x}') \Big]_{s'=-\infty}^{s'+\infty} = 0$, for $s' = t', x_i$ ⁵⁶.

Note that commutation with derivation is not satisfied if s' is not allowed to extend to infinite, that is, $G(t - t', \mathbf{x} - \mathbf{x}'; \square) \psi(t', \mathbf{x}') \Big]_a^b \neq 0$ if $a \neq -\infty$ or $b \neq +\infty$. This formally happens when any boundary of the flow is not at infinity, or when boundaries are not periodic. Later in this section, it will be discussed how points (t, \mathbf{x}) farther inside from the boundaries than a few times (Θ, Δ) , render the product $G(t - t', \mathbf{x} - \mathbf{x}'; \square) \psi(t', \mathbf{x}')$ almost zero. However, in general the condition of commutation with derivatives is not universal with filters, and in particular is not satisfied in the neighbourhood of flow boundaries.

For the moment, assume the flow conditions are such that the commutation of filter with derivative applies. Next, the FNSE will be obtained under this assumption. For convenience, the **conservation**

⁵⁶For this derivation holds the nomenclature $\partial_s \equiv \partial/\partial s$, $\partial_{s'} \equiv \partial/\partial s'$, and use is being made of Fubini's theorem, and the following meaning is given to the expression appearing in the integration by parts (e.g. for $s' = x'_1$):

$$\begin{aligned} &G(t - t', \mathbf{x} - \mathbf{x}'; \square) \psi(t', \mathbf{x}') \Big]_{x'_1=-\infty}^{x'_1=+\infty} \equiv \\ &\equiv \int_{t'=-\infty}^{t'+\infty} \int_{x'_2=-\infty}^{x'_2=+\infty} \int_{x'_3=-\infty}^{x'_3=+\infty} G(t - t', -\infty, x_2 - x'_2, x_3 - x'_3; \square) \psi(t', \infty, x'_2, x'_3) dt' dx'_2 dx'_3 - \\ &- \int_{t'=-\infty}^{t'+\infty} \int_{x'_2=-\infty}^{x'_2=+\infty} \int_{x'_3=-\infty}^{x'_3=+\infty} G(t - t', +\infty, x_2 - x'_2, x_3 - x'_3; \square) \psi(t', -\infty, x'_2, x'_3) dt' dx'_2 dx'_3 \end{aligned} \quad (3.264)$$

and similar results for $s' = t', x'_2, x'_3$. Note that no integration is carried out on x'_1 in these integrals.

form of Navier-Stokes equations will be used, namely⁵⁷

$$\partial_t u_i + \partial_j (u_i u_j) = -\frac{1}{\rho} \partial_i p + \partial_j [\nu (\partial_j u_i + \partial_i u_j)] + g_i \quad (3.265)$$

together with the continuity equation

$$\partial_i u_i = 0 \quad (3.266)$$

Every term in these equations will be filtered through convolution with a kernel $G(t, \mathbf{x}; \square)$. The flow fields u_i and p admit the filter decomposition⁵⁸

$$u_i(t, \mathbf{x}) = \underline{u}_i(t, \mathbf{x}) + u'_i(t, \mathbf{x}) \equiv U_i(t, \mathbf{x}) + u'_i(t, \mathbf{x}) \quad (3.267)$$

$$p(t, \mathbf{x}) = \underline{p}(t, \mathbf{x}) + p'(t, \mathbf{x}) \equiv P(t, \mathbf{x}) + p'(t, \mathbf{x}) \quad (3.268)$$

In terms of those components, the following FNSE are obtained:

$$\partial_t U_i + \partial_j (\underline{u}_i \underline{u}_j) = -\frac{1}{\rho} \partial_i P + \partial_j [\nu (\partial_j U_i + \partial_i U_j)] + \underline{g}_i \quad (3.269)$$

$$\partial_i U_i = 0 \quad (3.270)$$

If g_i is the gravity acceleration then $\underline{g}_i = g_i$, since the filter operator conserves the constants. One cannot help noticing the outstanding non-linear term $\underline{u}_i \underline{u}_j$, wherefrom the closure problem is arisen (see below).

It is very instructive to express these equations in Fourier space, with

$$\hat{U}_i(\omega, \boldsymbol{\kappa}) = \hat{G}(\omega, \boldsymbol{\kappa}) \hat{u}_i(\omega, \boldsymbol{\kappa}) \quad , \quad \hat{P}(\omega, \boldsymbol{\kappa}) = \hat{G}(\omega, \boldsymbol{\kappa}) \hat{p}(\omega, \boldsymbol{\kappa}) \quad (3.271)$$

The continuity equation (3.266) in Fourier space offers the first interesting piece of information:

$$\boldsymbol{\kappa} \cdot \hat{\mathbf{u}}(\omega, \boldsymbol{\kappa}) = 0 \quad (3.272)$$

The filtered version of this equation, which is (3.270) in Fourier space, adopts the form:

$$\boldsymbol{\kappa} \cdot \hat{\mathbf{U}}(\omega, \boldsymbol{\kappa}) = \boldsymbol{\kappa} \cdot \hat{G}(\omega, \boldsymbol{\kappa}) \hat{\mathbf{u}}(\omega, \boldsymbol{\kappa}) = 0 \quad (3.273)$$

From equation (3.272) it is clear that, for any point $(\omega, \boldsymbol{\kappa})$ in Fourier space, the set of solutions $\hat{\mathbf{u}}(\omega, \boldsymbol{\kappa})$ to the FNSE form a subspace orthogonal to $\boldsymbol{\kappa}$. Whatever the evolution of $\hat{\mathbf{u}}$ along the flow, it will be immersed in such orthogonal space. This leads to think that $\hat{\mathbf{u}}(\omega, \boldsymbol{\kappa})$ could be somehow expressed as

$$\hat{\mathbf{u}}(\omega, \boldsymbol{\kappa}) = \boldsymbol{\kappa} \wedge \hat{\mathbf{u}}(\omega, \boldsymbol{\kappa})$$

with $\hat{\mathbf{u}}(\omega, \boldsymbol{\kappa})$ an arbitrary function of $(\omega, \boldsymbol{\kappa})$.

⁵⁷The incompressible Navier-Stokes equations accept two equivalent formulations, the most frequently found in textbooks (3.35), called the **convective form**, and (3.265), known as the conservation or **conservative form**. As stated, both forms are equivalent for incompressible flow, since

$$\nabla \cdot \mathbf{u} = 0 \Rightarrow (\mathbf{u} \cdot \nabla) \mathbf{u} = \nabla \cdot (\mathbf{u} \otimes \mathbf{u})$$

However, upon discretising the Navier-Stokes equations in CFD simulations, the results are slightly different due to discretisation errors.

⁵⁸In this section the capital letter indicates the filtered field, $U_i \equiv \underline{u}_i$, $P \equiv \underline{p}$.

Even more interesting is the effect of the filter on the Fourier transformed field $\hat{\mathbf{u}}(\omega, \boldsymbol{\kappa})$. Equation (3.273) leads to think that, regardless of the action of the filter on the flow field, the filtered field $\hat{\mathbf{U}}(\omega, \boldsymbol{\kappa})$ will still be immersed in the subspace orthogonal to $\boldsymbol{\kappa}$. Moreover, since the filtered field could also be expressed as:

$$\hat{\mathbf{U}}(\omega, \boldsymbol{\kappa}) = \boldsymbol{\kappa} \wedge \hat{\mathbf{U}}(\omega, \boldsymbol{\kappa})$$

this, in turn, implies that the action of the filter is exerted only over the function $\hat{\mathbf{u}}(\omega, \boldsymbol{\kappa})$, leaving untouched the $\boldsymbol{\kappa} \wedge$ portion (or, at least, the filter does not change the direction of $\boldsymbol{\kappa}$). Thus, the filter does not change the property of the set of solutions of Navier-Stokes equations to be orthogonal to $\boldsymbol{\kappa}$ for each point $(\omega, \boldsymbol{\kappa})$ in Fourier space and, therefore, it could be stated that this orthogonal space is **invariant** under the FNSE operation.

From equation (3.269) follows the Fourier space version of the FNSE ⁵⁹

$$i\omega \hat{U}_i + \nu \kappa_j \widehat{u_i u_j} = -\frac{\nu \kappa_i}{\rho} \hat{P} - \kappa^2 \nu \hat{U}_i + \hat{g}_i \quad (3.274)$$

Should it not be for the awkward term $\widehat{u_i u_j}$, it would have been a relatively simple algebraic functional equation in Fourier space. Just like in the RANSE case, the convective non-linear term produces an odd field requesting special attention: be it $\langle u'_i u'_j \rangle$, $\widehat{u_i u_j}$ or $\widehat{u_i u_j}$, the closure problem readily manifests itself upon manipulation of Navier-Stokes equations.

However, in the statistical representation of turbulence the averages are Reynolds operators, which at least have the added benefit of splitting the average of the product:

$$\langle u_i u_j \rangle = \langle u_i \rangle \langle u_j \rangle + \langle u'_i u'_j \rangle \quad (3.275)$$

leaving only the Reynolds stress term $\langle u'_i u'_j \rangle$ subjected to modelling, be it the Boussinesq's hypothesis or any other assumption. But filters are not Reynolds operators and do not enjoy such property. There is no unique way to deal with $u_i u_j$ or $\widehat{u_i u_j}$. Actually, the response to this stalemate depends on whether the respondent is a Mathematician, a Physicist or an Engineer, and the order is not meant to be casual. The most general form to express the offending term in physical space-time is obtained from the filter decomposition (3.267):

$$\widehat{u_i u_j} = \widehat{(U_i + u'_i)(U_j + u'_j)} = \widehat{U_i U_j} + \widehat{U_i u'_j} + \widehat{U_j u'_i} + \widehat{u'_i u'_j} \quad (3.276)$$

because the filter is a lineal operator. Since the filter operator is not idempotent, no one of the four terms in (3.276) can be expressed as separated products of U_i and u'_j . Therefore, it is necessary to bring forth three Boussinesq-like hypothesis to account for each one of the possible types of products, $\widehat{U_i U_j}$, $\widehat{U_i u'_j}$ and $\widehat{u'_i u'_j}$. Last, but not least, the situation gets even worse since each term depends on the particular filter selected. This dependence is made explicit upon re-writing the FNSE in Fourier space (gravity is omitted)

$$(i\omega + \kappa^2 \nu) \hat{G}(\omega, \boldsymbol{\kappa}) \hat{u}_i + \nu \kappa_j \hat{G}(\omega, \boldsymbol{\kappa}) (\widehat{u_i u_j}) = -\frac{\nu \kappa_i}{\rho} \hat{G}(\omega, \boldsymbol{\kappa}) \hat{p} \quad (3.277)$$

In conclusion, U_i , u'_i and all possible products of both are filter-dependent and not expressible as separated products of U_i . In a sense, the situation is like some sort of magnified closure problem, compared to the RANS case.

⁵⁹If g_i is constant, like the gravity acceleration, then $\hat{g}_i = (2\pi)^4 g_i \delta(\omega) \delta(\boldsymbol{\kappa})$.

The conventional treatment for the $\underline{u}_i \underline{u}_j$ problem is to assume it can be expressed as (see [Leo74])

$$\underline{u}_i \underline{u}_j = \tau_{ij}^r + \underline{u}_i \underline{u}_j \equiv \tau_{ij}^r + U_i U_j \quad (3.278)$$

where $\rho \tau_{ij}^r$ is called the **residual stress tensor**, and is supposed to encompass and summarise the difference between $\underline{u}_i \underline{u}_j$ and $\underline{u}_i \underline{u}_j$. According to this decomposition, the FNSE now become

$$\partial_t U_i + \partial_j (U_i U_j) = -\frac{1}{\rho} \partial_i P + \partial_j [\nu (\partial_j U_i + \partial_i U_j)] - \partial_j \tau_{ij}^r + \underline{g}_i \quad (3.279)$$

The interpretation of τ_{ij}^r as a function of the terms appearing in (3.276) is beyond the scope of this Dissertation, and can be found in [Leo74] and [Sag06]. The relevant point herein is the presence of a mathematical artefact depending, among other factors, on the unresolved components u'_i , which could be modelled in a similar fashion as the Reynolds stress tensor through a **subgrid-scale viscosity** ν_s , as

$$\tau_{ij}^r = -\nu_s (\partial_i \underline{u}_j + \partial_j \underline{u}_i) \equiv -\nu_s (\partial_i U_j + \partial_j U_i) \quad (3.280)$$

with ν_s depending on u'_i , \underline{u}'_i , U_i and a complicated blend of filtered products of those fields. With the help of the subgrid-scale viscosity ν_s the FNSE adopt the form

$$\partial_t U_i + \partial_j (U_i U_j) = -\frac{1}{\rho} \partial_i P + \partial_j [(\nu + \nu_s) (\partial_j U_i + \partial_i U_j)] + \underline{g}_i \quad (3.281)$$

which is formally identical to the RANSE with Boussinesq's hypothesis (3.43), although the meaning of every quantity be different for each case, except ν and ρ , and possibly \underline{g}_i . Besides, as in the case of the statistical RANS approach to turbulence, the complexity of the closure problem is translated to the knowledge of a single quantity, ν_s . Whether this strategy would work for actual industry applications, depends on the ability of the practising Engineer to find an accurate enough model for ν_s in each particular problem.

Remains to say that Reynolds stress tensor has a clearer physical meaning than the residual stress tensor, which is a much more complicated and obscure quantity that can be decomposed into three other types of stresses (see [Leo74] or [Sag06]). Boussinesq's hypothesis might not be true, but it is not entirely false either. There is nothing alike for the residual stress tensor, which to present day lacks of a similar universally accepted hypothesis. ■

Note that in the limit $\square \rightarrow 0$ then $u'_i(t, \mathbf{x}) \rightarrow 0$, and the resolved component $U_i(t, \mathbf{x})$ coincides with the physical field $u_i(t, \mathbf{x})$. This limit occurs in the formalism called Direct Numerical Simulation (DNS), which leaves no unresolved portion of the flow field (always provided the mesh is fine enough). The relevant point herein is that, by selecting \square , one chooses the importance of u'_i relative to U_i . If \square is small enough then so would be u'_i , and the **problem of closure** would be reduced to that of determining the effect of small quantities upon large ones, which is a problem prone to have approximate solutions. This flexibility does not exist in the strict Reynolds decomposition formalism: for a given type of average it is not possible to have *à la carte* Reynolds stresses in RANSE. On the other hand, the filter formalism is mathematically more complex, since it depends upon the chosen kernel function form, the filter width \square , and the ability to bring Fourier transforms (and complex numbers) into CFD.

The filter does not represent so a radical approach to the turbulence representation problem as the average. Except in the case of ensemble average,⁶⁰ the statistical approach offers a mean field which has very little information in it, and sends most of the dynamics to the fluctuating component, which is rich in information. RANSE deal with mean fields almost devoid of Physics, and the most interesting behaviour is carried in the fluctuating fields, for which there is no equation. Reynolds operators routinely used in turbulence studies remove far more information from the physical fields than would be desirable. This hideout of the dynamics does not occur with the filter approach. The filter decomposition is not so clear-cut as the Reynolds decomposition, it is more physically realisable and less an ideal representation, although the residual stress tensor stands as a rather arbitrary mathematical artefact. Filters occur spontaneously in nature, whereas averages in the Reynolds sense are seldom present. Filters assume the turbulence phenomena to be deterministic, and do not attempt to picture the flow quantities as random fields. In the realm of turbulence filtering means *just removing the higher part of the spectrum*.

Since \cdot is not a Reynolds operator, its application over the Navier-Stokes equations will not yield RANSE. The turbulence researcher faces a dilemma: relatively simple RANSE with little information carried in the mean fields, or relatively complex FNSE with filtered fields richer in dynamical information. ■

In the derivation of the FNSE (3.269), the commutation of the filtering operator with the derivative has been assumed. In general this is not true, as it was already proven for the case of a cumulative time average filter in page 105, or as it could be seen in equation (3.263) for finite limits. In reference [BIL06] it is expressly mentioned and explained the non-commutative property of derivative and filter. Thus, in general for any turbulence field $\psi(t, \mathbf{x})$

$$\partial_s \psi \neq \underline{\partial}_s \psi \quad (s = t, x_i)$$

In the general case, the derivation of the FNSE is not possible, and it must be investigated under which conditions could the commutation of filter and derivative be taken for granted. It is not difficult to envisage that those conditions are related with the expected behaviour of any acceptable filter kernel $G(t - t', \mathbf{x} - \mathbf{x}'; \square)$, when the integration space-time variables (t', \mathbf{x}') are sufficiently far away from the filtered function space-time variables (t, \mathbf{x}) .

In order to prove that statement, it is convenient to write again the equation (3.246) with some modifications, to render it as general as possible:

$$\begin{aligned} \tilde{\psi}(t, \mathbf{x}) &= \int_{\mathbb{R}^4} G(t - t', \mathbf{x} - \mathbf{x}'; \square) \psi(t', \mathbf{x}') dt' d^3 \mathbf{x}' \approx \int_{n \square} G(t - t', \mathbf{x} - \mathbf{x}'; \square) \psi(t', \mathbf{x}') dt' d^3 \mathbf{x}' := \\ &:= \int_{t-n_0^- \Theta^-}^{t+n_0^+ \Theta^+} \int_{x_1-n_1^- \Delta_1^-}^{x_1+n_1^+ \Delta_1^+} \int_{x_2-n_2^- \Delta_2^-}^{x_2+n_2^+ \Delta_2^+} \int_{x_3-n_3^- \Delta_3^-}^{x_3+n_3^+ \Delta_3^+} G(t - t', \mathbf{x} - \mathbf{x}'; \square) \psi(t', \mathbf{x}') dt' dx'_1 dx'_2 dx'_3 \end{aligned} \quad (3.282)$$

with n_α^-, n_α^+ ($\alpha = 0, 1, 2, 3$) real numbers, although for practical reasons they will be frequently taken as integers, and $\Theta^-, \Theta^+, \Delta_i^-, \Delta_i^+$ ($i = 1, 2, 3$) arbitrary functions of (t, \mathbf{x}) , with the usual requirements of

⁶⁰In principle, ensemble averaged fields $\langle \psi(t, \mathbf{x}) \rangle$ could contain as much information as filtered fields $\tilde{\psi}(t, \mathbf{x})$, since nothing limits beforehand the complexity of $\langle \psi(t, \mathbf{x}) \rangle$. It is the practical impossibility of obtaining ensemble averages what move Engineers and Physicist alike to resort to time or space averages, and the RANSE hence derived. Unfortunately, these mean fields carry much less dynamical information than the filtered fields obtained from the same initial data. The remarks that follow in this paragraph apply only to non-ensemble averages.

differentiability. Note the difference between the upper and lower integral limits, and also the different limits for each primed variable (t', \mathbf{x}') . It is remarked, too, that the integral limits do not contain any primed variable (t', \mathbf{x}') . The integral in equation (3.282) is very approximately the filtered field $\psi(t, \mathbf{x})$, provided $G(t - t', \mathbf{x} - \mathbf{x}'; \square)$ tends to zero sufficiently rapid as $(t - t', \mathbf{x} - \mathbf{x}')$ is sufficiently larger than the filter width.

Although the integral which defines the filter encompasses \mathbb{R}^4 , in fact it could be extended only to $n\square \subset \mathbb{R}^4$, given by

$$n\square := \left(t - n_0^- \Theta^-, t + n_0^+ \Theta^+ \right) \times \left(x_i - n_i^- \Delta_i^-, x_i + n_i^+ \Delta_i^+ \right)^3$$

with n meaning the set of numbers n_α^-, n_α^+ , because any valid filter kernel $G(t, \mathbf{x}; \square)$ would be negligible outside $n\square$, provided the numbers within the set n are sufficiently large. For the boxcar function (3.101) this assertion is strictly true for $n_\alpha^- = n_\alpha^+ = 1$, because $G(t, \mathbf{x}; \square)$ is zero outside the filter range, and for a general filter it holds approximately for $n_\alpha^-, n_\alpha^+ \gtrsim 1$. The application of Leibniz's rule of differentiation under the integral sign, shows directly the conditions that should be met in order for the filter to commute with derivative (see [Fla73]). To avoid lengthy cumbersome mathematical expressions with factors x_{i-1} and x_{i+1} for the general i index, the derivation will only be carried out for the variable x_1 , with $\partial_1 \equiv \partial/\partial x_1$ and $\partial_{1'} \equiv \partial/\partial x_1'$. Similar results would be obtained for t , x_2 and x_3 . Making use also of Fubini's theorem, the derivative of the filtered field is expressed as:

$$\begin{aligned} \partial_1 \psi(t, \mathbf{x}) &= \partial_1 \int_{t-n_0^- \Theta^-}^{t+n_0^+ \Theta^+} \int_{x_1-n_1^- \Delta_1^-}^{x_1+n_1^+ \Delta_1^+} \int_{x_2-n_2^- \Delta_2^-}^{x_2+n_2^+ \Delta_2^+} \int_{x_3-n_3^- \Delta_3^-}^{x_3+n_3^+ \Delta_3^+} G(t-t', \mathbf{x}-\mathbf{x}'; \square) \psi(t', \mathbf{x}') dt' dx_1' dx_2' dx_3' = \\ &= \int_{n\square} \partial_1 G(t-t', \mathbf{x}-\mathbf{x}'; \square) \psi(t', \mathbf{x}') dt' dx_1' dx_2' dx_3' + \\ &+ (1 + n_1^+ \partial_1 \Delta_1^+) \int_{t-n_0^- \Theta^-}^{t+n_0^+ \Theta^+} \int_{x_2-n_2^- \Delta_2^-}^{x_2+n_2^+ \Delta_2^+} \int_{x_3-n_3^- \Delta_3^-}^{x_3+n_3^+ \Delta_3^+} G(t-t', -n_1^+ \Delta_1^+, x_2-x_2', x_3-x_3'; \square) \\ &\quad \psi(t', x_1 + n_1^+ \Delta_1^+, x_2', x_3') dt' dx_2' dx_3' - \\ &- (1 - n_1^- \partial_1 \Delta_1^-) \int_{t-n_0^- \Theta^-}^{t+n_0^+ \Theta^+} \int_{x_2-n_2^- \Delta_2^-}^{x_2+n_2^+ \Delta_2^+} \int_{x_3-n_3^- \Delta_3^-}^{x_3+n_3^+ \Delta_3^+} G(t-t', n_1^- \Delta_1^-, x_2-x_2', x_3-x_3'; \square) \\ &\quad \psi(t', x_1 - n_1^- \Delta_1^-, x_2', x_3') dt' dx_2' dx_3' \quad (3.283) \end{aligned}$$

The factors $(1 + n_1^+ \partial_1 \Delta_1^+)$ and $(1 - n_1^- \partial_1 \Delta_1^-)$ can exit the integral because they do not depend on primed variables (t', \mathbf{x}') . From equation (3.263), and the attached footnote (3.264), and taking into account that

$$\partial_s G(t-t', \mathbf{x}-\mathbf{x}'; \square) = -\partial_{s'} G(t-t', \mathbf{x}-\mathbf{x}'; \square) \quad (s = t, x_i)$$

the second integral can be integrated by parts as⁶¹:

$$\int_{n\square} \partial_1 G(t-t', \mathbf{x}-\mathbf{x}'; \square) \psi(t', \mathbf{x}') dt' d^3 \mathbf{x}' = - \int_{n\square} \partial_{1'} G(t-t', \mathbf{x}-\mathbf{x}'; \square) \psi(t', \mathbf{x}') dt' d^3 \mathbf{x}' = \quad (3.285)$$

⁶¹The general expression for the integration by parts of a n -dimensional integral is (see [DK04])

$$\int_{\Omega} \frac{\partial f}{\partial x_i} g d\Omega = \int_{\partial\Omega} f g \hat{n}_i d\Sigma - \int_{\Omega} f \frac{\partial g}{\partial x_i} d\Omega \quad (3.284)$$

$$= - G(t - t', \mathbf{x} - \mathbf{x}'; \square) \psi(t', \mathbf{x}') \Big]_{x'_1 = x_1 - n_1^- \Delta_1^-}^{x'_1 = x_1 + n_1^+ \Delta_1^+} + \int_{n \square} G(t - t', \mathbf{x} - \mathbf{x}'; \square) \partial_{1'} \psi(t', \mathbf{x}') dt' d^3 \mathbf{x}'$$

with the middle term equal to:

$$\begin{aligned} & G(t - t', \mathbf{x} - \mathbf{x}'; \square) \psi(t', \mathbf{x}') \Big]_{x'_1 = x_1 - n_1^- \Delta_1^-}^{x'_1 = x_1 + n_1^+ \Delta_1^+} = \\ &= \int_{t - n_0^- \Theta^-}^{t + n_0^+ \Theta^+} \int_{x_2 - n_2^- \Delta_2^-}^{x_2 + n_2^+ \Delta_2^+} \int_{x_3 - n_3^- \Delta_3^-}^{x_3 + n_3^+ \Delta_3^+} G(t - t', -n_1^+ \Delta_1^+, x_2 - x'_2, x_3 - x'_3; \square) \psi(t', x_1 + n_1^+ \Delta_1^+, x'_2, x'_3) dt' dx'_2 dx'_3 - \\ & - \int_{t - n_0^- \Theta^-}^{t + n_0^+ \Theta^+} \int_{x_2 - n_2^- \Delta_2^-}^{x_2 + n_2^+ \Delta_2^+} \int_{x_3 - n_3^- \Delta_3^-}^{x_3 + n_3^+ \Delta_3^+} G(t - t', n_1^- \Delta_1^-, x_2 - x'_2, x_3 - x'_3; \square) \psi(t', x_1 - n_1^- \Delta_1^-, x'_2, x'_3) dt' dx'_2 dx'_3 \end{aligned} \quad (3.286)$$

The last term in equation (3.285) is identical to $\partial_1 \psi$.

Now, grouping together all terms of equations (3.283), (3.285) and (3.286), the following relation is obtained for the commutation of filter and derivative:

$$\begin{aligned} & \partial_1 \psi(t, \mathbf{x}) - \partial_1 \psi(t, \mathbf{x}) = \\ & n_1^+ \partial_1 \Delta_1^+ \int_{t - n_0^- \Theta^-}^{t + n_0^+ \Theta^+} \int_{x_2 - n_2^- \Delta_2^-}^{x_2 + n_2^+ \Delta_2^+} \int_{x_3 - n_3^- \Delta_3^-}^{x_3 + n_3^+ \Delta_3^+} G(t - t', -n_1^+ \Delta_1^+, x_2 - x'_2, x_3 - x'_3; \square) \psi(t', x_1 + n_1^+ \Delta_1^+, x'_2, x'_3) d^3 \Sigma'_1 + \\ & + n_1^- \partial_1 \Delta_1^- \int_{t - n_0^- \Theta^-}^{t + n_0^+ \Theta^+} \int_{x_2 - n_2^- \Delta_2^-}^{x_2 + n_2^+ \Delta_2^+} \int_{x_3 - n_3^- \Delta_3^-}^{x_3 + n_3^+ \Delta_3^+} G(t - t', n_1^- \Delta_1^-, x_2 - x'_2, x_3 - x'_3; \square) \psi(t', x_1 - n_1^- \Delta_1^-, x'_2, x'_3) d^3 \Sigma'_1 \end{aligned} \quad (3.287)$$

where $d^3 \Sigma'_1 \equiv dt' dx'_2 dx'_3$ is the hypersurface element perpendicular to the X_1 axis. Similar expressions are obtained for $s = t, x_2$ and x_3 . Note the hypersurface integral terms in the integration by parts (3.286), annihilate identically the corresponding terms following the application of Leibniz's rule in equation (3.283). Equation (3.287) provides a **very general expression for the commutation error**, and constitutes a generalisation of similar relations obtained in references like [Sag06] or [BG05].

Therefore, the commutation between derivative ∂_s and filter operator is granted provided that:

$$\partial_s \Delta_s^+ = \partial_s \Delta_s^- = 0 \quad (s = t, x_1, x_2, x_3) \quad (3.288)$$

where $\Omega \in \mathbb{R}^n$ is an open domain, $\partial\Omega$ its oriented boundary, $d\Sigma$ an infinitesimal element of the hypersurface $\partial\Omega$, and \hat{n}_i the i^{th} component of the outward unit normal vector to $\partial\Omega$ at the element $d\Sigma$. In the present case

$$\Omega = \left(t - n_0^- \Theta^-, t + n_0^+ \Theta^+ \right) \times \left(x_i - n_i^- \Delta_i^-, x_i + n_i^+ \Delta_i^+ \right)^3$$

$d\Omega = dt' dx'_1 dx'_2 dx'_3$, \hat{n}_1 is directed along the X_1 axis, and $d\Sigma = dt' dx'_2 dx'_3$ is an element of hypersurface perpendicular to X_1 .

or, alternatively, provided that ⁶²

$$n_s^+ \Delta_s^+ = -n_s^- \Delta_s^- \quad (s = t, x_1, x_2, x_3) \quad (3.289)$$

In the first case (3.288), $\Delta_1^+ = \Delta_1^+(t, x_2, x_3)$ and $\Delta_1^- = \Delta_1^-(t, x_2, x_3)$ could be arbitrary functions as long as they do not depend on x_1 (and like assertions for $s = t, x_2, x_3$). In the second case (3.289), Δ_s^+ and Δ_s^- could depend on the four variables (t, x_1, x_2, x_3) , as long as they satisfy the expressed condition. In both cases, the annoying terms arising from the application of Leibniz's rule of differentiation under the integral sign vanish identically, and the derivative of the filter results in the simple expression:

$$\partial_s \psi = \underline{\partial}_s \psi \quad (3.290)$$

In other words, any filter defined with the integration limits as expressed in (3.282) commutes with the derivative ∂_s ($s = t, x_i$), because the disturbing terms cancel one another identically, either if

$$\begin{aligned} \partial_t \Theta^+ = \partial_t \Theta^- = 0 &\Rightarrow \Theta^+ = \Theta^+(x_1, x_2, x_3), \Theta^- = \Theta^-(x_1, x_2, x_3) \\ \partial_1 \Delta_1^+ = \partial_1 \Delta_1^- = 0 &\Rightarrow \Delta_1^+ = \Delta_1^+(t, x_2, x_3), \Delta_1^- = \Delta_1^-(t, x_2, x_3) \\ \partial_2 \Delta_2^+ = \partial_2 \Delta_2^- = 0 &\Rightarrow \Delta_2^+ = \Delta_2^+(t, x_1, x_3), \Delta_2^- = \Delta_2^-(t, x_1, x_3) \\ \partial_3 \Delta_3^+ = \partial_3 \Delta_3^- = 0 &\Rightarrow \Delta_3^+ = \Delta_3^+(t, x_1, x_2), \Delta_3^- = \Delta_3^-(t, x_1, x_2) \end{aligned} \quad (3.291)$$

or if equation (3.289) is satisfied. This interesting result finds immediate application in the design of LES algorithms for the solution of discretised Navier-Stokes equations. In practice, n_α^+ and n_α^- need only be small integers, since the filter kernel $G(t - t', \mathbf{x} - \mathbf{x}'; \square)$ drops rapidly to zero farther away than two or three filter's width units. Conditions (3.291) or (3.289) provide the desired assurance that the commutation of filter and derivative can be taken for granted. ■

The results (3.291) or (3.289) also pave the way to the coupling of filter operators with boundary conditions, in particular with walls and the no-slip condition. The complex problem of filtering in bounded domains is thoroughly studied in [BIL06]

Since the filtering through finite time T was already covered in section 3.2.2, with the equivalent concept of moving time average, the remainder of this section will be devoted to filtering in space coordinates \mathbf{x} . The reader interested in time filtering is also addressed to the references [Pru00], [PGGT03], [Pru08] and [Sag06].

Figure 3.12 shows the effect of boundaries on the filtered field $\underline{\psi}(t, \mathbf{x})$. In the case of a point like \mathbf{x}_1 , which is sufficiently far away from the boundary, the integral defining $\underline{\psi}(t, \mathbf{x}_1)$ extends across Δ ⁶³ without interference, and thus the integral limits do not depend on \mathbf{x} any further than the dependence the filter width Δ itself would have with \mathbf{x} .

$$\underline{\psi}(t, \mathbf{x}_1) = \int_{\Delta} G(t; \mathbf{x}_1 - \mathbf{x}'; \Delta) \psi(t, \mathbf{x}') \, d^3 \mathbf{x}'$$

⁶²Note that being n_s^+ and n_s^- constant numbers, equation (3.289) also implies

$$n_s^+ \partial_s \Delta_s^+ = -n_s^- \partial_s \Delta_s^-$$

The requirement (3.289) is usually related with the existence of periodic boundary conditions.

⁶³Here we return back to the previous nomenclature, with $\Delta_i^+ = \Delta_i^- = \Delta_i/2$, being Δ_i the filter width along the axis X_i .

However, in the case of a point like \mathbf{x}_2 , close to the boundary, the integral defining $\underline{\psi}(t, \mathbf{x}_2)$ has limits that depend on \mathbf{x} along the boundary, if only to denote the intersection of boundary and filter width:

$$\underline{\psi}(t, \mathbf{x}_2) = \int_{\Delta \cap \Omega} G(t; \mathbf{x}_2 - \mathbf{x}'; \Delta) \psi(t, \mathbf{x}') d^3 \mathbf{x}'$$

where $\Delta \cap \Omega$ means 'the integration is taken over the intersection of the sphere with centre in \mathbf{x}_2 and diameter Δ , and the flow domain Ω '.

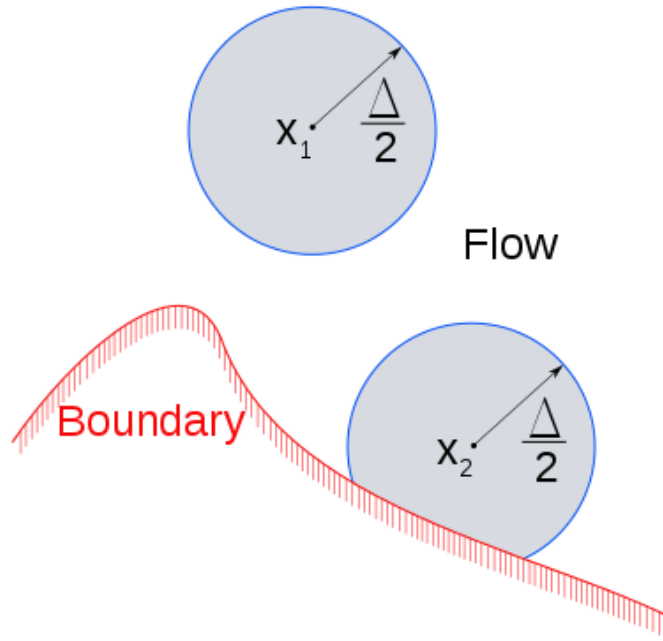


Figure 3.12: Filter range for point \mathbf{x}_1 within the flow, and for point \mathbf{x}_2 close to the boundary $\partial\Omega$.

The dependence of Δ_i^+ and Δ_i^- on x_i in the definition of $\underline{\psi}(t, \mathbf{x}_2)$ brings as a consequence that the derivative and filtering operations do not commute, that is

$$\partial_i \underline{\psi} \neq \underline{\partial}_i \psi$$

when the filtered field $\underline{\psi}(t, \mathbf{x}_2)$ is close to the boundaries. Therefore, the Navier-Stokes equations could only be filtered for points sufficiently far from the boundaries (see [BIL06]).

Alternatively, if the boundary conditions at the walls are periodic, with such a period that the filters' width Δ_i^+ and Δ_i^- satisfy equation (3.289), then it still would be possible to admit the filter-derivative commutation. Note this possibility would require an exquisite coordination of boundary conditions with filter's width definition, which seldom occurs in practice. Thus, it seems that FNSE and nearby walls are not an advisable combination.

Unfortunately, this is not the only thorny issue related with filters and boundaries. Another problem is the definition of the filtered velocity field $\underline{\mathbf{u}}(t, \mathbf{x})$ for walls. Assume the point \mathbf{x}_2 in figure 3.12 were exactly at the boundary, and assume the boundary were a wall with the no-slip condition⁶⁴. Such condition

⁶⁴The no-slip condition is so frequently invoked in Fluid Mechanics, that deserves some analysis regarding its overall validity. The approach followed herein is inspired by the noteworthy paper [Gre91]. See also [Lea07].

implies for the physical field $\mathbf{u}(t, \mathbf{x}_2) = 0$, $\forall t \in \mathbb{R}$, whereas for the filtered field the result is instead:

$$\underline{\mathbf{u}}(t, \mathbf{x}_2) = \int_{\Delta \cap \Omega} G(t; \mathbf{x}_2 - \mathbf{x}'; \Delta) \mathbf{u}(t, \mathbf{x}') d^3 \mathbf{x}' \neq 0 \quad (3.295)$$

with $\mathbf{u}(t, \mathbf{x}') = 0$, $\forall \mathbf{x}' \in \partial\Omega \cap \Delta \subset \Delta \cap \Omega$, being $\partial\Omega$ the oriented boundary surrounding the flow domain Ω .

Therefore, one does not know beforehand the actual value of $\underline{\mathbf{u}}$ at the walls, except that **for sure it is not zero**. A similar result is obtained for the velocity derivative: at the wall $\partial_i \underline{u}_j$ does not have foreseeable values. Dirichlet (\underline{u}_j undefined) and Neumann ($\partial_i \underline{u}_j$ undefined) boundary conditions are not possible at the walls, and consequently the attached mathematical problem of solving the FNSE becomes ill-posed. Note this situation is not shared with statistical methods based upon field averages, since the averages mimic the no-slip behaviour of the physical velocity $\mathbf{u}(t, \mathbf{x})$ at the walls (except the spatial average $\overline{\mathbf{u}(t)}$, which is never recommended when studying bounded flows). Thus, statistical methods are routinely used in models for bounded turbulent flows.

Thus, walls (and their neighbourhood) suffer from the combined effect of the non-commutativity of derivative and filtering, and the ignorance of the actual values of the filtered velocity field. This combination is the main reason why LES cannot be safely applied in the vicinity of walls, and alternative methods should be used in such cases. Probably, the most widely employed methods are those encompassed within the collective name of **Hybrid RANS-LES Turbulence Models (HRLTM)**, characterised by the use of statistical RANS methods near the walls, and LES with a suitable filter in the rest of the flow (see [Spa00] or [FT08]). One such model will be presented in the next Chapter.

Basically there are two kinds of HRLTM:

- i. Zonal Hybrid Methods. A region is defined near the wall in which the turbulent boundary layer model is solved. The transition from the RANS near-wall region to the LES outer region is determined explicitly in the boundary conditions established in the solver.
- ii. Blended Hybrid Methods. The transition between RANS and LES regions is made smoothly, according to algorithms defined in the solver itself.

Let $\Omega \subset \mathbb{R}^3$ be the domain occupied by the flow, $\partial\Omega$ its oriented boundary and $\overline{\Omega} = \Omega \cup \partial\Omega$ the closure of Ω . If Ω is a closed set then $\overline{\Omega} = \Omega$. The boundary $\partial\Omega$ is assumed to be a wall, or a wall-like surface, that contain the flow. Let $\mathbf{u}(t, \mathbf{x})$, $\mathbf{x} \in \overline{\Omega}$, be the flow's velocity field. Assume the boundary $\partial\Omega$ could be in movement, with a local velocity given by $\mathbf{v}_\Omega(t, \boldsymbol{\xi})$, $\boldsymbol{\xi} \in \partial\Omega$. Finally, let $\hat{\mathbf{n}}(t, \boldsymbol{\xi})$ be the unit outward normal vector to $\partial\Omega$ at the point $\boldsymbol{\xi} \in \partial\Omega$.

With those definitions, the boundary condition which requires that the fluid in contact with the wall have no relative tangential velocity, conventionally called the **no-slip condition**, is given by:

$$\mathbf{u}(t, \boldsymbol{\xi}) \wedge \hat{\mathbf{n}}(t, \boldsymbol{\xi}) = \mathbf{v}_\Omega(t, \boldsymbol{\xi}) \wedge \hat{\mathbf{n}}(t, \boldsymbol{\xi}) , \quad \boldsymbol{\xi} \in \partial\Omega \quad (3.292)$$

or alternatively

$$\mathbf{u}(t, \boldsymbol{\xi}) - [\hat{\mathbf{n}}(t, \boldsymbol{\xi}) \cdot \mathbf{u}(t, \boldsymbol{\xi})] \hat{\mathbf{n}}(t, \boldsymbol{\xi}) = \mathbf{v}_\Omega(t, \boldsymbol{\xi}) - [\hat{\mathbf{n}}(t, \boldsymbol{\xi}) \cdot \mathbf{v}_\Omega(t, \boldsymbol{\xi})] \hat{\mathbf{n}}(t, \boldsymbol{\xi}) , \quad \boldsymbol{\xi} \in \partial\Omega \quad (3.293)$$

Note that a wall at rest, $\mathbf{v}_\Omega(t, \boldsymbol{\xi}) = 0$, does not imply $\mathbf{u}(t, \boldsymbol{\xi}) = 0$, but rather $\mathbf{u}(t, \boldsymbol{\xi}) \wedge \hat{\mathbf{n}}(t, \boldsymbol{\xi}) = 0$ (or $\mathbf{u}(t, \boldsymbol{\xi}) - [\hat{\mathbf{n}}(t, \boldsymbol{\xi}) \cdot \mathbf{u}(t, \boldsymbol{\xi})] \hat{\mathbf{n}}(t, \boldsymbol{\xi}) = 0$): it is only the tangential velocity that is forced to be zero.

On the other hand, a wall, or wall-like surface, is expected to be impenetrable, that is, the flow cannot have a normal relative velocity at the wall. Thus, the **no-penetration condition** is another kind of boundary condition affecting to the flow (not occurring, for instance, with porous walls), which could be written as

$$\mathbf{u}(t, \boldsymbol{\xi}) \cdot \hat{\mathbf{n}}(t, \boldsymbol{\xi}) = \mathbf{v}_\Omega(t, \boldsymbol{\xi}) \cdot \hat{\mathbf{n}}(t, \boldsymbol{\xi}) , \quad \boldsymbol{\xi} \in \partial\Omega \quad (3.294)$$

In summary, the filter concept, while very useful and intuitive and in many respects closer to Physics than averages, suffer from the following problems, among others:

- The commutation between filter and derivative ∂_s is not guaranteed, unless the filter definition satisfy the conditions specified along this section: kernel function $G(t, \mathbf{x}; \square)$ strongly decreasing for $|\mathbf{x}| \gtrsim |\Delta|$, and $t \gtrsim \Theta$; either Δ_i should not depend on x_i or equation (3.289) ...
- Determining the acceptable values of integers n_α^+ and n_α^- for which the definition integrals extended to infinity could be replaced by integrals with finite limits, as in equation (3.282). This is related to the maximum admissible error level in the simulation.
- Selecting an appropriate filter width for each region of the flow, taking special care as the simulation approach the walls, where Δ ought to be chosen increasingly small. This, in turn, must be compatible with the request of Δ_i not depending on x_i , or with equation (3.289).
- Upon initiating the simulation, the mesh structure will ultimately determine whether the selected filter could indeed be applied and attain the expected performance. For structured meshes, the filter width along each axis is limited by the typical cell size in the corresponding direction, and in unstructured meshes the situation is even worse. In bounded flows it is customary to define graded meshes, with cell size increasingly smaller as the mesh approaches the wall. The filter width must be adjusted accordingly.
- The wall boundary conditions for filtered velocities are undefined, since $\mathbf{u}_{wall} = 0$ is not possible, and no result exists for $\partial_i u_j$ either. The absence of well-defined boundary conditions brings forward the use of RANS models to deal with the turbulence in the vicinity of walls. The outcome depends on the suitability of the chosen model, based on the Boussinesq's hypothesis.

On the other hand, one advantage of the filtering approach is that, as long as the filter is reasonably reproduced in the measuring instruments, the results obtained from the CFD simulation could be directly compared with experimental data. Filtering, that is, smoothing, is something that very naturally occurs in laboratory and industry alike. Filtering is a less radical solution than Reynolds decomposition except, perhaps, when it refer to pure ensemble average. But ensemble average is hardly possible in practice, whereas filters are routinely applied during the measurement of flow's quantities. The FNSE are not so *neat* as the RANSE, but they carry more dynamics in the fields, at least when compared to time averaged RANSE, which possibly be the most practised method.

3.4 Turbulence as an Additional Term to Laminar Solution

This section presents and discusses an altogether different, and perhaps also surprising, way of considering turbulence. The approach will be fully analytical and the averaged solutions will appear to be composed of two terms: one corresponding to the functional form of the quantity that would solve the laminar problem, and the second representing the contribution of the turbulence to the general average solution. That second term is generally a function of the Reynolds stress tensor for the flow

Again, in the case of a static wall the no-penetration condition implies $\mathbf{u}(t, \boldsymbol{\xi}) \cdot \hat{\mathbf{n}}(t, \boldsymbol{\xi}) = 0$, and it is only the normal component that is forced to be zero. Both conditions, the no-slip and the no-penetration, are usually enforced together at any wall. If so happens, the relative tangential **and** relative normal velocities must both be simultaneously zero at the wall, a condition that leads necessarily to $\mathbf{u}(t, \boldsymbol{\xi}) = 0$, which is the (somewhat misleading) no-slip condition claimed by many texts.

This Dissertation will adhere to the existing custom of associating the no-slip condition with $\mathbf{u}(t, \boldsymbol{\xi}) = 0$, although frequently a call will be made to this footnote, lest not be forgotten the true meaning of such expression.

being studied. Note this method does not make any provision for the fluctuating component of the quantity, since it refers only to its average component.

Two cases will be considered in the next subsections, one encompassing the other:

- i. The steady state case, already introduced and discussed in the brilliant and somewhat forgotten paper of [Pai53].
- ii. The general case which, to the author's knowledge, represents a genuine original contribution of this Dissertation to the problem of characterising analytically the turbulence.

3.4.1 Steady State Turbulence as an Additional Term to Laminar Solution

An unusual and interesting method to describe turbulence quantities is to decompose the mean turbulent field $\Psi(t, \mathbf{x})$ into two parts, the laminar and the pure turbulent ones:

$$\Psi(t, \mathbf{x}) = \psi_L(t, \mathbf{x}) + \Psi_T(t, \mathbf{x}) \quad (3.296)$$

Equation (3.296) will be called the **Laminar-Turbulent Decomposition** of the mean flow field Ψ , where ψ_L is the laminar solution to the Navier-Stokes equations, and Ψ_T is an additional term which accounts for the mean influence of turbulence on Ψ , added to the laminar solution.

Obviously this decomposition is only useful in flows for which a laminar solution is already available. Fortunately the steady flow of a Newtonian incompressible fluid in a pipe driven by constant pressure gradient is one the few examples with an exact analytical solution. This case is called Hagen-Poiseuille flow and its solution could be found in many reference textbooks (e.g. [Dur08])

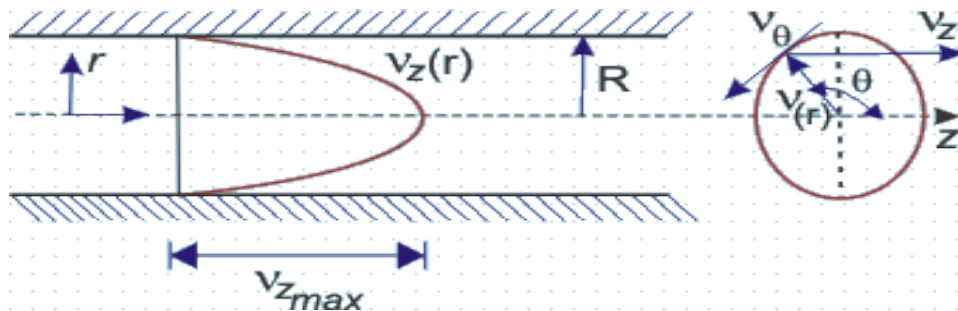


Figure 3.13: Geometry of Hagen-Poiseuille flow.

To not cause confusion, the laminar flow velocity will be denoted with \mathbf{v} , and the most common \mathbf{u} will be reserved for turbulent flow.

The solution for this one-dimensional problem is (see figure 3.13):

$$v_z = \frac{\Pi R^2}{4\mu} \left[1 - \left(\frac{r}{R} \right)^2 \right] = v_{z_{max}} \left[1 - \left(\frac{r}{R} \right)^2 \right] \quad (3.297)$$

where $\Pi = -\partial p / \partial z \geq 0$ is the (minus) constant pressure gradient along the pipe, R the pipe radius, μ the dynamic viscosity, cylindrical coordinates (r, θ, z) are used, and Z axis is coincident with the pipe's centreline. The maximum velocity occurs at the centreline and is given by $v_{z_{max}} = \Pi R^2 / 4\mu$.

The laminar-turbulent decomposition that is about to be developed for the steady⁶⁵ turbulent Hagen-Poiseuille flow is entirely based on the excellent paper presented in 1953 by Shih-I Pai, [Pai53]. The work [FDO2] arrives to a similar decomposition, although from a different starting point, and applied to plane channel flow.

The turbulent flow fields \mathbf{u} and p admit a Reynolds decomposition given by equations (3.10) and (3.11):

$$\mathbf{u}(t, \mathbf{x}) = \mathbf{U}(\mathbf{x}) + \mathbf{u}'(t, \mathbf{x}) \quad , \quad p(t, \mathbf{x}) = P(\mathbf{x}) + p'(t, \mathbf{x}) \quad (3.298)$$

In order to endow the coming derivation with the maximum generality, it will not be established at this point what kind of average represent the fields \mathbf{U} and P , although the fact that a mean steady flow is being considered hints to the use of time average as appropriate. In any case, average quantities will be denoted by the general symbol $\langle \cdot \rangle$ or by capital letters.

The assumptions made to obtain the announced results are not different than those expressed section 2.2:

- i. The mean flow is axially symmetric, that is, $\partial\Psi/\partial\theta = 0$ for any mean flow quantity Ψ .
- ii. The flow is incompressible and Newtonian, with density and dynamic and kinematic viscosities ρ , μ and ν , respectively.
- iii. No entrance or exit effects are considered, thus the pipe is assumed to have an infinite length $-\infty < z < +\infty$.
- iv. The mean velocity has only a non-zero component along the Z axis

$$\mathbf{U} = (U_r, U_\theta, U_z) = (0, 0, U_z) \equiv (0, 0, U)$$

(U and U_z will used interchangeably). Note that this assumption implies $u_r = u'_r$, $u_\theta = u'_\theta$ and $u'_z = u_z - U$.

- v. Gravity effects are neglected.
- vi. The statistical properties of the flow are the same at all sections of constant z ⁶⁶. In particular, this applies to the Reynolds stress tensor $R_{ij} = -\rho\langle u'_i u'_j \rangle$ which is assumed to be only function of r .

The same arguments mentioned in section 2.3.3, plus the assumptions made above, lead to the following dependence for the mean turbulence fields⁶⁷:

$$\mathbf{U} = \mathbf{U}(r) \quad , \quad P = P(r, z) \quad , \quad R_{ij} = R_{ij}(r) \quad (3.299)$$

Just as laminar Hagen-Poiseuille flow demands a constant pressure gradient along the pipe ($\partial p/\partial z = \text{const.}$), turbulent Hagen-Poiseuille flow requires a constant *mean* pressure gradient along the pipe ($-\partial P/\partial z = \Pi = \text{const.}$).

⁶⁵The flow is steady on average. The fluctuations need not be steady, and they cannot be so if the flow is to be turbulent. Therefore $\partial\Psi/\partial t = 0$ for any mean field Ψ , although $\partial\psi/\partial t = \partial\psi'/\partial t \neq 0$.

⁶⁶This is an important not straightforward assumption. It surely limits the range of solutions, but the assumption makes sense physically, and not much ought to be lost by considering a problem which has the same statistical properties at all sections of constant z .

⁶⁷In the laminar case the same assumptions lead to $p = p(z)$ only, because $p = p(r)$ imply $u_r \neq 0$ and there would be flow motion along the radius, against the assumption. But in turbulent flow the RANSE have an additional Reynolds stress component, thus $P = P(r, z)$ does not imply $U_r \neq 0$. See further below.

From the Navier-Stokes and continuity equations in cylindrical coordinates (see [Dur08]), the following RANS and averaged continuity equations are obtained

$$\begin{aligned} & \frac{\partial U_r}{\partial t} + \frac{1}{r} \frac{\partial r U_r^2}{\partial r} + \frac{1}{r} \frac{\partial U_r U_\theta}{\partial \theta} + \frac{\partial U_z U_r}{\partial z} - \frac{U_\theta^2}{r} = \\ & = -\frac{1}{\rho} \frac{\partial P}{\partial r} + \nu \left\{ \nabla^2 U_r - \frac{U_r}{r^2} - \frac{2}{r^2} \frac{\partial U_\theta}{\partial \theta} \right\} - \frac{1}{r} \frac{\partial r \langle u_r'^2 \rangle}{\partial r} - \frac{1}{r} \frac{\partial \langle u_r' u_\theta' \rangle}{\partial \theta} - \frac{\partial \langle u_r' u_z' \rangle}{\partial z} + \frac{\langle u_\theta'^2 \rangle}{r} \end{aligned} \quad (3.300)$$

$$\begin{aligned} & \frac{\partial U_\theta}{\partial t} + \frac{1}{r} \frac{\partial r U_\theta U_r}{\partial r} + \frac{1}{r} \frac{\partial U_\theta^2}{\partial \theta} + \frac{\partial U_z U_\theta}{\partial z} + \frac{U_\theta U_r}{r} = \\ & = -\frac{1}{r \rho} \frac{\partial P}{\partial \theta} + \nu \left\{ \nabla^2 U_\theta - \frac{U_\theta}{r^2} + \frac{2}{r^2} \frac{\partial U_r}{\partial \theta} \right\} - \frac{1}{r} \frac{\partial r \langle u_r' u_\theta' \rangle}{\partial r} - \frac{1}{r} \frac{\partial \langle u_\theta'^2 \rangle}{\partial \theta} - \frac{\partial \langle u_\theta' u_z' \rangle}{\partial z} - \frac{\langle u_r' u_\theta' \rangle}{r} \end{aligned} \quad (3.301)$$

$$\begin{aligned} & \frac{\partial U_z}{\partial t} + \frac{1}{r} \frac{\partial r U_r U_z}{\partial r} + \frac{1}{r} \frac{\partial U_z U_\theta}{\partial \theta} + \frac{\partial U_z^2}{\partial z} = \\ & = -\frac{1}{\rho} \frac{\partial P}{\partial z} + \nu \nabla^2 U_z - \frac{1}{r} \frac{\partial r \langle u_r' u_z' \rangle}{\partial r} - \frac{1}{r} \frac{\partial \langle u_z' u_\theta' \rangle}{\partial \theta} - \frac{\partial \langle u_z'^2 \rangle}{\partial z} \end{aligned} \quad (3.302)$$

$$\nabla \cdot \mathbf{U} = \frac{1}{r} \frac{\partial r U_r}{\partial r} + \frac{1}{r} \frac{\partial U_\theta}{\partial \theta} + \frac{\partial U_z}{\partial z} = 0 \quad (3.303)$$

Note that no mention is made as to which averaging method has been used to obtain the equations above. According to result (3.299) most of the terms above are zero. Discarding those zero terms, the equations result in:

$$-\frac{1}{\rho} \frac{\partial P}{\partial r} - \frac{1}{r} \frac{d(r \langle u_r'^2 \rangle)}{dr} + \frac{\langle u_\theta'^2 \rangle}{r} = 0 \quad (3.304)$$

$$-\frac{1}{r} \frac{d(r \langle u_r' u_\theta' \rangle)}{dr} - \frac{\langle u_r' u_\theta' \rangle}{r} = 0 \quad (3.305)$$

$$-\frac{1}{\rho} \frac{\partial P}{\partial z} + \nu \left(\frac{d^2 U_z}{dr^2} + \frac{1}{r} \frac{dU_z}{dr} \right) - \frac{1}{r} \frac{d(r \langle u_r' u_z' \rangle)}{dr} = 0 \quad (3.306)$$

The continuity equation is absent from this set because all of its terms are null. The second equation (3.305) is easily integrable:

$$\begin{aligned} & -\frac{1}{r} \frac{d(r \langle u_r' u_\theta' \rangle)}{dr} - \frac{\langle u_r' u_\theta' \rangle}{r} = 0 \Rightarrow r \frac{d \langle u_r' u_\theta' \rangle}{dr} + 2 \langle u_r' u_\theta' \rangle = 0 \Rightarrow \frac{d \langle u_r' u_\theta' \rangle}{dr} = -\frac{2 \langle u_r' u_\theta' \rangle}{r} \Rightarrow \\ & \Rightarrow \frac{d \langle u_r' u_\theta' \rangle}{\langle u_r' u_\theta' \rangle} = -2 \frac{dr}{r} \Rightarrow \ln \langle u_r' u_\theta' \rangle = -2 \ln r + C \Rightarrow \langle u_r' u_\theta' \rangle = \frac{C}{r^2} \end{aligned}$$

with C an integration constant. The constant is determined by the boundary condition $r = R \Rightarrow \langle u_r' u_\theta' \rangle = 0$. Therefore, $C = 0$ and

$$\langle u_r' u_\theta' \rangle = 0 \quad (3.307)$$

and one fewer unknown for the problem. Still, there are five unknowns

$$U_z(r) \equiv U(r), P(r, z), \langle u_r' u_z' \rangle(r), \langle u_r'^2 \rangle(r), \langle u_\theta'^2 \rangle(r)$$

and just two equations (3.304) and (3.306).

In order to obtain additional relationships among the five dependent variables, it is convenient to convert them into dimensionless form. Radius R is used as the reference length and thus the dimensionless coordinates are defined as:

$$\alpha = \frac{r}{R} \quad (0 \leq \alpha \leq 1), \quad \beta = \frac{z}{R} \quad (3.308)$$

The reference velocity will be the friction velocity u_τ , to be properly introduced in page 223, which is defined as

$$u_\tau = \sqrt{\frac{\tau_w}{\rho}}$$

with τ_w the shear stress at the wall, $\alpha = 1$. For the present derivation u_τ is to be considered constant, as no change in the velocity profile with time is expected. The dimensionless velocity will be

$$u^+ = \frac{U_z}{u_\tau} \quad (3.309)$$

and it has attached a friction Reynolds number given by

$$Re^+ = \frac{u_\tau R}{\nu} \quad (3.310)$$

Note that $U_z = U_z(r)$ implies $u^+ = u^+(\alpha, Re^+)$ ⁶⁸, even though Re^+ is constant for a given turbulent Hagen-Poiseuille flow.

The reference pressure is taken as ρu_τ^2 . Note that the mean pressure P only appears in the equations behind a derivative; therefore the same results are obtained if an arbitrary constant P_0 is added to P . As the boundary conditions are to be defined at the wall, $\alpha = 1$, P_0 will be selected such that the pressure boundary conditions at a given set of points of the wall is zero. Assume $P_0 = P(1, 0)$, that is, the value taken by P at the wall points given by coordinates $\alpha = 1$ and $\beta = 0$ (a circumference). Then the dimensionless pressure is defined by:

$$p^+ = \frac{P - P_0}{\rho u_\tau^2} \quad (3.311)$$

and $p^+ = p^+(\alpha, \beta, Re^+)$ The averaged squared velocity fluctuations in dimensionless form are expressed by:

$$\sigma_1(\alpha, Re^+) = \frac{\langle u_r'^2 \rangle}{u_\tau^2} \quad (3.312)$$

$$\sigma_2(\alpha, Re^+) = \frac{\langle u_\theta'^2 \rangle}{u_\tau^2} \quad (3.313)$$

$$\chi(\alpha, Re^+) = \frac{\langle u_r' u_z' \rangle}{u_\tau^2} \quad (3.314)$$

With the newly defined dimensionless quantities, and having into account that

$$\frac{d}{dr} = \frac{1}{R} \frac{d}{d\alpha}, \quad \frac{d^2}{dr^2} = \frac{1}{R^2} \frac{d^2}{d\alpha^2}, \quad \frac{d}{dz} = \frac{1}{R} \frac{d}{d\beta}$$

⁶⁸The velocity is said to be expressed in *outer variables* when written in this form. See page 223

the equations (3.304) and (3.306) become

$$\frac{\partial p^+}{\partial \alpha} + \frac{1}{\alpha} \frac{d(\alpha \sigma_1)}{d\alpha} - \frac{\sigma_2}{\alpha} = 0 \quad (3.315)$$

$$\frac{\partial p^+}{\partial \beta} - \frac{1}{Re^+} \left(\frac{d^2 u^+}{d\alpha^2} + \frac{1}{\alpha} \frac{du^+}{d\alpha} \right) + \frac{1}{\alpha} \frac{d(\alpha \chi)}{d\alpha} = 0 \quad (3.316)$$

subjected to the boundary conditions:

$$u^+(1, Re^+) = 0 \quad (3.317)$$

$$\left. \frac{du^+}{d\alpha} \right]_{\alpha=0} = 0 \quad (3.318)$$

$$\sigma_1(1, Re^+) = 0 \quad (3.319)$$

$$\sigma_2(1, Re^+) = 0 \quad (3.320)$$

$$\chi(1, Re^+) = 0 \quad (3.321)$$

$$p^+(1, 0, Re^+) = 0 \quad (3.322)$$

Equation (3.317) is the no-slip condition (see footnote 64 in page 146), (3.318) establishes that the mean velocity has a maximum at the centreline⁶⁹, (3.319)-(3.321) determine the flow in the vicinity of the wall to be laminar, and (3.322) sets $P = P_0$ at the circumference defined by $\alpha = 1$ and $\beta = 0$.

Equations (3.315) is integrated as follow:

$$\int \frac{\partial p^+}{\partial \alpha} d\alpha + \int \frac{1}{\alpha} \frac{d\alpha \sigma_1}{d\alpha} d\alpha - \int \frac{\sigma_2}{\alpha} d\alpha = K(\beta) \Rightarrow p^+(\alpha, \beta, Re^+) + \int \frac{1}{\alpha} \frac{d\alpha \sigma_1}{d\alpha} d\alpha - \int \frac{\sigma_2}{\alpha} d\alpha = K(\beta)$$

where $K(\beta)$ is a function which contains the dependence of p^+ on β . Since $\Pi = -\partial P/\partial z = const.$, then that dependence could only be linear and $K(\beta) = -\Pi^+ \beta + B$, with Π^+ the dimensionless version of $\Pi = -\partial P/\partial z$, and B a real constant.

The first integral is solved by parts:

$$\int \frac{1}{\alpha} \frac{d\alpha \sigma_1}{d\alpha} d\alpha = \int \frac{1}{\alpha} d(\alpha \sigma_1) = \left(\frac{1}{\alpha} \right) (\alpha \sigma_1) - \int \alpha \sigma_1 d\left(\frac{1}{\alpha} \right) = \sigma_1 + \int \frac{\sigma_1}{\alpha} d\alpha$$

and equation (3.315) yields the solution

$$p^+(\alpha, \beta, Re^+) + \sigma_1(\alpha, Re^+) + \int_1^\alpha \frac{\sigma_1 - \sigma_2}{\alpha'} d\alpha' = -\Pi^+ \beta + B \quad (3.323)$$

From the boundary conditions, for $\alpha = 1$ and $\beta = 0$, it results $B = 0$. Thus

$$p^+(\alpha, \beta, Re^+) = -\Pi^+ \beta - \sigma_1(\alpha, Re^+) + \int_1^\alpha \frac{\sigma_2 - \sigma_1}{\alpha'} d\alpha' \quad (3.324)$$

⁶⁹ Equation (3.318) is a Neumann-type boundary condition that avoids the definition of a Dirichlet-type boundary condition of the form

$$u^+(0, Re^+) = u_{max}^+$$

since u_{max}^+ is not assumed to be known beforehand. Should that be the case, the Neumann condition ought to be substituted by the Dirichlet condition.

with the last two terms function of α and Re^+ only. Equation (3.324) relates the mean pressure within the flow with the Reynolds stress tensor, and clearly separates the dependence of p^+ on α and β ⁷⁰. Besides, for the integral to converge for $\alpha \rightarrow 0$ it is necessary that either:

- $\sigma_1 \rightarrow 0$ and $\sigma_2 \rightarrow 0$ not slower than α , or
- $\sigma_1 - \sigma_2 \rightarrow 0$ not slower than α

Experimentally is found that σ_1 and σ_2 diminish upon approaching the pipe's centreline, but they do not vanish (see [Wil06]). Then it must be $\sigma_1 \approx \sigma_2$ in the proximity of the axis.

Equation (3.316) is solved with the help of equation (3.324), since

$$\frac{\partial p^+}{\partial \beta} = -\Pi^+$$

Multiply equation (3.316) times α

$$-\Pi^+ \alpha - \frac{\alpha}{Re^+} \frac{d^2 u^+}{d\alpha^2} - \frac{1}{Re^+} \frac{du^+}{d\alpha} + \frac{d\alpha\chi}{d\alpha} = 0$$

integrate

$$-\frac{\Pi^+ \alpha^2}{2} - \frac{1}{Re^+} \int \alpha \frac{d^2 u^+}{d\alpha^2} d\alpha - \frac{u^+}{Re^+} + \alpha\chi = C$$

with C a real integration constant. The integral is solved, as before, by parts:

$$\int \alpha \frac{d^2 u^+}{d\alpha^2} d\alpha = \alpha \frac{du^+}{d\alpha} - \int \frac{du^+}{d\alpha} d\alpha = \alpha \frac{du^+}{d\alpha} - u^+$$

and finally the equation is written as

$$-\frac{\Pi^+ \alpha^2}{2} - \frac{\alpha}{Re^+} \frac{du^+}{d\alpha}(\alpha, Re^+) + \alpha\chi(\alpha, Re^+) = C \quad (3.325)$$

C is easily determined by setting $\alpha = 0$. As χ and $du^+/d\alpha$ are both bounded real numbers $\forall \alpha \in [0, 1]$, then $C = 0$. Π^+ could be found upon realising that, in dimensionless units, the wall-shear-stress τ_w could be converted into

$$\tau_w = -\mu \left. \frac{dU_z}{dr} \right|_R \Rightarrow u_\tau^2 \rho = -\left. \frac{\mu u_\tau}{R} \frac{du^+}{d\alpha} \right|_{\alpha=1} \Rightarrow \frac{u_\tau R}{\nu} = Re^+ = -\left. \frac{du^+}{d\alpha} \right|_{\alpha=1}$$

Thus the equality

$$Re^+ = -\left. \frac{du^+}{d\alpha} \right|_{\alpha=1} \quad (3.326)$$

plus the boundary conditions yield, upon setting $\alpha = 1$ in equation (3.325), the result $\Pi^+ = 2$.

⁷⁰ The fact that $\partial p^+/\partial \alpha \neq 0$ does not mean that motion exist along the radial direction, which would contradict the assumption of motion exclusively along the Z axis. The mean radial pressure gradient is exactly compensated with equal variation on some Reynolds stress components, and does not affect the mean velocity (see equation (3.315)). The non-zero radial pressure gradient in turbulent pipe flow predicted by equation (3.324) has been effectively measured and reported. See, for instance, [PES67].

Finally, the solution for the turbulent Hagen-Poiseuille flow has been obtained:

$$p^+(\alpha, \beta, Re^+) = -2\beta - \sigma_1(\alpha, Re^+) + \int_1^\alpha \frac{\sigma_2 - \sigma_1}{\alpha'} d\alpha' \quad (3.327)$$

$$\frac{1}{Re^+} \frac{du^+}{d\alpha}(\alpha, Re^+) = \chi(\alpha, Re^+) - \alpha \quad (3.328)$$

Note that Reynolds stress $\langle u'_r u'_z \rangle$ (dimensionless χ) only affects to the mean velocity, whereas the transverse turbulent velocity intensities $\langle u_r'^2 \rangle$ and $\langle u_\theta'^2 \rangle$ (dimensionless σ_1 and σ_2) only influence the mean pressure. Besides, U has no effect over P and, *vice versa*, neither has P over U . Last, but not least, note that Reynolds stress $\langle u'_r u'_z \rangle$ is proportional to the mean velocity derivative (plus the term α), a result that seems to support the Boussinesq's hypothesis, except that this time it has been obtained theoretically and not presumed *ad hoc*.

Equations (3.327) and (3.328) have been obtained directly from the RANSE with few very reasonable general assumptions. Therefore they must be taken very seriously, The mean quantities correspond, in principle, to ensemble average, although they could be expressed as time averages, since all quantities are time independent (stationary) and the ergodic hypothesis clearly applies to this case.

It is still possible to go one step beyond. Boundary condition (3.318) could be established because of the flow's axial symmetry. Applying that boundary condition to equation (3.328), and making $\alpha = 0$, the following result is obtained:

$$\chi(0, Re^+) = 0 \quad (3.329)$$

The Reynolds stress $\langle u'_r u'_z \rangle$ is zero in the pipe's centreline. This theoretical result is also confirmed experimentally (see [Wil06]). Also, at the wall $\alpha = 1$ with boundary condition (3.321), equation (3.328) yields

$$\left. \frac{du^+}{d\alpha} \right|_{\alpha=1} = -Re^+$$

which is the expected result in dimensionless units.

Integrating equation (3.328) one obtains a direct expression for u^+ :

$$\int_1^\alpha \frac{1}{Re^+} \frac{du^+}{d\alpha'} d\alpha' = \int_1^\alpha \chi d\alpha' - \int_1^\alpha \alpha' d\alpha' \Rightarrow u^+(\alpha, Re^+) = Re^+ \int_1^\alpha \chi d\alpha' - Re^+ \left(\frac{\alpha^2}{2} - \frac{1}{2} \right) \Rightarrow$$

$$u^+(\alpha, Re^+) = \frac{Re^+}{2} (1 - \alpha^2) - Re^+ \int_\alpha^1 \chi d\alpha' \quad (3.330)$$

This expression for the mean velocity profile in steady state turbulent pipe flow is known as the Shih-I Pai analytical solution, [Pai53]⁷¹. Equation (3.330) has the form of laminar-turbulent decomposition

⁷¹Equations (3.328) and (3.330) would be written differently if another normalisation would have been chosen for velocity, instead of u_τ . For instance, in the next section the chosen reference velocity will be ν/R , for reasons that will be explained there. In such case, the equivalent equations to (3.328) and (3.330) in the new normalisation would be:

$$\frac{du^*}{d\alpha} = \varpi(\alpha) - \frac{\alpha}{2} \Pi^* \quad (3.331)$$

suggested in equation (3.296), in the form:

$$U(\alpha, Re^+) = v_L(\alpha) + U_T(\alpha, Re^+) \quad (3.333)$$

where U is the mean total velocity, v_L is the laminar Hagen-Poiseuille velocity profile (see equation (3.297)), and $U_T = -Re^+ \int_{\alpha}^1 \chi d\alpha'$ the mean component of turbulence velocity in U . That is a remarkable result, since it states that the difference between turbulent and laminar velocity distributions is directly a function of the Reynolds stress. Thus, Reynolds stress alone explains the generation of the turbulent component in the total velocity. Note that $\chi(\alpha, Re^+) = 0$ (i.e. $\langle u'_r u'_z \rangle = 0$) would reduce equation (3.333) to the laminar velocity profile given in equation (3.297), circumstance that leads to consider the Reynolds stress component $\langle u'_r u'_z \rangle$ as the most important to characterise the turbulence. ■

Amongst the contributions of [Pai53] stands out the analytical turbulent velocity profile that satisfies the differential equation (3.328) plus the boundary conditions (3.317) and (3.321), thus producing an exact solution of the RANSE. This solution is not unique, since the unknowns outnumber the available equations, but it provides an invaluable reference with which to compare potential empirical profiles and laboratory data. The announced solution takes the form

$$u^+(\alpha, Re^+) = u_m^+ \left(1 + b_2 \alpha^2 + b_{2n} \alpha^{2n} \right), \quad (n \geq 2, n \in \mathbb{N}) \quad (3.334)$$

where $n \geq 2$ is an integer, $b_n, b_{2n} \in \mathbb{R}$ are real numbers, and u_m^+ is the maximum of the velocity profile (3.330), which occurs at the pipe's axis:

$$u_m^+ = u^+(0, Re^+) = \left(\frac{1}{2} - \int_0^1 \chi d\alpha \right) Re^+ \quad (3.335)$$

just where the laminar velocity maximum is found. Note the velocity is an even function of α , as it corresponds to the radial symmetry of the flow within the pipe. Since $u_m^+ \geq 0$, then it must be

$$\frac{1}{2} - \int_0^1 \chi d\alpha \geq 0$$

The function (3.334) effectively satisfies the velocity equation (3.328):

$$\frac{u_m^+}{Re^+} (2b_2 \alpha + 2n b_{2n} \alpha^{2n-1}) = \chi(\alpha, Re^+) - \alpha \Rightarrow \left(b_2 + \frac{Re^+}{2u_m^+} \right) \alpha + n b_{2n} \alpha^{2n-1} = \frac{Re^+}{2u_m^+} \chi(\alpha, Re^+) \quad (3.336)$$

or

$$(b_2 + \vartheta) \alpha + n b_{2n} \alpha^{2n-1} = \vartheta \chi(\alpha, Re^+) \quad (3.337)$$

with

$$\vartheta = \frac{Re^+}{2u_m^+} \quad (\vartheta > 0) \quad (3.338)$$

and

$$u^*(\alpha) = \frac{\Pi^*}{4} (1 - \alpha^2) - \int_{\alpha}^1 \varpi(\alpha') d\alpha' \quad (3.332)$$

with u^* , Π^* and ϖ playing the same role as u^+ , Π^+ and χ , respectively, in the new normalisation.

Boundary condition (3.317) yields

$$\alpha = 1 \Rightarrow u^+(1, Re^+) = 0 \Rightarrow 1 + b_2 + b_{2n} = 0 \quad (3.339)$$

while boundary condition (3.321) and equation (3.336) lead to

$$\alpha = 1 \Rightarrow \chi(1, Re^+) = 0 \Rightarrow b_2 + \vartheta + n b_{2n} = 0 \quad (3.340)$$

Subtracting (3.339) from (3.340)

$$\vartheta + n b_{2n} - 1 - b_{2n} = 0 \Rightarrow b_{2n} = \frac{1 - \vartheta}{n - 1} \quad (3.341)$$

and b_2 is obtained from equation (3.339)

$$b_2 = \frac{\vartheta - n}{n - 1} \quad (3.342)$$

Therefore, the analytical velocity profile fulfilling the differential equation (3.328) and the boundary conditions (3.317) and (3.321) is given by

$$u^+(\alpha, Re^+) = u_m^+ \left(1 + \frac{\vartheta - n}{n - 1} \alpha^2 + \frac{1 - \vartheta}{n - 1} \alpha^{2n} \right), \quad (n \geq 2, n \in \mathbb{N}) \quad (3.343)$$

The coefficients of α^2 and α^{2n} are negative as long as $\vartheta < n$ and $\vartheta > 1$, respectively. Normally it is requested that those coefficients be negative for the solution to be physically sound. Equation (3.343) could also be expressed as

$$u^+(\alpha, Re^+) = u_m^+ \left[1 - \alpha^2 + \frac{\vartheta - 1}{n - 1} \alpha^2 (1 - \alpha^{2n-2}) \right], \quad (n \geq 2, n \in \mathbb{N}) \quad (3.344)$$

where the two components of the mean velocity are clearly shown:

- the laminar component corresponding to Hagen-Poiseuille flow

$$v_L(\alpha) = u_m^+(1 - \alpha^2) \quad (3.345)$$

- and the purely turbulent component derived from Reynolds stress

$$U_T(\alpha, Re^+) = u_m^+ \left(\frac{\vartheta - 1}{n - 1} \right) \alpha^2 (1 - \alpha^{2n-2}) \quad (3.346)$$

The Reynolds stress $\chi(\alpha, Re^+)$ is obtained from equation (3.337)

$$\begin{aligned} \left(\frac{\vartheta - n}{n - 1} + \vartheta \right) \alpha + n \left(\frac{1 - \vartheta}{n - 1} \right) \alpha^{2n-1} &= \vartheta \chi(\alpha, Re^+) \Rightarrow \\ \chi(\alpha, Re^+) &= \frac{n(\vartheta - 1)}{\vartheta(n - 1)} \alpha (1 - \alpha^{2n-2}) \end{aligned} \quad (3.347)$$

Equations (3.343)/(3.344) and (3.347) constitute one of the sets of fully analytical solutions to the problem of finding the velocity profile corresponding to a steady state turbulent Hagen-Poiseuille flow (Pai flow) in a circular pipe ⁷².

Note that, since $Re^+ = u_\tau R/\nu$, $u_m^+ = U_m/u_\tau$ and $u_\tau = \sqrt{\tau_w/\rho}$, then ϑ could be expressed as

$$\vartheta = \frac{Re^+}{2u_m^+} = \frac{u_\tau^2 R}{2\nu U_m} = \frac{\tau_w R}{2\mu U_m}$$

According to equation (3.297) the wall-shear stress for a laminar Hagen-Poiseuille flow whose maximum velocity were $v_{z_{max}} = U_m$, is given by

$$\tau_l = -\mu \left. \frac{dv_z}{dr} \right|_{r=R} = \frac{2\mu U_m}{R} \quad (3.349)$$

Therefore, the variable ϑ could be expressed as

$$\vartheta = \frac{\tau_w}{\tau_l} \quad (\vartheta \geq 1) \quad (3.350)$$

and represents the ratio of the wall-shear stress τ_w for a steady and fully developed turbulent flow in a pipe, to the wall-shear stress τ_l of a steady laminar flow with the same maximum velocity U_m , in the same circular pipe. Clearly $\vartheta > 1$, since the wall-shear stress is larger for turbulent flows than it is in the laminar case.

Note that $\vartheta = 1$ reduces equation (3.344) to the laminar case (3.297). Moreover, the Reynolds stress (3.347) is identically zero if $\vartheta = 1$

Figure 3.14 shows one of the turbulent analytic velocity profiles (3.343) that adjusts to the CFD simulation to be conducted in section 4.10.1, with $Re \simeq 1.2 \times 10^7$. This analytic velocity profile corresponds to a maximum dimensionless velocity $U_m = 2.2708$, and it has been obtained by setting $\vartheta = 13.4$ and $n = 16$ (n is always an integer). Figure 3.14 also shows the log-law velocity profile corresponding to the same CFD simulation (the log-law is explained in section 4.5). The agreement is remarkable, except near the wall, $\alpha = 1$, where the log-law and CFD profiles are much steeper. The outstanding coincidence near the wall between the CFD model and the log-law profiles could be due to the fact that the CFD solver uses the log-law as a wall-function to adjust the no-slip condition at the wall. Since the solution to the differential equations (3.327)-(3.328) is not unique, appropriate solutions must

⁷²To round things off, in reference [Pan90] is offered yet another analytical expression for the mean velocity profile of turbulent flow in a circular pipe. That equation takes the form, using the same variables introduced so far,

$$u^+ = u_{max}^+ + \frac{1}{0.15} \left[\sqrt{(1-\alpha)\alpha} - \arcsin \sqrt{\alpha} \right] \quad (3.348)$$

with 0.15 the result of modifying slightly the squared von Karman's constant, $\kappa = 0.41$, $\kappa^2 = 0.168 \approx 0.15$, to better adjust to experimental data, and u_{max}^+ the maximum mean velocity at the pipe's centreline. This equation presents a remarkable concordance with experimental data, specially for rough pipes. Unfortunately, (3.348) does not fulfil equation (3.328) for any function χ which also satisfy the boundary condition (3.321), because $du^+/d\alpha \neq Re^+$ at $\alpha = 1$. But this behaviour should not be so unexpected: the log-law does not satisfy it either (see equation (4.54)). This is due to the fact that neither (3.348) nor log-law are supposed to reproduce the turbulent flow dynamics at the very wall.

Regardless of the last remark, it seems startling that relatively simple expressions like (3.343)/(3.344) or (3.348) be not of widespread use in Engineering applications, at least as first approximations of the actual mean velocity profile.

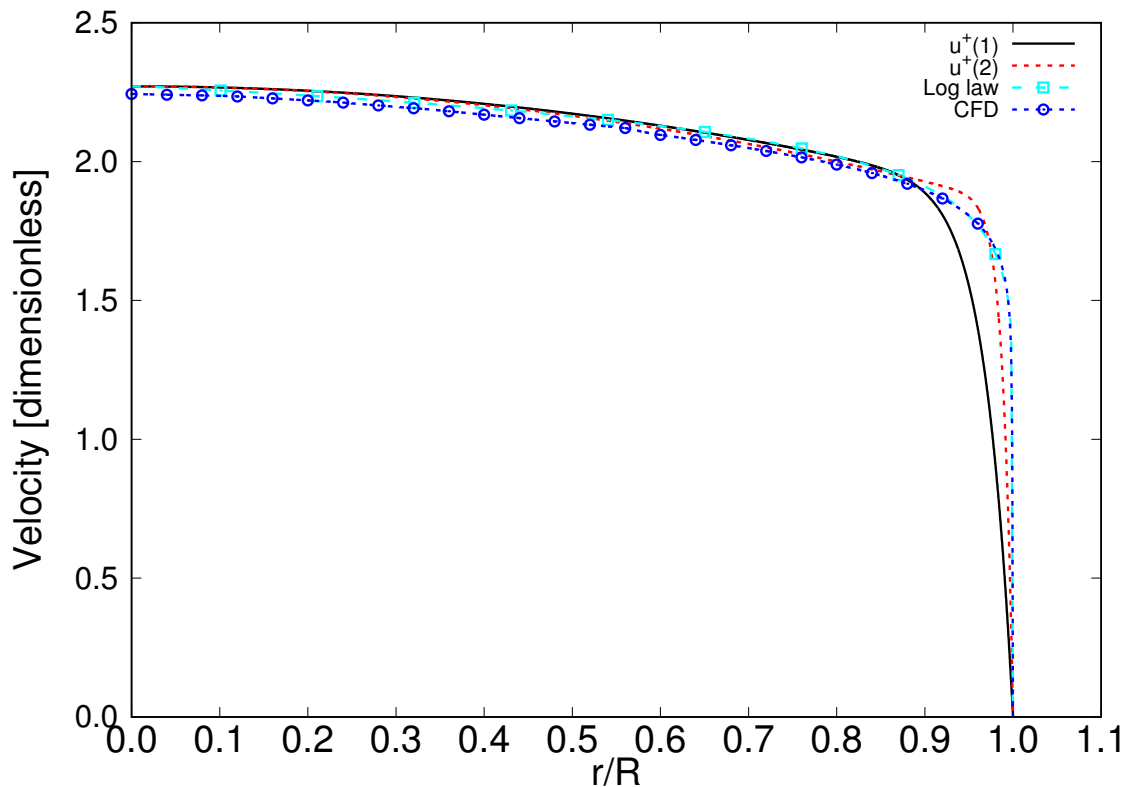


Figure 3.14: Analytic, log-law and CFD velocity profiles for turbulent Hagen-Poiseuille flow (analytic profiles with $U_m = 2.2708$: (1) $\vartheta = 13.4$, $n = 16$, and (2) $\vartheta = 36.8$, $n = 45$).

always be found by selecting the adjustable parameters ϑ and n . A second example is also presented in figure 3.14, which shows too the curve corresponding to an analytic solution given by $U_m = 2.2708$, $\vartheta = 36.8$ and $n = 45$. In this second profile the behaviour at the wall is steeper, although the shoulder of the curve raises above the log-law. In any case, the analytic model developed in [Pai53] is an invaluable tool for estimating the velocity profiles and other properties of steady turbulent flows in pipes.

Figure 3.15 depicts the dimensionless analytic Reynolds stress $\chi(\alpha, Re^+)$, given by equation (3.347), for the same sets of parameters: $U_m = 2.2708$, $\vartheta = 13.4$, $n = 16$ and $U_m = 2.2708$, $\vartheta = 36.8$ and $n = 45$. In both cases $Re \simeq 1.2 \times 10^7$ for the mean flow. The results show a remarkable qualitative agreement with equivalent profiles found in [Wil06], although for much smaller Reynolds numbers. Figure 3.15 also presents the Reynolds stress corresponding to a steady state CFD simulation carried out with the same turbulence model $k - \omega$ SSTSAS that appears in figure 3.14 (see section 4.10.1) for $Re \gtrsim 10^7$. The plot is represented in arbitrary units, since only qualitative results are relevant here. The different behaviour of the CFD model respect to the analytical case for $\alpha \equiv r/R \approx 1$, indicates the difficulty for the turbulence model to simulate the expected near-wall flow structure when the Reynolds number is so high. The near-wall cells are calculated in the simulation through wall-functions, that yield a result which is no longer supported by the chosen turbulence model algorithm when it is applied to cells farther away from the wall. Besides, the mesh employed in the CFD simulation is strongly graded near the wall (for an explanation of these concepts see section 4.6).

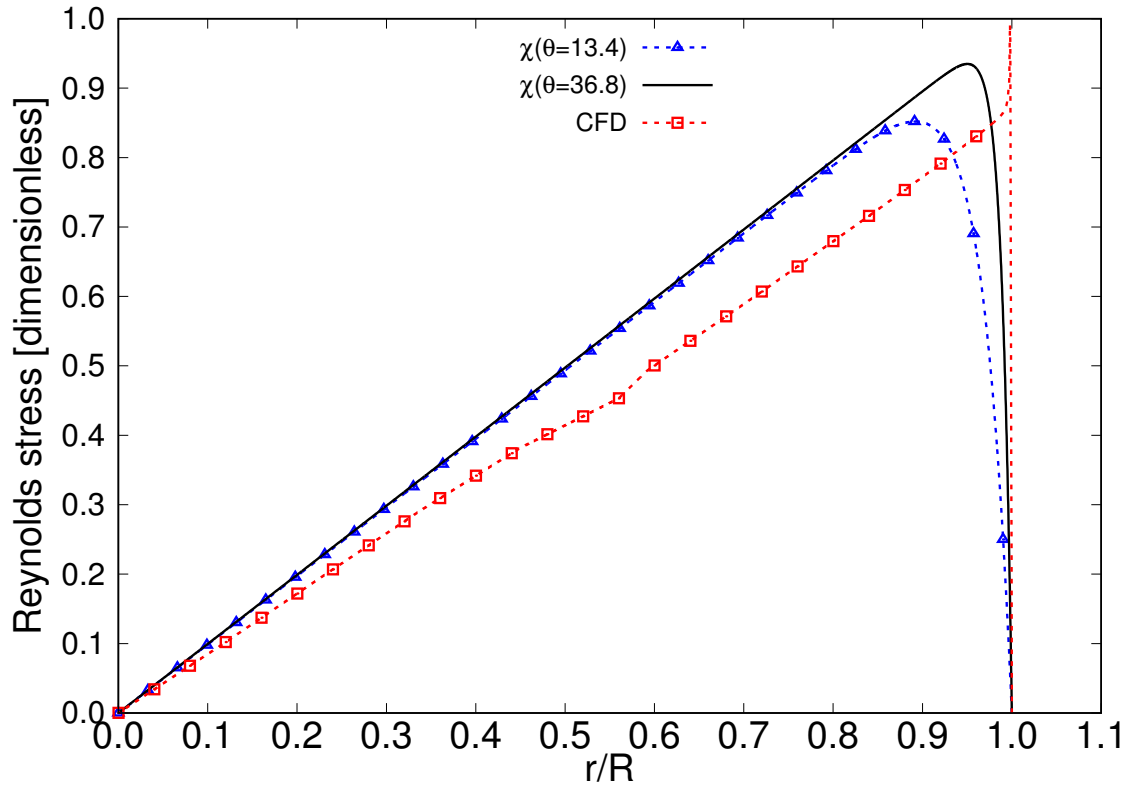


Figure 3.15: Analytic and CFD Reynolds stress profile for turbulent Hagen-Poiseuille flow (analytic with $U_m = 2.2708$, $\vartheta = 13.4$, $n = 16$ and $U_m = 2.2708$, $\vartheta = 36.8$ and $n = 45$).

3.4.2 General Transient/Unsteady Analytical Solution of RANSE for Incompressible Pipe Flow

Last section presented an analytical solution for the turbulent steady state incompressible pipe flow, after [Pai53], based on the Hagen-Poiseuille solution and depending directly on the components of the Reynolds stress tensor. Both solutions share the properties of being analytical, time-independent (correspond to steady state) and applicable to incompressible pipe flow.

In 1932 Piotr Szymanski published his work [Szy32]⁷³, in which he proposed the analytical solution for the transient problem of laminar incompressible pipe flow accelerating from rest, in response to a pressure step $\Delta p > 0$ suddenly applied to the fluid⁷⁴. The analytical solution takes the form:

$$v(t, r) = v_\infty \left[(1 - \alpha^2) - \sum_{n=1}^{\infty} \frac{8J_0(\lambda_n \alpha)}{\lambda_n^3 J_1(\lambda_n)} e^{-\lambda_n^2 \gamma} \right] \quad (3.351)$$

with $\alpha = r/R$ a dimensionless radial distance from the pipe's centreline, $\gamma = t\nu/R^2$ a dimensionless time, R and L the pipe's radius and length, ν the fluid's kinematic viscosity, $\mu = \rho\nu$ the dynamic

⁷³The interested reader may consult directly the source [Szy32], or alternatively try the more straightforward and modern approach offered by [Dur08]. Surprisingly, [Dur08] does not cite [Szy32] amongst its references.

⁷⁴A distinction is made in this Dissertation between *transient* and *unsteady* flow: a transient flow tends asymptotically to a steady state as $t \rightarrow \infty$, either because the forces decrease their action or because the flow adapts to the new situation. An unsteady flow is permanently time-dependent and shows no tendency to reach a steady state with $t \rightarrow \infty$.

viscosity; v_∞ is the steady state maximum velocity at the centreline, given by

$$v_\infty = \frac{\Delta p R^2}{4\mu L} \geq 0 \quad (3.352)$$

$J_0(x)$ and $J_1(x)$ are the Bessel functions of the first kind of order 0 and 1, respectively, and λ_n are the roots (or zeroes) of $J_0(x)$ ($J_0(\lambda_n) = 0 \forall n \in \mathbb{N}$).

So far there exists a set of three analytical solutions for incompressible pipe flow, duly expressed in table 3.1. The missing place corresponds to transient/unsteady turbulent pipe flow, whose General Analytical Solution (GAS) is going to be provided herein, along the lines set by [Szy32] on one hand, and [Pai53] on the other. The proposed solution is the most general, since it contains the laminar steady state, laminar transient, and turbulent steady state solutions as particular cases.

PIPE FLOW	Laminar	Turbulent
Steady State	Hagen-Poiseuille Flow	[Pai53]
Transient/Unsteady Regime	[Szy32]	This Dissertation

Table 3.1: Complete set of analytical solutions for incompressible pipe flow.

The starting point is similar to that one studied in section 3.4.1, except that now the main quantities depend also on t :

$$\mathbf{u}(t, \mathbf{x}) = \mathbf{U}(t, \mathbf{x}) + \mathbf{u}'(t, \mathbf{x}) \quad , \quad p(t, \mathbf{x}) = P(t, \mathbf{x}) + p'(t, \mathbf{x}) \quad (3.353)$$

The assumptions made to obtain the announced results are not very different than those expressed in section 3.4.1:

- i. The mean flow is axially symmetric, that is, $\partial\Psi/\partial\theta = 0$ for any mean flow quantity Ψ .
- ii. The flow is incompressible and Newtonian, with density and dynamic and kinematic viscosities ρ , μ and ν , respectively.
- iii. No entrance or exit effects are considered, thus the pipe is assumed to have an infinite length $-\infty < z < +\infty$ ⁷⁵.
- iv. The mean velocity has only a non-zero component along the Z axis

$$\mathbf{U} = (U_r, U_\theta, U_z) = (0, 0, U_z) \equiv (0, 0, U)$$

(U and U_z will be used interchangeably). Note that this assumption implies $u_r = u'_r$, $u_\theta = u'_\theta$ and $u'_z = u_z - U$.

- v. Gravity effects are neglected.
- vi. The statistical properties of the flow are the same at all sections of constant z (see footnote 66 in page 150). In particular, this applies to the Reynolds stress tensor $R_{ij} = -\rho\langle u'_i u'_j \rangle$ which is assumed to be only function of (t, r) .

⁷⁵Instead of considering the pressure gradient as a function of the total pressure drop Δp and pipe length L , $\Delta p/L$, as it is the case in [Szy32], herein a mean pressure gradient $\Pi(t) = -\partial P/\partial z$ is considered to be acting on the flow, with no reference whatsoever as to how it might be generated. Note $\Pi(t)$ cannot be a function of z , see section 2.3.3.

It could also be assumed that the flow reach a steady state as $t \rightarrow \infty$ (transient flow). That assumption, although true and useful in some cases, is not strictly necessary at this point, and will not be imposed. Thus, the results obtained in this section will find application in both, transient and unsteady flows.

The mean turbulent fields have the following dependence

$$\mathbf{U} = \mathbf{U}(t, r), P = P(t, r, z), R_{ij} = R_{ij}(t, r) \quad (3.354)$$

The general cylindrical RANSE (3.300) reduce in this case to:

$$-\frac{1}{\rho} \frac{\partial P}{\partial r} - \frac{1}{r} \frac{\partial(r \langle u_r'^2 \rangle)}{\partial r} + \frac{\langle u_\theta'^2 \rangle}{r} = 0 \quad (3.355)$$

$$-\frac{1}{r} \frac{\partial(r \langle u_r' u_\theta' \rangle)}{\partial r} - \frac{\langle u_r' u_\theta' \rangle}{r} = 0 \quad (3.356)$$

$$-\frac{1}{\rho} \frac{\partial P}{\partial z} + \nu \left(\frac{\partial^2 U_z}{\partial r^2} + \frac{1}{r} \frac{\partial U_z}{\partial r} \right) - \frac{1}{r} \frac{\partial(r \langle u_r' u_z' \rangle)}{\partial r} = \frac{\partial U_z}{\partial t} \quad (3.357)$$

since all other terms are zero, according to (3.354). The continuity equation is absent from this set because all of its terms are null and is a trivial equation. In this case the averaging method could only be the ensemble average, yielding RANSE *à la* ensemble average and Reynolds stress tensor *à la* ensemble average.

The second equation (3.356) is easily integrable following the same procedure used to integrate (3.305). An identical result is obtained:

$$\langle u_r' u_\theta' \rangle = 0 \quad (3.358)$$

and one fewer unknown for the problem. Still, there are five unknowns

$$U_z(t, r) \equiv U(t, r), P(t, r, z), \langle u_r' u_z' \rangle(t, r), \langle u_r'^2 \rangle(t, r), \langle u_\theta'^2 \rangle(t, r)$$

and just two equations (3.355) and (3.357). This fact illustrates dramatically the closure problem attached to RANSE.

In order to obtain additional relationships among the five dependent variables, it is convenient to convert them into dimensionless form, just as was done in section 3.4.1:

$$\alpha = \frac{r}{R} \quad (0 \leq \alpha \leq 1), \quad \beta = \frac{z}{R} \quad (3.359)$$

But now, contrary to the approach followed in section 3.4.1, care should be taken upon selecting the reference velocity, since the friction velocity u_τ is time-dependent and might not be such a good choice.

In principle, three approaches could be developed to find out the desired equations. They summarise in the following terms:

- Using a fully constant reference velocity, namely

$$u_{ref} = \frac{\nu}{R}$$

with no mention to the centreline or the friction velocities.

- Using the friction velocity $u_\tau(t)$ as the reference velocity, despite being time-dependent. This will allow direct comparison of results with those seen in section 3.4.1, since both use the same reference velocity.

- Using the maximum velocity $u_{max}(t)$ (that occurring at the pipe's centreline) as the reference velocity, despite being also time-dependent. This will allow direct comparison of results with those presented in [Szy32], since both use the same reference velocity.

In this Dissertation only the first approach will be followed, since it is clear and simple enough to illustrate the general method to obtain solutions. Advances in the other two directions are also planned for future work, as they are considered relevant in the distribution of mean velocity profiles for many Physics and Engineering applications.

Therefore, defining the reference velocity as

$$u_{ref} = \frac{\nu}{R} \quad (3.360)$$

the dimensionless mean velocity will be

$$u^*(\gamma, \alpha) = \frac{U_z R}{\nu} \quad (3.361)$$

With such definition, the dimensionless time is given by

$$\gamma = \frac{t\nu}{R^2} \quad (3.362)$$

being $t_{ref} = R^2/\nu$ the reference time.

Following the definition of dimensionless P made in section 3.4.1, the dimensionless mean pressure is now defined as

$$p^*(\gamma, \alpha, \beta) = \frac{(P - P_0) R^2}{\rho\nu^2} \quad (3.363)$$

with $p_{ref} = \rho\nu^2/R^2$ the reference pressure, and $P_0(t) = P(t, R, 0)$ the time-dependent reference of mean pressure at t , $r = R$, $z = 0$, which is supposed to define the external pressure exerted on the flow, in order to calculate the gradient therefrom. Note the dimensionless mean pressure gradient is now given by

$$\Pi^*(\gamma) = -\frac{\partial p^*}{\partial \beta}$$

and does not depend on α , although p^* does, since no mean fluid motion exists in the radial direction, according to assumption iv in page 161.

Additionally, the non-zero dimensionless Reynolds stress tensor components are given by

$$\varsigma_1(\gamma, \alpha) = \frac{\langle u_r'^2 \rangle R^2}{\nu^2} \quad (3.364)$$

$$\varsigma_2(\gamma, \alpha) = \frac{\langle u_\theta'^2 \rangle R^2}{\nu^2} \quad (3.365)$$

$$\varpi(\gamma, \alpha) = \frac{\langle u_r' u_z' \rangle R^2}{\nu^2} \quad (3.366)$$

and the derivatives by

$$\frac{\partial}{\partial r} = \frac{1}{R} \frac{\partial}{\partial \alpha}, \quad \frac{\partial^2}{\partial r^2} = \frac{1}{R^2} \frac{\partial^2}{\partial \alpha^2}, \quad \frac{\partial}{\partial z} = \frac{1}{R} \frac{\partial}{\partial \beta}, \quad \frac{\partial}{\partial t} = \frac{\nu}{R^2} \frac{\partial}{\partial \gamma}$$

With such dimensionless quantities, equations (3.355) and (3.357) result in

$$\frac{\partial p^*}{\partial \alpha} + \frac{1}{\alpha} \frac{\partial(\varsigma_1 \alpha)}{\partial \alpha} - \frac{\varsigma_2}{\alpha} = 0 \quad (3.367)$$

$$\frac{\partial u^*}{\partial \gamma} + \frac{\partial p^*}{\partial \beta} - \left(\frac{\partial^2 u^*}{\partial \alpha^2} + \frac{1}{\alpha} \frac{\partial u^*}{\partial \alpha} \right) + \frac{1}{\alpha} \frac{\partial(\varpi \alpha)}{\partial \alpha} = 0 \quad (3.368)$$

respectively, subjected to the following boundary and initial conditions:

BOUNDARY CONDITIONS

$$u^*(\gamma, 1) = 0 \quad (3.369)$$

$$\left. \frac{\partial u^*}{\partial \alpha} \right]_{\alpha=0} = 0 \quad (3.370)$$

$$\varsigma_1(\gamma, 1) = 0 \quad (3.371)$$

$$\varsigma_2(\gamma, 1) = 0 \quad (3.372)$$

$$\varpi(\gamma, 1) = 0 \quad (3.373)$$

$$p^*(\gamma, 1, 0) = 0 \quad (3.374)$$

INITIAL CONDITIONS

$$u^*(0, \alpha) = u_0^*(\alpha) \quad (3.375)$$

$$\varsigma_1(0, \alpha) = \varsigma_{1_0}(\alpha) \quad (3.376)$$

$$\varsigma_2(0, \alpha) = \varsigma_{2_0}(\alpha) \quad (3.377)$$

$$\varpi(0, \alpha) = \varpi_0(\alpha) \quad (3.378)$$

For the boundary conditions, equation (3.369) is the no-slip condition (see footnote 64 in page 146), (3.370) establishes that the mean velocity has a maximum at the centreline (see footnote 69 in page 153, which applies equally well herein), (3.371)-(3.373) determine the flow in the vicinity of the wall to be laminar, and (3.374) sets $P = P_0(t)$ at the circumference defined by $\alpha = 1$ and $\beta = 0$.

For the initial conditions⁷⁶, equations (3.375)-(3.378) establish the fluid to be at a given state in $\gamma = 0$. Note that no initial condition is defined for the mean pressure since it is directly related to the other mean quantities (see equation (3.379) below), and no further conditions ought to be imposed thereupon

⁷⁶For the transient problem being considered along this Dissertation, the initial state of the fluid is to be at rest,

$$u_0^*(\alpha) = 0, \quad \varsigma_{1_0}(\alpha) = 0, \quad \varsigma_{2_0}(\alpha) = 0, \quad \varpi_0(\alpha) = 0$$

with all turbulence quantities being also zero. But it is preferable to consider a general initial state, since the homogeneous problem (see equation (3.430) below) starting from rest has a trivial null solution. Once a general solution for the non-homogeneous problem is available, then it could be studied the case of motion suddenly started from rest; or the case of a steady state Hagen-Poiseuille laminar flow $u_0^*(\alpha) = u_{max}^*(1 - \alpha^2)$ at $\gamma = 0$ which is perturbed by the non-homogeneous source term $\Xi(\gamma, \alpha)$ (see equation (3.380)); or the case of a steady state Pai turbulent flow $u_0^+(\alpha, Re^+) = Re^+(1 - \alpha^2)/2 - Re^+ \int_{\alpha}^1 \chi \, d\alpha'$ at $\gamma = 0$ (see equation (3.330)), which is then perturbed by a $\Xi(\gamma, \alpha)$ source term; or any other seemingly reasonable flow which could be used as an initial state in any transient/unsteady flow experiment starting therefrom.

77.

Equation (3.367) is formally identical to (3.324) and, therefore, could be integrated along the lines followed to obtain (3.324) in section 3.4.1. The result is completely similar and reads

$$p^*(\gamma, \alpha, \beta) = -\beta \Pi^*(\gamma) - \varsigma_1(\gamma, \alpha) + \int_1^\alpha \frac{\varsigma_2(\gamma, \alpha') - \varsigma_1(\gamma, \alpha')}{\alpha'} d\alpha' \quad (3.379)$$

As established in footnote 70 in page 154, the existence of a non-zero mean radial pressure gradient $\partial p^*/\partial\alpha \neq 0$ does not imply any fluid motion along the radial direction, as stated in assumption iv of page 161, since that gradient is exactly compensated with equal variation on some Reynolds stress components and does not affect the mean velocity (see equation (3.379)).

Equation (3.368) has a much more elaborate solution. In principle, it could be written in an alternative form:

$$\frac{\partial u^*}{\partial\gamma} - \left(\frac{\partial^2 u^*}{\partial\alpha^2} + \frac{1}{\alpha} \frac{\partial u^*}{\partial\alpha} \right) = \Pi^* - \frac{1}{\alpha} \frac{\partial(\varpi\alpha)}{\partial\alpha} = \Xi(\gamma, \alpha) \quad (3.380)$$

where $\Xi(\gamma, \alpha)$ represents the non-homogeneous term, since it does not contain the dependent variable $u^*(\gamma, \alpha)$. In another context, it could be interpreted as a source term for the field $u^*(\gamma, \alpha)$.

The sensible way to obtain a solution for equation (3.380) is first to solve the homogeneous associated problem:

$$\frac{\partial w}{\partial\gamma} - \left(\frac{\partial^2 w}{\partial\alpha^2} + \frac{1}{\alpha} \frac{\partial w}{\partial\alpha} \right) = 0 \quad (3.381)$$

subjected to identical boundary and initial conditions, equations (3.369)-(3.378). Once a solution for the homogeneous problem is available, it could be attempted to find the corresponding solution for the non-homogeneous one.

The homogeneous problem (3.381) corresponds to a linear parabolic partial differential equation which could be solved using the Separation of Variables method. It is assumed the homogeneous solution could be expressed in the form:

$$w(\gamma, \alpha) = A(\alpha)\Gamma(\gamma) + w_\infty(\gamma, \alpha)$$

with the function $A(\alpha)$ depending only on α , and likewise for $\Gamma(\gamma)$ with γ , and $w_\infty(\gamma, \alpha)$ is a gauge function for which there are at least three options:

- $w_\infty(\gamma, \alpha)$ satisfies simultaneously both conditions:

$$\frac{\partial w_\infty}{\partial\gamma} = 0$$

and

$$\frac{\partial^2 w_\infty}{\partial\alpha^2} + \frac{1}{\alpha} \frac{\partial w_\infty}{\partial\alpha} = 0$$

⁷⁷Nevertheless, a reflection is in order in the particular case of initial rest conditions. In that case the mean pressure must satisfy $p^*(0, \alpha, \beta) = 0$, and this condition defines the initial mean pressure $P(0, r, z)$ to be constant $P_0(0)$ everywhere in the pipe. This last result should come as no surprise: since the fluid is initially at rest there is no pressure drop anywhere and the initial mean pressure does not depend on β . Besides, since gravity is neglected (assumption v in page 161), no hydrostatic effects are to be taken into consideration, and the initial mean pressure is also α -independent (even if gravity were not neglected, the fact that the pipe is horizontal, and relatively thin, conveys very small differences in hydrostatic pressure along the pipe's diameter, and thus the mean pressure would still be α -independent.). Therefore, should the initial state be that of rest, then $P(0, r, z)$ is constant everywhere and equal to $P_0(0)$.

The first one leads to $w_\infty = w_\infty(\alpha)$, since w_∞ does not depend on γ . The second one is fulfilled, for instance, with

$$w_\infty(\alpha) = k_1 \ln \alpha + k_2 \quad (3.382)$$

being k_1 and k_2 real constants chosen to satisfy the boundary and initial conditions.

- $w_\infty(\gamma, \alpha)$ satisfies equation (3.381) without having the form $w_\infty(\gamma, \alpha) = A(\alpha)\Gamma(\gamma)$. For instance, it could be:

$$w_\infty(\gamma, \alpha) = 4k\gamma - k(1 - \alpha^2) \quad (3.383)$$

- Any combination of the above.

$w_\infty(\gamma, \alpha)$ would be needed for those cases in which boundary and initial conditions are difficult to fulfil with *ordinary* functions. Since it is of secondary importance, this term will be plainly denoted w_∞ from now on.

Equation (3.381) is then written as:

$$\frac{\partial(A\Gamma + w_\infty)}{\partial\gamma} - \frac{\partial^2(A\Gamma + w_\infty)}{\partial\alpha^2} - \frac{1}{\alpha} \frac{\partial(A\Gamma + w_\infty)}{\partial\alpha} = 0 \Rightarrow A \frac{d\Gamma}{d\gamma} - \Gamma \frac{d^2A}{d\alpha^2} - \Gamma \frac{1}{\alpha} \frac{dA}{d\alpha} = 0$$

Divide this expression by $A\Gamma$, and it results in

$$\frac{1}{\Gamma} \frac{d\Gamma}{d\gamma} - \frac{1}{A} \frac{d^2A}{d\alpha^2} - \frac{1}{A\alpha} \frac{dA}{d\alpha} = 0 \Rightarrow \frac{1}{\Gamma} \frac{d\Gamma}{d\gamma} = \frac{1}{A} \frac{d^2A}{d\alpha^2} + \frac{1}{A\alpha} \frac{dA}{d\alpha}$$

Note the left-hand side of this equation depends only on γ , while the right-hand side depends solely on α . Therefore, both sides must be constant, depending neither on α nor γ . For convenience, this constant is called $-\lambda^2$, and the resulting equation is:

$$\frac{1}{\Gamma} \frac{d\Gamma}{d\gamma} = \frac{1}{A} \frac{d^2A}{d\alpha^2} + \frac{1}{A\alpha} \frac{dA}{d\alpha} = -\lambda^2 \quad (3.384)$$

Equation (3.384) could be split in two ordinary differential equations:

$$\frac{d\Gamma}{d\gamma} \equiv \dot{\Gamma} = -\lambda^2 \Gamma \quad (3.385)$$

$$\frac{d^2A}{d\alpha^2} + \frac{1}{\alpha} \frac{dA}{d\alpha} \equiv A'' + \frac{1}{\alpha} A' = -\lambda^2 A \quad (3.386)$$

where, adhering to the custom, the dot $\dot{\Gamma}$ denotes derivative respect to (dimensionless) time, whereas the prime A' derivative respect to (dimensionless) space. Both notations, dots and primes, or $d/d\gamma$ and $d/d\alpha$, respectively, will be used interchangeably in this section, upon convenience.

Equation (3.385) has a straightforward solution:

$$\Gamma(\gamma) = C_0 e^{-\lambda^2 \gamma}$$

with C_0 a real constant that will be adjusted later to satisfy boundary and initial conditions. Note that $\Gamma \rightarrow 0$ with $\gamma \rightarrow \infty$, and this behaviour might lead to think of transient solutions yielding steady state flows as time elapses sufficiently far. However, it will be seen that this exponential decay is compatible with unsteady, not transient, solutions, in which the time dependence would be inserted in other functions.

More interesting is the equation (3.386). It could be written in the following form:

$$\alpha \frac{d^2 A}{d\alpha^2} + \frac{dA}{d\alpha} = \frac{d}{d\alpha} \left(\alpha \frac{dA}{d\alpha} \right) \equiv \mathcal{L}A = -\lambda^2 \alpha A \quad (3.387)$$

where

$$\mathcal{L} = \frac{d}{d\alpha} \left(\alpha \frac{d}{d\alpha} \right) \quad (3.388)$$

is the so-called **Sturm-Liouville Operator** for the problem under consideration. And now it is convenient to stop along the way to briefly introduce the Sturm-Liouville methodology. ■

The general expression for a Sturm-Liouville operator is ⁷⁸

$$\mathcal{L} = \frac{d}{dx} \left(p(x) \frac{d}{dx} \right) + q(x) \quad (3.389)$$

corresponding to the general **Sturm-Liouville eigenvalue problem** (see [AG08], [Mac04] or [AM11]) ⁷⁹

$$\mathcal{L}\phi = \frac{d}{dx} \left(p(x) \frac{d\phi}{dx} \right) + q(x)\phi = -\lambda \varrho(x)\phi \quad (3.393)$$

⁷⁸In this Dissertation it will only be considered the real Sturm-Liouville eigenvalue problem, with all functions operating in \mathbb{R} . The complex Sturm-Liouville eigenvalue problem is of interest in other fields of Physics, but not in this context.

⁷⁹ The Sturm-Liouville problem is usually presented in two different ways, which result to be equivalent except for a normalisation constant. The first approach, which is the one used herein, is presented for example by [AM11], and defines the Sturm-Liouville problem by equation (3.393) and the attached inner product by equation (3.395).

The second approach is used by [Mac04] and defines the Sturm-Liouville problem by the following equation

$$l(x)\phi'' + m(x)\phi' + n(x)\phi = \lambda\phi \quad (3.390)$$

with the prime indicating derivative respect to x . The inner product attached to this equation is

$$\langle \phi, \psi \rangle = \int_a^b \phi(x)\psi(x)w(x) dx \quad (3.391)$$

with $w(x)$ a weighting function given by the following expression (which is related to the Wronskian of any two linearly independent solutions of equation (3.390)):

$$w(x) = \frac{1}{l(x)} \exp \left(\int_a^x \frac{m(x')}{l(x')} dx' \right) \quad (3.392)$$

As remarked above, both approaches are equivalent and yield the same results except for a normalisation constant, which happens to be $p(a)$:

$$w(x) = \frac{\varrho(x)}{p(a)}$$

For example, [AG08] uses both approaches shown herein, on different parts of the book. Therefore the reader is free to follow whichever approach he considers best.

To end up with this digression, some authors define the Sturm-Liouville problem on an open set (a, b) , while others use a closed set $[a, b]$. This really is unimportant provided the functions $p(x)$, $q(x)$, $\varrho(x)$, $l(x)$, $m(x)$, $n(x)$ and $w(x)$ be sufficiently regular and smooth. In that case, the Hilbert space of square integrable functions on (a, b) with weight function $\varrho(x)$, $L^2_{\varrho}(a, b)$, is equivalent to $L^2[a, b]$, and both notations could be used interchangeably (see [AG08]).

for $x \in [a, b] \subset \mathbb{R}$, $\phi = \phi(x)$ a twice continuously differentiable real function, subjected to the general non-trivial boundary conditions⁸⁰

$$\begin{aligned} a_0\phi(a) + a_1\phi'(a) &= 0, & a_0, a_1 &\in \mathbb{R} \\ b_0\phi(b) + b_1\phi'(b) &= 0, & b_0, b_1 &\in \mathbb{R} \end{aligned} \quad (3.394)$$

The real functions $p(x)$, $p'(x)$, $q(x)$ and $\varrho(x)$ are continuous in $[a, b]$, and $p(x) > 0$, $\varrho(x) > 0 \forall x \in (a, b)$.

A differential operator with the form given in (3.389) is guaranteed to be a self-adjoint operator (see [AG08] or [Mac04]) with respect to the inner product

$$\langle \phi, \psi \rangle := \int_a^b \phi(x)\psi(x)\varrho(x) dx \quad (3.395)$$

where $\varrho(x)$ is called the **weight function**. Besides, the Sturm-Liouville eigenvalue problem is linear: if ϕ_1 and ϕ_2 are solutions of (3.393) then any linear combination $a_1\phi_1 + a_2\phi_2$ is also a solution. One is in liberty to add any possible solution to another already determined.

The Sturm-Liouville operator is a self-adjoint operator and, as such, has eigenvalues and eigenfunctions. The eigenvalues $\{\lambda_n\}$ are guaranteed to be real, simple, countable, ordered and one of them is the smallest, called λ_1 . The eigenvalues can be ordered in a strictly increasing sequence

$$\lambda_1 < \lambda_2 < \lambda_3 < \dots < \lambda_n < \dots < \infty$$

with

$$\lim_{n \rightarrow \infty} \lambda_n = \infty$$

The set of eigenvalues $\{\lambda_n\}$ is numerable. For each eigenvalue λ_n there exists a unique eigenfunction ϕ_n , up to a normalisation constant, which satisfies

$$\mathcal{L}\phi_n(x) = -\lambda_n\varrho(x)\phi_n(x)$$

Besides, the n^{th} eigenfunction $\phi_n(x)$ has exactly $n-1$ zeroes in the open interval (a, b) (Sturm oscillation theorem, see [AM11])⁸¹. Therefore, the larger n , the more numerous and more rapid oscillations ϕ_n has in (a, b) .

If ϕ_n and ϕ_m are eigenfunctions corresponding to eigenvalues λ_n and λ_m , respectively, with $\lambda_n \neq \lambda_m$, then they are not only linearly independent but also mutually orthogonal with respect to the inner product defined by equation (3.395)

$$\langle \phi_n, \phi_m \rangle = \langle \phi_n, \phi_n \rangle \delta_{nm} \quad n, m \in \mathbb{N}$$

With a suitable normalisation constant they can easily be converted into a pair of orthonormal eigenfunctions verifying

$$\langle \phi_n, \phi_m \rangle = \delta_{nm}$$

⁸⁰In the present context, *non-trivial* means

$$|a_0| + |a_1| > 0$$

$$|b_0| + |b_1| > 0$$

(see [Mac04]).

⁸¹It could have n zeroes in the *closed* interval $[a, b]$, in those cases in which b is a zero of ϕ_n . See further below.

From now on, ϕ_n will denote eigenfunctions normalised to unity

$$\|\phi_n\| = \langle \phi_n, \phi_n \rangle^{\frac{1}{2}} = 1$$

The Sturm-Liouville eigenvalue problem defines a complete numerable set of eigenfunctions $\{\phi_n\}$ which constitute an orthonormal basis of the Hilbert space of square integrable functions in the interval (a, b) with respect to the weight function $\varrho(x)$, called $L^2_{\varrho}(a, b)$ ⁸² (also called $L^2_{\varrho}(a, b)$ if the interval were $[a, b]$, see footnote 79 in page 167). In this context, *complete* means that any square integrable function in the interval (a, b) , $\psi(x) \in L^2_{\varrho}(a, b)$, could be univocally expressed as a linear combination (generalised Fourier series) of the eigenfunctions $\{\phi_n\}$, namely

$$\psi(x) = \sum_{n=1}^{\infty} \langle \psi, \phi_n \rangle \phi_n(x) \tag{3.396}$$

with the inner product $\langle \psi, \phi_n \rangle$ defined by (3.395). Or, in other words, *complete* means that the set of eigenfunctions $\{\phi_n\}$ generate the following form of the identity operator $\mathbb{1}$ in $L^2_{\varrho}(a, b)$:

$$\mathbb{1} = \sum_{n=1}^{\infty} \langle \cdot, \phi_n \rangle \phi_n(x) \tag{3.397}$$

where this expression actually means:

$$\mathbb{1} \psi(x) = \sum_{n=1}^{\infty} \langle \psi, \phi_n \rangle \phi_n(x) = \psi(x) \tag{3.398}$$

for any function $\psi(x) \in L^2_{\varrho}(a, b)$. The series expansion (3.396) is a generalisation of the Fourier series for periodic functions introduced in section 3.2.3, in that it applies to *any* function $\psi(x) \in L^2_{\varrho}(a, b)$.

If $(a, b) \subset \mathbb{R}$ is a bounded set, then equation (3.393) plus the boundary conditions is called a **Regular Sturm-Liouville problem**; otherwise it receives the name of **Singular Sturm-Liouville problem**. ■

Returning back to the problem of solving the homogeneous equation associated with the GAS for incompressible pipe flow, the equation (3.387) corresponds to a Sturm-Liouville eigenvalue problem defined by equations (3.393) and (3.394) with the following values:

$$\begin{aligned} p(\alpha) &= \alpha \\ q(\alpha) &= 0 \\ \varrho(\alpha) &= \alpha \\ a &= 0 \\ b &= 1 \end{aligned} \tag{3.399}$$

⁸²A function $\psi(x)$ defined in $[a, b] \subset \mathbb{R}$ belongs to $L^2_{\varrho}(a, b)$ if and only if

$$\psi \in L^2_{\varrho}(a, b) \Leftrightarrow \|\psi\| = \langle \psi, \psi \rangle^{\frac{1}{2}} = \left(\int_a^b \varrho(x) |\psi(x)|^2 dx \right)^{\frac{1}{2}} < \infty$$

The functions which satisfy this condition form a normed vector space with an inner product given by $\langle \cdot, \cdot \rangle$. The normed vector space $L^2_{\varrho}(a, b)$ is a Hilbert space. See also footnote 35 in page 107

$$\begin{aligned} a_0 &= 0, \quad a_1 = 1 \\ b_0 &= 1, \quad b_1 = 0 \end{aligned}$$

Note the boundary conditions are not trivial. The attached inner product is given by

$$\langle \phi, \psi \rangle = \int_0^1 \alpha \phi(\alpha) \psi(\alpha) \, d\alpha \quad (3.400)$$

The solutions of equation (3.387) belong to the Hilbert space $L^2_\alpha(0, 1)$, for which there exists a unique series expansion in terms of the eigenfunctions $\{\phi_n\}$ of the Sturm-Liouville operator (3.388), which constitute a orthogonal basis of said Hilbert space $L^2_\alpha(0, 1)$. Armed with such a powerful toolkit, it is relatively straightforward to obtain the solution for the problem posed herein using the method of decomposition of functions in terms of series of eigenfunctions.

The equation (3.387) could be expressed as

$$\alpha^2 A'' + \alpha A' + \lambda^2 \alpha^2 A = 0 \quad (3.401)$$

which is almost the Bessel equation of order p (see [Kor02])

$$x^2 y'' + xy' + (x^2 - p^2)y = 0 \quad (3.402)$$

for the case $p = 0$. In order for (3.401) to have the form (3.402) suffices to perform the substitution of variables $\eta = \lambda\alpha$. In that case the derivatives read:

$$\frac{dA}{d\alpha} = \lambda \frac{dA}{d\eta}, \quad \frac{d^2 A}{d\alpha^2} = \lambda^2 \frac{d^2 A}{d\eta^2}$$

and equation (3.401) reduces to

$$\eta^2 \frac{d^2 A}{d\eta^2} + \eta \frac{dA}{d\eta} + \eta^2 A = 0 \quad (3.403)$$

which now is (3.402) for $p = 0$, whose general solution is (since $p = 0$ is integer, see [Kor02])

$$A(\eta) = C_1 J_0(\eta) + C_2 Y_0(\eta)$$

or

$$A(\alpha) = C_1 J_0(\lambda\alpha) + C_2 Y_0(\lambda\alpha) \quad (3.404)$$

In this general solution $J_0(\lambda\alpha)$ is the Bessel function of the first kind of order $p = 0$

$$J_p(x) = \sum_{n=0}^{\infty} \frac{(-1)^n \left(\frac{x}{2}\right)^{2n+p}}{n! \Gamma(p+n+1)} \quad (3.405)$$

$$J_0(\lambda\alpha) = \sum_{n=0}^{\infty} \frac{(-1)^n (\lambda\alpha)^{2n}}{n!^2 2^{2n}} = 1 - \frac{\lambda^2 \alpha^2}{2^2} + \frac{\lambda^4 \alpha^4}{2^2 4^2} - \frac{\lambda^6 \alpha^6}{2^2 4^2 6^2} + \dots \quad (3.406)$$

with $\Gamma(x)$ the Gamma function ($\Gamma(n+1) = n!$ for $n \in \mathbb{N}$), and $Y_0(\lambda\alpha)$ is the Bessel function of the second kind of order $p = 0$ (see figure 3.16), defined generically as

$$Y_p(x) = \begin{cases} \frac{J_p(x) \cos(p\pi) - J_{-p}(x)}{\sin(p\pi)} & p \notin \mathbb{Z}^+ \\ \lim_{s \rightarrow p} \frac{J_s(x) \cos(s\pi) - J_{-s}(x)}{\sin(s\pi)} & p \in \mathbb{Z}^+ \end{cases} \quad (3.407)$$

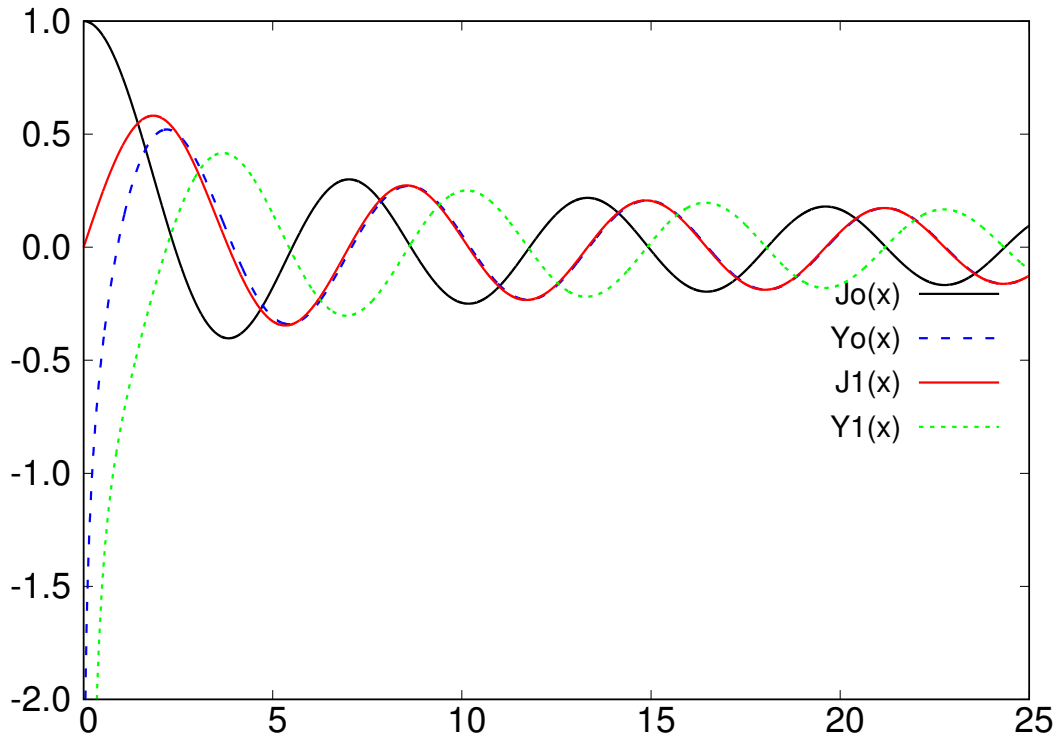


Figure 3.16: Bessel functions of the first and second kind $J_0(x)$, $Y_0(x)$, $J_1(x)$ and $Y_1(x)$. Note how similar are Y_0 and J_1 as $x \rightarrow \infty$.

Note $J_0(x)$ has an absolute maximum for $x = 0$, $J_0(0) = 1$. This is compatible with the mean velocity profile being maximum at the pipe's centreline.

The following relationships hold for Bessel functions (see [Kor02]), and are introduced herein as a reference to be used in the coming derivations:

$$J_{-p}(x) = (-1)^p J_p(x) \quad (p \in \mathbb{Z}^+) \quad (3.408)$$

$$J_p(-x) = (-1)^p J_p(x) \quad (p \in \mathbb{Z}^+) \quad (3.409)$$

$$J_p(x+y) = \sum_{k=-\infty}^{+\infty} J_k(x) J_{p-k}(y) \quad (p \in \mathbb{Z}) \quad (3.410)$$

$$Y_{-p}(x) = (-1)^p Y_p(x) \quad (p \in \mathbb{Z}^+) \quad (3.411)$$

$$J'_p(x) = \frac{1}{2} [J_{p-1}(x) - J_{p+1}(x)] \quad (3.412)$$

$$J'_0(x) = -J_1(x) \quad (3.413)$$

$$J_0(x) = \frac{1}{\pi} \int_0^\pi \cos(x \sin \theta) d\theta \quad (3.414)$$

$$J_1(x) = \frac{1}{\pi} \int_0^\pi \cos(x \sin \theta - \theta) d\theta \quad (3.415)$$

$$J_1(x) = \frac{x}{2} - \frac{x^3}{2^2 4} + \frac{x^5}{2^2 4^2 6} - \frac{x^7}{2^2 4^2 6^2 8} + \dots \quad (3.416)$$

$$Y_p'(x) = \frac{1}{2} [Y_{p-1}(x) - Y_{p+1}(x)] \quad (3.417)$$

$$Y_0'(x) = -Y_1(x) \quad (3.418)$$

$$\int x^p J_{p-1}(x) dx = x^p J_p(x) + C \quad (p \in \mathbb{N}) \quad (3.419)$$

$$\int x J_0(x) dx = x J_1(x) + C \quad (3.420)$$

$$\begin{aligned} \int x^n J_0(x) dx &= x^n J_1(x) + (n-1)x^{n-1} J_0(x) - \\ &- (n-1)^2 \int x^{n-2} J_0(x) dx + C \quad (n \geq -1, n \in \mathbb{Z}) \end{aligned} \quad (3.421)$$

$$\int x^2 J_0(x) dx = x^2 J_1(x) + x J_0(x) - \int J_0(x) dx + C \quad (3.422)$$

$$\int x^n J_1(x) dx = -x^n J_0(x) + n \int x^{n-1} J_0(x) dx + C \quad (n \geq -1, n \in \mathbb{Z}) \quad (3.423)$$

$$\int x J_p(ax) J_p(bx) dx = \frac{x (a J_p(bx) J_p'(ax) - b J_p(ax) J_p'(bx))}{b^2 - a^2} \quad (3.424)$$

$$\int x J_p^2(ax) dx = \frac{x^2}{2} [J_p'(ax)]^2 + \frac{x^2}{2} \left(1 - \frac{p^2}{a^2 x^2}\right) [J_p(ax)]^2 \quad (3.425)$$

$$\int x J_0(ax) J_0(bx) dx = \frac{x (a J_0(bx) J_1(ax) - b J_0(ax) J_1(bx))}{a^2 - b^2} \quad (3.426)$$

$$\int x J_0^2(ax) dx = \frac{x^2}{2} [J_1(ax)]^2 + \frac{x^2}{2} [J_0(ax)]^2 \quad (3.427)$$

$$\int_0^1 x J_0(ax) J_0(bx) dx = \frac{a J_0(b) J_1(a) - b J_0(a) J_1(b)}{a^2 - b^2} \quad (3.428)$$

$$\int_0^1 x J_0^2(ax) dx = \frac{1}{2} J_1^2(a) + \frac{1}{2} J_0^2(a) \quad (3.429)$$

Note $J_0(x)$ has some remote likeness with $\cos x$ and so does $J_1(x)$ with $\sin x$, as one could see upon examining their McLaurin series expansions (3.406) and (3.416). They even satisfy $J_0'(x) = -J_1(x)$, just as $\cos' x = -\sin x$.

$A(\alpha)$ must satisfy the boundary condition (3.370) for $\alpha = 0$

$$A'(0) = C_1 \lambda J_0'(0) + C_2 \lambda Y_0'(0) = -C_1 \lambda J_1(0) - C_2 \lambda Y_1(0) = 0$$

But upon looking at figure 3.16 it is clear that $Y_1(0) \neq 0$ and $J_1(0) = 0$. Therefore it must be $C_2 = 0$.

Also $A(\alpha)$ must fulfil the boundary condition (3.369) for $\alpha = 1$. Thus

$$A(1) = C_1 J_0(\lambda) = 0$$

and λ **must be a root of** $J_0(\alpha)$. Note $J_0(\alpha)$ has infinitely many roots, although they are not periodic like, for instance, those of $\cos \alpha$. The final form of the radial component $A(\alpha)$ is then given by

$$A(\alpha) = C_1 J_0(\lambda \alpha)$$

Therefore, the eigenfunctions of the Sturm-Liouville eigenvalue problem have the form $J_0(\lambda\alpha)$, with λ a root (a zero) of $J_0(\alpha)$. Those eigenfunctions have the property of completely spanning the Hilbert space $L^2_\alpha(0, 1)$, and they can be used to express any function of said space in terms of a Fourier-Bessel series.

Having an expression for $\Gamma(\gamma)$ and $A(\alpha)$, the solution of the homogeneous equation has the form

$$w(\gamma, \alpha) = C J_0(\lambda\alpha) e^{-\lambda^2\gamma} + w_\infty \quad (3.430)$$

with $C \in \mathbb{R}$ now playing the role of C_0C_1 , and λ a root of $J_0(\alpha)$. Note that λ also appears in the exponential, although in the derivation of the time equation it was not evident that λ^2 were to turn into a root of a Bessel function.

Since the homogeneous problem is fulfilled by infinitely many functions of the form (3.430), one for each possible root λ_n of $J_0(\alpha)$, $n \in \mathbb{N}$, then the general solution of the homogeneous problem subjected to the boundary and initial conditions established above takes the form of a so-called Fourier-Bessel series

$$w(\gamma, \alpha) = w_\infty + \sum_{n=1}^{\infty} a_n J_0(\lambda_n\alpha) e^{-\lambda_n^2\gamma} \quad (3.431)$$

with $e^{-\lambda_n^2\gamma}$ the set of functions that determines the time dependence of the solution, $\{J_0(\lambda_n\alpha)\}$ a set of orthogonal eigenfunctions with respect to the inner product

$$\langle J_0(\lambda_n\alpha), J_0(\lambda_m\alpha) \rangle = \int_0^1 \alpha J_0(\lambda_n\alpha) J_0(\lambda_m\alpha) d\alpha = \delta_{nm} \| J_0(\lambda_n\alpha) \|^2 \quad (3.432)$$

which constitute a basis of the Hilbert space $L^2_\alpha(0, 1)$, a_n are real constant coefficients which univocally determine $w(\gamma, \alpha)$ according to the relation (the time exponential is excluded from the integral, and only $w(\alpha)$ is written)

$$a_n = \frac{1}{\| J_0(\lambda_n\alpha) \|^2} \langle w(\alpha), J_0(\lambda_n\alpha) \rangle = \frac{1}{\| J_0(\lambda_n\alpha) \|^2} \int_0^1 \alpha w(\alpha) J_0(\lambda_n\alpha) d\alpha \quad (3.433)$$

and w_∞ is the gauge function which in general will be zero.

The roots of $J_0(\alpha)$ (and general $J_p(\alpha)$ functions) verify (see [Kor02]):

- i. For $p > -1$ the function $J_p(\alpha)$ has only real roots (that is, no complex roots). Therefore, $\lambda_n \in \mathbb{R}$. Besides, the roots of $J_p(\alpha)$ constitute a numerable infinite set of real numbers.
- ii. All roots of $J_p(\alpha)$ are simple (except, perhaps, $\alpha = 0$)
- iii. The functions $J_p(\alpha)$ and $J_{p+k}(\alpha)$, $k = 1, 2, 3, \dots$ have no common root except, perhaps, $\alpha = 0$.
- iv. The positive roots of $J_p(\alpha)$ form an increasing unbounded sequence, that is,

$$0 < \lambda_1 < \lambda_2 < \lambda_3 < \dots < \lambda_n < \dots \quad \lim_{n \rightarrow \infty} \lambda_n = \infty$$

- v. For each $n \in \mathbb{N}$ the function $J_0(\lambda_n\alpha)$ has exactly $n - 1$ roots in the open interval $(0, \lambda_n)$, corresponding to $\alpha \in (0, 1)$, and it has exactly n roots in the closed interval $[0, \lambda_n]$ (see footnote 81 in page 168).

For large n the roots λ_n of $J_0(\alpha)$ are given approximately by

$$\lambda_n \approx n\pi - \frac{\pi}{4} \quad (n \gg 1, n \in \mathbb{N}) \quad (3.434)$$

and for large x the value of $J_1(x)$ is approximately

$$J_1(x) \approx \sqrt{\frac{2}{\pi x}} \cos\left(x - \frac{3\pi}{4}\right) \quad (|x| \gg 0, x \in \mathbb{R}) \quad (3.435)$$

and thus the value of $J_1(\lambda_n)$ at the roots of $J_0(\alpha)$ for large n is approximately

$$J_1(\lambda_n) \approx (-1)^{n+1} \sqrt{\frac{2}{\pi \lambda_n}} \quad (n \gg 1, n \in \mathbb{N}) \quad (3.436)$$

Those approximate values will be useful when calculating particular cases.

According to equation (3.429), if λ_n is a root of $J_0(\alpha)$ then the norm of the eigenfunction $J_0(\lambda_n \alpha)$ is given by:

$$\|J_0(\lambda_n \alpha)\|^2 = \langle J_0(\lambda_n \alpha), J_0(\lambda_n \alpha) \rangle = \int_0^1 \alpha J_0^2(\lambda_n \alpha) d\alpha = \frac{1}{2} J_1^2(\lambda_n) \quad (3.437)$$

thus the set of normalised eigenfunctions $\{\phi_n(\alpha)\}$

$$\left(\frac{d^2}{d\alpha^2} + \frac{1}{\alpha} \frac{d}{d\alpha}\right) \phi_n(\alpha) = -\lambda_n^2 \phi_n(\alpha) \quad (3.438)$$

$$\phi_n(\alpha) = \frac{J_0(\lambda_n \alpha)}{\|J_0(\lambda_n \alpha)\|} = \frac{\sqrt{2}}{J_1(\lambda_n)} J_0(\lambda_n \alpha) \quad (3.439)$$

$$\langle \phi_n(\alpha), \phi_m(\alpha) \rangle = \delta_{nm} \quad (n, m \in \mathbb{N}) \quad (3.440)$$

constitutes an orthonormal basis of the Hilbert space $L_\alpha^2(0, 1)$, that is, the functional space in which the solutions to the Sturm-Liouville eigenvalue problem are developed. Besides, the following operator acts like the unit operator $\mathbb{1}$:

$$\left(\sum_{n=1}^{\infty} \phi_n \langle \cdot, \phi_n \rangle\right) \psi(\alpha) \equiv \left(\sum_{n=1}^{\infty} \frac{\sqrt{2}}{J_1(\lambda_n)} J_0(\lambda_n \alpha) \langle \cdot, \frac{\sqrt{2}}{J_1(\lambda_n)} J_0(\lambda_n \alpha) \rangle\right) \psi(\alpha) = \mathbb{1} \psi(\alpha) = \psi(\alpha) \quad (3.441)$$

Thus, the general solution to the homogeneous problem adopts the form of a Fourier-Bessel series, which in terms of the orthonormal basis $\{\phi_n(\alpha)\}$ is given by

$$w(\gamma, \alpha) = w_\infty + \sum_{n=1}^{\infty} w_n \frac{\sqrt{2}}{J_1(\lambda_n)} J_0(\lambda_n \alpha) e^{-\lambda_n^2 \gamma} = w_\infty + \sum_{n=1}^{\infty} w_n \phi_n(\alpha) e^{-\lambda_n^2 \gamma} \quad (3.442)$$

with w_n the coefficients of the Fourier-Bessel series corresponding to $\{\phi_n(\alpha)\}$ (differing from a_n in (3.431) above only in a normalisation constant).

In order to find w_n the initial condition (3.375) must be imposed. A new assumption must thus be introduced: the function $u_0^*(\alpha)$ which characterises the initial condition of $w(\gamma, \alpha)$ (and also of $u^*(\gamma, \alpha)$

in the non-homogeneous problem) belongs to $L^2_\alpha(0, 1)$, and therefore admits a unique decomposition in terms of the basis $\{\phi_n(\alpha)\}$. For $\gamma = 0$ it must then be:

$$w(0, \alpha) = u_0^*(\alpha) = w_\infty + \sum_{n=1}^{\infty} w_n \phi_n(\alpha) \quad (3.443)$$

with

$$w_n = \langle u_0^*(\alpha), \phi_n(\alpha) \rangle = \frac{\sqrt{2}}{J_1(\lambda_n)} \int_0^1 \alpha u_0^*(\alpha) J_0(\lambda_n \alpha) d\alpha \quad (3.444)$$

If $u_0^*(\alpha)$ has a regular expression as a Fourier-Bessel series of the eigenfunctions $\{\phi_n(\alpha)\}$, then the extra term w_∞ must be zero and should be removed, since the initial conditions are all contained in $u_0^*(\alpha)$. From now on w_∞ will not be written in the equations, although its role for non-regular initial or boundary conditions should not be forgotten.

The important point here is that the real coefficients w_n are determined univocally from the initial conditions of the problem, $u_0^*(\alpha)$, and that this function alone defines completely the solution of the homogeneous Sturm-Liouville problem. ■

For example, in the case of an initial Hagen-Poiseuille laminar flow for $\gamma \leq 0$, with

$$u_0^*(\alpha) = u_{max}^*(1 - \alpha^2)$$

and subjected to no external forces or pressure gradient for $\gamma > 0$ (that is, all external influence is switched off at $\gamma = 0$), the coefficients w_n are given by (see equations (3.420) and (3.421)):

$$w_n = \frac{\sqrt{2} u_{max}^*}{J_1(\lambda_n)} \int_0^1 \alpha(1 - \alpha^2) J_0(\lambda_n \alpha) d\alpha = \frac{\sqrt{2} u_{max}^*}{J_1(\lambda_n)} \left[\int_0^1 \alpha J_0(\lambda_n \alpha) d\alpha - \int_0^1 \alpha^3 J_0(\lambda_n \alpha) d\alpha \right] =$$

(doing $\eta = \lambda_n \alpha$ and remembering that $J_0(\lambda_n) = 0$)

$$\begin{aligned} &= \frac{\sqrt{2} u_{max}^*}{J_1(\lambda_n)} \left[\frac{1}{\lambda_n^2} \int_0^{\lambda_n} \eta J_0(\eta) d\eta - \frac{1}{\lambda_n^4} \int_0^{\lambda_n} \eta^3 J_0(\eta) d\eta \right] = \\ &= \frac{\sqrt{2} u_{max}^*}{J_1(\lambda_n)} \left[\frac{1}{\lambda_n^2} \lambda_n J_1(\lambda_n) - \frac{1}{\lambda_n^4} \left(\lambda_n^3 J_1(\lambda_n) + 2\lambda_n^2 J_0(\lambda_n) - 4 \int_0^{\lambda_n} \eta J_0(\eta) d\eta \right) \right] = \\ &= \frac{\sqrt{2} u_{max}^*}{J_1(\lambda_n)} \left[\frac{J_1(\lambda_n)}{\lambda_n} - \frac{1}{\lambda_n^4} \left(\lambda_n^3 J_1(\lambda_n) - 4\lambda_n J_1(\lambda_n) \right) \right] = \frac{\sqrt{2} u_{max}^*}{J_1(\lambda_n)} \frac{4J_1(\lambda_n)}{\lambda_n^3} \end{aligned}$$

or

$$w_n = \frac{4\sqrt{2}}{\lambda_n^3} u_{max}^* \quad (3.445)$$

Therefore, this particular example is characterised by the following two equations (in this case the term w_∞ is zero):

$$w(\gamma, \alpha) = 8 u_{max}^* \sum_{n=1}^{\infty} \frac{J_0(\lambda_n \alpha)}{\lambda_n^3 J_1(\lambda_n)} e^{-\lambda_n^2 \gamma} \quad (3.446)$$

and

$$u_0^*(\alpha) = u_{max}^*(1 - \alpha^2) = 8 u_{max}^* \sum_{n=1}^{\infty} \frac{J_0(\lambda_n \alpha)}{\lambda_n^3 J_1(\lambda_n)} \quad (3.447)$$

The flow has initially, at $\gamma = 0$, the known parabolic Hagen-Poiseuille profile; then as time elapses it loses the parabolic shape and behaves as determined by the Fourier-Bessel series with the time dependence included on it. Finally, for sufficiently long time (formally for $\gamma \rightarrow \infty$) the mean velocity reduces everywhere to zero and the liquid reaches a state of rest.

Equations (3.446) and (3.447) offer a neat interpretation of the behaviour shown by the transient laminar incompressible pipe flow described in [Szy32], equation (3.351), known as Szymanski flow. At $\gamma = 0$ both terms, the parabolic profile $(1 - \alpha^2)$ and the Fourier-Bessel series, are identical and cancel exactly each other: therefore the liquid is initially at rest. At $\gamma = 0$ the fluid suddenly begins to receive the constant pressure gradient, and starts to move following such stress. As time elapses, the parabolic profile and the Fourier-Bessel series are no longer identical and the cancellation is no longer possible: the flow shows some velocity profile which indicates its state of motion. As time grows sufficiently (again, formally $\gamma \rightarrow \infty$) the Fourier-Bessel series decreases to zero, leaving the parabolic term as the sole contribution to the velocity profile. The flow now is fully characterised by the Hagen-Poiseuille equation. Explaining the dynamics with such a fine detail is the main merit of the Szymanski's solution.

Incidentally, the derivation made herein illustrates the general procedure that must be followed in order to find the coefficients for the Fourier-Bessel series corresponding to any initial condition function $u_0^*(\alpha)$. Moreover, the fact that formulae for $\int \alpha^n J_0(\lambda_n \alpha) d\alpha$ exist, hints at the possibility of expanding the function $u_0^*(\alpha)$ in terms of McLaurin or Taylor series, truncate it in a polynomial function at the desired level of approximation, and apply such formulae to each resulting term, all with the general form of α^n .

In general, equation (3.442) shows an exponential decay behaviour of the solution with respect to time, given by the factor $e^{-\lambda_n^2 \gamma}$, typical of transient phenomena. Therefore, it corresponds to a transient flow that, given enough time, will lead to steady state flow. Nothing else could be expected from the homogeneous problem. Any unsteady, not transient, solution must have a factor of the order of $e^{\lambda_n^2 \gamma}$ to counteract the effect of the exponential decay. In the coming derivation it will be seen that is the case. ■

The orthonormal basis of eigenfunctions $\{\phi_n(\alpha)\}$ could be used to decompose any function belonging to $L^2_\alpha(0, 1)$ in terms of its components respect to that basis. In particular, by means of the Variation of Constants method, the general solution of the non-homogeneous problem might be expressed from the general solution of the homogeneous problem as (see [PR05])

$$u^*(\gamma, \alpha) = u_\infty + \sum_{n=1}^{\infty} u_n(\gamma) \frac{\sqrt{2}}{J_1(\lambda_n)} J_0(\lambda_n \alpha) = u_\infty + \sum_{n=1}^{\infty} u_n(\gamma) \phi_n(\alpha) \quad (3.448)$$

where the set of functions $\{u_n(\gamma)\}$ is defined through two different but complementary conditions:

- it must provide the fulfilment of the initial conditions (3.375)-(3.378), and
- it should satisfy the dependence on γ imposed by the non-homogeneous term

$$\Xi(\gamma, \alpha) = \Pi^*(\gamma) - \frac{1}{\alpha} \frac{\partial(\alpha \varpi)}{\partial \alpha} \quad (3.449)$$

Now it is pertinent to introduce another new assumption: $\Xi(\gamma, \alpha) \in L^2_\alpha(0, 1)$ (just as it was supposed above that $u_0^*(\alpha) \in L^2_\alpha(0, 1)$), and thus it can be univocally decomposed in a Fourier-Bessel series of the orthonormal basis of eigenfunctions $\{\phi_n(\alpha)\}$

$$\Xi(\gamma, \alpha) = \sum_{n=1}^{\infty} \Xi_n(\gamma) \phi_n(\alpha) \quad (3.450)$$

with

$$\Xi_n(\gamma) = \langle \Xi, \phi_n \rangle = \frac{\sqrt{2}}{J_1(\lambda_n)} \int_0^1 \alpha \Xi(\gamma, \alpha) J_0(\lambda_n \alpha) d\alpha \quad (3.451)$$

⁸³ The goal now is to express $u_n(\gamma)$ in terms of the coefficients $\Xi_n(\gamma)$ that define the non-homogeneous term, using the non-homogeneous equation (3.380). After that, the initial conditions will be used to find out the integration constants arising from such derivation.

Let's first determine $\partial u^* / \partial \gamma$ (remember: $\dot{u}_n \equiv \frac{du_n}{d\gamma}$):

$$\frac{\partial u^*}{\partial \gamma} = \frac{\partial}{\partial \gamma} \sum_{n=1}^{\infty} u_n \phi_n = \sum_{n=1}^{\infty} \dot{u}_n \phi_n$$

and then the derivatives in α :

$$\left(\frac{\partial^2}{\partial \alpha^2} + \frac{1}{\alpha} \frac{\partial}{\partial \alpha} \right) \sum_{n=1}^{\infty} u_n \phi_n = - \sum_{n=1}^{\infty} u_n \lambda_n^2 \phi_n$$

since each ϕ_n satisfies equation (3.438). Therefore, equation (3.380) implies:

$$\sum_{n=1}^{\infty} \dot{u}_n \phi_n + \sum_{n=1}^{\infty} u_n \lambda_n^2 \phi_n = \sum_{n=1}^{\infty} \Xi_n \phi_n \quad \Rightarrow \quad \sum_{n=1}^{\infty} [\dot{u}_n + \lambda_n^2 u_n - \Xi_n] \phi_n = 0 \quad (3.452)$$

Since the eigenfunctions $\{\phi_n(\alpha)\}$ are linearly independent, the series above is zero if and only if all of its coefficients are zero, that is

$$\dot{u}_n(\gamma) + \lambda_n^2 u_n(\gamma) = \Xi_n(\gamma) \quad (\forall n \in \mathbb{N}) \quad (3.453)$$

This is a first order linear ordinary differential equation whose solution requires an integrating factor (see [PRO5]). Since λ_n^2 is constant, the integrating factor adopts the simple form $e^{\lambda_n^2 \gamma}$. With the help of such integrating factor, the equation is now written as:

$$[\dot{u}_n(\gamma) + \lambda_n^2 u_n(\gamma)] e^{\lambda_n^2 \gamma} = \Xi_n(\gamma) e^{\lambda_n^2 \gamma} \quad \Rightarrow \quad \frac{d}{d\gamma} [u_n(\gamma) e^{\lambda_n^2 \gamma}] = \Xi_n(\gamma) e^{\lambda_n^2 \gamma}$$

⁸³The derivation of equation (3.451) is straightforward, having into account that $\{\phi_n(\alpha)\}$ is an orthonormal basis of $L^2_\alpha(0, 1)$:

$$\langle \Xi, \phi_n \rangle = \left\langle \sum_{m=1}^{\infty} \Xi_m(\gamma) \phi_m(\alpha), \phi_n(\alpha) \right\rangle = \sum_{m=1}^{\infty} \Xi_m(\gamma) \langle \phi_m(\alpha), \phi_n(\alpha) \rangle = \sum_{m=1}^{\infty} \Xi_m(\gamma) \delta_{nm} = \Xi_n(\gamma)$$

since the inner product is a linear functional, and any function not depending on α is treated as a constant which can exit the angled brackets. Actually, what is really meant by $\Xi(\gamma, \alpha) \in L^2_\alpha(0, 1)$ is: "that part of Ξ depending on α is square integrable in the interval $(0, 1)$ with weight function $\varrho(\alpha) = \alpha$ ".

and integrating from 0 to γ

$$u_n(\gamma)e^{\lambda_n^2\gamma} - u_n(0) = \int_0^\gamma \Xi_n(\gamma')e^{\lambda_n^2\gamma'} d\gamma' \quad (3.454)$$

or

$$u_n(\gamma) = u_{n0}e^{-\lambda_n^2\gamma} + \int_0^\gamma \Xi_n(\gamma')e^{-\lambda_n^2(\gamma-\gamma')} d\gamma' \quad (3.455)$$

with $u_n(0) = u_{n0} \in \mathbb{R}$. As expected, the general unsteady solution ought to contain a factor of the order of $e^{\lambda_n^2\gamma'}$, which could counteract the factor $e^{-\lambda_n^2\gamma}$ responsible for the transient behaviour.

The integration constant u_{n0} is found upon applying the initial condition (3.375). Note that, whatever the (bounded) value of the integrand, the integral term in equation (3.455) is zero for $\gamma = 0$. Therefore, being $u_0^*(\alpha)$ the initial condition for the mean velocity:

$$u^*(0, \alpha) = u_0^*(\alpha) = u_\infty + \sum_{n=1}^{\infty} u_n(0)\phi_n = u_\infty + \sum_{n=1}^{\infty} u_{n0}\phi_n$$

But, on the other hand, it has already been established that $u_0^*(\alpha) \in L_\alpha^2(0, 1)$, with a unique decomposition in terms of the basis of eigenfunctions $\{\phi_n(\alpha)\}$ given by (3.443) (with $w_\infty = 0$). Thus it could only be:

$$u_{n0} = w_n$$

with w_n given by equation (3.444), a vestige of the homogeneous problem. Since the integration constants u_{n0} are univocally determined by w_n , the term u_∞ could be considered null (just as w_∞ was found above to be zero if $u_0^*(\alpha)$ has a regular enough expansion in a Fourier-Bessel series of eigenfunctions).

Then, the general expression for the non-homogeneous mean velocity field is

$$u^*(\gamma, \alpha) = \sum_{n=1}^{\infty} \left[w_n e^{-\lambda_n^2\gamma} + \int_0^\gamma \Xi_n(\gamma') e^{-\lambda_n^2(\gamma-\gamma')} d\gamma' \right] \frac{\sqrt{2}}{J_1(\lambda_n)} J_0(\lambda_n\alpha) \quad (3.456)$$

or rather

$$u^*(\gamma, \alpha) = \sum_{n=1}^{\infty} w_n \frac{\sqrt{2}}{J_1(\lambda_n)} J_0(\lambda_n\alpha) e^{-\lambda_n^2\gamma} + \sum_{n=1}^{\infty} \frac{\sqrt{2}}{J_1(\lambda_n)} J_0(\lambda_n\alpha) \int_0^\gamma \Xi_n(\gamma') e^{-\lambda_n^2(\gamma-\gamma')} d\gamma' \quad (3.457)$$

where the first term could be considered a transient component, since it decreases exponentially as $\gamma \rightarrow \infty$, and the second term could be classified as unsteady, since the factors $e^{-\lambda_n^2\gamma}$ and $e^{\lambda_n^2\gamma'}$ compensate each other, more or less, and might not decrease to zero with $\gamma \rightarrow \infty$ ⁸⁴.

⁸⁴The same result would have been obtained if the following alternative derivation were carried out: Express $u^*(\gamma, \alpha)$ from the beginning as

$$u^*(\gamma, \alpha) = \sum_{n=1}^{\infty} u_n(\gamma) \frac{\sqrt{2}}{J_1(\lambda_n)} J_0(\lambda_n\alpha) e^{-\lambda_n^2\gamma} = \sum_{n=1}^{\infty} u_n(\gamma) \phi_n(\alpha) e^{-\lambda_n^2\gamma} \quad (3.458)$$

Some more information could still be squeezed from $\Xi_n(\gamma)$. Upon substitution of the non-homogeneous term $\Xi(\gamma, \alpha)$ by its components $\Pi^*(\gamma)$ and $-\frac{1}{\alpha}\partial(\alpha\varpi)/\partial\alpha$, some additional knowledge is to be gained. First with $\Pi^*(\gamma)$:

$$\begin{aligned}\langle \Pi^*, \phi_n \rangle &= \frac{\sqrt{2}}{J_1(\lambda_n)} \int_0^1 \alpha \Pi^*(\gamma) J_0(\lambda_n \alpha) d\alpha = \frac{\sqrt{2} \Pi^*}{J_1(\lambda_n)} \int_0^1 \alpha J_0(\lambda_n \alpha) d\alpha = (\text{with } \eta = \alpha \lambda_n) = \\ &= \frac{\sqrt{2} \Pi^*}{J_1(\lambda_n)} \int_0^{\lambda_n} \frac{\eta}{\lambda_n} J_0(\eta) \frac{d\eta}{\lambda_n} = \frac{\sqrt{2} \Pi^*}{J_1(\lambda_n) \lambda_n^2} \int_0^{\lambda_n} \eta J_0(\eta) d\eta = \frac{\sqrt{2} \Pi^*}{J_1(\lambda_n) \lambda_n^2} \lambda_n J_1(\lambda_n) = \frac{\sqrt{2} \Pi^*(\gamma)}{\lambda_n}\end{aligned}$$

where use has been made of equation (3.420). Thus

$$\langle \Pi^*(\gamma), \phi_n(\alpha) \rangle = \frac{\sqrt{2} \Pi^*(\gamma)}{\lambda_n} \quad (3.463)$$

Next with $\frac{1}{\alpha} \frac{\partial(\alpha\varpi)}{\partial\alpha}$:

$$\left\langle \frac{1}{\alpha} \frac{\partial(\alpha\varpi)}{\partial\alpha}, \phi_n \right\rangle = \frac{\sqrt{2}}{J_1(\lambda_n)} \int_0^1 \alpha \frac{1}{\alpha} \frac{\partial\alpha\varpi(\gamma, \alpha)}{\partial\alpha} J_0(\lambda_n \alpha) d\alpha = \frac{\sqrt{2}}{J_1(\lambda_n)} \int_0^1 \frac{\partial\alpha\varpi}{\partial\alpha} J_0(\lambda_n \alpha) d\alpha =$$

Note the presence of the exponential $e^{-\lambda_n^2 \gamma}$, which was already evident in the homogeneous problem (3.442). In this alternative derivation the γ dependence of $u_n(\gamma)$ ought to respond only to the non-homogeneous term $\Xi_n(\gamma)$, since the γ dependence attached to the dynamical equation itself is already contained in the exponential $e^{-\lambda_n^2 \gamma}$, which is present from the beginning in the expression of $u^*(\gamma, \alpha)$. Then the derivatives in γ and α turn out to be:

$$\frac{\partial u^*}{\partial \gamma} = \frac{\partial}{\partial \gamma} \sum_{n=1}^{\infty} u_n \phi_n e^{-\lambda_n^2 \gamma} = \sum_{n=1}^{\infty} \left[\dot{u}_n \phi_n e^{-\lambda_n^2 \gamma} - u_n \phi_n \lambda_n^2 e^{-\lambda_n^2 \gamma} \right]$$

and

$$\left(\frac{\partial^2}{\partial \alpha^2} + \frac{1}{\alpha} \frac{\partial}{\partial \alpha} \right) \sum_{n=1}^{\infty} u_n \phi_n e^{-\lambda_n^2 \gamma} = - \sum_{n=1}^{\infty} u_n \lambda_n^2 \phi_n e^{-\lambda_n^2 \gamma}$$

Equation (3.380) now converts into:

$$\begin{aligned}\sum_{n=1}^{\infty} \left[\dot{u}_n - u_n \lambda_n^2 \right] \phi_n e^{-\lambda_n^2 \gamma} + \sum_{n=1}^{\infty} u_n \lambda_n^2 \phi_n e^{-\lambda_n^2 \gamma} &= \sum_{n=1}^{\infty} \Xi_n \phi_n \Rightarrow \\ \sum_{n=1}^{\infty} \left[\dot{u}_n e^{-\lambda_n^2 \gamma} - \Xi_n \right] \phi_n &= 0\end{aligned} \quad (3.459)$$

or

$$e^{-\lambda_n^2 \gamma} \dot{u}_n(\gamma) = \Xi_n(\gamma) \Rightarrow \dot{u}_n(\gamma) = \Xi_n(\gamma) e^{\lambda_n^2 \gamma} \quad (\forall n \in \mathbb{N}) \quad (3.460)$$

This is a first order linear ordinary differential equation whose solution is:

$$u_n(\gamma) = w_n + \int_0^{\gamma} \Xi_n(\gamma') e^{\lambda_n^2 \gamma'} d\gamma' \quad (3.461)$$

and the general solution is:

$$u^*(\gamma, \alpha) = \sum_{n=1}^{\infty} w_n \frac{\sqrt{2}}{J_1(\lambda_n)} J_0(\lambda_n \alpha) e^{-\lambda_n^2 \gamma} + \sum_{n=1}^{\infty} \frac{\sqrt{2}}{J_1(\lambda_n)} J_0(\lambda_n \alpha) \left[\int_0^{\gamma} \Xi_n(\gamma') e^{\lambda_n^2 \gamma'} d\gamma' \right] e^{-\lambda_n^2 \gamma} \quad (3.462)$$

which is identical to (3.457).

$$= \frac{\sqrt{2}}{J_1(\lambda_n)} \int_0^1 \left(\varpi + \alpha \frac{\partial \varpi}{\partial \alpha} \right) J_0(\lambda_n \alpha) d\alpha = \frac{\sqrt{2}}{J_1(\lambda_n)} \int_0^1 \alpha \left(\frac{\varpi}{\alpha} + \frac{\partial \varpi}{\partial \alpha} \right) J_0(\lambda_n \alpha) d\alpha$$

Or in other words:

$$\left\langle \frac{1}{\alpha} \frac{\partial \alpha \varpi}{\partial \alpha}, \phi_n \right\rangle = \left\langle \frac{\varpi}{\alpha} + \frac{\partial \varpi}{\partial \alpha}, \phi_n \right\rangle = \left\langle \frac{\varpi}{\alpha}, \phi_n \right\rangle + \left\langle \frac{\partial \varpi}{\partial \alpha}, \phi_n \right\rangle \quad (3.464)$$

Therefore, putting together equations (3.463) and (3.464), the term $\Xi_n(\gamma)$ has now the more detailed expression:

$$\Xi_n(\gamma) = \frac{\sqrt{2} \Pi^*(\gamma)}{\lambda_n} - \left\langle \frac{\varpi}{\alpha}, \phi_n \right\rangle - \left\langle \frac{\partial \varpi}{\partial \alpha}, \phi_n \right\rangle \quad (3.465)$$

Calling conventionally

$$\varphi_n(\gamma) = \left\langle \frac{\varpi}{\alpha}, \phi_n \right\rangle = \frac{\sqrt{2}}{J_1(\lambda_n)} \int_0^1 \varpi(\gamma, \alpha) J_0(\lambda_n \alpha) d\alpha \quad (3.466)$$

and

$$\varpi'_n(\gamma) = \left\langle \frac{\partial \varpi}{\partial \alpha}, \phi_n \right\rangle = \frac{\sqrt{2}}{J_1(\lambda_n)} \int_0^1 \alpha \frac{\partial \varpi(\gamma, \alpha)}{\partial \alpha} J_0(\lambda_n \alpha) d\alpha \quad (3.467)$$

then the expressions for Ξ_n and u^* are

$$\Xi_n(\gamma) = \frac{\sqrt{2} \Pi^*(\gamma)}{\lambda_n} - \varphi_n(\gamma) - \varpi'_n(\gamma) \quad (3.468)$$

and (the **General Analytical Solution** (GAS))

$$\begin{aligned} u^*(\gamma, \alpha) &= \sum_{n=1}^{\infty} w_n \frac{\sqrt{2}}{J_1(\lambda_n)} J_0(\lambda_n \alpha) e^{-\lambda_n^2 \gamma} + \sum_{n=1}^{\infty} \frac{2}{J_1(\lambda_n) \lambda_n} J_0(\lambda_n \alpha) \int_0^{\gamma} \Pi^*(\gamma') e^{-\lambda_n^2 (\gamma - \gamma')} d\gamma' \\ &\quad - \sum_{n=1}^{\infty} \frac{\sqrt{2}}{J_1(\lambda_n)} J_0(\lambda_n \alpha) \int_0^{\gamma} (\varphi_n(\gamma') + \varpi'_n(\gamma')) e^{-\lambda_n^2 (\gamma - \gamma')} d\gamma' = \\ &= u_t^*(\gamma, \alpha) + u_p^*(\gamma, \alpha) + u_r^*(\gamma, \alpha) \end{aligned} \quad (3.469)$$

The mean velocity profile $u^*(\gamma, \alpha)$ has three different components with the following proposed names:

- the first term corresponds to the transient response of the mean initial velocity to external interactions, and thus will be called the **IniTrans component**, $u_t^*(\gamma, \alpha)$,
- the second term is the unsteady response to the time-dependent mean pressure gradient, called the **PressGrad component**, $u_p^*(\gamma, \alpha)$, and
- the third term is the unsteady component due to the turbulent Reynolds stress, with the name of **RStress component**, $u_r^*(\gamma, \alpha)$.

Equation (3.469) represents the most comprehensive analytical mean velocity profile for incompressible pipe flow. It describes the evolution of a turbulent incompressible pipe flow from an initial state at $\gamma = 0$

given by the initial conditions (3.375)-(3.378), which undergoes along the time the external influences defined by $\Xi(\gamma, \alpha)$. To the author's knowledge, it is the first time such equation has been written, and it probably constitutes the main contribution of the present Dissertation.

It ought to be remembered that the averaging method presumed to develop the RANSE is the most general available: the ensemble average. The equation could also describe the evolution of a laminar incompressible pipe flow simply by setting $\varpi(\gamma, \alpha) = 0$, since the mean velocity equals the instantaneous velocity when the fluctuating components are zero, a situation that is generally taken as a definition for the laminar regime.

Note the PressGrad and RStress components are zero for $\gamma = 0$, since they determine the flow evolution from the initial state, whereas the IniTrans component is zero for $\gamma \rightarrow \infty$. The IniTrans component also represents the initial inertia retained by the fluid, which is bound to be dissipated along the flow evolution, and replaced by the other components. No behaviour is assigned beforehand to the PressGrad or RStress components as $\gamma \rightarrow \infty$.

It stems from the GAS (3.469) the direct dependence of the mean velocity profile on the Reynolds stress $\varpi(\gamma, \alpha)$. Thus the Reynolds stress emerges as the main cause for the turbulent profile to depart from the laminar profile. The Reynolds stress $\varpi(\gamma, \alpha)$ can explain by itself the generation of the turbulent component within the total velocity.

This last assertion is better understood upon acknowledging a subtle difference between the PressGrad and RStress components. The integral in the PressGrad term has a single dependence on the index n , given by $e^{\lambda_n^2 \gamma}$. Were $\Pi^*(\gamma')$ of sufficiently slow variation, it could approximately exit the integral and the resulting exponentials would cancel each other:

$$\begin{aligned} u_p^*(\gamma, \alpha) &= \sum_{n=1}^{\infty} \frac{2}{J_1(\lambda_n)\lambda_n} J_0(\lambda_n\alpha) e^{-\lambda_n^2 \gamma} \int_0^{\gamma} \Pi^*(\gamma') e^{\lambda_n^2 \gamma'} d\gamma' \approx \\ &\approx \sum_{n=1}^{\infty} \frac{2}{J_1(\lambda_n)\lambda_n} J_0(\lambda_n\alpha) e^{-\lambda_n^2 \gamma} \Pi^* \int_0^{\gamma} e^{\lambda_n^2 \gamma'} d\gamma' \approx 2\Pi^* \sum_{n=1}^{\infty} \frac{J_0(\lambda_n\alpha)}{J_1(\lambda_n)\lambda_n^3} e^{-\lambda_n^2 \gamma} (e^{\lambda_n^2 \gamma} - 1) \approx \\ &\approx 2\Pi^* \sum_{n=1}^{\infty} \frac{J_0(\lambda_n\alpha)}{J_1(\lambda_n)\lambda_n^3} (1 - e^{-\lambda_n^2 \gamma}) \approx \frac{\Pi^*}{4} (1 - \alpha^2) - 2\Pi^* \sum_{n=1}^{\infty} \frac{J_0(\lambda_n\alpha)}{J_1(\lambda_n)\lambda_n^3} e^{-\lambda_n^2 \gamma} \end{aligned} \quad (3.470)$$

(see equation (3.447)). The PressGrad component is basically the Szymanski flow shown in equation (3.351), that is, the transient parabolic laminar velocity profile, which is a particular case of the general expression (3.469)⁸⁵. Therefore, not a very deformed velocity profile should be expected from the PressGrad term, since the integral in γ' does not significantly alter the relative weight of each eigenfunction ϕ_n in the final solution. Note the main mechanism the Fourier-Bessel series has to change the profile, that is, to significantly modify the dependence on α , is to assign very different relative weights to each eigenfunction, to modulate the share that each eigenfunction holds in the final solution, and this is not the case with the PressGrad term, which influences more or less uniformly to every eigenfunction.

However, in the RStress component the dependence on the index n is much stronger: each integrand changes significantly with changing n , being $\varphi_n + \varpi'_n$ very different from $\varphi_m + \varpi'_m$ if n and m are sufficiently far apart. Therefore, each eigenfunction ϕ_n has a noticeably different relative weight

⁸⁵Incidentally, the above derivation shows that the Szymanski flow is in reality a PressGrad term, that is, deriving exclusively from the pressure gradient when such gradient is constant.

in the Fourier-Bessel series, resulting in a remarkably altered velocity profile, with a not so familiar distribution of velocities along the radial α values. This different behaviour of the RStress term with changing n helps to understand the statement made above: the Reynolds stress alone almost explains the observed change in the turbulent velocity profile respect to the laminar counterpart. ■

It is already time to apply the GAS (3.469) to a particular case of incompressible pipe flow, which will serve as a benchmark to assess its effectiveness. This particular example has as limiting cases the already studied Hagen-Poiseuille, Szymanski and Pai flows. Imagine a fluid initially at rest in a pipe, filling it completely. At $\gamma = 0$ the fluid is suddenly subjected to a constant pressure gradient $\Pi^* \in \mathbb{R}$, which accelerates it in a transient flow until, for γ sufficiently high, it reaches a steady state with a turbulent mean velocity profile.

By now it should be evident the main drawback of the formalism herein developed: there are more unknowns than available equations; the old closure problem attached to the statistical description of turbulence. Either the Reynolds stress ϖ is calculated somehow, or a function ought to be proposed *ad hoc*. It is even possible a recursive method in which different candidate functions for Reynolds stress, $\varpi^{(n)}$, are being tested, each a bit more accurate than the preceding one, until a solution is obtained with a sufficient approximation to the experimental or simulation results. That method makes sense when testing successive terms in a truncated McLaurin or Taylor series that, once optimised, provides an approximate polynomial function for $\varpi(\gamma, \alpha)$, as accurate as desired. In any case, even with no *a priori* knowledge of the Reynolds stress ϖ , a wealth of qualitative or semi-quantitative results could be obtained from the general mean velocity profile (3.469), as it will be shown in the next Chapter.

A reasonable starting point is to suppose a Reynolds stress similar to that given by equation (3.347) in section 3.4.1. It could not be exactly the same because $\chi(\alpha, Re^+)$ is calculated with the friction velocity u_τ as reference velocity, whereas in this section that role has been played by ν/R . When the conversion of reference velocity is done on the differential RANSE that would otherwise lead to $u^+(\alpha, Re^+)$ and $\chi(\alpha, Re^+)$, the following expressions for the steady state quantities $u^*(\alpha, Re^+)$ and $\varpi(\alpha, Re^+)$ are obtained ⁸⁶:

$$u^*(\alpha, Re^+) = u_m^* \left(1 + \frac{\Theta - q}{q - 1} \alpha^2 - \frac{\Theta - 1}{q - 1} \alpha^{2q} \right) \quad , \quad (q \geq 2, q \in \mathbb{N}) \quad (3.471)$$

$$\varpi(\alpha, Re^+) = 2u_m^* \frac{q(\Theta - 1)}{q - 1} \alpha \left(1 - \alpha^{2(q-1)} \right) \quad , \quad (q \geq 2, q \in \mathbb{N}) \quad (3.472)$$

with

$$u_m^* = \frac{U_m R}{\nu}$$

the maximum mean velocity, attained at $\alpha = 0$, and Θ given by

$$\Theta = \frac{\Pi^*}{4u_m^*} \quad (\Theta \geq 1)$$

⁸⁶In order to avoid confusion with the index n of Fourier-Bessel series, the integer n in (3.347) is replaced by the integer q herein. Note u_m^* corresponds to the maximum mean velocity for a turbulent flow profile, which is different from the maximum velocity for a laminar profile, given by $\Pi^*/4$. Not noticing this difference at due time has caused the author much trouble during the resolution of this example.

From that steady state Reynolds stress the following unsteady Reynolds stress is proposed:

$$\varpi(\gamma, \alpha) = 2u_m^* \frac{q(\Theta - 1)}{q - 1} \alpha \left(1 - \alpha^{2(q-1)}\right) \Upsilon(\gamma) \quad , \quad (q \geq 2, q \in \mathbb{N}) \quad (3.473)$$

with $\Upsilon(\gamma)$ a function that would express the foreseeable evolution of ϖ with time, another degree of freedom (and of indeterminacy) of the formalism⁸⁷. $\Upsilon(\gamma)$ must satisfy the conditions $\Upsilon(0) = 0$ and $\Upsilon \rightarrow 1$ with $\gamma \rightarrow \infty$, since initially the flow is at rest and after a long time it would reach the steady state. Besides, it is convenient that the Reynolds stress growth be at a similar pace than the mean velocity itself, since the last fixes the Reynolds number which determines the former.

A sensible behaviour for ϖ is represented by the time function:

$$\Upsilon(\gamma) = 1 - e^{-\lambda^2 \gamma}$$

with $\lambda \in \mathbb{R}^+$ a parameter to be fixed, but which will foreseeably be some sort of average of the first few roots λ_n of J_0 , since they are the most significant in the Fourier-Bessel series. Note such $\Upsilon(\gamma)$ verifies $\Upsilon(0) = 0$ and $\Upsilon(\infty) = 1$, that is, no turbulence at the beginning and steady-state turbulence after a long time.

With all the reasoning made above, the Reynolds stress function considered in this problem is given by:

$$\varpi(\gamma, \alpha) = 2u_m^* \frac{q(\Theta - 1)}{q - 1} \alpha \left(1 - \alpha^{2(q-1)}\right) \left(1 - e^{-\lambda^2 \gamma}\right) \quad , \quad (q \geq 2, q \in \mathbb{N}) \quad (3.474)$$

Note the α -dependent part of ϖ belongs to $L_\alpha^2(0, 1)$ and, therefore, can be expanded in a Fourier-Bessel series.

Θ expresses the ratio of the maximum velocity for a laminar profile, $\Pi^*/4$, to the maximum mean velocity for a turbulent profile u_m^* . Note $\Theta \geq 1$ for the same cross-section averaged velocity (bulk velocity). When $\Theta = 1$ the flow must be interpreted as laminar. The expression 'switching off the turbulence' and doing $\Theta = 1$ will be considered equivalent in this text, since $\Theta = 1 \Rightarrow \varpi = 0$.

Note Θ as defined herein is different from ϑ defined in (3.338) and (3.350). In both cases the parameters express the ratio of a laminar quantity to a like turbulent quantity, but the chosen quantities are different for each case. Θ and ϑ share the property of being equal to 1 for laminar flow and > 1 for turbulent flow.

Equation (3.474) could be considered a simple model of turbulence, based on a polynomial expression for the spatial coordinate and an exponential growth in time. Its main merit is to reproduce with reasonable accuracy the expected curve for the steady state Reynolds stress: compare figure 3.15 with, either, figure 3.17 obtained from figure 7.3 of [Pop00], or with the curve $-\overline{u'v'}/u_\tau^2$ of figure 4.1 retrieved from [Wil06]. The agreement is noteworthy in both cases. Should a better match be required, one could always add more terms to the polynomial function. Unfortunately, no information could be found regarding the time evolution of that Reynolds stress profile. Therefore, the proposed exponential growth ought to be considered a first approximation to the actual build-up of turbulence along time, since no benchmark seems to be available to compare with.

⁸⁷Note U_m , u_m^* and Θ are in general time dependent in any unsteady/transient flow. But in equation (3.473) the quantities u_m^* and Θ would correspond to the steady state attained by the flow as $\gamma \rightarrow \infty$, if the spirit of equation (3.347) is meant to be preserved. Possibly they would be more illustrative if written like $u_{m_\infty}^*$ and Θ_∞ , but here it is considered unnecessary since all dependence of ϖ on γ is concentrated in the function $\Upsilon(\gamma)$, and u_m^* and Θ could only refer to said steady state. Note also that Θ herein has a different meaning than ϑ in equations (3.338) and (3.350). Confusing Θ with ϑ would only cause trouble during the resolution of this example.

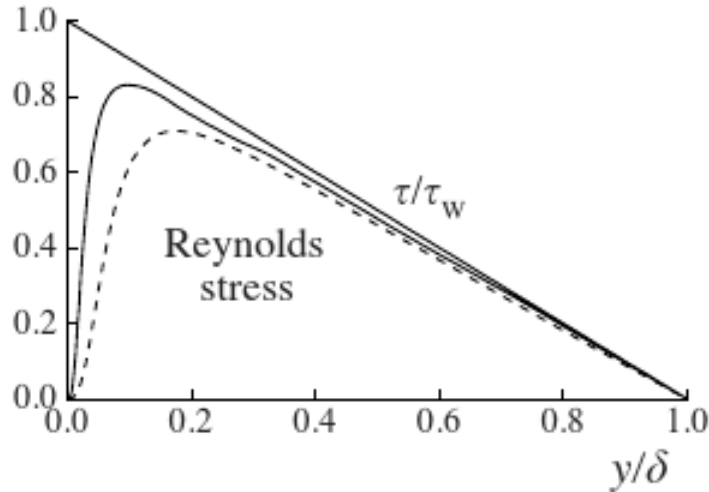


Figure 3.17: Profile of Reynolds stress in turbulent channel flow ($y/\delta = 1 - \alpha$). From fig. 7.3 of [Pop00].

Said turbulence model does not present some of the features the actual phenomenon is known to possess: intermittency, relaminarisation, continuous set of length scales, coherent structures, energy cascade... The solution obtained in this example will be valid as long as the Reynolds stress $\varpi(\gamma, \alpha)$ could be considered suitable to model the actual turbulence. Note $\varpi(\gamma, \alpha)$ is the single quantity the formalism uses to introduce the turbulence in the dynamic equations, since no other quantity plays that role. The efficacy of the method is directly related to the intelligent choice of a Reynolds stress function.

On the other hand, the method herein developed belongs to the realm of RANSE, that is, to the statistical description of turbulence in its simplest form. It is not related with the spectral distribution of turbulent energy, nor with the second- or third-order correlation tensor, nor with any other similarly powerful mathematical technique currently used in the study of turbulence. It would be unrealistic to expect from a simple scalar field $\varpi(\gamma, \alpha)$ a wealth of information it could by no means provide. Actually, one would think any function satisfying the condition (3.330) in steady state (or (3.332) in the current normalisation), which present a reasonable approximation with the expected Reynolds stress curve shown in figure 3.17, ought to be considered, in principle, a good-enough candidate for the formalism herein developed. Or perhaps not?

One simple example would shed some light onto this issue. The following function, proposed in a different context by [TM05], would at first sight seem a viable steady state Reynolds stress function:

$$\varpi_1(\alpha) = A \frac{1 - e^{(\alpha-1)/b}}{1 - e^{-1/b}} + A(\alpha - 1) \quad (3.475)$$

with $0 < A < 1$ and $b > 0$, $b \ll 1$, two real parameters. Note no further conditions are imposed on ϖ_1 : it is not associated with any normalisation and, in principle, it could be claimed to be expressed either with u_τ or ν/R as reference velocity, that is, it might correspond to either $\chi(\alpha, Re^+)$ in equation (3.330) or to $\varpi(\alpha)$ in (3.332). When plotted (see figure 3.18), the resulting curve is quite similar to the expected Reynolds stress profile of figure 3.17, a reassuring sign that it might indeed be an appropriate Reynolds stress for the problem. According to equation (3.330), to the Reynolds stress function $\varpi_1(\alpha)$

corresponds the following steady state mean velocity profile, expressed in the u_τ normalisation⁸⁸:

$$u_1^+(\alpha, Re^+) = \frac{Re^+}{2}(1 - \alpha^2) + \frac{Re^+ A}{2}(1 - \alpha)^2 - \frac{Re^+ A}{1 - e^{-1/b}} \left[1 - \alpha - b(1 - e^{(\alpha-1)/b}) \right] \quad (3.476)$$

Note Re^+ does not appear in equation (3.475), and then in (3.476) plays the role of a global scaling factor.

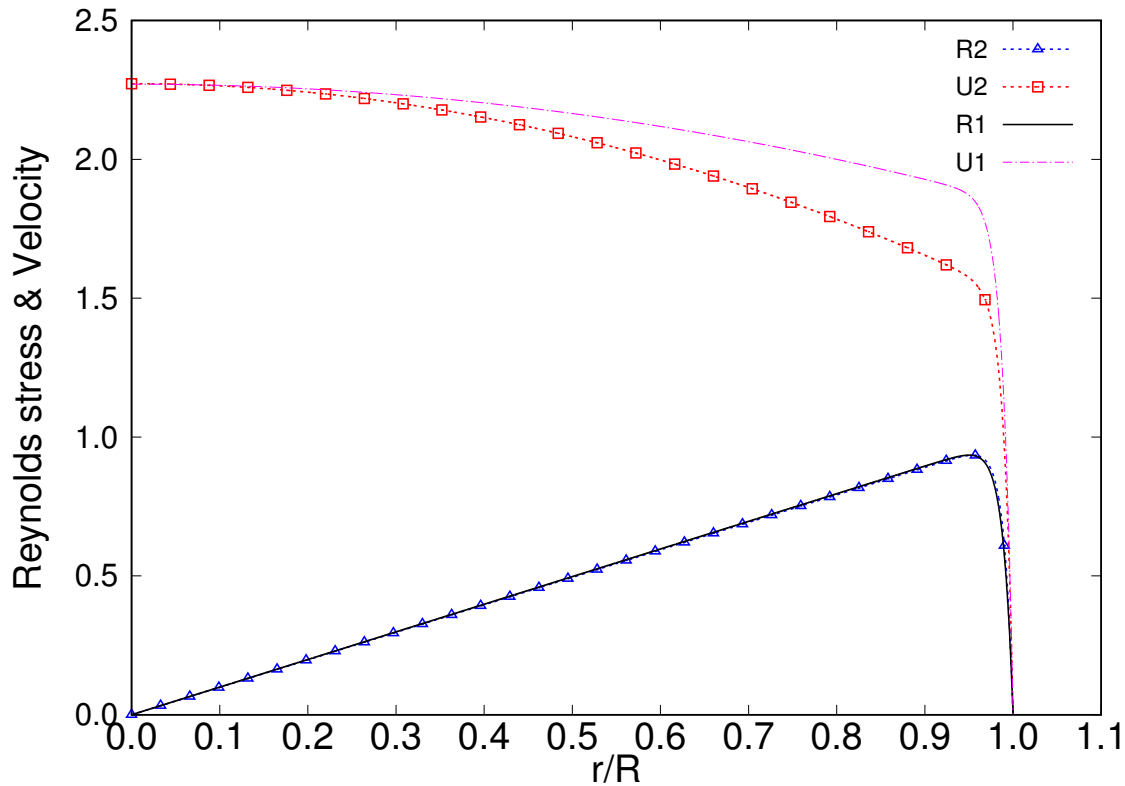


Figure 3.18: Reynolds stress and mean velocity profiles for equations (3.475) and (3.476) with $A = 0.99$, $b = 0.01$, $Re^+ = 152.5$ (R_2 , U_2), and for figures 3.14 and 3.15 (R_1 , U_1).

Figure 3.18 shows the functions $\varpi_1(\alpha)$ and $u_1^+(\alpha, Re^+)$ corresponding to equations (3.475) and (3.476), respectively, for the values $A = 0.99$, $b = 0.01$ and $Re^+ = 152.5$. Those curves are identified with the labels R_2 and U_2 . Figure 3.18 also shows the Reynolds stress (3.347) and mean velocity (3.343) functions that were already presented in figures 3.14 and 3.15 for the values $U_m = 2.2708$, $\vartheta = 36.8$ and $n = 45$, labelled R_1 and U_1 . Those functions R_1 and U_1 have already proved their good concordance with CFD data, they are expressed in u_τ normalisation, and their equivalent in ν/R normalisation is given by (3.472) and (3.471), respectively. The agreement between both Reynolds stress curves, R_1 and R_2 , is exceedingly good, to the point that they seem a single curve. But the velocity profiles are very different, having only in common the values in the vicinity of the centreline ($\alpha = 0$) and near the wall ($\alpha = 1$). It seems that the very tiny differences between R_1 and R_2 become hugely amplified when translated into U_1 and U_2 .

On the other hand, figure 3.19 shows the same curves with R_3 and U_3 corresponding to equations (3.475) and (3.476), respectively, for the values $A = 0.995$, $b = 0.011$ and $Re^+ = 169$. Now the agreement

⁸⁸The u_τ normalisation has been chosen because the resulting mean velocity profile (3.476) is meant to be compared with that plotted in figures 3.14 and 3.15, which is expressed in the u_τ normalisation. The results would not be directly comparable should (3.476) have been expressed in the ν/R normalisation.

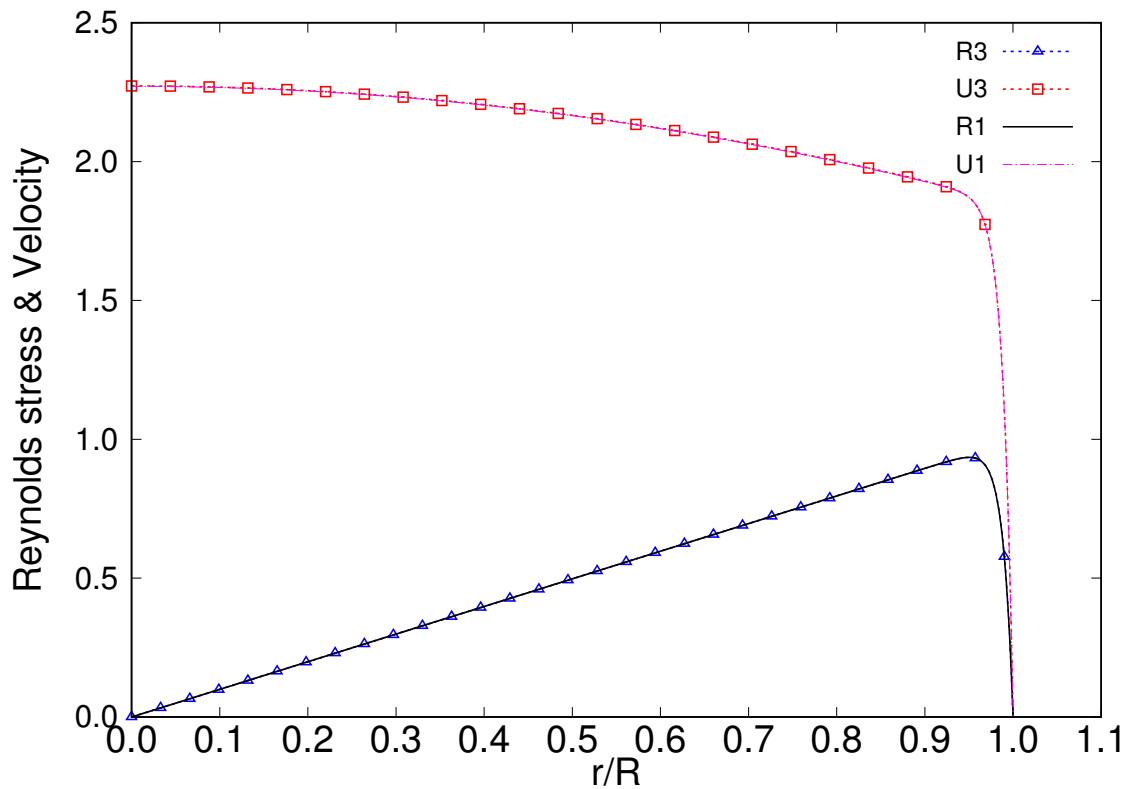


Figure 3.19: Reynolds stress and mean velocity profiles for equations (3.475) and (3.476) with $A = 0.995$, $b = 0.011$, $Re^+ = 169$ (R_3 , U_3), and for figures 3.14 and 3.15 (R_1 , U_1).

among all curves is complete, a feat achieved with just small variations on the parameters A and b (Re^+ is just a global scaling factor of u_1^+). The exponential function of equation (3.475) depends critically on the parameter b : very small variations of b translate into noticeable differences in u_1^+ .

Thus, it would seem it is not so straightforward to find a suitable steady state Reynolds stress function $\varpi(\alpha)$, and any proposed candidate should not be taken immediately for granted. Apart from satisfying equations (3.331) and (3.332), the only merit it must be requested to the model of turbulence is that it provide a steady state Reynolds stress function $\varpi(\alpha)$ **and** a mean velocity profile $u^*(\alpha)$ which are, **both**, reasonably coincident with experimental or simulation results. As a practical matter, Reynolds stress functions with polynomial form in α would be usually preferable to other functional forms, since they are easier to work with and they are not so critically dependent on small variations of its parameters. The polynomial functions (3.471) and (3.472) proposed in this example present, both, a remarkable agreement with CFD results and with the Law of the Wall, as it was already shown in figures 3.14 and 3.15 and the attached explanations therefrom. Therefore they ought to be considered an acceptable model for turbulence, duly applicable to the solution that is going to be obtained in the current example.

Regarding $\Pi^*(\gamma)$, it is taken as the Heaviside step function

$$\Pi^*(\gamma) = \begin{cases} 0 & \text{if } \gamma < 0 \\ \Pi^* & \text{if } \gamma \geq 0 \end{cases} \quad (3.477)$$

with $\Pi^* \in \mathbb{R}^+$ a constant value.

Boundary conditions for the problem are the familiar (3.369)-(3.374), whereas the initial conditions are easy to establish: u^* and ϖ are zero at $\gamma = 0$.

The PressGrad component has already been formulated above in an approximate way (see equation (3.470)). Now it can be accurately presented since Π^* is rigorously constant:

$$u_p^*(\gamma, \alpha) = \frac{\Pi^*}{4}(1 - \alpha^2) - 2\Pi^* \sum_{n=1}^{\infty} \frac{J_0(\lambda_n \alpha)}{J_1(\lambda_n) \lambda_n^3} e^{-\lambda_n^2 \gamma} = \frac{\Pi^*}{4} \left[(1 - \alpha^2) - \sum_{n=1}^{\infty} \frac{8 J_0(\lambda_n \alpha)}{J_1(\lambda_n) \lambda_n^3} e^{-\lambda_n^2 \gamma} \right] \quad (3.478)$$

For $\gamma \rightarrow \infty$ the PressGrad component corresponds to a laminar parabolic velocity profile with a maximum at the centreline given by

$$u_{pm}^* = \frac{\Pi^*}{4} \quad (3.479)$$

The RStress component is more elaborate and will require much attention. The $\varphi_n(\gamma)$ term is given by

$$\varphi_n(\gamma) = \left\langle \frac{\varpi}{\alpha}, \phi_n \right\rangle = \frac{2\sqrt{2} u_m^* q (\Theta - 1)}{J_1(\lambda_n) (q - 1)} (1 - e^{-\lambda^2 \gamma}) \int_0^1 \alpha (1 - \alpha^{2q-2}) J_0(\lambda_n \alpha) d\alpha \quad (3.480)$$

Since $\partial \varpi / \partial \alpha$ is given by

$$\frac{\partial \varpi}{\partial \alpha} = \frac{2u_m^* q (\Theta - 1)}{q - 1} (1 - e^{-\lambda^2 \gamma}) (1 - (2q - 1)\alpha^{2q-2}) \quad (3.481)$$

then the $\varpi'_n(\gamma)$ component adopts the form:

$$\varpi'_n(\gamma) = \left\langle \frac{\partial \varpi}{\partial \alpha}, \phi_n \right\rangle = \frac{2\sqrt{2} u_m^* q (\Theta - 1)}{J_1(\lambda_n) (q - 1)} (1 - e^{-\lambda^2 \gamma}) \int_0^1 \alpha (1 - (2q - 1)\alpha^{2q-2}) J_0(\lambda_n \alpha) d\alpha \quad (3.482)$$

which is very similar to that of φ_n , except for the integrand in $(2q - 1)\alpha^{2q-2}$. Actually, it is convenient to directly calculate the sum $\varphi_n + \varpi'_n$, which takes the form:

$$\varphi_n + \varpi'_n = \frac{4\sqrt{2} u_m^* q (\Theta - 1)}{J_1(\lambda_n) (q - 1)} (1 - e^{-\lambda^2 \gamma}) \int_0^1 (\alpha - q \alpha^{2q-1}) J_0(\lambda_n \alpha) d\alpha \quad (3.483)$$

In order to calculate this integral, equations (3.420)-(3.422) are necessary. The first integral is quite straightforward (as usual, the change of variables $\eta = \lambda_n \alpha$):

$$\int_0^1 \alpha J_0(\lambda_n \alpha) d\alpha = \frac{J_1(\lambda_n)}{\lambda_n}$$

The second integral requires a recursive algorithm ($J_0(\lambda_n) = 0$ and is thus omitted):

$$\begin{aligned} \int_0^1 q \alpha^{2q-1} J_0(\lambda_n \alpha) d\alpha &= q \int_0^{\lambda_n} \frac{\eta^{2q-1}}{\lambda_n^{2q-1}} J_0(\eta) \frac{d\eta}{\lambda_n} = \frac{q}{\lambda_n^{2q}} \left(\lambda_n^{2q-1} J_1(\lambda_n) - (2q - 2)^2 \int_0^{\lambda_n} \eta^{2q-3} J_0(\eta) d\eta \right) = \\ &= \frac{q}{\lambda_n^{2q}} \left(\lambda_n^{2q-1} J_1(\lambda_n) - (2q - 2)^2 \left[\lambda_n^{2q-3} J_1(\lambda_n) - (2q - 4)^2 \left\{ \dots - 4^2 \left(\lambda_n^3 J_1(\lambda_n) - 2^2 \lambda_n J_1(\lambda_n) \right) \dots \right\} \right] \right) \end{aligned}$$

Putting together both integrals and extracting the common factors, the following result is obtained for the eigenfunctions expansion of the RStress component⁸⁹ (choose any of both expressions, see [Ros16]):

$$\begin{aligned}\varphi_n + \varpi'_n &= \frac{4\sqrt{2}u_m^*q(\Theta - 1)}{q - 1} (1 - e^{-\lambda^2\gamma}) \left\{ \frac{1}{\lambda_n} - q \sum_{i=0}^{q-1} (-1)^i \left(\frac{(2q - 2)!!}{(2q - 2i - 2)!!} \right)^2 \lambda_n^{-2i-1} \right\} = \\ &= \frac{4\sqrt{2}u_m^*q(\Theta - 1)}{q - 1} (1 - e^{-\lambda^2\gamma}) \left\{ \frac{1}{\lambda_n} - q \sum_{i=0}^{q-1} (-1)^i \left(\frac{2^i(q - 1)!}{(q - i - 1)!} \right)^2 \lambda_n^{-2i-1} \right\}\end{aligned}\quad (3.484)$$

where $n!!$ is the double factorial defined by

$$n!! := \begin{cases} 1 & \text{if } n = 0 \\ \prod_{i=1}^{n/2} 2i & \text{if } n = \text{even} \\ \prod_{i=1}^{(n+1)/2} (2i - 1) & \text{if } n = \text{odd} \end{cases}\quad (3.485)$$

Note in this example $2q - 2$ is always even.

The RStress component itself is finally written as:

$$\begin{aligned}u_r^*(\gamma, \alpha) &= -\frac{8u_m^*q(\Theta - 1)}{q - 1} \sum_{n=1}^{\infty} \frac{J_0(\lambda_n\alpha)}{J_1(\lambda_n)} e^{-\lambda_n^2\gamma} \\ &\int_0^\gamma (1 - e^{-\lambda^2\gamma'}) \left\{ \frac{1}{\lambda_n} - q \sum_{i=0}^{q-1} (-1)^i \left(\frac{2^i(q - 1)!}{(q - i - 1)!} \right)^2 \lambda_n^{-2i-1} \right\} e^{\lambda_n^2\gamma'} d\gamma' = \\ &= -\frac{8u_m^*q(\Theta - 1)}{q - 1} \sum_{n=1}^{\infty} \frac{J_0(\lambda_n\alpha)}{J_1(\lambda_n)} e^{-\lambda_n^2\gamma} \left\{ \frac{1}{\lambda_n} - q \sum_{i=0}^{q-1} (-1)^i \left(\frac{2^i(q - 1)!}{(q - i - 1)!} \right)^2 \lambda_n^{-2i-1} \right\} \\ &\int_0^\gamma (1 - e^{-\lambda^2\gamma'}) e^{\lambda_n^2\gamma'} d\gamma'\end{aligned}$$

and a similar expression if the first sum with double factorials in (3.484) is chosen. The time integral is easily solved:

$$\begin{aligned}\int_0^\gamma (1 - e^{-\lambda^2\gamma'}) e^{\lambda_n^2\gamma'} d\gamma' &= \int_0^\gamma (e^{\lambda_n^2\gamma'} - e^{(\lambda_n^2 - \lambda^2)\gamma'}) d\gamma' = \int_0^{\lambda_n^2\gamma} \frac{e^\eta}{\lambda_n^2} d\eta - \int_0^{(\lambda_n^2 - \lambda^2)\gamma} \frac{e^\eta}{\lambda_n^2 - \lambda^2} d\eta = \\ &= \frac{e^{\lambda_n^2\gamma}}{\lambda_n^2} - \frac{1}{\lambda_n^2} - \frac{e^{(\lambda_n^2 - \lambda^2)\gamma}}{\lambda_n^2 - \lambda^2} + \frac{1}{\lambda_n^2 - \lambda^2}\end{aligned}$$

where the obvious change of variables $\eta = \lambda_n^2\gamma'$ and $\eta = (\lambda_n^2 - \lambda^2)\gamma'$ have been conducted for the first and second integrals, respectively.

⁸⁹Note it is also possible to define the time dependence of $\varphi_n + \varpi'_n$ in terms of $1 - e^{-\Lambda_n^2\gamma}$, with Λ_n a set of real constants which would have relationship with the roots λ_n of the Bessel function J_0 . That selection of time dependence would enable that each component of $\varpi/\alpha + \partial\varpi/\partial\alpha$ in the eigenfunctions Fourier-Bessel expansion have a different time modulation, instead of a single common time dependence $1 - e^{-\lambda^2\gamma}$ for all components, as it has been considered herein. Both approaches fulfil the main equation (3.469), and their suitability is to be assessed according to agreement with experimental or simulation data.

With those results, the RStress component is given by⁹⁰

$$u_r^*(\gamma, \alpha) = -\frac{8u_m^*q(\Theta - 1)}{q - 1} \sum_{n=1}^{\infty} \frac{J_0(\lambda_n \alpha)}{J_1(\lambda_n)} \left[\frac{1}{\lambda_n} - q \sum_{i=0}^{q-1} (-1)^i \left(\frac{2^i(q-1)!}{(q-i-1)!} \right)^2 \lambda_n^{-2i-1} \right] \left[\frac{1 - e^{-\lambda_n^2 \gamma}}{\lambda_n^2} + \frac{e^{-\lambda_n^2 \gamma} - e^{-\lambda^2 \gamma}}{\lambda_n^2 - \lambda^2} \right] \quad (3.488)$$

Finally, the IniTrans component $u_t^*(\gamma, \alpha)$ is blatantly zero, since the initial condition for velocity is $u_0^*(\alpha) = 0$, and the w_n coefficients of $u_t^*(\gamma, \alpha)$ are obtained directly from $u_0^*(\alpha) = 0$ (see equations (3.443) and (3.444)).

Now all ingredients are ready to provide the desired expression for the mean velocity profile corresponding to a fluid initially at rest, which is suddenly set in motion at time $\gamma = 0$ by exerting a constant pressure gradient Π^* , until the fluid reaches a turbulent steady state for $\gamma \rightarrow \infty$, whose Reynolds stress is given by (3.474). The said expression is ($u_t^*(\gamma, \alpha)$ is not written for being zero):

$$u^*(\gamma, \alpha) = u_p^*(\gamma, \alpha) + u_r^*(\gamma, \alpha) = \frac{\Pi^*}{4}(1 - \alpha^2) - 2\Pi^* \sum_{n=1}^{\infty} \frac{J_0(\lambda_n \alpha)}{\lambda_n^3 J_1(\lambda_n)} e^{-\lambda_n^2 \gamma} - \frac{8u_m^*q(\Theta - 1)}{q - 1} \sum_{n=1}^{\infty} \frac{J_0(\lambda_n \alpha)}{J_1(\lambda_n)} \left[\frac{1}{\lambda_n} - q \sum_{i=0}^{q-1} (-1)^i \left(\frac{2^i(q-1)!}{(q-i-1)!} \right)^2 \lambda_n^{-2i-1} \right] \left[\frac{1 - e^{-\lambda_n^2 \gamma}}{\lambda_n^2} + \frac{e^{-\lambda_n^2 \gamma} - e^{-\lambda^2 \gamma}}{\lambda_n^2 - \lambda^2} \right] \quad (3.489)$$

This general mean velocity profile satisfies three conditions:

- At $\gamma = 0$ the result is $u^*(0, \alpha) \equiv u_0^*(\alpha) = 0$ (fluid at rest), since all exponentials are equal to one, and $u_p^*(0, \alpha) = 0$ (see equation (3.447))
- Switching off the turbulence ($\Theta = 1 \Rightarrow \varpi = 0$) the RStress term is zero, $u_r^*(\gamma, \alpha) = 0$, and the solution is identical to the Szymanski flow, equation (3.351).

⁹⁰Note that if instead of a single time dependence with λ , a componentwise time dependence is chosen with a Λ_n for each eigenfunction (see footnote 89 in page 188), then the RStress component would take the form

$$u_r^*(\gamma, \alpha) = -\frac{8u_m^*q(\Theta - 1)}{q - 1} \sum_{n=1}^{\infty} \frac{J_0(\lambda_n \alpha)}{J_1(\lambda_n)} \left[\frac{1}{\lambda_n} - q \sum_{i=0}^{q-1} (-1)^i \left(\frac{2^i(q-1)!}{(q-i-1)!} \right)^2 \lambda_n^{-2i-1} \right] \left[\frac{1 - e^{-\lambda_n^2 \gamma}}{\lambda_n^2} + \frac{e^{-\lambda_n^2 \gamma} - e^{-\Lambda_n^2 \gamma}}{\lambda_n^2 - \Lambda_n^2} \right] \quad (3.486)$$

The main inconvenience of this approach is that a set of values for Λ_n would have to be provided *ad hoc*, and that could be a challenging task if $n \rightarrow \infty$. In the particular case of $\Lambda_n = \lambda_n$ the last term vanishes identically and the RStress component results in a somewhat more compact form

$$u_r^*(\gamma, \alpha) = -\frac{8u_m^*q(\Theta - 1)}{q - 1} \sum_{n=1}^{\infty} \frac{J_0(\lambda_n \alpha)}{J_1(\lambda_n)} \left[\frac{1}{\lambda_n^3} - q \sum_{i=0}^{q-1} (-1)^i \left(\frac{2^i(q-1)!}{(q-i-1)!} \right)^2 \lambda_n^{-2i-3} \right] \left[1 - e^{-\lambda_n^2 \gamma} \right] \quad (3.487)$$

with the familiar λ_n^{-3} dependence seen in Szymanski's equation (3.351).

- For $\gamma \rightarrow \infty$ the result is the superposition of laminar + turbulent flow given by equation (3.471), which is the ν/R -reference velocity version of (3.344) introduced in section 3.4.1. In effect, in the limit $\gamma \rightarrow \infty$ equation (3.489) is

$$u^*(\infty, \alpha) = \frac{\Pi^*}{4}(1 - \alpha^2) - \frac{8u_m^* q(\Theta - 1)}{q - 1} \sum_{n=1}^{\infty} \frac{J_0(\lambda_n \alpha)}{J_1(\lambda_n)} \left[\frac{1}{\lambda_n^3} - q \sum_{i=0}^{q-1} (-1)^i \left(\frac{2^i (q-1)!}{(q-i-1)!} \right)^2 \lambda_n^{-2i-3} \right] \quad (3.490)$$

On the other hand, equation (3.471) could be written in the form

$$u_s^*(\alpha) = u_m^* \left[1 - \alpha^2 + \frac{\Theta - 1}{q - 1} \alpha^2 (1 - \alpha^{2q-2}) \right] \quad (3.491)$$

with the subscript 's' indicating *steady state*, and u_m^* the maximum mean velocity appearing in the expression of ϖ (see (3.474)). This profile corresponds to that flow herein endowed with the name of Pai flow.

Comparing equations (3.490) and (3.491), it remains to demonstrate that

$$u^*(\infty, \alpha) = u_s^*(\alpha)$$

so that the assertion that (3.489) has Pai flow (3.491) as a steady state limit when $\gamma \rightarrow \infty$, could be considered true. The demonstration is somewhat elaborate and only some intermediate steps will be offered. The reader is encouraged to attempt the whole elaboration by himself.

First, a general expression should be found for α^2 :

$$\alpha^2 = \sum_{n=1}^{\infty} \frac{2 J_0(\lambda_n \alpha)}{\lambda_n J_1(\lambda_n)} \left[1 - \frac{4}{\lambda_n^2} \right] \quad (3.492)$$

Next a general expression for α^{2q} (see [Ros16])

$$\alpha^{2q} = \sum_{n=1}^{\infty} \frac{2 J_0(\lambda_n \alpha)}{J_1(\lambda_n)} \left[\sum_{i=0}^q (-1)^i \left(\frac{2^i q!}{(q-i)!} \right)^2 \lambda_n^{-2i-1} \right] \quad (3.493)$$

Now a curious representation of unity:

$$1 = \sum_{n=1}^{\infty} \frac{2 J_0(\lambda_n \alpha)}{\lambda_n J_1(\lambda_n)} \quad (3.494)$$

With the formulae above, $u_s^*(\alpha)$ yields:

$$u_s^*(\alpha) = u_m^* \left[1 - \sum_{n=1}^{\infty} \frac{2 J_0(\lambda_n \alpha)}{\lambda_n J_1(\lambda_n)} \left(1 - \frac{4}{\lambda_n^2} \right) + \frac{\Theta - 1}{q - 1} \sum_{n=1}^{\infty} \frac{2 J_0(\lambda_n \alpha)}{J_1(\lambda_n)} \left(\frac{1}{\lambda_n} - \frac{4}{\lambda_n^3} - \sum_{i=0}^q (-1)^i \left(\frac{2^i q!}{(q-i)!} \right)^2 \lambda_n^{-2i-1} \right) \right] \quad (3.495)$$

The term corresponding to $i = 0$ in the last sum equals

$$(-1)^0 \left(\frac{2^0 q!}{(q-0)!} \right)^2 \lambda_n^{-1} = \frac{1}{\lambda_n}$$

and annihilates identically the first $1/\lambda_n$. Thus

$$u_s^*(\alpha) = u_m^* \left[1 - \sum_{n=1}^{\infty} \frac{2 J_0(\lambda_n \alpha)}{\lambda_n J_1(\lambda_n)} \left(1 - \frac{4}{\lambda_n^2} \right) - \frac{\Theta - 1}{q - 1} \sum_{n=1}^{\infty} \frac{2 J_0(\lambda_n \alpha)}{J_1(\lambda_n)} \left(\frac{4}{\lambda_n^3} + \sum_{i=1}^q (-1)^i \left(\frac{2^i q!}{(q-i)!} \right)^2 \lambda_n^{-2i-1} \right) \right] \quad (3.496)$$

In the last sum perform the change of summation index $j = i - 1$. It yields

$$u_s^*(\alpha) = u_m^* \left[1 - \sum_{n=1}^{\infty} \frac{2 J_0(\lambda_n \alpha)}{\lambda_n J_1(\lambda_n)} \left(1 - \frac{4}{\lambda_n^2} \right) - \frac{\Theta - 1}{q - 1} \sum_{n=1}^{\infty} \frac{8 J_0(\lambda_n \alpha)}{J_1(\lambda_n)} \left(\frac{1}{\lambda_n^3} - \sum_{j=0}^{q-1} (-1)^j \left(\frac{2^j q!}{(q-j-1)!} \right)^2 \lambda_n^{-2j-3} \right) \right] \quad (3.497)$$

and ought to be compared with $u^*(\infty, \alpha)$ in (3.490).

In turn, (3.490) is converted into:

$$u^*(\infty, \alpha) = \frac{\Pi^*}{4} (1 - \alpha^2) - \frac{8u_m^*(\Theta - 1)}{q - 1} \sum_{n=1}^{\infty} \frac{J_0(\lambda_n \alpha)}{J_1(\lambda_n)} \left[\frac{q}{\lambda_n^3} - \sum_{i=0}^{q-1} (-1)^i \left(\frac{2^i q!}{(q-i-1)!} \right)^2 \lambda_n^{-2i-3} \right] \quad (3.498)$$

The q/λ_n^3 term is decomposed into

$$\frac{q}{\lambda_n^3} = \frac{q-1}{\lambda_n^3} + \frac{1}{\lambda_n^3}$$

Therefore

$$u^*(\infty, \alpha) = \frac{\Pi^*}{4} (1 - \alpha^2) - 8u_m^*(\Theta - 1) \sum_{n=1}^{\infty} \frac{J_0(\lambda_n \alpha)}{\lambda_n^3 J_1(\lambda_n)} - \frac{8u_m^*(\Theta - 1)}{q - 1} \sum_{n=1}^{\infty} \frac{J_0(\lambda_n \alpha)}{J_1(\lambda_n)} \left[\frac{1}{\lambda_n^3} - \sum_{i=0}^{q-1} (-1)^i \left(\frac{2^i q!}{(q-i-1)!} \right)^2 \lambda_n^{-2i-3} \right] \quad (3.499)$$

Upon close examination, it will be evident that the last term in equation (3.499) is identical to the like term in (3.497). Thus all that is lacking is to prove that the remainder of (3.499) equals the remainder of (3.497):

$$u_m^* - u_m^* \sum_{n=1}^{\infty} \frac{2 J_0(\lambda_n \alpha)}{\lambda_n J_1(\lambda_n)} \left(1 - \frac{4}{\lambda_n^2} \right) = \frac{\Pi^*}{4} (1 - \alpha^2) - 8u_m^*(\Theta - 1) \sum_{n=1}^{\infty} \frac{J_0(\lambda_n \alpha)}{\lambda_n^3 J_1(\lambda_n)}$$

Divide by u_m^*

$$1 - \sum_{n=1}^{\infty} \frac{2 J_0(\lambda_n \alpha)}{\lambda_n J_1(\lambda_n)} \left(1 - \frac{4}{\lambda_n^2} \right) = \Theta(1 - \alpha^2) - 8(\Theta - 1) \sum_{n=1}^{\infty} \frac{J_0(\lambda_n \alpha)}{\lambda_n^3 J_1(\lambda_n)}$$

or

$$1 - \sum_{n=1}^{\infty} \frac{2 J_0(\lambda_n \alpha)}{\lambda_n J_1(\lambda_n)} = \Theta(1 - \alpha^2) - 8\Theta \sum_{n=1}^{\infty} \frac{J_0(\lambda_n \alpha)}{\lambda_n^3 J_1(\lambda_n)}$$

Using equations (3.494) and (3.447), the last equality finally converts into a trivial one:

$$1 - 1 = \Theta(1 - \alpha^2) - \Theta(1 - \alpha^2)$$

and it emerges that

$$u^*(\infty, \alpha) = u_s^*(\alpha)$$

and thus Pai flow occurs as a limiting steady state case of the general transient flow (3.489)

The general expression (3.489) contains the Hagen-Poiseuille's (3.297), the Szymanski's (3.351) and the Pai's (3.344) solutions as particular cases, and it proves the claim established in table 3.1.

Note the solution (3.489) has the general form discussed on section 3.4.1 (see equation (3.296)), which was given the name of Laminar-Turbulent Decomposition:

$$u^*(\gamma, \alpha) = v_L^*(\gamma, \alpha) + u_T^*(\gamma, \alpha)$$

where v_L^* is the laminar Szymanski velocity profile (the PressGrad component) and u_T^* the contribution of turbulence to the final velocity profile (the RStress component). ■

A last example will be presented, to further illustrate the general method herein developed. It would be extremely convenient to find the analytical mean velocity profile for the kind of transient flow studied on this Dissertation: a sudden very high acceleration from rest until the pressure no longer balances the friction and the flow begins to decelerate. Unfortunately this is not possible with the formalism unfolded herein, mainly for two reasons:

- The flow represented by the AHM is two-phase, being the pipe initially empty of liquid that gradually fills it as the flow progresses. The general method does not contemplate a two-phase flow.
- The source term in the AHM depends on the velocity (actually on the time integral of the bulk velocity). Therefore it cannot be considered a non-homogeneous term of equation (3.380), since $\Xi(\gamma, \alpha)$ does **not** depend on velocity $u^*(\gamma, \alpha)$.

Thus the case which, possibly, most closely resembles the AHM is that of a liquid initially at rest, filling completely a pipe, that at $\gamma = 0$ undergoes a pressure gradient given by

$$\Pi^*(\gamma) = \begin{cases} 0 & \text{if } \gamma < 0 \\ \Pi_0^* + \frac{\Pi_1^*}{(b\gamma+1)^s} & (s \geq 1)(b, \Pi_0^*, \Pi_1^* \in \mathbb{R}^+) \text{ if } \gamma \geq 0 \end{cases} \quad (3.500)$$

where s fixes the rate at which the pressure gradient decays with time, and b is a parameter to modulate the progress of time. The liquid begins to accelerate in response to the pressure gradient until, for γ sufficiently high (formally for $\gamma \rightarrow \infty$) it reaches a turbulent steady state determined by the constant pressure gradient which is still active: Π_0^* . Note $\Pi^* = \Pi_0^* + \Pi_1^*$ at $\gamma = 0$, while $\Pi^* \rightarrow \Pi_0^*$ with $\gamma \rightarrow \infty$.

Figure 3.20 shows the pressure gradient evolution with time, in arbitrary dimensionless units, for the AHM model corresponding to the CFD model which was depicted in figures 3.14 and 3.15. The resulting

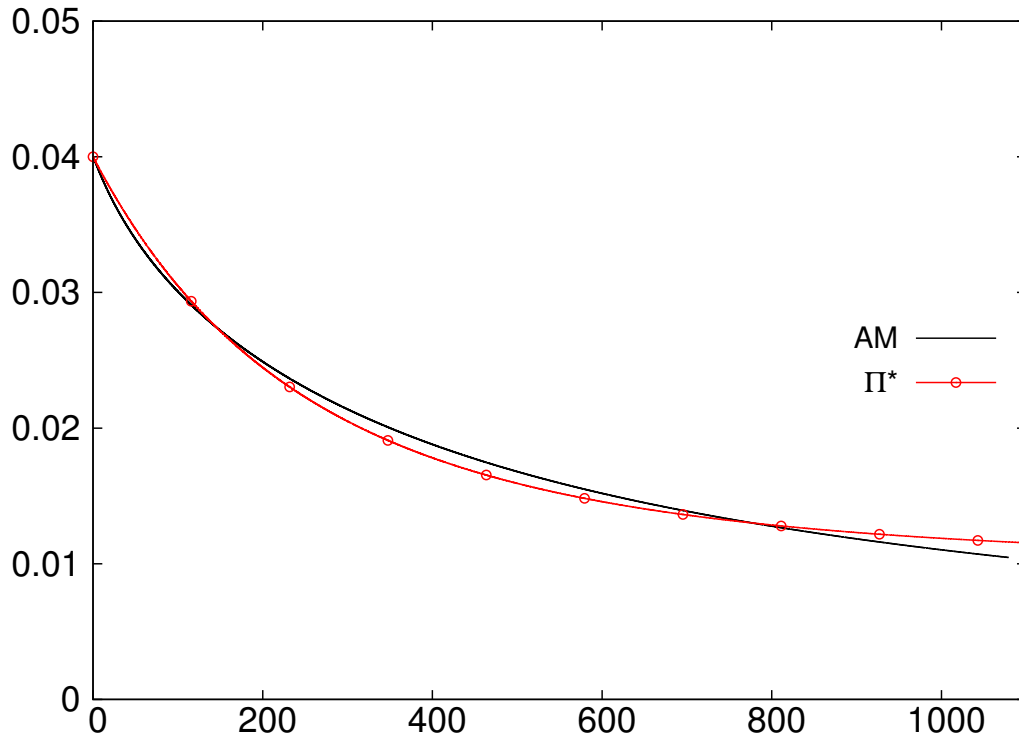


Figure 3.20: Decay of pressure gradient in pipe according to AHM and to $\Pi^*(\gamma) = 0.01 + \frac{0.03}{(0.001\gamma+1)^4}$.

curve has been obtained through the equations presented in section 2.4 That curve is compared with a pressure gradient of type (3.500) with $\Pi_0^* = 0.01$, $\Pi_1^* = 0.03$, $b = 0.001$ and $s = 4$, in the same dimensionless arbitrary units. The agreement is not perfect, but surely it is good enough to assume the mean velocity profile that will be obtained here, would not be noticeably different from that expected in the flow described by the corresponding AHM. The fact that $b = 0.001$ in equation (3.500) results equal to the geometrical factor $G_f = 0.001$ of the AHM is probably a coincidence, since no relationship is meant between both factors.

Just like in the previous case, it will be assumed that the steady state turbulent mean velocity profile is given by equation (3.491), corresponding to Pai flow. The time dependent Reynolds stress $\varpi(\gamma, \alpha)$ is also assumed to take the form given by (3.474).

It is expected that the solution to this example might serve as a benchmark for the AHM and the CFD model to be developed in the next Chapter. Although the flow corresponding to the present example is not fully equivalent to the AHM, at least is similar enough to provide valuable information.

The procedure that must be followed ought to be familiar by now. First it should be noticed the IniTrans component $u_t^*(\gamma, \alpha)$ is zero, because the initial state is that of rest. Then write the PressGrad component corresponding to $\Pi^*(\gamma)$

$$\begin{aligned}
 u_p^*(\gamma, \alpha) &= \sum_{n=1}^{\infty} \frac{2}{J_1(\lambda_n)\lambda_n} J_0(\lambda_n\alpha) \int_0^{\gamma} \Pi^*(\gamma') e^{-\lambda_n^2(\gamma-\gamma')} d\gamma' = \\
 &= \sum_{n=1}^{\infty} \frac{2}{J_1(\lambda_n)\lambda_n} J_0(\lambda_n\alpha) \int_0^{\gamma} \left(\Pi_0^* + \frac{\Pi_1^*}{(b\gamma' + 1)^s} \right) e^{-\lambda_n^2(\gamma-\gamma')} d\gamma' =
 \end{aligned}$$

$$= \sum_{n=1}^{\infty} \frac{2}{J_1(\lambda_n)\lambda_n} J_0(\lambda_n\alpha) e^{-\lambda_n^2\gamma} \left(\frac{\Pi_0^*(e^{\lambda_n^2\gamma} - 1)}{\lambda_n^2} + \Pi_1^* \int_0^{\gamma} \frac{e^{\lambda_n^2\gamma'}}{(b\gamma' + 1)^s} d\gamma' \right)$$

The last integral will be solved next. It requires the change of variables

$$\eta = b\gamma' + 1, \quad \gamma' = \frac{\eta - 1}{b}, \quad d\gamma' = \frac{d\eta}{b}$$

and results in

$$\int_0^{\gamma} \frac{e^{\lambda_n^2\gamma'}}{(b\gamma' + 1)^s} d\gamma' = \int_1^{b\gamma+1} \frac{e^{\lambda_n^2(\eta-1)/b}}{\eta^s} \frac{d\eta}{b} = \frac{e^{-\lambda_n^2/b}}{b} \int_1^{b\gamma+1} \frac{e^{\eta\lambda_n^2/b}}{\eta^s} d\eta$$

An integral like that has a recurrent solution (see [GRO7]):

$$\int \frac{e^{ax}}{x^n} dx = \frac{-e^{ax}}{(n-1)x^{n-1}} + \frac{a}{n-1} \int \frac{e^{ax}}{x^{n-1}} dx$$

The recurrence will go on indefinitely unless n is an integer, in which case it stops after a finite number of steps. Therefore, this example will be limited to such cases in which $s \in \mathbb{N}$, and an analytical mean velocity profile will be offered only for them. The integral is solved as:

$$\begin{aligned} \int_1^{b\gamma+1} \frac{e^{\eta\lambda_n^2/b}}{\eta^s} d\eta &= -e^{\eta\lambda_n^2/b} \sum_{i=1}^{s-1} \frac{\left(\frac{\lambda_n^2}{b}\right)^{i-1} (s-i-1)!}{(s-1)! \eta^{s-i}} \Bigg|_1^{b\gamma+1} + \frac{\left(\frac{\lambda_n^2}{b}\right)^{s-1}}{(s-1)!} \text{Ei}\left(\frac{\lambda_n^2}{b}\eta\right) \Bigg|_1^{b\gamma+1} = \\ &= e^{\lambda_n^2/b} \sum_{i=1}^{s-1} \frac{\lambda_n^{2i-2} (s-i-1)!}{(s-1)! b^{i-1}} \left[1 - \frac{e^{\lambda_n^2\gamma}}{(b\gamma+1)^{s-i}} \right] + \frac{\lambda_n^{2s-2}}{b^{s-1} (s-1)!} \left[\text{Ei}\left(\lambda_n^2\gamma + \frac{\lambda_n^2}{b}\right) - \text{Ei}\left(\frac{\lambda_n^2}{b}\right) \right] \end{aligned}$$

with $\text{Ei}(x)$ the so-called **Exponential Integral** function, a transcendental function given by the expression:

$$\text{Ei}(x) = - \int_{-x}^{\infty} \frac{e^{-t}}{t} dt = \aleph + \ln|x| + \sum_{n=1}^{\infty} \frac{x^n}{n n!} \quad (x \in \mathbb{R}, x \neq 0) \quad (3.501)$$

where \aleph is the Euler-Mascheroni constant defined by

$$\aleph := \lim_{n \rightarrow \infty} \left(-\ln n + \sum_{k=1}^n \frac{1}{k} \right) \approx 0.577215664 \dots \quad (3.502)$$

Note if $s = 1$ then the sum in i , $\sum_{i=1}^{s-1}$, is meaningless and only survives the last term involving the exponential integral functions. It will be supposed from now on that $s \geq 2$.

Thus the time integral in $u_p^*(\gamma, \alpha)$ adopts the form

$$\begin{aligned} \int_0^{\gamma} \Pi^*(\gamma') e^{-\lambda_n^2(\gamma-\gamma')} d\gamma' &= \frac{\Pi_0^*}{\lambda_n^2} (1 - e^{-\lambda_n^2\gamma}) + \\ &+ \frac{\Pi_1^*}{b} e^{-\lambda_n^2\gamma} \left\{ \sum_{i=1}^{s-1} \frac{\lambda_n^{2i-2} (s-i-1)!}{(s-1)! b^{i-1}} \left(1 - \frac{e^{\lambda_n^2\gamma}}{(b\gamma+1)^{s-i}} \right) + \right. \end{aligned}$$

$$\begin{aligned}
& + \frac{\lambda_n^{2s-2} e^{-\lambda_n^2/b}}{b^{s-1}(s-1)!} \left[\text{Ei} \left(\lambda_n^2 \gamma + \frac{\lambda_n^2}{b} \right) - \text{Ei} \left(\frac{\lambda_n^2}{b} \right) \right] \Big\} = \\
& = \frac{\Pi_0^*}{\lambda_n^2} (1 - e^{-\lambda_n^2 \gamma}) + \Pi_1^* \sum_{i=1}^{s-1} \frac{\lambda_n^{2i-2} (s-i-1)!}{(s-1)! b^i} \left(e^{-\lambda_n^2 \gamma} - \frac{1}{(b\gamma+1)^{s-i}} \right) + \\
& + \frac{\Pi_1^* \lambda_n^{2s-2} e^{-\lambda_n^2(\gamma+1/b)}}{b^s (s-1)!} \left[\text{Ei} \left(\lambda_n^2 \left(\gamma + \frac{1}{b} \right) \right) - \text{Ei} \left(\frac{\lambda_n^2}{b} \right) \right]
\end{aligned}$$

Finally, the PressGrad component is given by

$$\begin{aligned}
u_p^*(\gamma, \alpha) = & \sum_{n=1}^{\infty} \frac{2J_0(\lambda_n \alpha)}{J_1(\lambda_n) \lambda_n} \left\{ \frac{\Pi_0^*}{\lambda_n^2} (1 - e^{-\lambda_n^2 \gamma}) + \Pi_1^* \sum_{i=1}^{s-1} \frac{\lambda_n^{2i-2} (s-i-1)!}{(s-1)! b^i} \left(e^{-\lambda_n^2 \gamma} - \frac{1}{(b\gamma+1)^{s-i}} \right) + \right. \\
& \left. + \frac{\Pi_1^* \lambda_n^{2s-2} e^{-\lambda_n^2(\gamma+1/b)}}{b^s (s-1)!} \left[\text{Ei} \left(\lambda_n^2 \left(\gamma + \frac{1}{b} \right) \right) - \text{Ei} \left(\frac{\lambda_n^2}{b} \right) \right] \right\} \quad (s \geq 2, s \in \mathbb{N}) \quad (3.503)
\end{aligned}$$

In the particular case of $s = 1$, the PressGrad component adopts the simpler form of

$$\begin{aligned}
u_p^*(\gamma, \alpha) = & \sum_{n=1}^{\infty} \frac{2J_0(\lambda_n \alpha)}{J_1(\lambda_n) \lambda_n} \left\{ \frac{\Pi_0^*}{\lambda_n^2} (1 - e^{-\lambda_n^2 \gamma}) + \right. \\
& \left. + \frac{\Pi_1^* e^{-\lambda_n^2(\gamma+1/b)}}{b} \left[\text{Ei} \left(\lambda_n^2 \left(\gamma + \frac{1}{b} \right) \right) - \text{Ei} \left(\frac{\lambda_n^2}{b} \right) \right] \right\} \quad (s = 1) \quad (3.504)
\end{aligned}$$

For the RStress component there is no obstacle to employ the same expression that was used in the previous example, equation (3.488). The real parameter λ would have to be adjusted accordingly.

The GAS for the case which most closely resembles the type of flow studied along this Dissertation is thus, for $s \geq 2$

$$\begin{aligned}
u^*(\gamma, \alpha) = & u_p^*(\gamma, \alpha) + u_r^*(\gamma, \alpha) = \sum_{n=1}^{\infty} \frac{2J_0(\lambda_n \alpha)}{J_1(\lambda_n) \lambda_n} \left\{ \frac{\Pi_0^*}{\lambda_n^2} (1 - e^{-\lambda_n^2 \gamma}) + \right. \\
& + \Pi_1^* \sum_{i=1}^{s-1} \frac{\lambda_n^{2i-2} (s-i-1)!}{(s-1)! b^i} \left(e^{-\lambda_n^2 \gamma} - \frac{1}{(b\gamma+1)^{s-i}} \right) + \\
& \left. + \frac{\Pi_1^* \lambda_n^{2s-2} e^{-\lambda_n^2(\gamma+1/b)}}{b^s (s-1)!} \left[\text{Ei} \left(\lambda_n^2 \left(\gamma + \frac{1}{b} \right) \right) - \text{Ei} \left(\frac{\lambda_n^2}{b} \right) \right] \right\} - \quad (s \geq 2, s \in \mathbb{N}) \\
& - \frac{8u_m^*(\Theta - 1)}{q - 1} \sum_{n=1}^{\infty} \frac{J_0(\lambda_n \alpha)}{J_1(\lambda_n)} \\
& \left[\frac{q}{\lambda_n} - \sum_{i=0}^{q-1} (-1)^i \left(\frac{2^i q!}{(q-i-1)!} \right)^2 \lambda_n^{-2i-1} \right] \left[\frac{1 - e^{-\lambda_n^2 \gamma}}{\lambda_n^2} + \frac{e^{-\lambda_n^2 \gamma} - e^{-\lambda^2 \gamma}}{\lambda_n^2 - \lambda^2} \right] \quad (3.505)
\end{aligned}$$

and for $s = 1$

$$\begin{aligned}
u^*(\gamma, \alpha) = u_p^*(\gamma, \alpha) + u_r^*(\gamma, \alpha) = & \sum_{n=1}^{\infty} \frac{2J_0(\lambda_n \alpha)}{J_1(\lambda_n) \lambda_n} \left\{ \frac{\Pi_0^*}{\lambda_n^2} (1 - e^{-\lambda_n^2 \gamma}) + \right. \\
& \left. + \frac{\Pi_1^* e^{-\lambda_n^2 (\gamma + 1/b)}}{b} \left[\text{Ei} \left(\lambda_n^2 \left(\gamma + \frac{1}{b} \right) \right) - \text{Ei} \left(\frac{\lambda_n^2}{b} \right) \right] \right\} - \quad (s = 1) \\
& - \frac{8u_m^*(\Theta - 1)}{q - 1} \sum_{n=1}^{\infty} \frac{J_0(\lambda_n \alpha)}{J_1(\lambda_n)} \\
& \left[\frac{q}{\lambda_n} - \sum_{i=0}^{q-1} (-1)^i \left(\frac{2^i q!}{(q - i - 1)!} \right)^2 \lambda_n^{-2i-1} \right] \left[\frac{1 - e^{-\lambda_n^2 \gamma}}{\lambda_n^2} + \frac{e^{-\lambda_n^2 \gamma} - e^{-\lambda^2 \gamma}}{\lambda_n^2 - \lambda^2} \right]
\end{aligned} \tag{3.506}$$

With the development made in the previous example, now it is easy to prove that these solutions yield the turbulent steady state mean velocity profile $u_s^*(\alpha)$, equation (3.491), when $\gamma \rightarrow \infty$. The reader is invited to do it. ■

To round things of, a proposal for those with interest in the study of water hammer. Imagine a steady state turbulent flow with a mean velocity profile given by equation (3.491). Such profile is to be taken as the initial velocity $u_0^*(\alpha)$ for this problem: thus the IniTrans component will not be zero this time. This initial velocity is maintained through a constant pressure gradient $\Pi_0^* \in \mathbb{R}^+$. For $\gamma \geq 0$ the initially steady state flow undergoes the following additional pressure gradient:

$$\Pi^*(\gamma) = -\Pi_1^* \sin(\omega \gamma) e^{-b\gamma} \tag{3.507}$$

with $\Pi_1^* \in \mathbb{R}^+$ the initial amplitude of the new pressure gradient, $\omega \in \mathbb{R}^+$ a high angular frequency, and $b \in \mathbb{R}^+$ a damping parameter. Π_1^* should be chosen large enough to ensure the mean velocity changes direction under the influence of the sine's first quadrant; therefore $\Pi_1^* \gg \Pi_0^*$. It could also be considered that Π_0^* is switched off for $\gamma > 0$. After sufficiently long time (formally $\gamma \rightarrow \infty$) the flow reaches a state of rest, $u^*(\infty, \alpha) = 0$.

The reader is invited to propose a suitable Reynolds stress function $\varpi(\gamma, \alpha)$ for this toy model of water hammer, and to calculate the associated mean velocity profile $u^*(\gamma, \alpha)$ derived therefrom. ■

The main contribution of this section is not just the finding of a GAS for transient/unsteady incompressible turbulent pipe flow, but rather the proposal of an effective general method to solve a wide range of problems related with pipe flow, with only the hypothesised knowledge of a mean pressure gradient function $\Pi^*(\gamma)$, and the assumption of a given Reynolds stress $\varpi(\gamma, \alpha)$. Even if the request of *a priori* knowledge of the Reynolds stress could be felt like a flaw, in the very worst case at least a qualitatively correct solution could be obtained, wherefrom to extract information about the dynamical behaviour of the velocity profiles. The method opens new possibilities too: in the event of no available full-fledged Reynolds stress function, it would always be feasible to propose a few terms corresponding to a partial McLaurin or Taylor series expansion thereof, whose accuracy could be selected at will by only choosing where to truncate such series.

The solutions presented herein have, at the very least, a qualitative value, despite the fact that the Reynolds stress has been introduced *ad hoc*. Even quantitatively, the actual profiles ought not to be very

different from what has been deduced herein, since the proposed Reynolds stress functions adjust fairly well to experimental data. The readers are invited to try different functional forms for the Reynolds stress, provided they satisfy the equations (3.327),(3.328) and (3.330) in steady state (or (3.331) and (3.332) in the current normalisation), and they match acceptably with CFD or experimental results. It is a degree of freedom the formalism just developed allows to the researchers. Said general formalism should be considered the main contribution of this section to the problem of analytical description of turbulence.

3.5 Derivation of Navier-Stokes Equations from First Principles

This section is devoted to show that Navier-Stokes equations, despite being non-linear and presenting energy dissipation, can be derived from a variational Principle of Least Action (PLA), or Hamilton's principle, much in the same way than the equations of motion of Classical Mechanics or the dynamical equations of Classical Field Theory.

Derivation from a variational principle is, possibly, the most fundamental formulation of the laws of motion for a mechanical system or of the dynamical equations for a field, as the great principles of conservation for energy, linear momentum and angular momentum stem directly and seamlessly from primordial symmetries, manifested as invariance of the Lagrangian to time shift, space displacements and space rotations, respectively. These results are a consequence of Noether's theorem, which apply to those field theories that are invariant to the fundamental symmetry groups of Physics.

For a Classical Mechanics system whose state is defined by a set of generalised coordinates (q_1, q_2, \dots, q_n) and generalised velocities $(\dot{q}_1, \dot{q}_2, \dots, \dot{q}_n)$, and which is characterised by a Lagrangian function $L(q_1, q_2, \dots, q_n; \dot{q}_1, \dot{q}_2, \dots, \dot{q}_n; t)$ or $L(q, \dot{q}, t)$ for short, the PLA establishes that if the mechanical system occupies positions $q^{(1)}$ at instant t_1 , and $q^{(2)}$ at t_2 , then the system moves from $q^{(1)}$ to $q^{(2)}$ such that the integral

$$\mathfrak{S}(q_1, q_2, \dots, q_n) = \int_{t_1}^{t_2} L(q_1, q_2, \dots, q_n; \dot{q}_1, \dot{q}_2, \dots, \dot{q}_n; t) dt \quad (3.508)$$

has the minimum possible value. Note that $q = q(t)$ and $\dot{q} = \dot{q}(t)$ are functions $\mathbb{R} \rightarrow \mathbb{R}^n$. \mathfrak{S} is a functional over the function space defined by $q(t)$, the trajectories spanned by the generalised coordinates, and is called the **action** of the mechanical system.

Obtaining the minimum value of the action \mathfrak{S} in function space $q(t)$ is an extremal problem in the formalism of variational calculus. The variation of \mathfrak{S} is denoted by $\delta\mathfrak{S}$, and the minimum value for \mathfrak{S} implies that its variation be zero $\delta\mathfrak{S} = 0$. The variational calculus formalism yields the well-known Euler-Lagrange equations for an action given by equation (3.508):

$$\frac{d}{dt} \left(\frac{\partial L}{\partial \dot{q}_i} \right) - \frac{\partial L}{\partial q_i} = 0 \quad (i = 1 \dots n) \quad (3.509)$$

Thus the PLA is more fundamental than the Euler-Lagrange equations themselves.

The formalism just hinted for a finite set of generalised coordinates can also be applied, with some modifications, to continuous fields $\psi_i(t, \mathbf{x})$. Classical fields have an equivalent PLA, as it is shown in any Classical Field Theory book (see, for example, [Bur03]). The n -dimensional field $\psi(t, \mathbf{x}) = (\psi_1, \psi_2, \dots, \psi_n)$ obeys dynamical equations which are also obtained from a PLA. The field $\psi(t, \mathbf{x})$ plays the role of q in the Lagrangian, but as it is a continuous function of (t, \mathbf{x}) the Lagrangian now must

be expressed in terms of a Lagrangian density $\mathcal{L}(\psi_i, \partial_\alpha \psi_i; t, \mathbf{x})$, which depends on the fields ψ_i themselves and their first derivatives $\partial_\alpha \psi_i$, in the form:

$$L(t) = \int \mathcal{L}(\psi_i, \partial_\alpha \psi_i; t, \mathbf{x}) d^3 \mathbf{x} \quad (3.510)$$

with $i = 1, 2, \dots, n$ and $\alpha = 0, 1, 2, 3$, being $\partial_0 \equiv \partial_t$. The Lagrangian thus defined in (3.510) loses its original meaning of kinetic energy minus potential energy, and it turns into a intermediate function of limited utility and significance, transferring its role to the Lagrangian density \mathcal{L} . From now on no mention will be made to L , highlighting instead the primordial character of \mathcal{L} . The action \mathfrak{S} is now a functional over the function space $\psi(t, \mathbf{x})$ and is defined by:

$$\mathfrak{S}(\psi_i) := \int_{t_1}^{t_2} \int_{\Omega} \mathcal{L}(\psi_i, \partial_\alpha \psi_i; t, \mathbf{x}) d^3 \mathbf{x} dt \quad (3.511)$$

being $[t_1, t_2] \times \Omega$ the time-space domain which constitutes the support of the fields $\psi_i(t, \mathbf{x})$.

The version of the PLA valid for fields establishes that the dynamics of ψ_i is such that the action (3.511) is a minimum. The corresponding Euler-Lagrange equations are now expressed as:

$$\partial_\alpha \left(\frac{\partial \mathcal{L}}{\partial (\partial_\alpha \psi_i)} \right) - \frac{\partial \mathcal{L}}{\partial \psi_i} = 0 \quad (i = 1 \dots n) \quad (3.512)$$

Fluid Mechanics is the theory of the fields occurring in a flow and therefore it is pertinent to expect that their dynamics be explained in terms of a variational PLA. In particular the Navier-Stokes equations govern the behaviour of the velocity field in a Newtonian flow and they ought to be the specific form of the Euler-Lagrange equations for an appropriate Lagrangian density. The fact that those equations are dissipative complicates matters ostensibly, to the point that some attempts have been made to variational principles other than Hamilton's, which is known to be exact for non dissipative systems. In what follows the problem of finding a Lagrangian density will be focused on incompressible Newtonian flows.

The efforts to derive the steady incompressible Navier-Stokes equations from a variational Hamilton-like principle dates as back as [Mil29]. Later [Ros53] and [Her54] extended the formalism to general Newtonian incompressible flow, using a modified version of a variational principle due to Onsager, which is also summarised in [Sci04]. A different approach was essayed by [Ece80], which involves also the flow's vorticity field. A full solution for the Lagrangian density, obtained through the introduction of additional intermediate fields, is provided in [Sch14] using the novel concept of extended Lagrangian density. Finally, [Bur03] proposes a *classical* Lagrangian density defined in terms of covariant and contravariant components of the velocity field. Related to the problem of finding the Lagrangian density wherefrom to derive the Navier-Stokes equations, is the pursue of the Lagrangian density for dispersive waves in flows, initiated by [Whi65], and extended to wave turbulence by [MPW79]. A rigorous example for more complicated flows is found in [GG99].

By way of introduction, in order to illustrate how this formalism operates, here it will be derived the relatively simple Navier-Stokes equations corresponding to steady incompressible Newtonian flow

from a classical Lagrangian density.⁹¹ The derivation follows the Lagrangian density proposed in [Mil29]. The flow is assumed to develop with a null Lamb vector, defined as the vector product of velocity \mathbf{u} and vorticity $\boldsymbol{\zeta}$,

$$\mathbf{u} \wedge \boldsymbol{\zeta} = \mathbf{u} \wedge (\nabla \wedge \mathbf{u}) = 0$$

Lamb vector is zero either if $\boldsymbol{\zeta} = 0$ (irrotational flow) or if velocity and vorticity vectors are parallel, $\mathbf{u} \parallel \boldsymbol{\zeta}$. The Lamb vector is associated with the generation of eddies in turbulent flows. Many viscous flows of interest in Engineering, including Poiseuille flow, fulfil the required condition. For more examples the reader is referred to [JFW08]. The conditions that a flow must satisfy in order to have a zero Lamb vector are rigorously exposed in the excellent book [Tru54].

Being the flow steady, the time parameter is avoided in the Lagrangian density which can then be expressed entirely in terms of space variables \mathbf{x} . The field whose dynamics is to be determined through the PLA is the flow's vector velocity \mathbf{u} . The formalism demands that \mathbf{u} and its first derivatives $\partial_i \mathbf{u}$ be included in \mathcal{L} . The proposed Lagrangian density is

$$\mathcal{L}(u_i, \partial_j u_i) = u_i u_j \partial_j u_i + \frac{1}{\rho} u_i \partial_i p - u_i g_i + \frac{\epsilon}{2} \quad (i, j = 1, 2, 3) \quad (3.514)$$

where g_i is an external force field (typically the gravity) and ϵ is the **viscous dissipation function** given by⁹²:

$$\epsilon = \frac{\nu}{2} (\partial_i u_j + \partial_j u_i) (\partial_i u_j + \partial_j u_i) \quad (3.515)$$

(see equation (3.18)). The viscous dissipation function represents the rate of energy per unit mass dissipated in the flow through viscous forces.

The Euler-Lagrange equations adopt the form:

$$\partial_j \left(\frac{\partial \mathcal{L}}{\partial (\partial_j u_i)} \right) - \frac{\partial \mathcal{L}}{\partial u_i} = 0 \quad (i, j = 1, 2, 3) \quad (3.516)$$

Besides the velocity field \mathbf{u} is subjected to the continuity equation

$$\nabla \cdot \mathbf{u} = \partial_i u_i = 0$$

⁹¹ The derivation of the general time-dependent Navier-Stokes equations is quite a lengthy and complicated process, which scarcely contributes to illustrate the method any more than the chosen example. For the interested reader, it is offered herein the Lagrangian density that generates the complete incompressible Navier-Stokes equations for a Newtonian fluid, in terms of the covariant u_i and contravariant u^i components of the velocity vector, which must both be considered independent variables as it is customary in field theory:

$$\mathcal{L}(u_i, \partial_\alpha u_i) = \frac{\rho}{2} \left[u^i \partial_0 u_i - u_i \partial_0 u^i + u^i u^j \partial_i u_j - u^i u_j \partial_i u^j - u_j \partial_i (u^i u^j) \right] + \mu (\partial^i u^j) (\partial_i u_j) - u^i (\rho g_i - \partial_i p) \quad (3.513)$$

In order to obtain the desired equations, the variation of the action \mathfrak{S} should be executed with respect to the contravariant components u^i . The interested reader can request, via e-mail, the several-pages-long derivation to the author. Use any of the addresses jgarcia@integraciones.com, fjgg@icoiig.es or f.javier.garcia.garcia@udc.es, whichever is available. Or better still, the interested reader could try to obtain by himself the Navier-Stokes equations from the offered Lagrangian density: after all, the difficult part of the job has been deducing such Lagrangian density, and it is already done.

⁹²[Hin75] defines the rate of viscous dissipation per unit mass as

$$\epsilon = \nu (\partial_j u_i + \partial_i u_j) \partial_i u_j$$

The difference with (3.515) is the symmetrisation of the second $\partial_i u_j$, which is compensated with the factor 1/2.

In order to calculate the derivatives of the Lagrangian density, the following rules must be observed:

$$\frac{\partial u_i}{\partial u_k} = \delta_{ik} \quad (3.517)$$

$$\frac{\partial(\partial_j u_i)}{\partial(\partial_k u_l)} = \delta_{jk} \delta_{il} \quad (3.518)$$

$$\frac{\partial(\partial_j u_i)}{\partial u_k} = 0 \quad (3.519)$$

$$\frac{\partial u_i}{\partial(\partial_k u_l)} = 0 \quad (3.520)$$

that is, u_i and $\partial_j u_i$ are to be treated as independent variables.

The calculation of Euler-Lagrange equations follows:

TERMS IN $\frac{\partial \mathcal{L}}{\partial u_k}$

$$\frac{\partial}{\partial u_k} (u_i u_j \partial_j u_i) = (\delta_{ik} u_j + \delta_{kj} u_i) \partial_j u_i = u_j \partial_j u_k + u_i \partial_k u_i$$

$$\frac{\partial}{\partial u_k} \left(\frac{1}{\rho} u_i \partial_i p \right) = \frac{\delta_{ik}}{\rho} \partial_i p = \frac{1}{\rho} \partial_k p$$

$$\frac{\partial}{\partial u_k} (-u_i g_i) = -\delta_{ik} g_i = -g_k$$

$$\frac{\partial}{\partial u_k} \left(\frac{\nu}{4} (\partial_i u_j + \partial_j u_i) (\partial_i u_j + \partial_j u_i) \right) = 0$$

TERMS IN $\frac{\partial \mathcal{L}}{\partial(\partial_l u_k)}$

$$\frac{\partial}{\partial(\partial_l u_k)} (u_i u_j \partial_j u_i) = u_i u_j \delta_{lj} \delta_{ki} = u_k u_l$$

$$\frac{\partial}{\partial(\partial_l u_k)} \left(\frac{1}{\rho} u_i \partial_i p \right) = 0$$

$$\frac{\partial}{\partial(\partial_l u_k)} (-u_i g_i) = 0$$

$$\frac{\partial}{\partial(\partial_l u_k)} \left(\frac{\nu}{4} (\partial_i u_j + \partial_j u_i) (\partial_i u_j + \partial_j u_i) \right) = \frac{\nu}{2} (\partial_i u_j + \partial_j u_i) (\delta_{li} \delta_{kj} + \delta_{lj} \delta_{ki}) = \nu (\partial_l u_k + \partial_k u_l)$$

TERMS in $\partial_l \left(\frac{\partial \mathcal{L}}{\partial(\partial_l u_k)} \right)$

$$\partial_l (u_k u_l) = u_k \partial_l u_l + u_l \partial_l u_k = u_l \partial_l u_k$$

$$\partial_l 0 = 0$$

$$\partial_l 0 = 0$$

$$\partial_l (\nu (\partial_l u_k + \partial_k u_l)) = \nu (\partial_l \partial_l u_k + \partial_k \partial_l u_l) = \nu \partial_l \partial_l u_k$$

where use has been made of the continuity equation.

Putting together all terms above, the resulting equation is:

$$u_l \partial_l u_k + \nu \partial_l \partial_l u_k - u_j \partial_j u_k - u_i \partial_k u_i - \frac{1}{\rho} \partial_k p + g_k = 0$$

or, changing index names,

$$u_j \partial_i u_j = -\frac{1}{\rho} \partial_i p + \nu \partial_j \partial_j u_i + g_i \quad (3.521)$$

This is almost the steady Navier-Stokes equation. The awkward term $u_j \partial_i u_j$ is not quite the convection term $u_j \partial_j u_i$ one might expect. However $u_j \partial_i u_j = \frac{1}{2} \partial_i (u_j u_j)$ and resorting to the known vector identity

$$\frac{1}{2} \nabla(\mathbf{u} \cdot \mathbf{u}) = (\mathbf{u} \cdot \nabla) \mathbf{u} + \mathbf{u} \wedge (\nabla \wedge \mathbf{u}) \Leftrightarrow \frac{1}{2} \partial_i (u_j u_j) = u_j \partial_j u_i + \epsilon_{ijk} \partial_j u_k$$

and having into account that only flows with zero Lamb vector, $\mathbf{u} \wedge (\nabla \wedge \mathbf{u}) = 0$, are being considered, then it can be concluded that $u_j \partial_i u_j = u_j \partial_j u_i$. Therefore, the familiar steady Navier-Stokes equation is obtained:

$$u_j \partial_j u_i = -\frac{1}{\rho} \partial_i p + \nu \partial_j \partial_j u_i + g_i \quad (3.522)$$

and it can be successfully concluded that the dynamics of a steady incompressible Newtonian flow, with zero Lamb vector, emanates directly from the fundamental PLA for the Lagrangian density defined in (3.514). ■

Faced with this result, one might well feel tempted to conclude that the *real* Physics lies in the instantaneous fields \mathbf{u} and p and not in the averaged values \mathbf{U} and P derived therefrom. The remark made in page 77 points to this too, and highlights the fact that the equations describing the mean flow fields, the RANSE, cannot be directly derived from the general principles of Fluid Mechanics, but rather they are result of mathematical manipulations made over the solid dynamical equations themselves. However, [Hol05] presents a turbulence model based on averaged fields which follows directly from a variational Hamilton-like principle. The model is called the Navier-Stokes- α (NS- α) model, and produces a closed system of Lagrangian-averaged Navier Stokes- α (LANS- α) equations which can be used in CFD to simulate a number of flows. This model is also described in [FHT01] and the references cited therein. It could be argued that the Lagrangian density used to derive the LANS- α equations from is somewhat far-fetched, or that the NS- α model is quite different from the more familiar RANS model which so readily emerges from Navier-Stokes equations, but this approach greatly deserves to be taken into account as it sheds a new light into the turbulence description through averaged fields.

No further comment will be added regarding the statistical representation of turbulence except, perhaps, to point out at the growing evidence that some important Physics might rest into it, other than being mere mathematical tools to ease the description of an extremely complex phenomenon.

Chapter 4

3D CFD Model - Modelling with Wall Functions

4.1 Introduction to the 3D CFD Model

In Chapter 2 a 1D AHM was developed to describe the transient discharge flow, which seems to reproduce the few instances of similar flows found in the literature. Regrettably, a Hydraulic model cannot provide any information regarding the internal structure of the flow, and either one must resort to fully analytical 3D models, like that of section 3.4.2, or to more conventional CFD models, in order to obtain the desired information about the flow fields. Since the first approach is plagued with difficulties, it would seem sensible to begin with the second, and thus this Chapter is devoted to develop such 3D CFD model for discharge flow, with the expectation of gaining knowledge and insight on the structure and evolution of the flow fields.

However, there exist sound arguments to believe that current CFD turbulence models would have problems to correctly simulate so a transient and accelerated flow as this. Not many instances of $Re > 10^7$, transient, two-phase and highly accelerated internal flows are reported in the literature, possibly because it is indeed a difficult problem. Moreover, the present research could find no data, either experimental or analytical, with which to compare the results that might be output by such CFD model. The only available data to contrast the CFD model with, appear to be those provided by the AHM, even though they are referred to 1D quantities, rather than 3D fields. If any CFD model could reproduce the bulk velocity yielded by the AHM, chances are that the flow structure deriving from such CFD model correspond approximately to the actual discharge flow.

Summarising, this Chapter is devoted to develop a 3D CFD model which could reproduce the results obtained in Chapter 2 with the 1D (AHM), while providing additional information on the distribution of fields within the pipe that could help explain the observed flow dynamics. It will be seen that both models produce very similar results, and predict the evolution of cross-section averaged velocities from the very first instants of the discharge flow. Being a 3D model, it would be expected that some details regarding the structure of the turbulence, such as the mean velocity profile $U(t, \mathbf{x})$, the Reynolds stress tensor $R_{ij}(t, \mathbf{x})$, the energy dissipation rate per unit mass $\epsilon(t, \mathbf{x})$ or the turbulence kinetic energy per unit volume $k(t, \mathbf{x})$, generically called the Turbulence Quantities (Turbulence Quantities (TQ)), would emerge after discretise resolution of the governing equations¹. Those mean fields are written with the explicit full dependence of space-time variables because the flow is deeply unsteady and

¹In this introductory section a number of terms and concepts will be used without prior explanation. The reader is expected to be indulgent and patient, since all of them will be duly presented and explained in the sections to come.

inhomogeneous, and thus only ensemble averaged mean fields would describe adequately the mean flow.

Since the benchmark data to compare the 3D CFD model with is the 1D AHM itself, and this AHM does not provide any description of the flow structure within the pipe, the validation of the CFD data is limited to a coincidence of the cross-section averaged velocity for both models. Unfortunately, no detailed data of the flow's internal structure has been found in the literature for transient Reynolds numbers over 10^7 , a level reached by the model from the first split-second.

The case considered herein, besides its genuine interest in Engineering, offers a challenging amount of difficulties for a CFD solver to simulate it adequately. The only relatively easy feature of the model is the geometry of the problem: a long slender cylinder. Aside from this, it is by no means a trivial case: it is a two-phase problem with a rapidly changing interface, is very unsteady, very turbulent, the boundary conditions change with time and with the actual flow evolution, the friction forces (as important as the pressure gradient) are a direct consequence of the velocity distribution near the wall, the effects that high acceleration and deceleration have on the velocity profiles are far from being clear, the fast evolution of the TQ $k(t, \mathbf{x})$ and $\epsilon(t, \mathbf{x})$ is seldom reported in the literature... It is, indeed, a very interesting case. And the only available model with which to compare the CFD simulations is the 1D AHM, one that can provide no clue regarding the internal structure of the flow, other than a friction factor determined by the Colebrook-White correlation or the equivalent Moody diagram.

The attempt to model the behaviour of a liquid suddenly released to the atmosphere, driven by the action of an initial large pressure gradient plus an increasing wall-friction, encounters several major difficulties:

- i. The process is a transient, and a fast one, with high accelerations and decelerations alike. In order to guarantee stability to the algorithm, and to avoid a collapse due to excess accumulated error, the time step in the time-marching solution of the model must be very small. The Courant number ² which grants stability is well beyond unity, in the order of 0.01. That implies long execution times in any computer.
- ii. The flow is highly turbulent, although it starts from rest. The turbulence shoots up while the liquid barely starts progressing through the pipe's entrance. There is an added difficulty in trying to simulate a highly turbulent state several milliseconds after a zero velocity state. The turbulence model needs to be very stable not to diverge when the variations in TQ are very fast. As it will be explained later, a convenient way out of this problem is to establish initial conditions for the TQ different from zero.

²The Courant-Friedrichs-Lewy (CFL) condition is the criterion of stability for the numerical algorithms used to discretise the hyperbolic differential equations (see [VM07] or [FP02]). In a hyperbolic differential equation (e.g. the wave equation) there exists a *wave speed* c which determines the maximum velocity at which any perturbation can travel in space. Space points separated by Δx could have mutual interactions provided that the time between them is $\Delta t \geq \Delta x/c$. In physical space-time, the **domain of dependence** for a given *event* (t, x) is made up of all events (t', x') such that $|x - x'|/(t - t') \leq c$, that is, all events in the past from which any perturbation could propagate at a velocity equal or slower than wave speed c . Upon discretisation of a hyperbolic differential equation, the continuous set of events (t, x) is substituted by a discrete set of events (t_n, x_n) . The **differencing domain** for a given differencing scheme consists of all events (t_n, x_n) that such scheme uses to determine the next value of the solution. The CFL condition establishes that any discretisation of an hyperbolic differential equation would be stable if the time step Δt and the space resolution Δx are chosen so that $Co \leq 1$, where $Co = c\Delta t/\Delta x$ is called the **Courant number** for the discretisation scheme. In other words, if the differencing domain at a given event (t_n, x_n) is wider than its domain of dependence, then the discretisation algorithm is stable in the sense of CFL. On the contrary, if the differencing domain at a given event (t_n, x_n) is narrower than its domain of dependence, then the discretisation algorithm would be CFL unstable.

- iii. As the AHM repeatedly shows, a key aspect of the flow is the friction with the pipe's wall, which causes the high deceleration observed during most of the transient³. Being forced to simulate that friction with walls if the dynamics is meant to be reproduced, and noticing that the *locus* of the turbulent boundary layer where wall-friction is generated is extraordinarily thin, the computational mesh must then contain increasingly thinner cells near the wall, in order to be able to calculate the friction. If the nearest-wall cell were too tall, then it would miss the high velocity gradient at the wall producing the intense shear stress the AHM predicts, and it would be missed because an averaging is carried out within that first cell. Therefore, the number of cells near the wall must be very high and, correspondingly, the mesh contains great number of cells despite the simple geometry.
- iv. If the mesh is to represent adequately the flow's domain, the aspect-ratio of each cell should not be very high. The aspect-ratio is defined as the maximum ratio among any of the cell's dimensions: $\Delta x/\Delta y$, $\Delta x/\Delta z$, $\Delta y/\Delta z$ and their inverses. The algorithm produces poor results if a number a cells have a very unfavourable aspect-ratio. Since the height in the radial direction is determined by the capture of the wall-shear stress, and can only be very small, then the other cell's dimensions ought to be accordingly small in the vicinity of the wall, resulting again in a large number of cells for any significant portion of a pipe.
- v. The model represents an internal flow with most boundaries corresponding to walls. The proximity of walls suffer from two added complications: it is necessary to model the development of the turbulent boundary layer (usually through the use of wall-functions), and methods based on a pure filter approach (pure LES) ought to be avoided, according to the explanations offered in section 3.3.
- vi. In order to lessen the entrance effect in the pipe it is necessary to model a sufficiently long pipe, typically more than 20 diameters. This also increases the number of cells in the mesh.
- vii. The actual flow to be modelled is two-phase, in which there is a rapid advancement of a liquid phase (agent FK-5-1-12) into a gaseous phase (air), plus a strong mixing of liquid with the surrounding air, at least in the vicinity of the front/interface. This aspect was purposely omitted in previous Chapters, since it adds a difficulty not easy to deal with in the AHM. The CFD model, on the other hand, has this effect into account and solves a specific equation for it.

Note that very short time-step plus high number of cells implies greatly increased computational time, specially if several differential equations must be discretised and solved at each time-step. In summary, the phenomenon intended to be described herein is not geometrically difficult, but everything else is very complex. And the complexity has mainly to do with the turbulence that develops while the fluid is advancing through the pipe, causing an intense wall-friction that decelerates the flow. Modelling this turbulence is perhaps the greatest challenge of the proposed CFD model.



The model introduced herein is based on the formalism known as Finite Volume Method (FVM), a discretisation procedure that solves the integral form of the governing equations in each cell, considered as an elementary control volume where the continuity and Navier-Stokes equations could be applied. The general transport equation for a field $\phi(t, \mathbf{x})$ being transported by a flow of density $\rho(t, \mathbf{x})$ and

³Recall the acceleration stage is very short, and does not change much with varying initial conditions (see page 59). The slope of the velocity curve during the acceleration stage is roughly the same for most instances of flow shown in Chapter 2. It is in the deceleration stage where different conditions cause significant variations in the flow's dynamics.

velocity $\mathbf{u}(t, \mathbf{x})$ is given by (see [VM07])

$$\partial_t(\rho\phi) + \nabla \cdot (\rho\phi\mathbf{u}) = \nabla \cdot (\Gamma\nabla\phi) + S_\phi \quad (4.1)$$

where Γ is the diffusion coefficient attached to the field ϕ and S_ϕ represents its sources. The continuity equation corresponds to the particular case in which $\phi = 1$, $\Gamma = 0$ and $S_\phi = 0$, while the Navier-Stokes equations correspond to $\phi = u_i$, $\Gamma = \mu$ the viscosity and S_ϕ is the vector sum of the pressure gradient, the specific gravity and any other agent able to set a fluid in motion. The integral form of this general transport equation for a given control volume Ω with boundary $\partial\Omega$, and a time interval Δt , is written as (the Gauss theorem is applied to divergence $\nabla \cdot$ terms):

$$\left. \int_{\Omega} \rho\phi \, d\Omega \right|_{t+\Delta t} - \left. \int_{\Omega} \rho\phi \, d\Omega \right|_t + \int_{\Delta t} \int_{\partial\Omega} \rho\phi\mathbf{u} \cdot d\mathbf{S} \, dt = \int_{\Delta t} \int_{\partial\Omega} \Gamma\nabla\phi \cdot d\mathbf{S} \, dt + \int_{\Delta t} \int_{\Omega} S_\phi \, d\Omega \, dt \quad (4.2)$$

with $d\mathbf{S}$ the normal vector to the surface element in $\partial\Omega$.

The FVM begins by considering each cell in the computational mesh as a control volume Ω , then applying equation (4.2) to every cell in the domain, and finally approximating such integral equations with equivalent algebraic equations, a procedure called **discretisation**. There is no unique way to interpret the integral equation as an algebraic expression, and a whole mathematical formalism has been devised along the years to tackle this problem. It is beyond the scope of this Dissertation to penetrate any further into the FVM and the reader is addressed to some excellent classical references like [FP02], [VM07] or [Bla05].

Equations like (4.1) are said to be in **Conservation** or **Divergence form**. The name derives from the fact that such differential equations yield integral equations which guarantee the conservation of the transported quantity over any control volume Ω , or its balance if sources and sinks are also considered, as it is evident upon examining (4.2). For incompressible fluids ($\rho = \text{constant}$) the conservation form of the momentum equation ($\phi = u_i$) is the incompressible Navier-Stokes equation written in the following manner:

$$\partial_t u_i + \partial_j(u_i u_j) = -\frac{1}{\rho} \partial_i p + \partial_j(\nu \partial_j u_i) + g_i \quad (4.3)$$

The more familiar version of the Navier-Stokes equation is called the **Advective/Convective form**, or also the standard form:

$$\partial_t u_i + u_j \partial_j u_i = -\frac{1}{\rho} \partial_i p + \partial_j(\nu \partial_j u_i) + g_i \quad (4.4)$$

Both equations are identical in the analytical sense, since the continuity equation for the incompressible fluid, $\nabla \cdot \mathbf{u} = 0$, determines that \mathbf{u} be a zero-divergence (solenoidal) vector. They cannot be considered identical, though, when those equations are discretised and interpreted numerically, since the conservation of momentum is not fully implicit in the second and the discretisation errors cumulate as the simulation progresses in the computer. [Gre91] and [Gre92] explore and explain with great detail these interesting issues, and present a range of seemingly-equivalent forms of the incompressible Navier-Stokes equations, and study their different behaviour from an analytical point of view. Unfortunately, those papers do not study in detail the discretisation and numerical resolution of the various forms of Navier-Stokes equations explored in them.

The previous argumentation extends also to other aspects of the original differential equations. For example, a relevant issue appears with the diffusive term of (4.3)-(4.4) during its interpretation as an

algebraic equation. In principle there are two options for formulating such term; one that enhances the symmetric nature or the strain rate tensor

$$\frac{1}{2}\partial_j(\nu(\partial_j u_i + \partial_i u_j))$$

and other, the unmodified familiar form

$$\partial_j(\nu\partial_j u_i)$$

In some cases of numerical resolution the first instance leads to a better balance of the velocity components than the second, albeit they are fully equivalent in the analytical sense.

The remarks made above are particularly important when modelling turbulent flows, since in that case one works with RANSE rather than with pure Navier-Stokes equations, and the small numerical deviations observed from one form of equations to another tend to cumulate in the Reynolds stress tensor, sometimes with noticeable effects on the algorithm's stability. In such cases an intelligent choice of the discretisation method is particularly important, since it will not only affect to the RANSE, but also to the highly *customised*⁴ differential equations that govern some TQ like k , ϵ or ω .

The above comments ought to be sufficient to evince that the discretisation of differential equations is by no means a straightforward operation that proceeds almost automatically. On the contrary, a careful selection of algorithms and schemes must be performed in order to produce an accurate simulation of a given flow, although the guiding criteria for each possible choice is not usually explicit. Besides, even an unaccomplished discretisation scheme would still provide a solution that might, at first sight, seem to be a realistic simulation of the actual flow. This all contributes to the vague idea that CFD is more a craft than a science, when in all rigour it should be considered a branch of Mathematics, namely Numerical Analysis. This last thought brings to an end the general reflections expressed here on CFD and the numerical resolution of physical problems. The reader is again addressed to the mentioned references [FPO2], [VM07] or [Bla05], for further information and guidance on the various FVM discretisation procedures of Navier-Stokes and RANSE.



In order to facilitate the comparison of results yielded by the AHM and CFD models, all data will be dimensionless, expressed in units of the basic reference quantities seen in section 2.4.1. In other words, the 3D CFD model is constructed dimensionless from the beginning, with the same boundary and initial values that have been set in the AHM case. The notation and nomenclature used to denote the dimensionless quantities are also collected in section 2.4.1.

The main problem of the 3D CFD model introduced herein, is the simulation of a turbulence that grows and diminishes with the changing flow velocity that was made explicit during the presentation of the 1D AHM in Chapter 2. In order to visualise this turbulence, it is important to realise the order of magnitude of the Kolmogorov microscales associated therewith. The Kolmogorov microscales are defined in terms of the fluid's kinematic viscosity ν and the flow's average rate of dissipation of turbulence kinetic energy per unit mass ϵ , by the following expressions (see [TL72] or [Wil06]):

$$\eta = \left(\frac{\nu^3}{\epsilon} \right)^{\frac{1}{4}}$$

⁴The exact differential equations that describe TQ like k , ϵ or ω are extremely complicated, with many terms in the form of product of several strain rate components. Such equations are severely *clipped* ("...drastic surgery..." paraphrasing the words of [Wil06]) before being incorporated into turbulence models. That is the concrete meaning of the word "*customised*" used above. Therefore, those equations are even more dependent on the discretisation algorithm than standard governing differential equations. [Wil06] explains in great detail these issues.

$$\begin{aligned}\tau_\eta &= \left(\frac{\nu}{\epsilon}\right)^{\frac{1}{2}} \\ v_\eta &= \frac{\eta}{\tau_\eta} = (\nu\epsilon)^{\frac{1}{4}}\end{aligned}\quad (4.5)$$

The Kolmogorov microscales for a typical discharge of extinguishing agent FK-5-1-12 to the atmosphere, where Reynolds number Re could surpass 1.2×10^7 (see table 4.1), are estimated as ⁵

$$\eta = 1.88 \times 10^{-6} \quad , \quad \tau_\eta = 5 \times 10^{-5} \quad , \quad v_\eta = 0.0384$$

dimensionless length, time and velocity, respectively.

Those values provide an estimate of the limits within which to define the simulation. Since wall-friction has proven to be the main cause of failure for most standard turbulence models essayed in the 3D CFD simulations, the near-wall cells ought to be accordingly small for the solver to grasp the wall-shear stress generated in them. Small cells lead inevitably to small time-steps, to the point that the larger time-step that still grants algorithm's stability is of the order of magnitude of τ_η , the Kolmogorov time-scale. This gives an idea of the sort of computing power needed to solve the 3D CFD model introduced herein.

Although the RANSE written in the solver correspond to the mean velocity field $U(t, \mathbf{x})$, a provision is also made to calculate the cross-section averaged velocity $\tilde{U}(t)$ at each instant. Except for computational errors, $\tilde{U}(t)$ is not a function of z and could be safely obtained at any cross-section within the pipe. The CFD-calculated $\tilde{U}(t)$ will be compared with equal-time cross-section averaged velocity $\tilde{v}(t)$ obtained from the AHM ⁶, for a given set of adjustable parameters L_v , ζ_D and Δ_f (see Chapter 2).

The CFD simulation of this flow is tantamount to the simulation of the turbulence generated within. Since there is no geometrical complexity in the flow, all resources should be concentrated in studying the development and structure of the turbulence, which acquires very high intensity due to equally high Reynolds number. In order to quantify the degree of turbulence existing in a flow, it is convenient to resort to a set of fields known by the general name of Turbulence Quantities (TQ), which provide the most accurate picture compatible with CFD practice. The set used herein correspond to the following quantities:

- Reynolds stress tensor $R_{ij} = -\rho\langle u'_i u'_j \rangle$
- Specific average kinetic energy of turbulence $k = \frac{1}{2}\langle u'_i u'_i \rangle$
- Specific turbulent energy average dissipation rate $\epsilon = \frac{\nu}{2}(\partial_i U_j + \partial_j U_i)(\partial_i U_j + \partial_j U_i)$
- Specific turbulence average dissipation rate $\omega \sim \frac{\epsilon}{k}$
- Turbulent eddy viscosity (Boussinesq's hypothesis) $\nu_t \Rightarrow R_{ij} = \rho\nu_t(\partial_i U_j + \partial_j U_i) - \frac{2}{3}\rho k\delta_{ij}$
- Residual stress tensor (in LES) $\tau_{ij}^r = \underline{u_i u_j} - \underline{u_i} \underline{u_j}$
- Subgrid-scale viscosity (in LES) $\nu_s \Rightarrow \tau_{ij}^r = -\nu_s(\partial_i \underline{u_j} + \partial_j \underline{u_i})$

⁵ For agent FK-5-1-12 the kinematic viscosity at $20^\circ C$ is $\nu = 4 \times 10^{-7} m^2/s$, while a gross average value of ϵ is obtained from the very CFD simulation. For a pipe of $50 mm$ of diameter, $L_{ref} = D = 50 mm$, the Kolmogorov length scale represents only $\eta L_{ref} \simeq 10^{-4} mm$, a tenth of a micrometer.

⁶In order to avoid confusion, U , U_i and \tilde{U} will refer to mean velocities calculated from the 3D CFD model, while \tilde{v} and \bar{v} refer to velocities calculated with the AHM. Note the CFD velocities are always dimensionless by construction, and it is immaterial to write U , U_i and \tilde{U} or \mathbb{U} , \mathbb{U}_i and \mathbb{U} , respectively.

4.2 Brief Description of OpenFOAM

The open-source software package openFOAM has been chosen to carry out the CFD simulations included in the scope of this Dissertation. OpenFOAM stands for **Open Field Operation And Manipulation**, and it is a computer code designed specifically to work with general tensor fields (scalars, vectors, tensors...) in the realm of discretisation of differential equations. The OpenFOAM suite is described in [WTF98], [Jas96] and www.openfoam.org.

OpenFOAM is a set of libraries and applications, written in object-oriented code C++, aimed to be used for the development of solvers and utilities for Fluid Dynamics problems, as well as other kinds of situations which could be expressed through differential equations. Also, within the set there exist a number of ready-made solvers and utilities that can be used for the most common instances of flows, without implementing major changes in the code already available.

OpenFOAM is based on the discretisation technique for differential equations known as Finite Volume Method (FVM), a technique that relies heavily on the mesh topology (see below). FVM is thoroughly described in [VM07] or [FPO2]. In order to develop the model for a flow, one must define:

- i. A COMPUTATIONAL DOMAIN. Usually this is coincident with the physical domain where the flow develops, although a number of techniques exist (mirroring, boundary translation, cycling...) which can simplify the computational domain respect to the physical domain. The computational domain is expressed in a **mesh** or **grid**, composed of a number of **cells** of different sizes and shapes. The geometrical centre (centroid) of each cell is called a **node**, and they are important because the discretisation takes place in those nodes. Any cell is surrounded by **faces**. Most faces are common to two adjacent cells, although there exist faces which belong to a single cell. Those faces are part of the **boundary** of the computational domain. OpenFOAM always works with 3D meshes, although it is possible to simulate 2D and even 1D cases by simply defining a grid with one-cell depth and/or width.
- ii. A SET OF FIELDS. The fields characterise the dynamics and could adopt any tensorial form (scalar, vector, 2^{nd} -rank tensor, 3^{rd} -rank tensor...). In FVM the fields are solved for the mesh nodes, even though the CFD parlance sometimes refers to 'field values in the cells' or 'field values in the mesh', meaning actually the nodes. Usually the fields are given a value at each node of the mesh, although there are classes of fields that are only defined on surfaces or along lines.
- iii. A SET OF DIFFERENTIAL EQUATIONS. FVM is a technique to discretise and solve differential equations at the nodes of a mesh. The equations must be written in the solver's code. For each field there must exist an equation establishing the form to obtain its values at the nodes. Dynamical equations, usually in the form of partial differential equations, must also be included in the solver for the main conserved quantities of the flow.
- iv. A SET OF BOUNDARY AND INITIAL CONDITIONS. Let Ω be the physical domain of the flow and $\partial\Omega$ its boundary. Mathematically the boundary conditions can be classified as (see [PRO5])
 - Dirichlet. For a given field $\psi(t, \mathbf{x})$, $\mathbf{x} \in \Omega$, the Dirichlet boundary condition responds to the general form

$$\psi(t, \boldsymbol{\xi}) = f(t, \boldsymbol{\xi}), \quad \boldsymbol{\xi} \in \partial\Omega$$

for f a given piecewise continuous function defined on the boundary. The Dirichlet boundary condition fixes the value of the field ψ at the boundary.

- Neumann. For a given field $\psi(t, \mathbf{x})$ the Neumann boundary condition responds to the general form

$$\frac{\partial \psi(t, \boldsymbol{\xi})}{\partial n} := \mathbf{n} \cdot \nabla \psi(t, \boldsymbol{\xi}) = f(t, \boldsymbol{\xi}), \quad \boldsymbol{\xi} \in \partial\Omega$$

where \mathbf{n} is the unit vector normal to the boundary $\partial\Omega$ at the point $\boldsymbol{\xi} \in \partial\Omega$, and f as above. The Neumann boundary condition fixes the normal derivative of the field ψ at the boundary.

- Robin (or mixed). For a given field $\psi(t, \mathbf{x})$ the Robin or mixed boundary condition respond to the general form

$$\frac{\partial \psi(t, \boldsymbol{\xi})}{\partial n} + a(\boldsymbol{\xi}) \psi(t, \boldsymbol{\xi}) = f(t, \boldsymbol{\xi}), \quad \boldsymbol{\xi} \in \partial\Omega$$

where $a(\boldsymbol{\xi})$ is a continuous function defined on the boundary $\partial\Omega$, and f as above. The Robin boundary condition links both, the field ψ and its normal derivative at the boundary, although it fixes none of them.

OpenFOAM admits a wide variety of boundary conditions, most of which could be identified with any of the three above-mentioned fundamental types, although it also admits some particular forms to characterise situations that might be produced in CFD.

The initial conditions for a flow field $\psi(t, \mathbf{x})$ are defined as $\psi(0, \mathbf{x}) = f(\mathbf{x})$, $\mathbf{x} \in \Omega$, with f a piecewise continuous function defined in the domain.

- v. A SET OF DISCRETISATION SCHEMES. **Discretisation schemes** is the general name given to the methods whereby the continuous differential equations will be transformed into discrete algebraic equations, whose unknowns are the values of the fields at the mesh nodes. Being discretisation an intrinsically non-exact method of solution, the proper selection of the discretisation scheme for each particular case is of utmost importance to avoid the accumulation of errors during the CFD simulation.

Just as a mesh implements the discretisation of space, and a time-marching process through time-steps does the same with time, the discretisation schemes convert the continuous field equations into discrete algebraic equations. The general output of a discretisation algorithm, when applied to a differential equation, takes the following form for each time-step t (see [VM07] or [FPO2])⁷:

$$a_{ij} \psi_j^{[t]} = b_i \quad i, j = 1 \dots N \quad (4.6)$$

where N is the number of nodes in the mesh, a_{ij} are coefficients dependent on the geometry and transport properties of the flow, b_i are coefficients dependent on the boundary conditions or the source terms S_ϕ , and $\psi_j^{[t]}$ is the particular value taken by the field ψ on the j^{th} mesh-node at the time-step t .

The chosen discretisation scheme must satisfy two distinct needs of any numerical simulation: accuracy and stability. Being discretisation an approximation to the original equation, accuracy is better preserved by selecting a scheme which retain more than one term in the Taylor expansion. On the other hand, stability grossly means that the errors should not accumulate in the derivative always on the same side, that is, if a field is growing and positive errors add up in its derivative, then

⁷The coefficients a_{ij} are constant for a given simulation, always provided the transport properties and the mesh do not change with time. Some CFD models require a variable mesh, for instance, when simulating a flow on a moving domain (hydraulic machines, pistons...). In certain cases, e.g. when discretising the Laplacian of pressure, a_{ij} could contain values of the pressure field.

the field will grow even faster until it shows an exponential behaviour. Or it could have an oscillation pattern if the errors accumulate on the wrong side at each time-step. There are unconditionally stable schemes, but usually they are not very accurate, and when they are, normally involve high computing power. It might also happen that a scheme is suitable for a field, but unstable for another, or even that different schemes are needed for different terms of the same differential equation.

Particularly important is the right selection of the discretisation scheme for the advection term of the Navier-Stokes equations, since this non-linear term is related to most frequent problems of stability and convergence of any CFD algorithm. The advection term is also present in the equations describing the relevant fields for the simulation of turbulence, notably in the above-introduced TQ.

A treatment of the rich variety of available discretisation schemes and their properties is beyond the scope of this Dissertation. A detailed explanation could be found at [VM07] or [FPO2]. OpenFOAM includes in its libraries most of the schemes described in those references, and the simulation Engineer always has the possibility to write his own.

- vi. A SET OF MATRIX-SOLVING ALGORITHMS. The differential field equations that characterise the model, once discretised, adopt the form of colossal $N \times N$ matrices (a_{ij}), being N the number of nodes, a number that could easily surpass 10^6 for many complicated flows. Fortunately those matrices (a_{ij}) are almost empty, being zero the huge majority of all its components except those at the diagonal and in the neighbourhood thereof ($a_{ij} = 0$ for $i \neq j$). Such matrices with most components being zero are called **sparse matrices**, and there exists a full mathematical theory dealing with them (see [Tew73]) The OpenFOAM solvers are based on the theory of sparse matrices, and the many ingenious methods devised therein to solve the matrix equations with the barest minimum of operations.

There exists one such matrix for each field and for each time-step. In the case of transient phenomena, with small time-steps in order to capture the evolution of the flow, the computing power needed to solve the discretised model might reach astronomical levels. Therefore, selecting the right sparse matrix solving algorithm is an integral part of the simulation process which must be specifically addressed in the CFD code.

Equations like (4.6), with a_{ij} a sparse matrix, are generally solved through iterative algorithms: successive values of the field $\psi_j^{[t]}$ are inserted in (4.6) at each iteration, any of them more refined than the previous one, until finally the sequence converges and the field values are deemed sufficiently accurate, and the algorithm proceeds to the next time-step. *Convergence* is the key word herein. To measure the convergence rate the so-called residuals are introduced.

Let $^{(n)}\psi_j^{[t]}$ be the field value at the node j^{th} of the n^{th} iteration of equation (4.6) for time-step t . In order to ascertain whether each iteration is sufficiently accurate, the **residual**, or **residual error**, for the field ψ is defined at each mesh-node as

$$^{(n)}r_{\psi_i}^{[t]} = a_{ij} ^{(n)}\psi_j^{[t]} - b_i \quad i, j = 1 \dots N \quad (4.7)$$

Since most equations solved in CFD correspond to the conservation of any quantity, it would be concluded that in those cases the residuals measure the imbalance of a conserved quantity in the control volumes represented by each cell. Every cell in the grid has its own residual values corresponding to each of the differential equations being solved in the CFD model. As long as the residuals are kept low after each iteration, the solution is converging.

Residuals as defined in equation (4.7) are of limited usefulness in CFD, since each one refers to a unique node in the computational grid and some could be very low while others might appear intolerably high.

Note the residuals could be thought of as a N -vector $\{^{(n)}r_{\psi_i}^{[t]}\}$, with one component per node, which represents the overall behaviour of the mesh in a manner still to be specified. For such vector it is possible to define a **Residuals Vector Norm** (Residuals Vector Norm (RVN)), written $\|^{(n)}r_{\psi}^{[t]}\| \in \mathbb{R}^+$, which is a single positive figure that characterise the aggregate residual values at *all* node points in the mesh. It is known from the theory of normed vector spaces that the definition of a norm is not unique and, therefore, several norms could be proposed to evaluate the relative importance of the residuals after each iteration. A convenient and very useful norm is the residual Root-Mean-Square Error (RMSE) of the field ψ for the n^{th} iteration given by

$$\|^{(n)}r_{\psi}^{[t]}\| = RMSE_{\psi}^{(n)} = \sqrt{\frac{1}{N} \sum_{i=1}^N \left(^{(n)}r_{\psi_i}^{[t]}\right)^2} \geq 0 \quad (4.8)$$

Note this RVN allows for some residuals that grow large to be balanced by others resulting very small, thus some not-well-behaved nodes in the grid would be compensated by most others, and the (numerical) perturbations initiated in some area would spread to the whole domain. It is suitable in simulations where stability is not considered to be the main problem.

It is also possible another type of norm which only takes into account the **Residual Maximum Error**, that is, the largest absolute deviation produced anywhere in the n^{th} iteration:

$$\|^{(n)}r_{\psi}^{[t]}\| = \max_{i=1}^N \left|^{(n)}r_{\psi_i}^{[t]}\right| \geq 0 \quad (4.9)$$

This RVN is suitable in critical simulations where stability is not guaranteed and even at a single node could not be afforded a weak convergence of the iteration algorithm. No balancing out of residuals is contemplated on this norm.

It is yet possible to define a dimensionless residual simply dividing each residual by a quantity of the same dimensions, for example:

$$\frac{{}^{(n)}r_{\psi_i}^{[t]}}{b_i}$$

or any other convenient choice ⁸. The attached RVN would also be dimensionless.

Convergence of the iterative algorithm is strongly related with the norm of the N -vector $\{^{(n)}r_{\psi_i}^{[t]}\}$ being sufficiently small. Let $\varepsilon > 0$ be the maximum admissible deviation in the algorithm, also called the **tolerance**. When $\|^{(n)}r_{\psi}^{[t]}\| < \varepsilon$ then the iteration process is deemed to have converged, and the algorithm proceeds to the next time-step. Convergence in the sense of the RVN (4.9) would not tolerate that any one of the residuals, anywhere in the domain, be in absolute value larger than ε .

The RVN is thoroughly used in CFD to assess the quality of the simulations, and it will be mentioned frequently in this Dissertation.

- vii. A MODEL OF TURBULENCE. If turbulence is expected in a flow, it must be modelled. This is, probably, the most convoluted aspect of flow simulation. The Navier-Stokes equations ought to be replaced by the RANSE (statistical approach), or the FNSE (filtering approach), and room must be made for the new set of fields stemming from the averaging or filtering process. Note the Russian matryoshka

⁸For instance, OpenFOAM normalises the residuals to the first one, that is, the first residual is given the value of 1.0 and the remaining are normalised to that value.

doll structure: it is a model (turbulence) within another model (flow), and both have their own rules. The chosen model affects to all fields involved in the simulation, but particularly to the TQ.

Since the flow attempted to be modelled herein is very transient, the (only) right type of average needed to describe turbulence is the ensemble average. The more familiar time average is completely uncalled for in this case ⁹. Unfortunately, OpenFOAM does not have a tick-box where one could select what kind of average one wishes. Rather, the averaging method is indirectly defined by means of the equation written in the solver, and the variables it depends on. As the equation may be, so would be the resulting averaged field. Mathematically this approach makes sense: only the properly averaged field will satisfy its corresponding RANSE.

Now it should be recalled the different possibilities for the RANSE, as many as averaging methods. They will be repeated herein with their respective numbers as they were introduced in Chapter 3

- Ensemble average, equation (3.40):

$$\partial_t U_i + U_j \partial_j U_i = \partial_j \left[-\frac{P}{\rho} \delta_{ij} + \nu (\partial_j U_i + \partial_i U_j) - \langle u'_i u'_j \rangle \right] + \langle g_i \rangle$$

- Time average, equation (3.68):

$$U_j \partial_j U_i = \partial_j \left[-\frac{P}{\rho} \delta_{ij} + \nu (\partial_j U_i + \partial_i U_j) - \overline{u'_i u'_j} \right] + \bar{g}_i$$

- Spatial average, equation (3.80):

$$\partial_t U_i = \overbrace{u'_j \partial_j u'_i} + \overbrace{g_i}$$

- Phase average, equation (3.91):

$$\partial_t U_i + U_j \partial_j U_i = \partial_j \left[-\frac{P}{\rho} \delta_{ij} + \nu (\partial_j U_i + \partial_i U_j) - \overleftrightarrow{u'_i u'_j} \right] + g_i + \pi_i$$

Writing the time averaged equation (3.68) in the CFD code is not the only way to produce a set of time averaged flow fields. Usually there exists another method ¹⁰ to obtain them: one starts the simulation with the full (3.40) RANSE, until the solution stabilises in time and produces a steady state with no noticeable change in any of the fields being solved. Just by letting the solver go on for long enough, the solution has converted itself into a steady state time average, although the equation originally written in the solver include a time dependence. In this approach, the previous time-steps or time-frames where the solution was not yet a steady state should be neglected, and one ought to post-process only the last time-frame in which the solution is already steady-state. This last procedure guarantees a time average even if the equation originally written in the solver be not the one corresponding to such average because, given sufficient time, the ensemble average and the time average converge asymptotically.

⁹Even the finite time average (see URANS in section 3.2.2) is unsuitable for this simulation, as the resulting time-step is very, very short.

¹⁰The exception corresponds to the case in which the boundary conditions or the force density field g_i change with time not asymptotically during all flow.

The filtering approach does not pose those problems, since the filtered fields $\psi(t, \mathbf{x})$ are normally time and space dependent. Care must be taken, though, not to select a too long filter width Δ or Θ : such circumstance would lead to a loss of detail in the flow dynamics, as the interesting small structures will be blurred under the filter operator. The main drawback of the filtering approach for the model described in this work could be easily fathomed: an internal flow is fully surrounded by walls and a pure LES model of turbulence is out of question.

Turbulence modelling in CFD is masterfully described in the like-named reference [Wil06]. OpenFOAM boasts a comprehensive selection of turbulence models already written, ready to be used, in its libraries. Some of the turbulence models within the OpenFOAM suite will be described further in this Chapter, specially the most successful ones, since their knowledge will be convenient to understand the results obtained in the simulations of the transient discharge flow.

In the general case of a time dependent flow, the development of a simulation in OpenFOAM progresses in a time-marching sequence. It starts assigning to each field $\psi(t, \mathbf{x})$ the initial conditions defined in the model $\psi_i^{[0]}$ ($i = 1 \dots N$) for each mesh-node, and stores their values in files within a folder named after the initial time. The index i fully characterises each node and cell within the mesh. Those values $\psi_i^{[0]}$ are then used to calculate the new set of values $\psi_i^{[1]}$ corresponding to the next time-step for every node. These $\psi_i^{[1]}$ values are, in turn, used to calculate the $\psi_i^{[2]}$ set corresponding to the t_2 time-frame, and so continues the process until the end of the simulation.

The set of all flow fields for a given time t_n is called a **time-frame**. t_n progresses in discrete simulation time-steps Δt , adding it to the previous time t_{n-1} . Since OpenFOAM admits the use of variable time-steps Δt , it is not always possible to express a computing instant t_n as $t_n = t_0 + n\Delta t$ ($n = 0, 1 \dots$). Thus the time-frame is characterised by the actual time t_n instead of the integer index n .

Every time-frame t_n is kept in memory and it is used to calculate the next time-frame t_{n+1} . Standard time-discretisation schemes in OpenFOAM do not need time-frames earlier than past time-frame, i.e., t_n time-frame is calculated with t_{n-1} time-frame only, and time-frame t_{n-2} is not involved. Therefore, it is not necessary to keep in memory time-frame t_{n-2} .¹¹

One in every fixed number of time-frames is stored in hard-disk, and labelled with the corresponding time t_n . Such time-frames, containing the complete set of flow fields for all mesh-nodes, are used in the post-processing of data: calculating new fields, determining friction factors or wall-shear stresses... Each time-frame corresponds to a *picture* of the flow, which can be combined with other pictures to yield a *movie*. That movie constitutes the full simulation of the flow, since it contains the information generated in CFD. Whether this movie is a faithful representation of the actual flow depends on the ability of the simulation Engineer.

OpenFOAM uses the extraordinary post-processing software called ParaView. ParaView is an open-source, multi-platform data analysis and visualisation application. Extensive information about ParaView is found at www.paraview.org. Most of the figures shown in this Chapter have been obtained with ParaView, as a result of post-processing the data generated with OpenFOAM.

¹¹Of course, the user can create a time-discretisation scheme requiring t_{n-1} and t_{n-2} (and even further), but in such case must also write the algorithm to keep in memory the necessary past time-frames.

4.3 OpenFOAM's Solver Description

The physical phenomenon previously described in Chapter 2 with the AHM will be attempted to be reproduced in a 3D CFD simulation involving the complete tube, and the dimensionless cross-section averaged velocity $\tilde{v}(t)$ will be obtained for the time interval of interest. This bulk velocity curve will be compared with that offered by the AHM. Moreover, that comparison will allow to find out a suitable value for the otherwise undetermined degree of freedom L_v arisen in the AHM. To attain the widest generality of results all physical quantities within the CFD model are also dimensionless.

The flow which is intended to be simulated herein has some of the properties which make it difficult for CFD modelling: very high Reynolds number, extreme acceleration, wall-bounded, very unsteady, two-phase and with variable boundary conditions. Later on, it will be shown that just two of the acknowledged turbulence models used in industrial applications, yield predictions that approximate those offered by the AHM.

The open-source software package OpenFOAM has been chosen to carry out the CFD simulation. A new solver has been created within the OpenFOAM suite. It is very much based on the two-phase incompressible flow solver interFOAM, included in the standard OpenFOAM package introduced above. interFOAM is well described in [DAT12] and [Rus02], and is a CFD solver based on the so called Volume of Fluid (VoF) method, first introduced by [NHH80] and [HN81], which defines a scalar field $\alpha(t, \mathbf{x})$ in each mesh-node known as the **Liquid Fraction**. Consider a two-phase flow made up of immiscible liquid and gas; then the liquid fraction field α is defined by:

$$\alpha(t, \mathbf{x}) = \begin{cases} 1 & \text{if place } (t, \mathbf{x}) \text{ is occupied by liquid} \\ 0 < \alpha < 1 & \text{if place } (t, \mathbf{x}) \text{ is at the interface} \\ 0 & \text{if place } (t, \mathbf{x}) \text{ is occupied by gas} \end{cases} \quad (4.10)$$

with a similar definition for any two other non-miscible phases. With such a definition, it should be evident that α is no standard function; instead it must be included in the category of generalised functions or distributions.

The field $\alpha(t, \mathbf{x})$ makes possible the definition of global transport properties in a two-phase flow. In the case of a liquid-gas flow being considered, for example, the density and viscosity fields would be defined by¹²

$$\begin{aligned} \rho(t, \mathbf{x}) &= \rho_l \alpha(t, \mathbf{x}) + \rho_g(1 - \alpha(t, \mathbf{x})) \\ \mu(t, \mathbf{x}) &= \mu_l \alpha(t, \mathbf{x}) + \mu_g(1 - \alpha(t, \mathbf{x})) \\ \nu(t, \mathbf{x}) &= \nu_l \alpha(t, \mathbf{x}) + \nu_g(1 - \alpha(t, \mathbf{x})) \end{aligned} \quad (4.11)$$

and like expressions for any other transport property (thermal conductivity, specific heat capacity...). Thus the global fluid properties are weighted averages of the corresponding properties of each phase. $\alpha(t, \mathbf{x})$ is a field subjected to transport by advection, and responds to the continuity equation:

$$\partial_t \alpha + \nabla \cdot (\alpha \mathbf{u}) = 0 \quad (4.12)$$

which is equivalent to the conservation of phase fraction within the flow. In turbulent flow, the equation (4.12) could also be expressed with the mean velocity \mathbf{U} instead of the instantaneous velocity \mathbf{u} , being \mathbf{U}

¹²The VoF method considered herein assumes each phase as incompressible and Newtonian, thus $\rho_l, \rho_g, \mu_l, \mu_g, \nu_l$ and ν_g are supposed to be constant, although the global fields ρ, μ and ν may not be so.

the result of any of the averaging methods seen in Chapter 3

$$\partial_t \alpha + \nabla \cdot (\alpha \mathbf{U}) = 0 \quad (4.13)$$

Likewise, the global density defined in (4.11) satisfies also the continuity equation:

$$\partial_t \rho + \nabla \cdot (\rho \mathbf{u}) = 0 \quad (4.14)$$

It can be proven that the familiar continuity equation for each phase (that involving density) leads to the continuity equation for α (4.12).

The formalism could also be applied to other flow fields like the velocity \mathbf{u} . Assuming the velocities of liquid $\mathbf{u}_l(t, \mathbf{x})$ and gas $\mathbf{u}_g(t, \mathbf{x})$ could be different, then the global velocity and the mean global velocity are defined as

$$\begin{aligned} \mathbf{u}(t, \mathbf{x}) &= \mathbf{u}_l(t, \mathbf{x}) \alpha(t, \mathbf{x}) + \mathbf{u}_g(t, \mathbf{x}) (1 - \alpha(t, \mathbf{x})) \\ \mathbf{U}(t, \mathbf{x}) &= \mathbf{U}_l(t, \mathbf{x}) \alpha(t, \mathbf{x}) + \mathbf{U}_g(t, \mathbf{x}) (1 - \alpha(t, \mathbf{x})) \end{aligned} \quad (4.15)$$

and like expressions for other flow fields¹³.

interFOAM translates this VoF formalism into CFD code. For each cell completely full of liquid $\alpha = 1$, while another full of gas has $\alpha = 0$. Any value in between corresponds to an interface cell in which both phases coexist to certain degree.

Distributions like α , which have an unambiguous meaning in Continuous Mechanics, find it very difficult to be extrapolated into CFD. The discretisation algorithms would not respect the sharp step behaviour of field α , specially in turbulent flows, and would rapidly create numerical diffusion of α over finite lengths, spreading the interface in a volume instead of being a warped surface. The advection of the step distribution is plagued with computational problems in the FVM (and other discretisation methods as well). What starts up as a razor-sharp interface between both phases ends up being distributed among many cells, all of them having values for α different from 0 or 1, and the initially immiscible two-phase flow results in an increasingly mixed flow that no longer represents the physical situation being modelled. Therefore the equation (4.13) is almost impossible to satisfy in CFD and the numerical diffusion introduces an unbearable level of continuity error that must be avoided.

The usual approach to this problem is called the **interface compression**¹⁴, which is well explained in reference [Rus02], and entails the change of equation (4.13). According to this procedure, instead of applying to α the continuity equation (4.13), an additional somewhat artificial term must be introduced to avoid the interface spread, and the resulting equation that should be applied to α is the following

$$\partial_t \alpha + \nabla \cdot (\alpha \mathbf{U}) + \nabla \cdot (\mathbf{U}_r \alpha (1 - \alpha)) = 0 \quad (4.16)$$

where $\mathbf{U}_r = \mathbf{U}_l - \mathbf{U}_g$ is the relative velocity between both phases, also called the **compression velocity**, and it corresponds to a velocity field that would compress the interface and to a large extent would prevent it to spread. This artificially introduced compression term harnesses to a degree the trend of the CFD to diffuse the sharp interface that should exist between both phases.

¹³Note in equation (4.15) that even though \mathbf{U}_l and \mathbf{U}_g might not be function of t or \mathbf{x} , depending on the type of average, the global mean velocity $\mathbf{U}(t, \mathbf{x})$ is always a function of (t, \mathbf{x}) , inheriting this dependence at least through $\alpha(t, \mathbf{x})$.

¹⁴**Compression**, in the sense meant herein, has no relationship with the familiar compressible flow, caused by considering a finite sound velocity. The flow is still assumed incompressible.

\mathbf{U} in equation (4.16) is represented by the weighted average considered in equation (4.15), that is, the modified transport equation for α admits the possibility that both phases could have different velocities. Therefore, the modified VoF model should solve both phases separately, with transport equations for $\alpha(t, \mathbf{x})$ given by

$$\partial_t \alpha + \nabla \cdot (\alpha \mathbf{U}_l) = 0 \quad (4.17)$$

and

$$\partial_t (1 - \alpha) + \nabla \cdot ((1 - \alpha) \mathbf{U}_g) = 0 \quad (4.18)$$

and then the model couples together at the interface the results obtained in each phase with the third equation (4.16). This approach of the VoF model to the two-phase flow problem has the drawback that each phase could have a (slightly) different mean velocity, a situation which could hardly be considered very physical.

Note also that practically the compression term $\nabla \cdot (\mathbf{U}_r \alpha(1 - \alpha))$ is only active at the interface, since the factor $\alpha(1 - \alpha)$ would be negligible outside the thin domain occupied by the interface. Thus the compression term would not noticeably affect the general solution for $\alpha(t, \mathbf{x})$ outside that region, while hindering the numerical diffusion discussed above.

An interesting alternative approach to the modelling of two-phase flows is presented in [Dre83]. It is not the one followed herein, but its reading is undoubtedly recommended.

As mentioned at the beginning of this section, in order to simulate the discharge of extinguishing agent into the atmosphere a new solver based on interFOAM has been developed. The new solver modifies interFOAM to include the following characteristics of the model:

- a new field to account for the fluid volume that escapes from the pipe's outlet at each computational time-step, represented by the integral

$$\int_0^t \tilde{U} dt$$

where $\tilde{U}(t)$ is the cross-section average of the mean velocities calculated in the pipe (see equation (2.6)):

$$\tilde{U}(t) = \frac{2}{R^2} \int_0^R rU(t, r) dr \quad (4.19)$$

This field is necessary since a suitable definition for z_f is not readily available in CFD, as it is instead in the AHM,

- time-varying pressure in the vessel depending on the amount of liquid released from it, to account for the term

$$\frac{p_0}{\left(1 + G_f \int_0^t \tilde{U} dt\right)^\gamma} - p_\infty$$

of equations (2.72) and (2.76).

The new solver has been validated with some of the OpenFOAM standard cases and the results were identical to those yielded by the original interFOAM solver. It calculates the volume of fluid that crosses each cell, integrates it along the time, sums this volume for all cells belonging to the same cross-section to find out the total accumulated volume ejected from the pipe's outlet, and uses this value to modify the

vessel's pressure, which is used as a boundary condition for the pressure at the inlet. Such procedure guarantees that the CFD models is coincident in its dynamics with the AHM.

The computational domain has been chosen as a balance for high spatial resolution near the walls and a moderately high number of cells which could be readily solved in very short time steps. Therefore the tube is not long, resulting in high pressure gradients which cause large accelerations. All quantities are assigned dimensionless values. The liquid and air properties (density, viscosity...) are equal to those defined in the AHM.

4.4 Initial conditions for turbulence quantities

In most CFD simulations the initial conditions the flow fields must satisfy stem directly from the very definition of the model itself. Thus velocities, pressures or temperatures usually have unmistakable values at the beginning of the simulation. The evolution of the flow will determine the future values of such fields, but the initial conditions generally pose no doubts to the simulation Engineer.

But this situation, normally so clear for the main fields describing a flow, oftentimes is not so when it is affected by turbulence. Then it is not easy to determine beforehand which initial values should be assigned to fields like the Reynolds stress tensor R_{ij} or the specific energy dissipation rate ϵ , just to name a couple of them. It is, therefore, necessary to resort to any available correlation which can provide an estimate of the TQ for the requested flow conditions. Later on, as the CFD simulation progresses and reaches stability, the actual values adopted by the TQ could be used as initial conditions in a second attempt to perform the simulation with more reliable values, in a sort of recursive execution. This two-stage (and even three-stage or more) CFD simulation of turbulent flows is quite common in practice.

The situation is even worse when the flow to be modelled starts from rest conditions. In those cases, first a laminar flow is generated, then transition to turbulence occurs and, finally, a turbulent flow develops yielding, if conditions demand so, a fully developed turbulent regime. A CFD model with pretensions of being a faithful simulation must resolve the thorny problem of transition to turbulence, or at least attain an acceptable approximation thereof. The initiation of turbulence occurs very differently in the laboratory as it does in a computer, being an impossible task to find out which tiny fluid parcel will be the seed to cause the instability yielding turbulence. It is already complex enough to accurately simulate a very high-Reynolds fully developed steady turbulent flow, so it seems that attempting to reproduce the transition to turbulence from rest in a split-second would be a task beyond the scope of this Dissertation.

The model presented in this work is such a fast transient, reaching $Re \approx 10^5$ in less than one *ms*, that if initial conditions for TQ are set to zero (the obvious choice), then they would take too long to gain importance in the flow, contrary to what the high Reynolds number leads to think. The endeavour of simulating turbulence with zero initial conditions usually ends in failure, because the TQ will not acquire their final values in the simulation at the same rate as they would do in an actual laboratory experiment. Thus in the beginning part of a zero-initial-conditions simulation there normally exists an offset between the instantaneous Reynolds number and the corresponding calculated TQ values. This offset tends to vanish as the transient leads to a steady state.

Therefore, the TQ must be initiated with a set of non-zero values that, after a reduced number of tentative time-marching-steps, cancels that offset and produces a distribution of the TQ all over the flow compatible with the results the actual TQ be expected to achieve. Or in other words, the CFD model is set from the beginning with an artificial state of turbulence that is not very different from the one expected to be attained after not many execution time-steps. Then the turbulence model's differential

equations for the TQ will take care that such fields adopt the expected values at each mesh-node, since the initial values they start from are not far away from the destination state. This procedure is, in general, more efficient than trying to numerically generate a state of turbulence from scratch. Some useful correlations to approximate the initial values of the TQ will be deduced and explored in this section.

Since the initial conditions are needed for TQ according to Reynolds-Averaged Simulation (RAS) ($k, \epsilon, \nu_t, \omega, R_{ij}$), it is convenient to employ the most general Reynolds decomposition, based on ensemble average:

$$u_j(t, \mathbf{x}) = \langle u_j \rangle(t, \mathbf{x}) + u'_j(t, \mathbf{x}) \equiv U_j(t, \mathbf{x}) + u'_j(t, \mathbf{x}) \quad (4.20)$$

and similarly for other quantities (see section 3.2).

The procedure presented herein to initiate these turbulence fields is based on the Blasius correlation for pipe flow, and on the concept of **Turbulence Intensity**. The turbulence intensity along the axis j is defined as (no sum over indices):

$$I_j = \frac{\sqrt{\langle u_j'^2 \rangle}}{U_j} \quad (4.21)$$

Following this, the turbulence intensity is defined as (sum over repeated indices is implicit)

$$I = \frac{\sqrt{\langle u'_j u'_j \rangle}}{\sqrt{U_j U_j}} = \frac{\sqrt{2k}}{\sqrt{U_j U_j}} \quad (4.22)$$

In the particular case of isotropic turbulence, the intensity is given by

$$I = \frac{\sqrt{\frac{2}{3}k}}{U} \quad (4.23)$$

where U is the mean flow velocity magnitude.

Blasius offers the following correlation for the Fanning friction factor C_f (also called skin friction coefficient) corresponding to the fully developed turbulent flow inside a pipe (see [Sch79], [MY71] or [DKL⁺96]):

$$C_f = \frac{\tau_w}{\frac{1}{2}\rho\tilde{v}^2} = 0.0791 Re^{-1/4} \quad (4.24)$$

where τ_w is the wall-shear stress and Re is the Reynolds number corresponding to the bulk¹⁵ velocity \tilde{v} in the pipe

$$Re = \frac{\tilde{v} D}{\nu} \quad (4.25)$$

But τ_w , in terms of the friction velocity u_τ , is expressed as $\tau_w = \rho u_\tau^2$. Substituting in equation (4.24)

$$C_f = 2 \left(\frac{u_\tau}{\tilde{v}} \right)^2 \quad (4.26)$$

or

$$\left(\frac{u_\tau}{\tilde{v}} \right)^2 = 0.0396 Re^{-1/4} \quad (4.27)$$

¹⁵The bulk velocity \tilde{v} verifies $Q = A\tilde{v}$, where Q is the volumetric flow, and has been called cross-section averaged velocity in Chapter 2.

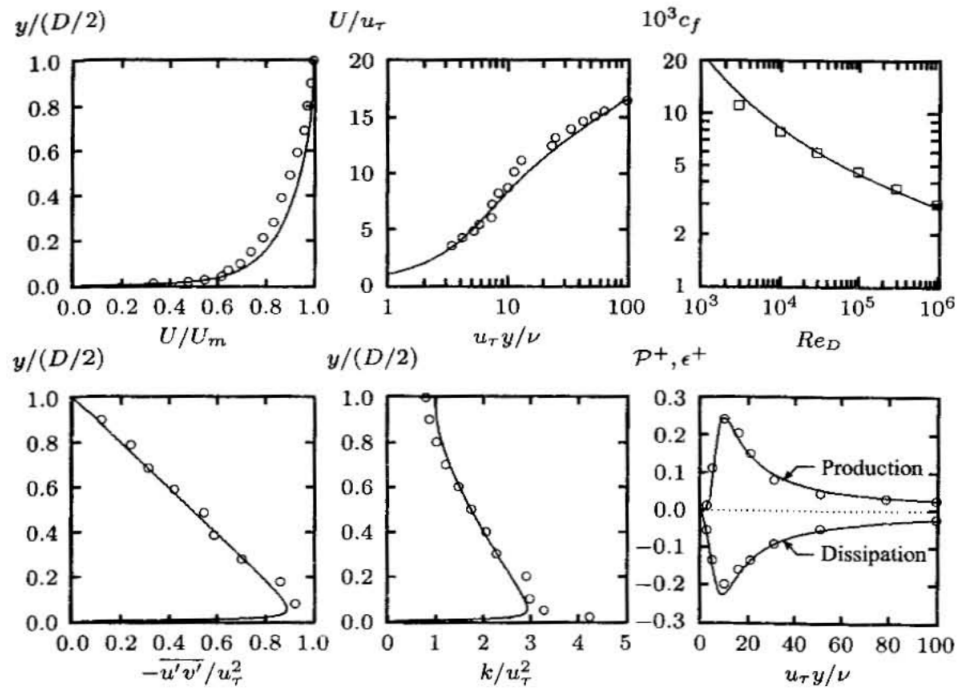


Figure 4.1: Figure 4.29 of reference [Wil06].

with the interesting result

$$\frac{u_\tau}{\tilde{v}} = 0.1989 Re^{-1/8} \quad (4.28)$$

Figure 4.29 of [Wil06], reproduced herein as figure 4.1, shows that for turbulent flow in pipes

$$1 \lesssim \frac{k}{u_\tau^2} \lesssim 3 \quad (4.29)$$

Actually, for $y/(D/2) > 0.4$ this ratio is less than 2, that is, in the core of the pipe k and u_τ^2 are not only of the same order of magnitude, but approximately equal as well. This result can also be observed in figure 12, page 394, of [Cha00], reproduced herein as figure 4.2.

Thus an initial estimate for pipe turbulent flow is $k = \alpha u_\tau^2$ with $1 \leq \alpha \leq 2$. Substituting in (4.27)

$$\frac{k}{\alpha \tilde{v}^2} = 0.0396 Re^{-1/4} \quad (4.30)$$

or

$$\frac{2k}{3\tilde{v}^2} = \alpha 0.0264 Re^{-1/4} \quad (4.31)$$

The left hand side of this equation is the square of the isotropic turbulence intensity I for a pipe. Then

$$\sqrt{\frac{2k}{3\tilde{v}^2}} = I = \sqrt{\alpha} 0.1625 Re^{-1/8} \quad (4.32)$$

But $1 \leq \alpha \leq 2$, and $\alpha = 1.5$ can be assumed as an acceptable approximation. Then for turbulent pipe flow the initial conditions for the turbulence intensity can be estimated from the following result:

$$I \approx 0.2 Re^{-1/8} \quad (4.33)$$

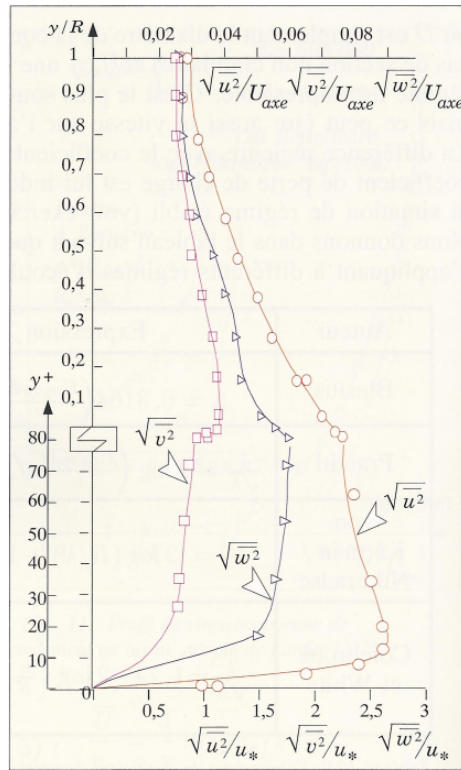


Figure 4.2: Figure 12, page 394 of reference [Cha00].

Turbulence intensity is an useful parameter to help estimate the TQ of a flow, since there exist correlations based on I .

The $k - \epsilon$ turbulence model (see section 4.10.2 and [Wil06]) establishes differential equations to determine the quantities k and ϵ (one equation per quantity), and then uses the calculated values of the fields k and ϵ to obtain the turbulent eddy viscosity field as

$$\nu_t = C_\mu \frac{k^2}{\epsilon} \quad (4.34)$$

with $C_\mu = 0.09$ a constant of the model. This eddy viscosity is then inserted in the RANSE, adding to the molecular viscosity in the diffusion term.

The initial conditions for the $k - \epsilon$ model's TQ are estimated from the following equations:

$$k = \frac{3}{2}(\tilde{v}I)^2 \quad (4.35)$$

$$\epsilon = C_\mu^{3/4} \frac{k^{3/2}}{\mathcal{L}} \quad (4.36)$$

where \mathcal{L} is called the **turbulence length scale**, and represents a characteristic size of the eddies containing most of the turbulence energy, the largest ones. In this study \mathcal{L} will be taken as the integral length scale (see page 114) corresponding to the most energetic eddies¹⁶, which for fully developed

¹⁶The integral length scale corresponds to the maximum of the turbulence energy spectrum of the flow, $E(k)$, expressed as a function of the wave-number k .

turbulent pipe flow is an $\mathcal{O}(1)$ to $\mathcal{O}(10^{-1})$ fraction of the geometric length scale of the flow field (the pipe diameter). Thus it will be assumed

$$\mathcal{L} = 0.1 D$$

The $k - \omega$ turbulence model (see section 4.10.1 and [Wil06]) sets differential equations to determine the quantities k and ω (one equation per quantity), and then uses the calculated values of the fields k and ω to obtain the turbulent eddy viscosity field as

$$\nu_t = \frac{k}{\omega} \quad (4.37)$$

Note that this equation implies the following relationship among k , ϵ and ω

$$\epsilon = C_\mu \omega k \quad (4.38)$$

Finally, it is also convenient to provide an estimate for initial values of the Reynolds stress components. Here it must be distinguished between diagonal components R_{ii} and off-diagonal components $R_{i \neq j}$. Diagonal components can be approximated to

$$R_{ii} \approx \frac{2}{3} \rho k \quad (\text{no sum implied})$$

because ρk is equal to half the (R_{ij}) matrix's trace. The most important off-diagonal component for pipe flow is R_{rz} . This quantity is represented in figure 4.29 of [Wil06] with the notation $-\overline{u'v'}$ (reproduced here as figure 4.1), or $-\langle u'_r u'_z \rangle$ in the notation adopted herein. Leaving aside the zero value at the wall, which is fixed by the boundary conditions, the functional form of R_{rz} could be approximated to a straight line depending on $y = R - r$

$$R_{rz}(r) = -\rho u_\tau^2 \left(1 - \frac{y}{R}\right) = -0.0396 \rho \tilde{v}^2 Re^{-1/4} \frac{r}{R} = -0.0791 \rho \left(\frac{\nu}{D}\right)^2 Re^{7/4} \frac{r}{D}$$

Since the average value of r/D is $1/4$, then an approximate initial value for R_{rz} is given by

$$R_{rz} \approx -0.0198 \rho \left(\frac{\nu}{D}\right)^2 Re^{7/4}$$

It is assumed that the diameter D and the transport properties of the fluid (density ρ and kinematic viscosity ν) are known beforehand. Then the initial conditions for the TQ could be expressed as a function of the estimated Re number as follows:

$$\begin{aligned} I &= 0.2 Re^{-\frac{1}{8}} \\ k &= \frac{3}{2} \left(\frac{Re \nu}{D} I\right)^2 = 0.06 \left(\frac{\nu}{D}\right)^2 Re^{\frac{7}{4}} \\ \epsilon &= 0.0242 \frac{\nu^3}{D^4} Re^{\frac{21}{8}} \\ \nu_t &= 0.0134 \nu Re^{\frac{7}{8}} \\ \omega &= 4.4815 \frac{\nu}{D^2} Re^{\frac{7}{8}} \\ R_{ii} &= -0.04 \rho \left(\frac{\nu}{D}\right)^2 Re^{\frac{7}{4}} \quad (\text{no sum implied}) \end{aligned} \quad (4.39)$$

$$R_{rz} = -0.0198 \rho \left(\frac{\nu}{D} \right)^2 Re^{\frac{7}{4}}$$

The correlations (4.39) are used to fix the initial conditions values of the TQ for all internal mesh-nodes (those not in boundaries). The boundary mesh-nodes are fixed by the boundary conditions. Then the CFD simulation is run and, after not many execution time-steps, the TQ acquire values in the mesh-nodes that are compatible with the Re being attained in the flow at each time-frame. For most CFD simulations, an initial $Re = 10^7$ has been considered, since it corresponds to $\tilde{v} = 2$, a bulk velocity attained after a small number of time steps.

4.5 Near-Wall Modelling

As pointed out by [Geo13], without the presence of walls or surfaces, turbulence in the absence of density fluctuations could not exist. The vorticity-generation effect caused by walls is fundamental to initiate and propagate the turbulence in the flow. Turbulence is particularly concentrated in zones of the flow where shear stress (vorticity) is significantly high. From there it spreads to the rest of the fluid, conditioning the evolution of the physical quantities that describe the flow. Thus, the steepest changes in velocity and other quantities occur in those vorticity-rich zones of the flow, notably near of the walls which are important generators of vorticity. Actually the gradients are so large that very small cell sizes must be adopted in those zones, in order to grasp the rapid changes that take place in the flow's physical quantities, specially the velocity.

The behaviour of wall-bounded turbulent flows is radically different near the walls than it is in the cross-section's centre. As a matter of fact, more than 50% of the total turbulent kinetic energy is produced within the first 5% of radial distance to the wall. Therefore, the flow in this near-wall region conditions completely the overall regime in the pipe. The influence of walls on turbulent pipe flow is masterfully presented and explained in [Tow76]: through the use of relatively simple equations, the author reaches the conclusion that the velocity profile in the core region of the pipe must have a more flattened form than that corresponding to laminar flow.

Fortunately for the physical description of turbulence, the behaviour of any turbulent flow near the walls seems to be quite independent of the flow itself, that is, it appears to be an universal property of all (smooth) turbulent flows to a high degree of approximation. The so-called Law of the wall, or log-law for short, describes the structure of the mean velocity profile in the immediate vicinity of a wall. Thus the CFD model must only take care that the wall-nearest cell in the mesh has its node (centroid) located within the range of applicability of the log-law. If so happens, then the mean velocity at that node could be calculated from an algebraic expression, instead of having to solve a differential equation in an environment of high gradients and rapid changes.

The gradient of most turbulence fields is very significant in the near-wall region. Hence a very fine mesh must be defined therein to fully grasp the steep variation of these quantities, with the attached computational cost. In high Re flows such provisions are usually impractical, beyond current computing capabilities, even for relatively simple geometries. Thus the simulation Engineer must face the prospect of having to model, rather than calculate, the turbulence fields near the wall. The standard procedure to realise that model is through the use of **wall-functions**. The main role of wall-functions is to extend the no-slip boundary condition typical of walls a step further, and to create a new boundary condition at the wall-nearest mesh node instead of the wall itself (see footnote 64 in page 146). With the aid of wall-functions the main turbulence fields are fixed at those wall-nearest nodes, and can be used as an effective boundary condition for the whole flow domain. The fixed field values at those wall-nearest

nodes, are the best replacement to the very steep gradients existing on the wall for all turbulence fields. Therefore, if properly set the wall-functions, there is no need to capture the gradients since they are duly synthesised at the near-wall nodes, or so the theory claims. The main drawback about those new boundary conditions is that one does not know, beforehand, which value they take, as it depends on the flow's friction velocity.

In this section the convention of using the y coordinate to designate the distance from the wall will be followed. Therefore, $y = R - r$ will be written throughout the section to express such distance. The convention also establishes to call y and U the **physical variables**. Note that in this section U refers to the mean velocity component along the flow direction (U_z for pipe flow, since most of the mean velocity develops along the Z axis.). Near the wall the natural dimensionless variables in the configuration space are the so-called **inner variables** or wall coordinates. They are based on the **friction velocity** or shear velocity:

$$u_\tau = \sqrt{\frac{\tau_w}{\rho}} \quad (4.40)$$

which, again, is the natural scale of velocity close to the wall. The natural distance scale is ν/u_τ , called the friction (or inner, or wall) length scale, or also the wall-unit. Both natural scales yield the inner variables:

$$u^+ = \frac{U}{u_\tau} \quad , \quad y^+ = \frac{yu_\tau}{\nu} \quad (4.41)$$

in which the TQ close to the wall should be expressed. Attached to the friction velocity is the friction Reynolds number

$$Re^+ = \frac{u_\tau R}{\nu} \quad (4.42)$$

which is a measure of the pipe radius expressed in the friction length scale. By the same token, other TQ could also be dimensionlessly expressed in this natural scale (see [KMID05])

$$\nu_t^+ = \frac{\nu_t}{\nu} \quad , \quad k^+ = \frac{k}{u_\tau^2} \quad , \quad \omega^+ = \frac{\omega\nu}{u_\tau^2} \quad , \quad \epsilon^+ = \frac{\epsilon\nu}{u_\tau^4} \quad (4.43)$$

As the flow description withdraws from the wall a new set of variables become more suitable for its characterisation. They are called the **outer variables** and are defined by:

$$\check{y} = \frac{y}{\delta} \quad , \quad \frac{U_\infty - U}{u_\tau} \equiv u_\infty^+ - u^+ \quad (4.44)$$

where $\delta = \delta(z)$ is the boundary layer height at longitudinal coordinate z , and U_∞ is the mean velocity at the pipe's centreline. It should be stressed that not every author uses the outer variables as defined in equation (4.44). For instance, [MY71] or [Sch79] use $\check{y} = y/R$ as outer variable, being R the pipe radius. Both are identical far enough from the pipe's inlet in fully developed flow.

Some authors (see [Geo05]) define

$$\delta^+ = \frac{u_\tau \delta}{\nu} = \frac{y^+}{\check{y}} \quad (4.45)$$

as the ratio of inner to outer length scales. It is also called the **local** Reynolds number, since it expresses the height of the turbulent boundary layer in wall-units. Note that $Re^+ = \delta^+$ for fully developed turbulent flows at sufficient distance from the pipe's inlet, as $\delta = R$ in such circumstances.

The turbulent boundary layer thickness δ establishes the outer region length scale, and this is expressed in the definition of the outer variable \check{y} . For fully developed turbulent flow, far away from the pipe's inlet,

δ also represents the mean flow length scale, also known as the integral scale in the turbulence energy wavenumber spectrum. The **overlap layer** (see below) is the region where the flow could be described by either type of variables.

As it will be seen next, a major part of the complication related with wall-bounded flow is caused by the interplay between those two independent length scales, and the distinct structures created by the turbulence in each region is determined by its corresponding length scale, and the interaction and transfer of energy between both types of structures is related to the different character of each length scale: one based on the viscous friction with the wall, the other based on the boundary layer thickness (see [Jim04]).

As it has been established above, the use of wall-functions could be avoided if the mesh were so fine near the wall that everywhere the requirement $y^+ \approx 1$ be satisfied. Thus the large gradients generated by the wall would be duly captured by the FVM algorithm. As that cannot be the case for the transient model presented in this study, the flow's wall-behaviour must be modelled rather than calculated. This is the role played by the wall-functions: to simulate the steep near-wall gradients generated during the flow.

The following example illustrates the necessity of using wall-functions to properly predict the wall-friction generated by the wall-shear stress. Assume for a moment a flow in which:

- No use is made of wall-functions.
- The mesh is not very fine near the wall.

Let y_1 be the height of the first wall-near node in the mesh, and U_1 the mean velocity value calculated by the FVM solver from the no-slip boundary condition and the interpolation algorithm it use. The standard way to calculate the wall-shear stress would be:

$$\tau_w = \mu \left[\frac{\partial U}{\partial y} \right]_{y=0} = \mu \frac{U_1}{y_1} \quad (4.46)$$

because $U = 0$ and $y = 0$ at the wall.

Since the velocity gradient from y_1 to $y = 0$ is much smaller than the actual velocity gradient existing as $y \rightarrow 0$, then the wall-shear stress would be greatly underestimated. If instead of using U_1 as calculated by the solver it could be employed an U_1 provided by a wall-function, then the result for the wall-shear stress would be closer to the real one.

The introduction to the wall-functions require the knowledge of the turbulent boundary layer structure. This is well explained in several excellent reference books ([Sch79], [Whi06], [MY71], [Cha00], [CS74], [Hin75], [Pop00]...), extensively and thoroughly analysed in [Cas97], and here only the main results will be presented without proof. Although some small differences could be found in the development and conclusions of these authors, those do not alter the general structure of the turbulent boundary layer they present. The set of wall-functions introduced herein are found in [Wil06] and [Bre00].

- **INNER REGION** ($y^+ \lesssim 200$)

The viscous (molecular) shear dominates or is not negligible in this region. Most of the energy dissipation in the flow occurs here, and adopts the form of skin friction or wall-friction. In the inner region is valid the inner law

$$u^+ = f(y^+) \quad (4.47)$$

expressed in inner variables. The inner region is divided into the following layers and sublayers, according to the value of y^+ :

– **Viscous layer** ($y^+ < 30$)

The viscous shear plays an important role here. Actually the viscosity must not be negligible as $Re \rightarrow \infty$, if the no-slip condition is to be held as a valid boundary condition for the RANSE (see footnote 64 in page 146). The existence of this layer in the vicinity of a pipe's wall could be interpreted as if the actual turbulent flow were contained in a stationary tube made of the same fluid, with viscous forces acting in the interface. The viscous layer is typically below 1% of the pipe's diameter.

The viscous layer subdivides into:

* **Laminar sublayer** ($y^+ < 5$)

Also called the linear sublayer, because the inner law (4.47) takes the linear form

$$u^+ = y^+ \quad (4.48)$$

The following wall-functions for the TQ can be applied in this sublayer:

$$u^+ = y^+ \quad (4.49)$$

$$k^+ = C_1 y^{+2} \quad (4.50)$$

$$\epsilon^+ = C_2 \quad (4.51)$$

with $C_1 = 0.1$ and $C_2 = 0.2$ (constants for wall-function in the linear sublayer).

* **Buffer layer** ($5 < y^+ < 30$)

Also called the **transition region**. Some authors locate this buffer layer within slightly different limits ($5 < y^+ < 40$, or even $5 < y^+ < 70$).

The wall-functions are intermediate between the ones introduced for the laminar sublayer, and the corresponding to the logarithmic inertial layer to be seen next. According to [SPL⁺99] and [NNO4] the following correlation due to Spalding could be used in this buffer layer:

$$y^+ = u^+ + e^{-\kappa B} \left[e^{\kappa u^+} - 1 - \kappa u^+ - \frac{(\kappa u^+)^2}{2} - \frac{(\kappa u^+)^3}{6} \right] \quad (4.52)$$

which is based on a power-series interpolation scheme joining the laminar sublayer to the logarithmic inertial layer. Clearly this equation adjusts to the general form demanded by the inner law (4.47).

– **Logarithmic inertial layer** ($30 < y^+ \lesssim 200$)

Also called the inertial or log-law layer. It is characterised by a viscous shear stress less than 1% of the Reynolds shear stress, so it can be ignored. Therefore the viscous term in the RANSE is negligible and only the inertial term $\partial \langle u'v' \rangle / \partial y$ from the fluctuating motion remains (v' is the fluctuating component of velocity normal to the wall.). In not too high Reynolds number flows, most of the turbulent energy is generated within this layer (see [Jim04]). The inertial layer extends until the mean convection term in RANSE begins to be important, which happens beyond $\check{y} \gtrsim 0.1$. With a negligible viscous term and a still small

mean convection term, the inertial term is the only one of importance in the inertial layer, and the following approximate relationship holds:

$$u_\tau^2 \approx -\langle u'v' \rangle \quad (4.53)$$

Therefore the Reynolds shear stress is almost constant in this layer.

In the inertial layer the inner law (4.47) adopts the so-called log-law form

$$u^+ = \frac{1}{\kappa} \ln y^+ + B \quad (4.54)$$

with $\kappa = 0.41$ the von Karman's constant, and $B \approx 5.57$ the additive inner layer scaling constant. These values are taken directly from OpenFOAM source code. Since the OpenFOAM suite is the one used herein for 3D CFD simulations, it is deemed suitable to adhere to those values, because later it will be evident the need to compare curves from different sources, including OpenFOAM. Other authors offer slightly different values, notably [ASKS07] have found $\kappa \approx 0.421$ and $B \approx 5.6$ from careful experiments carried out at the Princeton University Superpipe Facility. The von Karman's constant is believed to be universal, since it depends on the properties of the logarithmic inertial layer¹⁷. The additive constant B is determined by means of the no-slip boundary condition at the wall (see [Jim04]). B represents the value assigned to u^+ when $y^+ \approx 1$ and therefore $\ln y^+ \approx 0$. Since equation (4.54) is accurate for $y^+ \gg 1$ and does not reach to describe the viscous layer, the value of B depends on the structure of the buffer and viscous layers and measures the influence caused by such layers on the mean velocity profile. The values offered above are valid only for smooth walls.

Some authors also call this layer the **overlap layer**, because the inner region and the outer region have it in common.

Figure 4.3 shows the velocity profiles obtained from equation (4.54), using the constants κ and B values implemented in OpenFOAM and those found in the paper [ASKS07], for a friction velocity $u_\tau = 1$. The velocity peak in the pipe's centreline is non-physical, as the curve should be flat with value U_∞ in the vicinity of that axis. The [ASKS07] values produce a somewhat flatter velocity profile, actually around 2% smaller.

It is customary, specially in the realm of CFD applications, the use of a slightly different version of the log-law:

$$u^+ = \frac{1}{\kappa} \ln(Ey^+) \quad (4.55)$$

where

$$E = e^{\kappa B} \quad (4.56)$$

it is just the replacement of an additive constant B for a multiplicative one $E = 9.8$.

The following wall-functions for the TQ can be applied in the inertial layer¹⁸:

$$U = \frac{u_\tau}{\kappa} \ln y^+ + B^* = \frac{u_\tau}{\kappa} \ln(Ey^+) \quad (4.58)$$

¹⁷[NC08] discusses that the von Karman coefficient κ is not universal and exhibits dependence on the pressure gradient and flow geometry. Should that statement be true, some aspects of turbulence theory for wall-bounded flows would have to be questioned, and likewise for all modelling efforts carried out for such flows.

¹⁸The meaning of equations (4.58) - (4.62) in CFD is the following (see [Maj02]). Let P be the wall-near node with height coordinate y_P .

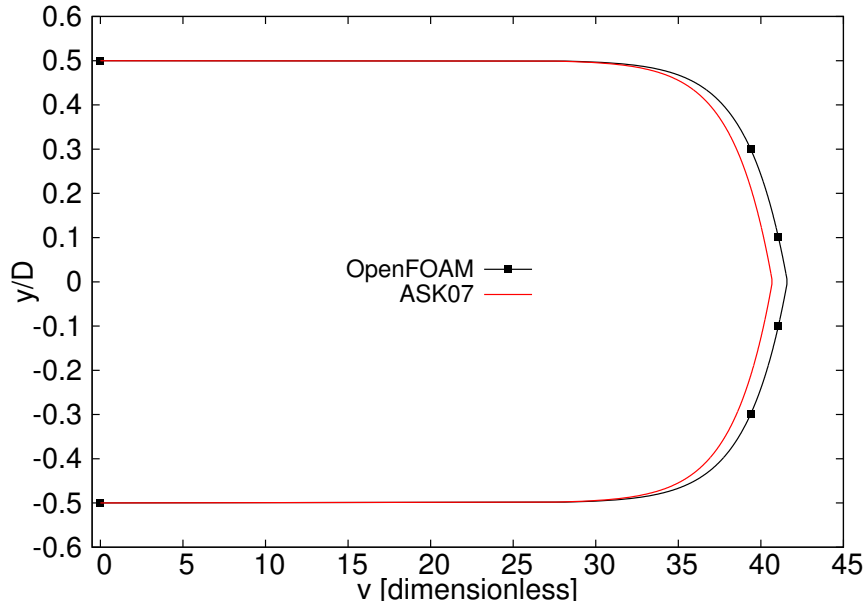


Figure 4.3: Theoretical velocity profiles for κ and B according to OpenFOAM and [ASKS07].

$$k = \frac{u_\tau^2}{\sqrt{C_\mu}} \quad (4.59)$$

$$\omega = \frac{u_\tau}{\sqrt{C_\mu \kappa y}} \quad (4.60)$$

* In the wall-near node P take

$$U_P = \frac{u_\tau}{\kappa} \ln(E y_P^+)$$

* In the same node P make

$$k_P = \frac{u_\tau^2}{\sqrt{C_\mu}}$$

since u_τ and C_μ do not depend on position y .

* Take ϵ in P to be

$$\epsilon_P = \frac{u_\tau^3}{\kappa y_P}$$

* Make ω in P equal to

$$\omega_P = \frac{u_\tau}{\sqrt{C_\mu \kappa y_P}}$$

* Finally the eddy viscosity ν_t in P is

$$\nu_{t_P} = u_\tau \kappa y_P$$

Only the friction velocity u_τ is not known beforehand and must be determined through an iterative algorithm involving the values u_τ , U_P , k_P , ϵ_P , ω_P and ν_{t_P} . When the iterative process is over then the set of TQ is defined in P and this information can be used as a makeshift *boundary condition* to determine the TQ in the second-wall-node, and so on until mesh completion.

The commonly used expression for the shear stress at the wall τ_w , assuming the fields mentioned above are known for the nearest-wall node P , and P is located within the log-law region, is

$$\tau_w = \frac{\kappa C_\mu^{1/4} \rho U_P k_P^{1/2}}{\ln \left(E y_P k_P^{1/2} C_\mu^{1/4} / \nu \right)} \quad (4.57)$$

Note that wall-functions attempt to impose the no-slip condition through a modification of the boundary conditions, not by changing the dynamic equations themselves (see footnote 64 in page 146).

$$\epsilon = \frac{u_\tau^3}{\kappa y} \tag{4.61}$$

$$\nu_t = u_\tau \kappa y \tag{4.62}$$

with $B^* = Bu_\tau$ and $C_\mu = 0.09$ a constant of the $k - \epsilon$ turbulence model adjusted to experimental data (see section 4.10.2).

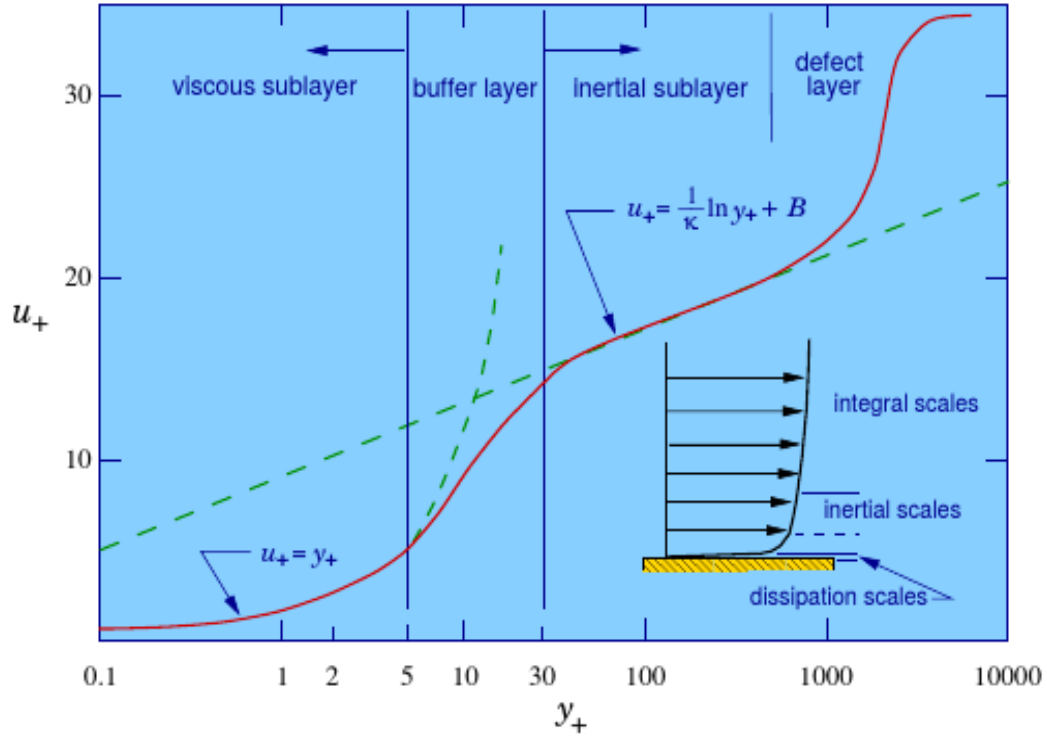


Figure 4.4: Turbulent Boundary Layer according to [McD07].

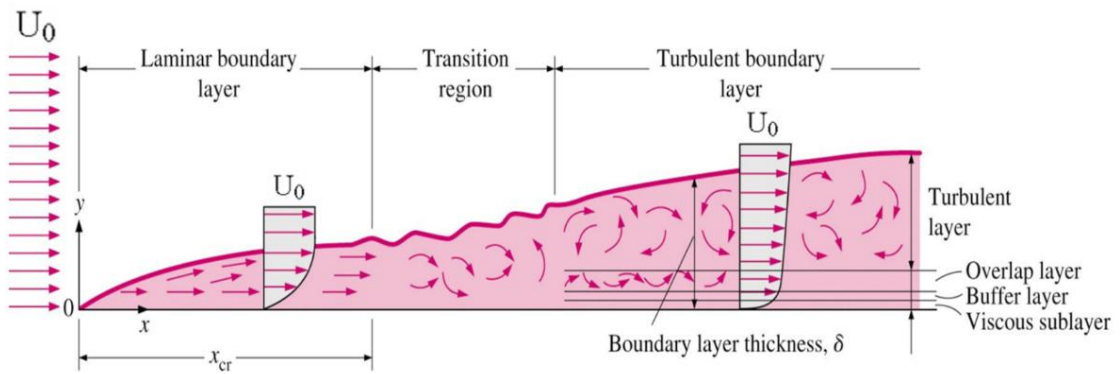


Figure 4.5: Turbulent Boundary Layer evolution.

OpenFOAM employs the following equation to calculate y^+

$$y^+ = y \frac{C_\mu^{1/4} k^{1/2}}{\nu} = y \frac{u_\tau}{\nu} \tag{4.63}$$

where $u_\tau = k^{1/2}C_\mu^{1/4}$ is determined through an iterative algorithm that is executed any time a boundary condition of type wall-function is declared for any TQ. The threshold value for the laminar sublayer in OpenFOAM is

$$y_{lam}^+ = 10.97$$

and corresponds to the y^+ value for which the laminar and log-law velocity profiles intersect each other. For each cell having a face declared as wall boundary, herein called near-wall node, the solver calculates y^+ and according to the result assigns the following values to the TQ of said wall-node:

- Case $y^+ < y_{lam}^+$. In this case the solver considers the flow as laminar for that near-wall node and makes

$$u^+ = y^+, \quad k = 0, \quad \epsilon = 0, \quad \nu_t = 0, \quad \omega = 0$$

- Case $y^+ \geq y_{lam}^+$. In this case the solver considers the flow as turbulent for that near-wall node, and with the calculated $u_\tau = k^{1/2}C_\mu^{1/4}$ value makes

$$u^+ = \frac{1}{\kappa} \ln(Ey^+), \quad k = \frac{u_\tau^2}{\sqrt{C_\mu}}, \quad \epsilon = \frac{u_\tau^3}{\kappa y}, \quad \nu_t = u_\tau \kappa y, \quad \omega = \frac{u_\tau}{\sqrt{C_\mu \kappa y}}$$

- **OUTER REGION** ($y^+ \gtrsim 100$)

The outer region can be defined as that part of the turbulent boundary layer where viscous shear stress is negligible and, therefore, the viscous diffusion term can be dropped from the RANSE. On the other hand, the turbulence shear stress is of importance since it is the mean convection term. Besides, the flow in this region is sensitive to the mean pressure gradient $\partial P/\partial z$, and it will appear in the equations for the mean velocity U in the form of a dimensionless parameter ξ which will be defined below.

The relevant length scale at that distance from the wall is the boundary layer thickness itself δ , since the turbulent structures developed therein have a typical size limited by δ . The outer region is naturally described using outer variables, as the flow fields scale with $\check{y} = y/\delta$. The scale separation between the inner and outer regions is given by the following Reynolds number (see equation (4.45))

$$\delta^+ = \frac{\delta u_\tau}{\nu}$$

which measures the ratio of the natural outer length scale δ to the natural inner length scale ν/u_τ .

In the outer region is valid the **Outer Law**

$$U = U_\infty - u_\tau g(\check{y}, \xi) \tag{4.64}$$

with

$$\xi = \frac{\delta}{\tau_w} \frac{\partial P_e}{\partial z} \tag{4.65}$$

being P_e the mean pressure at the pipe's centreline, and $\partial P_e/\partial z$ the local mean pressure gradient. The outer law is often called the **velocity-defect law** because $u_\infty^+ - u^+$ is the defect velocity or retardation of the flow due to wall effects.

The outer law is not always presented as it has just been done in this work. According to [Geo05], three different formulations have been established for the velocity defect-law

$$\frac{U - U_\infty}{u_\tau} = g(\check{y}, \delta^+, *) \quad (\text{von Karman}) \quad (4.66)$$

$$\frac{U - U_\infty}{U_\infty} = g(\check{y}, \delta^+, *) \quad (\text{George \& Castillo}) \quad (4.67)$$

$$\frac{U - U_\infty}{U_\infty} = \frac{\delta_*}{\delta} g(\check{y}, \delta^+, *) \quad (\text{Zagarola \& Smits}) \quad (4.68)$$

where '*' means 'other factors', and δ_* is the **displacement thickness** defined as

$$\delta_* = \int_0^\infty \left(1 - \frac{U}{U_\infty}\right) dy \quad (4.69)$$

The von Karman formulation is most widespread, and it is the one this study herein adheres to. It can be proven that, in any of the formulations above, the function $g(\check{y}, \delta^+, *)$ is generally small and U is almost constant in this region ($U \approx U_\infty$). Therefore the mean velocity profile in the pipe is almost flat, except for the wall-near region where it satisfies the log-law.

Equation (4.64) is not very practical for actual CFD applications. An alternative equation also valid in the outer region is the **Coles' Law of the Wake** given by (see [Col56], [Jim04] or [Whi06])

$$u^+ = \frac{1}{\kappa} \ln y^+ + B + \frac{2\Pi}{\kappa} W\left(\frac{y}{\delta}\right) = \frac{1}{\kappa} \ln y^+ + B + \frac{2\Pi}{\kappa} W(\check{y}) \quad (4.70)$$

where $W(y/\delta) \equiv W(\check{y})$ is the **wake function**, with values

$$W(0) = 0, \quad W(1) = 1, \quad 0 \leq W(\check{y}) \leq 1$$

and Π is called the **Coles' wake parameter** which varies with the pressure gradient ξ . Note the law of the wake is expressed with both, inner y^+ and outer \check{y} variables.

The wake function $W(\check{y})$ represents the deviation of the mean velocity profile from the log-law observed in the outer layer. This deviation is generally small for pipes and channels, since the wake term $2\Pi W(\check{y})/\kappa$ is $\mathcal{O}(1)$ in such cases. Thus, the logarithmic inertial layer defined by equation (4.54) is responsible for some 80% of the overall mean velocity difference observed across the whole boundary layer, from 0 at the very wall to U_∞ at the centreline (see [Jim04]). This percentage increases with growing δ^+ .

The wake term for $\check{y} = 1$, conventionally normalised to $2\Pi/\kappa$, measures the contribution of the outer layer flow to the mean velocity profile, just in a similar way that B in equation (4.54) measures the influence of the near-wall layer on said mean velocity profile (see [Jim04]). In his paper [Col56] Coles interprets the deviation as a manifestation of a large-scale mixing process similar to that of the flow in a wake, in that it is constrained primarily by inertia rather than by viscosity.

[Whi06] proposes for $W(\check{y})$ a 'S' shape curve given approximately by any or the two following expressions:

$$W(\check{y}) \approx \sin^2\left(\frac{\pi}{2}\check{y}\right) \approx 3\check{y}^2 - 2\check{y}^3 \quad (4.71)$$

A considerably more sophisticated expression for $W(\check{y})$ could be found in [NC08], with special application to pipe and channel flows. [NC08] also introduces a single composite velocity profile for the turbulent boundary layer which is not without interest. The accuracy of those approximations for the actual $W(\check{y})$ depends on the type of flow being considered.

The outer region comprises the following layers:

- **Logarithmic overlap layer** ($y^+ \gtrsim 100$, $\check{y} \lesssim 0.1$)

The lower part of this layer is also conventionally included within the logarithmic inertial layer, therefore it is a shared zone between the inner and the outer regions, hence the name *overlap* layer. The distinction between logarithmic inertial layer and logarithmic overlap layer is somewhat artificial and it is not remarked by many authors. In this layer the log-law is quite accurate, as the main assumptions for its derivation are valid within that range.

The wall-functions corresponding to this layer are also represented by equations (4.58)-(4.62), although the accuracy tends to diminish as the distance to the wall increases.

- **Outer layer** ($\check{y} \gtrsim 0.1$)

In this part of the turbulent boundary layer the mean velocity follows with reasonable accuracy the velocity-defect law (4.64). But, contrary to the other layers, herein there is no universality regarding the function $g(\check{y}, \xi)$, whose form is derived in each case to fit experimental data. Thus there exists no, *a priori*, valid function $g(\check{y}, \xi)$ which could be generally implemented in a CFD code to attend to any foreseeable turbulent flow.

Therefore, it has traditionally been considered bad practice to locate the first wall-node in the mesh within the outer layer, since no general wall-function is available with sufficient accuracy, because the node is too far from the wall. As a consequence, if the nearest wall-node falls in this outer layer, it would be very difficult for the CFD model to reproduce the wall-shear stress and skin friction measured in the actual turbulent flow.

Should the logarithmic inertial layer for the actual flow be so thin that it would be very costly to reach it with the first wall-node, then it is possible to use the law of the wake (4.70) to provide a mean velocity value for a wall-node seating at the outer layer. In that case any of the approximations given by equation (4.71) could be used for the wake function $W(\check{y})$, and hope for it to be accurate enough. If the wall-shear stress or skin friction measured in the actual turbulent flow do not match the simulations results, then some modifications must be introduced in the approximations (4.71).

It should be pointed out that questions have arisen regarding the validity of the universal law of the wall for very high Re (see [M⁺10], [Geo05], [Geo07]), at least in the form it has traditionally been accepted. The value of the constants κ and B , as well as the reach of the logarithmic overlap layer, might not be as stated in orthodox textbooks for such high Re .



Once the general structure of the turbulent boundary layer has been described, it is pertinent to explain the general method to obtain a CFD model which can simulate with reasonable accuracy the wall-shear stress attached to a high Re flow.

The method of wall behaviour simulation through the use of wall-functions, in order for it to be accurate enough, requires that the first near-wall node be located within the buffer layer of the wall boundary

layer, corresponding to approximately $5 < y^+ < 30$, or in the lower logarithmic inertial layer $30 < y^+ \lesssim 100$, give or take some wall-units, and then the wall-shear stress is determined through equations (4.58)-(4.62). Therefore it is important to select an appropriate y^+ value, combined with the right turbulence model.

A general method will be presented next to calculate the correct first cell height y based on the desired y^+ value. This is an important first step in any CFD turbulence simulation, since the global mesh resolution will also be affected by this near-wall mesh, as well as by Re and the domain geometry. The subsequent steps are the selection of the differencing method for each term of the RANSE and other governing equations for the TQ ($k, \epsilon, \omega, \dots$), and the iteration algorithm to solve the sparse matrices obtained through the FVM application. But those subsequent steps will be dealt with later.

The proposed general method to find the right first wall-cell height is:

- Resolving the laminar sublayer.

This involves the full resolution of the turbulent boundary layer and is required where wall-bounded effects are a high priority in the simulation, for instance in cases with adverse pressure gradients, aerodynamic drag, pressure drop, skin friction, surface heat transfer... Of course, in such cases the simulation is limited to moderate Re .

Wall adjacent grid height must be $y^+ = \mathcal{O}(1)$ in wall-units. An appropriate low- Re turbulence model must be selected, like Launder-Sharma $k - \epsilon$ or the Shear Stress Transport Model (SSTM). In that case it is not necessary to use wall functions, since the interpolation algorithm will provide the right value from the boundary conditions, due to the linearity reigning in this sublayer.

- Adopting a wall function grid.

This method involves modelling the turbulent boundary layer using a log-law wall function (4.58). This approach is suitable for cases where wall-bounded effects are of secondary importance, or the flow undergoes geometry-induced separation (such as bluff bodies immersed in a stream), or Re is so high that it is impractical to reach the laminar sublayer. Wall adjacent grid height should ideally reside in the log-law region where $30 < y^+ \lesssim 100$, and most turbulence models are readily applicable (e.g. SSTM or $k - \epsilon$ with scalable wall-functions).

- Height estimation.

The first wall-node of the mesh must be positioned during the pre-processing stage, before deciding the actual mesh characteristics. Since the node is located at the centroid of the cell, the problem is equivalent to calculate the first cell height (Δy_1), because the node height is $y_1 = \Delta y_1/2$. The wall-near node height in wall-units is y_1^+ , and it would be convenient for it to fall within the desired range (eg. the logarithmic inertial layer). The computed flow-field will dictate the actual y^+ value which in reality will vary along the wall, as it depends on the friction velocity u_τ . In some cases, it might be necessary to locally refine the mesh in order to achieve the desired y^+ value in all regions. The procedure to calculate y_1 is as follow:

- Select a suitable value for y_1^+ , so that it falls within the desired layer. For example, $y_1^+ = 80$ for the logarithmic inertial layer.
- Calculate the Reynolds number Re for the flow model, based on the characteristics scales and dimensions of the domain geometry L , on the expected free-stream or centreline mean velocity U_∞ , or the bulk velocity \tilde{U} , and, of course, on the fluid kinematic viscosity ν . The

characteristic length L may be taken as the pipe diameter, the channel width, the body length, etc.

- iii. Estimate the wall-shear stress τ_w for the model. It need not be an accurate calculation. A good practice is to find τ_w from the skin friction coefficient C_f , also called the Fanning friction factor, such that ¹⁹

$$\tau_w = \frac{1}{2} C_f \rho \tilde{U}^2 \quad \text{or} \quad \tau_w = \frac{1}{2} C_f \rho U_\infty^2$$

C_f can in turn be estimated from two empirical correlations:

- INTERNAL FLOWS: Blasius correlation (4.24) for internal flows, which is repeated here:

$$C_f = 0.0791 Re^{-1/4}$$

- EXTERNAL FLOWS: a simplified form of Fernholz correlation is proposed for external flows (see [Sch79]):

$$C_f = 0.0576 Re^{-1/5} \quad (4.72)$$

These estimates should pose no problem, since Re has already been obtained in the previous step. Therefore, from C_f it is possible to compute τ_w , and from it the friction velocity $u_\tau = \sqrt{\tau_w/\rho}$.

- iv. With the friction velocity just obtained, calculate the height of the near-wall node as $y_1 = \nu y_1^+ / u_\tau$. The near-wall cell height should then be $\Delta y_1 = 2y_1$. From this cell it is then possible to construct the rest of the mesh, probably with some grading to have refined mesh in the vicinity of the wall.
- v. If the model has a simple geometry, and the flow is not complex, this method should yield quite accurate positions for the near-wall node, meaning that the actual y^+ value obtained from the CFD simulation be very similar to the y_1^+ value calculated herein. However, if the model has a complex geometry or a complicated flow pattern, then it might be necessary to refine the mesh in the vicinity of the wall to attain the desired y^+ value. A good practice is to input these values into the CFD model, execute the solver for a short time until the flow reaches some stability, read the y^+ values provided by the solver, and readjust the mesh accordingly. After a few such steps a good quality mesh should have been created for the model.

The actual first wall-node height for the CFD simulation conducted in this work will be shown in section 4.6.

The application of wall-functions to some of the most widely used turbulence models based on RANSE is well explained in [KMID05]. It is the main method to tackle with the intense gradients generated at the wall in turbulent flows, when employing RAS model. Since turbulence models based on FNSE (i.e. LES models) should not be applied in the proximity of walls, being instead necessary the use of hybrid RAS-LES models for such cases, then it must be concluded that inserting wall-functions into the code of RAS models is generally an acceptable method for any CFD simulation, be it RAS or LES.

¹⁹For pipe flow, it could found in the references in both forms:

$$\tau_w = \frac{1}{2} C_f \rho \tilde{U}^2 \quad \text{and} \quad \tau_w = \frac{1}{2} C_f \rho U_\infty^2$$

Herein, the first one is preferred.



Use of wall-functions is not the only way to deal with the no-slip boundary condition in CFD. It has been explained that wall-functions attempt to introduce some modifications in the boundary conditions, so that they extend a bit farther, to the first wall-node; but they do not intend to alter the dynamic equations themselves.

There also exists another method to insure the TQ satisfy the requested behaviour near the wall: introducing some (artificial) changes in the dynamic transport equations that govern the TQ. These changes take the form of so-called **damping functions** (see [Maj02], [Bla05] or [Wil06]). Damping functions represent a different proposal to approach the problem of simulating the behaviour of fluids near the walls. They will be made explicit for some turbulence models in section 4.10.

An example will serve to illustrate the rationale behind the use of damping functions, to reproduce the high gradients attained in the viscous sublayer and the logarithmic inertial layer within the turbulent boundary layer.

In this example attention is drawn to a couple of TQ, namely the specific average turbulence kinetic energy k and the specific turbulent energy dissipation rate ϵ . These fields are the basis for the so-called $k - \epsilon$ turbulence model. The exact dynamic transport equations for those fields are derived from RANSE and they present the following expression *à la* ensemble average (see [Hin75], [Pop00] or [Wil06], and specially [MKM87]).

$$\partial_t k + U_j \partial_j k = -\frac{1}{\rho} \partial_i \langle u'_i p' \rangle - \frac{1}{2} \partial_i \langle u'_j u'_j u'_i \rangle + \nu \partial_j \partial_j k - \langle u'_i u'_j \rangle \partial_j U_i - \nu \langle \partial_j u'_i \partial_j u'_i \rangle \quad (4.73)$$

$$\begin{aligned} \partial_t \epsilon + U_j \partial_j \epsilon = & -2\nu \left[\left(\langle \partial_k u'_i \partial_k u'_j \rangle + \langle \partial_i u'_k \partial_j u'_k \rangle \right) \partial_j U_i + \langle u'_k \partial_j u'_i \rangle \partial_k \partial_j U_i + \right. \\ & \left. + \langle \partial_k u'_i \partial_l u'_i \partial_l u'_k \rangle + \nu \langle \partial_k \partial_l u'_i \partial_k \partial_l u'_i \rangle - \frac{1}{2} \partial_j \left(\partial_j \epsilon - \langle u'_j \partial_l u'_i \partial_l u'_i \rangle - \frac{2}{\rho} \langle \partial_l p' \partial_l u'_j \rangle \right) \right] \end{aligned} \quad (4.74)$$

with the following meaning for the terms of the k transport equation ²⁰:

- Turbulence production

$$\mathfrak{P} = -\langle u'_i u'_j \rangle \partial_j U_i$$

- Turbulence dissipation

$$\epsilon = -\nu \langle \partial_j u'_i \partial_j u'_i \rangle$$

- Turbulent transport

$$\mathcal{T} = -\frac{1}{2} \partial_i \langle u'_j u'_j u'_i \rangle$$

- Molecular viscous transport or molecular diffusion

$$\nu \partial_j \partial_j k$$

²⁰The terms in the ϵ equation are too complex to have a physical meaning that could be highlighted herein. Nevertheless, [MKM87] is recommended for a characterisation of each term.

- Turbulent pressure diffusion

$$-\frac{1}{\rho} \partial_i \langle u_i p' \rangle$$

On the other hand, it is known (see [Bla05] or [Maj02]) that the asymptotic behaviour of the TQ as they approach the wall is given by

$$U_i \sim y \quad k \sim y^2 \quad \epsilon \sim y^0 \equiv 1 \quad \nu_t \sim y^3 \quad \frac{\epsilon}{k} \sim \frac{2\nu}{y^2} \quad \langle u_i' u_j' \rangle \sim y^3 \quad (i \neq j) \quad (y \rightarrow 0) \quad (4.75)$$

where y denotes, as usual, the coordinate normal to the wall.

Instead of attempting to introduce the complicated equations (4.73) and (4.74) in a CFD solver, the proposed method aims to transform, somewhat artificially, those equations into simpler ones that still could retain some of the dynamics of turbulence, while their solutions satisfy the limiting behaviour shown in the expression (4.75). The modified equations make use of the Boussinesq's hypothesis, but what really matters here is the appearance of a new set of functions, the damping functions, which condition the solution to provide the expected result in the viscous sublayer on the wall (see [MKM87]). The resulting $k - \epsilon$ turbulence model thus derived is apt for simulating low Reynolds number flows, since the standard no-slip boundary conditions suffice to provide solutions satisfying the near-wall profiles, with no additional hypothesis (see footnote 64 in page 146). Thus the $k - \epsilon$ models with damping functions are also collectively called low- Re turbulence models.

The low- Re $k - \epsilon$ model used in this work is known as the Launder-Sharma $k - \epsilon$ model (see [LS74]), defined by the equations:

$$\partial_t k + U_i \partial_i k = \mathfrak{P} - \epsilon + \partial_i \left[\left(\nu + \frac{\nu_t}{\sigma_k} \right) \partial_i k \right] \quad (4.76)$$

$$\partial_t \tilde{\epsilon} + U_i \partial_i \tilde{\epsilon} = C_{\epsilon 1} f_1 \frac{\tilde{\epsilon}}{k} \mathfrak{P} - C_{\epsilon 2} f_2 \frac{\tilde{\epsilon}^2}{k} + \partial_i \left[\left(\nu + \frac{\nu_t}{\sigma_\epsilon} \right) \partial_i \tilde{\epsilon} \right] + \mathfrak{E} \quad (4.77)$$

$$\epsilon = \tilde{\epsilon} + \mathfrak{D} \quad (4.78)$$

$$\nu_t = C_\mu f_\mu \frac{k^2}{\tilde{\epsilon}} \quad (4.79)$$

with \mathfrak{P} the already introduced production term; C_μ , $C_{\epsilon 1}$, $C_{\epsilon 2}$, σ_k , σ_ϵ are constants, and the five factors f_μ , f_1 , f_2 , \mathfrak{D} and \mathfrak{E} are collectively known as the **damping functions**. The damping functions depend on Re and y , are determined empirically for each type of low- Re turbulence model (for example, Launder-Sharma), and are meant to assure the proper limiting behaviour of k and ϵ at the wall. The reader is referred to [Wil06] for a full set of damping functions for the most used low- Re $k - \epsilon$ models.

Note the conspicuous difference between equations (4.73)-(4.74) on one hand, and equations (4.76)-(4.77) on the other. This last set of equations could feasibly be programmed in a CFD code, and have the possibility of generating turbulence fields which would serve as acceptable simulations of actual flows. The turbulence models which use damping functions will be called **dampened turbulence models** in this work.

Note also that equation (4.77) refers to $\tilde{\epsilon}$ while (4.76) involves the true specific turbulent energy dissipation rate ϵ . The difference between both has been called \mathfrak{D} , which is the value of the dissipation rate at the wall and represents an offset for ϵ . Therefore, $\tilde{\epsilon}$ is the dissipation rate that occurs above the

level attained at the wall. Is typical of dampened models to work with $\tilde{\epsilon}$ instead of ϵ . The term \mathfrak{E} in equation (4.77) receives the name of **explicit wall-term** (see [Bla05]), and it is supposed to condition the behaviour of $\tilde{\epsilon}$ near the wall.

The reader would have probably noticed the modified expression (4.79) for ν_t , instead of the most familiar one (4.34) which is reproduce herein.

$$\nu_t = C_\mu \frac{k^2}{\epsilon}$$

The altered definition of the eddy viscosity is one of the changes introduced in the Low- Re models that distinguish them from the standard $k - \epsilon$ model. The Launder-Sharma $k - \epsilon$ model presents differences respect to the standard $k - \epsilon$ turbulence model which are beyond the scope of this section ²¹.

It would also have been noticed that low- Re turbulence models are hardly applicable to the transient case which is being presented in this work, characterised by very high Re . According to what herein has been explained, it would seem so. The main conclusion of the damping function approach to the near-wall turbulence problem, is that with such models there is no need to use special boundary conditions, like those represented by the wall-functions, since dampened turbulence models predict by themselves the behaviour of the flow near the walls, with the sole use of standard no-slip boundary conditions.

The simulations carried out in this work, though, has made use of both resources: a dampened turbulence model with wall-functions to properly simulate the friction on the walls. The dampened model which has performed best is the Launder-Sharma $k - \epsilon$. Although this use of the dampened model is beyond the original purpose of its authors, [LS74], the simulation has attained an acceptable quality whose results will be presented in section 4.10.2. It seems that the combined effect of both approaches works reasonable well in the case of transient high Re flows.



The *universal* law of the wall seen so far is only valid provided the duct's walls are smooth enough. Wall-roughness has an important influence on turbulent flow which must be duly taken into account whenever such conditions cannot be ignored. Rough-wall turbulent boundary layer is more complex and still harbours many unanswered questions to be of straightforward application into CFD. The problem of rough-wall boundary layer is very well presented in the like-named paper [Jim04], in [MY71] or in [Tow76], among other classical references.

In page 225 it was mentioned that the existence of the viscous layer permits to consider the turbulent flow within a pipe as if it were flowing through a stationary tube made of the same fluid, with viscous forces acting in the interface. Again, this statement is true as long as the pipe is sufficiently smooth, that is, the wall-roughness is not so high to disrupt the laminar sublayer within the viscous layer. The remainder of this section is devoted to introduce the concepts that permit to characterise the wall-rough flow, the models which have been developed to predict and explain its behaviour, and the translation such models might have into CFD codes in general, and OpenFOAM in particular.

The first point to remark is that there is not a unique way to characterise roughness, since at least two quantities could be used for that: the dimensionless effective or equivalent sand roughness ζ_s^+ and the roughness function Δu^+ , and some authors even add a third one, the dimensionless roughness length ζ_0^+ . All these quantities are going to be introduced and explained in the coming paragraphs.

²¹The differences are not limited to the appearance of the five damping functions, the use of $\tilde{\epsilon}$ instead of ϵ and the newly defined eddy viscosity.

Let ζ_r be the average height of the roughness protrusions in the wall as measured with a micrometer, also called the **absolute roughness**²². For example, in standard Schedule-40 or Schedule-80 steel pipe, very much used in fire extinction applications with clean agents, the typical absolute roughness is $\zeta_r = 4.5 \times 10^{-5} \text{ m}$ (see [RH12]), while according to the AFTA Manual (<http://www.afta-asociacion.com/>) the galvanised steel pipe (also employed in FPE applications) has an absolute roughness of about $3.3 \times 10^{-5} \text{ m}$. In the dimensionless units used herein, $\zeta_D = \zeta_r/D = 1.125 \times 10^{-3}$ and $\zeta_D = \zeta_r/D = 8.25 \times 10^{-4}$, respectively, for the standard pipe (see page 59).

ζ_r acts like a length scale for rough-walled flows. If ζ_r is not negligible compared to the friction length scale ν/u_τ , then the rough character of the wall must be taken into account. The average protrusion height is conveniently expressed in wall units as:

$$\zeta_r^+ = \frac{\zeta_r u_\tau}{\nu} \quad (4.80)$$

and is called the **roughness Reynolds number**. For $\zeta_r^+ \gtrsim 4$ the buffer-layer is perturbed and some of the features that have just been studied become modified by the presence of roughness. For $\zeta_r^+ \gtrsim 60$ the buffer-layer is almost absent. Therefore, in general terms ζ_r^+ determines what the buffer-layer would be like.

According to the value of ζ_r^+ the regime of a turbulent flow could be divided into (see [MY71] or [Whi06])

$$\begin{aligned} \zeta_r^+ < 4 & \text{ hydraulically smooth flow} \\ 4 \leq \zeta_r^+ \leq 60 & \text{ transitional - rough flow} \\ \zeta_r^+ > 60 & \text{ fully rough flow} \end{aligned} \quad (4.81)$$

Other authors establish the fully rough flow for $\zeta_r^+ > 70$, and even for $\zeta_r^+ > 90$, but the principle is similar. Note that a hydraulically smooth flow corresponds roughly to that flow whose laminar sublayer $y^+ < 5$ is still above the average roughness protrusions of the wall $\zeta_r^+ < 4$, since both y^+ and ζ_r^+ are measured in the same wall units. It should be remarked that [Jim04] challenges the interpretation that $\zeta_r^+ < 4$ imply hydraulically smooth flow.

Therefore, as the flow Reynolds number increases so does the roughness Reynolds number ζ_r^+ and the flow itself evolves from hydraulically smooth to transitional-rough and to fully rough, with the same absolute wall roughness. This effect is explained in figure 4.6, where δ_L is the height of the laminar sublayer corresponding to the flow's Reynolds number, while ζ_r is the average height of roughness protrusions²³. The flow will be considered hydraulically smooth as long as the wall-roughness height

²²It is customary to denote by k and k^+ the average roughness height and its dimensionless counterpart, and thus can be seen in most references. In this Dissertation, though, it is preferred to reserve k for the turbulence kinetic energy.

²³In practical terms, the height of the laminar sublayer could be found through the Darcy-Weisbach friction factor f in the following way (since $y^+ \approx 5$ marks the limits of the laminar sublayer):

$$\delta_L = 5 \frac{\nu}{u_\tau} = 5\nu \sqrt{\frac{\rho}{\tau_w}} = 5\nu \sqrt{\frac{\rho}{\frac{f}{8} \rho \tilde{v}^2}} = 5 \frac{\nu}{\tilde{v}} \sqrt{\frac{8}{f}}$$

with \tilde{v} the bulk velocity of the flow. Therefore, the laminar sublayer height could be estimated at

$$\delta_L \approx \frac{5D}{Re} \sqrt{\frac{8}{f}} \quad (4.82)$$

with D the pipe's diameter. Aided with the Moody chart it is easy to get all those values for a given flow. δ_L decreases rapidly with increasing Re .

ζ_r^+ is smaller than the thickness of the laminar sublayer $\delta_L^+ \approx 5$, because then it will have a negligible influence on the viscous layer and, for extension, on the outer turbulent flow. In such conditions a turbulent flow would be directly comparable with a laminar flow in that the pressure drop along the pipe is a function of the properties of the fluid, the mean velocity and the diameter, with no regard to other factors. Thus in hydraulically smooth turbulent flows, at the same Reynolds number, all fluids appear to behave in a similar way regardless of its composition and nature, that is, they seem to share the same mean turbulence patterns.

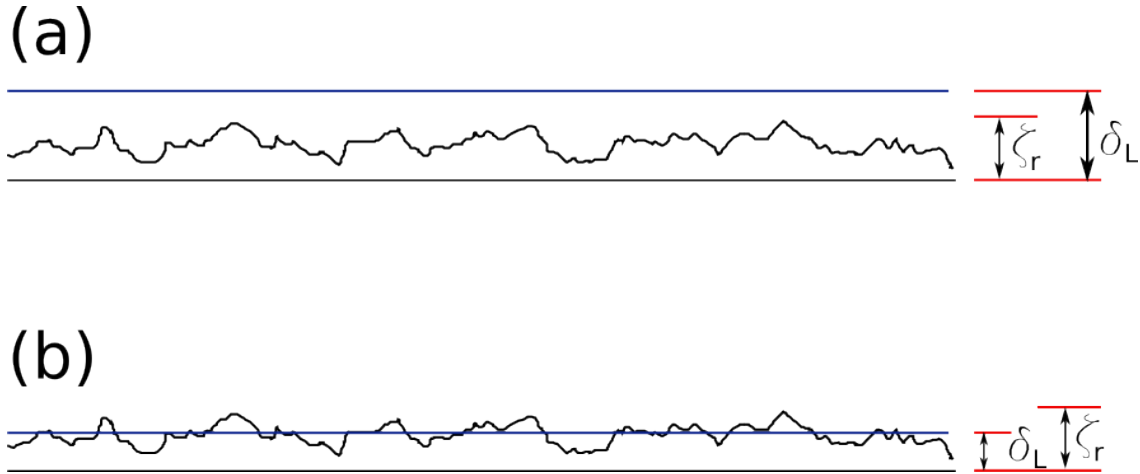


Figure 4.6: (a) Low Re , the pipe is considered smooth; (b) high Re , it behaves as rough.

In fully rough flow the laminar sublayer is missing, since it would be located well within the wall-roughness, the viscous layer is almost absent and hardly deserves such name, and the near-wall flow is constituted mostly by eddies created around each wall protrusion, which propagate into the core flow adding intensity to the turbulent mixing. The resulting mean velocity profile does not depend on the viscosity ν . In such conditions the pressure drop along the pipe is independent of viscosity, and starts to depend on the wall-roughness measured in terms of the equivalent sand roughness (see below), rather than in the physical roughness height itself. The outstanding work of Nikuradse in [Nik50] demonstrates that beyond certain point the Darcy-Weisbach friction factor f becomes independent of Re , and only responds to variations in wall roughness. Therefore the pressure drop along the pipe depends on wall roughness instead of the properties of the fluid.

The most ubiquitous effect of roughness in the turbulent flow is the modification of the mean velocity profile in the vicinity of the wall, with the attached effect of changing the wall-shear stress and the skin friction coefficient.

From Nikuradse's experiments with sand-roughened pipes (see [Nik50]), emerged a new velocity profile which could be approximately defined as

$$u^+(y) = \frac{1}{\kappa} \ln \left(\frac{y}{\zeta_s} \right) + 8.5 + \frac{2\Pi}{\kappa} W \left(\frac{y}{\delta} \right) \quad (4.83)$$

which is valid in the overlap layer and outer region of the turbulent boundary layer. It is worth remarking that the von Karman's constant is still valid in the case of rough walls, since it is not affected by roughness, and that u^+ is no longer a function of y^+ , but of y instead²⁴ The validity of von Karman's

²⁴The dependence of u^+ on y was also seen in the law of the wake, equation (4.70), so it might be considered a similar situation at first sight. But the law of the wake is only applicable to the outer layer of smooth flows, and in equation (4.70) u^+ still retains a dependence on y^+ . Thus the situation is not comparable.

constant means that the velocity profile maintains the same slope, namely $1/\kappa$, than in the smooth wall case, and thus the resulting mean velocity profile should be parallel to that obtained from equation (4.54) or (4.70).

Equation (4.83) is considered the functional definition of the **equivalent** or **effective sand roughness** ζ_s of the wall. Thus absolute roughness ζ_r is measured by the actual mean size of surface protrusions, while the equivalent sand roughness ζ_s adopts the value which provides the best fit of expression (4.83) with experimental data. ζ_s is a property of the flow, while ζ_r is a property of the surface texture. In principle, they are of the same order of magnitude, but different. From ζ_s stems $\zeta_s^+ = \zeta_s u_\tau / \nu$, which is used to characterise roughness. In the fully rough regime the pressure drop along the pipe, that is the Darcy-Weisbach friction factor f , depends on ζ_s^+ rather than on Re . Thus the measurement of pressure drop provides a method for quantifying the surface roughness though its effect on the turbulent flow, yielding ζ_s , instead of directly measuring the surface texture, yielding ζ_r .

An alternative expression for u^+ is given by:

$$u^+(y) = \frac{1}{\kappa} \ln y^+ + B + \frac{2\Pi}{\kappa} W\left(\frac{y}{\delta}\right) - \Delta u^+ \quad (4.84)$$

Note that now u^+ depends on y^+ and y/δ . Actually the first three terms correspond to the law of the wake for smooth walls (4.70), and the expression for u^+ is corrected by an additional term Δu^+ called the **roughness function**, which represents a downward shift in the law of the wake equation (see [SF07]). Note that for the logarithmic inertial layer the wake function $W(y/\delta)$ is negligible and can be removed from equation (4.84) even for rough walls. In that case the roughness function Δu^+ represents a down shift in the log-law for smooth walls (4.54).

[Jim04] still suggests another equation for the mean velocity profile in rough-walled flows:

$$u^+(y) = \frac{1}{\kappa} \ln\left(\frac{y}{\zeta_o}\right) + \frac{2\Pi}{\kappa} W\left(\frac{y}{\delta}\right) \quad (4.85)$$

with

$$\zeta_o = 0.033\zeta_s \quad (4.86)$$

representing the so-called **roughness length**. Either of these quantities ζ_s^+ , Δu^+ or ζ_o^+ characterises the roughness equally well.

The effect of roughness on the mean velocity profile is limited to the inner region (see [SF07]), and represents a shift of the curve in both axis y^+ and u^+ , as it can be seen in figure 4.7 taken from figure 4.25, page 128 of [Ceb13], where the meaning of the offset Δu^+ is explained. The logarithmic inertial layer still exists but, as ζ_r^+ increases, the effective intercept B moves downward in an amount given by Δu^+ , while the effective wall position begins to move outward by

$$\Delta y^+ \approx \ln \zeta_r^+ \quad (4.87)$$

Δu^+ does not only depend on ζ_r^+ , but also on the type and geometry of roughness in a very elaborate way. [Whi06], [Jim04] or [Ceb13], to name just a few, offer slightly different expressions for Δu^+ , like

$$\Delta u^+ \approx \frac{1}{\kappa} \ln \zeta_r^+ - 3.5, \quad \Delta u^+ \approx \frac{1}{\kappa} \ln(1 + 0.3\zeta_r^+), \quad \Delta u^+ \approx \frac{1}{\kappa} \ln \zeta_s^+ - 3.4$$

and even more elaborate formulae also found in [Ceb13] (see equation (4.89)) Note that if $\zeta_r^+ \lesssim 4$ in the first expression for Δu^+ above, or $\zeta_s^+ \lesssim 4$ in the third one, then $\Delta u^+ < 0$ and the skin friction for rough

wall would be smaller than the corresponding for smooth wall, since u_{rough}^+ in (4.84) would be greater than u_{smooth}^+ in (4.70), *caeteris paribus*. This appears as a surprising result, since nowhere in the Moody diagram (see figure 2.12) has a smooth pipe a higher friction factor than a rough one for the same Re . However, [Jim04] reports cases in which moderately rough surfaces reduce drag respect to equivalent smooth ones.

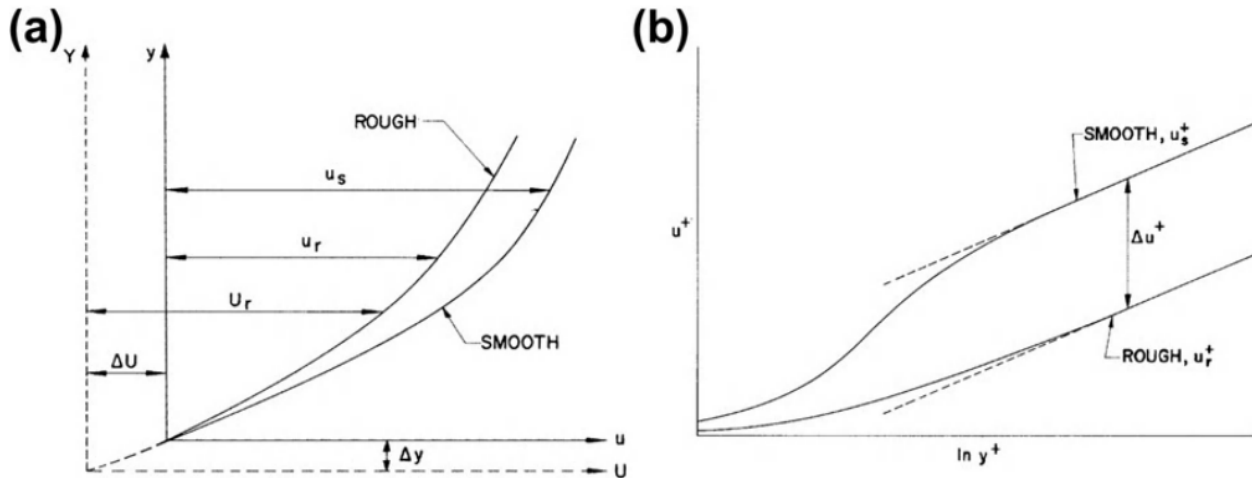


Figure 4.7: Meaning of velocity offset Δu^+ due to rough wall (from figure 4.25 of [Ceb13]).

Figure 4.8, obtained from figure 3 of [SF07], shows how for hydraulically smooth flows, $\zeta_r^+ < 4$ (depicted in the figure as k_s^+ to denote our ζ_s^+ , which although not equal to ζ_r^+ is of the same order of magnitude), the mean velocity profile is coincident with the log-law, except when reaching the outer region $y^+ \gtrsim 200$. As Reynolds number increases, which is to say as ζ_s^+ increases, the downward shift appreciated in the mean velocity profiles also increases. Such offset is a measure of the roughness function Δu^+ corresponding to each Re , although the profiles retain a similar shape because the slope $1/\kappa$ does not change for smooth or rough walls. All curves correspond to the same absolute roughness ζ_r .

Also, figure 4.9 taken from [SAS06] shows a similar result: the nearly parallel velocity profiles correspond to different Reynolds numbers for a rough pipe. The vertical offset between any pair of curves is a measure of Δu^+ in equation (4.84). That is, the main effect that roughness induces on the mean velocity profile: a displacement of the outer region velocities to lower values, thus increasing friction, since friction is directly related to the mean velocity acquired by the flow. Therefore, the velocity defect in the outer region is independent of surface roughness (see [SF07]), and the flow in the outer region is not affected by roughness. This statement is fully consistent with Nikuradse's results presented in [Nik50].

According to [SF07], there is strong experimental evidence about the outer-layer similarity of the turbulence structure over smooth and rough walls. This **wall similarity hypothesis** (as it is known in the literature) states that at high Re the turbulent motions for rough-wall flow are independent of the wall roughness and viscosity outside the so-called **roughness sublayer**, just as they are independent of viscosity outside the viscous layer, in the case of smooth walls. In other words, the core flow is similar in the case of smooth and rough walls.

The roughness sublayer, a concept commonly used in boundary layer meteorology, is the region

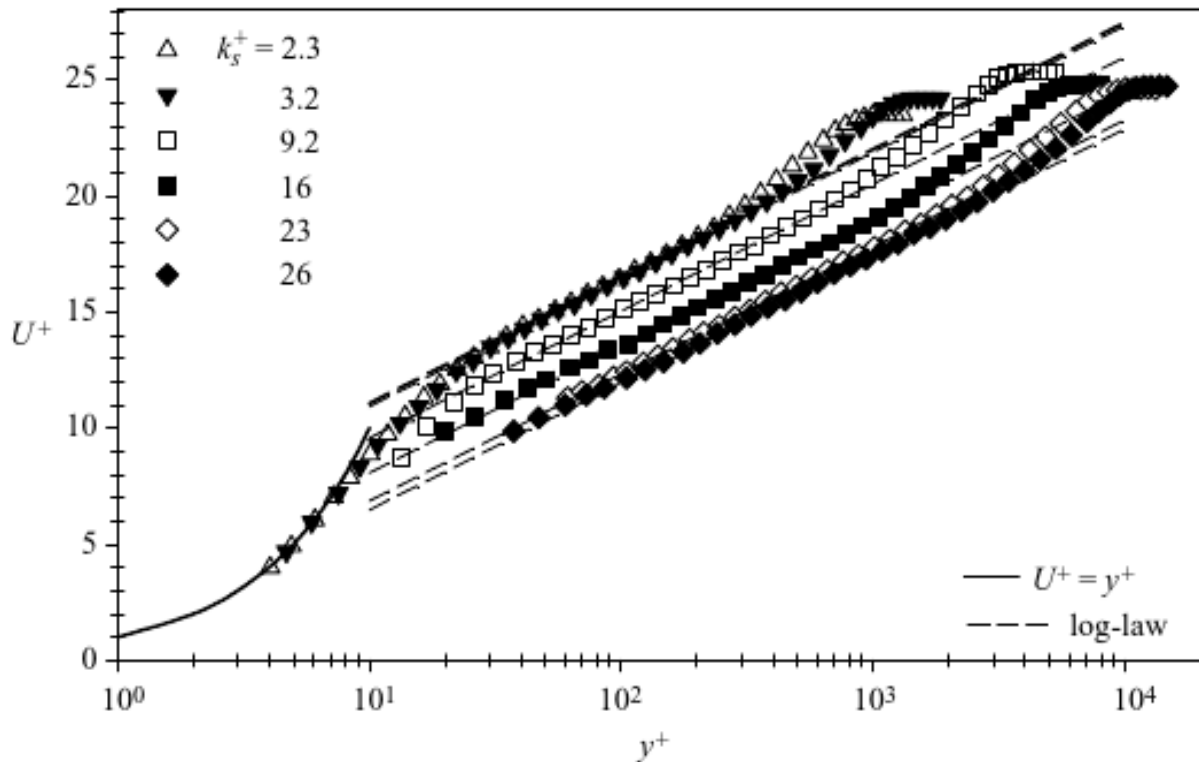


Figure 4.8: Mean velocity profiles for smooth ($\zeta_r^+ < 4$) and transitional-rough flows (from figure 3 of [SF07]).

extending about $5 \zeta_r$ from the wall, with ζ_r the absolute roughness height²⁵, just as the laminar sublayer extends some $5 \nu/u_\tau$ above the wall, being ν/u_τ the natural smooth-wall length scale. In that region the turbulence is directly influenced by the roughness length scale ζ_r . The roughness sublayer plays a similar role for rough walls as the laminar sublayer does for smooth walls.

[Jim04] noted that the key parameter for the wall similarity is the quotient ζ_r/δ , where δ is the boundary layer thickness. If $\zeta_r/\delta < 1/50$ then the effect of roughness should be confined to the inner region and wall similarity will hold (provided the Reynolds number is high enough), that is, the outer region flow would be similar to that corresponding to smooth walls. However, if the roughness height is not much smaller than the boundary layer thickness ($\zeta_r/\delta \gtrsim 1/50$), then the roughness effects on the turbulence may extend across the entire boundary layer, and the wall similarity hypothesis would be invalid. This possibility has profound implications on the modelling of turbulence, since some assumptions taken for granted far away from the wall might no longer be valid. Thus two requirements must be met in order to call for the wall similarity hypothesis: Reynolds number high enough and ratio ζ_r/δ small enough.

Henceforth the ratio ζ_r/δ will be called **dynamic relative roughness**²⁶. The model studied in this Dissertation fulfils both requirements for the wall similarity hypothesis to be applicable: the Reynolds number is very high ($Re \gtrsim 10^7$), and the absolute roughness of typical pipes used in fire extinction with

²⁵Roughness height normally means that height within which most of the protruding microscopic relieves of the wall are contained. In figure 4.6 ζ_r measures properly the roughness height, since most of the relief is not higher than ζ_r .

²⁶Note that what herein is called *dynamic relative roughness* is different from the ratio $\zeta_D = \zeta_r/D$ appearing in the Colebrook-White formula (2.64) (D the pipe inner diameter), which is called *relative roughness* by many authors. The difference, though, might not be large.

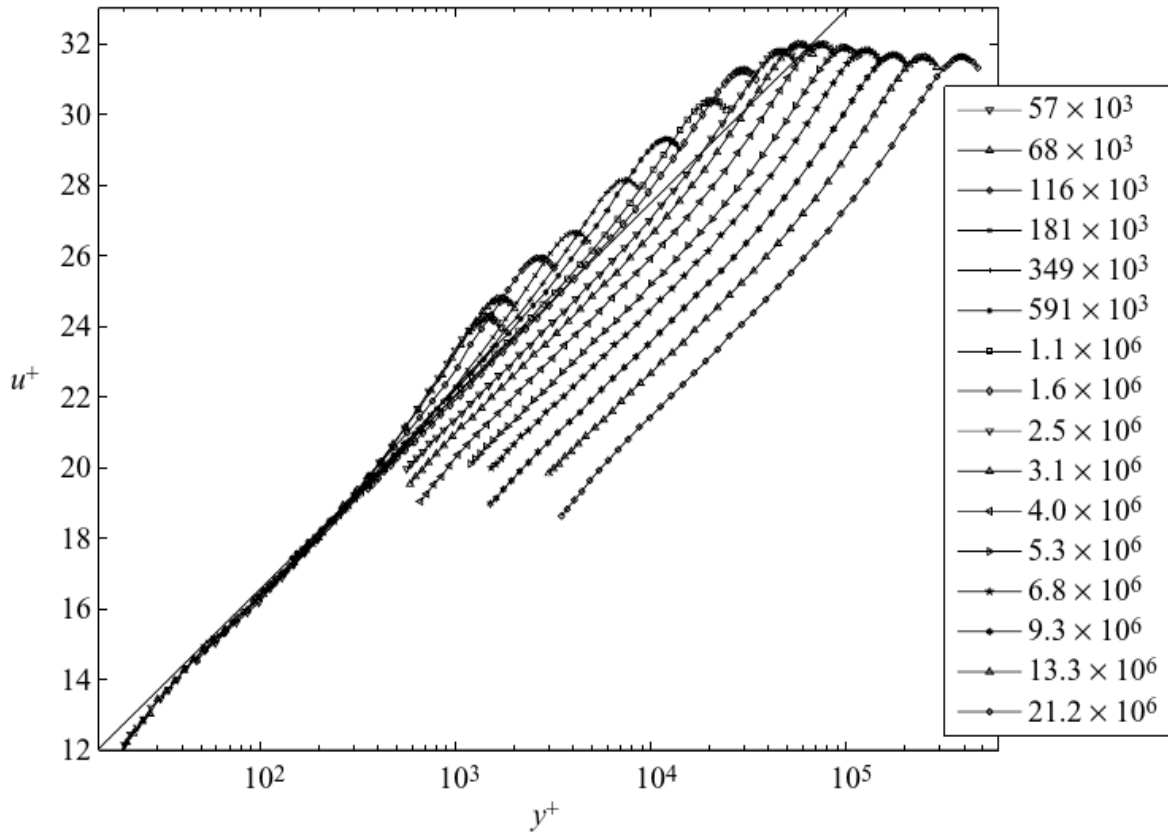


Figure 4.9: Mean velocity profiles for a range of Re in rough-walled pipe (from [SAS06]).

clean agents (either Schedule-40, Schedule-80 or AFTA galvanised steel) is very small ($\zeta_r/\delta \approx 10^{-3}$). Therefore, it is justified to apply standard turbulence models to the problem in the CFD simulation, since the flow developing in the outer region is similar to that occurring in the case of smooth wall flows, for which such turbulence models were devised.

The surface roughness in OpenFOAM, and in most CFD codes as well, is defined by means of two quantities: the equivalent sand roughness in wall coordinates ζ_s^+ and the roughness function Δu^+ . ζ_s^+ determines univocally Δu^+ and vice versa. Obviously, it would be extremely difficult to simulate the wall roughness directly in the mesh²⁷; therefore the simulation Engineer must resort to wall-functions in order to set suitable boundary conditions that characterise the CFD model.

The mean velocity profile for rough walls is defined in OpenFOAM as²⁸:

$$u^+ = \frac{1}{\kappa} \ln(Ey^+) - \Delta u^+ \quad (4.88)$$

with $E = 9.8$ and $\kappa = 0.41$. Thus OpenFOAM assumes that the shape of the mean velocity profile in the overlap layer and outer region for the rough wall is the same one as that of the smooth wall, but displaced

²⁷One attempt to directly introduce periodic wall-roughness as boundary conditions in a CFD model is provided in [APV00]. Periodic wall-roughness is just a crude approximation to the actual wall-roughness of any physical wall, but it provides a convenient first analogy to tackle the problem from a mathematical point of view. The approach is analytical and easily generalisable to CFD codes, although the periodicity of the wall-roughness introduces some *ringing* in the solution, which is only dampened if an artificial truncation is executed in the equations.

²⁸In OpenFOAM nomenclature, ζ_s^+ is denoted by K_s^+ and Δu^+ by ΔB .

by Δu^+ below it. The value of Δu^+ follows the model offered in section 4.5 of [Ceb13] (see [LABP11])

$$\Delta u^+ = \begin{cases} 0 & \zeta_s^+ \leq 2.5 \\ \frac{1}{\kappa} \ln \left(\frac{\zeta_s^+ - 2.25}{87.75} + C_s \zeta_s^+ \right) \sin \left(0.4258 \left(\ln \zeta_s^+ - 0.811 \right) \right) & 2.5 < \zeta_s^+ < 90 \\ \frac{1}{\kappa} \ln \left(1 + C_s \zeta_s^+ \right) & \zeta_s^+ > 90 \end{cases} \quad (4.89)$$

with C_s a coefficient, called the **roughness constant**, which depends on the shape and distribution of the roughness protrusions. Typically $0.2 \lesssim C_s \leq 1$. Besides, y^+ and ζ_s^+ are taken in OpenFOAM's rough-wall function as

$$y^+ = y \frac{\rho C_\mu^{\frac{1}{4}} k^{\frac{1}{2}}}{\mu} \quad (4.90)$$

and

$$\zeta_s^+ = \zeta_s \frac{\rho C_\mu^{\frac{1}{4}} k^{\frac{1}{2}}}{\mu} \quad (4.91)$$

with $C_\mu = 0.09$ a constant of the $k - \epsilon$ turbulence model to be introduced ahead, and k the turbulent specific kinetic energy. Equations (4.90) and (4.91) are valid provided the first wall-node height is $y^+ > 20$ (that is, somewhere above roughness Reynolds number ζ_r^+ for at least transitional-rough flow). With those results, the rough-wall function of OpenFOAM estimates the turbulent viscosity as (see [LABP11])

$$\nu_t = \nu \left(\frac{y^+ \kappa}{\ln(Ey^+) - \kappa \Delta u^+} - 1 \right) \quad (4.92)$$

When dealing with rough walls it does not make much sense to bring the nearest node very close to the wall, since for small values of y^+ the boundary conditions represented by rough-wall functions are somewhat misleading. As a matter of fact, a simulation was carried out in OpenFOAM for the model being studied in this Dissertation, with the turbulence model $k - \omega$ SST SAS (see section 4.10.1) that has proven to be successful, keeping everything as it is known to yield good results, except with the single variation of changing the boundary conditions from smooth to rough walls. The outcome was very illustrative: despite everything else being equal, the rough-walled model was unable to simulate the wall-friction, and the acceleration did not cease to be positive until finally the execution was halted at $t = 35$. The mesh, so appropriate for the case of smooth walls, was unsuitable for a rough wall simulation.

Finally, an additional interesting proposal for the modelling of wall-roughness into CFD codes could be found in [SCIO6], later improved and generalised by [Aps07]. The authors introduce the concept of zero-eddy-viscosity height in the mesh, and make it a function of roughness. Such height determines the threshold of the viscosity-dominated sublayer in which the flow is hardly turbulent.

4.6 Mesh Selection

'Who owns the mesh owns the solution': that is probably the most repeated motto a simulation Engineer ought to hear or say along his career. Arguably it may well be true. Therefore no energy should be spared to devise the best possible mesh, within computational reason, while confronting the CFD simulation of any physical flow. With a mesh fine enough it is of lesser importance whether the discretisation algorithm or the differentiation scheme is first or second order accurate, just to name a typical basic modelling decision. Fortunately the current simulation has a very simple geometry, a cylindrical pipe, and the problems are expected to arise somewhere else. Regardless, a good enough mesh is basic for an accurate solution to the problem.

The geometrical mesh defined for this 3D CFD model is shown in figure 4.10, in a perspective that illustrates the indisputable importance assigned to the near-wall flow. Figure 4.11 shows a cross-section of it, revealing how the cells are becoming increasingly thin as they approach the pipe's wall. The strategy followed to design the mesh is in accordance with standard procedures in CFD modelling of turbulent flows, such as the one described in [SC09].

Here it will be shown that the wall-nearest node of the proposed model is located within the applicability range of the Law of the wall and, thus, a direct calculation of the mean velocity, and other TQ, for such node is possible and accurate enough.

The mesh encompasses the computation domain, including its boundaries. It has two distinct subdomains, the core flow with cells of medium size and the near-wall flow where cells are much smaller in the radial direction, with a high aspect-ratio²⁹. In this near-wall subdomain the cell size is strongly graded until it ends with the cell nearest to the wall, which is thin enough to sink within the logarithmic layer, near the buffer layer, even for the highest Re attained in the flow. OpenFOAM would not tolerate cells with an extreme aspect ratio, therefore there is a strict limit set by the meshing library in this regard. Near-wall cells have indeed a high aspect ratio, although within limits, and their width would not tolerate any further reduction without also reducing the other dimensions, leading to still higher computational cost. It is easily seen that the simulation does not offer difficulty regarding the geometry: it is a simple cylindrical pipe, the second simplest internal flow geometry after the square channel. It will be seen that difficulties arise from other aspects.

The pipe's axis runs along Z , while X and Y axes define the cross-section. The mesh has unit diameter $D = 1$, and a length of $L = 25$ diameters, since a shorter length would not be completely free from entrance effects along all tube. There are $2100 \times 192 = 403200$ cells in the mesh -192 along the Z axis- and it has passed the standard quality control performed by OpenFOAM, and is fit for modelling. The two most successful models, namely the Detached Eddy Simulation (DES) $k - \omega$ SST SAS and RAS $k - \epsilon$ Launder-Sharma, have also been tested with a refined mesh of $4400 \times 192 = 844800$ cells, each cell with equal radial size and half transversal size than the first mesh. The results were almost identical despite the added resolution, thus proving the mesh independence of the model for meshes of resolution higher than 403200 cells (see sections 4.10.1 and 4.10.2).

The domain has 3 distinct boundaries:

- the *inlet*, with boundary conditions defined by liquid fraction $\alpha = 1$ and pressure p given by equation (2.52);
- the *outlet*, with the boundary condition $p = p_\infty$, and where the cross-section averaged velocity $\tilde{U}(t)$ is calculated and then incorporated to the inlet pressure equation;
- and the pipe *wall* characterised by the no-slip boundary condition and with wall-functions acting on the wall-nearest nodes, to make sure they receive velocity values compatible with the Universal Law of the Wall (see footnote 64 in page 146). The wall-functions also define boundary conditions for all TQ in the flow ($k, \epsilon, \omega, \rho u'_i u'_j, \nu_t, \nu_{SGS} \dots$).

²⁹A cell is said to possess a low aspect-ratio if

$$\frac{\Delta x}{\Delta y} \approx \frac{\Delta x}{\Delta z} \approx \frac{\Delta y}{\Delta z} \approx 1$$

with Δx , Δy and Δz the cell dimensions along each coordinate axis. Near-wall cells in the mesh of figure 4.10 have an aspect-ratio well in excess of 400.

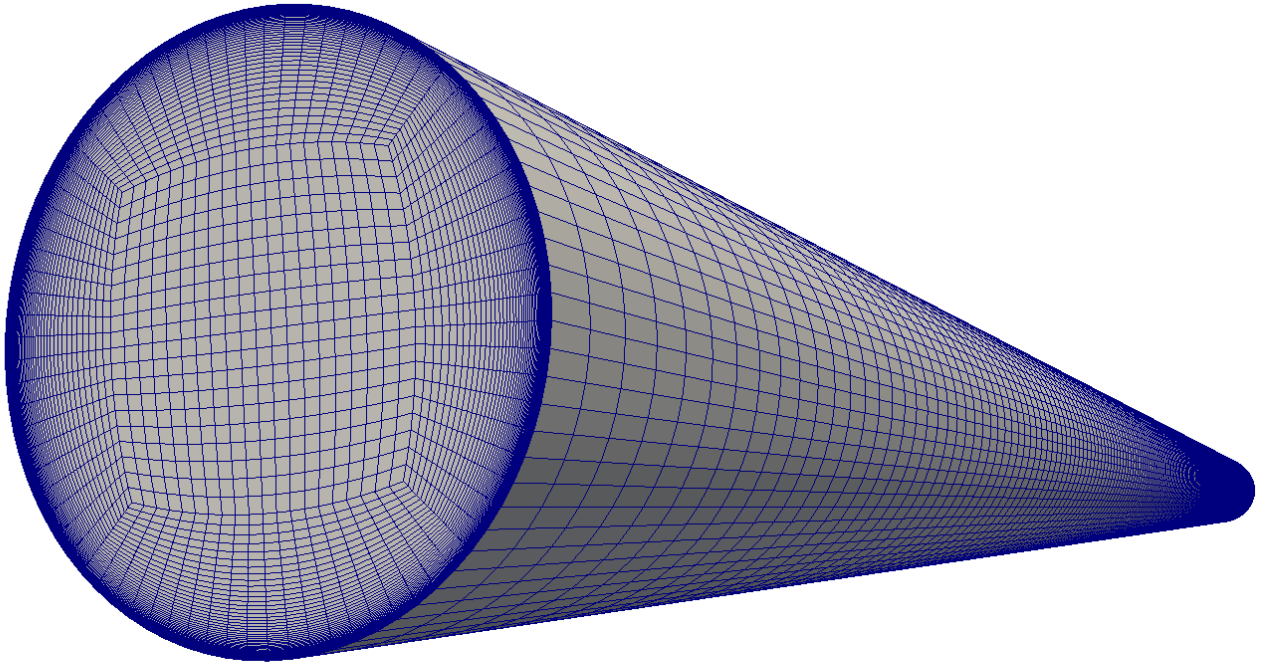


Figure 4.10: Complete mesh for the CFD model.

Special care has been taken in order to capture the logarithmic layer. The radial distance from the wall to the nearest node is $y = 1.5407 \cdot 10^{-4}$, in diameter units. Depending on the bulk velocity attained during the flow evolution, the expected values of y^+ are shown in table 4.1, calculated from the Blasius correlation (4.24). In all cases the first node is properly set within the log-law layer ($y^+ \lesssim 200$), not too far from the buffer layer ($5 \leq y^+ \leq 30$). Thus the wall-functions provided by OpenFOAM can be safely used since the first node is set within specifications, and the turbulence fields values for that node are given by the law of the wall.

It might be recalled that, according to [PPS06], the use of wall functions is based on three main assumptions:

- The near-wall cell is located within the logarithmic inertial layer.
- The validity of the law of the wall in such circumstances, for any turbulent smooth flow.
- The establishment of a turbulent local equilibrium in the near-wall region

$$\mathfrak{P} = \epsilon \Rightarrow \mathfrak{P} = \nu_t \left(\frac{\partial U}{\partial y} \right)^2 \quad (4.93)$$

where the production \mathfrak{P} and dissipation of ϵ of turbulent kinetic energy are locally equal (see [Wil06]), and the production could be expressed in terms of the eddy viscosity ν_t . This assumption is inherent to the $k - \epsilon$ and $k - \omega$ turbulence models.

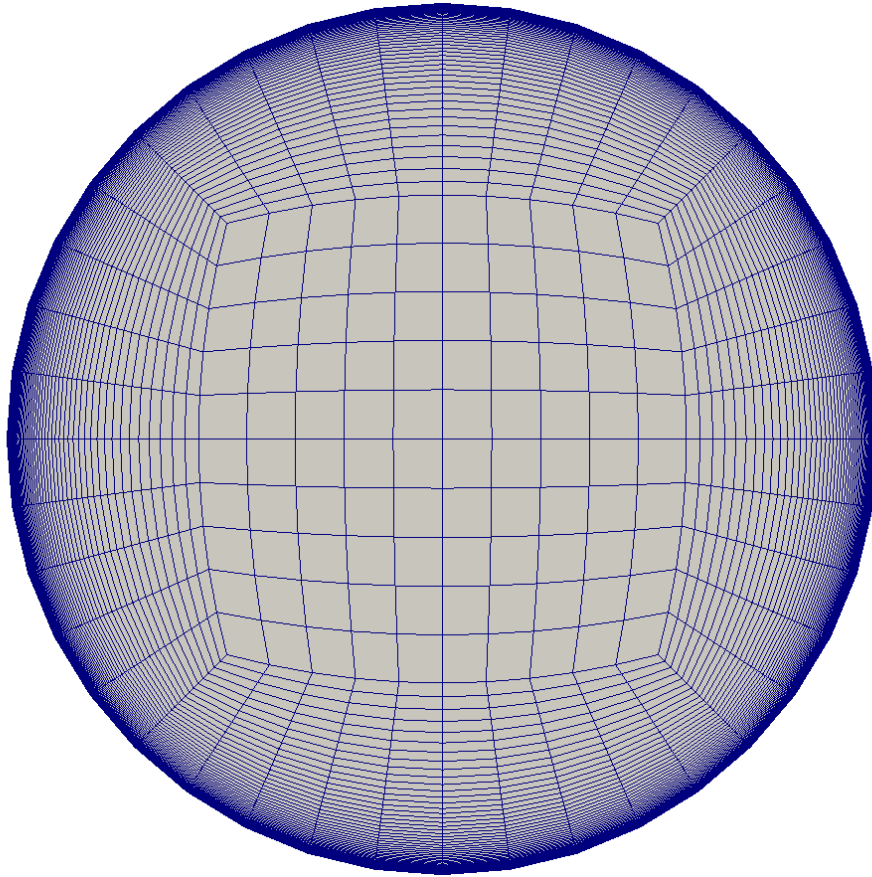


Figure 4.11: Cross-section of the mesh for the CFD model.

As a conclusion, the use of wall-functions in the current model is called for, since the three conditions above are met by the turbulence models used in the CFD simulations.

The execution of this CFD model in the computer is carried out through parallel processing, where each processor takes up several slices of the cross section shown along the Z axis. There is no parallel processing along the axes X and Y . That decomposition has proven the fastest and most suitable for the current problem.

\tilde{U}	Re	u_τ	y^+
2.00	$1.04306 \cdot 10^7$	0.05276	42.39
2.25	$1.17345 \cdot 10^7$	0.05849	47.00
2.50	$1.30383 \cdot 10^7$	0.06414	51.54
2.75	$1.43421 \cdot 10^7$	0.06972	56.02
3.00	$1.5646 \cdot 10^7$	0.07523	60.45

Table 4.1: y^+ for first wall-node for bulk velocities \tilde{U} , according to Blasius correlation (4.24).

Recall in page 207 the Kolmogorov length scale for the current model was estimated at $\eta = 1.88 \times 10^{-6}$, in diameter units. Therefore the first wall-node height is only some 82 times η , a fact that hints at the sort of resolution needed for the CFD model to capture that part of the turbulent boundary layer where the wall-friction is generated. Figure 4.12 shows a sketch of the mean velocity profile near the wall, and how the steep slope is seized within the first wall-cell. That slope is a measure of the intense gradient

undergone by the mean velocity, which is translated into a high friction with the wall and with the lower liquid layers through viscosity. Later it will be seen that even with such high spatial resolution, most turbulence models within the OpenFOAM suite fail to simulate the wall-friction caused by the flow's highly accelerated motion.

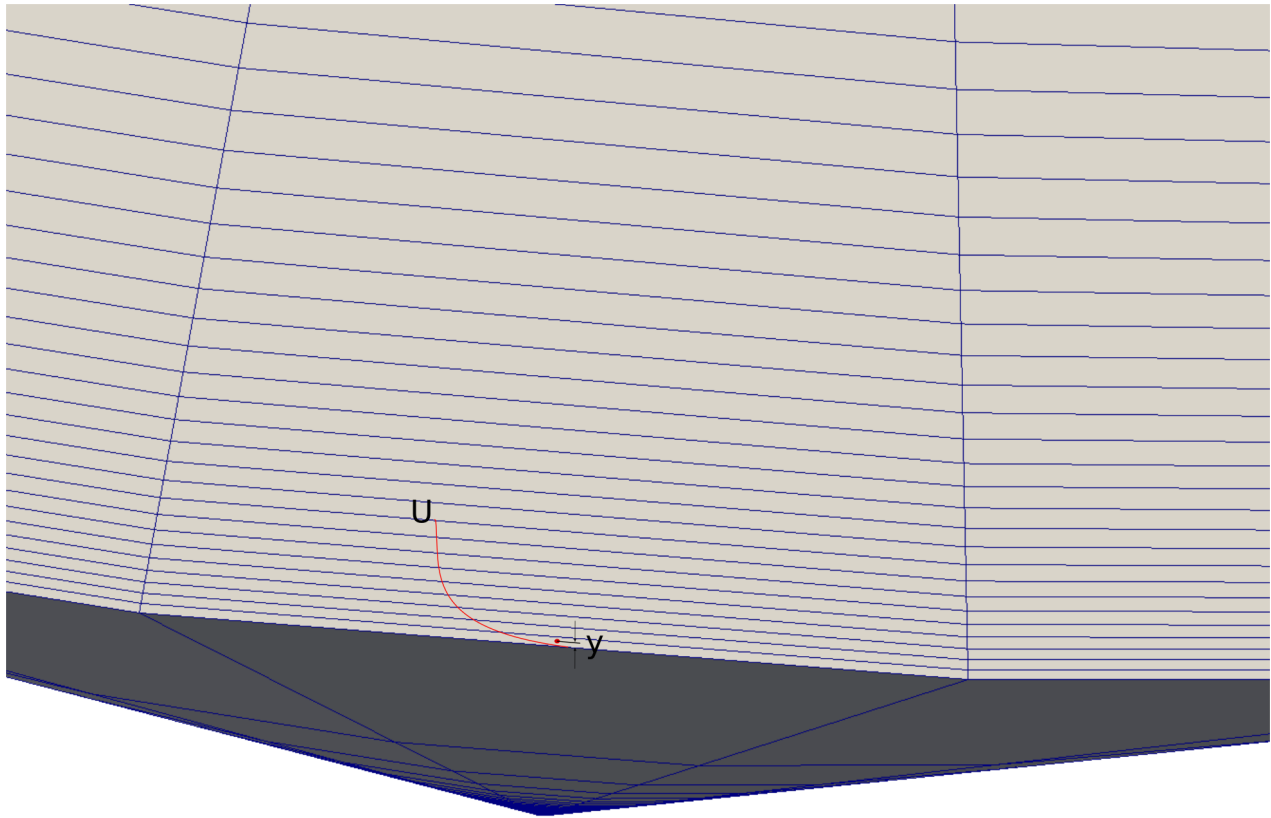


Figure 4.12: The log-layer develops within the first wall-cell.

Besides, it is expected that the enhanced spatial resolution could shed some light onto the issue raised in section 2.3.5, regarding the adequacy of Colebrook-White correlation to calculate the Darcy-Weisbach's friction factor f for the case of intensely accelerated internal flows. Such study and discussion is beyond the scope of this Dissertation and will be postponed to a future research work, including some analytical findings on transient wall-friction attained from the general equations developed in section 3.4.2 (see Conclusions in Chapter 5).

4.7 Discretisation Method and Differencing Scheme

In the realm of CFD *discretisation* usually refers to the method by which a continuous boundary value problem, comprised of partial differential equations defined in a domain with boundary conditions, is transformed into a huge set of discrete difference algebraic equations which can be solved with advanced matrix methods. Discretisation encompasses the following aspects:

- discretisation of space: a mesh
- discretisation of time: a marching algorithm

- discretisation of equations themselves: conversion of partial differential equations into a set of algebraic equations for each node in the mesh. Herein the FVM is selected because OpenFOAM is based thereof.

More specifically, within the CFD community when reference is made to *discretisation* often is meant *differencing scheme*, or rather, the procedure to discretise the convection term of the Navier-Stokes equations, because there lies a major issue in any flow simulation. The discretisation of the convection term is typically a source of problems in CFD modelling, since it affects critically to the stability and accuracy of the algorithm. This topic is beyond the scope of this Dissertation, and the reader is referred to the classical literature: [VM07], [FPO2] or [Bla05].

Upwind differencing scheme has generally been used for convective velocity, mainly because other schemes normally turned unstable with such rapidly changing speed. The liquid movement occurs essentially in one direction, parallel to the main cell edges, with negligible transversal components, Peclet number $Pe \gg 1$, thus the flow is overtly dominated by convection and negligible numerical diffusion is expected. With such conditions the use of upwind differencing scheme is justified, and one might even say called for. Besides, the two most successful CFD models, DES $k - \omega$ SSTSAS and RAS $k - \epsilon$ Launder-Sharma, have also been run with a more sophisticated and accurate Total Variation Diminishing (TVD)³⁰ scheme based on van Leer's flux limiter, and no significant difference has been observed. Thus upwind has proven accurate enough for this application. It should be stressed that upwind differencing scheme has been used not only for the momentum equation, but also for the TQ governing equations.

More care demands the time discretisation. Since all processes happen very fast, an explicit temporal discretisation would have required a very small time step in order to warrant a stable time-marching algorithm, rendering it almost impossible for the application. Hence an implicit Crank-Nicolson differencing scheme has been employed for temporal evolution, and even that has not avoided the use of small time steps, although not so small as explicit counterparts. The Courant number must be kept as low as $Co \approx 0.01$ for the solver to fully grasp the extreme accelerations attained during the first instants of the simulation. Later on, when the flow is well within the deceleration stage, it is possible to gradually increase such number up to $Co \approx 0.02$ at the end of the simulation. The Crank-Nicolson scheme is well described in the classical references [VM07], [FPO2] or [Bla05].

Another important aspect of the simulation is the existing coupling between two fields whose governing equations are very different: the mean (vector) velocity and the mean (scalar) pressure. Both fields appear intertwined in the Navier-Stokes equations, since an excess local pressure will boost up velocity while a local velocity reduction will increase pressure. Actually, the mutual influence could extend spatially many diameters beyond the point where the perturbation occurs, assuming a diameter is the natural length unit for the flow. Such mutual influence must be accounted for in the solver which embodies the algorithm conducting to a solution for the CFD problem. Normally, this is carried out with iterative procedures in which an initial estimate of the pressure field at each node is provided; then the discretised Navier-Stokes equations are solved with that initial pressure field. The fields obtained are checked with the continuity equation. Since they probably would not satisfy it with the desired level of error, a corrector is calculated for velocity and pressure fields. The newly corrected fields are inserted again in the discretised Navier-Stokes equations, and this iterative process goes on until the continuity error sinks below a predefined threshold value.

³⁰TVD schemes constitute a remarkable development in the numerical solution of hyperbolic differential equations, and its origins and initial applications can be traced to [HL81], [Har83], [Har84] and [Swe84], among others.

Note this algorithm uses the continuity equation to judge if the attained velocity field is accurate enough, thus revealing the relevant role awarded to that equation. The continuity error herein described is different from the residual (4.7) introduced in section 4.2. Residuals, through the figure of merit given by the RVN, measure the convergence rate of the iteration algorithm conducting to a solution of equation (4.6) for a particular field ψ . On the other hand, continuity errors measure the imbalance in the coupling of the fields mean velocity $\mathbf{U}(t, \mathbf{x})$ and mean pressure $P(t, \mathbf{x})$. There are two equations, Navier-Stokes and continuity, for two fields, \mathbf{U} and P . The fact that P do not appear explicitly in the continuity equation does not mean it is not part of the set; both are needed to obtain both fields.

Pressure Implicit with Splitting of Operator (PISO) algorithm has been used to solve the pressure-velocity coupling in the equations (see [Iss86] or [FPO2]). Usually three full PISO-loop iterations were sufficient to couple pressure and velocity, although each loop requires a high number of matrix-solver iterations to achieve low residual error, again as rapid changes in velocity and pressure render the coupling between them very awkward. Due to the low tolerance values set for the residuals, the continuity errors also resulted very low, since even levels acceptable in other types of simulations have proven to yield stability problems in this fast transient flow. All those circumstances put together result in long computation time for each time step. Typically, a 403200 cells simulation run at CESGA with 24 cores elapses some 57 hours, while a 844800 cells needs some 122 hours. In a powerful eight-core computer, the typical results are 180 hours for 403200 cells and 305 hours for a 844800 cells simulation.

Usually, a very convenient way to deal with pressure-velocity coupling in OpenFOAM is through the so-called PIMPLE algorithm. PIMPLE is a sort of blend of PISO and Semi-Implicit Method for Pressure-Linked Equations (SIMPLE), and it is much used in unsteady problems. Unfortunately, PIMPLE has proven not suitable for this transient flow, since it tends to increase Δt when the Courant number is small, and that smoothens the gradients and tends to decrease noticeably the accelerations. In other words, it introduces too much numerical diffusion. On the other hand, PISO does not exhibit that behaviour and yields accelerations compatible with those attained with the AHM.

Multidimensional Universal Limiter with Explicit Solution (MULES) algorithm is used to solve the equation for the liquid fraction field α which was introduced in section 4.3. MULES is a particular instance of the general Flux-Corrected Transport (FCT) scheme, used to guarantee boundedness in the solution of hyperbolic equations, like the one governing α given by (4.12) or (4.13). The theory behind the FCT is very intuitively explained in [KLT12] by its own creators, and the reader is encouraged to have a look at it. MULES is the particular implementation of FCT in OpenFOAM code. A convenient description of the specific aspects of MULES could be found in [MD13].

4.8 Independence of the Results with Mesh, Δt and Differencing Schemes

The title of this section is, possibly, somewhat misleading. After all that has been discussed in past sections, it might seem odd to even suggest that CFD results could be independent of mesh, Δt or differencing schemes. What have those sections done but to stress the importance of designing a proper mesh, choosing a Δt small enough, or selecting a stable, non-diffusive and accurate differencing scheme for each equation written in the solver, that is, for each quantity being solved?

In the present context, *independence* conveys the following meaning: once a mesh, a Δt and a set of differencing schemes have been chosen, any moderate improvement in any of them does not deliver a

noticeable increment in the accuracy of CFD results³¹. Therefore, to claim that some results are *mesh-independent* is tantamount to admit that a sort of asymptotic region has been reached, and further mesh refining would not provide any significant improvement in data quality. Likewise, a CFD model is said to be *differencing-scheme-independent* if the use of any more sophisticated and supposedly more accurate algorithm than the one selected, does not translate into a meaningfully better simulation.

Standard practice in CFD modelling also contemplates to check the model has reached the threshold that guarantee independence with respect to those key aspects. When that occur, one could be reasonably certain to have attained a stable, robust and relatively accurate CFD model, *relatively* implying that the accuracy might be determined by other factors not related to such independence.

In order to check the independence three figures of merit are typically considered, which also have a direct relationship with convergence of algorithms:

- i. A measure of convergence provided by a RVN. The concept of RVN was defined in section 4.2, and is related to the discretisation error for the conservation equation at each cell. For a simulation to have a moderate convergence, the RVN should be kept below 10^{-4} (in dimensionless units). $RVN < 10^{-5}$ is acceptable, while $RVN < 10^{-6}$ is generally considered a proof of convergence. Those figures are offered herein without any rigour, are part of the diffuse background knowledge associated with CFD Engineering, and ought to be considered as general rules of thumb.
- ii. Monitor points or probes. Certain nodes (probes) in the mesh are usually monitored in real time during the computer execution of the simulation, in order to check that the behaviour of the fields does not depart unacceptably from the expected evolution. This is particularly useful when simulating a steady state flow, since the probes should provide approximately constant values once the initial numerical transient fades away. Should the probes yield increasing/decreasing or oscillating values after a relatively long execution time, there would be reason to suspect the steady state simulation is not converging.
- iii. Imbalances in domain. Let ψ be a conserved quantity. Consider the flux of ψ over the boundary face of every cell located in the domain's boundary. In steady state, the domain imbalance for ψ is the sum of all such boundary fluxes (with their signs), minus the value of the sources and sinks of ψ (with their signs) existing in the computational domain. If the algorithm is sufficiently conservative, the sum of the boundary fluxes should equal the sources and sinks of ψ within the domain. If the domain has no source nor sink then the boundary flux of ψ ought to be zero, and the domain imbalance would equal its departure from zero. If there exist sources or sinks, then the domain imbalance would equal to departure of the boundary flux from the aggregate value of all sources/sinks, each with its sign. A relatively high domain imbalance for ψ would indicate an algorithm which does not globally conserve it. Even if RVN is low, a high domain imbalance would suggest that most errors tend to cumulate on the same side, thus causing a significant aggregate value. Convergence is generally considered dubious if domain imbalance is high. Obviously, in case of unsteady flow the time derivative of ψ must also be accounted for in the balance.

A recommended procedure to check if a model is mesh-independent is the following. It does not mean to be rigorous but frequently is very useful:

³¹ *Moderate improvement* is one which does not change the nature of the simulation being carried out. For example, if an Engineer is modelling a flow using the methods of RAS, it would always be possible to switch to the finest mesh demanded by DNS, but then it would be a different kind of simulation and the concept of mesh-independence would not apply for such modification. Doubling the mesh resolution should not change much the results if a model is already mesh-independent, but a tenfold increase would be an altogether different matter.

- STEP 1. Start with a computational mesh which has passed the standard quality tests most CFD codes perform. Make sure the height of the first wall-node be sufficiently low to be seated on the logarithmic inertial layer or below, if wall-functions are to be used. Run the simulation and verify the RVN is below 10^{-4} , since that hints at moderate convergence. Check the probes show a consistent behaviour (are almost constant in steady state flow), and domain imbalances are kept below 1% for all conserved quantities. When all that is fulfilled, proceed to the next step.
- STEP 2. Refine the mesh globally, so that all cells are smaller. As a rule of thumb, the number of cells in the domain should be some 50% higher than in the first grid. Run the simulation with the new mesh and check the RVN is better than 10^{-4} , domain imbalance is below 1% for all conserved quantities, and probes behave properly. Compare the values of the probes obtained in this step with the ones attained previously. If they are similar, within the tolerance levels, then the mesh at the *previous* step was good enough for the simulation, and the results would be mesh-independent. Use the smaller mesh that provide independence, since it would be sufficiently accurate and would reduce computing time. On the other hand, if the probes at step 2 are not alike those at the previous step, then the added resolution of the mesh is changing significantly the results and the simulation is not yet mesh-independent. In such case, proceed to step 3.
- STEP 3. Refine the mesh further, for instance another 50%, and repeat step 2.

A similar procedure is followed in order to check the independence respect to differencing scheme. In that case, a more sophisticated (and supposedly more accurate) differencing scheme should be used in step 2. If the probes shed similar values, then the initial differencing scheme is accurate enough. Otherwise, yet more sophisticated schemes have to be used until the probes yield results alike, within tolerance. Use the less sophisticated scheme granting independence, since it would be accurate enough and would reduce computing time.

Independence with respect to time step Δt is usually simpler to check, since the Courant number regulates that Δt be within reason. In particular, OpenFOAM includes in certain solvers the ability to fix a threshold Courant number Co , and the solver automatically adjusts Δt to keep the calculated Co approximately equal to the fixed Co . Therefore, with such solvers independence respect to Δt is equivalent to independence respect to Co : once a sufficiently small threshold Co number has been chosen, any decrement therein will not bring noticeably better results.

The 3D CFD model described in this Dissertation has reached independence with higher figures of merit than those recommended above:

- RVN is below 10^{-7} in all cases, because higher residuals would in general turn the solution unstable. Even the turbulence models that have failed to simulate the wall-friction (see next section), were executed with such a small RVN.
- The grid with 403200 nodes is accurate enough, and a refined one with 844800 nodes did not make any significant improvement.
- Upwind differencing scheme also proved accurate enough, since more sophisticated schemes did not provide significantly better results.
- Δt was chosen extremely small, of the order of Kolmogorov time scale, since Courant numbers above 0.02 were dubious to yield accurate results. Most simulations have been run with $Co \approx 0.01 \sim 0.015$. Simulations with $Co \lesssim 1$ were completely unstable for all turbulence models tested.

4.9 Turbulence Modelling

The main feature that outlines the physical phenomenon being studied in this Dissertation is the transient character of its dynamical behaviour: everything happens very fast, including the development of turbulence within the liquid. The presence of very high accelerations does not help either, since the increments of velocity are significant from one time-step to the next, and are likely to be underestimated in the discretisation algorithms.

In order to fully grasp the flow evolution, and to avoid the CFD model's collapse due to unstable time marching algorithms, a very small time step Δt must be selected. This is also limited by the Courant number Co associated with the simulation. The simulations carried out usually do not converge for $Co > 0.05$, and with some turbulence models not for $Co > 0.01$, values any of them much smaller than 1, being $Co < 1$ the usual requirement for CFD codes to grant stability. A consequence of this convergence criterion is quite extreme: a Δt one order of magnitude larger than Kolmogorov time $\tau_\eta = (\nu/\epsilon)^{1/2}$ does not warrant stability of the time marching algorithm, not being unlikely its collapse³². Thus, a careful consideration of the acceleration field must be envisaged in order to have a meaningful simulation of the discharge flow. It will be shown that only two out of the twenty tested turbulence models included in the OpenFOAM suite, offer a good enough simulation of the wall-friction that causes the flow deceleration.

One of the first studies on the structure of turbulence in accelerated pipe flow is [MKM76]. The authors experiment on stepwise changes on the Reynolds number, typically increases from $Re \approx 3 \cdot 10^3$ to $Re \approx 10^4$, and decreases from $Re \approx 2 \cdot 10^4$ to $Re \approx 10^4$. They report the generation of new coherent turbulence structures associated with the transient flow changes.

[Lef88] is also another reference which considers the evolution of turbulence when a constant acceleration is present in a pipe flow. The PhD Thesis describes the experimental studies conducted at the Naval Underwater System Centre (NUSC) by the author. [HJ00] also describes the detailed experimental work on pipe flow carried out by the authors, in which they study the build-up of turbulence in various instances of accelerating flow, ranging from initial $Re = 7000$ to final $Re = 45200$. This investigation also considers decelerating flows, from Re up to 45200 to Re down to 7000. The authors introduce the so-called dimensionless ramp parameter which characterises the acceleration undergone by the flow, and also the delay parameter to characterise the observed delay in turbulence development when acceleration is present. [JC12] studies a LES model of an accelerated turbulent pipe flow, with constant acceleration from $Re = 7000$ to $Re = 36000$, and compares the results with the previously mentioned paper [HJ00]. It is not very clear how the authors calculate the filtered quantities at the wall, since it is known that LES is not very accurate in the proximity of boundaries (see section 3.3).

Along similar lines than [HJ00] progresses the work [GM04]. The authors present the experimental results of rapidly accelerating a flow from $Re \approx 31000$ to $Re \approx 82000$. Attention is paid to the flow relaminarisation caused by the acceleration. The high ramp parameter considered in the experiments described on this paper seems to cause some turbulent structures near the wall. [GM04] hints at the generation of velocity profile inflections with growing acceleration.

Of a different nature is the study of turbulence modelling for unsteady flows presented in [BM93]. The authors develop a turbulence model based on the so-called Rapid Distortion Theory, and compare the

³²As explained in section 4.1, Kolmogorov microscales are estimated for this problem as $\eta = 1.88 \cdot 10^{-6}$, $\tau_\eta = 5 \cdot 10^{-5}$, $\nu_\eta = 0.0384$ in dimensionless units. Time steps around 10^{-5} , total simulation time up to $t = 100$, and 403200 cells in the mesh provide the measure of the computational power required.

simulation results with actual experimental data, with noticeable agreement. The resultant turbulent flow is oscillatory, with frequencies below 10 Hz and Reynolds number below 12 000.

[SHVO14] presents a DNS of a linearly accelerating channel flow, with Re ranging from 2818 to 7402. The paper is most centred on the transition to turbulence of a flow that initially is laminar-like and later becomes fully turbulent.

[GSA⁺14] assesses the performance of various classic turbulence models upon simulating unsteady flows where acceleration is present, some of which can also be found in OpenFOAM. The work is limited to relatively modest constant accelerations and does not consider the case of deceleration, which has proven to be the behaviour that most turbulence models fail to simulate, at least in this Dissertation. The $k - \epsilon$ Launder-Sharma model fares relatively well in the tests carried out in [GSA⁺14], and so occurs in the case presented herein.

During the accelerating stage the friction is relatively less important than the impulsive force represented by the strong pressure gradient, that is, the diffusive term (where the friction resides) is negligible. This explains that all turbulence models tested herein simulate reasonably well the acceleration stage: the wall-friction is relatively unimportant and the potential failure of those models to reproduce it would pass unnoticed on the simulation of the flow. With increasing bulk velocity the diffusive term becomes important, since the velocity gradient at the wall is no longer negligible. The intense wall-shear stress causes the deceleration, and it is no longer irrelevant that a turbulence model reproduce poorly the wall-friction. Although the pressure gradient is still high, the diffusive term is even higher and growing in importance. Remember the pressure at the vessel decreases rapidly with each litre of liquid leaving therefrom.

The previous remark is pertinent to understand an important point: although it seems that most turbulence models fail to simulate the wall-friction *only* during the deceleration stage, the truth is that they fail equally in reproducing the wall-friction along the acceleration stage. This last effect goes unnoticed on the CFD results, because the lesser importance of the diffusive term during the acceleration stage seems to boost the turbulence models' performance, regardless of its ability to simulate the wall-friction at that stage. In the coming pages data will be presented to conclude that only two turbulence models, out of the twenty tested (see table 4.2), reproduce reasonably well the wall-friction, and the rest fail to do so regardless of its partial success in simulating the acceleration stage, since diffusion plays a minor role in such stage and any model would do equally well.



Modelling the rapid turbulence evolution is probably one of the most demanding aspects of this study, and basically the only guide available is a match of results with those yielded by the 1D AHM. The suite OpenFOAM offers Reynolds-Averaged Simulation (RAS), Detached Eddy Simulation (DES), LES and DNS models. With Δt of the order of Kolmogorov time scale, DNS and pure LES are precluded for being very computationally expensive.

Most of the available RAS and DES turbulence models of OpenFOAM have been tested in this study, up to twenty of them. This includes RAS with the Boussinesq's hypothesis of eddy viscosity, RAS with Shear Stress Transport (SST) or with Reynolds Stress Transport Method (RSTM), DES with eddy viscosity hypothesis, and DES with SST models. Table 4.2 lists the twenty OpenFOAM turbulence models that have been tested in the CFD simulations, the two most successful ones shown in *italics*. The description of those twenty turbulence models is beyond the scope of the present Dissertation, and the reader is referred to the website www.openfoam.org and to the classic handbook [Wil06]. DES $k - \omega$ with SST

and Scale Adaptive Simulation (SAS), or $k - \omega$ SSTSAS, deserves a special mention. $k - \omega$ SSTSAS is described in [ME05] and [ME10]. $k - \epsilon$ Launder-Sharma model is described in [LS74] and [BHC97].

OpenFOAM model	Turbulence Model Description
SpalartAllmaras	Spalart-Allmaras one-equation mixing-length
kEpsilon	Standard high Re $k - \epsilon$
kOmega	Standard high Re $k - \omega$
<i>LaunderSharmaKE</i>	Low Re Launder-Sharma $k - \epsilon$
RNGkEpsilon	Renormalisation group $k - \epsilon$
NonlinearKEShih	Non-linear Shih $k - \epsilon$
realizableKE	Realisable $k - \epsilon$
LamBremhorstKE	Low Re Lam-Bremhorst $k - \epsilon$
LienCubicKELowRe	Low Re Lien cubic $k - \epsilon$
LienLeschzinerLowRe	Low Re Lien-Leschziner $k - \epsilon$
kOmegaSST	Shear Stress Transport $k - \omega$
LRR	Launder-Reece-Rodi Reynolds-Stress transport
LaunderGibsonRSTM	Launder-Gibson RSTM with wall-reflection terms
SpalartAllmarasIDDES	Spalart-Allmaras Improved Delayed DES
mixedSmagorinsky	Mixed Smagorinsky scale similarity
oneEqEddy	k -equation eddy-viscosity
dynOneEqEddy	Dynamic k -equation eddy-viscosity
LRDDiffStress	Launder-Reece-Rodi differential stress
DeardorffDiffStress	Deardorff differential stress
<i>kOmegaSSTAS</i>	$k - \omega$ Shear-Stress-Transport Scale-Adaptive-Simulation

Table 4.2: Turbulence models tested in CFD simulations.

The Boussinesq's hypothesis possibly deserves some further remarks. It has already been discussed, for instance in Chapter 3 or in section 4.5, that upon deducing the RANSE some additional quantities appear therein which were not present in the classic Navier-Stokes equations they stem from. Those new quantities account for the fluctuating effect of the turbulence that is not smeared out by the averaging process. Such appearance causes the so-called **closure problem**: there are more unknowns than equations in RANS formalism. The new quantities constitute a tensor field, the Reynolds stress tensor, defined by

$$R_{ij}(t, \mathbf{x}) = -\rho \langle u'_i u'_j \rangle$$

where the most general ensemble average is considered (note $R_{ij} = R_{ji}$). In principle, six new equations are needed to determine the six new independent quantities that have sprouted.

Most of the classic RAS turbulence models, notably the ever-popular $k - \epsilon$, $k - \omega$ and their offspring, are based on a shift of the number of unknown variables causing the closure problem: instead of six independent quantities R_{ij} , only two are needed, in principle, to account for the fluctuating effects of turbulence: the eddy viscosity ν_t and the specific average turbulence kinetic energy (per unit mass) k . Thus the Reynolds stress tensor $R_{ij}(t, \mathbf{x})$ is replaced by the scalar fields $\nu_t(t, \mathbf{x})$ and $k(t, \mathbf{x})$, according to

the following definition that constitutes the Boussinesq's hypothesis³³

$$R_{ij}(t, \mathbf{x}) = -\rho \langle u'_i u'_j \rangle = \rho \nu_t \left(\partial_j U_i + \partial_i U_j \right) - \frac{2}{3} \rho k \delta_{ij} \quad (4.94)$$

with

$$U_i(t, \mathbf{x}) = \langle u_i(t, \mathbf{x}) \rangle$$

the average velocity and

$$k(t, \mathbf{x}) = \frac{1}{2} \langle u'_i u'_i \rangle$$

Now it is only necessary to provide two additional equations for the two unaccounted for variables ν_t and k . It would seem that with such smart move up to four unknowns have been precluded from the turbulence model. The exact governing equation for k is long and complicated, was already presented in (4.73) and is repeated here for convenience (see [Wil06]) :

$$\partial_t k + U_i \partial_i k = -\langle u'_i u'_j \rangle \partial_j U_i - \nu \langle \partial_j u'_i \partial_j u'_i \rangle - \frac{1}{\rho} \partial_i \langle p' u'_i \rangle + \nu \nabla^2 k - \partial_j \langle u'_j \frac{u'_i u'_i}{2} \rangle$$

and again new quantities appear in a never-ending progression: $\langle u'_i u'_j \rangle$, $\langle p' u'_i \rangle$, $\langle u'_j u'_i u'_i \rangle$, $\langle \partial_j u'_i \partial_j u'_i \rangle$... The traditional way out of this outward spiralling process is to stop at three additional quantities: k , ν_t and³⁴

$$\epsilon = \nu \langle \partial_j u'_i \partial_j u'_i \rangle \quad (4.95)$$

and propose governing equations for them which are free from *foreign* quantities. The only fields admitted in those equations are U_i , k , ν_t and ϵ , and the only equations considered are the RANSE, the simple relationship linking directly k , ν_t and ϵ

$$\nu_t = C_\mu \frac{k^2}{\epsilon} \quad (4.96)$$

and the conveniently modified transport equations for k and ϵ :

$$\partial_t k + U_i \partial_i k = \mathfrak{P} - \epsilon + \partial_i \left[\left(\nu + \frac{\nu_t}{\sigma_k} \right) \partial_i k \right] \quad (4.97)$$

$$\partial_t \epsilon + U_i \partial_i \epsilon = C_{\epsilon 1} \frac{\epsilon}{k} \mathfrak{P} - C_{\epsilon 2} \frac{\epsilon^2}{k} + \partial_i \left[\left(\nu + \frac{\nu_t}{\sigma_\epsilon} \right) \partial_i \epsilon \right] \quad (4.98)$$

with \mathfrak{P} the production term expressed only through the selected quantities

$$\mathfrak{P} = \frac{\nu_t}{2} (\partial_i U_j + \partial_j U_i) (\partial_i U_j + \partial_j U_i) \quad (4.99)$$

Each particular RAS turbulence model endows a different set of values to the constants C_μ , σ_k , $C_{\epsilon 1}$, $C_{\epsilon 2}$, σ_ϵ , and some models even introduce additional constants and terms, like the low-Reynolds model seen in equations (4.76)-(4.79) of section 4.5, or some others to be presented in the coming sections.

³³Some authors provide good reason to doubt about the validity of the Boussinesq's hypothesis. See, for instance, [Sch07] and [Cha00]. Should that be generically true, most of RAS turbulence models ought to be reformulated and some of them even discarded.

³⁴The expression (4.95) for ϵ is an useful simplification. ϵ is rigorously defined in equations (3.21) and (3.22).

Although a detailed discussion of turbulence models is beyond the scope of this Dissertation, and the reader is addressed to the excellent text [Wil06], it has been deemed convenient to highlight these points herein, if only to evidence the playing field in which most of the turbulence modelling has been, and still is, developed. The pruning of equations and the blossoming of constants, factors and terms finds no mathematical justification³⁵, and it is only supported by the (partial) agreement that such CFD models show with experimental results, at least in some relatively simple flows. Even the Boussinesq's hypothesis itself is seriously questioned by an ever-growing number of researchers (see footnote 33 in page 255). It is no novelty in the History of Science that some arbitrariness be ruefully admitted while no acceptable theory yet exists, and that seems to be the case with turbulence modelling.



As frequently employed, RAS models are, in principle, less suited for the simulation of transient effects, since they normally rely on Reynolds Decomposition *à la* time average, which does not leave much room for time-dependent average quantities, much less for *very* time-dependent ones, although it has been reported that URANS can handle slowly time-varying average fields. URANS methods are expected to produce acceptable results for problems with simple geometry, in which the time variation of the mean fields develops in a frequency spectrum much smaller than that corresponding to fluctuating components (see section 3.2.2). But such is clearly not the case of this simulation, with a transient part already on the same order of magnitude than Kolmogorov time. Therefore, all simulations carried out, shown in table 4.2, have considered from the beginning a Reynolds Decomposition *à la* ensemble average.

Promising turbulence models like Realisable $k - \epsilon$ or Renormalisation Group $k - \epsilon$ did not meet the expectations, and also reproduced poorly the wall-friction. Realisable $k - \epsilon$ is presented in papers [SZL93] and [SLS⁺94]. The use of Renormalisation Group techniques in turbulence modelling is discussed in [YO86], [YOT⁺92], [Lam92], [SGF91] and [Cho93]. [ZO98] applies those techniques to high Reynolds number pipe flow.

The approach of calculating directly the Reynolds stress was also followed with two of the RSTM turbulence models listed in table 4.2. Despite the added equations and supposedly higher accuracy, those models also could not yield a wall-friction so high as that obtained with the 1D AHM. RSTM turbulence models are didactically described in [LW07].

Finally, HRLTM were also tested despite the added computational cost they imply. HRLTM represent a blend between LES and RAS methods, and were briefly described in page 147. The LES modelling is used in the main flow, sufficiently apart from the walls, whereas RAS is applied near the walls since, both, RAS presents a better approximation to DNS and to experimental data, and LES is not even theoretically feasible in the proximity of walls (see section 3.3). A first attempt was carried out with a HRLTM technique known by the general name of Improved Delayed Detached Eddy Simulation (IDDES), which is well described in [SSST08]. The turbulence model Spalart-Allmaras IDDES produced a surprising result: the time-velocity curve obtained matches very accurately the equivalent 1D AHM, provided the wall-friction were exactly one half of that attained by the AHM. Thus it would seem that Spalart-Allmaras IDDES underestimate the friction by a sharp factor of 2. A revision of the OpenFOAM code did not reveal any programming error, so it would be assumed that is, indeed, the turbulence model behaviour for rapidly accelerating flows.

A HRLTM emerged as the most successful turbulence model for the flow being considered: the already

³⁵The foregoing statement notwithstanding, it is remarkable the mathematical approach presented in [MP94] for the $k - \epsilon$ turbulence model, which could be extended to other RAS models.

mentioned DES $k - \omega$ SST/SAS. The results will be amply discussed in the next section.

4.10 Results and Discussions

After the introduction made in the previous sections, herein will now be presented the main results concerning the 3D CFD successful models and their comparison with equivalent 1D AHM. Both models, 1D AHM and 3D CFD, share the same geometry, boundary conditions, initial pressure and fluid properties. The relevant dimensionless values for the problem are: initial pressure $p_0 = 1.04224$, diameter $D = 1$, pipe's length $L = 25$, geometrical factor $G_f = 10^{-3}$, liquid's density $\rho = 1$ and kinematic viscosity $\nu = 1.9174 \cdot 10^{-7}$, corresponding to typical values for fire extinction agent FK-5-1-12 (Novec-1230)³⁶. Besides, for the CFD model the following transport quantities are also relevant: surface tension of FK-5-1-12 $\sigma = 1.1871137 \cdot 10^{-7}$, density of air $\rho_{air} = 7.582563 \cdot 10^{-4}$ and kinematic viscosity of air $\nu_{air} = 6.6768045 \cdot 10^{-6}$. Note the air viscosity is more than ten times higher than FK-5-1-12's.

A wide selection of turbulence models has been tested (see table 4.2). All simulations carried out show an acceptable agreement with the AHM in the acceleration stage, in which the dominant force is not the wall-friction (see discussion in page 253). But only DES $k - \omega$ SST/SAS and RAS $k - \epsilon$ Launder-Sharma turbulence models provide an acceptable behaviour in the deceleration stage. Most turbulence models within the OpenFOAM suite fail to simulate the wall-friction originated in the liquid's decelerated motion: regardless of the adjustment made on L_v , ζ_D or Δ_f , no analytical curve could approximate the results yielded by the corresponding CFD model.

Also all tested turbulence models, without exception, fail to reproduce the transition stage, that part of the time-velocity curve around the maximum. This stage corresponds to a major deformation in the cross-section turbulent velocity profile within the pipe, in which some portions of the fluid still have accelerated motions while others begin to suffer decelerations. Therefore, the shear stress reaches its maximum value in this period and the production of turbulence also attains a peak. That turbulence would be very difficult to simulate by any foreseeable model, let alone the RAS and DES models available in OpenFOAM.

On the other hand, some good news: the *vi*th assumption made in section 2.2, regarding a non-zero pressure gradient exclusively in the wet zone, is confirmed in all CFD simulations. The pressure is maintained approximately equal to atmospheric in the dry zone, with no noticeable longitudinal gradient.

In this section the results obtained from the CFD simulations are presented in order of agreement with the AHM. The equations that define the turbulence models, as they are implemented in OpenFOAM, are obtained from [Wil06], [Cha00], [Mor10] and the OpenFOAM code itself. The symbols that will appear in the equations shown in the next sub-sections are named after the OpenFOAM code. The extraordinary complexity attained by some models, with tens of arbitrary constants, factors, quantities, terms, uncanny functions and mathematical artefacts, reveals the lack of physical ground afflicting much of the current modelling (see remarks posed in page 255)

4.10.1 $k - \omega$ SST/SAS

The $k - \omega$ SST/SAS turbulence model could be generically classified as a HRLTM, within the subclass of DES. The model blends the $k - \omega$ SST, which is itself a RAS model, with the concept of SAS near the wall,

³⁶All dimensionless data are expressed in units of the basic reference quantities seen in section 2.4.1. The notation and nomenclature used to denote the dimensionless quantities are also collected in section 2.4.1.

and with LES in the core flow. The model is generically described in [ME05] and [ME10]

It is also classified as a two-equation turbulence model, since two turbulence fields are directly calculated through their governing equations, namely k and ω . $k - \omega$ SST is a high Re model with wall-functions: it models turbulence in the boundary layer with standard $k - \omega$ while it switches to $k - \epsilon$ elsewhere, since $k - \omega$ is known to be more accurate and robust near solid boundaries. Where the mesh is fine enough (and sufficiently far away from walls) to allow for LES to be accurate, it automatically switches thereto; *mesh fine enough* meaning that the filter width (which in turn determines the minimum resolvable turbulence length scale) be larger than the maximum cell size.

The implementation of $k - \omega$ SSTSAS model into the OpenFOAM code is explained in [Lin14] and [Gra12]. OpenFOAM implements this model into the following equations³⁷:

$$\frac{\partial k}{\partial t} + \nabla \cdot (\mathbf{U}k) - (\nabla \cdot \mathbf{U})k - \underbrace{\nabla \cdot (D_{k,eff}(F_1)\nabla k)}_{\text{Diffusion}} = \underbrace{\min(G, C_1\beta^*k\omega)}_{\text{Production}} - \underbrace{\beta^*k\omega}_{\text{Dissipation}} \quad (4.100)$$

$$\frac{\partial \omega}{\partial t} + \nabla \cdot (\mathbf{U}\omega) - (\nabla \cdot \mathbf{U})\omega - \underbrace{\nabla \cdot (D_{\omega,eff}(F_1)\nabla \omega)}_{\text{Diffusion}} = \underbrace{2\gamma(F_1)S^2}_{\text{Production}} - \underbrace{\beta(F_1)\omega^2}_{\text{Dissipation}} + \underbrace{(1 - F_1)C_{Dk\omega}}_{\text{Cross-diffusion}} + Q_{SAS} \quad (4.101)$$

with the following quantities and parameters:

- Effective diffusivity for k : $D_{k,eff}(F_1)$

$$D_{k,eff}(F_1) = \nu + \nu_{SGS} \alpha_k(F_1) \quad (4.102)$$

- Effective diffusivity for ω : $D_{\omega,eff}(F_1)$

$$D_{\omega,eff}(F_1) = \nu + \nu_{SGS} \alpha_\omega(F_1) \quad (4.103)$$

- Subgrid-scale viscosity: ν_{SGS}

$$\nu_{SGS} = \frac{a_1 k}{\max(a_1 \omega, F_2 \sqrt{2S^2})} \quad (4.104)$$

- Turbulence production: G

$$G = 2\nu_{SGS} S_{ij}S_{ij} = \frac{\nu_{SGS}}{2} (\partial_i U_j + \partial_j U_i)(\partial_i U_j + \partial_j U_i) \quad (4.105)$$

- Mean total strain rate squared: S^2

$$S^2 = 2(\partial_i U_j + \partial_j U_i)/2 (\partial_i U_j + \partial_j U_i)/2 = \frac{1}{2} (\partial_i U_j + \partial_j U_i)(\partial_i U_j + \partial_j U_i) \quad (4.106)$$

- Cross-diffusion factor: $C_{Dk\omega}$

$$C_{Dk\omega} = \frac{2\alpha_\omega}{\omega} \nabla k \cdot \nabla \omega \quad (4.107)$$

³⁷Although for incompressible flows the continuity equation reads $\nabla \cdot \mathbf{U} = 0$ and it would seem preferable to ignore it, nevertheless OpenFOAM code solves the term $\nabla \cdot \mathbf{U}$ because it is non-zero while convergence is being achieved, and keeping it in the calculations helps the solver to improve the stability and convergence rate.

- First blending function : F_1

$$F_1 = \tanh \left[\left[\min \left(\min \left(\max \left(\frac{\sqrt{k}}{\beta^* \omega y}, \frac{500\nu}{y^2 \omega} \right), \frac{4\alpha_{\omega 2} k}{\max(C_{Dk\omega}, 10^{-10}) y^2} \right), 10 \right) \right]^4 \right] \quad (4.108)$$

- Second blending function : F_2

$$F_2 = \tanh \left[\left[\min \left(\max \left(\frac{2\sqrt{k}}{\beta^* \omega y}, \frac{500\nu}{y^2 \omega} \right), 100 \right) \right]^2 \right] \quad (4.109)$$

- Additional term for Scale Adaptive Simulation : Q_{SAS}

$$Q_{SAS} = F_{SAS} \cdot \max \left[2\zeta_2 \kappa S^2 \left(\frac{L}{L_{vk2}} \right)^2 - \frac{2k}{\alpha_\phi} \max \left(\frac{\nabla k \cdot \nabla k}{k^2}, \frac{\nabla \omega \cdot \nabla \omega}{\omega^2} \right), 0 \right] \quad (4.110)$$

- Turbulence length scale : L

$$L = \frac{\sqrt{k}}{\omega C_\mu^{\frac{1}{4}}} \quad (4.111)$$

- Grid length scaling factor for DES : L_{vk2}

$$L_{vk2} = \max \left[\frac{\kappa \sqrt{2S^2}}{\sqrt{(\partial_i \partial_i U_j)(\partial_k \partial_k U_j) + 10^{-18}}}, C_S \Delta \right] = \max \left[\frac{\kappa \sqrt{2S^2}}{\sqrt{\nabla^2 \mathbf{U} \cdot \nabla^2 \mathbf{U} + 10^{-18}}}, C_S \Delta \right] \quad (4.112)$$

- Blending of constants α_{k1} and α_{k2} : α_k

$$\alpha_k(F_1) = (\alpha_{k1} - \alpha_{k2})F_1 + \alpha_{k2} \quad (4.113)$$

- Blending of constants $\alpha_{\omega 1}$ and $\alpha_{\omega 2}$: α_ω

$$\alpha_\omega(F_1) = (\alpha_{\omega 1} - \alpha_{\omega 2})F_1 + \alpha_{\omega 2} \quad (4.114)$$

- Blending of constants β_1 and β_2 : $\beta(F_1)$

$$\beta(F_1) = (\beta_1 - \beta_2)F_1 + \beta_2 \quad (4.115)$$

- Blending of constants γ_1 and γ_2 : $\gamma(F_1)$

$$\gamma(F_1) = (\gamma_1 - \gamma_2)F_1 + \gamma_2 \quad (4.116)$$

- And the constants:

$$a_1 = 0.31 \quad (4.117)$$

$$C_S = 0.262 \quad (4.118)$$

$$C_1 = 10 \quad (4.119)$$

$$C_\mu = 0.09 \quad (4.120)$$

$$F_{SAS} = \frac{5}{4} \quad (4.121)$$

$$\alpha_{k1} = 0.85034 \quad (4.122)$$

$$\alpha_{k2} = 1.0 \quad (4.123)$$

$$\alpha_{\omega1} = 0.5 \quad (4.124)$$

$$\alpha_{\omega2} = 0.85616 \quad (4.125)$$

$$\alpha_\phi = \frac{2}{3} \quad (4.126)$$

$$\beta_1 = 0.075 \quad (4.127)$$

$$\beta_2 = 0.0828 \quad (4.128)$$

$$\beta^* = 0.09 \quad (4.129)$$

$$\gamma_1 = 0.5532 \quad (4.130)$$

$$\gamma_2 = 0.4403 \quad (4.131)$$

$$\Delta = \max(\Delta x, \Delta y, \Delta z) \quad (4.132)$$

$$\kappa = 0.41 \quad (4.133)$$

$$\zeta_2 = 1.755 \quad (4.134)$$

(Δ is the maximum linear size of a cell)



The CFD model was executed in three different configurations, with OpenFOAM version 2.3.1. The resulting time-velocity curves are shown in figure 4.13. The features of each execution are the following:

- Label 1 indicates a mesh with 403200 cells and upwind differencing scheme for the convective term in the equations for velocity and TQ (k, ω).
- Label 2 indicates a mesh with 844800 cells and upwind differencing scheme for the convective term in the equations for velocity and TQ.
- Label 3 indicates a mesh with 403200 cells and TVD scheme based on van Leer's flux limiter for the convective term in the equation for velocity, and Self-Filtered Central Differencing (SFCD) schemes in the convective terms of TQ.

As it can be seen, the curves match one another almost perfectly, thus proving the model's independence on the mesh and differencing scheme. The time interval Δt is automatically adjusted by the solver upon fixing the maximum acceptable Courant number Co , therefore independence respect to Δt is equivalent to independence respect to Co number. Upwind differencing scheme, despite being less accurate than others, has shown to be perfectly suitable for the application. Therefore it is fully justified its use, as it was explained above.

Figure 4.14 shows the time-velocity curve obtained from the DES $k - \omega$ SSTSAS model simulation, and

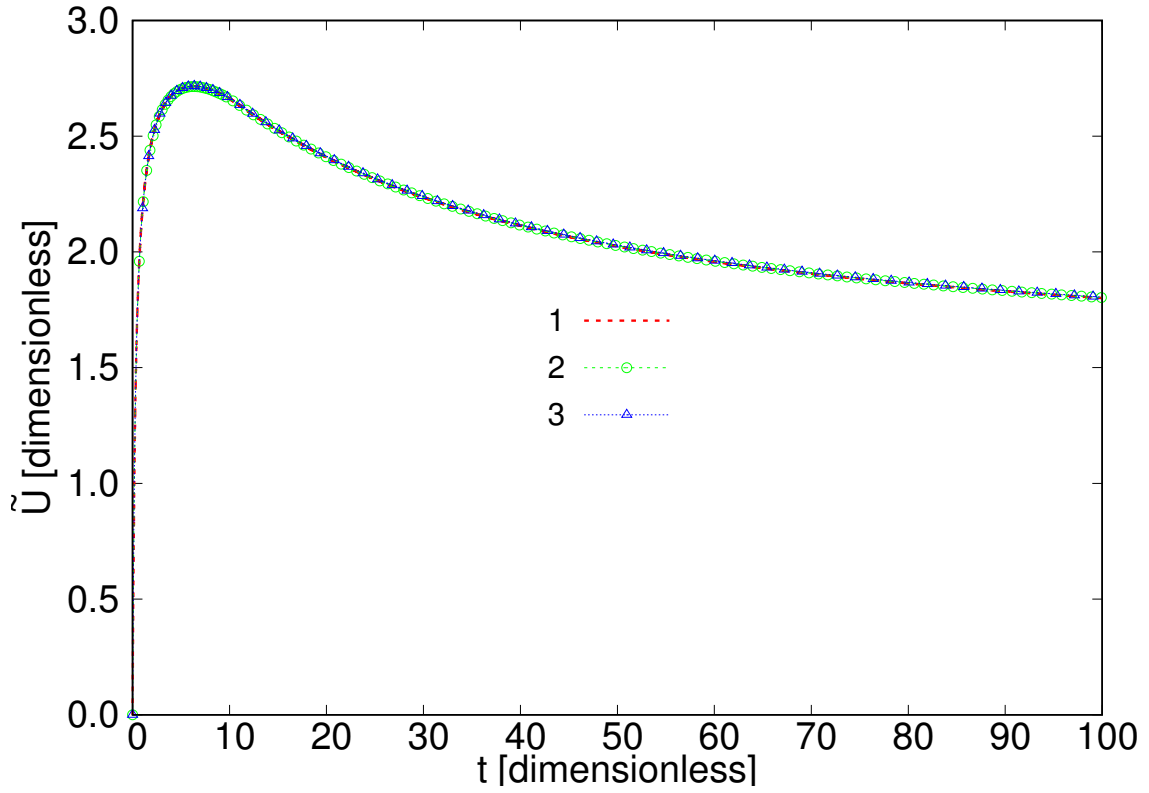


Figure 4.13: Velocity curves for $k - \omega$ SSTSAS model in 3 different solver executions.

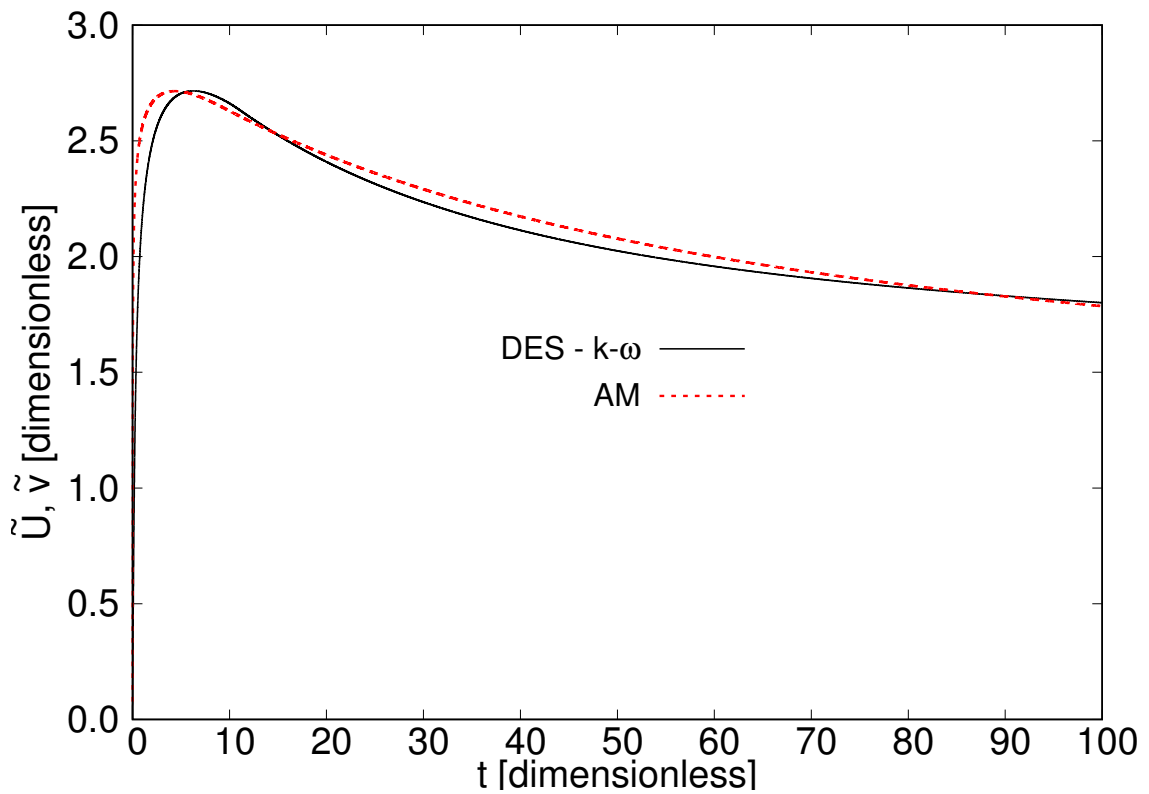


Figure 4.14: Velocity curves for DES simulation and AM ($L_v = 7.6 \cdot 10^{-3}$, $\zeta_D = 8.75 \cdot 10^{-5}$, $\Delta_f = 1$).

compares it with the AHM for the parameters which most closely adjust the curve:

$$L_v = 7.6 \cdot 10^{-3} \quad \zeta_D = 8.75 \cdot 10^{-5} \quad \Delta_f = 1$$

The agreement is excellent -excluding the transition stage- indeed the best of all tested models to simulate the turbulence within the tube and the interaction with the wall. The CFD model mimics very accurately the dynamics predicted by the AHM, which is entirely based on first principles. The dynamical behaviour in the transition stage is very complex to be accurately reproduced with the available Engineering turbulence models (see remarks on page 257).

The liquid reaches the outlet at $t_f \approx 10$ in this CFD simulation, while $t_f = 9.4546$ for the AHM. The small difference could be explained by the slightly larger acceleration in the AHM, since the maximum velocity is attained earlier in the AHM. The maximum flow velocity is reached while the pipe is not yet completely full of liquid, and the friction starts to overcome the pressure even with some inner surface still dry. The pipe's relative roughness, $\zeta_D = 8.75 \cdot 10^{-5}$, is nearly equal to half the height of the first wall-node, $y = 1.5407 \cdot 10^{-4}$. In wall-units $\zeta_r^+ = 31.41$ at the velocity maximum, calculated from the Blasius correlation (4.24), and the pipe can be considered transitionally rough ($\zeta_r^+ < 60$) for all the flow. The CFD model confirms the extreme acceleration (several thousands g) undergone by the liquid in the first few time units, as predicted by the AHM.

The table 4.3 presents the most significant flow events for both, 3D CFD and 1D AHM models. The instant at which the liquid reaches the outlet is only approximate in the 3D CFD model, as it is very difficult to determine it with accuracy. On the other hand, the AHM allows the exact determination of such events.

EVENT	3D CFD		AHM	
	t	\tilde{U}	t	\tilde{v}
Flow reaches maximum velocity	6.303	2.7144	4.360	2.7149
Liquid reaches outlet	≈ 10	≈ 2.66	9.455	2.6410

Table 4.3: Comparison of flow events for 3D CFD and 1D AHM models.

Figure 4.15 shows the evolution of the liquid front as it is being discharged through the pipe, according to the CFD model. Note the velocity maximum is produced sometime between $t = 6$ and $t = 7$ (actually the maximum is reached at $t = 6.3026576$ with $\tilde{U}_{\max} = 2.7144151$). It can be appreciated that the liquid front is gradually attaining a parabolic shape, starting from a plug-like flow at $t = 1$. Whether the CFD simulation reproduce faithfully the actual evolution of the interface, is a matter that ought to be settled experimentally. To the author's knowledge, such rapidly evolving interface has not been reported yet in the literature.

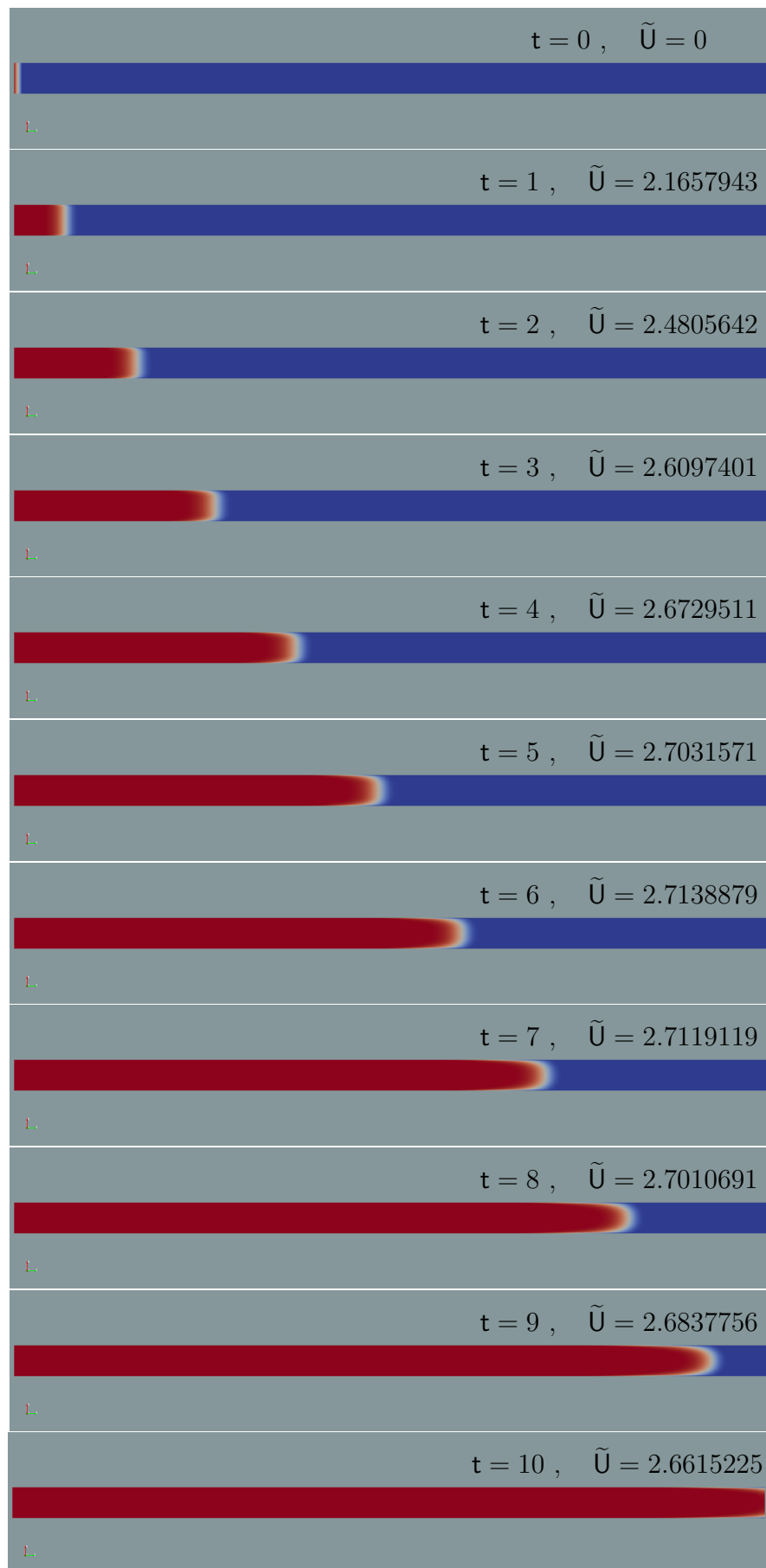
Some attention requires the mean acceleration reported by the CFD model. Following the convention, the instantaneous acceleration vector field is expressed through the Reynolds decomposition as

$$\mathbf{a}(t, \mathbf{x}) = \mathbf{A}(t, \mathbf{x}) + \mathbf{a}'(t, \mathbf{x}) \equiv \langle \mathbf{a}(t, \mathbf{x}) \rangle + \mathbf{a}'(t, \mathbf{x})$$

while the vector modulus is

$$a(t, \mathbf{x}) = A(t, \mathbf{x}) + a'(t, \mathbf{x}) \equiv \langle a(t, \mathbf{x}) \rangle + a'(t, \mathbf{x})$$

where angled brackets $\langle \cdot \rangle$ denote the ensemble average, and primes the fluctuating components resulting from the averaging process. The cross-section averaged dimensionless acceleration, or bulk

Figure 4.15: Sequence of discharge of liquid in the pipe for $k - \omega$ SSTSAS model.

acceleration, for the 1D AHM is defined by

$$\tilde{a}(t) = \frac{d\tilde{v}(t)}{dt} \quad (4.135)$$

with $\tilde{v}(t)$ the dimensionless cross-section averaged velocity, or bulk velocity, defined in Chapter 2; while for the 3D CFD model is

$$\tilde{A}(t) \equiv \tilde{\tilde{A}}(t) = \frac{d\tilde{U}(t)}{dt} \quad (4.136)$$

with $\tilde{U}(t) \equiv \tilde{\tilde{U}}(t)$ the cross-section averaged mean velocity, or bulk velocity, introduced in section 4.1 (see also footnote 6 in page 207.).

Nominally the acceleration stage elapses from $t = 0$ to $t = 6.3026576$, when the maximum velocity is achieved, and the deceleration stage runs for $t > 6.3026576$. The truth is that from $t \gtrsim 3$ the acceleration, although still positive, is much smaller than the values attained during the first time unit. Nevertheless it should not be forgotten that the reference unit for acceleration is very high, $a_{ref} = 7.420082 \cdot 10^4 \text{ m/s}^2$; therefore even accelerations as *small* as $\tilde{A} = 0.01$ still correspond to many g (see table 2.2 of reference quantities and units in page 61).

Figure 4.16 shows the mean acceleration during the full discharge process, from $t = 0$ to $t = 100$. Since $\tilde{A}(t)$ decreases several orders of magnitude in few time units, the curves are displayed in two vertical and horizontal scales:

- The left-down axis covers from $t = 0$ to $t = 5$, and positive accelerations from $\tilde{A} = 12$ to $\tilde{A} = 0$.
- The right-upper axis covers from $t = 5$ to $t = 100$, and positive/negative accelerations from $\tilde{A} = 0.01$ to $\tilde{A} = -0.04$.

The sharp positive and negative peaks at nearly $t = 10$ correspond to the narrow interval in which the interface liquid-air reaches the pipe's outlet, and ought to be considered a minor flaw in the solver. They could have been removed from the curves, but it has been preferred not to edit them. The solver developed for this application calculates the cross-section averaged velocity at exactly the pipe's end section $z = 25$, and that would explain the appearance of the peaks at that position. At $t = 100$ the deceleration, although much tamed, is still above $15 g$.

Figure 4.17 shows the pressure distribution along the pipe's centreline, which has been taken as the Z axis, from $z = 0$ to $z = L = 25$. The vi^{th} assumption of page 33 is confirmed in the CFD simulation (see figure 2.10). Thus the 3D CFD model is also coincident with the AHM in this respect: the pressure gradient develops exclusively in the wet zone of the pipe. The dry zone, where only air exists, presents no noticeable pressure gradient³⁸. The longitudinal distribution of pressure is shown for the same instants considered in figure 4.15. From $t > 10$ the whole tube is full of liquid and the pressure gradient involves the total length L .

The pressure gradient is constant for all instants up to $t = 8$. At time $t = 9$ the liquid-air interface is very near the outlet and the coupling pressure-velocity CFD algorithm makes the variation of p with z to adopt a parabolic-like behaviour (another minor flaw in the solver). That dependence of $\partial p / \partial z$ on z must manifest itself onto a dependence of \tilde{U} with z as well (see remarks on page 43). This is confirmed in the CFD simulation curves, and an example thereof is presented in figure 4.18 for instants $t = 9, 10$, where

³⁸That statement makes sense upon realising that air density is some 1600 times smaller than liquid density (FK-5-1-12). Therefore, any pressure gradient in the dry zone, however small, is directly converted into air motion with negligible inertia, thus rendering a near-zero pressure gradient therein.

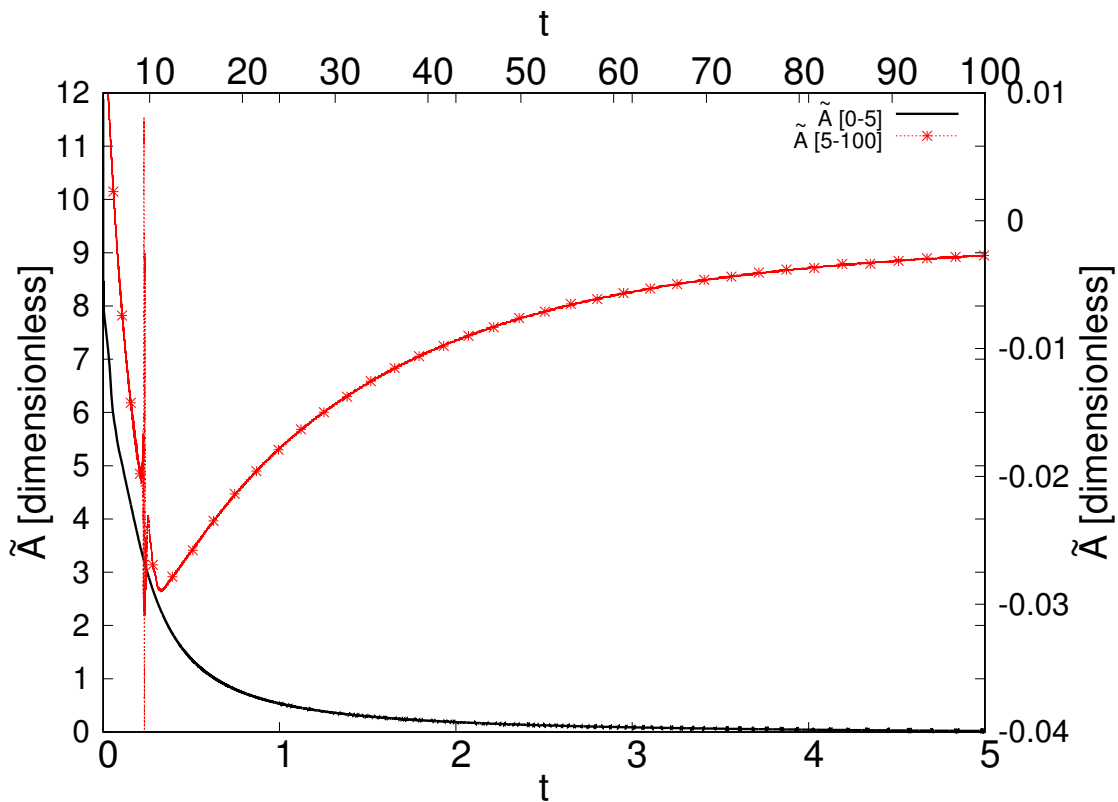


Figure 4.16: Cross-section averaged flow acceleration for $k - \omega$ SST SAS model.

it is also evident the centreline mean velocity decreases in just one dimensionless time unit. Besides, for $t \geq 6$ the pressure at the liquid-air interface is below the atmospheric pressure³⁹. This surely be a numerical effect introduced by interFOAM, which might have problems following such a fast-evolving interface, and be probably related with the parabolic-like form of the liquid front seen in figure 4.15. Of course, the results discussed herein refer only to the pipe's centreline, being different for other points within the pipe's cross-section. Upon averaging through the cross-section, all those particular effects compensate one another to produce an unique $U(t)$ free from them.

■

The comparison between 1D AHM and 3D CFD model would not reach much further than what has already been discussed. It is now time to see what sort of internal structure for the flow predicts the CFD, since the AHM offers none. To this end it is convenient to compare the resulting unsteady flow structure with that of a more familiar steady state flow. Aside from the transient CFD model described along this Chapter, a parallel steady state model has also been prepared. The CFD steady state has every property identical to the transient: geometry, solver, differencing schemes, turbulence model... The only and single difference is that in the former the pressure has been set constant at the inlet throughout the simulation. For the sake of brevity, the unsteady/transient CFD will be called the **U-model**, while the other will be the **S-model**.

The S-model has been set so that to obtain a sufficiently high velocity, which could then be compared

³⁹Most incompressible flow solvers within the OpenFOAM suite, including interFOAM and the specific solver herein derived therefrom, take the atmospheric pressure as zero. Therefore, the calculated pressures are relative to atmosphere or **gauge pressures**. This aspect has already been taken into account upon preparing the 3D CFD model, since the pressures in the 1D AHM *must* be absolute.

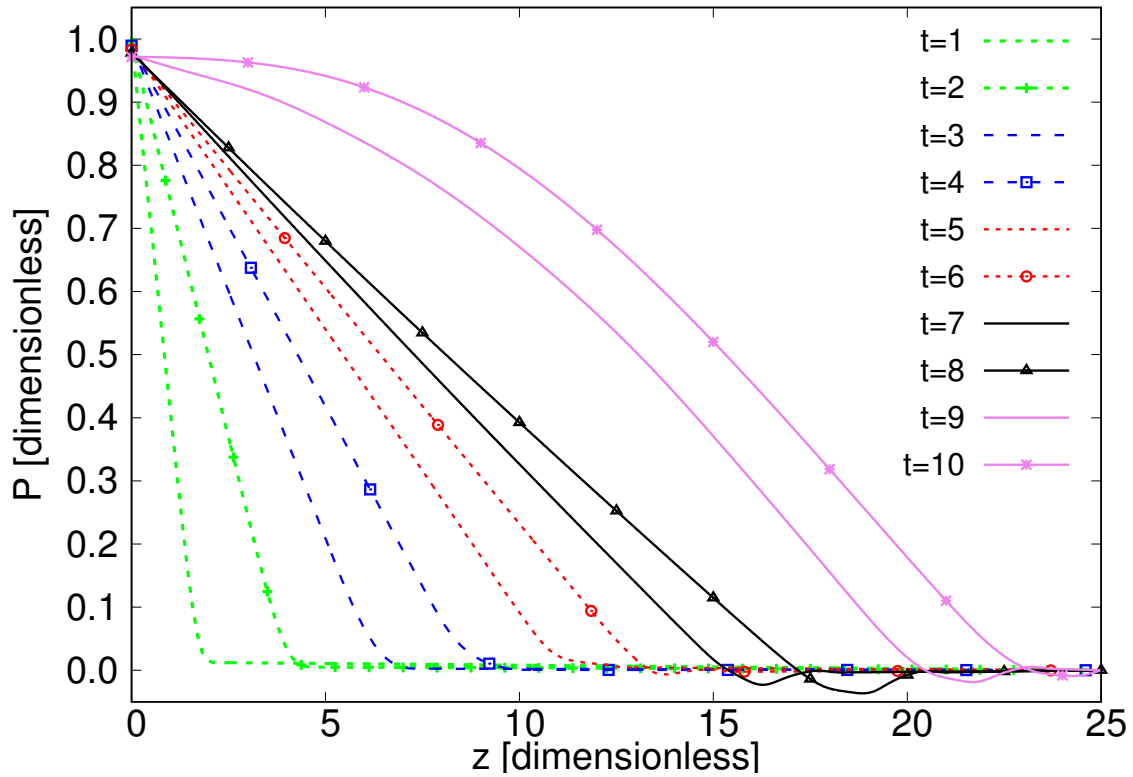


Figure 4.17: Mean pressure along Z axis at instants in fast stage for $k-\omega$ SSTSAS model.

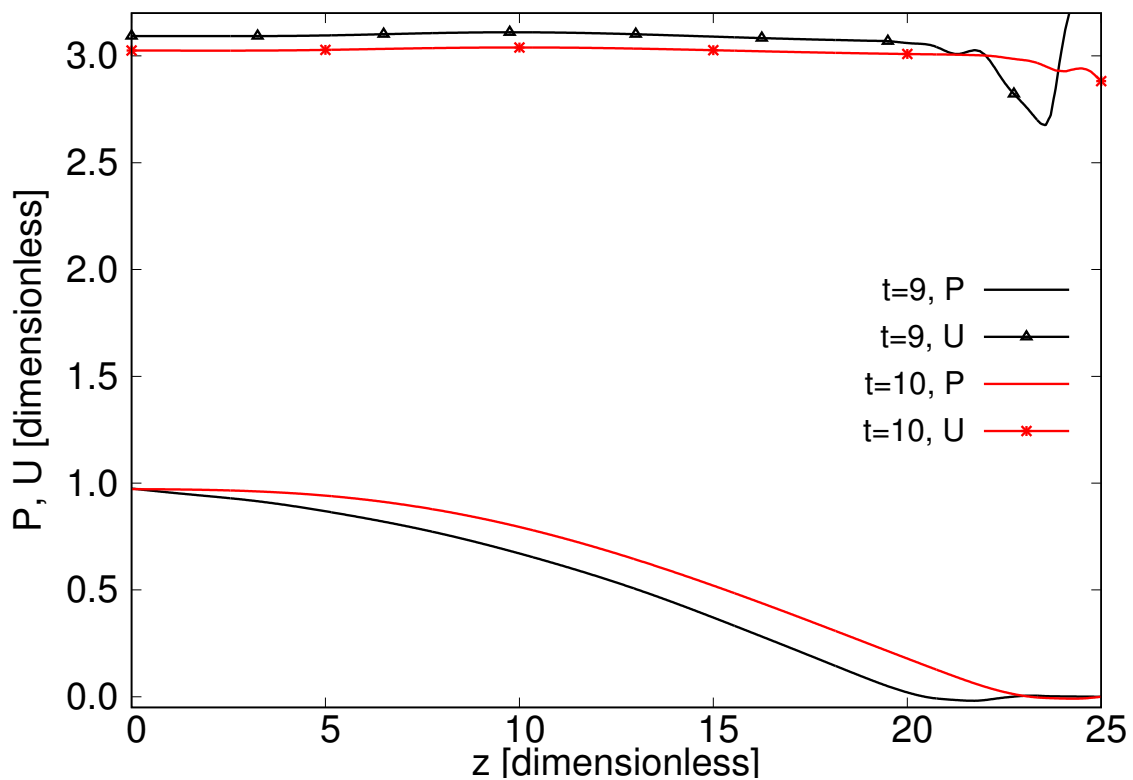


Figure 4.18: Mean pressure and velocity along centreline at $t=9, 10$, $k-\omega$ SSTSAS model.

with a similar one in the deceleration stage, not too far from the maximum. The S-model has been run until a steady bulk velocity has been achieved. When it was fully stabilised, to the point that it was a rigorous steady state flow, the resulting bulk velocity was 2.03463. This S-model bulk velocity matches almost exactly the U-model velocity corresponding to time $t = 49$, which happens to be 2.03465, and differs from the S-model's bulk velocity less than 0.001%. For the U-model, $t = 49$ corresponds to the deceleration stage. The Reynolds numbers for each simulation also match to $1.06 \cdot 10^7$ with 0.001% accuracy.

Figure 4.19 shows the cross-section mean velocity profiles for the U-model at $t = 49$. They correspond to positions $z = 5, 12.5, 20, 24.5$, so that they could be assessed at the entrance and fully developed regions of the flow (the outlet is located at $z = L = 25$). They are labelled with 'u'. Also, the cross-section mean velocity profiles for the S-model are shown for the same positions. They are labelled with 's'. Finally, figure 4.19 shows the theoretical log-law profile according to equation (4.54) (curve labelled 'Theor.'). All curves are made up of 10^4 equally spaced points across the diameter (5000 across the radius); therefore they depict the profiles quite finely, so much indeed that the first point ($y = 10^{-4}$) is nearer to the wall than the wall-nearest node in the mesh ($y = 1.5407 \cdot 10^{-4}$). The unsteady profiles along the tube superimpose one another almost perfectly, thus fulfilling the condition $\partial U / \partial z = 0$. This result is general in all simulation tests carried out: the velocity profiles are z -dependent in the acceleration stage, and virtually z -independent in the deceleration stage. The theoretical and steady state profiles match one another almost perfectly, thus indicating that the steady-state case reproduces very well the log-law, as might be expected. Both curves depart from the U-model profiles in the shoulders, where they are not so abrupt, thus presenting the unsteady profiles a larger velocity gradient near the wall, that is, a larger skin friction coefficient⁴⁰. Nevertheless the agreement steady-unsteady is noteworthy, having into account that at $t = 49$ the unsteady bulk velocity is 2.03465, the bulk acceleration is -0.00787 (some $-60 g$) and the Reynolds number is $1.06 \cdot 10^7$.

Some remarkable sets of velocity profiles for unsteady accelerating pipe flow are those offered by members of the Tallinn Technical University (see [Ann11], [AKSA13], and [ALSL81]). Unfortunately, such profiles have been obtained in conditions not directly comparable with the application described herein, since the pipe is initially full of liquid and the accelerations and velocities are much smaller than those provided by either 1D AHM or 3D CFD model, and they would not serve as plausible benchmark for the profiles of figure 4.19.

Figure 4.20 shows the law of the wall results for the U-model ($t = 49, z = 20$) and the S-model ($z = 20$). Note $y = R - r$ corresponds to the radial distance to the wall, and $y^+ = y u_\tau / \nu$ is that distance in wall-units. Average wall-shear stress along pipe's wall at $z = 20$ for U-model is $\tau_w = 0.1024$, corresponding to an average friction velocity of $u_\tau = \sqrt{\tau_w / \rho} = 0.32$. The average y^+ in the same circumference at $z = 20$ for the U-model, as calculated by OpenFOAM, results $y^+ = 108.8$. For the S-model, the calculated average y^+ at $z = 20$ is $y^+ = 53.21$ ⁴¹. Since the mesh geometry is identical, it corresponds a friction velocity of $u_\tau = 0.1565$. With those values, the law of the wall for U-model and S-model has been drawn

⁴⁰This would indicate that the unsteady friction factor is larger than the steady state counterpart.

⁴¹Note OpenFOAM yields y^+ values somewhat higher than Blasius correlation (4.24) for the S-model (check table 4.1), and more than double for the U-model. Possibly, this is due to how OpenFOAM calculates the wall-shear stress:

$$\tau_w = \rho(\nu + \nu_t) \left. \frac{\partial U}{\partial y} \right]_{y=0} \quad (4.137)$$

Usually $\nu_t = 0$ for $y \rightarrow 0$, because at the laminar sublayer there is no turbulence. However, in the U-model (and in the S-model to less extent) the laminar sublayer is so far behind the first wall-node, that the eddy viscosity ν_t plays a relevant role and increases τ_w considerably.

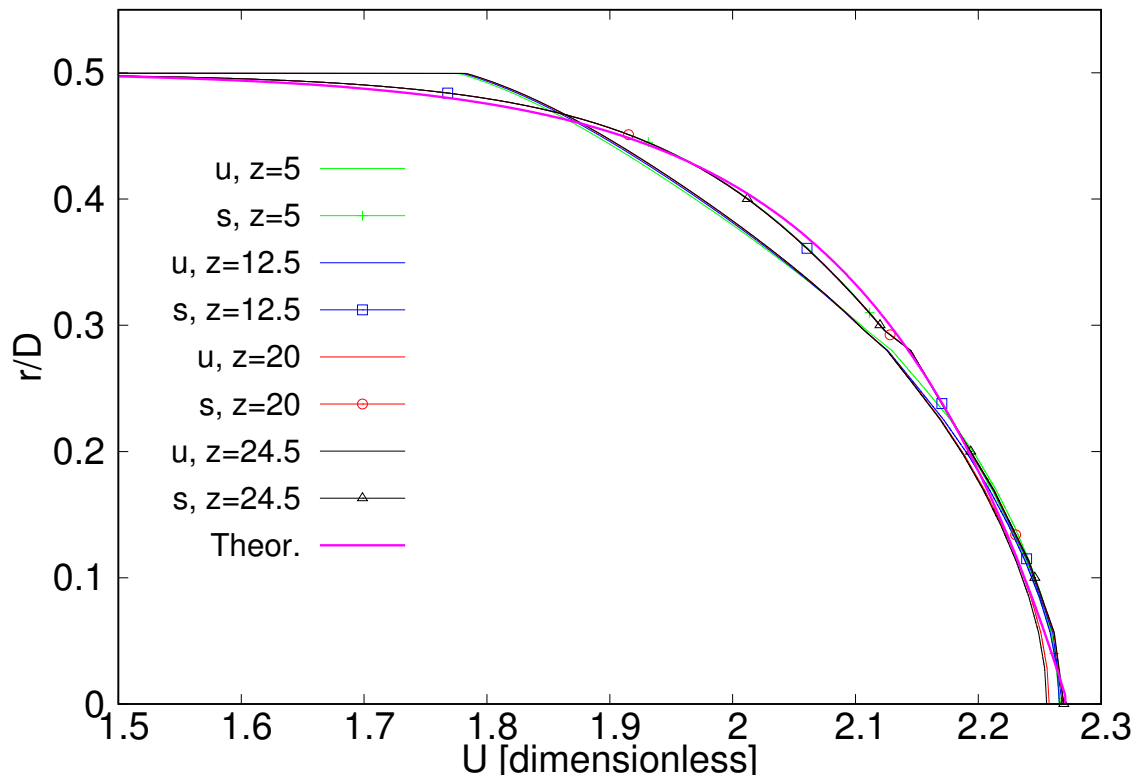


Figure 4.19: Mean velocity profiles for unsteady $t = 49$ (u) and steady (s) flow in $k - \omega$ SSTSAS model for positions $z = 5, 12.5, 20$ and 24.5 . Also theoretical log-law profile.

in figure 4.20. Unfortunately, both CFD simulations of the log-law do not appear to contain many points, so the resulting curves are not very smooth. Figure 4.20 also displays the theoretical smooth-walls log-law, equation (4.54), with $\kappa = 0.41$ and $B = 5.57$, which are the values adopted by OpenFOAM. Finally, also the rough-wall profiles according to equation (4.88) which better match the U-model and S-model are drawn. For the U-model the offset is given by $\Delta u^+ = 16.8$, whereas for the S-model is $\Delta u^+ = 14.3$. Thus, the theoretical rough-wall velocity profiles are given, respectively, by:

$$u_u^+ = \frac{1}{\kappa} \ln y^+ - 11.23 \quad u_s^+ = \frac{1}{\kappa} \ln y^+ - 8.73$$

The result would suggest that OpenFOAM is considering a very hydraulically rough flow for both models, meaning that the wall-functions are ignoring completely the laminar sublayer, since it falls deep under the wall roughness, or in other words, the first wall-node is too far above the laminar sublayer to even consider it. The first remarkable outcome is that two flows with the **same** Reynolds number could provide so different profiles: although both are reasonably parallel (at least up to $y^+ \approx 900$), the U-model presents a stronger wall-shear stress, because it is distinctly displaced downwards. On the other hand, the S-model seems to have a correct behaviour for a hydraulically fully rough flow: it follows a displaced log-law which is itself parallel to the theoretical smooth-wall log-law. In this regard, the OpenFOAM solver appears to yield consistent results, despite having just a few available nodes within the log-layer. That agreement with the rough-wall log-law would explain the match of velocity profiles for S-model and 'Theor.' in figure 4.19.

There is a second interesting outcome. Below $y^+ \approx 150$ and above $y^+ \approx 900$ the U-model departs noticeably from the log-law behaviour: below because the mesh has no available nodes; above because

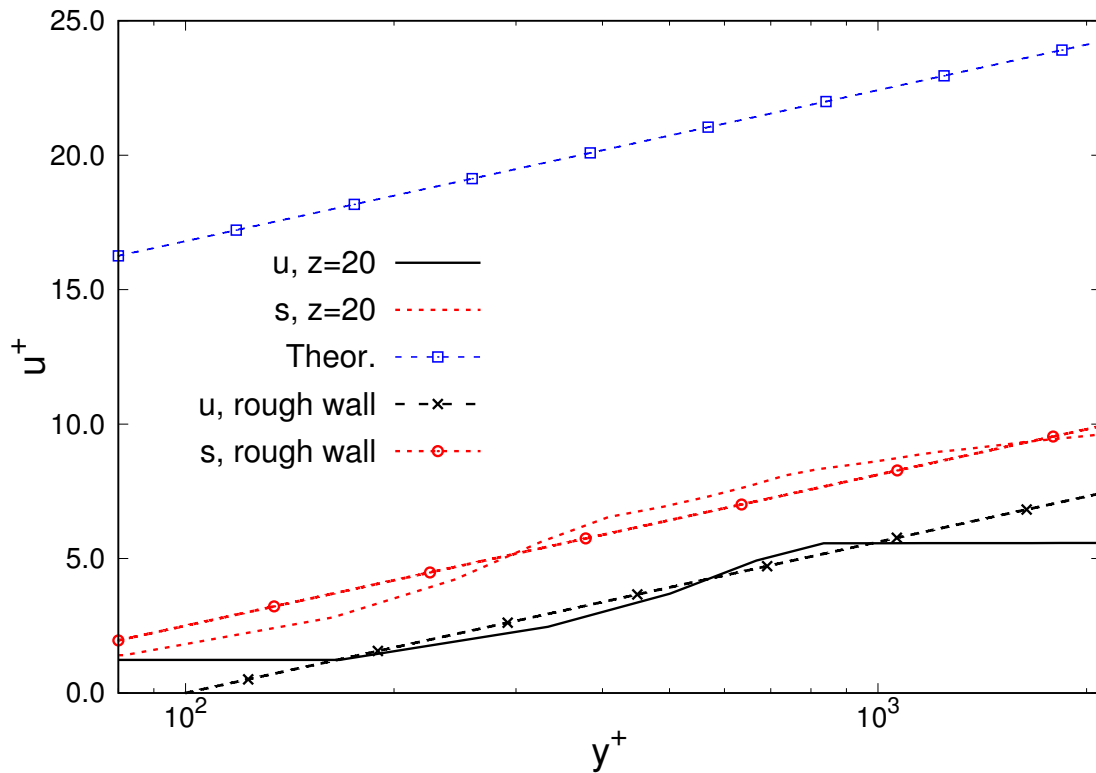


Figure 4.20: Law of the wall for unsteady $t = 49$ (u), steady (s) and theoretical (Theor.) flows in $k - \omega$ SSTSAS model for position $z = 20$

the flow appears not to obey any longer the logarithmic pattern, always provided the OpenFOAM simulation is at least qualitatively correct. The departure from the log-law is not in itself extraordinary: most turbulent flows do that above certain value of y^+ (see figures 4.8 and 4.9). The unforeseen result is the U-model departing abruptly from its twin- Re S-model above $y^+ \approx 900$. Before that point, both models were approximately parallel, only separated by an offset $\Delta u^+ = 2.5$. This different behaviour could only be caused by the intense acceleration undergone by the U-model flow. The observed departure of U-model from S-model above $y^+ \approx 900$, will aid in explaining some of the interesting flow structures the U-model appears to possess, which will be discovered next upon studying the TQ profiles for both flows. Note $y^+ = 900$ corresponds to $y = 1.08 \cdot 10^{-3}$, and check the coming profiles at $y \approx 10^{-3}$

Figure 4.21 shows the Reynolds stress component R_{xz} for the flow, in both cases of U-model for $t = 49$ and S-model. Logarithmic scales has been used, since otherwise details are not visible. Only the R_{xz} component is presented, as the mean motion is along the Z axis. The vertical axis in figure 4.21 correspond to the radial distance to the wall $y = R - r$, and the log-scale starts at $y = 10^{-4}$ (the distance to the first point of the curve and almost the height of the first wall-node), and ends at $y = 0.5$, the pipe's centreline⁴². A third profile obtained from the literature would have been desirable to compare with the two shown herein. Unfortunately no turbulence profile could be found for such high Re as 10^7 . The profile behaviour is as expected, including $R_{xz} = 0$ at the centreline (not shown because the scale is logarithmic). The U-model profile is some 10 times larger than the S-model's, except when approaching the wall. The U-model peak near the wall is over 10^3 times larger than the S-model's, and that occurs at

⁴²This configuration for the vertical axis will be maintained for figure 4.21, and is different from that used in figure 4.19.

$y \approx 10^3$ when the U-model departs from the S-model (see figure 4.20). In the core flow region, where the velocity profiles are almost coincident, still is the U-model Reynolds stress 10 times larger than the S-model's. Roughly speaking the deceleration seems to cause 10 times more turbulence for the same Re . That effect is greatly amplified near the wall, perhaps because the velocity profiles for U-model and S-model are not so coincident therein.

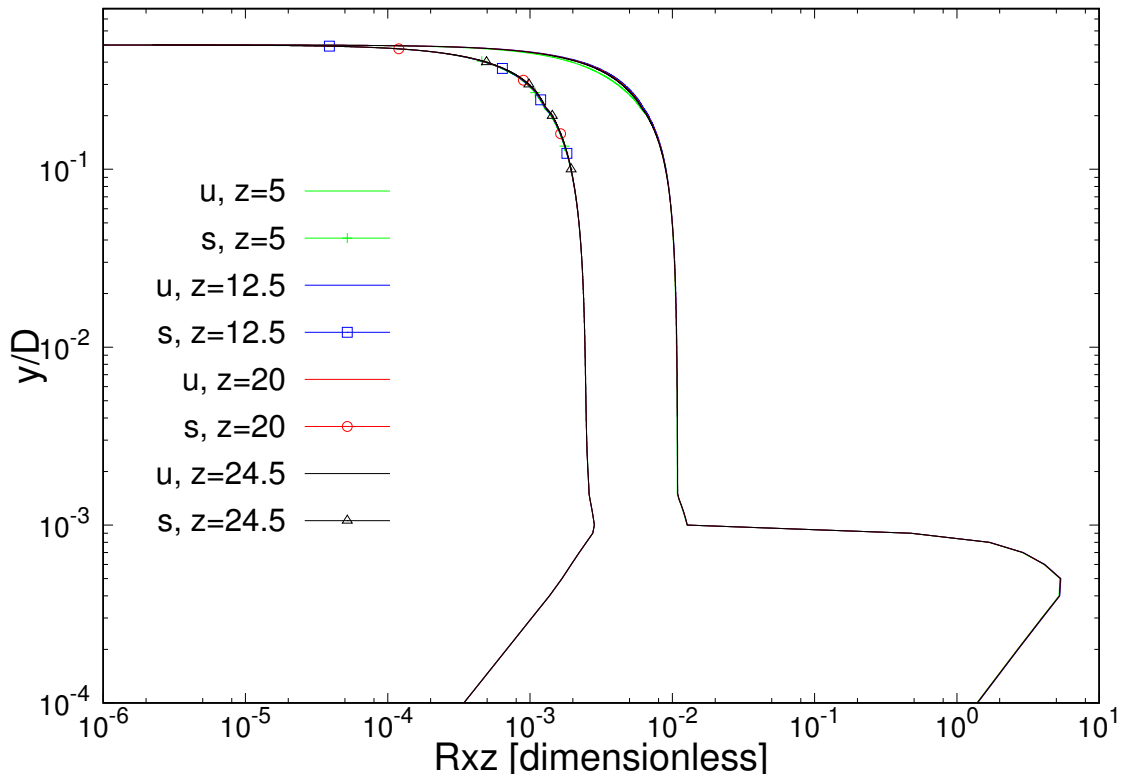


Figure 4.21: Reynolds stress R_{xz} profiles for unsteady $t = 49$ (u) and steady (s) flow in $k - \omega$ SSTSAS model for positions $z = 5, 12.5, 20$ and 24.5 .

Figure 4.22 shows the profiles for the dimensionless specific turbulent kinetic energy k , in both U-model for $t = 49$ and S-model cases. Regretfully, no third curve from the literature could be found for such high Re as $1.06 \cdot 10^7$. The expected behaviour for k is illustrated in figure 4.1, and could be summarised as: $k = 0$ at the wall (laminar sublayer, although be not modelled), followed by a sharp increase to attain its maximum very near the wall; then smoothly decreases up to the pipe's centreline. This expected behaviour is observed in both profiles, except that the log-scale does not reach to the wall ($y = 0$). In the core flow region k is $10 \sim 100$ times larger for the U-model than for the S-model, despite being very coincident the velocity profiles in such region. Close to the wall, at $y \lesssim 10^3$, that relationship increases to $10^3 \sim 10^4$ times larger, implying that the energy contained in the turbulence is likewise larger when the deceleration is present. There is a difference in the position of the maxima too: for the S-model the maximum is located at $y = 10^{-3}$, whereas for the U-model that occurs at $y = 10^{-4}$. In the S-model the k wall-function assigns a small value to k at the first wall-node, $k \approx 10^{-3}$, an indication that y^+ was small enough at that wall-node. In U-model the wall-node has a greater y^+ because the friction velocity u_τ is larger, and thus the k wall-function assigns a large value to k in the same wall-node: $k \approx 5$, almost $5 \cdot 10^3$ times larger. There is a slight but noticeable difference in the U-model k profile for $z = 5$ and the rest, probably due to entrance effects in the pipe. In the core flow region the radial gradient is much steeper in the U-model, when compared with the S-model.

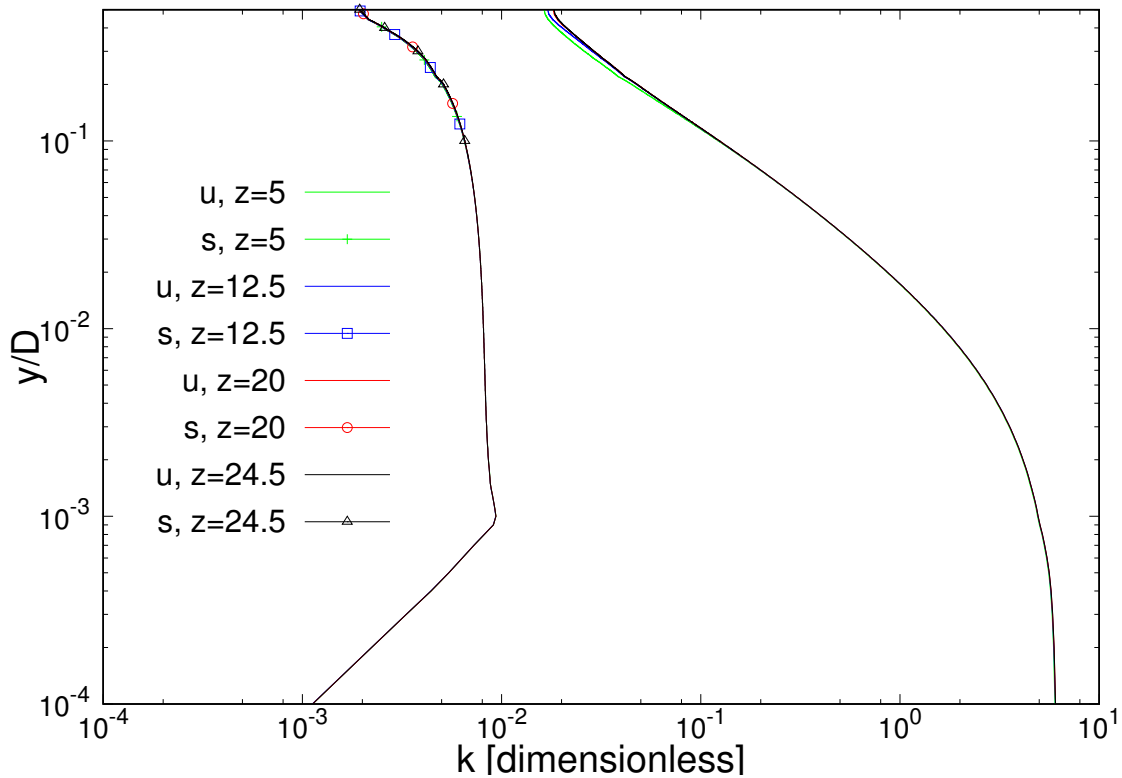


Figure 4.22: Turbulent kinetic energy k profiles for unsteady $t = 49$ (u) and steady (s) flow in $k - \omega$ SSTSAS model for positions $z = 5, 12.5, 20$ and 24.5 .

Figure 4.23 shows the profiles for the dimensionless specific turbulent kinetic energy dissipation ϵ , for both U-model at $t = 49$ and S-model, with no third curve to serve as reference. For ϵ it is expected a similar behaviour than that seen for k : $\epsilon = 0$ at the wall (laminar sublayer, although be not modelled), whereas it reaches its maximum very near the wall; then a smooth decrease up to a minimum at the pipe's centreline (see figure 4.1). This is duly observed in the profiles. Within the core flow region ϵ is $10 \sim 100$ times larger for the U-model than it is for the S-model, despite being very coincident the velocity profiles in such region. Close to the wall (again for $y \lesssim 10^3$), that relationship increases to $10^3 \sim 10^4$ times larger, implying that the energy dissipated in the turbulence is likewise larger when the deceleration is present. There is also a difference in the position of the maxima, just as in the case of k : for the S-model the maximum is located at $y = 10^{-3}$, whereas for the U-model that occurs at $y = 10^{-4}$. In the S-model the ϵ wall-function assigns a small value to ϵ at the first wall-node, $\epsilon \approx 3 \cdot 10^{-1}$, an indication that y^+ was small enough at that wall-node. In U-model the wall-node has a greater y^+ because the friction velocity u_τ is larger, and thus the ϵ wall-function assigns a large value to ϵ in the same wall-node: $\epsilon \approx 10^3$, almost $5 \cdot 10^3$ times larger. There is also a slight but noticeable difference in the U-model ϵ profile for $z = 5$ and the rest, possibly due to entrance effects in the pipe. In the core flow region the radial gradient is not so steeper in the U-model, when compared with the S-model, as it was in the k case.

Figure 4.24 shows the profiles for the dimensionless specific dissipation rate of turbulence ω , in both U-model for $t = 49$ and S-model cases, again with no third curve to compare to. The already described general behaviour is also expected for ω and thus appear in the profiles. It should be noticed that the profiles corresponding to U-model and S-model cross at around $y \approx 10^{-3}$ (where else?). That situation is compatible with the behaviour seen above for k and ϵ , since both are related by $\omega \sim \epsilon/k$. This time the

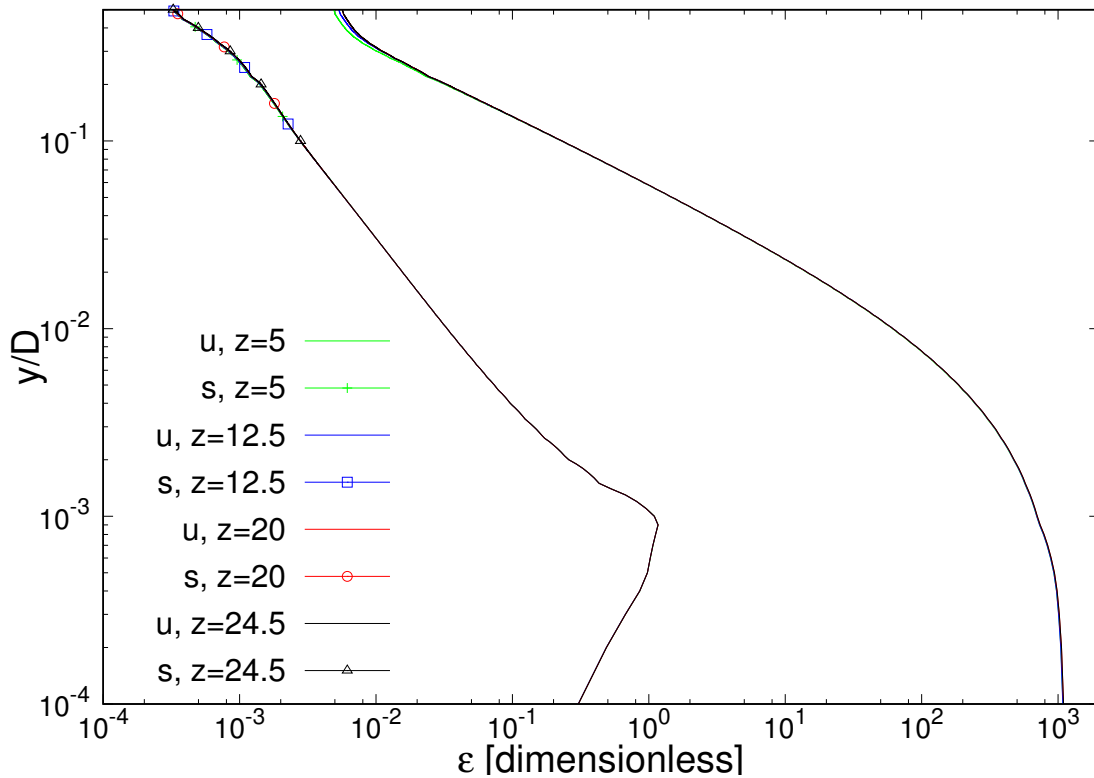


Figure 4.23: Turbulent energy dissipation ϵ profiles for unsteady $t = 49$ (u) and steady (s) flow in $k - \omega$ SSTSAS model for positions $z = 5, 12.5, 20$ and 24.5 .

maximum for S-model also occurs at $y = 10^{-4}$, just like the U-model. With ω the general trend seen so far is inverted: as $r \rightarrow R$ ($y \rightarrow 0$) the simulations predict some 26 times more dissipation rate for steady state $\omega \approx 53400$, than for unsteady regime $\omega \approx 2050$. There is also a slight difference in the U-model ω profile for $z = 5$ and the rest, probably due to entrance effects in the pipe.

Figure 4.25 shows the profiles for the dimensionless mean vorticity ζ , for both U-model at $t = 49$ and S-model. As it might be expected, the vorticity ζ increases in the radial direction as the wall is approached from the centreline. While the S-model grows smoothly across the radius, the U-model's ζ shoots up around $y \approx 10^{-3}$ by a factor $\gtrsim 100$. If vorticity preludes turbulence, one would say that most turbulence is concentrated near the wall, according to the U-model. That jump near $y \approx 10^{-3}$ shows resemblance with the one presented by R_{xz} at the same position (see figure 4.21). There is nothing in the model's mesh geometry that could cause such jumps: the transition from coarse to fine grid occurs at $y \approx 0.25$ (see figure 4.11). Thus, no other explanation could be offered but the often-mentioned departure of U-model from S-model at $y \approx 10^{-3}$ observed in figure 4.20. It is also noteworthy that both, U-model and S-model, profiles cross at around $y \approx 10^{-3}$, with the U-model ζ more than doubling the S-model's as $r \rightarrow R$, $\zeta_u \approx 7800$ vs. $\zeta_s \approx 3450$. There is a slight but noticeable difference in the U-model ζ profile for $z = 5$ and the rest, possibly due to entrance effects in pipe.

■

In summary, there are three types of profiles: a theoretical log-law, a set of calculated steady state, and a set of calculated transient profiles. Strictly the same solver with the same settings and configuration (except the boundary conditions for pressure) yields the S-model and U-model data. The S-model and theoretical profiles are coincident within 0.05% in figure 4.19, and present consistent behaviour in figure

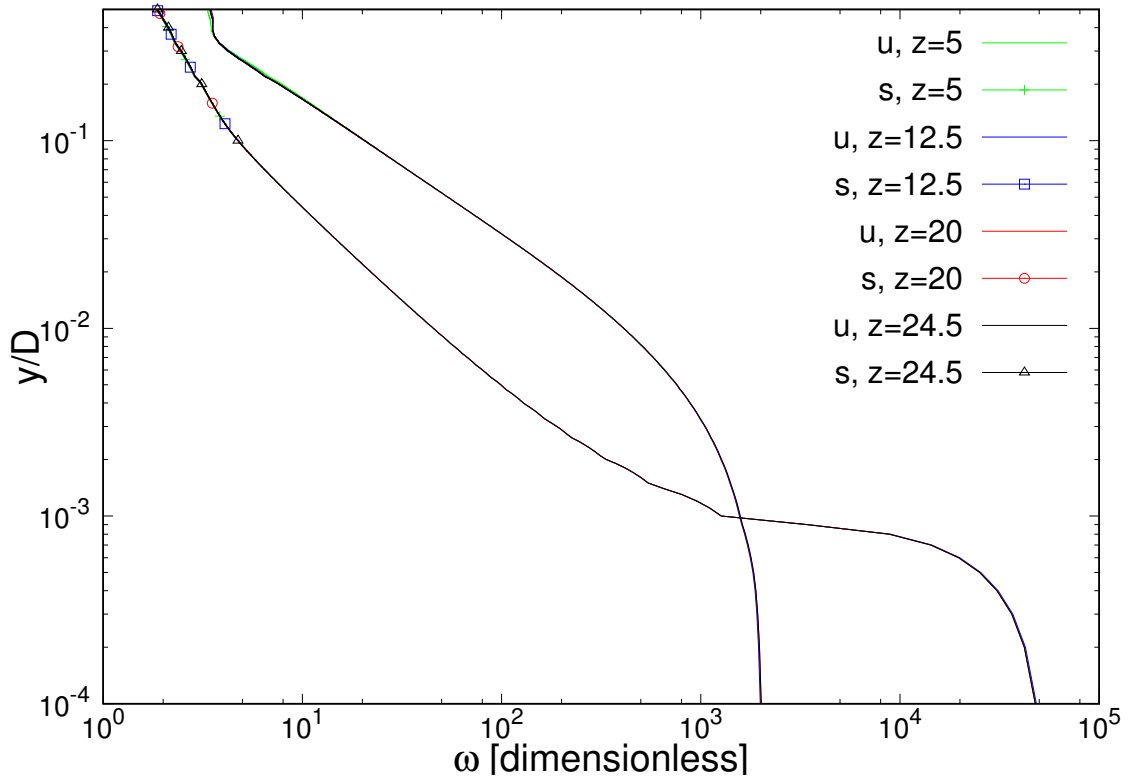


Figure 4.24: Turbulence dissipation rate ω profiles for unsteady $t = 49$ (u) and steady (s) flow in $k - \omega$ SSTSAS model for positions $z = 5, 12.5, 20$ and 24.5 .

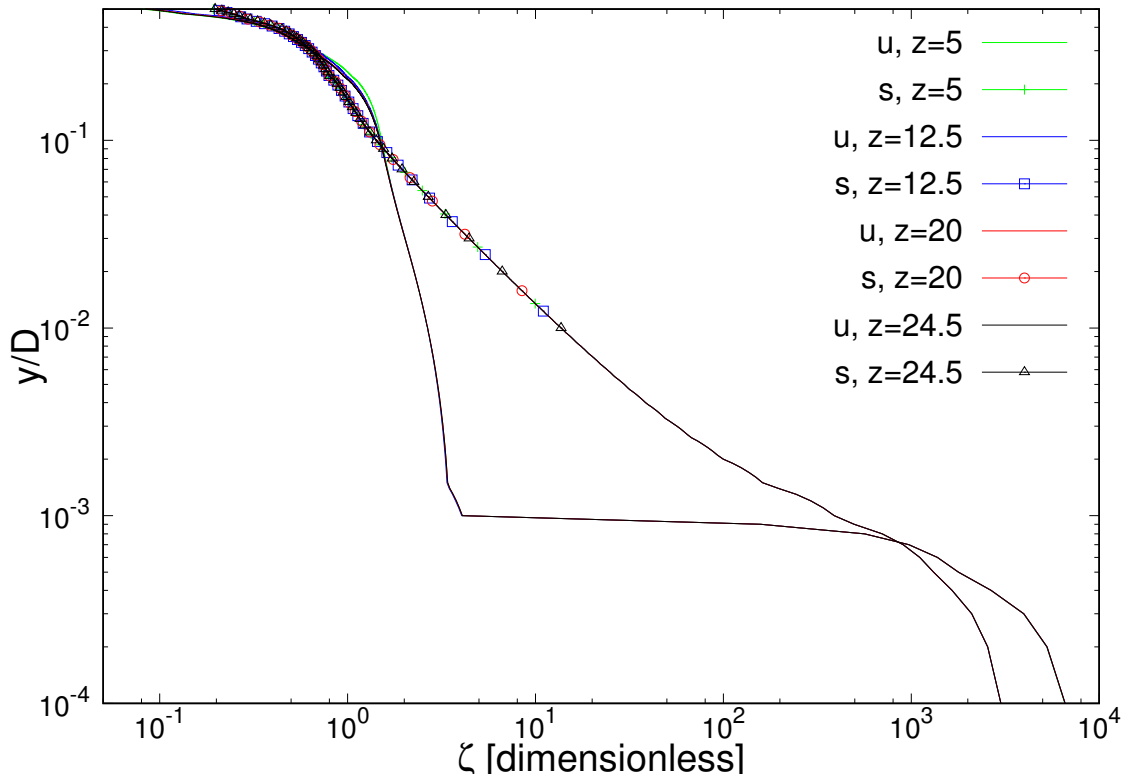


Figure 4.25: Vorticity ζ profiles for unsteady $t = 49$ (u) and steady (s) flow in $k - \omega$ SSTSAS model for positions $z = 5, 12.5, 20$ and 24.5 .

4.20. Therefore, there are reasons to believe the solver is performing well and one could, in principle, endorse its results. Besides, the U-model is also quite coincident with the 1D AHM, another reason not to entirely distrust the solver. One of those results shows that the U-model velocity profiles present larger gradient near the wall than the S-model, ensuing in a modified velocity profile which differs from the theoretical log-law. This is also confirmed by the observed departure of U-model from S-model in the log-law at around $y \approx 10^{-3}$, figure 4.20. The difference could be explained through the very high values attained by the TQ, R_{xz} , k , ϵ , ζ , beyond the departure point $y \approx 10^{-3}$ in the U-model. This remarkable thousandfold difference in the TQ is the main clue the 3D CFD model furnishes to justify the deformed unsteady velocity profiles seen in figure 4.19. It is worth a further research on the influence of acceleration in the generation of turbulent structures within the flow, which causes the unsteady log-law to be altered with respect to steady-state flow.

Hence, high deceleration brings forward higher values for TQ⁴³. This extra turbulence shapes the mean velocity profile and changes its usual form, specially near the wall where the highest velocity gradient concentrates. Thus high deceleration appears to contribute to high velocity gradient, higher than in steady state flows (at least in the studied cases). Despite having the same Reynolds number Re for S-model and U-model, the turbulence intensity is much higher in the later (some $10^{3/2}$ higher). Therefore it could be concluded that Re by itself is not sufficient to characterise the turbulence when acceleration is present, because the same Re yields a thousandfold higher turbulence energy for decelerating flows. The U-model suggests a relevant role for acceleration/deceleration on the production of turbulence.

Reference [Hin75] forecasts this effect for decelerating flows, while [PBPOO] describes it in detail for accelerating flows, although for much smaller accelerations than those considered herein. It is important to highlight the U-model achieves a high deceleration rate without any adverse pressure gradient, contrary to what is frequently described in the literature. At no instant of the bulk-velocity curves of figure 4.14 is $\partial P/\partial z > 0$ in any point of the pipe. Everywhere, every time, is the gradient $\partial P/\partial z < 0$ in the direction of the flow, and the deceleration is produced exclusively through friction. The dimensionless acceleration parameter $K = (\nu/U_\infty^2)(dU_\infty/dz)$ used in [PBPOO] is hardly applicable to pipe flow, since continuity equation implies $dU_\infty/dz = 0$ in this case. A new dimensionless number seems to be necessary to characterise the additional turbulence production due to deceleration in the flow. In this Dissertation the following dimensionless acceleration number is proposed

$$GF = \frac{\tilde{a} D^2}{\nu \tilde{v}} \quad (4.138)$$

being \tilde{v} the bulk velocity and \tilde{a} the cross-section averaged acceleration (bulk acceleration) of the flow. Figure 4.26 shows the curve for GF corresponding to the U-model simulation (the sharp peak around $t = 10$ is not omitted).

For the interested reader, the accelerating turbulent boundary layer is discussed in [DHOJ56], [KM86], [Lef88], [PBPOO], [GMO4], [PKPB07], [JC12], [HS13] and [SHVO14]. Further research is being conducted to characterise the production of turbulence from strongly accelerated/decelerated flows. Some CFD models are being exploited in order to provide an useful relationship linking the turbulence intensity with the GF number for a wide spectrum of Re . Keeping the geometry simple for the moment, the

⁴³It would be expected that high acceleration present a like effect, although this cannot be safely confirmed by the U-model, since the acceleration stage is short, the pipe is not yet full of liquid, the influence of the liquid-air interface on the flow cannot be neglected, the entrance effect is not entirely absent, the initial conditions for the TQ have probably still not settled (see section 4.4) and, most important of all, the acceleration values attained in this stage are enormous. On the other hand, the deceleration stage offers a wide range of bulk-velocity values to work with, affected by relatively *moderate* decelerations.

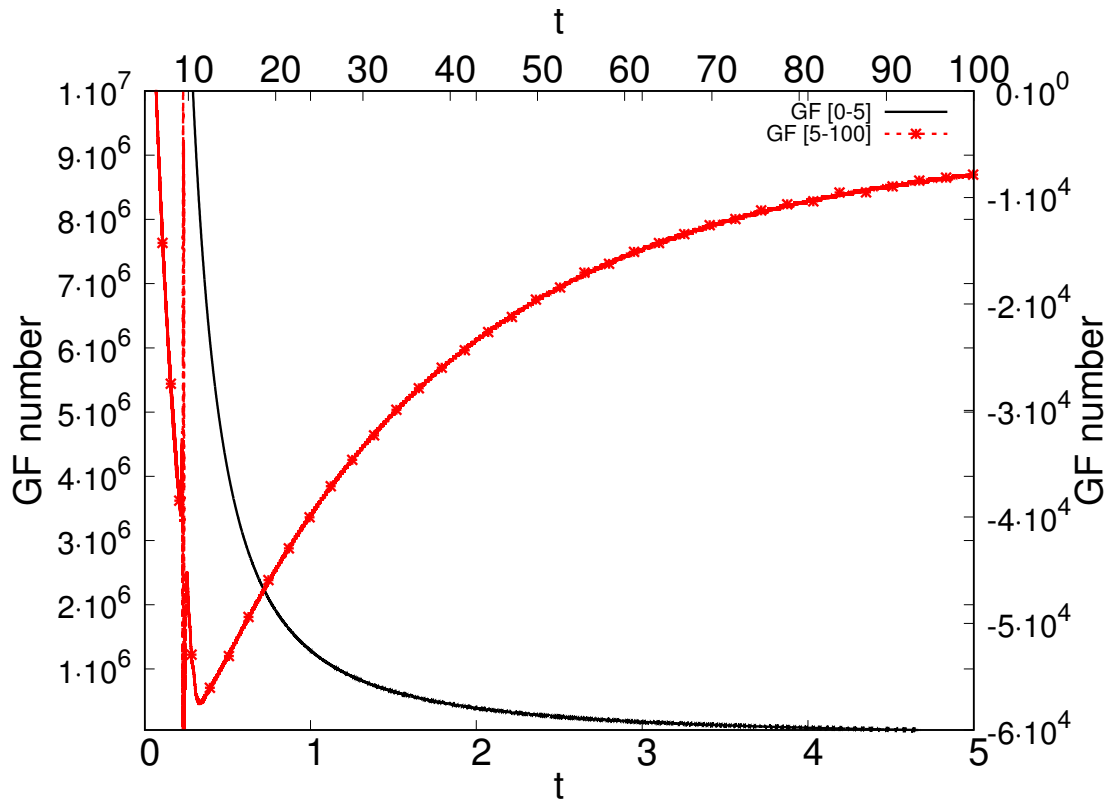


Figure 4.26: Dimensionless number evolution for $k - \omega$ SSTSAS model.

CFDmodels are offering very interesting and massive data which is yet to be analysed and ordered into structured information.

4.10.2 $k - \epsilon$ Launder-Sharma

$k - \epsilon$ Launder-Sharma was developed as a low Re turbulence model by Launder and Sharma [LS74]. The damping functions are inserted in the equations to account for the near-wall damping effect on the movement. It is a two-equations RAS turbulence model because two turbulence fields are directly calculated, namely k and ϵ , or rather $\tilde{\epsilon}$ as it will be seen next. It responds to the following set of equations and parameters (the symbols are named after the OpenFOAM code):

$$\frac{\partial k}{\partial t} + \nabla \cdot (\mathbf{U}k) - \underbrace{\nabla \cdot (D_{k,eff} \nabla k)}_{\text{Diffusion}} = \underbrace{G}_{\text{Production}} - \underbrace{(\tilde{\epsilon} + D)}_{\text{Dissipation}} \quad (4.139)$$

$$\frac{\partial \tilde{\epsilon}}{\partial t} + \nabla \cdot (\mathbf{U}\tilde{\epsilon}) - \underbrace{\nabla \cdot (D_{\epsilon,eff} \nabla \tilde{\epsilon})}_{\text{Diffusion}} = \underbrace{C_{\epsilon 1} \frac{\tilde{\epsilon}}{k} G}_{\text{Production}} - \underbrace{C_{\epsilon 2} f_2 \frac{\tilde{\epsilon}^2}{k}}_{\text{Dissipation}} + E \quad (4.140)$$

with the following quantities and parameters:

- Isotropic eddy dissipation rate of the turbulent kinetic energy : $\tilde{\epsilon}$ (subgrid dissipation rate)

$$\tilde{\epsilon} = \epsilon - D \quad (4.141)$$

- Effective diffusivity for k : $D_{k,eff}$

$$D_{k,eff} = \nu + \nu_t \quad (4.142)$$

- Effective diffusivity for ϵ : $D_{\epsilon,eff}$

$$D_{\epsilon,eff} = \nu + \alpha_\epsilon \nu_t \quad (4.143)$$

- Turbulent viscosity : ν_t

$$\nu_t = C_\mu f_\mu \frac{k^2}{\epsilon} \quad (4.144)$$

- Turbulence production : G

$$G = 2\nu_t S_{ij} S_{ij} = \frac{\nu_t}{2} (\partial_i U_j + \partial_j U_i) (\partial_i U_j + \partial_j U_i) \quad (4.145)$$

- Damping function : E (provides correct near-wall viscous sublayer behaviour)

$$E = 2\nu\nu_t |\nabla\nabla\mathbf{U}|^2 = 2\nu\nu_t \left(\frac{\partial^2 U_i}{\partial x_j \partial x_k} \frac{\partial^2 U_i}{\partial x_j \partial x_k} \right) \equiv 2\nu\nu_t (\partial_j \partial_k U_i) (\partial_j \partial_k U_i) \quad (4.146)$$

- Damping function : f_2

$$f_2 = 1 - 0.3 \exp \left\{ - \min \left(\left(\frac{k^2}{\nu\epsilon} \right)^2, 50 \right) \right\} \quad (4.147)$$

- Damping function : f_μ

$$f_\mu = \exp \left(\frac{-3.4}{\left(1 + \frac{k^2}{50\nu\epsilon} \right)^2} \right) \quad (4.148)$$

- Damping function : D (accounts for turbulence anisotropy at the wall)

$$D = 2\nu |\nabla\sqrt{k}|^2 = 2\nu (\partial_i \sqrt{k}) (\partial_i \sqrt{k}) \quad (4.149)$$

- And the constants:

$$\alpha_\epsilon = 0.76923 \quad (4.150)$$

$$C_{\epsilon 1} = 1.44 \quad (4.151)$$

$$C_{\epsilon 2} = 1.92 \quad (4.152)$$

$$C_\mu = 0.09 \quad (4.153)$$

Originally thought for low Re flows, the Launder-Sharma $k - \epsilon$ model normally does not need wall-functions, and it is frequently sufficient to use only damping functions to simulate simple turbulent flows. The CFD model developed herein obviously needs wall-functions, and use is made of both, wall-functions and damping functions. It is, perhaps, this combined effect of both types of functions what makes the model effective in grasping the wall-friction along the pipe flow.

The model was executed 6 times, each with a different configuration. They are listed in table 4.4, which characterises the velocity curves generated by the model. Cases 1 – 4 (OpenFOAM version 2.1.0) were run at CESGA⁴⁴. Results are shown in figure 4.27

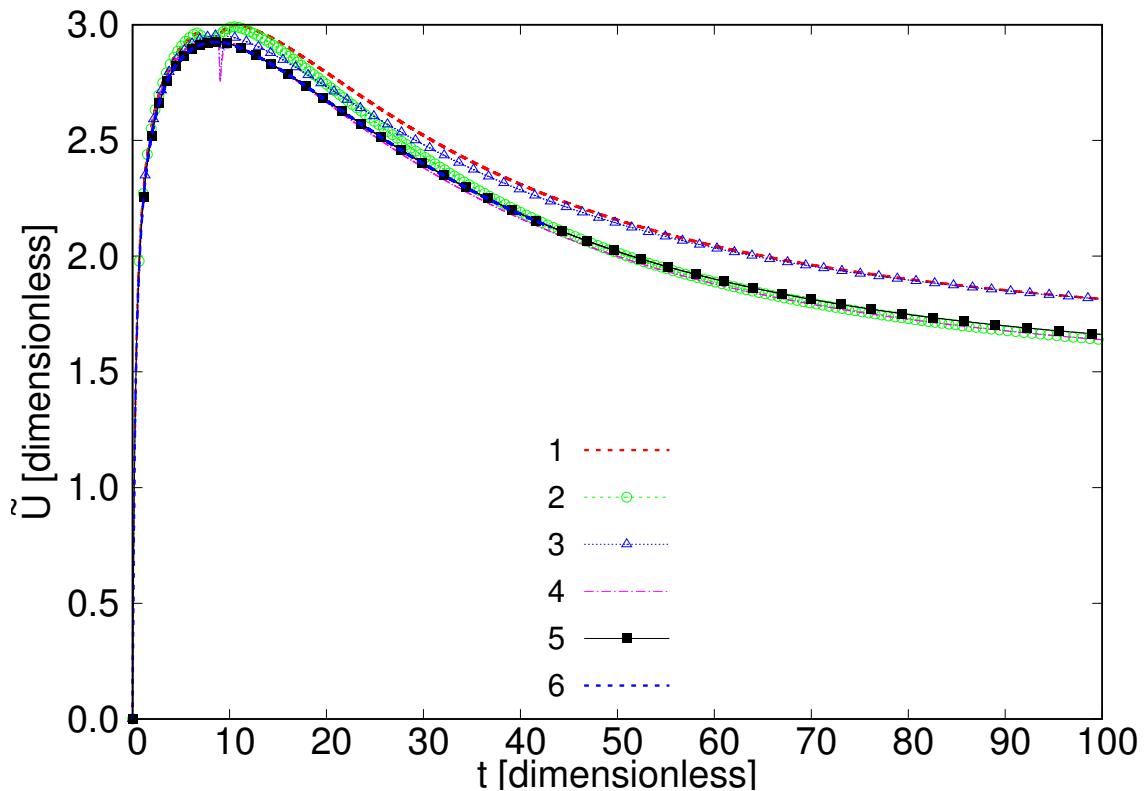


Figure 4.27: Velocity curves for $k - \epsilon$ Launder-Sharma model in 6 different solver executions.

Label	No.cells	Diff.Sch. U	Diff.Sch. $k - \epsilon$	OF ver.	Cores	Exec.Time
1	403200	Upwind	Upwind	2.1.0	24	53 hour
2	844800	Upwind	Upwind	2.1.0	24	130 hour
3	403200	TVD vanLeer	SFCD	2.1.0	24	57 hour
4	844800	TVD vanLeer	SFCD	2.1.0	24	122 hour
5	844800	TVD vanLeer	SFCD	2.3.1	8	180 hour
6	403200	TVD vanLeer	SFCD	2.4.0	8	305 hour

Table 4.4: Features of the 6 models executed in figure 4.27.

Curves 1 and 3 present a lesser friction in deceleration stage than the others, therefore the velocity in that stage is some 10% higher. Curves 4, 5 and 6 show a lower peak than the others. Peak in 3 is between both groups.

The results in 5 and 6 prove that the model is mesh-independent for TVD and SFCD schemes. Models executed in OpenFOAM 2.1.0 always present a sharp notch in the velocity curve when the liquid reaches the pipe's outlet. However this notch is not present in OpenFOAM 2.3.1 nor in 2.4.0. This poor accuracy in capturing the fast-evolving liquid front as it reaches the pipe's outlet, could explain the slight mesh-dependency shown by the models for OpenFOAM 2.1.0. As it could be seen, the curves have some differences, specially in the deceleration stage.

Figure 4.28 shows the curve \tilde{U} obtained from the $k - \epsilon$ Launder-Sharma simulation. Also shows the

⁴⁴The execution times of cases 1 and 3 do not appear to be compatible with those of cases 2 and 4, but those were the actual results as measured by the execution time clock included in OpenFOAM.

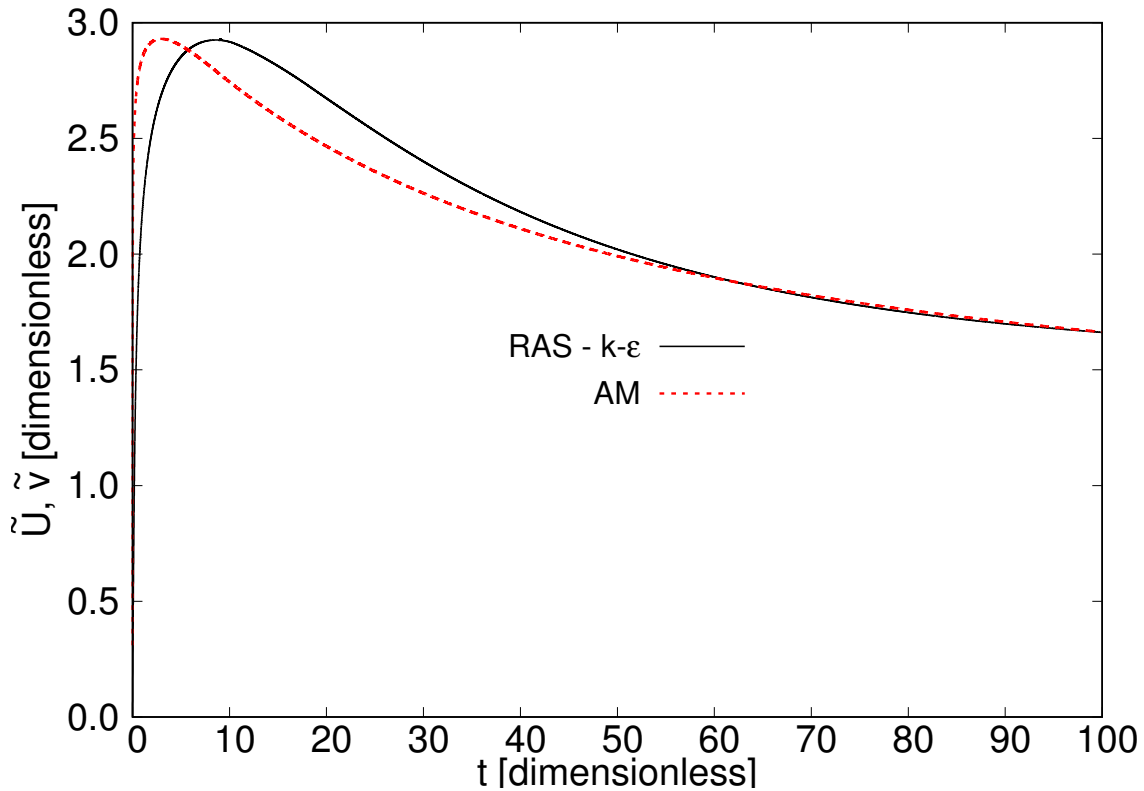


Figure 4.28: Velocity curves for $k - \epsilon$ simulation and AHM ($L_v = 1.833 \cdot 10^{-3}$, $\zeta_D = 2.0 \cdot 10^{-4}$, $\Delta_f = 1$).

AHM bulk velocity \tilde{v} with the set of parameters which most closely adjust to the CFD results:

$$L_v = 1.833 \cdot 10^{-3} \quad \zeta_D = 2.0 \cdot 10^{-4} \quad \Delta_f = 1$$

Note the relative roughness ζ_D is slightly higher than the first wall-node, yielding $\zeta_r^+ = 76.88$ at the velocity maximum, and $\zeta_r^+ = 55.03$ at $\tilde{v} = 2.0$ when the CFD and AHM curves begin to overlap, calculated by means of the Blasius correlation (4.24). Therefore the flow could be considered fully rough ($\zeta_r^+ > 60$) over the transition stage where the CFD and AHM agreement is poor, and transitional-rough during most of the deceleration stage, where both curves match very well. The liquid reaches the outlet in the AHM at $t_f = 8.75$, whereas in the CFD simulation this happens at $t_f \approx 9.5$ (see table 4.5). This difference could be explained because at the transition stage the acceleration is larger in the AHM. The results are mesh independent and do not change significantly with other differencing schemes.

EVENT	3D CFD		AHM	
	t	\tilde{U}	t	\tilde{v}
Flow reaches maximum velocity	9.07	2.9305	2.95	2.9303
Liquid reaches outlet	≈ 9.50	≈ 2.922	8.75	2.7860

Table 4.5: Comparison of flow events for 3D CFD and 1D AHM models.

The curves corresponding to the bulk acceleration \tilde{A} and dimensionless number $GF = aD^2/\nu U$ for the $k - \epsilon$ Launder-Sharma simulation, are shown in figures 4.29 and 4.30, respectively. The positive and negative peaks at around $t = 10$ are due to the liquid-air interface reaching the pipe's outlet, as it was remarked in page 264. The peak at around $t = 65$ corresponds to a halt in the solver execution. Sometime

after $t = 65$ the computer was accidentally switched off and, upon restart of the solver at $t = 65$, it did not reproduce exactly the previous Δt due to stabilisation of Courant Co number. It has been preferred not to edit the curve to remove the glitch.

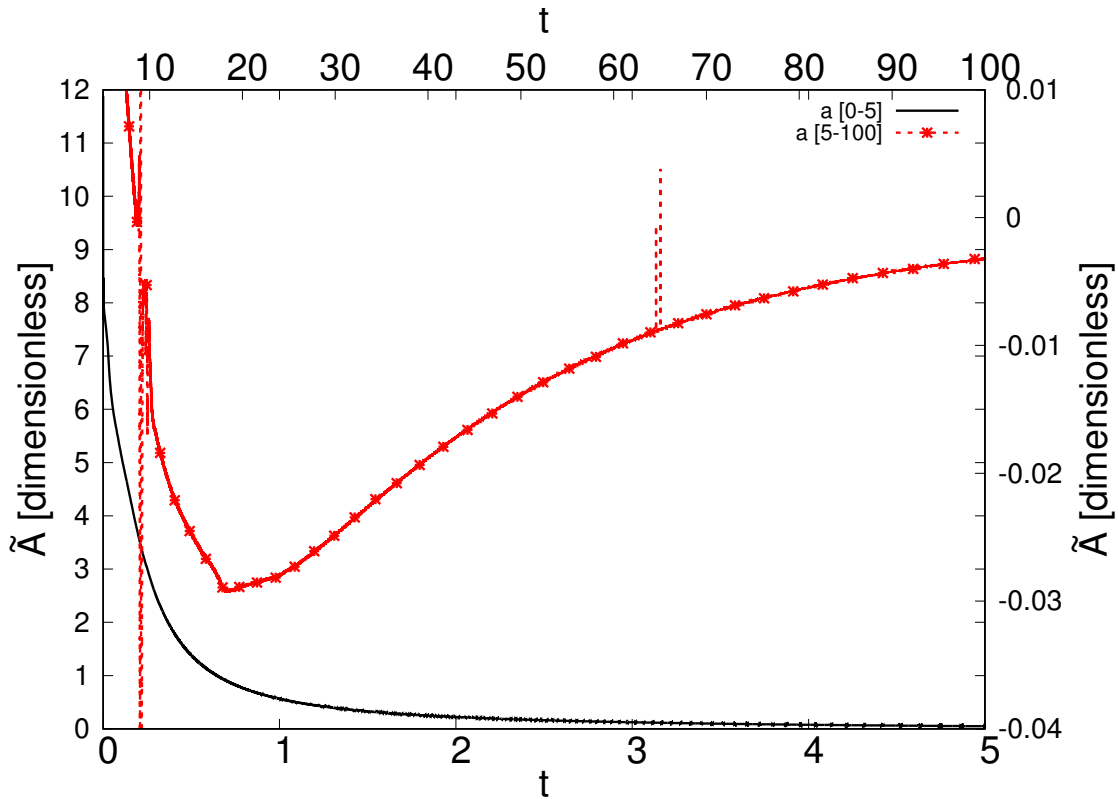


Figure 4.29: Cross-section averaged flow acceleration for $k - \epsilon$ Launder-Sharma model.

Figure 4.31 shows the evolution of the liquid front as it is being discharged through the pipe, according to the CFD model. Note the velocity maximum is produced sometime between $t = 9$ and $t = 10$ (actually it occurs at $t = 9.0722883$ with $\tilde{U}_{\max} = 2.9304531$). It can be appreciated that, according to the simulation, the liquid front maintains a plug-like flow in every step, not achieving a parabolic-like interface at any time. The $k - \epsilon$ Launder-Sharma simulation differs from the $k - \omega$ SSTAS in this respect, since $k - \omega$ predicts a parabolic-like liquid-air interface from $t \gtrsim 2$ (see figure 4.15).

Figure 4.32 presents the mean velocity profiles for the $k - \epsilon$ Launder-Sharma turbulence model, both in unsteady and steady state simulations. They will be called the U-model and S-model, respectively, in a similar fashion to page 265. In order to elaborate those profiles, an interval has been selected within which CFD and AHM curves were almost coincident, namely $t \gtrsim 50$ (see figure 4.28). Then, a steady state simulation (S-model) has been run until the output velocity was sufficiently constant. The S-model yields a bulk velocity of $\tilde{U} = 1.9833$. The U-model reaches at $t = 53$ the bulk velocity $\tilde{U} = 1.9807079$, which differs only in a 0.1% with the S-model. Note $t = 53$ is an acceptable point for the CFD U-model, since its bulk velocity curve is also quite coincident with the AHM's at that instant.

Therefore, three sets of profiles are available:

S-model: Obtained for pipe positions $z = 5, 12.5, 20, 24.5$, with $\tilde{U} = 1.9833$, and labelled 's' in figure 4.32. The steady profiles match one another almost perfectly, revealing that they do not depend on z in the deceleration stage.

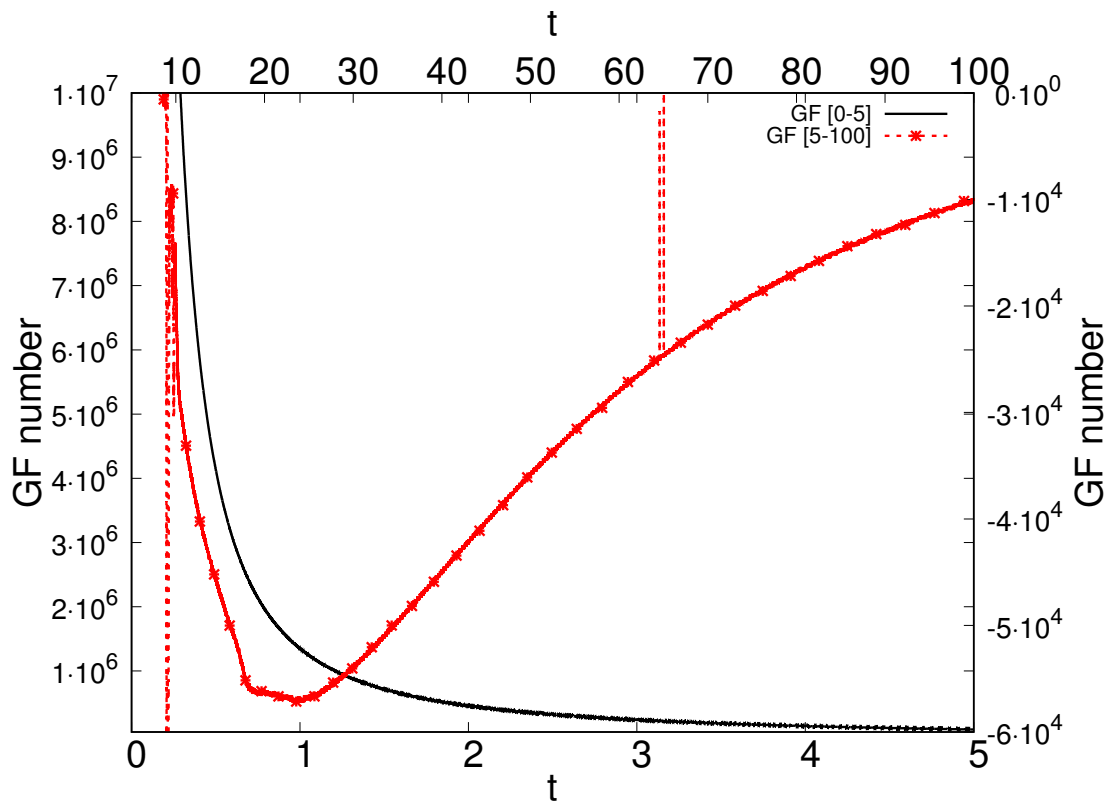
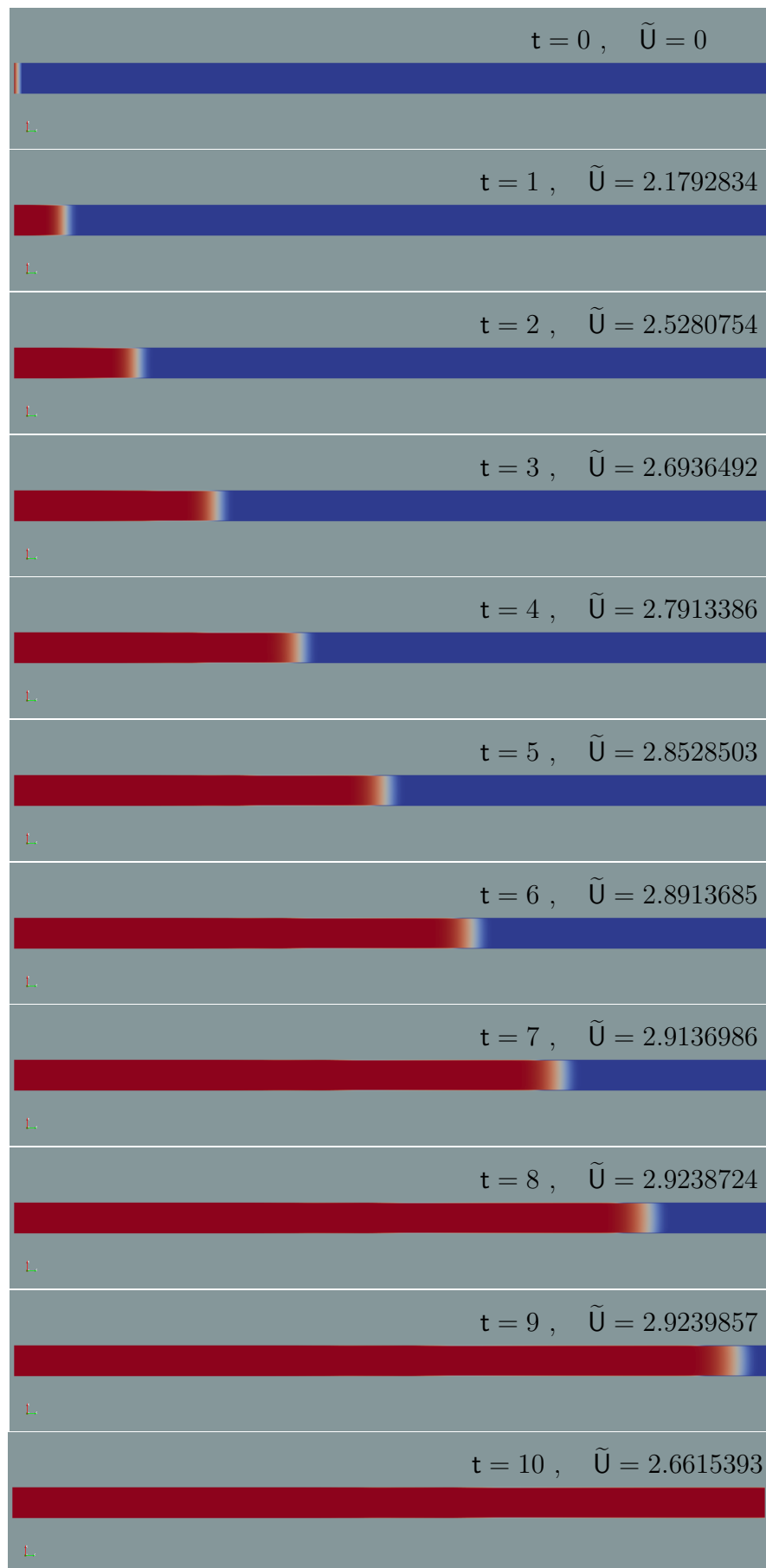


Figure 4.30: Dimensionless number evolution for $k - \epsilon$ Launder-Sharma model.

- U-model : Obtained for the same positions at time $t = 53$, with $\tilde{U} = 1.9807079$, and labelled 'u' in figure 4.32. The profiles match one another very well except at $z = 24.5$, surely because of the outlet proximity (at $z = 20$ there is also a slight mismatch).
- Log-law : The theoretical log-law profile corresponding to bulk velocity $\tilde{U} = 1.9825373$ is also shown, since the AHM is developed with a friction factor f based on the Law of the wall. Labelled 'Theor.' in figure 4.32.

The Reynolds numbers for each simulation also match to $1.03435 \cdot 10^7$ with 0.1% accuracy. The most remarkable feature of figure 4.32 is the ostensible disagreement between the S-model and the log-law theoretical profile. The departure is not limited to the curve's shoulder, but rather extends to the whole profile. Such lack of agreement casts doubts about the reliability of the $k - \epsilon$ Launder-Sharma turbulence model to simulate so a high Re flow. It would be within expectations that U-model profiles differ from theoretical log-law, according to what has been discussed about a transient friction factor being different from Darcy-Weisbach's. However, the disagreement between S-model and log-law reveals an untrustworthy model, and it would be meaningless to conduct an analysis of TQ ($R_{xz}, k, \epsilon, \omega, \zeta, \dots$) similar to the one carried out in section 4.10.1. A final remark: at $t = 53$ the bulk acceleration predicted by the U-model is $\tilde{A} = -0.01266$ (some 96 g).

The $k - \epsilon$ Launder-Sharma turbulence model is only partially successful in reproducing the behaviour emerged from the 1D AHM: it simulates reasonably well the Hydraulics of the flow, but it cannot properly explain its underlying Hydrodynamics (see footnote 3 in page 3). The deformed velocity profile of the U-model would have been interesting to explore, had it been the S-model sufficiently close to the theoretical log-law. In reality, it could be concluded that only the $k - \omega$ SSTSAS turbulence model, out of the twenty tested models of table 4.2, yields significant results when applied to the highly transient discharge flow

Figure 4.31: Sequence of discharge of liquid in the pipe for $k - \epsilon$ Launder-Sharma model.

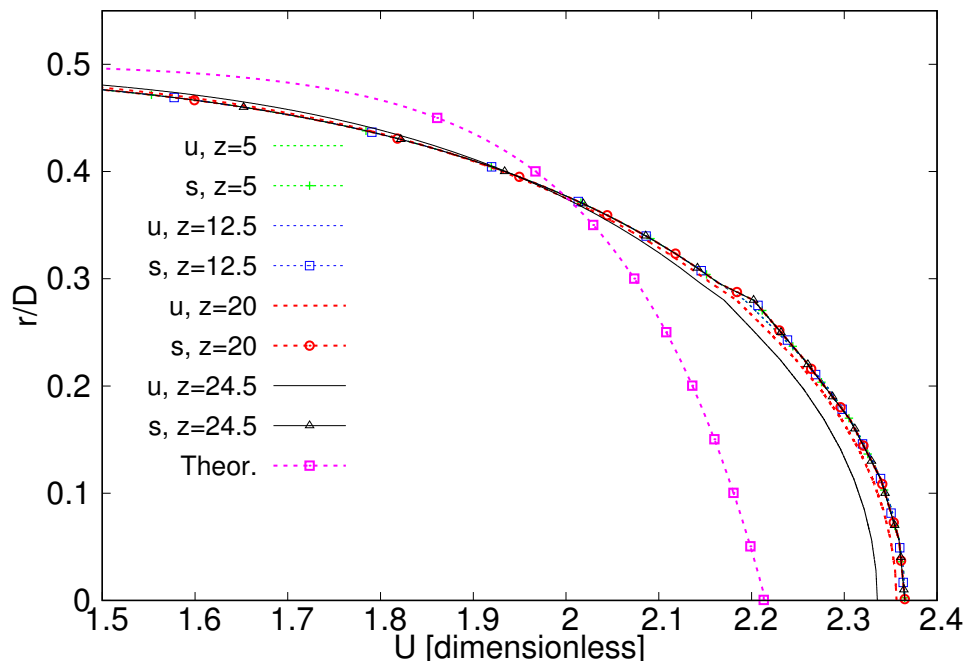


Figure 4.32: Mean velocity profiles for unsteady (u) and steady (s) flow in $k - \epsilon$ Launder-Sharma model for time $t = 53$ and positions $z = 5$, $z = 12.5$, $z = 20$ and $z = 24.5$.

considered in this Dissertation.

Chapter 5

Conclusions and Research Program

A specialised type of flow has been considered in this Dissertation, present in FPE applications and other Engineering fields whence a fluid is kept under pressure and could be subjected to discharge or accidental leakage. Whenever possible, emphasis has been placed in FPE, whose Professionals would possibly obtain the highest benefit from the offered results.

A new set of tools have been developed to approach the problem, each one comprehensibly described along the text:

- A 1D AHM, together with a computer program, to rapidly characterise the expected flow according to the conditions of the application, and which hopefully would help the practitioner Engineer in designing more efficient fire extinction systems. The AHM provides detailed data of bulk velocity, pressure, pressure drop, mass flow rate, volume, remaining mass in vessel, etc. versus time, for as long as the discharge process elapses. It could be used for a variety of clean agents, always provided they undergo relatively low vaporisation during the discharge.
- A 3D CFD model to obtain detailed information on the structure and evolution of the flow during the complete discharge process. Such information includes the profiles for mean velocity, Reynolds stress tensor, turbulent kinetic energy, turbulent energy dissipation, turbulence dissipation rate, vorticity and a variety of other turbulence fields deduced therefrom. It is also possible to study the development of the turbulent boundary layer near the wall, for any time during the discharge flow or any cross-section along the pipe. The model permits too the extraction of Hydraulics information from the 3D data, such as bulk velocity or mean pressure versus time, or mean pressure along the pipe length.
- A fully analytical general solution (GAS) for unsteady turbulent incompressible pipe flow, which could be used to assess the validity of the velocity profiles yielded by CFD models for such flows. The GAS depends on the choice of a well-behaved Reynolds stress function, which must possess a functional form shown in figure 3.17. The GAS would be a remarkable tool when performing unsteady CFD simulations not backed-up by experimental data, since it would serve as a benchmark to assess the CFD model's accuracy.

Being turbulent friction the main cause for the intense deceleration observed in the flow, modelling turbulence has been a capital issue in this Dissertation and, thus, the description of turbulence has occupied many pages thereof. A thorough presentation of the available methods for field averaging has been developed, including their mathematical properties, the type of averages produced, the functional form of the resulting RANSE, and the range of applicability. Averaging gives rise to the Reynolds

decomposition of physical fields. To each averaging method corresponds an unique set of averaged fields, a specific functional form of the RANSE, and an unique set of fluctuating fields. Each averaging method has a scope which is clearly established in the text, and accuracy is only granted within specified limits. The error attached to a potential misuse of RANSE, for applications beyond the scope of the averaging method corresponding to its functional form, has also been considered and explained.

Another method of describing turbulence, namely that based on filtered fields, has also been discussed. The physical flow fields are decomposed into filtered fields and fluctuating or unresolved fields, the later having no relationship with like-named fluctuating fields of Reynolds decomposition. The key issue here is that, in general, the operations of derivative and filtering do not commute. The FNSE have been obtained in conditions granting commutativity, whereas a general expression has been found for the commutation error, in those cases where it cannot be avoided. General properties of the solutions of FNSE in Fourier space have also been examined. Usually the non-commutativity is related with the proximity of boundaries. The HRLTM are briefly introduced as a convenient solution to the problem of modelling turbulence through filtering in presence of boundaries.

The last, and potentially most important and fruitful, method for describing turbulence is the analytical method, based on finding solutions to the actual RANSE with given boundary and initial conditions. Due to the closure problem, the system of RANSE is under-determined and a function must be provided in order to obtain a solution. The pre-defined function is normally the Reynolds stress, which could be obtained as the polynomial function best-fitting the experimental data. Some examples of Reynolds stress functions are offered in the text. Relatively simple Reynolds stress functions yield mean velocity profiles which fit incredibly well the theoretical or experimental available data. Several particular cases have been fully calculated, and a general method to obtain solutions has been offered. Foreseeably, a great number of qualitative and quantitative results ought to be expected from the GAS which has just been developed. Note such GAS stems directly from the RANSE themselves, obtained through the most general averaging method available, the ensemble average.

After explaining with care the details of the 3D CFD model, including the mesh geometry, the wall-functions, the differencing schemes and the solver itself, the outcome of the CFD simulations has been presented. Being the 1D AHM bulk velocity curve the only available data to compare with, after testing up to twenty different turbulence models provided by the suite OpenFOAM, only two of them were able to reproduce the intense friction giving rise to the bulk flow deceleration observed in the AHM. The results and 3D data of those two promising models have been discussed. Two versions of each one have been prepared: the unsteady flow for all instants of the discharge process (U-model), and a steady state flow simulation with exactly the same conditions (S-model). Within the U-model, it has been selected the time-frame having the same Re than the corresponding S-model. Then, a comparison has been performed between the profiles yielded by the U-model and S-model, for identical Re . Unfortunately, one of them provides poor agreement between the S-model and the expected theoretical results (law of the wall), therefore it has been discarded as unreliable. That leaves just one single model, namely the $k - \omega$ SSTSAS turbulence model, out of the twenty tested models of table 4.2, yielding significant results when applied to the highly transient discharge flow considered in this Dissertation. This sole surviving U-model suggests a relevant role of deceleration in the production of turbulence, particularly near the wall. It should be noted that in this transient flow the deceleration is produced exclusively by friction, since no adverse pressure gradient exists. This situation is scarcely studied in the literature, at least when high decelerations are present.

The issues dealt with in this Dissertation also bring forward some new challenging and stimulating research tasks, which could constitute a **Research Program** of its own:

- i. The 1DAHM should be improved and upgraded to include pipe bending and branching, considering fittings like elbows, Tees, diameter-reducing couplings, middle valves, nozzles, manifolds, chokes, etc. This will allow the design of complex pipe networks for agent's release. Besides, the AHM would employ a transient friction factor in its algorithm, instead of the current Colebrook-White correlation (see point vii below).
- ii. The 1D AHM could be improved too by considering the air within the pipe, ahead of the liquid's front, as a compressible fluid which will oppose a certain resistance to the liquid's motion. That would be the case in FPE applications with very narrow nozzles, in which the air is close to choking conditions and cannot vacate the pipe fast enough. This last consideration means that the term p_∞ in equations (2.72) and (2.76) is no longer constant, and it would have to be replaced by $p_{air}(t)$, which must be found from the theory of unsteady one-dimensional flow for a compressible fluid (see [Sha54]). In that case, the deceleration in the flow would be caused by the combined effect of friction and an adverse pressure gradient.
- iii. The 1D AHM could also consider explicitly agents with significant vaporisation while being discharged through the pipe network. The agent's phase diagram and equations of state for each phase should be included in the solver. It would also be possible to interface the AHM's solver with existing Thermophysics software, preferably open-source.
- iv. New turbulence models are being developed every year, some of them quite promising. Evaluation of new turbulence models should continue, in order to assess its suitability in simulating rapid transient flows with high accelerations. Hopefully, some of those new models might confirm, or even improve with further details, the interesting and rich flow structure the $k - \omega$ SSTSAS turbulence model has just begun to unearth.
- v. The 3D CFD model ought to be endowed with solvers for temperature, heat flux, Thermophysics quantities, species concentration, etc. Thus, the study of turbulence under acceleration would be extended to transient heat transfer. Possibly, new phenomena related with transient accelerated turbulent transport might emerge from such enhanced CFD model.
- vi. New Reynolds stress functions $\varpi(\gamma, \alpha)$ must be found, aside from those already introduced in the text. This would include piecewise continuous functions too, with one patch being derived from the log-law, so that it could be accurately reproduced in the velocity profile (recall the log-law itself does not fulfil the boundary conditions (3.369) and (3.373)). The new $\varpi(\gamma, \alpha)$ would have to represent more faithfully the actual turbulent stresses occurring in various flows. Presumably, some Reynolds stress functions would be more suitable for certain applications than others. A wider palette of Reynolds stress functions would increase the applicability of the GAS (3.469).
- vii. It is already within reach to obtain a general analytical expression for the transient friction factor, $f_t(t)$, using as departure point the GAS (3.469)

$$f_t(t) = \frac{8\tau_w}{\rho\tilde{U}^2} = \frac{2 \left. \frac{\partial u^*(\gamma, \alpha)}{\partial \alpha} \right|_{\alpha=1}}{\left[\int_0^1 \alpha u^*(\gamma, \alpha) d\alpha \right]^2} \quad (5.1)$$

There exists already an analytical expression for every factor in equation (5.1), thus, it is simply a matter of arduous and careful mathematical craftsmanship. The solution will be offered soon in a paper to be published. Possibly, a simplified version of f_t (perhaps the first few terms of its Taylor series expansion) could be included in the AHM solver to increase its accuracy (see point i above).

- viii. The GAS for unsteady turbulent incompressible pipe flow (3.469), could easily be modified to include other geometries, notably the rectangular duct.
- ix. The GAS for unsteady turbulent incompressible pipe flow (3.469) has been obtained for a particular normalisation scheme, defined by equations (3.359)-(3.364). That GAS should be upgraded to include other normalisation strategies (see remarks in page 162). It would allow direct comparison with other results expressed in wall-units, like u^+ in the log-law layer, or normalised to centreline velocity. This task is far from trivial, since there is great difficulty in the reference velocity being time-dependent ($u_\tau(t)$, $U_\infty(t)$).
- x. A GAS for unsteady heat transfer in turbulent incompressible pipe flow is also within reach. The development would proceed along similar lines to those followed in section 3.4.2, but applied to the transport equation of temperature instead. That GAS would serve as a benchmark for those CFD simulations of unsteady turbulent heat transfer with no available experimental data to be compared with. Foreseeably, such GAS will soon be ready for publishing.
- xi. Finally and most important of all: the findings of this Dissertation are still awaiting experimental confirmation... or refutation. Current technology makes it possible to measure with accuracy and high speed, the two main requirements for the type of flows being considered herein. In particular, turbulence in presence of high acceleration/deceleration deserves a systematic study, since accelerated turbulent flows appear to possess their own particular structures, not entirely similar to those already known to exist for steady state turbulent flows. Note the decelerated flow considered herein is not caused by an adverse pressure gradient, but rather by sheer friction against the walls. The predicted departure of the log-law for strongly decelerated pipe flow, respect to that observed in steady state flow of identical Reynolds number Re , seems to hint at the fact that, perhaps, Re is not the only dimensionless number needed to characterise the turbulence when deceleration is present (see figure 4.20). Presumably, the GAS for unsteady turbulent incompressible pipe flow (3.469), would shed some light onto that problem for any given flow, provided a suitable Reynolds stress function is available for it.

Anexo A

Resumen en Castellano



En el campo de la Ingeniería de Protección Contra Incendios, no es infrecuente el uso de agentes extintores que se mantienen a alta presión en el interior de recipientes, para ser rápidamente descargados a través de difusores dentro de espacios protegidos en caso de alarma de incendios. Este método tan eficaz de extinción de fuegos incipientes se suele efectuar con agentes que se vaporizan rápidamente en condiciones normales de presión y temperatura (20 °C y 1 atm), aunque en el interior de los recipientes presurizados se encuentran en estado líquido. Se denomina **flujo de descarga** al que desarrolla un líquido sometido a altas presiones aguas arriba, que avanza por una tubería que desemboca en un ambiente de presión baja empujado por el gradiente de presiones y sin otra restricción que la fricción con las paredes. La presente Tesis Doctoral explora la dinámica de tales flujos transitorios de descarga, suponiendo un líquido incompresible que fluye a lo largo de un tubo recto de diámetro constante.

En el **PRIMER CAPÍTULO** se realiza una investigación acerca del Estado del Arte existente en la literatura que trata sobre el flujo de descarga aplicado a la Ingeniería de protección contra incendios. Inicialmente se relata la evolución histórica del uso de agentes con propiedades refrigerantes, en las aplicaciones de extinción automática y precoz de conatos de fuego en espacios confinados, y el origen del término **agente limpio**. Se explica el contenido de la técnica utilizada en este tipo de sistemas, así como las propiedades termofísicas de los agentes extintores más comúnmente empleados. Se presentan y comentan los trabajos de investigación más relevantes sobre flujo de descarga que existen en la literatura relativa a la Ingeniería de protección contra incendios, resaltando las características que más adelante se intentarán reproducir en los modelos que se desarrollan en el texto. Se comprobará que la mayor parte de dichas investigaciones tratan al flujo de descarga como si fuese un proceso en régimen estacionario, descartando el hecho de que el transitorio dura tanto como la propia descarga. Se explican y analizan los mecanismos de extinción de incendios empleados por dos de los agentes limpios más frecuentemente utilizados en aplicaciones reales, y dicha explicación se elabora sobre sus diagramas presión-entalpía. Se justifica que, posiblemente, no se cometa un error inasumible por suponer que la descarga de agentes HFC a través de tubos suficientemente cortos se realice en régimen de flujo monofásico, evitando los complejos y probablemente poco exactos modelos de descarga en régimen bifásico que actualmente se utilizan en la industria. Se obtiene como conclusión la necesidad de desarrollar modelos analíticos y computacionales que tengan en cuenta, desde el inicio, el carácter fuertemente transitorio del flujo de descarga.

En el **SEGUNDO CAPÍTULO** se desarrolla un **modelo hidráulico unidimensional** de flujo de descarga, que describe y explica la dinámica que acontece durante la descarga de un líquido incompresible desde

un depósito presurizado mediante un gas ideal. El modelo asume un flujo transitorio rápido a través de una tubería recta y abierta por un extremo, sometido a una alta aceleración rápidamente variable con el tiempo, y sujeto exclusivamente a la acción de las fuerzas de presión y fricción, que alternan su importancia relativa a lo largo del desarrollo del flujo. El motor del movimiento se supone que es la expansión politrópica adiabática de un gas ideal, N_2 , que está encerrado en el mismo depósito que contiene al líquido. Se asume que en el interior del depósito existe equilibrio mecánico entre el líquido y el gas ideal, es decir, ambos comparten la misma presión en todo instante.

Se han obtenido unas ecuaciones dinámicas que deben proporcionar una solución exacta dentro de las limitaciones, suposiciones e hipótesis del modelo hidráulico unidimensional. Estas ecuaciones dinámicas resultan ser ecuaciones integro-diferenciales ordinarias no lineales, para las que no se ha podido determinar una solución analítica directa. Para hacer su aplicación lo más universal posible, se han adimensionalizado todas las magnitudes tomando como referencias la longitud, densidad y presión. Adicionalmente, el modelo presenta tres grados de libertad que se pueden adaptar de forma conveniente para que los resultados que predice se ajusten a los datos experimentales o de simulación computacional. Se ha desarrollado un programa informático para resolver numéricamente el problema de flujo unidimensional. Dicho programa incluye algoritmos bien conocidos, adecuados para una solución punto a punto de ecuaciones diferenciales ordinarias, así como para realizar operaciones de integración numérica.

El modelo hidráulico unidimensional se estudia exhaustivamente, incluyendo un análisis detallado de sensibilidad respecto a cualquier magnitud o parámetro de que puedan depender las ecuaciones dinámicas. Se muestran las curvas de velocidad frente a tiempo para una gran variedad de situaciones de flujo de descarga, con la expectativa de que sean posteriormente reproducidas por un modelo CFD en tres dimensiones. Una de las principales características del flujo de descarga es que, transcurridos los instantes iniciales, el líquido pasa la mayor parte del tiempo desacelerando bajo los efectos de la fricción. Se comprobará que este comportamiento es el que menos consiguen simular los distintos modelos computacionales (CFD) que se han ensayado en el desarrollo del presente trabajo.

En el **CAPÍTULO TERCERO**, debido al papel relevante desempeñado por la turbulencia en el desarrollo de estos flujos transitorios, se propone una discusión general sobre los distintos métodos de representar los campos turbulentos, antes de proceder a describir los modelos CFD tridimensionales desarrollados en esta Tesis Doctoral. Se evalúa de un modo general lo complicado del movimiento turbulento, haciendo referencia al enorme número de grados de libertad que posee, y a cómo se puede simplificar su descripción con métodos que reduzcan significativamente dicho número. Se presenta, a modo tentativo, un paralelismo entre una posible representación de la turbulencia, y la descripción que la Mecánica Estadística Clásica realiza de los fenómenos termodinámicos, basada en la reducción casi completa de los grados de libertad de los sistemas físicos.

Se discute primero el enfoque estadístico, basado en el concepto de **media estadística**, incluyendo aquellas propiedades de la operación de promediado que son necesarias para originar **Ecuaciones de Navier-Stokes Promediadas según Reynolds** (ENSPR) viables, a partir de su aplicación a las propias ecuaciones de Navier-Stokes, siguiendo los conceptos de descomposición de Reynolds y operador de Reynolds. Se presentan con gran detalle los distintos métodos disponibles de promediado para flujos incompresibles, incluyendo sus propiedades matemáticas, la forma funcional de las ENSPR que de ellos se derivan, y el alcance y límites dentro de los cuales permanecen válidas. Dichos métodos de promediado son: la **media de conjunto**, la **media general espacio-temporal**, la **media temporal**, la **media espacial** y la **media de fase**. Se hace hincapié en el hecho de que cada método de promediado da lugar a un único juego de ENSPR que son exactas únicamente dentro de los límites especificados. Se

discute la forma funcional del tensor de tensiones de Reynolds producido en cada uno de los métodos de promediado, haciendo notar que sus valores son diferentes en cada caso, a pesar de que desempeñan papeles análogos de difusión de la turbulencia en todos ellos. Se examina también el error cometido al no respetar los límites de validez de cada método de promediado, y se introduce una ecuación general para estimar dicho error, en particular cuando se utilizan métodos URANS con campos medios obtenidos mediante promediado temporal finito, un práctica harto frecuente. Para ello, se estudian promedios temporales que no verifican las condiciones de Reynolds, es decir, que no son operadores de Reynolds, como son la **media temporal móvil de intervalo T** y la **media temporal acumulada**. Aunque de uso frecuente en la literatura, estas medias temporales no originan ENSPR exactas y deben ser utilizadas con sumo cuidado en simulación CFD. También se discute la llamada **triple descomposición**, en la que las magnitudes turbulentas son expresadas como suma de tres términos: uno estacionario, otro periódico y el último correspondiente a la fluctuación. Se resaltan algunas inexactitudes existentes en la formulación que frecuentemente se emplea en la literatura, al tiempo que se ofrece una formulación alternativa libre de inconsistencias matemáticas.

En segundo lugar se introduce un enfoque de descripción de la turbulencia basado en el procedimiento de filtrado, fundado sobre la **integral de convolución**. Se introduce el concepto de filtro y su amplitud, tanto en el espacio como en el tiempo, y se deducen los conceptos equivalentes en el espacio de Fourier, definido por la frecuencia y el vector número de onda. Al aplicarse sobre campos físicos, la operación de filtrado da lugar a **campos filtrados** y **campos fluctuantes**, lo que constituye una descomposición similar a la de Reynolds para el enfoque estadístico, aunque no idéntica. Las operaciones de derivación y filtrado, en general, no conmutan, lo que complica el desarrollo de las ecuaciones de gobierno de las magnitudes filtradas. Se estudian las condiciones que garantizan la conmutación de ambas operaciones y, en esas circunstancias, se derivan las **Ecuaciones Filtradas de Navier-Stokes (EFNS)**, y los conceptos asociados de **tensor de tensiones residuales** y **viscosidad a escala sub-malla**, que pueden considerarse parientes lejanos de las magnitudes similares estudiadas durante el enfoque estadístico. También se ofrece una expresión general para estimar el error cometido cuando dicha conmutación no está garantizada, el llamado error de conmutación, así como el grado de exactitud previsible de las EFNS cuando se utilizan fueran de su ámbito de aplicación. Se discute el modo de establecer las condiciones de contorno para las EFNS, deteniéndose especialmente en el caso en que el contorno sea una pared. En esos casos, la condición de no-deslizamiento implica una indefinición de las condiciones de contorno, que lleva a que los métodos de filtrado no puedan ser utilizados con confianza en las proximidades de paredes sólidas. Por último, dentro de este apartado se estudian los métodos que combinan la aplicación de magnitudes filtradas para el flujo principal, y magnitudes promediadas en las proximidades de las paredes.

En tercer lugar, se ha ideado un acercamiento completamente analítico al problema de describir el campo de velocidad en un flujo turbulento, incluyendo los casos no estacionarios y transitorios. Se repasan todas las **soluciones analíticas** conocidas para el flujo incompresible en tuberías: la de Hagen-Poiseuille (ca. 1840) para flujo estacionario laminar, la de Piotr Szymanski (1932) para flujo transitorio laminar y la de Shih-I Pai (1953) para flujo turbulento estacionario. Utilizando la operación estadística de promedio de conjunto sobre las ecuaciones de Navier-Stokes, se obtienen las ENSPR en forma adimensional, que se resuelven proporcionando una **solución analítica general (SAG)** para el flujo incompresible no estacionario y turbulento en tuberías, cerrando así el círculo de soluciones analíticas mencionado. Se trata de una SAG obtenida directamente a partir de Primeros Principios, y posiblemente, sea la contribución más relevante de la presente Tesis Doctoral. La SAG está compuesta por tres términos que corresponden a distintos generadores de momento, cuya descripción detallada se ofrece en el texto: el término inicial que representa la inercia existente en el fluido en el instante cero, el término de respuesta al gradiente de presiones existente y el término propiamente turbulento

que responde a las tensiones de Reynolds. Se aplica la SAG a algunos ejemplos de flujos simples, como ilustración del método general que debe seguirse para obtener soluciones analíticas a problemas más complejos.

Por último, se ha realizado el ejercicio de derivar una versión estacionaria simplificada de las ecuaciones de Navier-Stokes directamente del **Principio de Mínima Acción de Hamilton**, uno de los fundamentos de la Mecánica Clásica.

En el **CUARTO CAPÍTULO** se ha desarrollado un modelo CFD tridimensional con el fin de obtener un conocimiento detallado de la estructura interna de este flujo transitorio de descarga. El modelo CFD está basado en la *suite* de software en código abierto **OpenFOAM**, basada a su vez en el formalismo del **Método de Volúmenes Finitos**. Inicialmente se enumeran las dificultades que debe afrontar el modelo CFD: debe ser fuertemente transitorio, altamente turbulento aunque parta del reposo, está sujeto a una intensa fricción, el flujo es interno y está completamente rodeado de paredes, se espera que la subcapa laminar sea extraordinariamente fina por lo que será un flujo hidráulicamente rugoso, la longitud de la tubería debe ser suficiente para reducir los efectos de entrada y, por último, en los momentos iniciales el flujo debe ser considerado bifásico, con una interfase líquido-aire que va avanzando rápidamente conforme progresa el transitorio. Se introduce brevemente el fundamento del método de volúmenes finitos y la forma que adoptan las **ecuaciones discretizadas de Navier-Stokes**. Se hace una breve descripción del software OpenFOAM, incluyendo los elementos principales que deben ser definidos para efectuar cualquier simulación: una malla formada por celdas, nodos, caras y contorno, un conjunto de campos que adoptan valores en dichos nodos y caras, el conjunto de ecuaciones diferenciales que obedecen los campos y que es preciso discretizar, las condiciones iniciales y de contorno que se van a imponer sobre el flujo, los esquemas de discretización y diferenciación que se van a aplicar, los métodos de resolución de las matrices dispersas que resultan del anterior proceso de discretización y, por último, el modelo de turbulencia que se va a considerar para el flujo. Se ha desarrollado un programa que resuelve las ecuaciones (*solver*), basado en otro existente en OpenFOAM denominado interFOAM, que considera el carácter bifásico del flujo, las condiciones de contorno cambiantes y la dependencia de éstas con el caudal de líquido que sale por la tubería. Este *solver* se describe brevemente en el texto.

Se presentan con detalle las principales características del modelo CFD que se ha elaborado en esta Tesis Doctoral. Se discute el modo en que se introducen las condiciones iniciales, sobre todo para las magnitudes turbulentas, ofreciéndose una serie de correlaciones que permiten estimar estos valores iniciales. En el flujo real la turbulencia se desarrolla muy rápido, aunque se espera que el modelo CFD no sea capaz de reproducir tal generación de turbulencia. Por tanto, se seguirá una estrategia mixta: se establecerán unos valores iniciales de los campos turbulentos no nulos, a pesar de que se parte de condiciones de reposo. En pocos instantes el flujo alcanza tal velocidad que los valores establecidos de turbulencia ya no son incompatibles con los que corresponden a los números de Reynolds que se obtienen, produciéndose entonces el correcto acoplamiento entre las magnitudes turbulentas en las celdas y las ecuaciones discretizadas que las gobiernan. Se estudian también las condiciones de contorno, que en el caso propuesto coinciden con condiciones de modelización del flujo en las paredes. Se describe la estructura de la **capa límite turbulenta**, y se proponen **funciones de pared** adecuadas para cada una de las zonas de las que se compone dicha capa límite. En concreto, se presta especial atención a la **capa inercial logarítmica**, en la que se desarrolla la **ley universal de la pared**. Se hace especial hincapié en que la primera celda de la malla debe tener su nodo central en el interior de dicha capa logarítmica, a fin de que sea posible la aplicación de las condiciones de contorno correctas a través de la función de pared logarítmica universal. Se ofrece un procedimiento general para estimar la altura de la primera celda de pared, a fin de garantizar que esté situada en el interior de la capa logarítmica. También se analizan las funciones de pared que corresponden a paredes rugosas, y el modo general de abordar este

problema en simulación CFD.

A la vista de la información obtenida anteriormente, se describe con detalle el diseño de la malla en que se desarrolla el modelo CFD. Se muestra su estructura, sus contornos y la altura del primer nodo de pared. Se comprueba que dicho nodo está sumergido en el interior de la capa inercial logarítmica del flujo, incluso en las condiciones más desfavorables de velocidad, por lo que la aplicación de funciones de pared como condiciones de contorno queda plenamente justificada. Se discuten los métodos de discretización y los esquemas de diferenciación que se han aplicado en el modelo CFD. Se justifica la utilización de métodos simples e incondicionalmente estables, puesto que el potencial peaje en exactitud que podrían implicar es completamente asumible. También se describe brevemente el algoritmo de acoplamiento entre velocidad y presión, y cómo se resuelve este problema con un intervalo de tiempo de integración Δt pequeño y ajustable, a pesar de que el flujo es un transitorio muy acusado. Se discuten las condiciones que llevan a la independencia de los resultados del modelo con respecto a la resolución de la malla, al intervalo Δt de integración y a los esquemas de diferenciación. Se ofrece un procedimiento general para comprobar esta deseada independencia.

Se presenta el complicado asunto de modelar la turbulencia que se espera en el flujo. Se han ensayado hasta veinte de los modelos de turbulencia disponibles en OpenFOAM, realizando simulaciones de descargas idénticas con cada uno de ellos. Como no se pudieron encontrar datos experimentales para un flujo transitorio tan rápido, las curvas de velocidad-tiempo proporcionadas por el modelo hidráulico unidimensional han sido la única referencia disponible para contrastar los modelos CFD. De todos los modelos de turbulencia probados, sólo dos consiguieron reproducir la intensa fricción causante de la gran deceleración observada en el flujo, denominados $k - \omega$ SSTAS y $k - \epsilon$ Launder-Sharma. Se presentan ambos modelos y se describen las ecuaciones que lo definen y los valores de los grados de libertad del modelo hidráulico unidimensional que mejor se ajustan a sus predicciones. De estos dos modelos de turbulencia, el $k - \epsilon$ Launder-Sharma da lugar a un perfil de velocidades medias cercano a la pared que no es compatible con las predicciones de la ley de la pared, por lo que fue descartado como poco fiable. El único modelo de turbulencia que superó todas las pruebas, el $k - \omega$ SSTAS, muestra un perfil de velocidades medias compatible con la ley de la pared, en su versión de flujo completamente rugoso. Se comparan los perfiles de todas las magnitudes turbulentas de interés que ofrece el modelo transitorio, con los correspondientes a un flujo estacionario con el mismo número de Reynolds y el resto de condiciones idénticas. Dicho de otro modo, en el instante en que se comparan ambos flujos únicamente se distinguen en la presencia de aceleración en uno de ellos, siendo nula para el modelo estacionario. Además, este modelo CFD predice un papel importante para la deceleración en la descripción de la turbulencia para flujos transitorios rápidos, ya que los valores de sus campos turbulentos son órdenes de magnitud superiores a los que muestra un flujo idéntico estacionario. Se deduce del análisis que el número de Reynolds por sí solo no basta para caracterizar la turbulencia de este tipo de flujos, y que es preciso tener en cuenta la aceleración para explicar la intensidad de la turbulencia, en particular junto a la pared.

Finalmente, en el **QUINTO CAPÍTULO** se presentan las conclusiones del presente estudio y se propone un programa de investigación para continuar explorando los diversos caminos que se abren tras el descubrimiento de la SAG, incluyendo el diseño de experimentos que pudieran confirmar la interesante, y de momento no reportada, estructura interna de la turbulencia que predice el modelo CFD para flujo fuertemente decelerado en tuberías.

Bibliography

- [AG08] M A Al-Gwaiz. *Sturm-Liouville theory and its applications*. Springer-Verlag, 2008. 167, 168
- [AKSA13] I Annus, T Koppel, L E Sarv., and L Y Ainola. Development of accelerating pipe flow starting from rest. *Journal of Fluids Engineering*, 135(111204):1–10, 2013. 31, 50, 267
- [AL⁺81] J L Achard, G M Lespinard, et al. Structure of the transient wall-friction law in one-dimensional models of laminar pipe flow. *Journal of Fluid Mechanics*, 113:283–298, 1981. 50
- [ALSL81] L Y Ainola, Y Y Lamp, L E Sarv., and U R Liiv. Transient processes in a compressible fluid in pipes by means of numerical methods. *Hydrotechnical Construction*, (15):14–19, 1981. 31, 267
- [AM11] F V Atkinson and A B Mingarelli. *Multiparameter eigenvalue problems. Sturm-Liouville theory*. CRC Press - Taylor & Francis Group, 2011. 167, 168
- [Ann11] I Annus. *Development of accelerating pipe flow starting from rest*. PhD thesis, 2011. 31, 50, 267
- [Ant91] H M Antia. *Numerical Methods for Scientists and Engineers*. Tata McGraw-Hill Pub.Co.Ltd., 1991. 57
- [Aps07] D Apsley. CFD calculation of turbulent flow with arbitrary wall roughness. *Flow Turbulence Combust*, 78:153–175, 2007. 243
- [APV00] Y Achdou, O Pironneau, and F Valentin. New unsteady wall laws for incompressible Navier-Stokes equations. In *European Congress on Computational Methods in Applied Sciences and Engineering - ECCOMAS-2000*, September 2000. 242
- [ASKS07] J. J. Allen, M. A. Shockling, G. J. Kunkel, and A. J. Smits. Turbulent Flow in Smooth and Rough Pipes. *Philosophical Transactions: Mathematical, Physical and Engineering Sciences*, 365(1852):699–714, March 2007. xii, 226, 227
- [BBFY08] T K Blanchat, A L Brown, V Figueroa, and S S Yoon. Benchmark enclosure fire suppression experiments and modeling. In *Suppression and Detection and Applications-A Technical Working Conference (SUPDET 2008)*, 2008. 2, 11
- [Ben06] J M Bennett. Verification of NGP Fire Suppression Principles. In R G Gann, S R Burgess, K C Whisner, and P A Reneke, editors, *Halon Options Technical Working Conferences (HOTWC)-2006*, volume NIST Speci. National Fire Protection Association, May 2006. 3
- [BG05] F van der Bos and B J Geurts. Commutator errors in the filtering approach to large-eddy simulation. *Physics of Fluids*, 17(035108):1–20, 2005. 144
- [BGF⁺95] E B Bird, H D Giesecke, T J Friderichs, A Maranghides, and R S Sheinson. Results of Benchmark Comparisons of Calculated and Measured Flow Parameters for Discharges of Halon Replacement Chemicals. In *Halon Options Technical Working Conferences (HOTWC)-1995*. National Institute of Standards and Technology, May 1995. 2, 17

- [BGH⁺94] E B Bird, H D Giesecke, J A Hillaert, T J Friderichs, and R S Sheinson. Development of a Computer Model to Predict the Transient Discharge Characteristics of Halon Alternatives. In *Halon Options Technical Working Conferences (HOTWC)-1994*. National Institute of Standards and Technology, May 1994. 17
- [BHC97] J E Bardina, P G Huang, and T J Coakley. Turbulence Modeling Validation, Testing, and Development. Technical Report 110446, April 1997. 254
- [BIL06] L C Berselli, T Iliescu, and W J Layton. *Mathematics of Large Eddy Simulation of Turbulent Flows*. Springer-Verlag Berlin Heidelberg, 2006. 73, 77, 132, 133, 142, 145, 146
- [BJPV98] T Bohr, M H Jensen, G Paladin, and A Vulpiani. *Dynamical Systems Approach to Turbulence*. Cambridge University Press, 1998. 72
- [BK92] G J Brereton and A Kodal. A frequency-domain filtering technique for triple decomposition of unsteady turbulent flow. *Journal of Fluids Engineering*, 114:45–51, March 1992. 115
- [Bla05] J Blazek. *Computational fluid dynamics: Principles and applications*. Elsevier Inc., 2nd edition, 2005. 205, 206, 234, 235, 236, 248
- [BM93] G J Brereton and R R Mankbadi. A Rapid-Distortion-Theory Turbulence Model for Developed Unsteady Wall-Bounded Flow. Technical Report 106249, July 1993. 252
- [Boi61] G P Bois. *Tables of Indefinite Integrals*. Dover Publications Inc., 1961. 119, 127
- [Bra00] R N Bracewell. *The Fourier transform and its applications*. McGraw-Hill, 3rd ed. edition, 2000. 104, 105, 106
- [Bra09] O Bratland. *Pipe Flow I: Single-phase Flow Assurance*. e-book www.drbratland.com, 2009. 49
- [Bre00] J Bredberg. On The Wall Boundary Condition for Turbulence Models. Technical Report Internal Report 00/4, Chalmers University of Technology, 2000. 224
- [Bur03] M Burgess. *Classical covariant fields*. Cambridge University Press, 2003. 197, 198
- [Cas97] L Castillo. *Similarity Analysis of Turbulent Boundary Layers*. PhD thesis, Faculty of the Graduate School, 1997. 224
- [Ceb13] T Cebeci. *Analysis of Turbulent Flows with Computer Programs*. Butterworth-Heinemann Ltd., 3rd edition, 2013. xii, 239, 240, 243
- [CGY94] T G Cleary, W L Grosshandler, and J C Yang. Flow of Alternative Agents in Piping. In *Halon Options Technical Working Conferences (HOTWC)-1994*. National Institute of Standards and Technology, May 1994. 17, 18, 19
- [Cha00] P Chassaing. *Turbulence en Mecanique des Fluides*. Cepadues Editions, 2000. xii, 219, 220, 224, 255, 257
- [CHM92] R N Coward, J A Hillaert, and D M McCrory. Analytical methods for modeling discharge characteristics of Halon 1301 fire protection systems. In *Halon Alternatives Technical Working Conference-1992*. National Institute of Standards and Technology, May 1992. x, 17, 18, 60
- [Cho93] D Choudhury. Introduction to the Renormalization Group Method and Turbulence Modeling. Technical Report TM-107, August 1993. 256
- [Cla09] D Clamond. Efficient resolution of the Colebrook equation. *Ind.Eng.Chem.Res.*, 48(7):3665–3671, 2009. 49

- [Col56] D Coles. The Law of the wake in the turbulent boundary layer. *Journal of Fluid Mechanics*, 1(2):191–226, 1956. 230
- [Con80] F Constantinescu. *Distributions and their applications in Physics*. Pergamon Press, 1980. 86, 87
- [Coo93] L Y Cooper. Discharge of Fire Suppression Agents from a Pressurized Vessel: A Mathematical Model and its Application to Experimental Design. *NISTIR*, (5181), May 1993. 3, 15, 31
- [Coo94] L Y Cooper. Dispersion of Fire Suppression Agents Discharged From High Pressure Vessels: Establishing Initial/Boundary Conditions for the Flow Outside the Vessel. In *Liquid Atomization and Spray Systems, 6th International Conference Proceedings.*, volume ICLASS, 1994. 2, 3
- [Cor89] C Corduneanu. *Almost Periodic Functions*. Chelsea Pub.Co., 2nd ed. edition, 1989. 131
- [CS74] T Cebece and A M O Smith. *Analysis of Turbulent Boundary Layers*. Academic Press, Inc., 1974. 224
- [CYK⁺95] T G Cleary, J C Yang, M D King, C I Boyer, and W L Grosshandler. Pipe flow characteristics of alternative agents for engine nacelle fire protection. In *Proceedings on Halon Options Technical Working Conference-1995*. National Institute of Standards and Technology, May 1995. x, 18, 19
- [DAT12] S S Deshpande, L Anumolu, and M F Trujillo. Evaluating the performance of the two-phase flow solver interFoam. *Computational Science & Discovery*, 5(014016), 2012. 214
- [Dei84] R G Deissler. Turbulent solutions of the equations of fluid motion. *Review of Modern Physics*, 56, No-2, Part I:223–254, April 1984. 73
- [Den09] G S Denton. *CFD Simulation of Highly Transient Flows*. Phd, University College London, 2009. 30, 49
- [Dev89] R L Devaney. *An Introduction to Chaotic Dynamical Systems*. Addison-Wesley Publishing Co. Inc., 2nd edition, 1989. 82
- [DFF⁺94] P J DiNenno, E W Forssell, M J Ferreira, C P Hanauska, and B A Johnson. Modeling of the Flow Properties and Discharge of Halon Replacement Agents. In *Proceedings on Halon Options Technical Working Conference-1994*. National Institute of Standards and Technology, 1994. x, 16, 17
- [DHOJ56] J W Daily, W L Hankey, R W Olive, and J M Jordaan. Resistance coefficients for accelerated and decelerated flows through smooth tubes and orifices. *Transactions of the ASME*, 78:1071–1077, 1956. 274
- [DiN02] P J DiNenno. *Halon Replacement Clean Agent Total Flooding Systems*, volume SFPE Handb, chapter 4-7. National Fire Protection Association, 3rd edition, 2002. 8, 11
- [DiN03] P J DiNenno. *Direct Halon Replacement Agents and Systems*, volume NFPA Fire of NFPA Fire Protection Handbook, vols. I & II, chapter 11-2. National Fire Protection Association, 19th edition, 2003. 8, 11
- [DK04] J J Duistermaat and J A C Kolk. *Multidimensional Real Analysis II: Integration*. Cambridge University Press, 2004. 143
- [DKL⁺96] F Durst, H Kikura, I Lekakis, J Jovanovic, and Q Ye. Wall shear stress determination from near-wall mean velocity data in turbulent pipe and channel flows. *Experiments in Fluids*, 20:417–428, 1996. 218
- [DR05] D Drikakis and W Rider. *High-Resolution Methods for Incompressible and Low-Speed Flows*. Springer-Verlag, 2005. 57
- [Dre83] D A Drew. Mathematical modeling of two-phase flow. *Annu. Rev. Fluid Mech.*, 15:291–291, 1983. 216

- [Dur08] F Durst. *Fluid Mechanics. An Introduction to the Theory of Fluid Flows*. Springer-Verlag Berlin Heidelberg, 2008. 29, 149, 151, 160
- [Ece80] A Ecer. Variational formulations of viscous flow. *Int. J. Num. Meth. Eng.*, 15:1355–1361, 1980. 198
- [EGK⁺84] D G Elliot, P W Garrison, G A Klein, K M Moran, and M P Zydowicz. Flow of nitrogen-pressurized Halon 1301 in Fire Extinguishing Systems. *Jet Propulsion Laboratory*, JPL Public(84-62), 1984. 16, 18, 19
- [FD02] H Frahnert and U C Dallman. Examination of the Eddy-Viscosity Concept Regarding its Physical Justification. In S Wagner, U Rist, H J Heinemann, and R Hilbig, editors, *New Results in Numerical and Experimental Fluid Mechanics III - Contributions to the 21st STAB/DGLR Symposium. Stuttgart, Germany 2000*, page 255–262. Springer-Verlag Berlin Heidelberg, 2002. 150
- [FHT01] C Foias, D D Holm, and E S Titi. The Navier-Stokes-alpha model of fluid turbulence. *Physica D*, 152 - 153:505–519, 2001. 201
- [Fla73] H Flanders. Differentiation Under the Integral Sign. *The American Mathematical Monthly*, 80(6):615–627, July 1973. 39, 143
- [FPO2] J H Ferziger and M Peric. *Computational Methods for Fluid Dynamics*. Springer-Verlag, 3rd edition, 2002. 203, 205, 206, 208, 209, 210, 248, 249
- [Fri95] U Frisch. *Turbulence. The legacy of A. N. Kolmogorov*. Cambridge University Press, 1995. 71, 98
- [Fri03] R Friedman. *Theory of Fire Extinguishment*, chapter 2-5, page 2–96. NFPA Fire Protection Handbook, vols. I & II. National Fire Protection Association, 19th edition, 2003. 3
- [FT08] J Froehlich and D von Terzi. Hybrid LES/RANS methods for the simulation of turbulent flows. *Progress in Aerospace Sciences*, 44:349–377, 2008. 147
- [Gan95] R G Gann. Next Generation Fire Suppression System Technology: A National Research Plan. In *Halon Options Technical Working Conferences (HOTWC)-1995*. National Institute of Standards and Technology, May 1995. 2
- [Gan98] R G Gann. Next-Generation Fire Suppression Technology Program. In *Halon Options Technical Working Conferences (HOTWC)-1998*. National Institute of Standards and Technology, May 1998. 2
- [Gan03] R G Gann. Next Generation Fire Suppression Technology Program: FY2003 Progress. In *Halon Options Technical Working Conferences (HOTWC)-2003*. National Institute of Standards and Technology, May 2003. 2
- [Gan05] R G Gann. Next Generation Fire Suppression Technology Program: FY2005 Progress. In *Halon Options Technical Working Conferences (HOTWC)-2005*. National Institute of Standards and Technology, May 2005. 2
- [GCC07] L A Gimenez-Curto and M A Corniero. Accurate calculation of friction in tubes, channels, and oscillatory flow: A unified formulation. *Journal of Geophysical Research*, 112(CO2007):1–14, 2007. 49
- [Geo05] W K George. Recent advancements toward the understanding of turbulent boundary layers. In *4th AIAA Theoretical Fluid Mechanics Meeting, 6-9 June 2005, Toronto, ON, Canada*, number AIAA-2005-4669, 2005. 223, 230, 231
- [Geo07] W K George. Is There a Universal Log Law for Turbulent Wall-Bounded Flows? *Philosophical Transactions: Mathematical, Physical and Engineering Sciences*, 365(1852):789–806, March 2007. 231
- [Geo13] W K George. *Lectures in Turbulence for the 21st Century*. January 2013. 222

- [Ger92] M Germano. Turbulence: the filtering approach. *Journal of Fluid Mechanics*, 238:325–336, 1992. 132
- [GG99] S Gavriluk and H Gouin. A new form of governing equations of fluids arising from Hamilton’s principle. *International Journal of Engineering Science*, 37:1495–1520, 1999. 198
- [GGP94] W L Grosshandler, R G Gann, and W M Pitts, editors. *Evaluation of Alternative In-Flight Fire Suppressants for Full-Scale Testing in Simulated Aircraft Engine Nacelles and Dry Bays*, volume SP. National Institute of Standards and Technology, 1994. 2, 12
- [GHCP00] W L Grosshandler, A Hamins, S R Charagundla, and C Presser. Suppression Effectiveness Screening for Impulsively Discharged Agents. *Halon Options Technical Working Conference*, May 2000. 2
- [GHL96] T B Gatski, M Y Hussaini, and J L Lumley, editors. *Simulation and Modeling of Turbulent Flows*. Oxford University Press, Inc., 1996. 77, 82, 115
- [Gib91] C H Gibson. Fossil two-dimensional turbulence in the ocean. In F Durst et al., editors, *Turbulent Shear Flows 7 - Selected papers from the Seventh International Symposium on Turbulent Shear Flows*, page 63–78. Springer-Verlag Berlin Heidelberg, 1991. 72
- [GM84] R S R Gorla and P E Madden. A variational approach to non-steady non-Newtonian flow in a circular pipe. *Journal of Non-Newtonian Fluid Mechanics*, (16):251–265, 1984. 30
- [GM04] D Greenblatt and E A Moss. Rapid temporal acceleration of a turbulent pipe flow. *Journal of Fluid Mechanics*, 514:65–75, 2004. 252, 274
- [GR07] I S Gradshteyn and I M Ryzhik. *Table of Integrals, Series and Products*. Elsevier - Academic Press, 7th edition edition, 2007. 118, 194
- [Gra85] C C Grant. Computer-aided Halon 1301 Piping Calculations. *Fire Safety Journal*, 9:171–179, 1985. 26
- [Gra12] M Gramlich. Numerical Investigations of the Unsteady Flow in the Stuttgart Swirl Generator with OpenFOAM. Master’s thesis, Chalmers University of Technology - Department of Applied Mechanics, 2012. 258
- [Gre91] P M Gresho. Incompressible Fluid Dynamics: Some fundamental formulation issues. *Annu. Rev. Fluid Mech.*, (23):413–453, 1991. 57, 146, 205
- [Gre92] P M Gresho. Some Interesting Issues in Incompressible Fluid Dynamics, Both in the Continuum and in Numerical Simulation. In J W Hutchinson and T Y Wu, editors, *Advances in Applied Mechanics*, volume 28, page 46–140. Academic Press, Inc., 1992. 57, 205
- [GS08] C T Goudar and J R Sonnad. Comparison of the iterative approximations of the Colebrook-White equation. *Hydrocarbon Processing*, 87(8):79–84, 2008. 49
- [GSA⁺14] S Gorji, M Seddighi, C Ariyaratne, A E Vardy, T O’Donoghue, D Pokrajac, and S He. A comparative study of turbulence models in a transient channel flow. *Computers & Fluids*, 89:111–123, 2014. 253
- [Haa95] D ter Haar. *Elements of Statistical Mechanics*. Butterworth-Heinemann Ltd., 3rd edition, 1995. 74, 97
- [Har83] A Harten. High resolution schemes for hyperbolic conservation laws. *Journal of Computational Physics*, 49:357 – 393, 1983. 248
- [Har84] A Harten. On a class of high resolution total-variation-stable finite-difference schemes. *SIAM J. Numer. Anal.*, 21(1):1 – 23, 1984. 248
- [Her54] J W Herivel. A general variational principle for dissipative systems. *Proc. Royal Irish Acad.*, 56, sect. A:37–44, April 1954. 198

- [HGG⁺94] A Hamins, G Gmurczyk, W L Grosshandler, R G Rehwoldt, I Vazquez, T G Cleary, C Presser, and K Seshadri. *Flame Suppression Effectiveness*, volume NIST-SP 86 of *Evaluation of Alternative In-Flight Fire Suppressants for Full-Scale Testing in Simulated Aircraft Engine Nacelles and Dry Bays*, chapter 4. National Institute of Standards and Technology, 1994. 2, 3
- [Hin75] J O Hinze. *Turbulence*. McGraw-Hill, 2nd edition edition, 1975. 72, 80, 199, 224, 234, 274
- [HJ00] S He and J D Jackson. A study of turbulence under conditions of transient flow in a pipe. *Journal of Fluid Mechanics*, 408:1–38, 2000. 252
- [HL81] A Harten and P D Lax. A random choice finite difference scheme for hyperbolic conservation laws. *SIAM J. Numer. Anal.*, 18(2):289 – 315, 1981. 248
- [HN81] C W Hirt and B D Nichols. Volume of Fluid (VOF) Method for the Dynamics of Free Boundaries. *Journal of Computational Physics*, 39:201–225, 1981. 214
- [Hol05] D D Holm. Taylor’s hypothesis, Hamilton’s principle and the LANS-alpha model for computing turbulence. *Los Alamos Science*, (29):172–180, 2005. 201
- [HP58] J C Hesson and R E Peck. Flow of Two-phase Carbon Dioxide Through Orifices. *AIChE Journal*, 4(2):207–210, June 1958. 24
- [HR70] A K M F Hussain and W C Reynolds. The mechanics of an organized wave in turbulent shear flow. *Journal of Fluid Mechanics*, 41(2):241–258, 1970. 77, 93, 115, 118, 120, 122, 123, 129, 131
- [HS13] S He and M Seddighi. Turbulence in transient channel flow. *Journal of Fluid Mechanics*, 715:60–102, 2013. 274
- [HTSC94] A Hamins, D Trees, K Seshadri, and H K Chelliah. Extinction of Nonpremixed Flames With Halogenated Fire Suppressants. *Combustion and Flame*, 99(2):221–230, 1994. 2, 3
- [Hus86] A K M F Hussain. Coherent structures and turbulence. *Journal of Fluid Mechanics*, 173:303–356, 1986. 72
- [Iss86] R I Issa. Solutions of the Implicitly Discretised Fluid Flow Equations by Operator-Splitting. *Journal of Computational Physics*, (62):40–65, 1986. 249
- [Jas96] H Jasak. *Error analysis and estimation for the finite volume method with applications to fluid flows*. PhD thesis, Department of Mechanical Engineering, June 1996. 208
- [JC12] S Y Jung and Y M Chung. Large-eddy simulation of accelerated turbulent flow in a circular pipe. *International Journal of Heat and Fluid Flow*, 33:1–8, 2012. xi, 50, 51, 252, 274
- [JFW08] D Joseph, T Funada, and J Wang. *Potential flows of viscous and viscoelastic fluids*. Cambridge University Press, 2008. 199
- [Jim04] J Jimenez. Turbulent flows over Rough Walls. *Annu. Rev. Fluid Mech.*, 36:173–196, 2004. 224, 225, 226, 230, 236, 237, 239, 240, 241
- [Jov13] V Jovic. *Analysis and modelling of non-steady flow in pipe and channel networks*. John Wiley & Sons, Ltd, 2013. 30
- [KA06] T Koppel and L Y Ainola. Identification of transition to turbulence in a highly accelerated start-up pipe flow. *Transactions of the ASME*, 128:680–686, 2006. 31, 50

- [KCB⁺10] V Kitsios, L Cordier, J P Bonnet, A Ooi, and J Soria. Development of a nonlinear eddy-viscosity closure for the triple-decomposition stability analysis of a turbulent channel. *Journal of Fluid Mechanics*, 664:74–107, 2010. 115
- [KE81] M E Kim-E. The possible consequences of rapidly depressurizing a fluid. Msc, Massachusetts Institute of Technology, 1981. 30
- [KLA⁺11] T Koppel, J Laanearu, I Annus, M Raidmaa, et al. Using transient flow equations for modelling of filling and emptying of the large-scale pipeline. In K A Lansey, C Y Choi, A Ostfeld, and I L Pepper, editors, *Proceedings of the 12th Annual Conference on Water Distribution Systems Analysis, held in Tucson, Arizona, September 12-15, 2010.*, page 112–121, 2011. xi, 31, 60, 61
- [KLG94] S K Kim, T J Lestina, H D Giesecke, and R S Sheinson. Development of Computer Models for the Discharge of Halon Alternatives. In *Halon Options Technical Working Conferences (HOTWC)-1994*. National Institute of Standards and Technology, May 1994. 17
- [KLT12] D Kuzmin, R Loehner, and S Turek, editors. *Flux-Corrected Transport. Principles, algorithms and applications*. Springer, 2nd edition, 2012. 249
- [KM86] J Kurokawa and M Morikawa. Accelerated and Decelerated Flows in a Circular Pipe. *Bulletin of JSME*, 29(249):758–765, 1986. 49, 50, 274
- [KMID05] G Kalitzin, G Medic, G Iaccarino, and P Durbin. Near-wall behaviour of RANS turbulence models and implications for wall functions. *Journal of Computational Physics*, (204):265–291, 2005. 223, 233
- [Kor02] B G Korenev. *Bessel functions and their applications*. Taylor & Francis, 2002. 170, 171, 173
- [KOYS01] H Kashiwagi, S Oshikawa, J Yui, and Y Saso. Effect of Fire Size on Suppression Characteristics of Halon Replacement Total-Flooding Systems. In *Halon Options Technical Working Conferences (HOTWC)-2001*. National Institute of Standards and Technology, 2001. 3
- [KSMKK96] A K Kim, J Z Su, J R Mawhinney, and M Kanabus-Kaminska. Full-Scale Fire Testing of HFC-227ea and HCFC Blend A. In *Halon Options Technical Working Conferences (HOTWC)-1996*. National Institute of Standards and Technology, May 1996. 3
- [KY78] C A Kot and C K Youngdahl. Transient Cavitation Effects in Fluid Piping Systems. *Nuclear Engineering and Design*, 45:93–100, 1978. 49
- [L⁺12] J Laanearu et al. Emptying of large-scale pipeline by pressurized air. *Journal of Hydraulic Engineering*, 138(12):1090–1100, 2012. 31
- [LABP11] G A Lima, M N Arima, N N Branco, and M M Pimenta. Proposed wall function models for heat transfer around a cylinder with rough surface in cross flow. Technical Report 2011-38-0023, 2011. 243
- [Lam92] S H Lam. On The RNG Theory of Turbulence. *Phys. Fluids A*, 4:1007–1017, May 1992. 256
- [Lea07] L G Leal. *Advanced Transport Phenomena. Fluid Mechanics and Convective Transport Processes*. Cambridge University Press, 2007. 146
- [Lef88] P J Lefebvre. *Characterization of Accelerating Pipe Flow*. PhD thesis, University of Rhode Island, 1988. 252, 274
- [Leo74] A Leonard. Energy cascade in large-eddy simulations of turbulent fluid flows. *Advances in Geophysics*, A18:237–248, 1974. 141
- [Lin06] G T Linteris. NGP Research on Fire Suppression Chemistry. In *Halon Options Technical Working Conferences (HOTWC)-2006*. National Institute of Standards and Technology, May 2006. 2, 3

- [Lin14] D Lindblad. Implementation and run-time mesh refinement for the k-omega SST DES turbulence model when applied to airfoils. Technical report, January 2014. 258
- [LS74] B E Launder and B I Sharma. Application of the energy-dissipation model of turbulence to the calculation of flow near a spinning disc. *Letters in Heat and Mass Transfer*, 1:131–138, 1974. 235, 236, 254, 275
- [Lum98] J L Lumley. *Stochastic Tools in Turbulence*. Dover Publications Inc., 1998. 74
- [LW07] R Leighton and D Walker. Reynolds stress modeling for rough wall turbulence: An invited paper. In *37th AIAA Fluid Dynamics Conference and Exhibition, 25-28 June 2007, Miami FL*, number AIAA-2007-4615, 2007. 256
- [M⁺10] I Marusic et al. Wall-bounded turbulent flows at high Reynolds numbers: Recent advances and key issues. *Physics of Fluids*, 22(065103):1–24, 2010. 231
- [Mac04] C R MacCluer. *Boundary Value Problems and Fourier Expansions*. Dover Publications Inc., revised edition, 2004. 167, 168
- [Maj02] S Majumdar. Modeling of Near Wall Turbulent Flows. In G Biswas and V Eswaran, editors, *Turbulent Flows - Fundamentals, Experiments and Modeling*. Alpha Science International Ltd., 2002. 226, 234, 235
- [McD07] J M McDonough. *Introductory Lectures on Turbulence. Physics, Mathematics and Modeling*. 2007. xii, 228
- [MD13] S Marquez-Damian. *An Extended Mixture Model for the Simultaneous Treatment of Short and Long Scale Interfaces*. PhD thesis, Facultad de Ingenieria y Ciencias Hidricas, 2013. 249
- [MDK98] B Moghtaderi, B Z Dlugogorski, and E M Kennedy. Detailed Chemical Kinetic Modelling Study on High Temperature Ignition of Methane/Air Mixtures Doped With C3F7H. In *Halon Options Technical Working Conferences (HOTWC)-1998*. National Institute of Standards and Technology, May 1998. 2, 3
- [ME05] F R Menter and Y Egorov. *A Scale-Adaptive Simulation Model using Two-Equation Models*. 43rd AIAA Aerospace Sciences Meeting and Exhibit. American Institute of Aeronautics and Astronautics, jan 2005. 254, 258
- [ME10] F R Menter and Y Egorov. The Scale-Adaptive Simulation Method for Unsteady Turbulent Flow Precisions. Part 1: Theory and Model Description. *Flow Turbulence Combust*, (85):113–138, 2010. 254, 258
- [Mil29] C B Millikan. On the steady motion of viscous, incompressible fluids; with particular reference to a Variation Principle. *Phil. Mag. S.7*, 7(44):641–662, April 1929. 198, 199
- [MKM76] T Maruyama, T Kuribayashi, and T Mizushima. The Structure of the Turbulence in Transient Pipe flows. *Journal of Chemical Engineering of Japan*, 9(6):431–439, 1976. 252
- [MKM78] T Maruyama, Y Kato, and T Mizushima. Transition to turbulence in starting pipe flows. *Journal of Chemical Engineering of Japan*, 11(5):346–353, 1978. 31
- [MKM87] N N Mansour, J Kim, and P Moin. Near-wall k-epsilon turbulence modeling. Technical Report 89461, Ames Research Center, jun 1987. 234, 235
- [MOR06] H Mahgerefteh, A O Oke, and Y Rykov. Efficient numerical solution for highly transient flows. *Chemical Engineering Science*, 61(15):5049–5056, 2006. 30
- [Mor10] P Moradnia. CFD of Air Flow in Hydro Power Generators. Master's thesis, Chalmers University of Technology - Department of Applied Mechanics, 2010. 257

- [Mos89] E A Moss. The identification of two distinct laminar to turbulent transition modes in pipe flows accelerated from rest. *Experiments in Fluids*, 78:271–274, 1989. 31
- [MP94] B Mohammadi and D Pironneau. *Analysis of the k-epsilon turbulence model*. John Wiley & Sons, Ltd, 1994. 256
- [MPW79] J D Meiss, N Pomphrey, and K M Watson. Numerical analysis of weakly nonlinear wave turbulence. *Proc. Natl. Acad. Sci USA*, 76(5):2109–2113, May 1979. 198
- [MS00] J Mathieu and J Scott. *An Introduction to turbulent flow*. Cambridge University Press, 2000. 111
- [MY71] A S Monin and A M Yaglom. *Statistical Fluid Mechanics. Mechanics of Turbulence. Vol.I*. Dover Publications Inc., 1971. 72, 77, 86, 98, 111, 218, 223, 224, 236, 237
- [MY75] A S Monin and A M Yaglom. *Statistical Fluid Mechanics. Mechanics of Turbulence. Vol.II*. Dover Publications Inc., 1975. 73, 74
- [MY10] Y S Muzychka and M M Yovanovich. Unsteady viscous flows and Stokes’s first problem. *International Journal of Thermal Sciences*, 49:820–828, 2010. 30
- [NBHT98] T Noto, V Babushok, A Hamins, and W Tsang. Inhibition Effectiveness of Halogenated Compounds. *Combustion and Flame*, 112(1/2):147–160, 1998. 2
- [NBZR10] A Nouri-Borujerdi and M Ziaei-Rad. Numerical modeling of transient turbulent gas flow in a pipe following a rupture. *Transaction B: Mechanical Engineering*, 17(2):108–120, 2010. 30
- [NC08] H M Nagib and K A Chauhan. Variations of von Kármán coefficient in canonical flows. *Physics of Fluids*, 20(10):1518, 2008. 226, 231
- [Nel94] M Nelkin. Universality and scaling in fully developed turbulence. *Advances in Physics*, 43(2):143–181, 1994. 72
- [NFPO8] NFPA-2001. {NFPA}-Standard on Clean Agent Fire Extinguishing Systems. National Fire Protection Association, 2008. 22
- [NHH80] B D Nichols, C W Hirt, and R S Hotchkiss. SOLA-VOF: A solution algorithm for transient fluid flow with multiple free boundaries. Technical report, 1980. 214
- [Nik50] J Nikuradse. Laws of low in rough pipes. Technical report, 1950. 238, 240
- [NN04] R H Nichols and C C Nelson. Wall function Boundary Conditions Including Heat Transfer and Compressibility. *AIAA Journal*, 42(6):1107–1114, June 2004. 225
- [OMER03] A O Oke, H Mahgerefteh, I Economou, and Y Rykov. A transient outflow model for pipeline puncture. *Chemical Engineering Science*, 58(20):4591–4604, 2003. 30
- [Pai53] S I Pai. On Turbulent flow in a circular pipe. *Journal of The Franklin Institute*, 256(4):337–352, October 1953. 149, 150, 155, 156, 159, 160, 161
- [Pan90] S A Pankratov. Velocity distribution of turbulent pipe flow. *Power Technology and Engineering*, 24:715–718, 1990. 158
- [PBPO0] U Piomelli, E Balaras, and A Pascarelli. Turbulent structures in accelerating boundary layers. *Journal of Turbulence*, 1:1–16, 2000. 274
- [PES67] G K Patterson, W J Ewbank, and V A Sandborn. Radial pressure gradient in turbulent pipe flow. *Physics of Fluids*, 10, 1967. 154

- [PGGT03] C D Pruett, T B Gatski, C E Grosch, and W D Thacker. The temporally filtered Navier-Stokes equations: Properties of the residual stress. *Physics of Fluids*, 15(8), August 2003. 145
- [Piq99] J Piquet. *Turbulent flows. Models and Physics*. Springer-Verlag Berlin Heidelberg, revised 2nd printing edition, 1999. 72
- [PKPB07] G de Prisco, A Keating, U Piomelli, and E Balaras. Large-eddy simulation of accelerating boundary layers. In M Oberlack et al., editors, *Progress in Turbulence II - Proceedings of the iTi Conference in Turbulence 2005*. Springer-Verlag Berlin Heidelberg, 2007. 274
- [PMN08] D Pokrajac, I McEwan, and V Nikora. Spatially averaged turbulent stress and its partitioning. *Experiments in Fluids*, 45:75–83, 2008. 115
- [Pop00] S B Pope. *Turbulent Flows*. Cambridge University Press, 2000. xi, 71, 80, 82, 85, 112, 183, 184, 224, 234
- [PPS06] D Panara, M Porta, and T Schoenfeld. LES and URANS unsteady boundary layer strategies for pulsating and oscillating turbulent channel flows applications. In *ECCOMAS CFD 2006: Proceedings of the European Conference on Computational Fluid Dynamics*. Delft University of Technology, 2006. 245
- [PRO5] Y Pinchover and J Rubinstein. *An introduction to partial differential equations*. Cambridge University Press, 2005. 176, 177, 208
- [Pru00] C D Pruett. Eulerian Time-Domain Filtering for Spatial Large-Eddy Simulation. *AIAA Journal*, 38(9), September 2000. 145
- [Pru08] C D Pruett. Temporal large-eddy simulation: theory and implementation. *Theoretical Computational Fluid Dynamics*, 22:275–304, 2008. 145
- [PYB⁺06] W M Pitts, J C Yang, R A Bryant, L G Blevins, and M L Huber. Characterization and Identification of Super-Effective Thermal Fire Extinguishing Agents. Final Report. NGP Project 4C/1/890. Technical Report NIST Technical Note 1440, National Institute of Standards and Technology, 2006. 2, 3
- [PYBG93] W M Pitts, J C Yang, B Breuel, and G Gmurczyk. Dynamics of the release of alternate Halon replacement agents from pressurized bottles. In *Halon Alternatives Technical Working Conference-1993*. National Institute of Standards and Technology, May 1993. 15
- [PYG⁺94] W M Pitts, J C Yang, G Gmurczyk, L Y Cooper, W L Grosshandler, W G Cleveland, and C Presser. *Fluid Dynamics of Agent Discharge*, volume SP of *Evaluation of Alternative In-Flight Fire Suppressants for Full-Scale Testing in Simulated Aircraft Engine Nacelles and Dry Bays*, chapter 3. National Institute of Standards and Technology, 1994. x, 3, 13, 14, 15, 16
- [RFS05] M L Robin, E W Forssell, and V Sharma. Pressure Dynamics of Clean Agent Discharges. In *Halon Options Technical Working Conferences (HOTWC)-2005*. National Institute of Standards and Technology, May 2005. x, 19, 20, 21
- [RH72] W C Reynolds and A K M F Hussain. The mechanics of an organized wave in turbulent shear flow. Part 3. Theoretical models and comparisons with experiments. *Journal of Fluid Mechanics*, 54(Part 2):263–288, 1972. 115, 116, 118, 120, 122, 123, 126, 129, 130, 131
- [RH12] D C Rennels and H M Hudson. *Pipe Flow. A practical and comprehensive guide*. John Wiley & Sons, Inc., 2012. 237
- [RHC98] W M Rohsenow, J P Hartnett, and Y I Cho, editors. *Handbook of Heat Transfer*. McGraw-Hill, 3rd edition, 1998. 49
- [RKO6] A R Rao and B Kumar. Friction factor for turbulent pipe flow. 2006. 49

- [Ros53] P Rosen. On variational principles for irreversible processes. *Journal of Chemical Physics*, 21(7):1220–1221, July 1953. 198
- [Ros16] W Rosenheinrich. *Tables of some indefinite integrals of Bessel functions*. Erns - Abbe -Hochschule Jena, University of Applied Sciences, Germany, 2016. 188, 190
- [RRC01] M L Robin, T F Rowland, and M D Cisneros. Fire Suppression Testing: Extinguishment of Class A Fires With Clean Agents. In *Halon Options Technical Working Conferences (HOTWC)-2001*. National Institute of Standards and Technology, 2001. 2, 3
- [Rus02] H Rusche. *Computational fluid dynamics of dispersed two-phase flow at high phase fractions*. PhD thesis, Department of Mechanical Engineering, December 2002. 214, 215
- [SAA⁺03] R S Sheinson, S Ayers, R Anleitner, D Morse, D Szwarc, L Levenberry, and A Maranghides. Combining a Water Spray Cooling System With Heptafluoropropane for Total Flooding Fire Suppression. In *Halon Options Technical Working Conferences (HOTWC)-2003*. National Institute of Standards and Technology, May 2003. 3
- [SAAM04] R S Sheinson, S Ayers, R Anleitner, and A Maranghides. Heptafluoropropane With Water Spray Cooling System as a Total Flooding Halon 1301 Replacement: System Implementation Parameters. In *Halon Options Technical Working Conferences (HOTWC)-2004*. National Institute of Standards and Technology, May 2004. 3
- [Sag06] P Sagaut. *Large Eddy Simulation for Incompressible Flows. An Introduction*. Springer-Verlag Berlin Heidelberg, 3rd ed. edition, 2006. 133, 141, 144, 145
- [Sas01] Y Saso. Roles of Inhibitors in Global Gas-Phase Combustion Kinetics. In *Halon Options Technical Working Conferences (HOTWC)-2001*. National Institute of Standards and Technology, 2001. 2, 3
- [SAS06] M. A. Shockling, J. J. Allen, and A J Smits. Roughness effects in turbulent pipe flow. *Journal of Fluid Mechanics*, 564:267–285, 2006. xii, 240, 242
- [SC09] S M Salim and S C Cheah. Wall y^+ Strategy for Dealing with Wall-bounded Turbulent Flows. In *Proceedings of the International Multiconference of Engineers and Computer Scientist_IMECS 2009*, volume II, 2009. 244
- [Sch66] L Schwartz. *Mathematics for the Physical Sciences*. Hermann, 1966. 86, 87
- [Sch79] H Schlichting. *Boundary-Layer Theory*. McGraw-Hill, 7th edition, 1979. 218, 223, 224, 233
- [Sch07] F G Schmitt. About Boussinesq’s turbulent viscosity hypothesis: historical remarks and a direct evaluation of its validity. *C.R. Mecanique*, 335:617–627, 2007. 255
- [Sch08] B S W Schroeder. *Mathematical analysis: a concise introduction*. John Wiley & Sons, Inc., 2008. 39
- [Sch14] M Scholle. Variational formulations for viscous flow. *Proc. Appl. Math. Mech.*, 14:611–612, 2014. 198
- [Sci04] E Sciuuba. Flow exergy as a Lagrangian for the Navier-Stokes equations for incompressible flow. *Int. J. Thermodynamics*, 7(3):115–122, September 2004. 198
- [SCI06] K Suga, T J Craft, and H Iacovides. An analytical wall-function for turbulent flows and heat transfer over rough walls. *International Journal of Heat and Fluid Flow*, 27:852–866, 2006. 243
- [Sen01] J A Senecal. New Technology Delivery System for FM-200 Clean Agent. In *Halon Options Technical Working Conferences (HOTWC)-2001*. National Institute of Standards and Technology, 2001. 2

- [SF07] M P Schultz and K A Flack. The rough-wall turbulent boundary layer from the hydraulically smooth to the fully rough regime. *Journal of Fluid Mechanics*, 580:381–405, 2007. xii, 239, 240, 241
- [SG06] J R Sonnad and C T Goudar. Turbulent flow friction factor calculation using a mathematically exact alternative to the Colebrook-White equation. *J. Hydraulic Engineering*, 132(8):863–867, 2006. 49
- [SGF91] C G Speziale, T B Gatski, and N Fitzmaurice. An analysis of RNG based turbulence models for homogeneous shear flow. Technical Report 187552, April 1991. 256
- [Sha53] A H Shapiro. *The Dynamics and Thermodynamics of Compressible Fluid Flow, vol.1*, volume I. The Ronald Press Company, 1953. 13
- [Sha54] A H Shapiro. *The Dynamics and Thermodynamics of Compressible Fluid Flow, vol.2*, volume II. The Ronald Press Company, 1954. 13, 285
- [Shu95] E B Shuy. Approximate wall shear equation for unsteady laminar pipe flows. *Journal of Hydraulic Research*, 33(4):457–469, 1995. 50
- [Shu96] E B Shuy. Wall shear stress in accelerating and decelerating turbulent pipe flows. *Journal of Hydraulic Research*, 34(2):173–183, 1996. 50
- [SHVO14] M Seddighi, S He, A E Vardy, and P Orlandi. Direct Numerical Simulation of an Accelerating Channel Flow. *Flow Turbulence Combust*, 92:473–502, 2014. 253, 274
- [Ska02] R R Skaggs. Assessment of the Fire Suppression Mechanics for HFC-227ea Combined With NaHCO₃. In *Halon Options Technical Working Conferences (HOTWC)-2002*. National Institute of Standards and Technology, May 2002. 3
- [SL93] N Shamsundar and J H Lienhard. Equations of state and spinodal lines - a review. *Nuclear Engineering and Design*, 141:269–287, 1993. 27
- [SLS⁺94] T H Shih, W W Liou, A Shabbir, Z Yang, and J Zhu. A new k-epsilon eddy viscosity model for high Reynolds number turbulent flows-Model development and validation. Technical Report 106721, 1994. 256
- [SP95] J A Senecal and R C Prescott. FM-200 Suppression Systems: A Conservative Discharge Test Method and In-Room Pressure Variance Upon Discharge. In *Halon Options Technical Working Conferences (HOTWC)-1995*. National Institute of Standards and Technology, May 1995. x, 19
- [Spa00] P R Spalart. Strategies for turbulence modelling and simulations. *International Journal of Heat and Fluid Flow*, 21:252.–263, 2000. 147
- [Spe87] C G Speziale. On the decomposition of turbulent flow fields for the analysis of coherent structures. *Acta Mechanica*, 70:243–250, 1987. 115
- [SPL⁺99] T H Shih, L A Povinelli, N S Liu, M G Potapczuk, and J L Lumley. A Generalized Wall Function. Technical Report ICOMP-99-08, July 1999. 225
- [SSST08] M L Shur, P R Spalart, M K Strelets, and A K Travin. A hybrid RANS-LES approach with delayed-DES and wall-modelled LES capabilities. *International Journal of Heat and Fluid Flow*, 29:1638–1649, 2008. 256
- [Stu03] R B Stull. *An Introduction to Boundary Layer Meteorology*. Kluwer Academic Publishers, 2003. 108
- [Swe84] P K Sweby. High resolution schemes using flux limiters for hyperbolic conservation laws. *SIAM J. Numer. Anal.*, 21(5):995 – 1011, 1984. 248

- [SZL93] T H Shih, J Zhu, and J L Lumley. A Realizable Reynolds Stress Algebraic Equation Model. Technical Report 105993, 1993. 256
- [Szy32] G Szymanski. Quelques solutions exactes des equations d'hydrodynamique du fluide visqueux dans le cas d'un tube cylindrique. *Journal de Mathematiques pures et Appliquees*, 9^o serie(tome 11):67–108, 1932. 29, 160, 161, 163, 176
- [Tan64] R S Tankin. Turbulent flow in a Pipe. *Rheologica Acta*, 3(3):143–147, 1964. 29
- [TCK05] J B Taylor, A L Carrano, and S G Kandlikar. Characterization of the effect of surface roughness and texture on fluid flow-Past, present and future. *Proceedings of ICMM2005*, 3rd Intern, 2005. 49
- [Tel81] D P Telionis. *Unsteady Viscous Flows*. Springer-Verlag Berlin Heidelberg, 1981. 30, 115
- [Tew73] R P Tewarson. *Sparse Matrices*. Academic Press, Inc., 1973. 210
- [TL72] H Tennekes and J L Lumley. *A first course in turbulence*. The MIT Press, 1972. 111, 206
- [TM05] R Temam and A Miranville. *Mathematical modeling in continuum Mechanics*. Cambridge University Press, 2nd edition, 2005. 184
- [Tow76] A A Townsend. *The Structure of Turbulent Shear Flow*. Cambridge University Press, 2nd edition, 1976. 29, 222, 236
- [TPC⁺00] K Tuzla, T Palmer, J C Chen, R K Sundaram, and W S Yeung. Development of computer program for fire suppressant fluid flow-Final technical report. Technical report, Lehigh University, 2000. 19
- [Tru54] C Truesdell. *The kinematics of vorticity*. Indiana University Press, 1954. 199
- [Tuc01] P G Tucker. *Computation of unsteady internal flows*. Springer Science+Business Media B.V., 2001. 97
- [TYF07] C Tropea, A L Yarin, and J F Foss, editors. *Springer Handbook of Experimental Fluid Mechanics*. Springer-Verlag Berlin Heidelberg, 2007. 114
- [Vah86] G De Vahl Davis. *Numerical Methods in Engineering & Science*. Allen & Unwin (Publishers) Ltd., 1986. 57
- [Val98] E Valero Sanchez. *Analisis del proceso de descarga de fluidos sometidos a altas presiones y temperaturas*. PhD thesis, E.T.S. Ingenieros Aeronauticos, Madrid, 1998. x, 30, 60
- [VM07] H K Versteeg and W Malalasekera. *An Introduction to Computational Fluid Dynamics - The Finite Volume Method*. Pearson - Prentice Hall, 2nd edition, 2007. 203, 205, 206, 208, 209, 210, 248
- [VW07] J G Vasconcelos and S J Wright. Comparison between the two-component pressure approach and current transient flow solvers. *Journal of Hydraulic Research*, 45(2):178–187, 2007. xi, 60, 61
- [WC96] T Wysocki and B Christensen. Inert gas fire suppression systems using IG541 (INERGEN). Solving the hydraulic calculation problem. In *Proceedings on Halon Options Technical Working Conference-1996*. National Institute of Standards and Technology, 1996. 19
- [Whi65] G B Whitham. A general approach to linear and non-linear dispersive waves using a Lagrangian. *Journal of Fluid Mechanics*, 22(2):273–283, 1965. 198
- [Whi06] F M White. *Viscous Fluid Flow*. McGraw-Hill, 3rd edition, 2006. 224, 230, 237, 239
- [Wil76] H.V. Williamson. Halon 1301 flow in pipelines. *Fire Technology*, 12(1):18–32, 1976. 24
- [Wil06] D C Wilcox. *Turbulence Modeling for CFD*. DCW Industries, Inc, 3rd edition, 2006. xii, 154, 155, 159, 183, 206, 213, 219, 220, 221, 224, 234, 235, 245, 253, 255, 256, 257

- [WTJF98] H G Weller, G Tabor, H Jasak, and C Fureby. A tensorial approach to computational continuum mechanics using object-oriented techniques. *Computers in Physics*, 12(6), December 1998. 208
- [Wys96] T Wysocki. Single point flow calculations for liquefied compressed gas fire extinguishing agents. In *Proceedings on Halon Options Technical Working Conference-1996*. National Institute of Standards and Technology, May 1996. x, 15, 16, 26
- [YK06] J C Yang and D R Keyser. Fluid Dispensing and Dispersion. In *Halon Options Technical Working Conferences (HOTWC)-2006*. National Institute of Standards and Technology, May 2006. 3
- [YO86] V Yakhot and S A Orszag. Renormalization Group Analysis of Turbulence. I. Basic Theory. *Journal of Scientific Computing*, 1(1):3–51, 1986. 256
- [YOT⁺92] V Yakhot, S A Orszag, S Thangam, T B Gatski, and C G Speziale. Development of turbulence models for shear flows by a double expansion technique. *Phys. Fluids A*, 4(7):1510–1520, July 1992. 256
- [Zie66] W Zielke. *Frequency dependent friction in transient pipe flow*. PhD thesis, Department of Civil Engineering, 1966. 29
- [ZO98] Y Zhang and S A Orszag. Two-equation RNG transport modeling of high Reynolds number pipe flow. *Journal of Scientific Computing*, 13(4):471–483, 1998. 256
- [ZW96] R Zalosh and W Wang. Mathematical modeling of FM-200 discharge and leakage from an enclosure. In *Proceedings on Halon Options Technical Working Conference-1996*. National Institute of Standards and Technology, May 1996. 17

Index

- Absolute roughness, 237
Acceleration number, 274
Acceleration parameter, 274
Acceleration stage, 50, 59, 63–66, 69, 204, 253, 257, 264, 267, 274
Action of a mechanical system, 197
Adiabatic index, 33, 45, 52, 58, 61
Advective/convective form, 205
AHM, iv
Angular frequency, 102, 134
Aspect-ratio, 204, 244
Avogadro's number, 74

Bernoulli's principle, 15, 22, 54
Bessel equation, 170
Bessel function of the first kind, 161, 170, 173
Bessel function of the second kind, 170
Bessel functions, 171
Blasius correlation, 218, 233, 245, 262, 267, 278
Blended hybrid RANS-LES, 147
Boussinesq's hypothesis, 85, 92, 140, 141, 148, 155, 235, 253–256
Buffer layer, 225, 244, 245
Bulk acceleration, 264, 267, 274, 278, 280
Bulk velocity, 38, 40, 45, 49, 51, 62–68, 70, 183, 192, 214, 218, 237, 245, 253, 264, 267, 274, 279, 280

Chaos, 76
Clean agent, 1–5, 8, 15, 17, 28, 31–33, 53, 57, 59, 62, 237, 242
Closure problem, 81, 82, 139–141, 162, 182, 254, 284
Coherent turbulent structure, 72
Colebrook-White correlation, 34, 49, 51, 53, 57, 67, 70, 203, 247, 285
Commutation condition, 87
Commutation error, 144
Compression velocity, 215
Conservation form, 205
Conservation form of equations, 139
Continuity equation, 35, 90, 92, 96
Continuity error, 248, 249
Convection velocity, 114
Convective form of equations, 84, 139
Convolution, 101, 102, 104–106, 133, 138, 139

Correlation time, 112, 114
Courant number, 203, 248, 249, 251, 252, 260, 279
Courant-Friedrichs-Lewy condition, 203
Crank-Nicolson differencing scheme, 248
Cross-section average, 3, 38, 41
Cumulative average, 100, 103, 105, 142
Cut-off frequency, 134
Cut-off wavenumber, 134

Damping function, 234–236, 275, 276
Darcy-Weisbach friction factor, 29, 34, 40, 48, 49, 57, 58, 67, 68, 71, 203, 237–240, 247, 280
DC component, 116, 117, 122, 123, 126, 129–131
Deceleration stage, 60, 63, 64, 66, 67, 69, 204, 248, 253, 257, 264, 267, 274, 277–279
Dirac's delta distribution, 88, 107, 137
Dirichlet boundary condition, 147, 208
Discretisation scheme, 209, 210
Displacement thickness, 230
Distribution, 86
DNS, 141, 256
Dry zone, 34–36, 264
Dynamic pressure, 40
Dynamic relative roughness, 241

Eddy turnover time, 71
Eddy viscosity, 85, 236, 254, 267
Effective friction factor, 53, 67
Effective sand roughness, 236
Ensemble average, v , 31, 78, 81–85, 88, 90, 92, 96–98, 111–115, 142, 148, 155, 162, 181, 203, 212, 218, 234, 254, 256, 262, 284
Equivalent sand roughness, 236, 238, 242
Ergodic hypothesis, 97–99, 114, 155
Ergodic theorem, 98, 99
Euler-Lagrange equations, 197–199
Eulerian representation, 42
Exponential integral function, 194

Fanning friction factor, 40, 49, 218, 233
Fast stage, 36, 40, 45, 47, 55, 56, 58, 59, 62, 69, 70
Favre average, 82
Filter decomposition, 137, 139, 140, 142

- Filter width, 132–134, 137, 141, 143, 145, 146, 148, 213, 258
 Finite time average, 113
 FK-5-1-12, 4–6, 8–12, 20–24, 31, 33, 34, 52–54, 57, 59, 62, 64,
 204, 207, 257, 264
 Flash point, 21
 Floor function, 117
 Flux-corrected transport, 249
 FM-200, 31
 FNSE, 138, 211
 Fourier series, 116, 126
 Fourier space, 134–136, 139, 140, 284
 Fourier transform, 101, 102, 132, 134–136, 141
 Fourier-Bessel series, 173–178, 181–183, 188
 FPE, iv, 29, 31, 35, 237
 Friction force, 40, 69
 Friction length scale, 223, 237, 241
 Friction modulator, 52, 53, 59, 65, 67–69
 Friction Reynolds number, 152, 223
 Friction velocity, 152, 162, 218, 223, 226, 232, 233, 267, 270,
 271
 Fubini's theorem, 89, 91, 93, 138, 143
 Fully rough flow, 238

 Gauss theorem, 205
 Gaussian filter, 136, 137
 General boxcar function, 100, 104
 General space-time average, 86–89, 91, 93, 97
 General transport equation, 204, 205
 Generalised function, 86–88
 Geometric factor, 11, 55, 58
 Geometric length scale, 114, 221
 GWP, 2, 4, 5

 Hagen-Poiseuille flow, 149, 150, 152, 155–158, 160, 164, 175,
 176, 182, 199
 Haloalkanes, 1, 2, 5, 19, 28
 Hamilton's principle, 81, 197
 Heaviside step function, 101, 186
 HFC-227ea, 2, 5, 7, 8, 10–12, 14–17, 19–21, 24–28, 31, 34
 Hilbert space, 132, 167, 169, 170, 173, 174
 HOTWC, 1
 Hybrid RANS-LES, 147

 IDDES, 256
 Ideal low pass filter, 135
 Idempotent condition, 78, 83, 87, 89, 92, 94, 104–106, 108,
 114, 132, 137
 Identity operator, 169
 IG541, 19, 20
 Inertial layer, 225, 226
 Inertial length scale, 71
 Inertial time scales, 71
 IniTrans component of mean velocity, 180, 181, 189, 193,
 196
 Inner law, 224–226
 Inner length scale, 223
 Inner product, 167–170, 173
 Inner region, 224, 226, 229, 239, 241
 Inner variables, 223, 224
 Integral length scale, 71, 112, 114, 220, 224
 Integral of motion, 72
 Integral time scale, 71, 112, 114
 Interface compression, 215
 interFOAM, 214–216, 265, 290

 k - ϵ Launder-Sharma, 277, 279–281
 k - ϵ Launder-Sharma, 232, 235, 236, 244, 248, 253, 254,
 257, 275–280, 291
 k - ϵ model, 220, 228, 232, 234–236, 254
 k - ϵ realisable, 256
 k - ω SST, 257
 k - ω SSTSAS, 159, 243, 244, 248, 254, 257, 258, 260, 279,
 280, 284, 285, 291
 Karman constant, 226
 Kernel function, 132
 Kolmogorov length scale, 71, 72, 113, 207, 246
 Kolmogorov microscales, 206, 207, 252
 Kolmogorov time scale, 71, 251, 253, 256

 Lagrangian density, 198–201
 Lagrangian function, 197
 Lagrangian-averaged Navier-Stokes- α equations, 201
 Lamb vector, 199, 201
 Laminar sublayer, 71, 73, 225, 229, 232, 237, 238, 241, 267,
 268, 270, 271
 Laminar-turbulent decomposition, 149, 155
 Law of the wake, 230, 231, 238, 239
 Law of the wall, v, 186, 222, 231, 244, 245, 267, 269, 280,
 284
 Leibniz's rule, 39, 103, 105, 143–145
 Linear sublayer, 225
 Liquid fraction, 244
 Liquid fraction field, 214, 249
 Local Reynolds number, 223
 Locally isotropic turbulence, 73
 Log-law, 158, 222, 226, 230, 231, 267–269, 274, 280, 285,
 286
 Log-law layer, 225, 239, 245, 268, 286
 Logarithmic inertial layer, 225, 226, 230–232, 239, 244,
 245, 251
 Logarithmic overlap layer, 231
 Lyapunov exponent, 72

- Mean periodic field, 95
- Mean value, 76
- Moody diagram, 34, 49, 50, 203, 237, 240
- Moving average, 99–103, 105, 106, 108, 110, 114, 145
- MULES, 249

- Navier-Stokes equations, 42, 84, 90, 92, 140, 145, 210, 211
- Navier-Stokes- α model, 201
- Neumann boundary condition, 147, 209
- Newton's Law of viscosity, 44
- NGP, 1
- NIST, 2
- No-penetration condition, 147, 148
- No-slip condition, 43, 94, 145–148, 153, 158, 164, 222, 224–227, 234–236, 244
- Noether theorem, 197
- Noise, 73
- Normalisation condition, 83
- Normalised boxcar function, 100, 101, 104, 106, 143
- Novac-1230, 4, 31
- NTP, iv, v, 45

- OpenFOAM, v, 85, 208–214, 216, 226–229, 236, 242–245, 247–249, 251–253, 256–258, 260, 265, 267–269, 275–277, 284, 290, 291
- Oscillating component, 124, 131
- Outer law, 229
- Outer layer, 230, 231, 238
- Outer length scale, 223
- Outer region, 226, 229–231, 240, 242
- Outer variables, 152, 223, 229
- Overlap layer, 224, 226

- Pai analytical solution, 155
- Pai flow, 155, 158, 164, 182, 190, 192, 193
- Parameter's standard values, 59, 62
- ParaView, 213
- PessGrad component of mean velocity, 192, 193, 195
- Phase average, 88, 93–97, 115, 118, 119, 122, 123
- Physical variables, 223
- PIMPLE algorithm, 249
- PISO, 249
- PLA, 197
- Polytropic index, 33, 45, 52, 58, 61
- Potentially periodic field, 94, 95, 117, 119, 131
- Potentially periodic flow, 94, 97
- PressGrad component of mean velocity, 180, 181, 187
- Pressure force, 40, 69
- Pressure, dynamic, 40
- Pressure-enthalpy diagram, 21, 24
- Principle of Least Action, 81, 197

- Probability density function, 74

- Quasi-periodic field, 131
- Quasi-periodic flow, 131

- Random field, 73, 76
- Random-spike function, 121–123
- RANS equations, 77, 83, 88, 95, 117, 124, 130, 156, 220
- RANS oscillating equation, 131
- Realisation, 82
- Rect function, 100–104, 135
- Rectangular function, 100
- Regular Sturm-Liouville problem, 169
- Residual, 210, 249
- Residual maximum error, 211
- Residual RMS error, 211
- Residual stress tensor, 141, 142
- Residuals vector norm, 211
- Resolved component, 137, 141
- Reynolds conditions, 77, 78, 81–83, 87–89, 91, 94, 103
- Reynolds decomposition, 77, 78, 80, 81, 85, 90, 92, 96, 110, 111, 137, 141, 142, 148, 218, 256, 262
- Reynolds operator, 78, 81, 83, 84, 87, 88, 90, 92, 95, 105, 132, 137, 140, 142
- Reynolds shear stress, 225, 226
- Reynolds stress, 81, 82, 85, 131, 140, 141, 155, 156
- Reynolds stress tensor, 81, 90, 92, 96, 97, 141, 148, 150, 154, 156–161, 165, 180–184, 186, 189, 193, 196, 197, 202, 206, 217, 221, 254, 256, 283–286
- Reynolds' transport theorem, 39
- Robin boundary condition, 209
- Roughness constant, 243
- Roughness function, 236, 239, 240, 242
- Roughness length, 236, 239
- Roughness Reynolds number, 237, 243
- Roughness sublayer, 240, 241
- Roughness, absolute, 237, 241
- RStress component of mean velocity, 180–182, 187–189, 195
- Running average, 99

- Separation of variables method, 165
- SFCD, 260
- Singular Sturm-Liouville problem, 169
- Skin friction, 224, 231, 239
- Skin friction coefficient, 34, 40, 49, 50, 218, 233, 238, 267
- Slow stage, 36, 42, 45, 48, 56, 58, 59, 62, 69, 70
- Smooth wall, 226
- SNSE, 73
- Space average, 88
- Sparse matrix, 210

- Spatial average, 90–92, 147
- Spatial wavenumber, 134
- Spectral gap problem, 108
- Spectral space, 134
- Spinodal lines, 27
- SSTM, 232
- Standard pipe, 59, 60, 62–68, 70, 237
- Statistical averages, 82
- Statistical representation of turbulence, 73
- Steady state, 3, 31, 36
- Stochastic Navier-Stokes equations, 73
- Sturm-Liouville eigenvalue problem, 167–169, 173–175
- Sturm-Liouville operator, 167, 168, 170
- Subgrid-scale viscosity, 141, 207, 258
- Surface average, 37
- Szymanski analytical solution, 160
- Szymanski flow, 160, 176, 181, 182, 189

- Taylor length scale, 113
- Taylor’s frozen turbulence hypothesis, 114
- Time average, 88–90, 115, 117–120, 122, 212
- Tolerance, 211
- Transient regime, 3, 31, 36
- Transition region, 225
- Transition stage, 59, 60, 63, 64, 66, 69, 257, 262, 278
- Triple decomposition, 115, 117, 123, 131
- Turbulence intensity, 114, 218, 219
- Turbulence length scale, 220, 258
- Turbulence quantities, 78, 207, 210, 212, 217, 218, 220, 222, 223, 225, 226, 232, 244, 260
- Turbulent boundary layer, 71, 204, 246, 258
- TVD, 248, 260

- Unit operator, 174
- Unresolved component, 137
- Upwind differencing scheme, 248, 260
- URANS, 97, 108, 110, 111

- Valve length, 67
- van Leer’s flux limiter, 248, 260
- Vapour pressure, 6, 7, 9, 10, 21
- Vapour quality, 24, 26
- Velocity-defect law, 229, 231
- Viscosity, eddy, 220, 221
- Viscosity, molecular, 220
- Viscous dissipation, 199
- Viscous dissipation function, 199
- Viscous layer, 225
- Viscous shear stress, 224, 225
- Viscous sublayer, 234
- VoF, 214

- Vorticity, 80
- Wake function, 230, 231, 239
- Wake parameter, 230
- Wall length scale, 223
- Wall similarity, 241
- Wall similarity hypothesis, 240, 241
- Wall-friction, 59, 60, 207, 224, 247, 252, 253, 256, 257, 276
- Wall-function, 158, 159, 204, 222–227, 229, 231–234, 236, 242–246, 251, 258, 270, 271, 276, 284
- Wall-shear stress, 31, 34, 40, 44, 45, 49–51, 158, 204, 207, 218, 224, 231–233, 238, 253, 267
- Wall-units, 223, 232, 267, 286
- Weighting function, 132
- Wet zone, 33, 35, 36, 40, 69, 264

- Zonal hybrid RANS-LES, 147